Lava Emplacement Dynamics

Stewart Anthony Stansfield

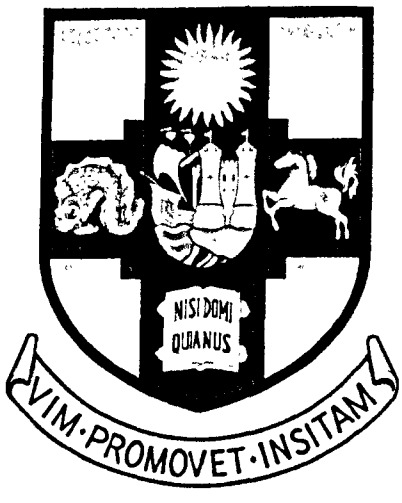

A dissertation submitted to the University of Bristol in accordance with the requirements of the degree of PhD in the Faculty of Science, Department of Earth Sciences

Abstract

Recent advances in the study of lava emplacement dynamics have focused on the numerical solutions of increasingly complex fluids, frequently with an onus on visco-plasticity. The effects of temperature-dependent viscosity in the extrusion of lava have been under-investigated, particularly with reference to experimental analogues.

Golden syrup displays a strongly temperature-dependent viscosity, and in a series of experiments was extruded from a point source onto a slope in a cooled environment. The long flows underestimated the isothermal numerical predictions of Lister (1992) in spatial extent, and can be modelled to expand according to basic isothermal theory, but with a time-dependent bulk viscosity that varies with time to the power of β, which takes the values 0.25 to 0.79 and increases with increasing viscosity ratio and decreasing Peclet number. Cooled flows developed considerably greater height profiles than in isothermal experiments, leading to steep flow fronts and bulked-up flow plateaus.

The flows developed clear central channels of hot syrup, bordered by margins of cooled, rippled and/or torn skin, with small-scale fold wavelengths (L_1) of 1 mm. Channel widths are found to be linear functions of flow rate, and at given flow rates and ambient temperatures, relative widths are a function of the cotangent of the angle of slope. Larger second-generation folds (L_2) developed downstream, and the ratio Λ (L_2/L_1) is of the range 10.5 to 29.5. Flow margins were perturbed and developed overflow crease structures.

Fieldwork in Cameroon investigated the character and morphologies of the 1999 lava flows, and their relation to local and source dynamics. Structures are analysed qualitatively and quantitatively; more detailed arguments are developed on the processes of levee formation, and systematic links between flow dynamics and levee-channel interface geometry are presented in light of Cameroonian examples. Modern field analyses are supported by a historical, archive-sourced investigation of past activity that collates and interprets prior observations for the modern volcanologist.

Acknowledgements

The sciences, each straining in their own direction have hitherto harmed us little; but some day the piecing together of dissociated knowledge will open up such terrifying vistas of reality, and our frightful position therein, that we shall either go mad from the revelation or flee from the deadly light into the peace and safety of a new dark age.

Howard Phillips Lovecraft

First and foremost, I'd like to thank my supervisor, Steve Sparks, for his friendly support and encouragement (and forbearance) over the period of my research; especially as without his tireless efforts, this thesis would be twice as verbose and long-winded as it already is! Secondly, the aid and advice of Anne-Marie Lejeune was crucial during the experimental phase of this project, and her efforts are greatly appreciated. As are those of Fred Wheeler, Mike Drury and Phil Boyd in the workshop, whose patience with my queries and engineering talents produced a super bit of kit. Simon Powell kindly prepared the prints of field photographs for use in this thesis.

The field analyses in Cameroon could not have been completed without the kind hospitality, advice and expertise of Sam Ayonghe, Edwin, Steve Njome, George and, especially, Emmanuel Suh and his family. I'd also like to thank Gerald Ernst for his friendly help and discussions in the field and after, alongside Steve and myself. On a no less important note, I wish to express my appreciation of the efforts of Shelly Ardener, and Prince Henry Mbain, whose friendly assistance and expertise in the National Archives of Cameroon in Buea allowed me to collate hitherto unused evidence. When back in Bristol Kim Berlo kindly provided invaluable aid in the translation of German documents.

John Lister provided critically useful mathematical support to a benighted geologist such as myself, and aided me greatly in the discussion of his model. In Bristol and via e-mail, brief discussions with Tim Barrass, Rob Craster, Andrew Hogg and Jeremy Philips also proved highly useful. Sadly my research moved away from the domes that took his fancy, but my early chats with Rob Watts on actual lava processes were enlightening and enjoyable. A special mention should be made of Joseph Walder, whose advice and experimental designs considerably further my research, and whose loan of two video cameras was vitally important. I even managed to get one of them back in one piece (eventually)!

Thanks are also directed at the organisers of GEFD 2000, Don Dingwell's magmas, fluids and melts course, IAVCEI 2000 in Bali and the fieldtrip to Santorini. Throughout the years my mates and office companions proved a constant source of friendly diversion, especially Jon Blower, Ed Llewellin and David Mallard, who gave advice on scientific matters too. Though a special mention should be made in honour of a large pair of Bush headphones, which preserved my sanity—and freedom from detainment at Her Majesty's pleasure—in critical stages. Sadly they finally gave up the ghost a few weeks back, and I honour their memory.

Labwork was made all the more bearable by Toto IV, and if future generations can never remove that veneer of sticky syrup from the lab floor, I heartily apologise. Additional nods of thanks go to (in no apparent order): Patrick O'Brian; Crom; Maiden; the Metallers; the Southmead Hospital infectious diseases ward and Tim, Col and Caroline for their assistance; Club 977; and my map of the British Empire, which reminded me of the Briton's greatness, and constantly reinforced the axiom that no thesis-born foes could confound any clean-limbed son of Albion in his endeavours.

Finally, and most importantly, I'd like to thank my family: my Dad and my Gran, for their loving care and support throughout my life, and in these difficult times. This thesis is dedicated to the memory of my mother, without whose constant love and wise counsels none of this would have been possible.

For Mum.

AUTHOR'S DECLARATION

I declare that the work in this dissertation was carried out in accordance with the Regulations of the University of Bristol. The work is original except where indicated by special reference in the text and no part of the dissertation has been submitted for any other degree. Any views expressed in this dissertation are those of the author and in no way represent those of the University of Bristol. The dissertation has not been presented to any other University for examination either in the United Kingdom or overseas.

SIGNED:..... DATE:.....

IN MEMORIAM

Barbara Ann Stansfield

1949-2000

Contents

List of Figures

List of Tables

List of Plates

Chapter 1: Lava emplacement dynamics—an introduction

1.1 Motivation

Lava, the expression of molten or partially-molten magma extruded onto the Earth's surface, forms an integral element of our planet. Flows, domes and other constructs of lava can be deposited in a subaerial or submarine environment, and form volumetrically important building blocks in the lithosphere. Eruptions of lava, driven by the natural buoyancy of the magma, and exacerbated by processes such as thermal and chemical transport and pressures arising from the exsolution of dissolved volatiles in the melt, likewise illustrate the very forces that give them existence.

Thus the investigation of the surface habits, chemistry and emplacement patterns of lava flows yield far more than a simple explanation of their styles of motion. Such data can illuminate a variety of system processes, from the geochemistry and thermal development of the mantle to the geochronology and tectonic development of the Earth itself. Lavas display a suite of physical and chemical features that are of profound use in the study of our own and other planets' development.

Yet beyond the purely geological factors, lava flows and other volcanic phenomena dictate an influence on the human environment that has profound effects across the globe. Though sudden episodes of explosive volcanism pose the greatest immediate risk to human life, flows of lava still possess heat, mass and mobility in considerable amounts, and can cause the widespread damage and destruction of land, property and important social infrastructure. From these primary depredations arise the greatest threats to human society: death, disease and injury from exposure, poor sanitation and health provision, and a lack of food and water.

Studies of the emplacement dynamics of lava allow volcanologists to understand and predict the kinematics of erupted flows. Estimates of lava velocity, direction and extent aid in the mitigation of hazards to property and populace alike. The extent of lava propagation is also dependent on the small and large-scale morphologies of units, which can focus or halt lava flow. Analyses of these in conjunction with the local topography permit the assessment of increasingly complex models and predictions of flow development for at risk volcanic theatres.

The study of lava flow emplacement therefore allows geologists to gain a better comprehension of the geological environment, and also an understanding of the ways in which we can adapt our human environment to mitigate the risks posed by its interaction with the geological environment. This thesis seeks to build on the established literature, and via experimental, field and historical analyses, further our understanding of the character, dynamics and risks of lava emplacement.

1.2 Modelling lava

Lavas extruded across the planet display a great variety in chemical and physical properties. Furthermore, the initial character of local lava, defined by its individual and unique pre-eruption history, can vary considerably through time and space. Changes in the chemistry, crystallinity and thermal properties of the source magma throughout an eruption are compounded by the similar changes experienced by lava on the Earth's surface, as a function of cooling.

In any analysis of lava emplacement dynamics, the key property of lava one must consider is its *rheology*. Lava rheology depends on a suite of factors: the level of polymerisation within the melt (dependent on the lava's chemistry—including dissolved volatiles—and temperature); the proportion, size and habit of crystals suspended within the melt phase; and the degree and character of vesiculation within the fluid.

Changes in melt polymerisation and crystallinity are driven by effective cooling—in its nominal form, as a function of a drop in lava temperature on exposure to a cooler substrate or atmosphere; or in the form of *undercooling*, wherein the exsolution of volatiles reduces fluid pressure and alter the position of the liquidus in the mineralogical systems (e.g. Sparks and Pinketon 1978). The choice of rheological phenotype used in formulating any model defines its applicability to natural systems. As lava rheology is usually complex in form, and varies in space and time, many models choose simplifying rheological laws to model real lavas, and even then applicability can be limited to certain regimes.

Silicate melts are well approximated by a simple Newtonian rheology, with a purely linear relationship between the application of stress to a fluid and the resultant rate of strain experienced (McBirney and Murase 1984, Webb and Dingwell 1990, Pinkerton and Stevenson 1992). With cooling, melt polymerisation increases, leading to an increase in viscosity (Shaw 1972, Webb and Dingwell 1990). As cooling induces other changes, including crystallisation, lava rheology is frequently approximated by a simple Bingham flow law, and possessing of a yield stress; when shearing stresses overcome this value the lava deforms linearly (see for example Shaw et al. 1968, Shaw 1969; Murase and McBirney 1973, McBirney and Murase 1984)

$$\sigma = \tau + \eta \dot{\varepsilon} \tag{1.1}$$

where σ is the shearing stress, τ the yield stress, η the plastic viscosity, and $\dot{\varepsilon}$ the strain rate.

The crystallinity of the lava influences both elements of lava rheology—yield value and actual viscosity. With cooling, the volume fraction and habit of crystals interact with the melt to define an apparent suspension viscosity. The specifics of such interactions will necessarily vary among lavas erupted with a range of source and emplacement parameters, but research has commonly adopted the concept that the viscosity of a Basaltic mixture can be modelled by an Einstein-Roscoe relationship (Roscoe 1952, 1953; Marsh 1981; Dragoni, 1989; Pinkerton and Stevenson 1992)

$$\eta = \eta_0 \left(1 - \frac{\varphi}{\varphi_{max}}\right)^{-2.5} e^{\gamma(T_0 - T)} \tag{1.2}$$

where η is the viscosity at a given temperature T, η_0 a reference viscosity for an homogenous melt (e.g. at vent eruption temperature, T_0), φ is the crystal volume fraction, φ_{max} the maximum crystal volume fraction that will allow flow (as shall be explained below), and γ is a constant. Formulations of this type were derived to attempt to describe the hydrodynamics of small rigid spheres, with particular reference to a serial size distribution of particles (Roscoe 1952, 1953).

Roscoe (1952) further noted that the presence of solid particles in a liquid phase could result in a fixed or interactive framework, whose interactions would supply an impediment to flow in the suspension – i.e. an apparent yield strength that must be overcome before visible motion ensues (Kerr and Lister 1991). The manner of such an impediment was theorised to be dependent upon the packing of particles, their size distributions, and their habits: hexagonally packed, smooth spheres of equal size might allow a *theoretical* φ_{max} of 0.74; smooth spheres with a serial size distribution would provide φ_{max} of 1; while disordered, loose or close packed suspensions of variably sized or shaped particles would provide ever diminished values of φ_{max} (Roscoe 1952). Furthermore the value of the exponent of the crystal fraction term—in (eq. 1.2) –2.5—can be varied, to take into account forces other than the hydrodynamic in the modelling of a given suspension (see, for example, Lejeune and Richet 1995).

The issue of an apparent yield strength must always be treated with caution, as its definition varies, and its 'presence' very much dependent on the scales of observation (Barnes 1999). In experimental lava dynamics, certain studies have assumed plastic rheologies (e.g. Fink and Griffiths 1990, 1992), when the analogue itself describes a more complex viscoplastic rheology (Balmforth et al. 1999). Nevertheless, the use of apparent yield values renders a great many problems more readily tractable, and renders accessible solutions without supplying undue over-simplification; models using yield values are highly useful, so long as reference is given to the data and circumstances that encourage its use.

Reference to the Einstein-Roscoe equation and the study of field data have led workers to estimate that the apparent viscosity of a silicate suspension becomes sufficiently extreme to be treated as a yield value for crystal volume fractions of 0.55 to 0.6 (Marsh 1981), values that are corroborated by the recent research of Lejeune and Richet (1995). Cashman et al. (1999b) suggest a slightly lower volume fraction for the regime transfer in Hawaiian basalts (0.45-0.5), and Lejeune and Richet (1995) themselves highlight the development of strongly non-Newtonian behaviour at crystal volume fractions ~0.4.

In basalts, field measurements of yield strength show an increase with cooling; at crystal volume fractions of 0.7, yield values of 10^2 to 10^3 Pa are common (Pinkerton and Sparks 1978, Pinkerton and Stevenson 1992). In more silicic eruptions, it is not uncommon for exceptionally crystalline flows to be extruded, as a function of extended cooling and degassing in the vent, producing lava that is effectively solid, and deforms in a radically-different manner (Sparks et al. 2000). In basalts such extreme conditions are rarely encountered, and crystal volume fractions at the vent are typically less than 0.05 at the source.

The influence of temperature and crystallinity on the viscosity and yield strength of a lava are the most commonly cited factors of lava flow models. Beyond these, a variety of other processes and more complex rheological changes are evidenced in the field. All lavas are affected by the process of near-surface solidification, which brings lava into the regime of brittle behaviour and solid mechanics. A function of significant crystallisation, or rapid vitrification as the lava is erupted into a cooler environment, considerable solidification yields a crust that cannot be modelled by simple fluid mechanics; instead references to solid and elastic deformation (e.g. Dance et al. 2001), and a more applicable Mohr-Coulomb, fragmentary rheology would prove more accurate.

Furthermore, crystal and bubble populations can provide rheologic effects that are further dependent on time and strain rate. A useful overview of some of the prior research into these factors is contained in Chester et al. (1985), but more recent studies are considerably furthering concepts of lava rheology, with workers such as Smith (1997) indicating the importance of dilatancy in highly crystalline flows. More complex analyses of viscosity, with reference to melt relaxation (e.g. Webb and Dingwell 1990) and the influence of bubbles (Manga and Stone 1994, Manga et al. 1998, Llewellin et al. 2002), also further our models, investigating the visco-elastic properties of a melt. An increasing array of constitutive rheological models now exist from which volcanologists can consider the study of actual emplacement dynamics.

1.3 The development of dynamical models of lava emplacement

The first models of lava emplacement focused on situations and systems that were tractable, given the volcanological knowledge, theory and analytical techniques of the time. As the morphologies and rheology of lava flows are typically complex and locally-variable, efforts focused on systems that gave the opportunity to simplify one, or both, of these two factors. Furthermore, volcanologists recognised that two natural extreme cases suggested themselves for study: (i) lava domes, extruded onto a relatively horizontal surface, and typically limited in horizontal propagations; and (ii) longer flows extruded on a slope, developing self-propagating channel structures, and coming to a rest an order of magnitude or more beyond their domed counterparts.

1.3.1 Flows extruded onto a horizontal base

Lava domes' frequently axisymmetric profile provides a simplified theoretical system, and thus renders analysis easier; coupled with low Reynolds number (frequently approaching ~ 10^{-9}, or lower) and use of thin-layer theory (see, for example, Batchelor 1967), domes provided a natural focus of study. Huppert et al. (1982) used the theoretical and numerical analyses of an isothermal viscous drop, spreading on a flat plane, to investigate a basaltic andesite dome, extruded on the Soufrière of St Vincent in 1979. The theory (Huppert 1982, Didden and Maxworthy 1982) assumed a fluid of a simple Newtonian rheology, spreading in a dynamic equilibrium between viscous and buoyancy forces; thus the fluid drop would expand indefinitely.

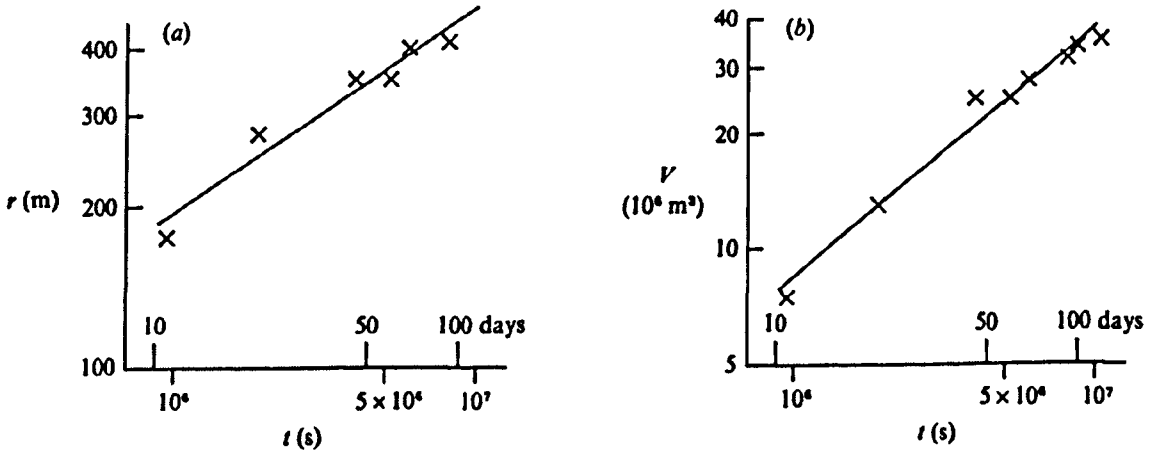

Figure 1.1 Huppert's (1986; p. 572) representation of the data for radial (r) and volumetric (V) growth with time (t) of the Soufrière of St Vincent dome, discussed in Huppert et al. (1982). The lines of best fit—which suggest $r \sim 90t^{0.39}$ and $V \sim 933t^{0.66}$—are argued to give a general approximation to Huppert's theory for an isoviscous fluid (1982).

Huppert et al. (1982) found that the dome's behaviour mimicked that of the model in some elements, but that the formulation required a viscosity much higher than that predicted by petrological analysis. This Huppert et al. attributed to the effects of cooling, and the development of non-Newtonian properties, not least of all a strongly cooled skin that dominated the bulk dynamics; subsequently Jaupart (1991) suggested that vesicular lava compressibility could account for a part of the viscosity difference. Although the radial fit was moderately accurate, the theory failed to adequately model the development of dome height.

In the light of the veracity of this model, the investigations of Blake (1990) focused on a different rheological system: that of a spreading plastic fluid accommodating to a static balance between buoyancy forces and an internal yield strength. Blake's model, building on the work of Nye (1952), found good agreement with experimental flows of kaolin-water slurries. Furthermore his scaling analyses produced a model that provided a better fit to the St. Vincent data than that of Huppert et al. (1982). From these bases, Blake also derived simple time scalings for when the changing ratios of viscous to plastic retardational forces would indicate one force dominant.

A further development was driven by the considerations of surface solidification. Iverson (1990) developed a theoretical model wherein an expanding, pressurised dome was overlain by a solid crust, the interaction between the two defining dome development. On a different tack, Fink and Griffiths (1990, 1992) investigated the development of a solid crust experimentally. Following on from the analogue suggested by Hallworth et al. (1987), they extruded a relatively inviscid polyethylene glycol (PEG) wax into cold water, and found that a range of highly interesting morphological regimes ensued. These were well quantified by reference to a single, non-dimensional parameter, Ψ: a ratio of the timescale for cooling of the surface from source to solidification temperatures, to the timescale for the advection of fluid over a scaled distance.

Fink and Griffiths (1990, 1992) noted a transition through five regimes. At the lowest values of Ψ, denoting rapid cooling or small flux, the PEG developed a bulbous, pillow-like habit; with increasing Ψ most of the flow was mantled by rigid, solid plates, interspersed with interstitial rifts; at higher values again, the solid crust was more widely apparent, but thinner, allowing the generation of folds, ridges and a ropy surface; as Ψ increased further, the crust was marginalized, forming levees; while at the highest values of Ψ no solid crust formed within the lifetime of the experiments. These morphologies proved useful analogies to real basaltic flows.

Rather than dealing with a plastic or solidifying analogue, Stasiuk et al. (1993) worked from the experimental base of Huppert (1982), using golden syrup as an analogue. Golden syrup displays a Newtonian rheology, but possesses a strongly temperature-dependent viscosity. Stasiuk et al. extruded warm golden syrup into a tank of cooled sucrose solution, and saw that experimental

morphologies and rates of propagation rapidly departed from the isothermal theory (Huppert 1982, Didden and Maxworthy 1982), as the flow developed a cooled viscous boundary layer.

Stasiuk et al. (1993) sought to model this as a function of a bulk viscosity. While this would effectively increase in time as the boundary layer developed (Griffiths and Fink 1993), Stasiuk et al. modelled it as a single value, derived from apparently steady flow propagation at longer timescales. This 'late-time' constant bulk viscosity was found to depend on the ratio of surface to vent viscosities, and the Peclet number (itself a ratio of heat transfer via conduction to that effected via advection). Lister and Kerr (1994) concurred, and produced a somewhat simpler formulation.

While lava does possess a strongly temperature-dependent viscosity, the relative importance of retardational forces in a given system was arguable. Griffiths and Fink (1993) therefore defined a full range of scales for flows existing in a variety of force balances. Building on the works of Huppert (1982), Blake (1990) and Iverson (1990), Griffiths and Fink's scaling relationships were centred on a two-component system, with an isothermal homogenous interior and a cooled carapace. Analyses could then define the balance of forces present within this system as they required: the driving force—a function of buoyancy or overpressure; and the retarding force—a function of viscosity or yield strength, with stresses focused in the skin, or along the dome base.

Building on this theory, Griffiths and Fink (1997) established the most complex and developed experimental system yet, when they investigated the effects of plasticity and surface solidification. Using a PEG-kaolin slurry, they developed a range of experimental morphologies that differed from those of their earlier work. Using a slightly modified parameter Ψ_B, Griffiths and Fink produced a sequence that ran from no apparent solidification effect at high Ψ_B (rapid extrusion and/or little effective cooling); through the generation of strong plates and ridges in an increasingly non-axisymmetric form; to the development of clear lobes, typically five in number; and finally at lowest Ψ_B (slow extrusion and/or rapid cooling) the flow developed as sluggishly extruded spines, that toppled under their own weight.

1.3.2 Flows extruded onto an inclined plane

Conversely, studies of what are frequently called 'long lava flows', extruded over varied topography and commonly down a slope, must reference a more complex theoretical frame. One cannot approximate flows as axisymmetric, but may attempt other simplifications. Longer lava flows on slopes are often produced by less viscous, mafic lava (although this definition has no defined petrological or geometrical flow prerequisite), though slumps or coulees of highly viscous lava are not uncommon. Slope-borne lava flows offer a bewilderingly large array of flow features, dependent upon an equally substantial array of flow parameters: flow rate and its fluctuation with

time; local flow velocity; and flow stress regimes; total extruded volume; flow viscosity and rheology (itself dependent upon flow temperature, chemistry, crystal content, and rate of shear) and underlying slope and topography.

Most analyses seeking to explain the bulk dynamics of lava flows thus simplify the model system, ignoring second order features and opting for a simple, uniform flow rheology or a noncomplex flow geometry. As a prime example, lava is generally viscous enough to be approximated by laminar flow, particularly in creeping, silicic flows. However, high flow velocities and low initial lava viscosities have been measured for many mafic long lava flows near the vent, implying Reynolds numbers of O (1-10^3), and a crossover into a transitional or turbulent regime. This feature is sometimes used to imply that the flow is thermally well mixed, and hence isothermal in the vertical plane, though the effects of turbulence in dynamical formulations of flow motion are often ignored (e.g. Bruno et al. 1996), but not in the case of Huppert and Spark's (1985) investigation of Komatiites.

In theoretical studies into the dynamics of lava flows on slopes, workers have usually taken one of two approaches. Either they have assumed the flow to be an unbounded fluid spreading on an inclined plane, with a tangible lateral free surface; or they have simplified the model by ignoring the lateral free surface, either by considering the flow to behave as an infinite sheet flow (or even more simply, as a 2D flow), or by assuming rigid lateral boundaries, as in a channelled flow. Both approaches have their merits and their flaws.

In terms of global dynamics, the first approach offers the most rigorous analysis, but the complexity of the solutions means that such analyses are only readily applied to simple rheological systems (i.e. a pure Newtonian fluid). As such, only a few workers have taken this route. Smith (1973) obtained a similarity solution for the downstream behaviour of a Newtonian fluid extruded from a point source, with a constant flux. The solution, which matches the free lateral boundary as a function of the distance from the source, gave good agreement when compared with rudimentary experiments using silicone oil.

Lister (1992) presented the most detailed and rigorous analysis of the problem so far. In studying the extrusion of viscous flows on an inclined plane, from both point and line sources, he showed that the flow changed from an initial regime wherein its motion was predominantly driven by the down-slope height gradient, to one where it was dominated by the influence of the slope itself. He derived early and late time solutions for a variety of cases, and provided experimental data that conforms well to the numerical and analytical solutions obtained. Lister also highlighted that the complexities of dealing with the free lateral flow boundary in addition to considering the evolution of the flow height through space and time render the this approach somewhat complex already;

instilling an effect like a temperature-dependent viscosity into the model and coupling the momentum and energy equations would further complicate the issue.

Both the above analyses considered an isothermal (and hence isoviscous) flow. Bruno et al. (1996), following Smith (1973), solved for the near source region, but also attempted to include the effects of cooling. Rather than include the process of heat transfer *per se*, they instead applied an arbitrary function for viscosity, dependent on distance from the source i.e. as a given flow parcel travels further downstream it will have cooled more. Again, the flow is considered isothermal in the vertical. Such a simplified approach allows some tractability, but must be held against effects of channelling, which can preserve heat and hence keep viscosity low far from the source.

The second approach has many merits. Whilst it does not attempt to solve the dynamics of a realistic lava flow profile, the use of simplified geometries allow more complex rheologies to be used and can better incorporate the effects of cooling. Hulme (1974) attempted to model basaltic lunar and terrestrial flows by way of considering them as an infinite sheet flow of a Bingham liquid in between plastic levees. For the latter, Hulme considered that lateral motion ceased as the cross-slope pressure gradient was balanced by a basal yield stress, allowing the formation of stagnant levees. The width of these levees could then be analysed with reference to other flow parameters (slope and local pressure gradient). Theoretical predictions for levee height found good agreement with experimental extrusions of a plastic kaolin slurry.

These theoretical and experimental observations have had a lasting impact in volcanology, particularly with regard to the formation of lava levees. Although Hulme's theory considered only the cross-slope basal stress, and neglected field observations of the variation in how levees can form, it has nevertheless proven highly enduring. Hulme (1974) mimics the effective features of cooling by use of an isothermal analogue with a yield stress. Other workers have sought to incorporate the varied effects of cooling in different ways. These have typically consisted of two-dimensional—effectively depicting intra-channel flow—two-component models of Bingham flows with an isothermal interior and cooled crust, cooling by a mixture of surface radiation and internal conduction (Dragoni 1989; Dragoni and Tallarico 1994; Crisp and Baloga 1990, 1994).

1.4 Recent advances in research

In his review of the research into lava flow dynamics, Ross Griffiths called the previous quarter of a century a 'golden age' in the study of the field (Griffiths 2000). A considerable amount of research has furthered knowledge in the behaviour of lava flows to a great extent. The most recent advances in the experimental and analytical study of lava flows have expanded on the work cited previously;

most typically, they have shed new light on older theoretical systems with the application of improved and more efficacious numerical techniques. Sansom (2000) and King et al. (2000) have developed full numerical models to examine the experimental and theoretical system of Stasiuk et al. (1993). In a series of papers, numerical and theoretical analyses have shed increased light on: isothermal viscoplastic domes (Balmforth et al. 1999); easily cooled—low thermal diffusivity—flows of viscoplastic fluid with a temperature-dependent viscosity (Balmforth and Craster 2000); shallow viscoplastic flow on an inclined plane (Balmforth et al. 2002); and a more appropriate model of Bingham flows with a temperature dependent viscosity, with a low thermal diffusivity (Balmforth et al. 2003).

Experimental analyses have also seen important advances. Osmond and Griffiths (1998, 2001) applied elements of the viscoplastic theory of Blake (1990) and Griffiths and Fink (1993) to flow on an incline, and investigated coulee morphology. Gregg and Fink (2000) expanded the earlier work of Fink and Griffiths (1990, 1992) to study the effect of slope on solidification PEG wax and the morphology produced. Increases in underlying slope were found to displace the observed morphological regimes to lower values of Ψ, with the additional appearance of channelisation, lava tubes and far greater flow front extension. Hoover et al. (2001) investigated the development of yield strength in a novel analogue—poppy seeds and other particles suspended in isothermal syrup.

Elsewhere research has focused on the development of flow channels. Solutions for the behaviour of a viscous flow in a semicircular channel or filled rectangular duct are well known (e.g. White 1991). By taking one such solution as a starting point, Tallarico and Dragoni (1999) and Sakimoto and Gregg (2001) derived series solutions for the velocity distribution of a Newtonian flow in a rectangular channel. In the near source region, such a simple model proves remarkably accurate. Tallarico and Dragoni (1999) compared the field results taken from Arenal Volcano, in Costa Rica (Linneman and Borgia, 1993) with theoretical predictions, and find good agreement with their simple model.

As already discussed, significant cooling of more mafic flows can lead to significant crystallisation, and the onset of a yield strength; Hulme's (1974) simple, semi-analytical model for an isothermal Bingham flow in a channel has been advanced by further research. Sakimoto and Deane (1997) arrived at a general solution for flow rate in such a system from computational fluid dynamics and dimensional analysis. A more rigorous solution, however, was derived by Tallarico and Dragoni (2000). A further multi-component model for the progress of channel-bound lava flows has been developed by Harris and Rowland (2001).

As this piece is written, therefore, the field of lava emplacement dynamics is in rude health. A considerable range of experimental and field data are supported by a collection of applicable scaling

analyses and simple theoretical arguments, which have proven robust and useful in investigating and explaining to a leading order (and often greater) the processes of lava flow expansion and development.

These studies have been supported with a growing roster of numerical investigations that seek to solve the systems of coupled equations accompanying real lava flows and complex analogues. Yet relative to these studies there has been a decrease in the number of detailed experiments that accompany and test their numerical predictions. The recent studies of viscoplastic flow—with a temperature-dependent viscosity—have had no recourse to experimental verification of the model. In the field of experimental volcanology, a study of such a fluid over a wide and controlled parameter range is a necessary check on the models' veracity. A suspension of neutrally buoyant particles in variably cooled golden syrup—as suggested by the studies of Hoover et al. (2001)—would provide a possible analogue.

Despite its factoring in the numerical approaches of Balmforth and Craster (2000) and Balmforth et al. (2003) temperature-dependent viscosity has been somewhat ignored in the last ten years, in favour of analyses investigating the effects of solidification and yield strength. In part this is a function of a decision to focus on a different given property in the interests of tractability. It is also a decision made with reference to timescales and non-dimensional parameters derived to define the relative importance of viscous and plastic forces over a flow's spatial and temporal evolution. While scaling analyses such as these can predict that viscous forces become less important than the plastic effects in many flow regimes, a little further consideration is needed.

Static equilibrium models typically incorporate a purely plastic rheology—that the equilibrium profile for a give mass of material is formed by the immediate accommodation of the fluid to the new balance. While the yield stress may be considerable in even moderately crystalline lava, as a function of crystal frameworks and further mechanical interactions, the interstitial fluid can often prove a highly viscous medium for particle movement. The catchall term of a 'yield strength' can perhaps incorporate such viscous factors, if due care is taken as to its definition, simplifying first-order models. Yet with numerical analyses now making strong forays into visco-plastic systems with strong cooling effects, the importance of strong melt-phase viscosity gradients necessitates their study in greater detail. Models of the development of real lava need to be made with reference to detailed studies of the actual effects of a temperature-dependent viscosity on laboratory analogue and theoretical systems.

Lava flows develop a great variety of structures during emplacement, and while qualitative models for their creation have been assessed, direct quantitative models for the processes of fold formation (e.g. Biot 1961, Fink and Fletcher 1978, Fink 1980) or spine-fed dome growth are limited in

number and application. The formation of in situ lava channels is little understood or quantified; the majority of studies take their presence as given, to facilitate analysis of bulk flow parameters. The formation and growth of these conduits of lava propagation, when coupled with a three-dimensional form and moving contact-line—itself the focus of considerable thermal and rheological change—provide a highly complex theoretical system; but in the absence of numerical analyses careful experimental approaches can yield many insights. Distinct changes in manner of basaltic flows, such as those entailed in the pahoehoe-aa transition, are also governed and exacerbated by a variety of structural process at micro- and macroscale levels (see Cashman et al. 1999 for a coherent overview).

1.5 Thesis approach and structure

This thesis seeks to investigate the emplacement dynamics of lava, with special reference to the development of longer flows extruded onto an incline, using a combination of experimental, theoretical, field and historical analyses. Though elements of the analysis are particular to the study of basaltic flows, the experiments performed provide data that may prove applicable to a wider range of lava compositions. Special reference is given to Mount Cameroon volcano, whose recent extensive eruptions provide a hitherto little analysed field laboratory for the physical volcanologist. Theoretical investigations into lava emplacement dynamics are framed against specific examples provided by the Mount Cameroon lava flows and the laboratory work performed in Bristol.

In this manner, the author seeks to tackle this broad topic on three levels: (i) the experimental study of cooled extrusions of golden syrup, effused onto a slope at constant flow rate, in closely monitored and controlled environmental conditions; (ii) an historical analysis of the documentary reports of the 1909 and 1922 eruptions of Mount Cameroon, which form a repository of volcanological data on flows beyond the ken of modern volcanologists; and (iii) field studies of the recently extruded 1999 flows of Mount Cameroon.

The study of cooled viscous flows on a slope has attracted little research, and none in an experimental context. The use of a temperature-dependent viscosity alone in the experiments does not constitute a belief on the part of the author that it is the most crucial factor in the lava flow development. Such would be misguided and over-simplified; the author freely accepts the importance of a yield strength and surface solidification in the propagation of real lava flows. Rather, it is a suggestion that this factor retains a considerable level of importance and requires further investigation—particularly with reference to long, slopeborne flows.

This chapter has sought to give a brief overview of the current status of the study of lava emplacement dynamics, and the theories currently investigated and discussed. Chapters 2 and 3 discuss the experimental approach to the problem, with the study of extrusions of cooled viscous flows on a slope. The former explains the properties of the analogue fluids used to mimic lava, and describes the apparatus into which they are extruded; the latter presents in considerable detail the experimental data, with discussions of qualitative trends and the morphological regimes produced. It is also accompanied by a brief explanation of Lister's (1992) isothermal model, and references to isothermal experiments, by way of contrast.

Chapter 4 provides an overview of the 1999 phase of activity on Mount Cameroon, and proceeds to develop a full field analysis of the distal and proximal flows produced. Discussion of field micro-, macro- and megascale morphologies seeks to provide new understandings on the interactions between lava structures and dynamics. In the final section, Chapter 5, the thesis takes elements from field, experimental and historical data, and draws them together in a final analysis. Key processes in the field of lava emplacement dynamics are analysed with special reference to the flows of Mount Cameroon. Quantitative explanations for some phenomena are offered, and conclusions from the process and results drawn.

Experimental data for isoviscous and cooled experiments are contained in Appendix A. Appendix B shifts the scene considerably, forming an historical analysis of primary and secondary data pertaining to the early 20th Century eruptions of Mount Cameroon. In collating and discussing these observations—the vast majority hitherto unconsidered by volcanologists—it is hoped to provide for a greater knowledge of previous eruptive activity, past examples of lava dynamics, and supply a background to Chapter 4.

Chapter 2: Experimental materials and methods

2.1 Experimental Materials

Sugar syrups have seen much usage as analogue fluids in experimental volcanology (e.g. Huppert 1982, Whitehead and Helfrich 1991, Stasiuk et al. 1993, Hammer et al. 1998, Hoover et al. 2001). *Lyle's Golden Syrup*® is the most common brand found in the United Kingdom. The syrup is produced by the heating and acidification of the by-products of sugar cane refining, and is a partially inverted refiners' syrup, being an aqueous solution of 47.0-51.3% inverted fructose and glucose, and 30.0-33.0% sucrose.

The viscosity characteristics of Golden Syrup are largely derived from the temporary hydrogen bonds that form between sugar molecules, or between the sugars and water. The former bonds are stronger, and dilute syrup solutions display markedly lower viscosities (see for example Lejeune et al., in press). Over periods a few hours in length (in excess of the experimental timescales, see Chapter 3), syrup dehydrates, losing water to the atmosphere and producing a viscous skin.

Irrespective of dehydration, syrup can develop heterogeneities naturally if left to stand for weeks or months. Sugar crystals nucleate in the fluid, and settle to the container base, forming a soft crystal mush. This has no permanent effect on the bulk chemistry or properties and, if gently heated and stirred to remove the crystals, produces syrup with an identical rheology to the pre-crystalline case (see, for example, Stasiuk 1993). In the experiments described herein, batches of syrup were used within the timescale of a week, and crystallisation never became a problem.

The density of Golden Syrup is found to be temperature dependent, and varies from batch to batch; using volumetric analyses, Llewellin (2002) found that the density to vary according to

$$\rho = mT + c \tag{2.1}$$

where ρ is the syrup's density, T is the temperature in °C, m = -0.6166 kg m^{-3} and c = 1453 kg m^{-3}. In contrast, Lejeune et al. (in press), analysed the same syrup batch as used in the experiments of this thesis and measured a room-temperature picnometer reading of 1422 kg m^{-3}. As the density of Llewellin (2002) varies only weakly with temperature, we adopt Lejeune et al.'s value in this thesis, for all temperatures. We take the surface tension of Golden Syrup, Γ, to equal 0.08 N m^{-1}. This is the figure measured by Llewellin (2002), and shows good correlation with other measurements for

sugar solutions given in the literature, e.g. Manga and Stone (1995) give a value for corn syrup of 0.07 N m^{-1}, and there is no evidence to suggest that Γ is anything other than temperature invariant.

Most importantly, Golden Syrup displays a strongly temperature-dependent viscosity. This has been analysed in detail before (White 1988, Davaille and Jaupart 1991, Llewellin 2002), but the slight variation from batch to batch requires independent analysis. The viscosity of the Golden Syrup used in these experiments was analysed quantitatively, using a Haake RV20 rotational viscometer, and SVII concentric cylinder cup system; the cup was jacketed by a water-bath, which was connected to a Haake Phoenix C-40P refrigerating/heating circulator.

As a controlled-rate rheometer, the angular velocity of the sensor head is controlled by the user, and the necessary torque to facilitate that rate measured and logged as the dependent variable. The resultant flow-curves are plotted and the rheometer software used to find the syrup viscosity. The bath temperature is regulated by the attached circulator, and altered between runs to construct a batch of flow curves for different syrup temperatures. The sample temperature is monitored via a sensor in the rheometry system, and increases in temperature (and a subsequent shear-thinning behaviour) as a result of viscous dissipation were not observed under the strain regimes modelled (strain rates encountered in experiments are typically of the order 1 to 10^{-3} s^{-1}, there is little danger of such processes or extreme strain regimes occurring in the experiments).

At a given temperature, Golden Syrup behaves as a Newtonian fluid, with no observed dilatant or pseudo-plastic behaviour. Recorded values of viscosity are plotted as a function of temperature on **Figure 2.1**. Difficulties arise in the use of the RV20 rheometer at sub-zero temperatures; the C-40P circulator can function as a sub-zero refrigerator but the RV20 system is inaccurate at such high viscosities. Furthermore, increasing levels of condensation and the high temperature difference between the bath and the ambient room temperature lead to errors and issues of practicality.

The viscosity of syrup at sub-zero temperatures is instead calculated using the falling sphere method. A square-sectioned (12 cm x 12 cm) Perspex-fronted container 1 m high is placed in the Cold Room (see 2.2.2) and filled with syrup. The room (and syrup) are cooled to a set temperature, monitored by a thermometer placed in the translucent syrup. A small steel sphere (typically 0.99 cm in diameter and 4.031 g in mass) is dropped into the syrup, and its progress measured as a function of time; given the high viscosity of the syrup at sub-zero temperatures, they rapidly reach their terminal velocity in the fluid. Knowing the particles' velocities the application of Stokes' Law

$$V = \frac{2gr^2(\rho_s - \rho_l)}{9\mu} \tag{2.2}$$

(where V is the sphere's velocity, g the acceleration due to gravity, r the sphere's radius, ρ_s the density of the sphere, ρ_l the density of the liquid and μ the liquid's Newtonian viscosity) can readily supply the cooled syrup's viscosity. Stokes' Law is applicable in this case as particle Reynolds numbers in these scenarios are of the order 10^{-7} to 10^{-12}, very much less than the ~ 0.1 required for application of the model. These data are also plotted on **Figure 2.1**. The data show excellent agreement with those of Llewellin (2002) and Lejeune et al. (in press). Furthermore, over the recorded temperature range –20°C to 25°C, they are consistent with the empirical relation found by Davaille and Jaupart (1991):

$$\eta = 4.1148\times10^{-8}\exp\left(\frac{1}{-7.6346\times10^{-7}T^2+3.8693\times10^{-4}T+0.039992}\right) \tag{2.3}$$

where η is the viscosity and T the temperature of the syrup. Golden Syrup possesses a hyper-exponential temperature-dependent viscosity and hence has strong similarities to silicate melts (Shaw 1972, Webb and Dingwell 1990).

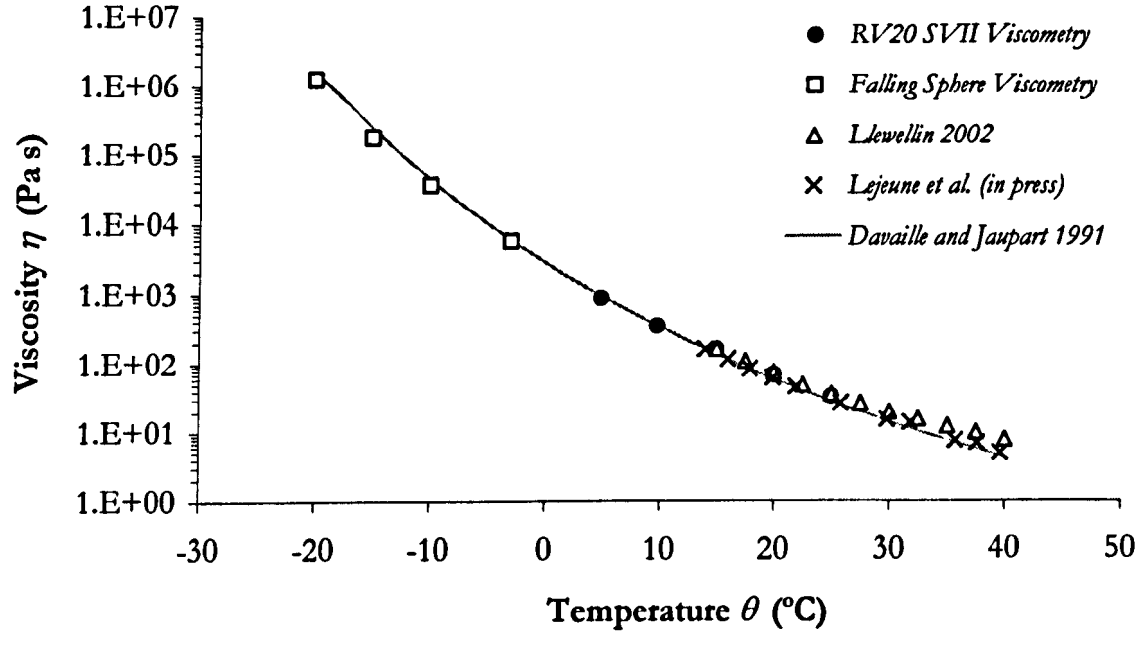

Figure 2.1 Viscosity data for Golden Syrup at a range of temperatures; at a given temperature syrup is Newtonian, but the magnitude of the viscosity displays a strong thermal dependence. Although the specific characteristics of batches vary in small amounts, the commonality of the trends is clear. The line refers to the empirical relationship defined by Davaille and Jaupart (1991).

2.2 Experimental Methods

2.2.1 Experimental apparatus

All the experimental work was conducted using the same apparatus: in keeping with past work (Stasiuk et al. 1993) the experimental system is moderately simple, consisting of a Perspex tank and a pressure vessel, built by the University of Bristol Department of Earth Sciences Workshop. **Figure 2.2** shows a schematic representation of the apparatus. The tank is constructed of 2 cm-thick Perspex plates, fitted so as to render an open topped box of interior dimensions 1.5 m long by 0.5 m wide, and 0.2 m deep. The tank itself is attached to a wheeled steel frame, which can be accurately levelled. The joints between the tank and frame are not fixed, but freely pivot. The two rear joints connect to a lifting mechanism, which consists of two hollow steel bars. The bars are drilled at fixed distances with small holes; the tank frame has two similarly sized holes drilled in its sides. The rear of the tank can thus be raised, pivoted about the front two joints and then fixed in place at a new angle, with steel rods placed through the holes in the bars and frame. This mechanism can impart a stable, fixed slope to the tank, in 5° gradations (up to a maximum of 30°).

A 4 cm diameter hole had been drilled in the tank base, centred half way across the tank's width, and at a distance of 50 cm from the rear wall (allowing a maximum run out distance of ~100 cm for any analogue flows). This is the experimental vent, and the aperture through which the liquid analogues will enter the tank. To allow experiments with different vent diameters, the workshop engineered 4 cm diameter plastic Perspex cylinders of interior bore 2 cm and 1 cm, which can be fitted into the tank vent if desired.

The apparatus was designed for flexibility, to enable the analysis of conduit flow processes, so that the liquid analogue enters the tank via a glass and plastic conduit-system. The clear conduit allows the user to watch and record conduit processes during experimental eruptions. The experimental conduit consists of a clear glass tube (0.8 m long; external diameter 4 cm, interior diameter 3.75 cm), which is connected to the tank base via a socketed ball joint. Below the ball joint, the tube is fixed within a sealed, hollow plastic cylinder, which serves as a heated water jacket. Glass was used for the inner tube as Perspex degrades on contact with acetone, an organic solvent often used to clean the apparatus. This whole arrangement allows the conduit to freely accommodate the tank tilt, whilst itself remaining vertical. Once the tank is fixed at a given angle, the base of the conduit can be secured against the tank frame.

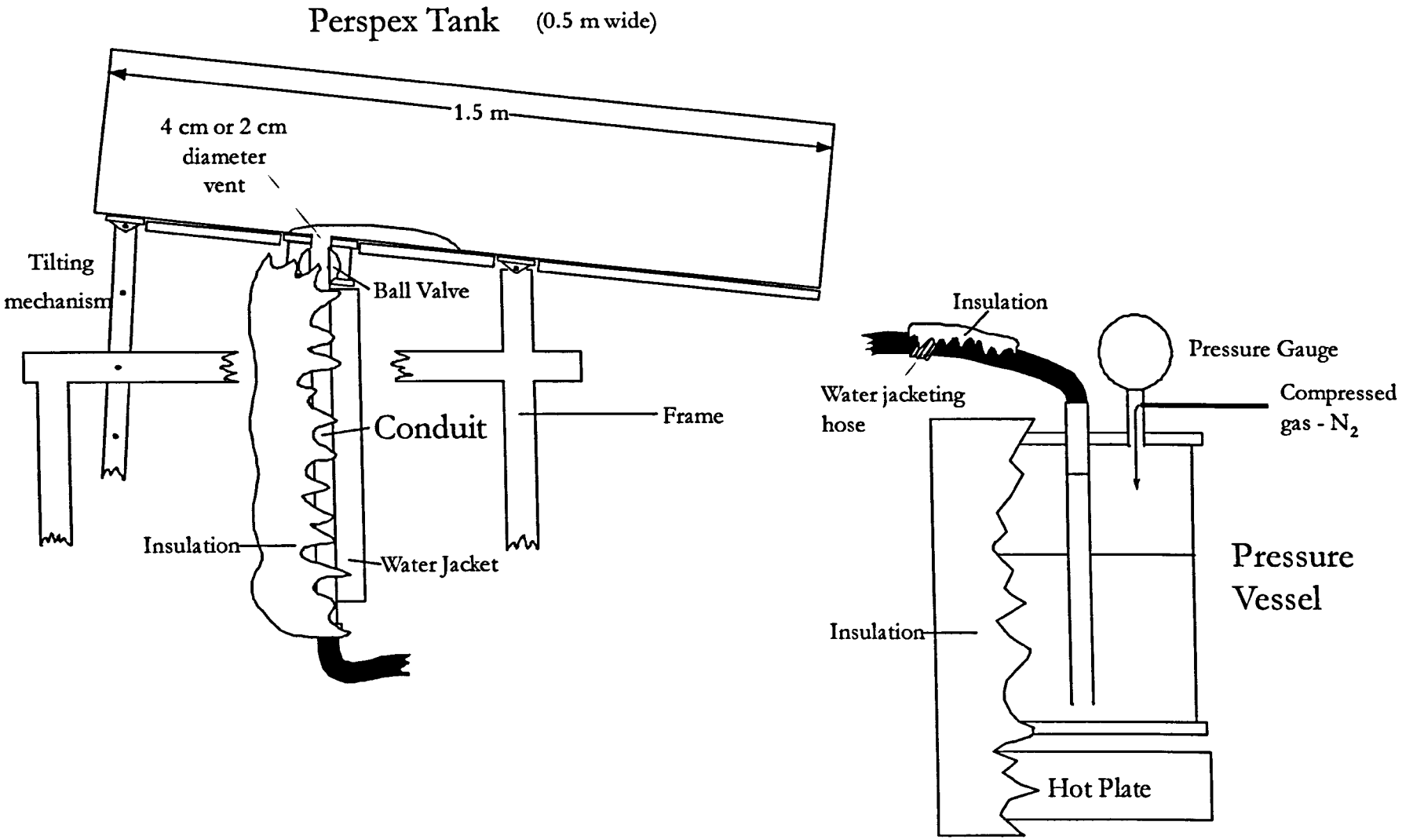

Figure 2.2 Schematic representation of the experimental apparatus (not to scale).

The pressure vessel consists of a stainless steel, sealable cylinder. The cylinder has a capacity of 20 litres. The liquid analogue is placed in the pressure vessel before a series of experiments, and the vessel then sealed shut. The only exit is through a long stainless steel tube, which reaches down into the reservoir itself, and exits by way of an outlet at the top of the pressure vessel. Oxygen free Nitrogen (N_2) is pumped into the vessel from a pressurised gas cylinder, regulated by a pressure gauge, so as to impart a constant driving pressure in the experimental 'magma chamber'. The pressure vessel itself is tested and guaranteed up to pressure of 3 bars at 100°C. In the interests of safety, however, a blast valve has been installed, which will burst and release all the gas at a pressure of 2.5 bars. As any given experiment will generally result in the extrusion of no more than 5 litres of liquid analogue, the system allows several experiments to be performed concurrently, with minimal inter-experimental maintenance and cleaning.

The pressure vessel itself rests upon a hot plate, which can be set to reach temperatures of up to 250°C. This enables the analogue fluid to be kept at a pre-determined temperature, which can be monitored by means of a thermocouple in the pressure vessel. A hardened polystyrene foam casing fits around the pressure vessel, so as to insulate the system and minimise heat loss. While the experimental tank is kept within the sealed cold room, the pressure vessel is held outside. The analogue fluid is transported from the pressure vessel to the tank by means of a water jacketed, insulated hose, which is affixed to the outlet on the pressure vessel, wherefrom it passes through a flange in the cold room wall and connects to a pipe section at the base of the conduit.

2.2.2 Experimental procedures

Previous experimental work analysing the extrusion of gravity currents into a cooled environment has featured either the extrusion of a hot analogue into an environment at ambient room temperature (e.g. Fink and Griffiths 1992, Griffiths and Fink 1993; Gregg et al. 1998), or a ~room temperature analogue into a moderately cooled environment (i.e. golden syrup into cold sucrose solution, Stasiuk et al. 1993). In the experiments described here, it was considered important to obtain a temperature difference (ΔT) between the erupted analogue and the ambient that is larger than has been obtained before, whether to better simulate more rapid cooling and higher skin viscosities. To achieve a large value of ΔT, the tank, conduit and frame were placed inside the Geological Fluid Dynamics (GFD) group 'Cold Room'. The Cold Room is a sealed environment of dimensions 3.75 m long x 2 m wide x 2.5 m high. Air is refrigerated in a circulator system using HCFCs and HFCs, and then circulated around the room with Searle model KS20-6 and KS45-6 fans. A single heat and vapour-sealed, windowed door opens onto the room, and provides a portal through which to monitor experiments at a distance.

Built using technology developed for the retail and food industries, the Cold Room provides a controlled, refrigerated environment within which to conduct our experiments. The room does not provide an environment of constant ambient temperature. Given the needs of the food industry, it operates on a principle whereby it seeks to maintain the temperature of any object *within* the room, not the ambient air itself, whilst minimising operating costs. When engaged, the fans will cool the room down to a temperature ~1°C below that set on the control panel, and then shut off. The room will proceed to warm slowly over time, until the ambient temperature reaches a value ~2°C above the set temperature, when the fans will re-engage.

Figures 2.3 and **2.4** show typical temperature profiles recorded by a thermocouple placed in the centre of the Cold Room, when cooled down to two different ambient temperatures. The cycle of heating and cooling produced by the episodic operation of the circulation system can clearly be seen, with both runs displaying a cyclic temperature fluctuation with period of ~20 minutes. Over the course of the thermocouple recordings, the oscillations produced an average room temperature comparable to the set value. As with any refrigeration system, there exists the potential for equipment to frost, and then ice up, if

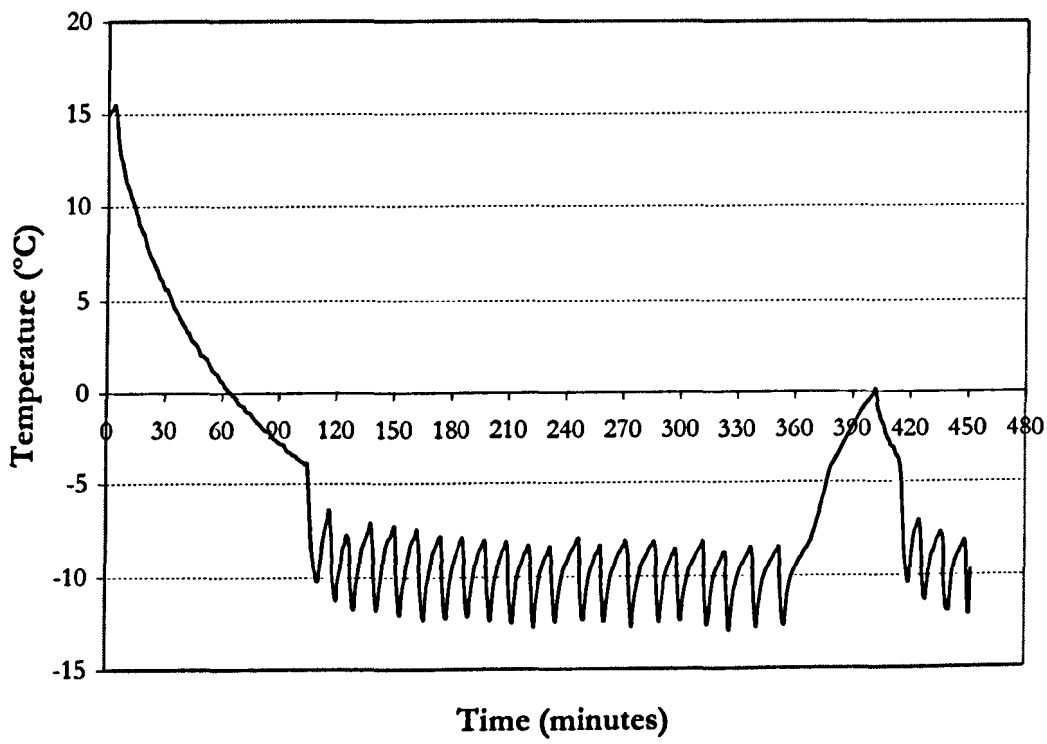

Figure 2.3 Temperature profile recorded by a Type-T thermocouple placed in the Cold Room (set to -10°C) over several hours. Note the initial temperature fall as the room cools down, and the peak at ~415 minutes, which signifies a defrost cycle, where the room is allowed to warm, preventing ice build-up.

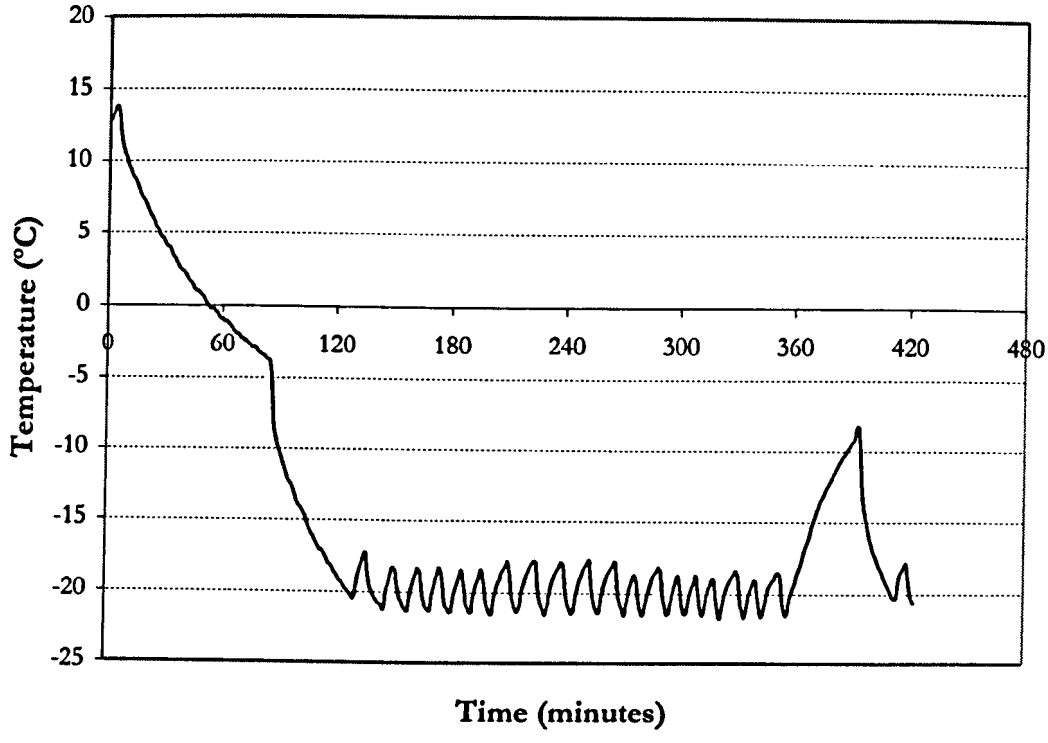

Figure 2.4 Temperature profile recorded by a Type-T thermocouple placed in the cold room (set to -20°C).

left in a freezing environment with significant moisture present. Experimental run-times never exceeded 1 hour, and saw negligible icing, and actual physical work and observation in the Cold Room was kept to a minimum.

As it was imperative to have the liquid analogue at a well-defined, constant eruption temperature, measures were introduced to minimise heat loss from the system. The water jackets for the conduit and connecting hose were connected to heating circulators placed outside the Cold Room. At various stages in the course of experiments, Haake N3-T, DC5-K15 and Phoenix C-40P refrigerating/heating circulators were used for this task. They maintained a constant circulation of water (for golden syrup experiments) or polyethylene glycol (for gum rosin), which kept the analogue in the system as close to the required temperature as possible. Heat loss from the system was further minimised by fully encasing the conduit, hose, connecting pipe fittings and water jackets (including their attached, feeding hoses) with aluminium foil-covered, fibre-glass insulation from E.J. Berry Ltd. On average the insulation resulted in a 4-6 cm thick barrier between the system and the ambient environment, and thermocouples placed in the lagged intersection between the conduit and hose registered no discernible heat loss during the timescale of an experiment.

Although the basal cooling of lava flows and theoretical fluids has been analysed in other studies, and incorporated in some models (e.g. Sansom 2000), it is simplest to assume no heat loss through the base of the flow, and no basal thermal (and hence rheological) boundary layer. Since many of

the models and experiments to which we compare our experimental data use such an assumption, and basal cooling itself can be shown to be minimal with respect to the global flow heat flux (e.g. Neri 1998), an effort was made to reduce heat loss through the tank base to a minimum.

With the tank horizontal, a layer of polystyrene board was laid on top of the tank base, with a hole cut to match the tank vent. The insulation was covered with a 0.1 mm thick layer of Mylar plastic, which provides a smooth surface that can be annotated with a scale. Along one radial axis, the underlying polystyrene was scored into a channel in which the thermocouple wires could rest without impinging upon the flow. A pin was used to punch small holes in the plastic, through which the thermocouple head could then be placed. This enabled an array of thermocouples to be located along the tank base, following one radial axis, which could measure basal flow temperatures as the flow extruded. Several experiments were performed as in Stasiuk et al. (1993), with room temperature syrup extruded into a sub-zero ambient environment, and the basal thermocouple readings analysed.

Thermocouples initially read values concordant with the cold environment, until the overflow of warmer syrup caused a considerable rise. At a given thermocouple, the initial post overflow readings measured somewhat cooler than the extrusion temperature, concordant with the overflow of a partially cooled syrup front. Recorded temperatures rapidly increased with the advection of hotter syrup from the source, and remained at the extrusion temperature throughout the duration of the experiments (up to 30 minutes). Clearly there was no rheological stiffening along the base of the analogue flows.

The polystyrene insulator, however, comes naturally bowed; a property exaggerated by the continual heating and cooling the apparatus undergoes during and between experiments. This imparted a heterogeneity to the surface profile of the tank, which significantly affected the flow in early trials, especially in 'axisymmetric' isothermal and cooled experiments with syrup.

To avoid this problem, the insulation layer was attached to the underside of the tank floor. Although the upper surface of the tank floor will still be exposed to the cooled air of the Cold Room, and there will be some minor initial cooling of the flow as it rides over the cold base, the insulation prevents an extreme thermal gradient from persisting along the tank base for the duration of the experiment. Effectively, a small time after an area has been covered in hot analogue fluid, the Perspex base warms to some value close to the eruption temperature. Continual advection of heat by the flow along the tank floor provides a constant thermal boundary condition on the upper side, whilst the insulation prevents heat loss from the underside. Undoubtedly, there would be a small, lateral conductive heat flux between uncovered areas of the tank floor and those

underlain by the analogue, but we assume this to be negligible. This altered set-up prevented the measurement of basal temperatures, but provided a workable, insulated system.

2.2.3 Measurement

Any dynamic model of highly viscous gravity currents will require an accurate description of several key parameters: volumetric flow rate (Q); liquid analogue density (ρ_l) and viscosity (η); ambient fluid density (ρ_a); and in the case of cooling, the temperature of the ambient environment and the flow itself. The character and variation in analogue fluid properties were described in section 2.1; this section shall explain the manner in which these parameters were measured during the experiments. As all experiments were extruded into air, we take $\rho_a \sim 0$ kg m^{-3}.

i) *Flow Rate*

The nature and environment of the experimental system preclude many types of flow rate measurement that might be available in other experimental systems. Golden syrup has sufficiently high viscosity that flow rates of only 0.1-10 cm^{3}s^{-1} are obtainable using this apparatus; this results in pipe-flow velocities that are at the extreme lower limit of accuracy for most small ultrasonic flow meters. Similarly, the highly viscous nature of analogue rules out the use of simple mechanical flow meters, like the ball viscometer. Visual approximations of flow rate, using the speed of flow front propagation up the conduit, cannot be applied during non-isothermal experiments, as the whole conduit is lagged and insulated. The pressure vessel has a cross-sectional area of ~700 cm^2; given that ultrasonic level metres, usually used for large capacity water tanks, commonly give an error in vertical measurement of ±3 cm, this would have produced volumetric error too large to measure flow rate accurately in this system, due to the small flow rates (~ 1-10 cm^3 s^{-1}) and extruded volumes (~ 1000 cm^3) involved.

Flow rate was therefore measured using two thermocouples, which were situated at different heights in the source region. In experiments lacking the 2 cm interior diameter nozzle, these were placed in the upper region of the glass conduit, with one positioned 4 cm above the other. In experiments using the plastic nozzle, they were placed in the engineered fittings, as shown in **Figure 2.5**. Although ideally the ambient temperature throughout the interior of the conduit should be consistent with the eruption temperature of the analogue (T_i), the proximity of the upper conduit regions to the cooled air circulating in the Cold Room means that any thermocouples placed in the conduit will inevitably measure some temperature lower than that of T_i. When the comparatively warmer liquid analogue first passes the thermocouples, there will be a sharp inflection in the temperature data (**Figure 2.6**). This onset of rapid temperature rise can be identified to an accuracy of ±1 s.

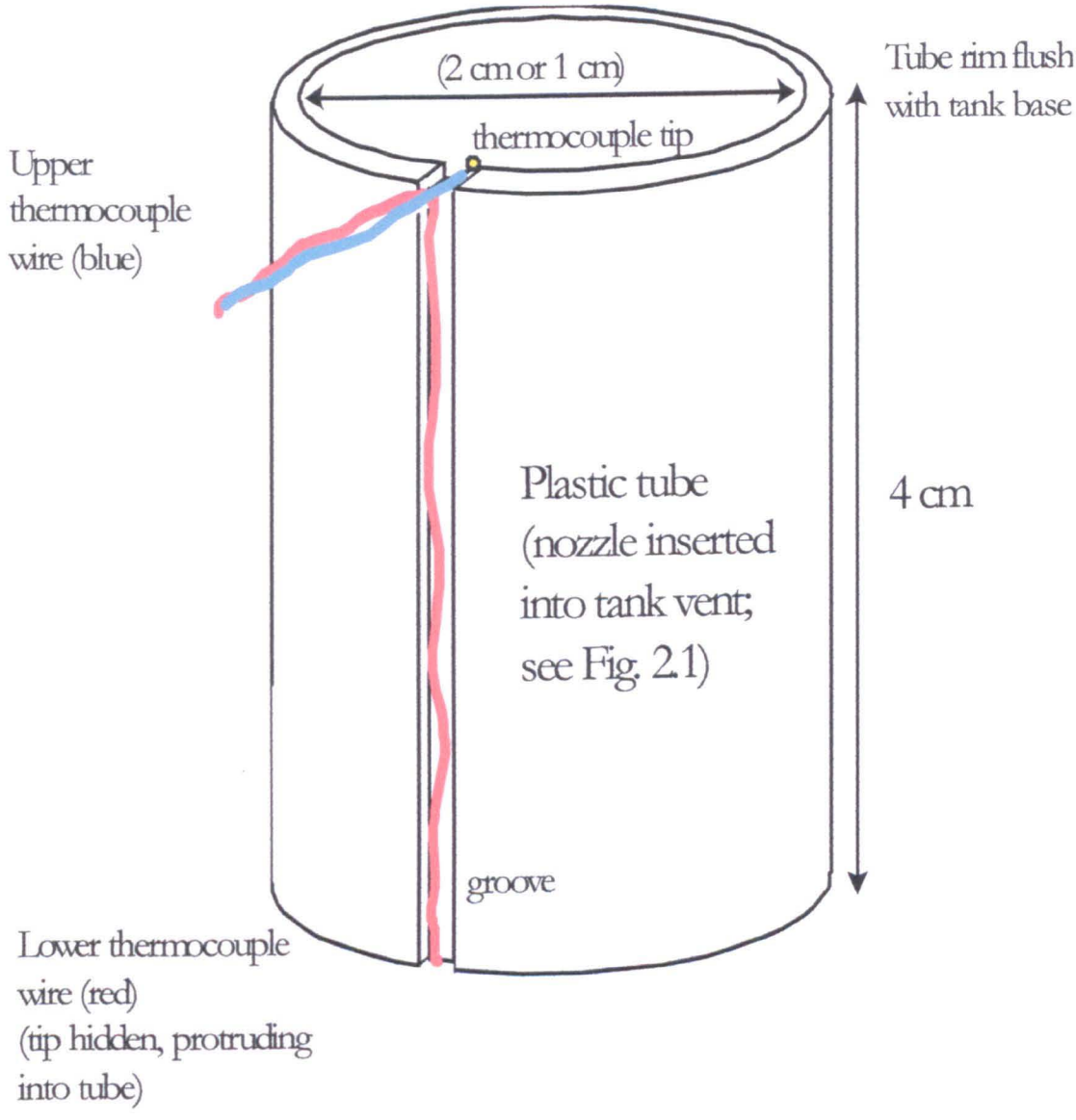

Figure 2.5 Schematic representation of the grooved plastic fittings that are placed inside the tank vent (not to scale). The outer diameter is 4 cm. Note the upper thermocouple (coloured blue) and the lower thermocouple (coloured red), which are used to record flow transit, and hence flow-rates.

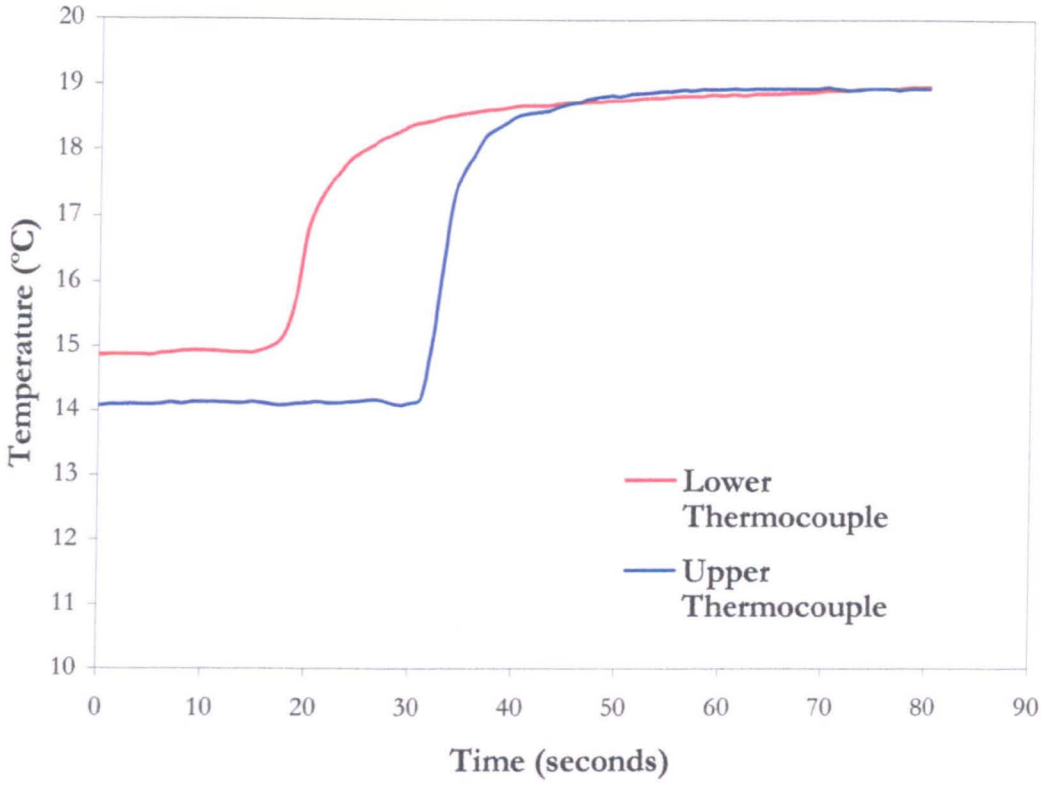

Figure 2.6 Plot showing recorded temperature vs. time for the two thermocouples placed in the conduit for experiment GS-10_20_3. The thermocouples are coloured similarly to those on Fig 2.4.; although in this experiment the thermocouples were attached to the insides of the glass conduit, not to the plastic tube. The time difference between the two initial inflections in temperature is used to calculate conduit transit time and hence flow-rate.

The transit time between the two inflections in the temperature readout was measured. As one knows the radius of the cylinder and the distance between the thermocouples, the cylindrical volume lying between them can be calculated. Assuming that the syrup flow profile in the cylinder remains similarly parabolic as it passes the thermocouples, the time difference between the two registered temperature spikes indicates the time taken to emplace a measured volume of fluid. This method therefore gives a value for flow rate at the very top of the conduit, and therefore an accurate effusion rate for the flows themselves. Inherent in this calculation is the assumption that the mass of syrup that builds above the conduit as the extrusion progresses contributes a negligible pressure head, and will not reduce the flux at the vent by any noticeable amount over that measured in the conduit.

The above method could only be used to measure flow rate at the very start of the experiment. Accurate validation of such measurements from secondary volumetric methods can be achieved, to ensure that the flux does not wax nor wane with time. The simplest method used to achieve this was to temporarily seal a gradated Perspex ring to the tank floor, sides equidistant from the vent

aperture. Syrup was extruded into this temporary measuring cylinder at a constant pressure for a known amount of time, and the volume calculated with time. The cylinder was wide enough to produce extrusion depths on the order of those achieved in experiments, preventing the creation of an excessive backpressure. These data corroborated the initial flow measurements within an accuracy of 10%.

ii) *Temperature*

In order to study the effects of cooling accurately, it was necessary to record the extrusion (or 'eruption') temperature of the analogue (T_e), and the ambient temperature of the cool environment (T_a). Furthermore, it was frequently useful to record temperature profiles at various instances across experimental flows. All temperature measurements were made using Type-T Cu/Cu-Ni thermocouples. These were routed to an RS Datascan 7220 Data-logger, which was itself connected to a lab PC. The data-logger has sixteen channels, allowing sixteen different thermocouple measurements to be recorded simultaneously, at an accuracy of ±0.1°C. For each channel, a measurement was taken once every second.

iii) *Viscosity*

The variation of viscosity with temperature for Golden Syrup is explained and characterised in section 2.1. From temperature measurements taken at the conduit vent, we could easily define an eruption viscosity η_e. This was taken as the basic viscosity of the uncooled fluid analogue, before any rheological stiffening has taken effect. Similarly, temperature measurements taken by floating thermocouples immersed in the flow during an experimental run could be used to calculate a local (time- and spatially dependent) viscosity.

Chapter 3: Experimental analysis of gravity currents extruded from a point source onto an inclined plane, with temperature-dependent viscosity

3.1 Introduction

The investigation of the literature in Chapter 1 described the key elements affecting the development of a lava flow: the rate of extrusion, the effect of cooling on lava rheology (a strongly temperature-dependent viscosity and similarly dependent viscoplasticity and solidification) and the nature of the underlying topography. Studies have typically focused on one or two of these factors, for the suite as a whole proves a complex system. Variable flux, radially symmetric gravity currents on a horizontal plane, with a temperature-dependent viscosity have been analysed by Stasiuk et al. (1993), Griffiths and Fink (1993), Bercovici (1994), Sakimoto and Zuber (1995), Bercovici and Lin (1996), King et al. (2000) and Balmforth et al. (2003); while Blake (1990), Griffiths and Fink (1993, 1997), Balmforth and Craster (2000) and Balmforth et al. (1999, 2003) have focused on the importance of yield strengths and other non-Newtonian properties as a result of cooling.

The addition of a non-horizontal basal boundary complicates matters considerably. Lister (1992) analysed the growth of variable flux, three-dimensional viscous flows on an inclined plane, but did not consider the effects of cooling. Osmond and Griffiths (2001) and Balmforth et al. (2002) investigated a similar paradigm to Lister, but considered the effects of a viscoplastic rheology.

Here we seek to investigate experimentally the extrusion of hot, viscous gravity currents from a point source onto an inclined plane in a cooled environment, building on the work of Lister (1992). Whilst it is accepted that an increase in viscoplasticity, engendered by crystallisation, is an important component of the rheological changes experienced by cooling lavas, we suggest that the current level of theory precludes a full analysis of viscoplastic effects in addition to those provided by a temperature dependent viscosity. Our aim is to focus on the effects of cooling on the downslope flow of a Newtonian liquid with strongly temperature-dependent viscosity, as a first step in the elucidation of more complex lavas.

In analysing the evolution of slope-formed, cooling viscous flows with strongly temperature dependent viscosities, we hope to better understand the dynamic interactions between slope, eruption rate and temperature in lava flows, and provide a basis of understanding from whence the model can be further developed.

3.2 Experimental Procedure

To investigate experimentally the effects of cooling on gravity currents on an inclined plane, we take an analogue fluid with a known temperature-dependent viscosity, and extrude it into a tilted tank, systematically observing the influence of key parameters (flow rate, slope and temperature differential) on flow dynamics and morphologies. Golden syrup is an ideal such analogue, in that it possesses a simple Newtonian rheology with a known viscosity dependence on temperature (section 2.1.1). It has been used in previous experimental studies of viscous gravity currents (Huppert 1982, Lister 1992; Stasiuk et al. 1993). Furthermore, syrup does not crystallise or vitrify in the experimental conditions used herein, and was believed not develop a 'strength' of any kind.[1] Although this simplicity limits its use in direct comparison with real lava flows, whose rheology may often possess elements of plasticity or elasticity, it simplifies the dynamical system we wish to analyse. This study provides a useful and necessary entrée, for we need to better understand cooled viscous flows before more complex analogues are studied experimentally.

The syrup was extruded into free air along the tank (described in Chapter 2) base. Syrup flows hold qualitatively well to a basal no-slip condition, and no basal, rough grid was needed. The base of the tank was marked with a measured, inked scale grid, in 2 cm gradations. Continuous measurements of the flow plan and down slope profiles were recorded using a Sony TRV330E digital video camcorder, and a Kohu video camera or another Sony digital camcorder, respectively. The digital flow plan data were captured and saved as .avi files via 'firewire' based capture software, at a rate of one frame every five seconds. These files were then analysed using a computer video analysis software package, which allowed measurement of flow features to a minimum accuracy of ± 1 mm (at maximum depth of field). Height profiles in the downslope section were either captured and analysed in the same way as the flow plan data (if digitally recorded; a scale was placed in the centre of the tank - corresponding to the centreline of the flow - prior to extrusion), or obtained using a televisual data retrieval system. Temperature, viscosity and flow rate data were recorded as described in section 2.2.3.

A matrix of experiments was constructed for varying slopes and flow rates at two values of T_a: -10°C and -20°C. Given the nature of the experimental system, we were unable to specify an exact metric flow rate before the experiment began; rather we specified a chamber pressure, and then recorded the flow rate as per section 2.2.3. Whilst this precluded a perfectly pre-planned series of experiments, with an exact and identical sequence of flow rates common to all extrusions, care taken to match parameters as closely as possible allows good comparative analysis of data.

[1] *N.B. This is shown to be slightly misplaced in these experiments. When cooled, the rippled syrup skin appears to possess a very small tensile strength. See section 3.5.2.*

In addition, six isothermal experiments were performed with both the syrup and ambient environment at room temperature (insulation was discarded in these runs, and flow rates were obtained by visually measuring transit times in the upper portion of the glass conduit). These served to check the functionality of the apparatus (in relation to the predictions and results of Lister, 1992), and to provide data for direct comparison between the isothermal and cooled runs. These experiments are described in section 3.4.

Table 3.1 shows the matrix of experiments, and the eruption parameters for each. Experiments are coded in the form:

$$\mathbf{Gs}a\_b\_c$$

where GS signifies golden syrup; a is the ambient temperature (-ISO signifies room temperature); b is the slope angle in degrees; and c is an arbitrary run number.

Throughout the following sections 3.4 and 3.5 of this thesis, the spatial and temporal data are depicted without error bars. Small potential errors in flow-rate have been described in Chapter 2, but the key spatial measurements recorded in the experiments were accurate to ± 1 mm, as noted above. In considering the downslope expansion of experimental flows, which quickly obtain values of the order of ~ 0.1 m, and extend to ~ 1 m, such inaccuracies produce errors of no more than 1% at early times, depreciating to 0.1% at long times. In the less-developed lateral, cross-slope expansion of the experiments, such errors will typically be ~ 1%.

Furthermore, such potential errors in down- and cross-slope expansion remain small when spatial variables are normalised by the length scales inimical to the theory, which are described in the following section. Error bars resulting from potential errors of such low orders are far smaller than the symbols used to signify the data themselves, and are therefore not included. Where such errors would be more easily depicted, as for low values on logarithmic plots, they are not depicted as a matter of coherence, with due reference to their small size. The notable exception is in **Figures 3.33** to **3.39**, wherein the ± 1 mm degree of inaccuracy is important, relative to the small values of vertical expansion (~ 2 cm) achieved in the experiments, and error bars are included.

Potential errors in temporal measurements are also small, as such data are taken from single frames of digital video footage, typically captured at accurately defined 5 second intervals by computer software. Error bars in secondary data, such as the velocities derived from recorded heights, times, and cross- and downslope extents in **Figures 5.11** to **5.14**, are included, if only with reference to spatial inaccuracies. Further clarification of any individual errors is included in the relevant sections of Chapter 5.

Name	Ambient Temp. (°C)	Eruption Temp. (°C)	Slope (°)	Erupt. Pressure (x 10^{-1} M Pa)	Flow Rate (x 10^{-6} m^3 s^{-1})	Viscosity (Pa s)	T^* (s)	X^* & Y^* (cm)
GS-ISO_20_1	22	22	20	0.6	1.9	43.3	6.3	3.2
GS-ISO_10_1	21	21	10	1	3.1	50.5	25.9	7.7
GS-ISO_10_3	23	23	10	0.6	1.9	37.3	23.2	6.3
GS-ISO_15_1	23.5	23.5	15	0.4	1.3	34.6	10.5	3.7
GS-ISO_15_2	23.8	23.8	15	0.8	3.1	33	8.3	4.6
GS-ISO_5_1	22	22	5	0.5	1.8	43.3	105.6	13.0
GS-20_10_3	-19	20.75	10	0.6	4.3	52.5	24.5	8.4
GS-20_10_4	-19	21	10	1	8.6	50.5	20.0	9.9
GS-20_10_6*	-18.5	19	10	0.4	1.0	69.4	43.0	6.3
GS-20_20_1	-19	18.75	20	0.4	1.5	72.3	9.9	3.4
GS-20_20_2	-19	18	20	0.6	2.3	81.7	9.7	3.9
GS-20_20_6	-18.5	21	20	1.1	6.1	50.5	5.3	4.5
GS-20_20_7	-18	22	20	0.8	3.3	43.3	5.5	3.7
GS-20_20_8	-19	21	20	0.3	0.7	50.5	9.0	2.6
GS-20_15_1*	-20	20	15	0.4	1.3	69.4	18.0	4.4
GS-20_15_2	-19.5	19.5	15	0.7	4.3	64	12.5	5.9
GS-20_15_3	-19	20	15	1.1	7.2	69.4	11.7	6.8
GS-20_5_1	-18.5	19	5	0.5	1.8	69.4	151.5	14.6
GS-20_5_2	-18.5	19	5	1	5.4	69.4	115.1	19.2
GS-10_5_1	-9	19.5	5	0.8	3.3	64	122.3	16.7
GS-10_5_2	-8.5	20	5	0.4	1.3	59	146.3	12.8
GS-10_5_3	-7.5	22	5	1.2	10.8	43.3	67.9	20.3
GS-10_15_1	-10	18.5	15	0.8	4.8	75.3	13.7	6.3
GS-10_15_2	-10	18.5	15	0.4	1.8	75.3	17.6	4.9
GS-10_15_3	-9.5	20.5	15	1.2	8.6	54.6	9.3	6.7
GS-10_10_1	-9.5	19	10	0.8	4.8	69.4	29.4	9.3
GS-10_10_2	-10	19.5	10	0.5	1.7	64	35.8	7.0
GS-10_10_3	-8.5	21	10	1.2	10.8	50.5	18.9	10.5
GS-10_20_2	-10	18.5	20	0.4	1.4	75.3	10.3	3.4
GS-10_20_3	-9	20	20	0.6	3.1	59	7.1	3.9
GS-10_20_4	-10	20	20	0.8	6.1	59	5.9	4.6
GS-10_20_5	-9	20	20	1.2	8.6	59	5.5	5.1

Table 3.1 Experimental runs and their parameters. The eruption temperature refers to the temperature of the syrup measured at the point of extrusion into the tank, while the eruption pressure is that placed upon the syrup in the pressure vessel. Flow rate is measured as stated in section 2.2, and viscosity is calculated from the eruption temperature, using the relationships described in section 2.1. T^*, X^* and Y^* are represented time and length scales, based on the work of Lister (1992), and explained in detail in section 3.3. The asterisked experiments used the smaller (2 cm) diameter injection nozzle.

3.3 Isothermal experiments—the theoretical framework of Lister (1992)

Rigorous investigations into the behaviour of isothermal, Newtonian viscous flows on a slope have already been completed by Lister (1992): hereafter abbreviated as 'Lister'). The experiments investigated in this thesis are identical in concept to those studied by Lister, but with the addition of cooling effects. Thus there is an added component of a temperature dependent viscosity. The new experiments can be compared with the isothermal cases, to better identify the effects of cooling. Furthermore, in describing the flow dynamics and features, it will often prove efficacious to illustrate them with respect to certain key dynamical concepts and scales derived by Lister.

Lister analysed the flow of syrup down an inclined plane, from both line and point sources. Given the nature of our experiments, I shall only make reference here to the three-dimensional case of extrusion from a point source; furthermore, although I shall highlight the dependence of the theory on a time-dependent flux, in my experiments the flow rate was constant, leading to further simplification.

Lister considered the extrusion of a fluid of constant Newtonian viscosity, μ, and constant density, ρ, onto a plane inclined at an angle to the horizontal of θ (**Fig 3.1**). In defining a co-ordinate system to describe these experiments, x is chosen to be downslope co-ordinate (positive in the downslope direction and 0 at the point of release), y the cross-slope coordinate (both positive and negative; taken from a midline (y=0) running down the centre of the tank and passing through the source), and z the coordinate normal to the inclination of the plane (**Fig. 3.1**).

At any time (t), the dimensions of the flow margin are described by: $x_T(t)$ and $x_N(t)$, the maximum upslope and downslope extents, respectively; the perimeter $y_P(x, t)$, or cross-slope extent, at a given value of x in $x_T(t) < x < x_N(t)$; and the depth of the flow in the z-axis, $h(x,y)$.

We can simplify the problem and magnify its tractability by assuming the effects of (i) inertia and (ii) surface tension to be negligible in the system. Such an assumption will only be valid if we can (i) show that the Reynolds number << 1 and (ii) the Bond number is >> 1.

The Reynolds number can be estimated using the mechanical and rheological properties of Golden Syrup, given in Chapter 2 for experimental conditions. Typically, given the dimensions of the flows (~2 cm high) and their velocities (1-0.1 cm s^{-1}) encountered in our experiments and those of Lister, Huppert (1982) and Stasiuk (1993), Reynolds numbers in the region of 0.01 to 10^{-6} are estimated, and hence inertial effects are considered to negligible.

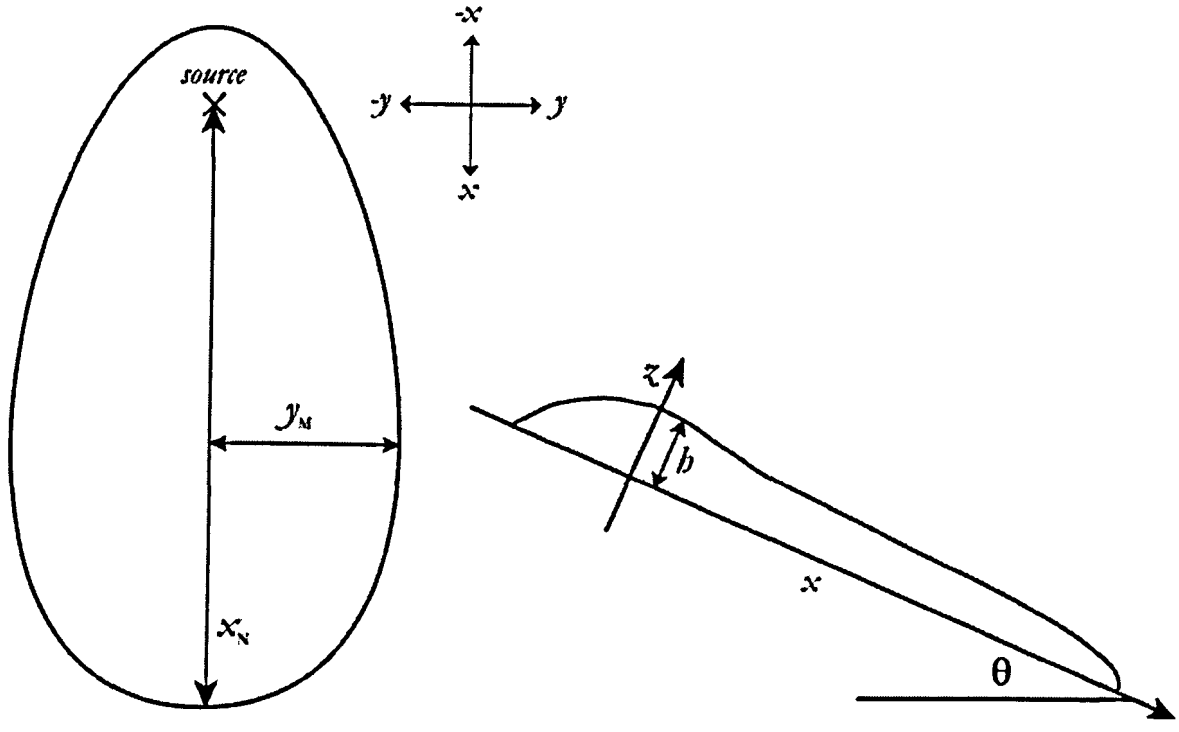

Figure 3.1 Diagram describing the geometry and notation of the theoretical and experimental system of Lister (1992).

The dimensionless Bond number (B) is equal to $\rho g L^2/\Gamma$, where ρ is the density, g the acceleration due to gravity, L a typical length scale, and Γ the coefficient of surface tension. For golden syrup, given typical values for the above parameters ($\rho \sim 1440$ kg m^{-3}, g ~9.81 m s^{-2}, $\Gamma \sim 0.8$ N m^{-1}; see Chapter 2), B ~ 175000 L^2, with the final value dependent on the length scale chosen. Given the geometry of the flows we shall extrude, cross- and downslope flow extents rapidly reach values O (0.10 m), yielding an $L^2 \sim 0.01$ m^2. This results in, at the very least, B~1750, significantly in excess of 1. Therefore, to a leading order solution of the problem, we can expect surface tension effects to be negligible.

We now preset a dynamical model for the advance of viscous flows down uniform slopes, following the work of Lister. Lister simply gives (3.1), (3.5), (3.8) and (3.10) *et sequentia*, any remaining, or intermediary steps were derived from first principles, and are presented here for clarity. In the absence of inertial or surface tension effects, a thin layer of fluid, spreading under viscous-buoyancy force balance on an inclined plane of angle θ, possesses a fluid pressure given by

$$p = \rho g[(h - z)\cos\theta - x\sin\theta] \tag{3.1}$$

which therefore varies according to

$$\nabla p = \frac{\partial p}{\partial x} + \frac{\partial p}{\partial y} = \rho g \frac{\partial h}{\partial x} \cos\theta + \rho g \frac{\partial h}{\partial y} \cos\theta - \rho g \sin\theta$$

(3.2)

As the momentum equation for a thin layer of fluid spreading in a viscous-buoyancy balance (the 'lubrication' or 'thin-layer' approximation; see for example Batchelor, 1967) reduces to

$$0 = -\nabla p + \mu \nabla^2 \mathbf{u}$$

(3.3)

wherein μ is the Newtonian viscosity and the velocity $\mathbf{u}$ only really varies with z. ∇p can be integrated with respect to z to obtain the flow velocity, using the stress-free surface and no-slip boundary conditions ($\partial \mathbf{u}/\partial z = 0$ at $z = h$; and $\mathbf{u} = 0$ at $z = 0$) to fix the constants, giving

$$u_x = -\frac{\rho g}{2\mu} \left\{ \frac{\partial h}{\partial x} \cos\theta \left(2hz - z^2\right) - \sin\theta \left(2hz - z^2\right) \right\}$$

$$u_y = -\frac{\rho g}{2\mu} \frac{\partial h}{\partial y} \cos\theta \left(2hz - z^2\right)$$

(3.4a,b)

Or, to simplify

$$\mathbf{u} = u_x + u_y = -\frac{1}{2\mu} z(2h - z) \nabla p$$

(3.5)

At any single time-step one may convert this to a local flux (per unit of the flow in the direction of flow) by integrating the velocity profile across $h(x, y, t)$, so that

$$Q = \int_0^h \mathbf{u} \, dz$$

(3.6a)

$$\therefore Q = -\frac{\rho g \sin\theta}{3}\left(\cot\theta h^3 \frac{\partial h}{\partial x} + \cot\theta h^3 \frac{\partial h}{\partial y} - h^3\right)$$

(3.6b)

It follows, therefore, that locally the depth-averaged equation of continuity for the flow can be stated as:

$$\frac{\partial h}{\partial t} + \nabla Q = 0$$

(3.7a)

i.e.

$$\frac{\partial h}{\partial t} = -\left(\frac{\partial Q_x}{\partial x} + \frac{\partial Q_y}{\partial y}\right)$$

(3.7b)

Finally, by differentiating (3.6) with respect to x and y, and inserting into (3.7), one obtains the following equation

$$\frac{\partial h}{\partial t} = \frac{\rho g \sin\theta}{3\mu}\left\{\cot\theta \frac{\partial}{\partial y}\left(h^3 \frac{\partial h}{\partial y}\right) + \cot\theta \frac{\partial}{\partial x}\left(h^3 \frac{\partial h}{\partial x}\right) - \frac{\partial h^3}{\partial x}\right\}$$

(3.8a)

which we combine with the volume constraint

$$Volume = \int_{x_T}^{x_N} \int_{-y_P(x)}^{y_P(x)} h \, dy \, dx = St^{\alpha}$$

(3.8b)

where S is a constant of proportionality between the flow volume and t^{α}; when $\alpha = 1$, $S = Q$, the uniform flow rate, with units of $m^3 s^{-1}$. If one can solve (3.8), which describes the evolution of the height of the flow, one can map the boundaries of the flow in space and time. To achieve this, in non-dimensionalising (3.8), one first needs to derive typical spatial and temporal scales for the system. This can be achieved through the simple dimensional analysis of (3.8), converting the equations to purely dimensional relationships of H (a 'height'), L (i.e. a 'length' distinct from the far

smaller magnitude height, H) & T ('time'). Assuming that through simple geometric considerations X~Y~L and that H $\cot\theta \sim$ X, one arrives at

$$\frac{H}{T} \sim R\left(\cot\theta\frac{H^4}{L^2}+\cot\theta\frac{H^4}{L^2}-\frac{H^3}{L}\right)$$

(3.9a)

and

$$\text{Volume} \sim \mathcal{S}T^{\alpha} \sim HL^2$$

(3.9b)

where $R=\rho g \sin\theta/3\mu$. By substituting (3.9b) in (3.9b), the following scales become apparent

$$T^*=\left(\frac{\cot^5\theta}{\mathcal{S}R^3}\right)^{1/\alpha+3} \quad \text{and} \quad L^*=X^*=Y^*=H^*\cot\theta=\left(\frac{\mathcal{S}\cot^{2\alpha+1}\theta}{R^{\alpha}}\right)^{1/\alpha+3}$$

(3.10a,b)

Lister then uses the above scales to define the following dimensionless variables $T=t/T^*$, $X=x/X^*$, $Y=y/Y^*$ and $H=h/H^*$, and recasts (3.8) in these dimensionless variables, resulting in

$$\frac{\partial H}{\partial T}=\frac{\partial}{\partial Y}\left(H^3\frac{\partial H}{\partial Y}\right)+\frac{\partial}{\partial X}\left(H^3\frac{\partial H}{\partial X}\right)-\frac{\partial H^3}{\partial X}$$

(3.11a)

$$\int_{X_T}^{X_N}\int_{-Y_P(X)}^{Y_P(X)} H\,dY\,dX = T^{\alpha}$$

(3.11b)

In analysing (3.11), and looking for asymptotic balances, which may indicate regimes of behaviour at both early and later stages of the evolution, Lister rescales (3.11) to show bimodal, time-dependent modes of behaviour. For the sake of brevity, these 'early' and 'long-time' rescalings of (3.11) are not presented in formulation here, but the outcomes of such rescalings are important and shall be discussed.

In the early stages of the flows evolution, the solution of a rescaled (3.11) is identical to that given by Huppert (1982) for the spread of a gravity current on a horizontal plane, with the dominant factor in its extension being the surface gradient of the flow. This is considerably in excess of the tank incline in the initial stages (i.e. $\partial h/\partial x >> \tan\theta$): slope is unimportant and the gradient of current thickness defines spreading dynamics.

Then, at some time ~ T^*, there is a transition in flow behaviour towards the long-time scaling, as the length of the flow increases and the surface gradient over the flow becomes very much less than the angle of the slope (i.e. $\tan\theta >> \partial h/\partial x$). The latter is now the dominant factor, and of far greater magnitude than the gradient of current thickness. At the time of transition between early and long-time cases, the current dimensions x_N, y_M and h are typically equal to the scales X^*, Y^* and H^*.

From these early- and long-time rescalings, one can then derive dimensionless relationships for the progression of X_N and Y_M in terms of T (where X_N and Y_M are the maximum down- and cross-slope extents x_N and y_M, normalised by X^* and Y^*). For the early-time case, the asymptotic dependence of the these dimensions can be deduced from the scalings, giving

$$X_N = Y_M \sim T^{\frac{3\alpha+1}{8}} \tag{3.12}$$

which dimensionalises (on application of X^* or Y^*, and T^*) to

$$x_N = y_M \sim \left(S^3 \mathrm{R}' \cos\theta t^{3\alpha+1}\right)^{\frac{1}{8}} \tag{3.13}$$

Similarly from the long-time rescalings, the following dimensionless relationships are obtained:

$$X_N \sim T^{\frac{4\alpha+3}{9}} \qquad \text{and} \qquad Y_M \sim T^{\frac{\alpha}{3}} \tag{3.14a,b}$$

These can also be dimensionalised, using the scales X^*, Y^* and T^* (3.10), to gain

$$x_N \sim \left(\frac{S^4 R'^3 \sin^5\theta t^{4\alpha+3}}{\cos^2\theta} \right)^{\frac{1}{9}} \quad \text{and} \quad y_M \sim \left(\frac{S\cos\theta t^{\alpha}}{\sin\theta} \right)^{\frac{1}{3}} \tag{3.15a,b}$$

where in both (3.13) and (3.15) $R' = \rho g/3\mu$.

These asymptotic scalings provide some interesting information. Firstly, at early times ($t<<T^*$, and dependent on the magnitudes of $\partial h/\partial x$ and $\tan\theta$) the gravity current behaves in a manner similar to an extrusion on a horizontal slope. Secondly, when has fluid has spread for long enough so that $\tan\theta >> \partial h/\partial x$ ($t>>T^*$) the cross-slope extent advances wholly independently of viscosity, and is only dependent on the angle of the incline and the fluid flow rate.

Lister investigated a variety of solutions for different cases of flow behaviour, including similarity solutions of the structure near the source and the contact line in the long-time regime, analytical solutions of two-dimensional cases, and actual numerical solutions of the evolution equations for a variety of values of α. Here we will consider only two: the solution to (3.11), which is gained by numerically integrating that equation (or an equation for the approach to the long-time similarity solution derived from its form), and the simple scalings (3.14, 3.15) produced from the long-time rescalings of (3.11). The results of these analyses shall be reviewed and compared with actual isothermal experimental data in the next section.

3.4 Isothermal experiments—experimental observations

Five isothermal experiments were conducted to test the functionality of the apparatus and compare the subsequent results obtained with those of Lister (1992). The procedure for these experiments was as described in Section 3.2, with both the ambient and the extrusion temperatures being held at ~21°C (room temperature). The parameters for these experiments are listed in **Table 3.1** (see Section 3.1.2).

Data were taken for the flow length, maximum width, height and aspect ratio of these extrusions. As will be shown, these isothermal experimental data gave excellent agreement with both the experimental data and theoretical predictions of Lister (1992), and confirmed the ability of the apparatus to maintain a steady flux onto the tank base. The brief following analysis of these data will provide an illuminating and useful isothermal experimental benchmark with which we may compare later, cooled extrusions.

To reprise: initially, at very early times, Lister (1992) predicts that the extruded isothermal Golden Syrup should spread according to the similarity solution of Huppert (1982), with flow advance being driven by the local surface gradients of the fluid; i.e. the flow was not affected by the slope angle ($\partial h/\partial y$ and $\partial h/\partial x$ both >> $\tan\theta$). Given a steady, constant flux at the source, the flows should advance at an approximate rate of $x_N \sim t^{1/2}$ (eq. 3.13).

As the flow propagates in the downslope direction, it will eventually reach a point where $\partial h/\partial x <<$ $\tan\theta$, and the downslope expansion will change from a process dominated by surface depth gradients to one dominated by the downslope component; the change visibly occurring at earlier times for flows of lower flow rates and/or on steeper slopes, as predicted by (eq. 3.10a). Lister (1992) showed that this 'transition time' is a strong function of slope angle and flow rate, and can be readily obtained by dimensional analysis. For an isoviscous flow of continual flow rate from a point source it can be scaled as:

$$T^* \sim \left(\frac{27\mu^3 \cot^5\theta}{S\rho^3 g^3 \sin^3\theta} \right)^{\frac{1}{4}} \tag{3.16}$$

where the notation is described in section 3.3. Typically, for the parameters inherent in the five isothermal experiments, $T^*<10$ (see **Table 3.1**). The benefit of such small values of T^* is that for the majority of their extrusion history flows will lie within the long-time spreading regime. This will

prove important in the later study of cooled flows, as any changes witnessed can be ascribed to the effects of cooling, rather than an affect peculiar to the isothermal model.

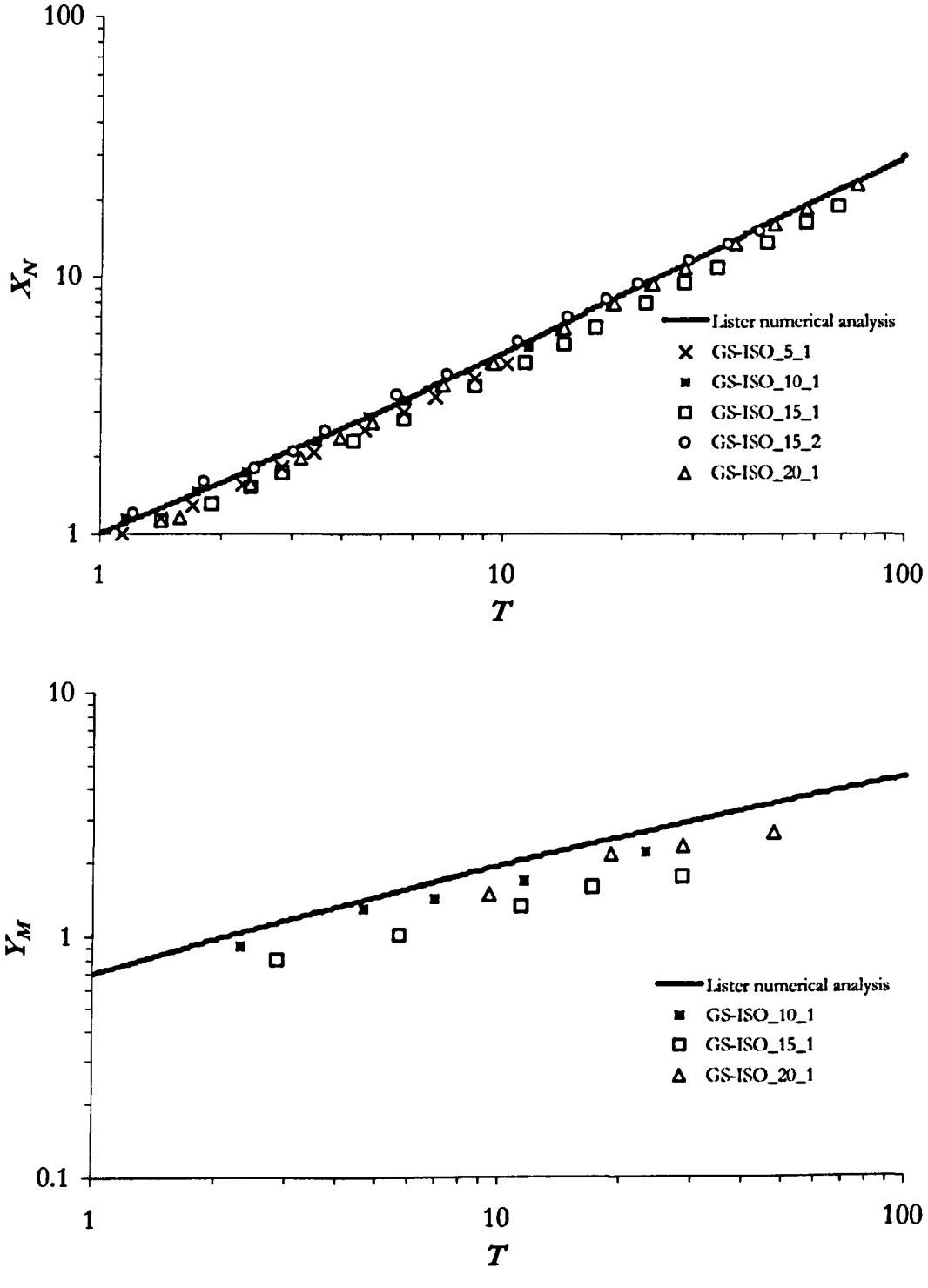

Figure 3.2 Plots of dimensionless downslope (X_N) and cross-slope (Y_M) extent versus dimensionless time (T). Observed experimental values of x_N and y_M at any given t have been normalised by the scales X^*, Y^* and T^*, respectively. The scales are calculated using (eq. 3.10), and representative values are collected in **Table 3.1.** They are compared with an unsmoothed numerical solution of (eq. 3.11), using a scheme as noted in section 3.3, kindly provided by John Lister. Due to an equipment malfunction, values for y_M were not recorded for GS-ISO_5_1 and GS-ISO_15_2.

Although T^* is a useful scale, there is no sudden transition between regimes at this value, and a full solution of (eq. 3.11) shows that flows display a behaviour intermediate to the early and long time solutions over a range of times of magnitude ~ $0.1T^*$ to $10T^*$ (see Lister 1992: Figure 1). Given the values of T^* encountered in the isothermal experiments, ~ 6 to 100 s (see **Table 3.1**), it is not possible to spot any extended spreading accordant to the early-time solution alone, even in the experiment GS-ISO_5_1.

A brief analysis suffices to show that the experimental data mimic Lister's model well: **Figure 3.2** uses an unsmoothed plot of Lister's own raw numerical results to (eq. 3.11) (including numeric 'noise'), kindly provided for this thesis. Lister noted that for the extrusion of some of his analogues in air, there was a slight deviation in the experimental values from those predicted by the model. He found that the advance of the flow toe downslope was increased relative to the predictions of the model, while cross-slope spreading was decreased relative to that predicted by the numerical model.

Similarly, the flows extruded in our isothermal experiments displayed little deviation from the numerical analysis. In the downslope direction, one can find no evidence of lengthening relative to the model predictions (**Fig. 3.2**). Cross-slope spreading, however, was slightly less than predicted by the solution of (eq. 3.11), as was also witnessed in the experimental flows of Lister. The absolute values of cross-slope propagation alone are reduced; the trend of expansion itself closely follows the numerical predictions. Accurate height measurements across the flow could not be adequately measured to the degree that we can incontrovertibly account for the extra volume vertically, but the stability of the flux in the apparatus (see section 2.2) would indicate that the minimal volume lost from the flanks was 'bulked up' rather than focused down flow, resulting in a greater flow thickness.

Irrespective of the magnitude of data points relative to those predicted by Lister's model, the trends of cross- and downslope advance still conform excellently to the power-law relationships predicted, and provide a useful and stable analytical base from which we can investigate the effects of cooling. The influence of experimental parameters on the flow at any point in time can be analysed with reference to the dimensionless parameters X_N, Y_M and T. For example, **Plate 3.1** shows three snapshots of isothermal flows, taken at the same absolute time in their evolution (~ 100 s) at similar flow rates (~ 2 $cm^3\ s^{-1}$), but different values of θ. One can clearly see that (c) has advanced considerably further downslope than (a), has less of an axisymmetric profile as it is well-advanced into the late-time solution $x_N \sim t^{1/9}$. Conversely analysis of video data shows that (a) is at present still spreading in the upslope direction, whilst at a similar time both (b) and (c) are stagnant. Still, there is considerable elongation of (a) in the downslope direction, highlighting the fact that the influence of the slope can be felt long before T^*.

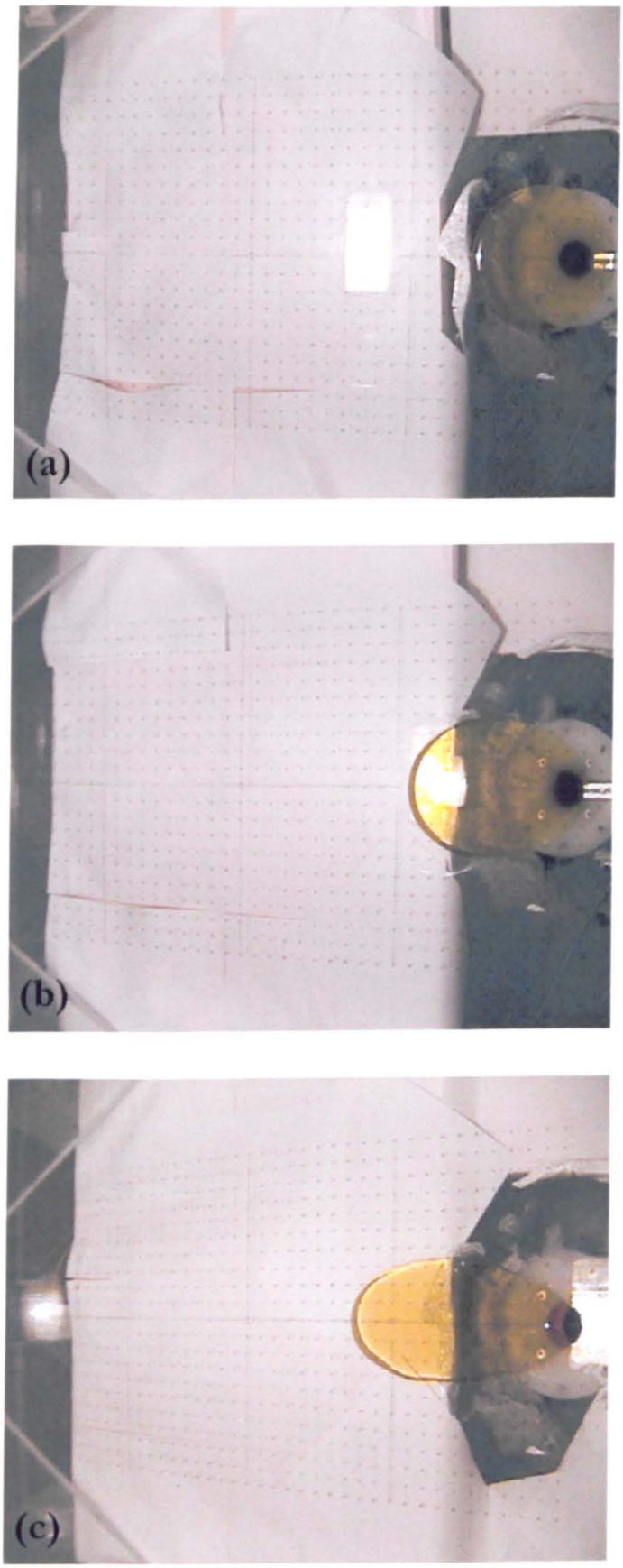

Plate 3.1 Photographs of three flows of similar flow rates, taken after c. 100 seconds: (a) GS-ISO_5_1: Q~1.84cm^{3}s^{-1}; t~T^*; (b) GS-ISO_10_3: Q~1.92cm^{3}s^{-1}; t~$4T^*$; (c) GS-ISO_20_1: Q~1.90cm^{3}s^{-1}; t~$17T^*$.

3.5 Cooled experiments—experimental observations

The twenty-six experiments wherein cooling was a factor displayed a wealth of interesting and novel flow features. Both morphologically and dynamically, the cooled syrup flows differed from the theoretical predictions and experimental precedents set for isothermal syrup flows by workers such as Huppert (1982) and Lister (1992). The observed differences between the flow behaviour of cooled and isothermal flows will be separated, with discussion of variances on both a quantitative (with reference to kinematic and spatial characteristics) and qualitative level. The implications and extended analytical approaches to these results, and their comparison with real lavas witnessed in the field, are presented in Chapter 5.

3.5.1 Kinematic and spatial observations

The maximum downslope (x_N) and cross-slope (y_M) extents of analogue flows at any given time (t) were collated from digitised flow-plan images. Similarly, central flow heights at a given downslope coordinate (x) and time-step were collected for many flows. Where pertinent, elements of these data are presented in the following text, but a more comprehensive overview of the experimental results and raw data is contained within **Appendix A.**

3.5.1.1 Development of downslope extent with time

It has been demonstrated (e.g. Stasiuk et al. 1993) that for similar values of flow rate and eruption viscosity, cooled viscous flows are significantly retarded in their expansion relative to the isothermal case. The gross mechanism for this effect is readily apparent, in that with the interaction of cooling and a strongly temperature-dependent viscosity, a cooled, highly viscous boundary layer forms. Locally, this sluggish layer acts as a bulwark to expansion, and the flow as a whole behaves as if it possesses a 'bulk viscosity' somewhere between the viscosity of syrup at the ambient temperature (T_a) η_a, and viscosity at eruption temperature (T_e) η_e, if such a concept is remotely applicable (Stasiuk et al. 1993, Lister and Kerr 1993, Griffiths 2000).

Raw data, listing values of x_N with respect to t are displayed in **Appendix A.** A sample of these data is presented in **Figure 3.3a.** It is readily seen that the cooled flows spread more slowly than is predicted by Lister's numerical model (eq. 3.11) or long-time similarity solution (eq. 3.14): at any given point in time, their magnitude of advance (x_N) and rate of advance ($\partial x_N / \partial t$) are retarded relative to the isothermal case. While the depiction of data in this manner is useful, we also present the results in a non-dimensional fashion, normalising recorded values of x_N and t with the scales X^* and T^*, respectively. **Figures 3.4a** to **3.7b** display plots of X_N vs. T, arranged by temperature and slope.

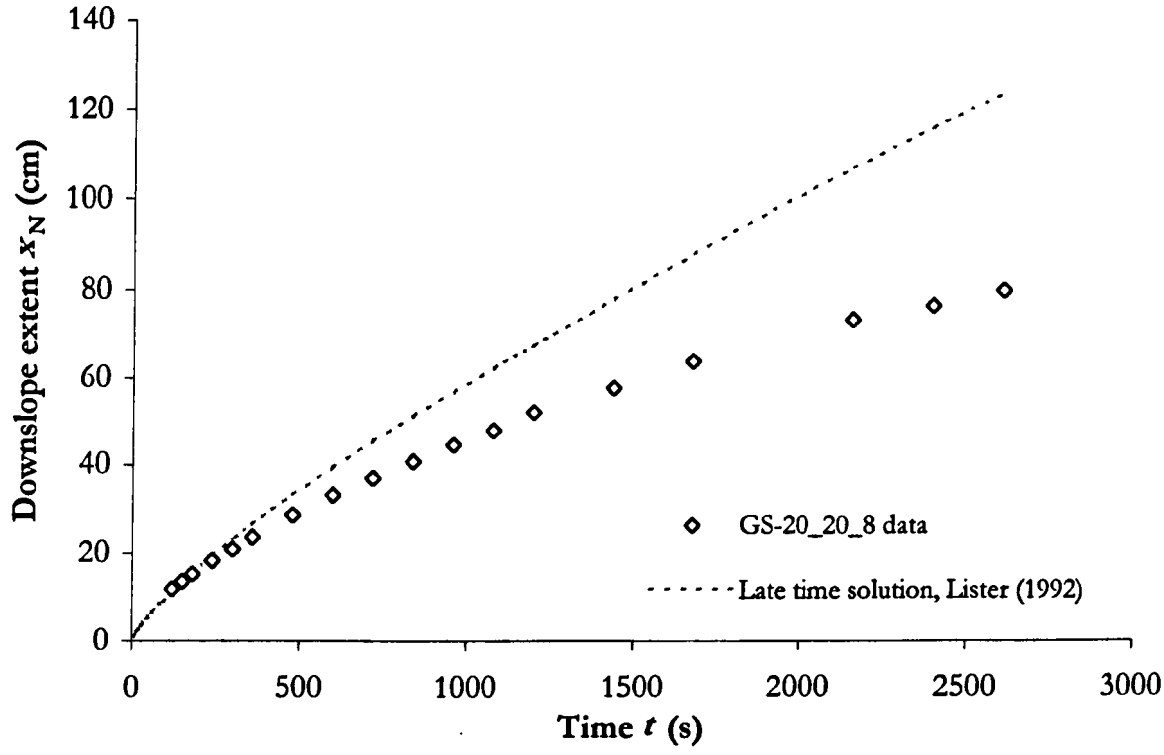

Figure 3.3a Plot showing the development of downslope extent (x_N) with time (t) for a sample flow, in this case extruded at 0.7 cm s^{-1} onto a slope of 20° in an ambient environment of –19°C. The extents predicted by Lister's (1992) long-time similarity solution are shown for comparison.

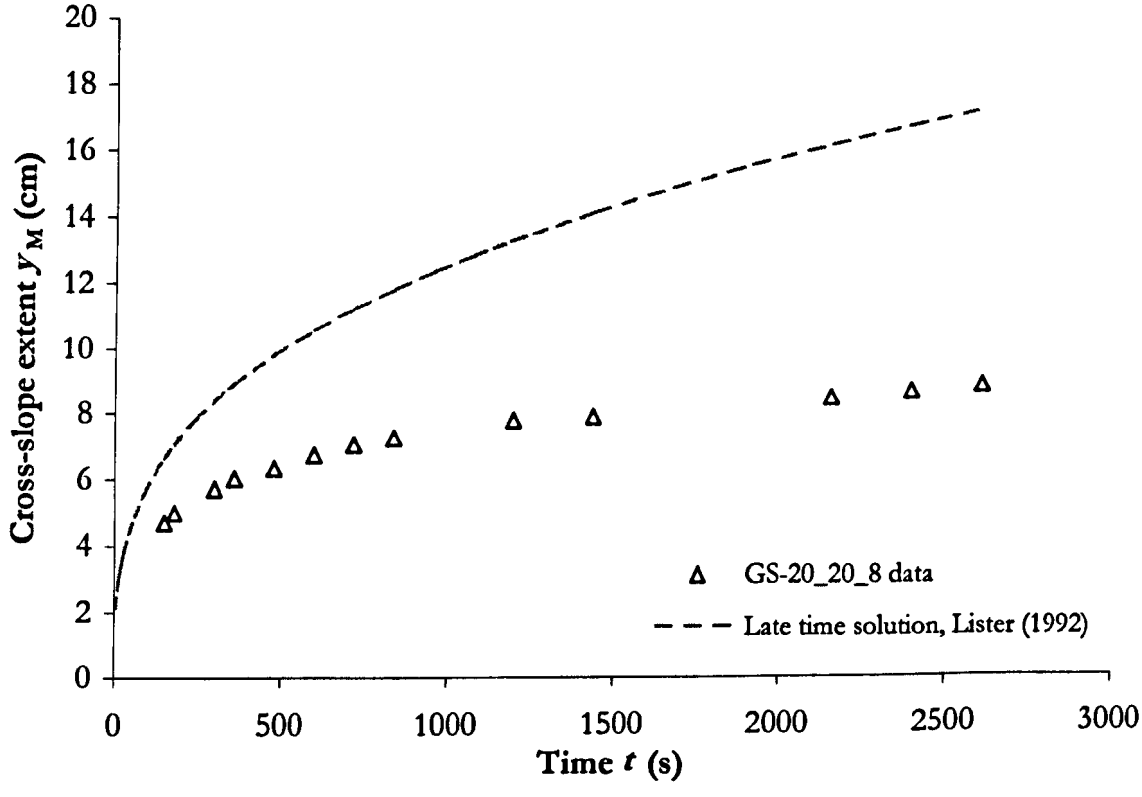

Figure 3.3b Plot showing the development of cross-slope extent (y_M) with time (t) for a sample flow, in this case extruded at 0.7 cm s^{-1} onto a slope of 20° in an ambient environment of –19°C. The extents predicted by Lister's (1992) long-time similarity solution are shown for comparison.

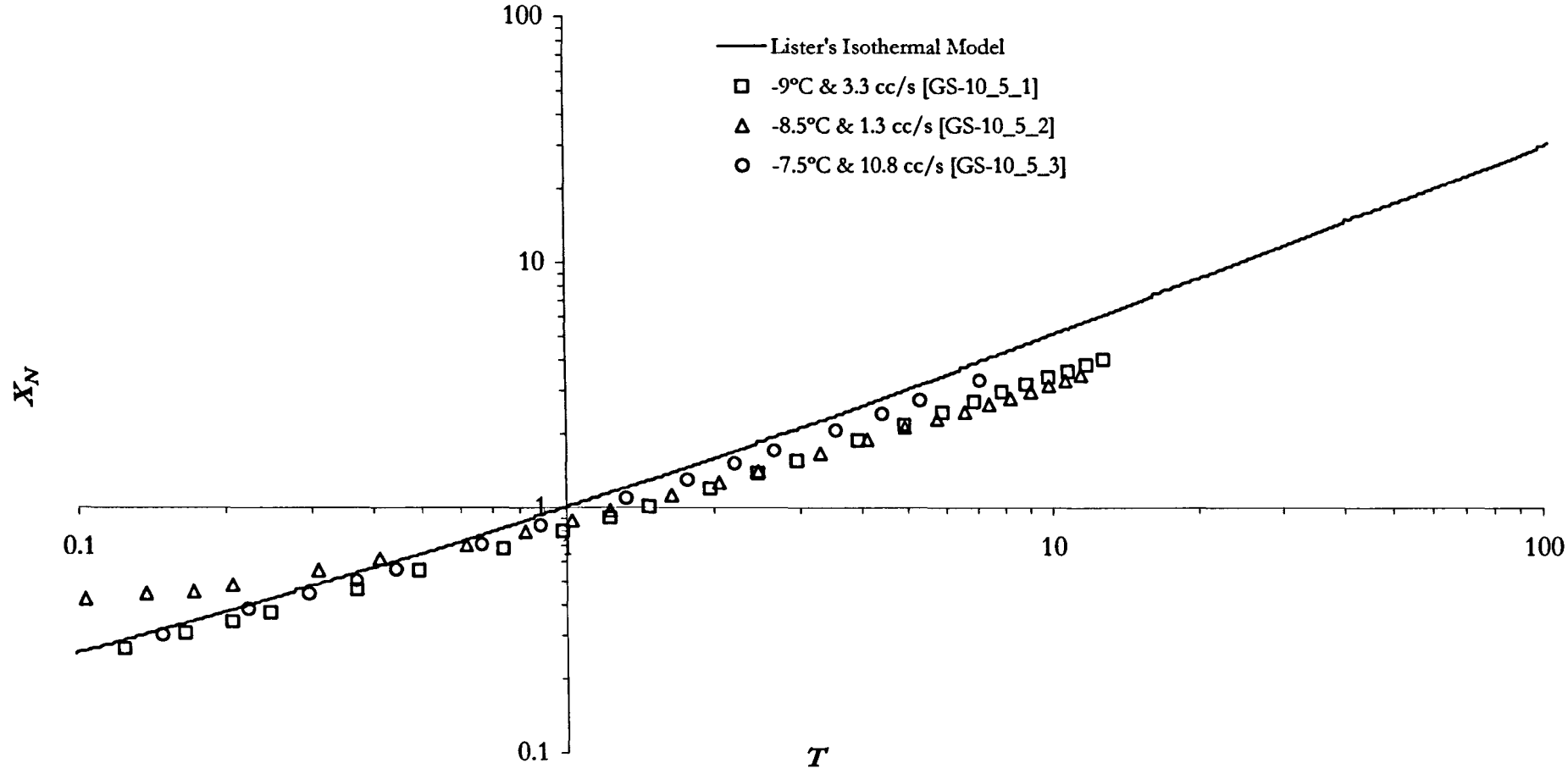

Figure 3.4a Comparison of cooling flows with the same ambient temperature (-10°C), same slope (5°) and different flow rates, plotted as the maximum dimensionless downslope extents of the flow (X_N) with dimensionless time (T). Recorded experimental values of x_N for a given t are normalised by the scales X^* and T^*, respectively. Experimental parameters: **GS-10_5_1**—T_a –9°C, T_e 19.5°C, Q 3.3 x10^{-6} m^3 s^{-1}, X^* 16.7, T^* 122.3, η_e 64 Pa s, η_a ~34,000 Pa s; **GS-10_5_2**—T_a –8.5°C, T_e 20°C, Q 1.3 x10^{-6} m^3 s^{-1}, X^* 12.8, T^* 146.3, η_e 59 Pa s, η_a ~29,000 Pa s; **GS-10_5_3**—T_a –7.5°C, T_e 22°C, Q 10.8 x10^{-6} m^3 s^{-1}, X^* 20.3, T^* 67.9, η_e 43.3 Pa s, η_a ~ 22,000 Pa s.

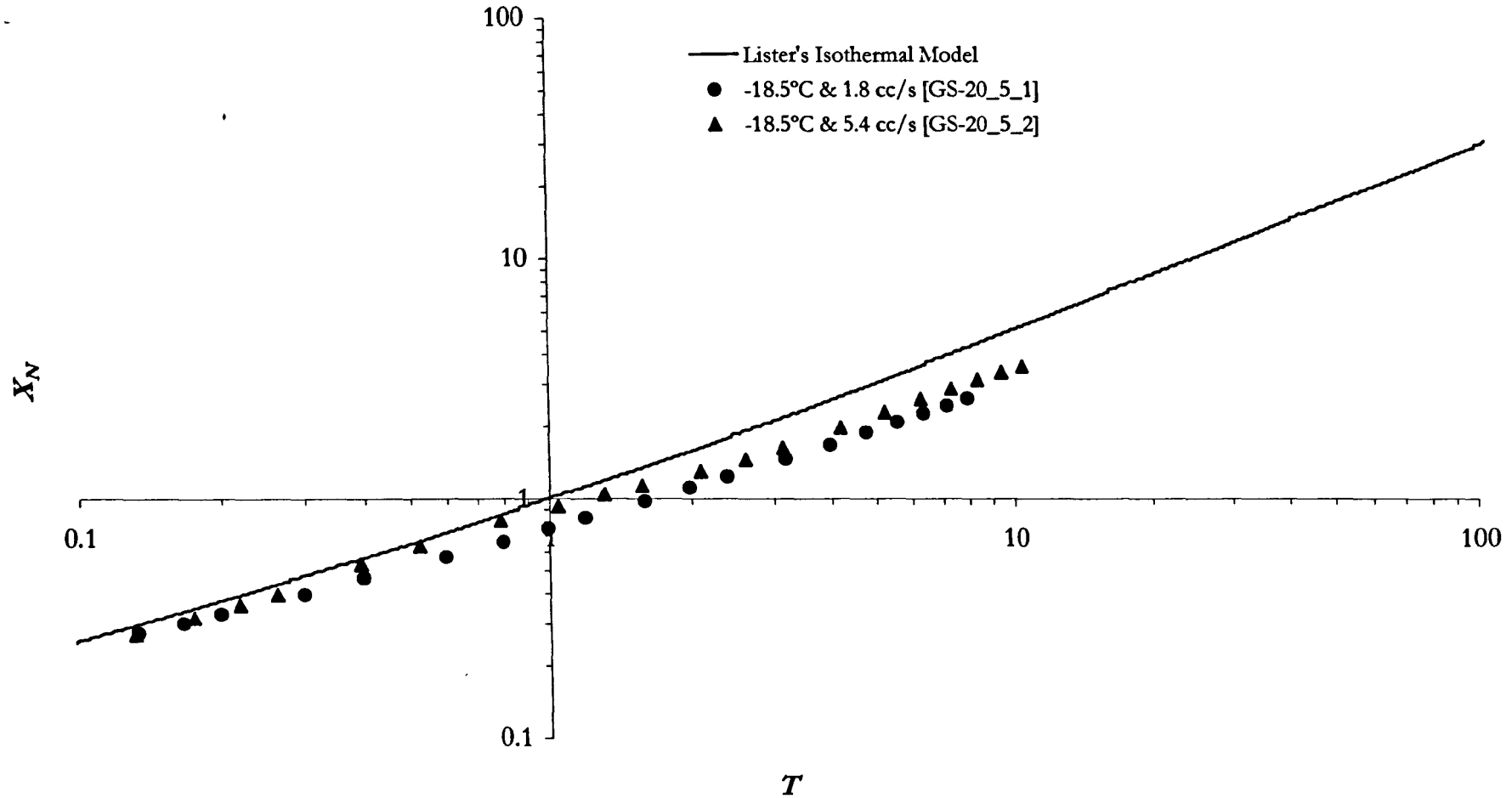

Figure 3.4b Comparison of cooling flows with the same ambient temperature (-20°C), same slope (5°) and different flow rates, plotted as the maximum dimensionless downslope extents of the flow (X_N) with dimensionless time (T). Recorded experimental values of x_N for a given t are normalised by the scales X^* and T^*, respectively. **GS-20_5_1**—T_a –18.5°C, T_c 19°C, Q 1.8 x10^{-6} m^3 s^{-1}, X^* 14.6, T^* 151.5, η_c 69.4 Pa s, η_a ~8.9 x10^5 Pa s; **GS-20_5_2**—T_a –18.5°C, T_c 19°C, Q 5.5 x10^{-6} m^3 s^{-1}, X^* 19.2, T^* 115.1, η_c 69.4 Pa s, η_a ~8.9 x10^5 Pa s.

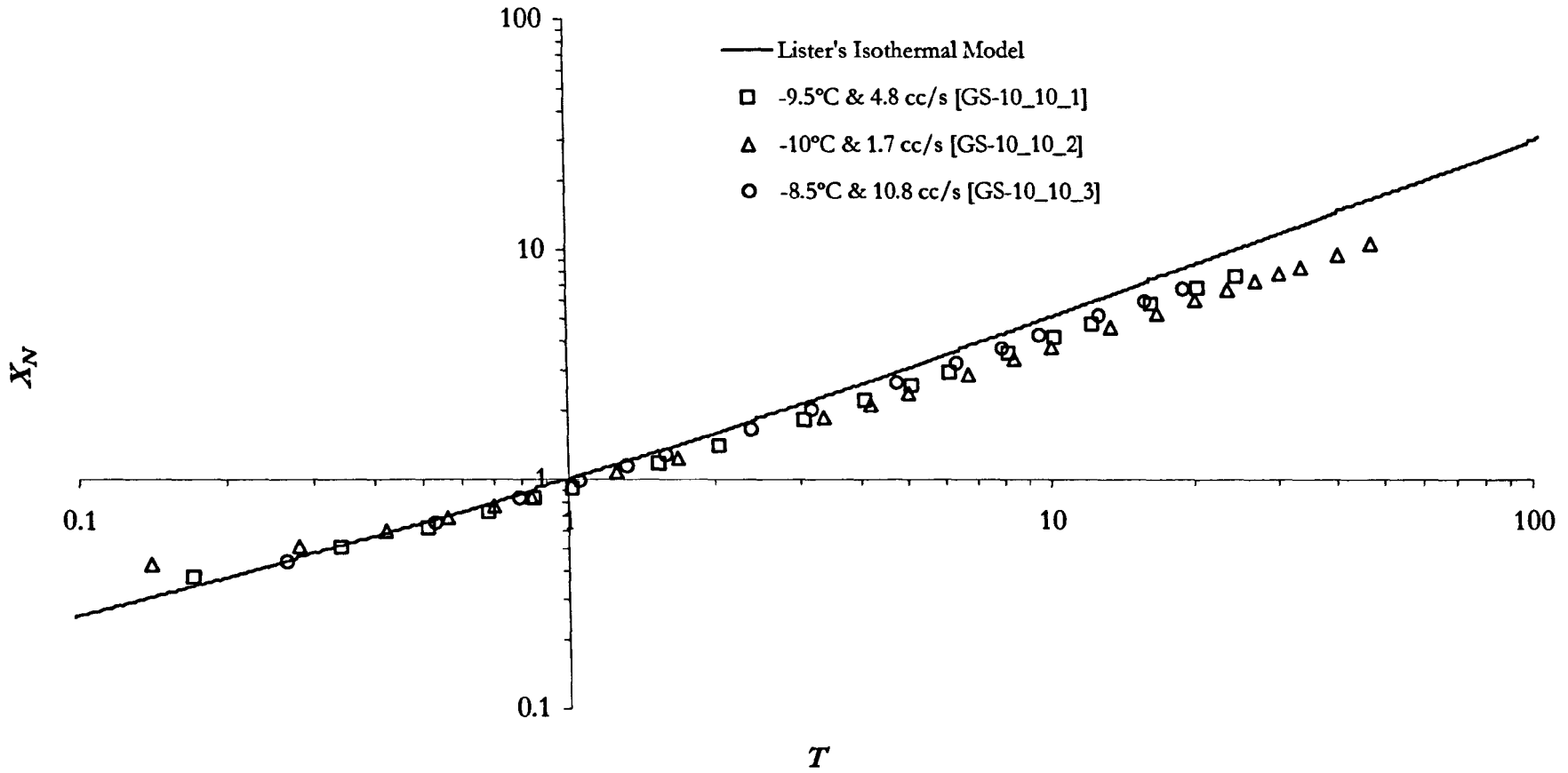

Figure 3.5a Comparison of cooling flows with the same ambient temperature (-10°C), same slope (10°) and different flow rates, plotted as the maximum dimensionless downslope extents of the flow (X_N) with dimensionless time (T). Recorded experimental values of x_N for a given t are normalised by the scales X^* and T^*, respectively. Experimental parameters: **GS-10_10_1**—T_a –9.5°C, T_c 19°C, Q 4.8 x10^{-6} m^3 s^{-1}, X^* 9.3, T^* 29.4, η_c 69.4 Pa s, η_a ~39,500 Pa s; **GS-10_10_2**—T_a –10°C, T_c 19.5°C, Q 1.7 x10^{-6} m^3 s^{-1}, X^* 7.0, T^* 35.8, η_c 64 Pa s, η_a ~46,000 Pa s; **GS-10_10_3**—T_a –8.5°C, T_c 21°C, Q 10.8 x10^{-6} m^3 s^{-1}, X^* 10.5, T^* 18.9, η_c 50.5 Pa s, η_a ~ 29,000 Pa s.

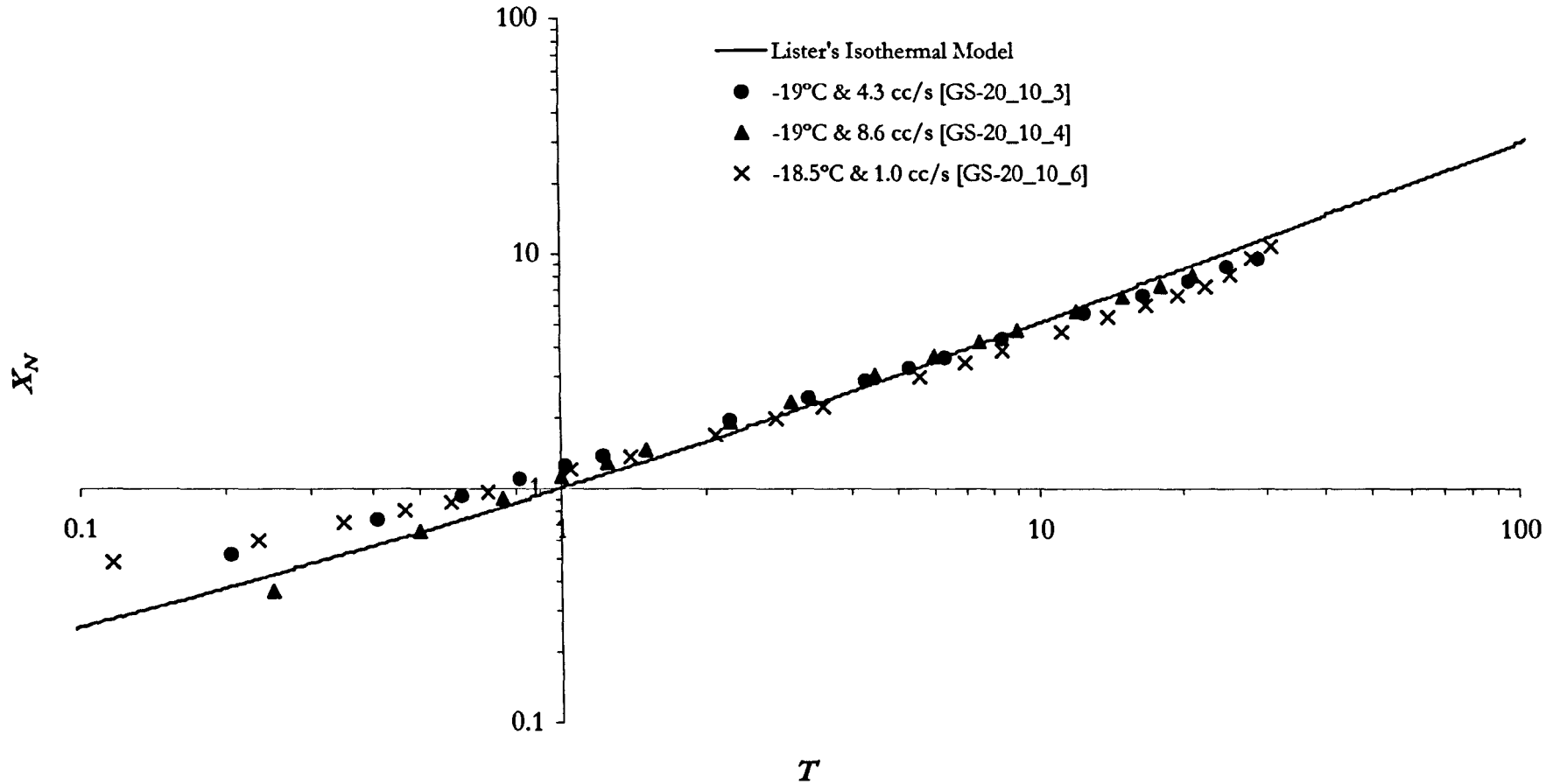

Figure 3.5b Comparison of cooling flows with the same ambient temperature (-20°C), same slope (10°) and different flow rates, plotted as the maximum dimensionless downslope extents of the flow (X_N) with dimensionless time (T). Recorded experimental values of x_N for a given t are normalised by the scales X^* and T^*, respectively. Experimental parameters: **GS-20_10_3**—T_a –19°C, T_c 20.75°C, Q 4.3 x10^{-6} m^3 s^{-1}, X^* 8.4, T^* 24.5, η_c 52.5 Pa s, η_a ~1.1 x10^6 Pa s; **GS-20_10_4**—T_a –19°C, T_c 21°C, Q 8.6 x10^{-6} m^3 s^{-1}, X^* 9.9, T^* 20.0, η_c 50.5 Pa s, η_a ~1.1 x10^6 Pa s; **GS-20_10_6**—T_a –18.5°C, T_c 19°C, Q 1.0 x10^{-6} m^3 s^{-1}, X^* 6.3, T^* 43.0, η_c 69.4 Pa s, η_a ~8.9 x10^5 Pa s.

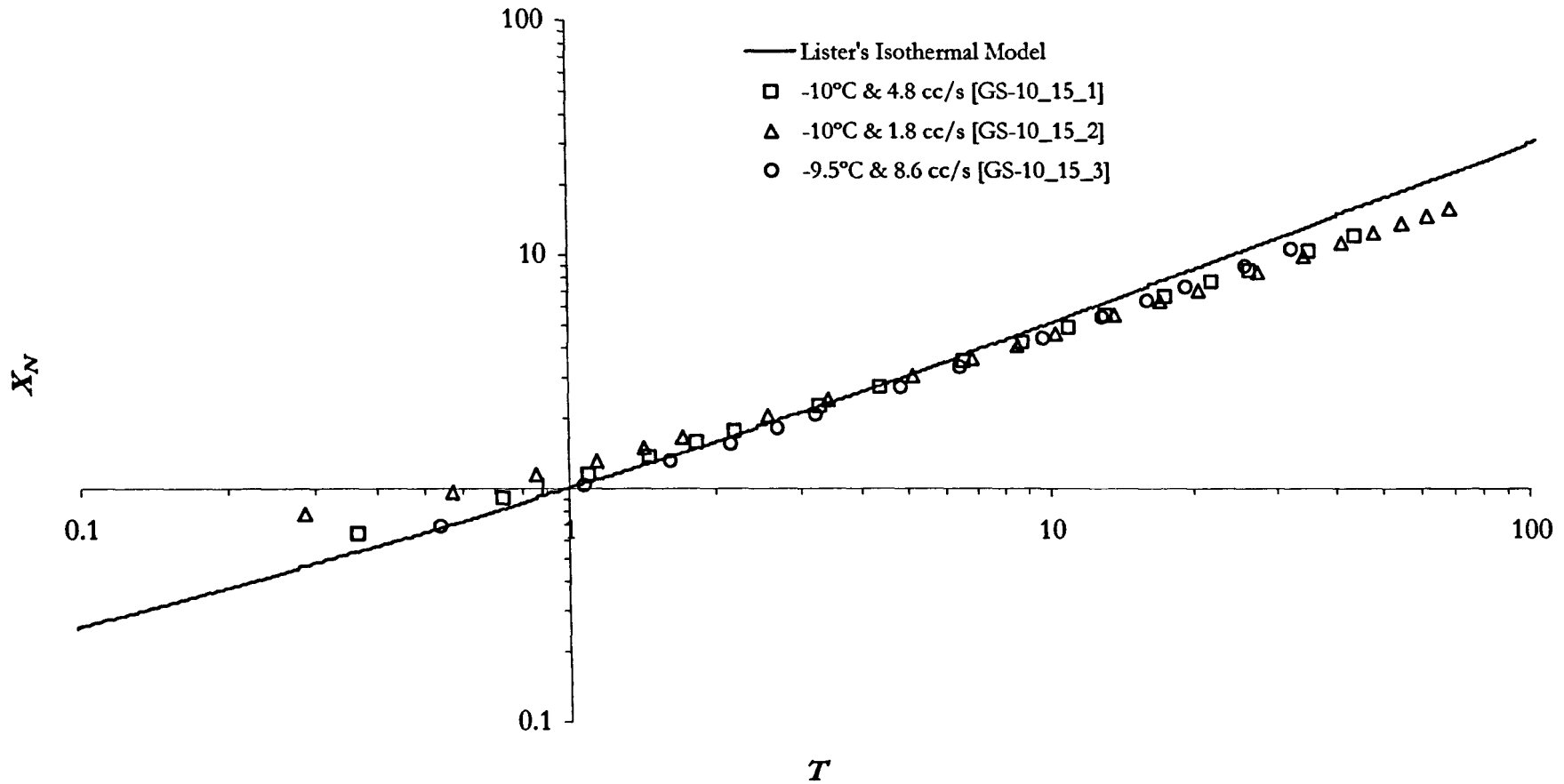

Figure 3.6a Comparison of cooling flows with the same ambient temperature (-10°C), same slope (15°) and different flow rates, plotted as the maximum dimensionless downslope extents of the flow (X_N) with dimensionless time (T). Recorded experimental values of x_N for a given t are normalised by the scales X^* and T^*, respectively. Experimental parameters: **GS-10_15_1**—T_a –10°C, T_c 18.5°C, slope angle 15°, Q 4.8 x10^{-6} m^3 s^{-1}, X^* 6.3, T^* 13.7, η_c 75.3 Pa s, η_a ~46,000 Pa s; **GS-10_15_2**—T_a –10°C, T_c 18.5°C, slope angle 15°, Q 1.8 x10^{-6} m^3 s^{-1}, X^* 4.9, T^* 17.6, η_c 75.3 Pa s, η_a ~46,000 Pa s; **GS-10_15_3**—T_a –9.5°C, T_c 20.5°C, slope angle 15°, Q 8.6 x10^{-6} m^3 s^{-1}, X^* 6.7, T^* 9.3, η_c 54.6 Pa s, η_a ~ 39,500 Pa s.

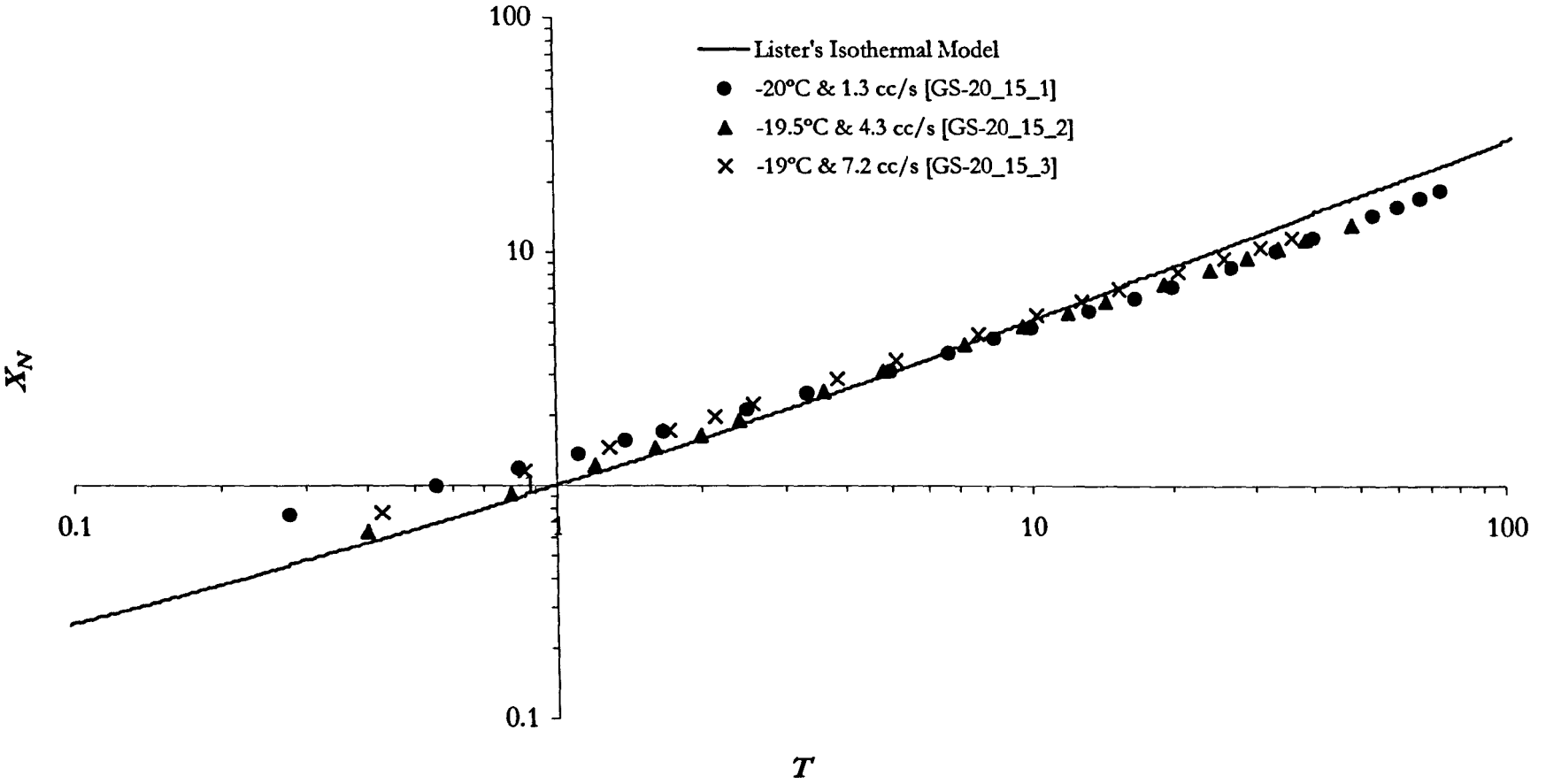

Figure 3.6b Comparison of cooling flows with the same ambient temperature (-20°C), same slope (15°) and different flow rates, plotted as the maximum dimensionless downslope extents of the flow (X_N) with dimensionless time (T). Recorded experimental values of x_N for a given t are normalised by the scales X^* and T^*, respectively. Experimental parameters: **GS-20_15_1**—T_a –20°C, T_c 20°C, Q 1.3 x10^{-6} m^3 s^{-1}, X^* 4.4, T^* 18.0, η_c 69.4 Pa s, η_a ~1.6 x10^6 Pa s; **GS-20_15_2**—T_a –19.5°C, T_c 19.5°C, Q 4.3 x10^{-6} m^3 s^{-1}, X^* 5.9, T^* 12.5, η_c 64 Pa s, η_a ~1.3 x10^6 Pa s; **GS-20_15_3**—T_a –19°C, T_c 20°C, Q 7.2 x10^{-6} m^3 s^{-1}, X^* 6.8, T^* 11.7, η_c 69.4 Pa s, η_a ~1.1 x10^6 Pa s.

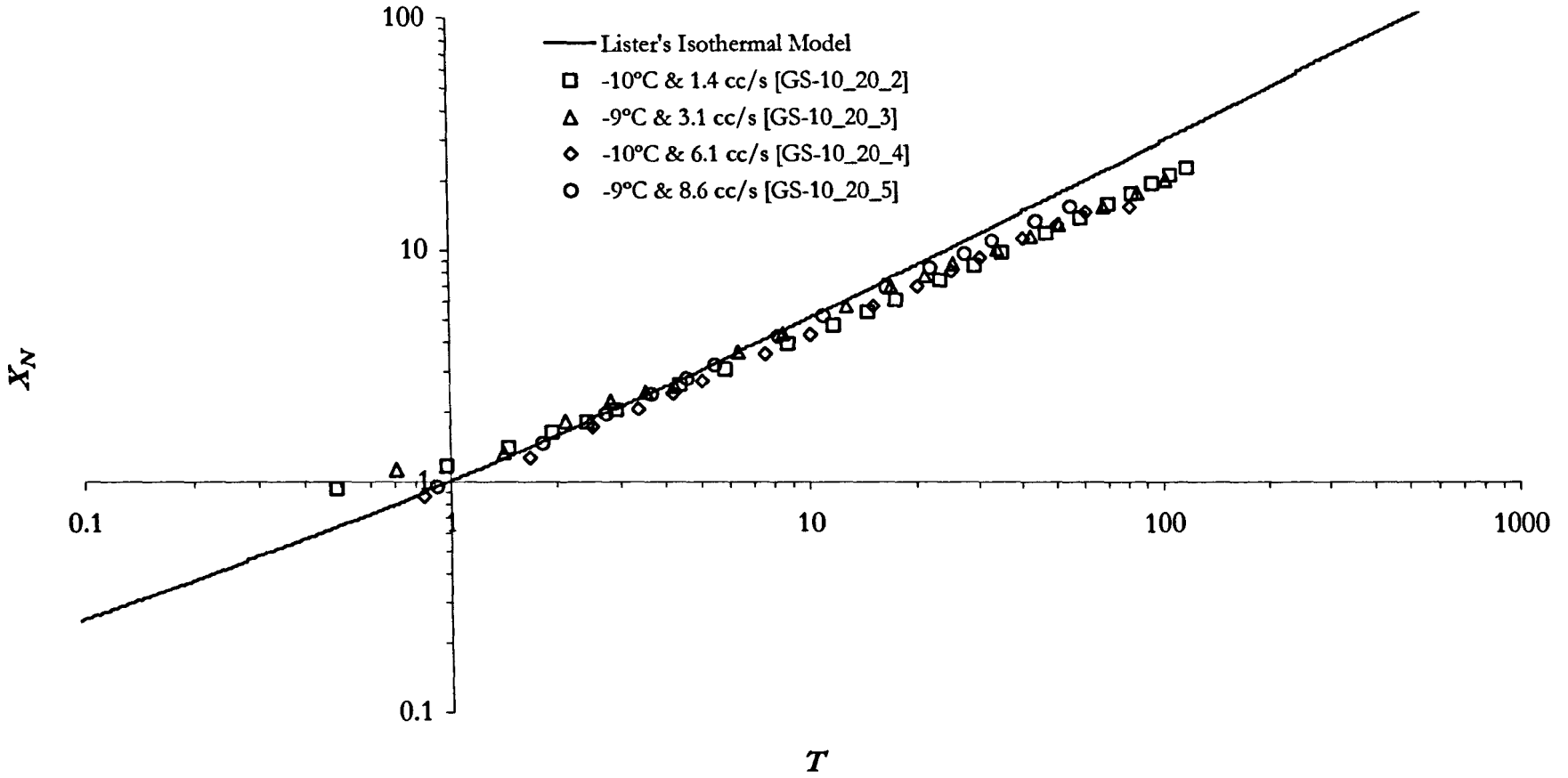

Figure 3.7a Comparison of cooling flows with the same ambient temperature (-10°C), same slope (20°) and different flow rates, plotted as the maximum dimensionless downslope extents of the flow (X_N) with dimensionless time (T). Recorded experimental values of x_N for a given t are normalised by the scales X^* and T^*, respectively. Experimental parameters: **GS-10_20_2**—T_a –10°C, T_c 18.5°C, Q 1.4 x10^{-6} m^3 s^{-1}, X^* 3.4, T^* 10.3, η_c 75.3 Pa s, η_a ~46,000 Pa s; **GS-10_20_3**—T_a –9°C, T_c 20°C, Q 3.1 x10^{-6} m^3 s^{-1}, X^* 3.9, T^* 7.1, η_c 59 Pa s, η_a ~34,000 Pa s; **GS-10_20_4**—T_a –10°C, T_c 20°C, Q 6.1 x10^{-6} m^3 s^{-1}, X^* 4.6, T^* 5.9, η_c 59 Pa s, η_a ~ 46,000 Pa s; **GS-10_20_5**—T_a –9°C, T_c 20°C, Q 8.6 x10^{-6} m^3 s^{-1}, X^* 5.1, T^* 5.5, η_c 59 Pa s, η_a ~ 34,000 Pa s.

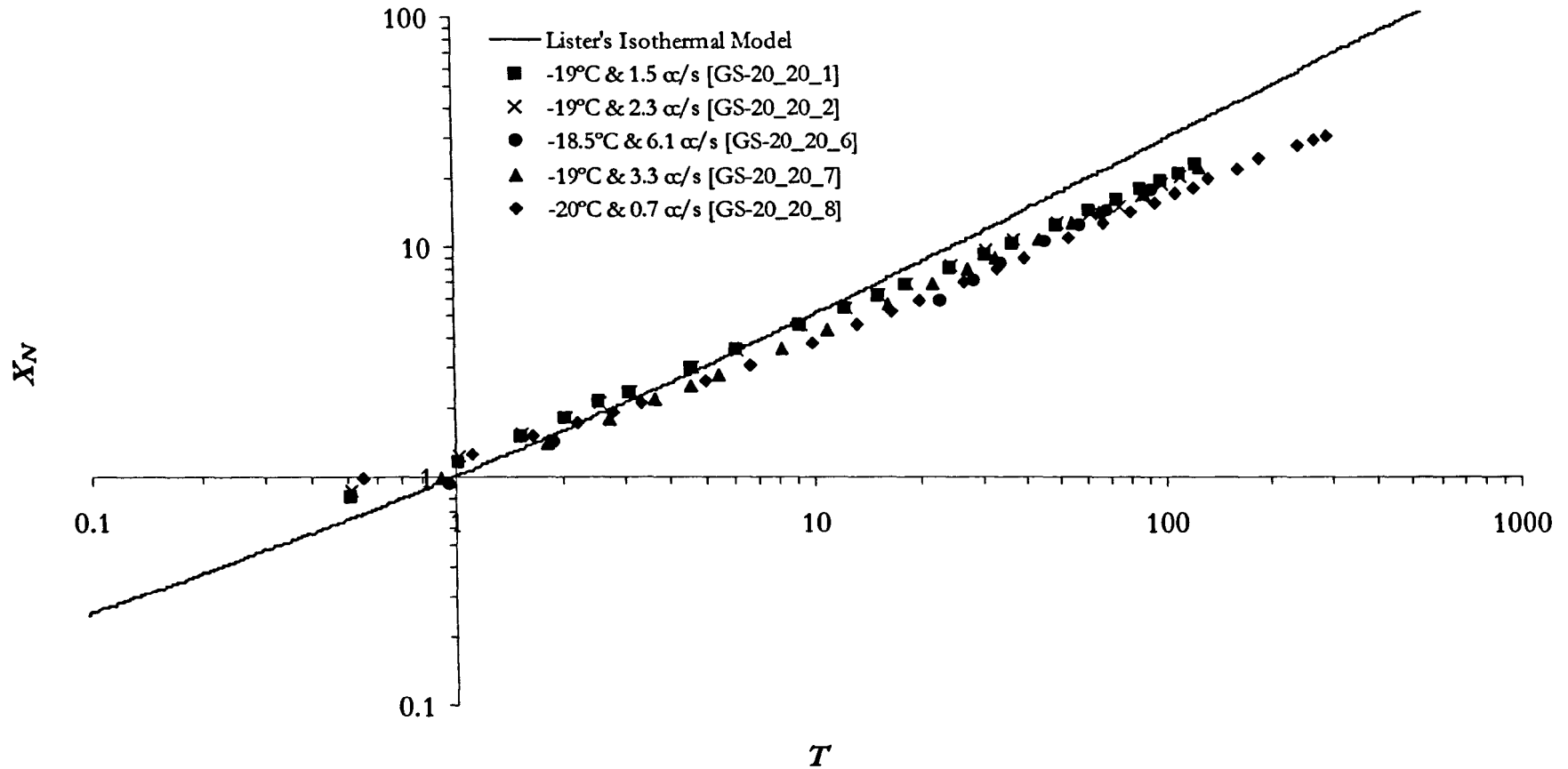

Figure 3.7b Comparison of cooling flows with the same ambient temperature (-20°C), same slope (20°) and different flow rates, plotted as the maximum dimensionless downslope extents of the flow (X_N) with dimensionless time (T). Recorded experimental values of x_N for a given t are normalised by the scales X^* and T^*, respectively. Experimental parameters: **GS-20_20_1**—T_a –19°C, T_e 18.75°C, Q 1.5 x10^{-6} m^3 s^{-1}, X^* 3.4, T^* 9.9, η_e 72.3 Pa s, η_a ~1.1 x10^6 Pa s; **GS-20_20_2**—T_a –19°C, T_e 18°C, Q 2.3 x10^{-6} m^3 s^{-1}, X^* 3.9, T^* 9.7, η_e 81.7 Pa s, η_a ~1.1 x10^6 Pa s; **GS-20_20_6**—T_a –18.5°C, T_e 21°C, Q 6.1 x10^{-6} m^3 s^{-1}, X^* 4.5, T^* 5.3, η_e 50.5 Pa s, η_a ~8.9 x10^5 Pa s; **GS-20_20_7**—T_a –18°C, T_e 22°C, Q 3.3 x10^{-6} m^3 s^{-1}, X^* 3.7, T^* 5.5, η_e 43.3 Pa s, η_a ~7.3 x10^5 Pa s; **GS-20_20_8**—T_a –19°C, T_e 21°C, Q 0.7 x10^{-6} m^3 s^{-1}, X^* 2.6, T^* 9.0, η_e 50.5 Pa s, η_a ~1.1 x10^6 Pa s.

These dimensionless plots permit a more ready correlation of different data sets, as they allow the examination of flows of different parameters on the same figure. While plotting multiple experiments possessing identical values in two of the controlling parameters we can investigate the influence of the third—in this manner we can assess the relative interaction of flow rate, level of cooling and slope angle on the flows' dynamics.

The scale X^* should have no dynamical bearing on the cooled flows themselves. As explained in Section 3.3, this scale is derived and calculated with sole regard to Lister's (1992) isothermal case, and cannot describe the influence of a temperature-dependent viscosity on the transition between early and long-time spreading regimes. Nevertheless, by treating the cooled flows in this 'isothermal manner' we can qualitatively observe the differences between theory and practice. The implications of altering the theory to accommodate heterogeneous viscosities are discussed in Chapter 5.

Figures 3.4a to **3.7b** all depict flows that vary from the isothermal numerical model of Lister, and the close correlation depicted in **Figure 3.2.** A change in the magnitude or gradient of X_N vs. T indicates a variance from the isothermal model: either in magnitude of X_N at a given T, or in the rate of change of X_N with T. On a simple level, we would expect cooled flows to depart from the model in both these criteria, as evidenced by Stasiuk et al. (1993), and the experimental results conform to these expectations.

Generally speaking, the flows show a substantially reduced value of X_N at a given T, relative to the model. This reduction increases with decreasing flow rate, at constant ambient temperature and tank slope angle. Furthermore, the rate of increase of X_N with T is also retarded relative to the model, with the magnitude of retardation broadly and inversely proportional to the flow rate.

At temperatures of –10°C, experimental series GS-10_5 (**Figure 3.4a**) and GS-10_10 (**Figure 3.5a**) display a clear reduction in the magnitude of X_N relative to the model, exacerbated at larger values of T. Series GS-10_15 (**Figure 3.6a**) and GS-10_20 (**Figure 3.7a**) show a far smaller and less simple retardation. Clearer in all GS-10 series are well-evidenced changes in dX_N/dT, as experimental gradients decrease with decreasing flow rate, and splay away from Lister's numerical predictions, adopting shallower values.

These same features are broadly mimicked in series GS-20_5 (**Figure 3.4b**) and GS-20_10 (**Figure 3.5b**). Yet while the results depict an increasing retardation of X_N (T) relative to the model with decreasing flow rate, the variance is slight. Furthermore, though values of dX_N/dT for experiments do depart from Lister's prediction, it is impossible to distinguish changes in gradient between individual experiments themselves. These elements are compounded in series GS-20_15 (**Figure 3.6b**) and GS-20_20 (**Figure 3.7b**). In the former, an extremely weak range in magnitudes of X_N

(T) is apparent, but there is no clear distinction in the gradients dX_N/dT, other than that they are clearly shallower than in Lister's model. In GS-20_20, the data defy any attempt to characterise relative magnitudes of X_N (T) with Q, but do display some clear variations in dX_N/dT: particularly with regard to GS-20_20_1 and GS-20_20_8, which clearly depart from the steeper trends set by more rapidly effused flows.

Within this paradigm, certain experimental features must be reiterated. Firstly, the experimental lifetimes are typically of the order 10-100T^*. Many of the flows spend a considerable portion of their evolution in the transitional regime (typically evident over 0.1 to 10T^*), between Lister's early and long-time similarity solutions (eq. 3.14). Though flow development in this period is adequately modelled by Lister's numerical model (eq. 3.11), the experimental data should show change in dX_N/dT that is unrelated to the processes of cooling, and themselves exacerbated by the presence of a 4 cm (or 2 cm) diameter entry nozzle, whereas the model assumes a point-source.

Secondly the vicissitudes inherent to the size of the experimental system raise several qualms. Experimental series GS-10_10 shows an unfortunate 'creep' in ambient temperatures experienced, with room temperatures achieved increasing with increasing flow rate. Though the increase in ambient temperature is small, the nature of $d\eta_c/d\theta$ complicates direct conclusions about the effect of flow rate. Nevertheless, the trends of decreasing X_N (T) and dX_N/dT with decreasing flow rate are evidenced with regard to GS-10_5_1 and GS-10_5_2, where the most retarded case was extruded in a slightly warmer environment than its closest counterpart in flow rates, and in series GS-10_15, wherein all flows were cooled at the same ambient temperature. Series GS-20_5 and GS-20_10 reinforce these cases.

Figures 3.8 to **3.11** display the effects of temperature on downslope evolution, pairing flows of equivalent slopes and flow rates, but cooled at different ambient temperatures. Comparison of experiments GS-20_10_3 and GS-10_10_1 (**Figure 3.8**) shows that the more strongly cooled flow is more retarded than the one extruded at ~–10°C. This trend is continued in **Figures 3.9** and **3.10**, and at well-developed T, **Figure 3.11.**

Beyond these correlations, it is difficult to discern definite trends within the data. Whereas one might expect to find that dX_N/dT was smaller at lower temperatures, there is some evidence that 'warmer flows', cooled to –10°C, actually develop shallower dX_N/dT gradients at long time-scales (see, for example, **Figures 3.9** & **3.10**). Clearly analyses of X_N (T) alone fail to illuminate the full complexity of the dynamical problem, and we shall return to this later in the chapter.

Interestingly, the function of slope has a similarly pronounced effect on the divergence of data from the predictions of the model. At identical flow rates and ambient temperatures, the

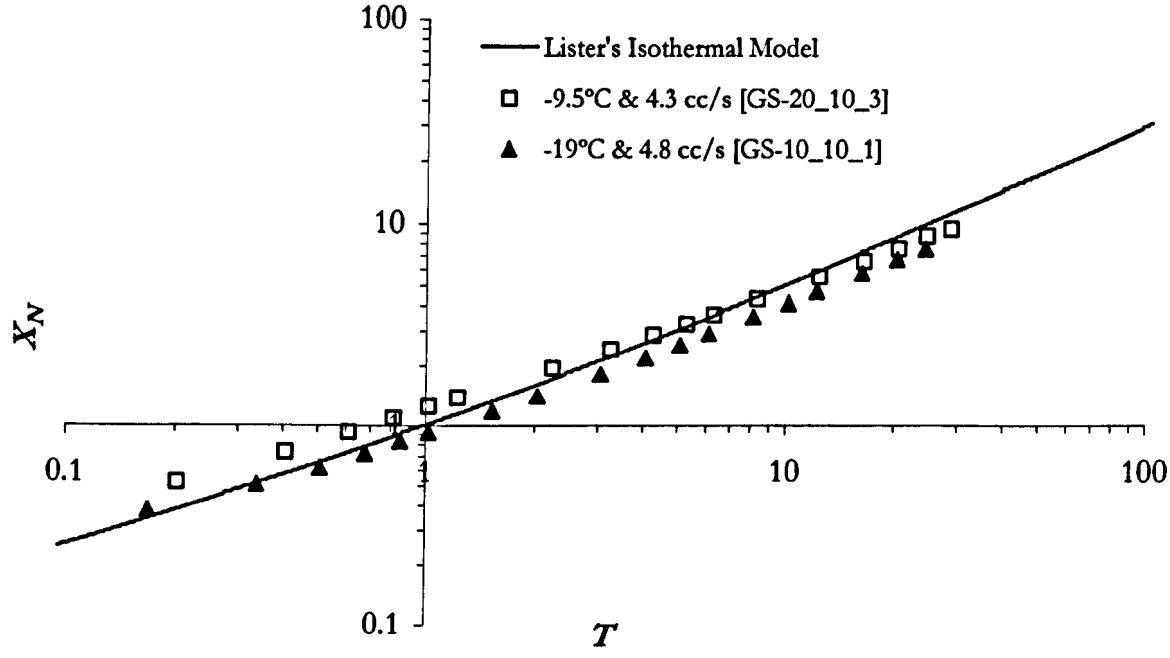

Figure 3.8 Plot of the maximum dimensionless downslope extents of two flows (X_N) with dimensionless time (T), extruded onto the same slope (10°) at similar flow rates. Recorded experimental values of x_N for a given t are normalised by the scales X^* and T^*, respectively. Experimental parameters: **GS-20_10_3**—T_a –19°C, T_c 20.75°C, Q 4.3 x10^{-6} m^3 s^{-1}, X^* 8.4, T^* 24.5, η_c 52.5 Pa s, η_a ~1.1 x10^6 Pa s; **GS-10_10_1**—T_a –9.5°C, T_c 19°C, Q 4.8 x10^{-6} m^3 s^{-1}, X^* 9.3, T^* 29.4, η_c 69.4 Pa s, η_a ~39,500 Pa s.

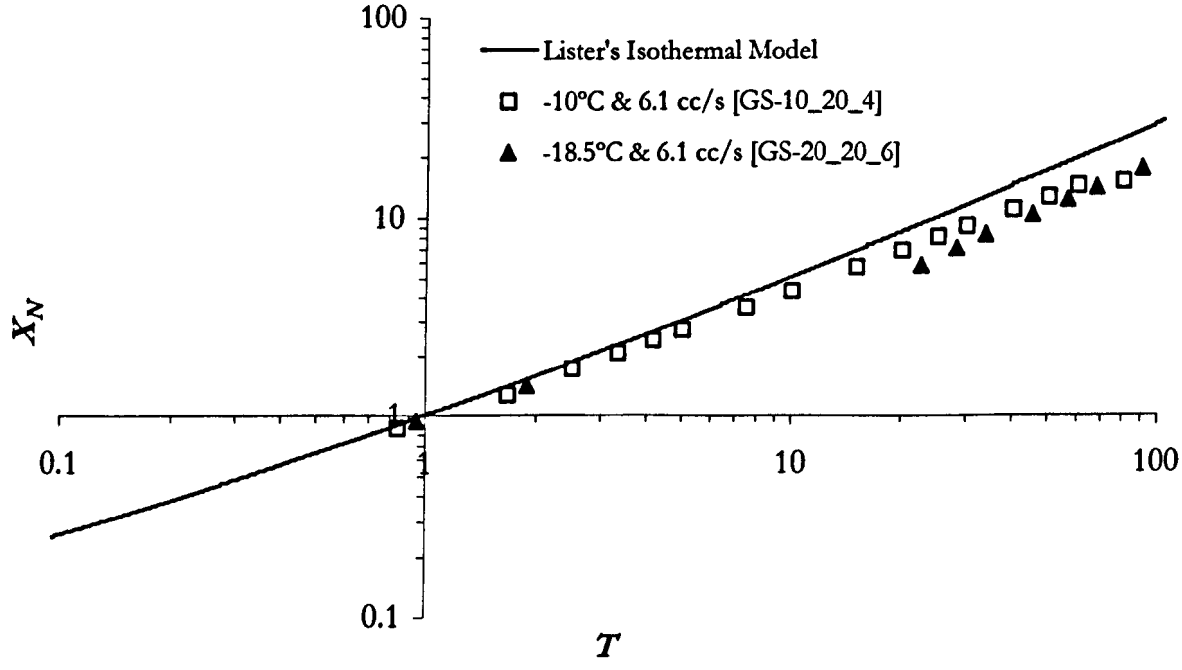

Figure 3.9 Plot of the maximum dimensionless downslope extents of two flows (X_N) with dimensionless time (T), extruded onto the same slope (20°) at similar flow rates. Recorded experimental values of x_N for a given t are normalised by the scales X^* and T^*, respectively. Experimental parameters: **GS-10_20_4**—T_a –10°C, T_c 20°C, Q 6.1 x10^{-6} m^3 s^{-1}, X^* 4.6, T^* 5.9, η_c 59 Pa s, η_a ~ 46,000 Pa s; **GS-20_20_6**—T_a –18.5°C, T_c 21°C, Q 6.1 x10^{-6} m^3 s^{-1}, X^* 4.5, T^* 5.3, η_c 50.5 Pa s, η_a ~8.9 x10^5 Pa s.

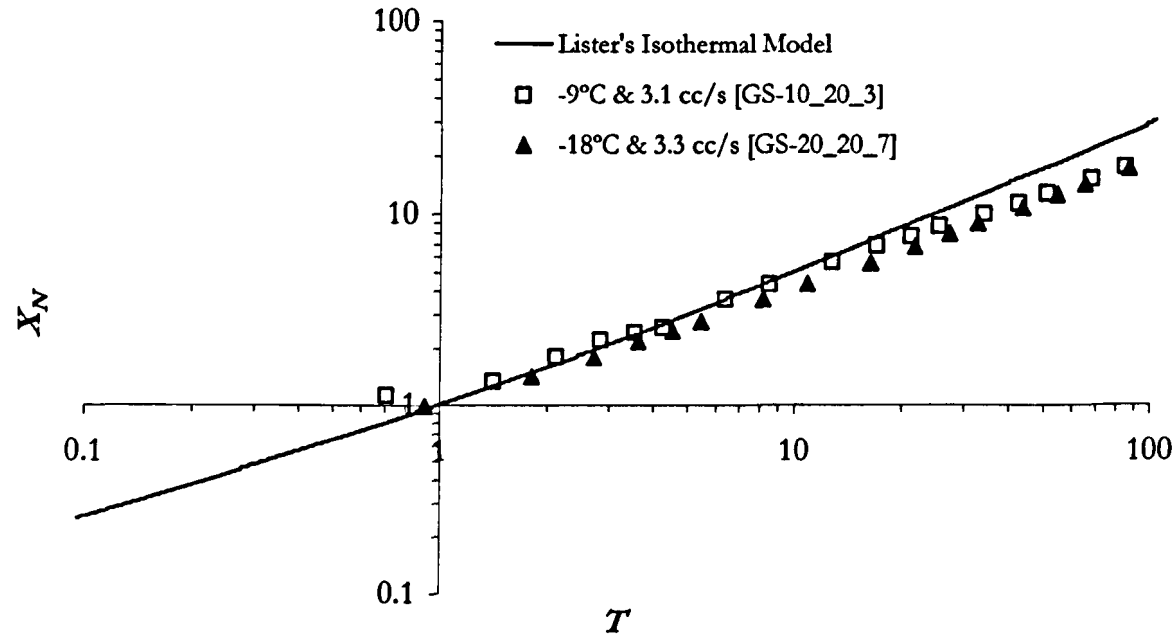

Figure 3.10 Plot of the maximum dimensionless downslope extents of two flows (X_N) with dimensionless time (T), extruded onto the same slope (20°) at similar flow rates. Recorded experimental values of x_N for a given t are normalised by the scales X^* and T^*, respectively. Experimental parameters: **GS-10_20_3**—T_a –9°C, T_c 20°C, Q 3.1 x10^{-6} m^3 s^{-1}, X^* 3.9, T^* 7.1, η_c 59 Pa s, η_a ~34,000 Pa s; **GS-20_20_7**—T_a –18°C, T_c 22°C, Q 3.3 x10^{-6} m^3 s^{-1}, X^* 3.7, T^* 5.5, η_c 43.3 Pa s, η_a ~7.3 x10^5 Pa s.

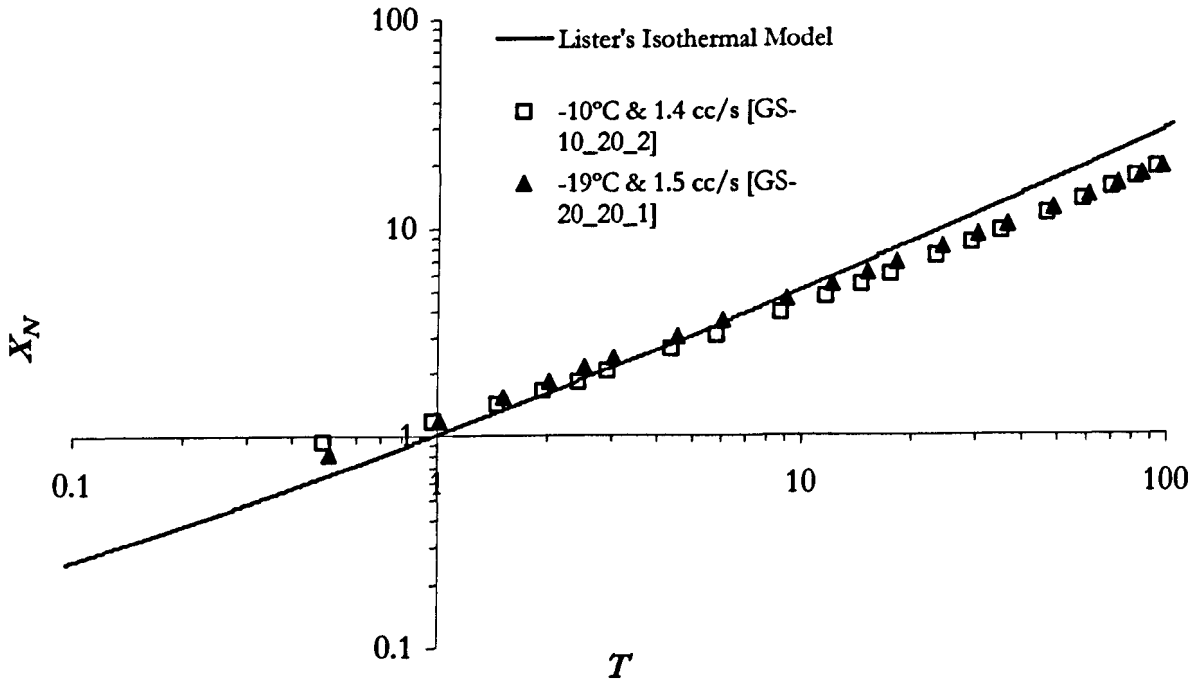

Figure 3.11 Plot of the maximum dimensionless downslope extents of two flows (X_N) with dimensionless time (T), extruded onto the same slope (20°) at similar flow rates. Recorded experimental values of x_N for a given t are normalised by the scales X^* and T^*, respectively. Experimental parameters: **GS-10_20_2**—T_a –10°C, T_c 18.5°C, Q 1.4 x10^{-6} m^3 s^{-1}, X^* 3.4, T^* 10.3, η_c 75.3 Pa s, η_a ~46,000 Pa s; **GS-20_20_1**—T_a –19°C, T_c 18.75°C, Q 1.5 x10^{-6} m^3 s^{-1}, X^* 3.4, T^* 9.9, η_c 72.3 Pa s, η_a ~1.1 x10^6 Pa s.

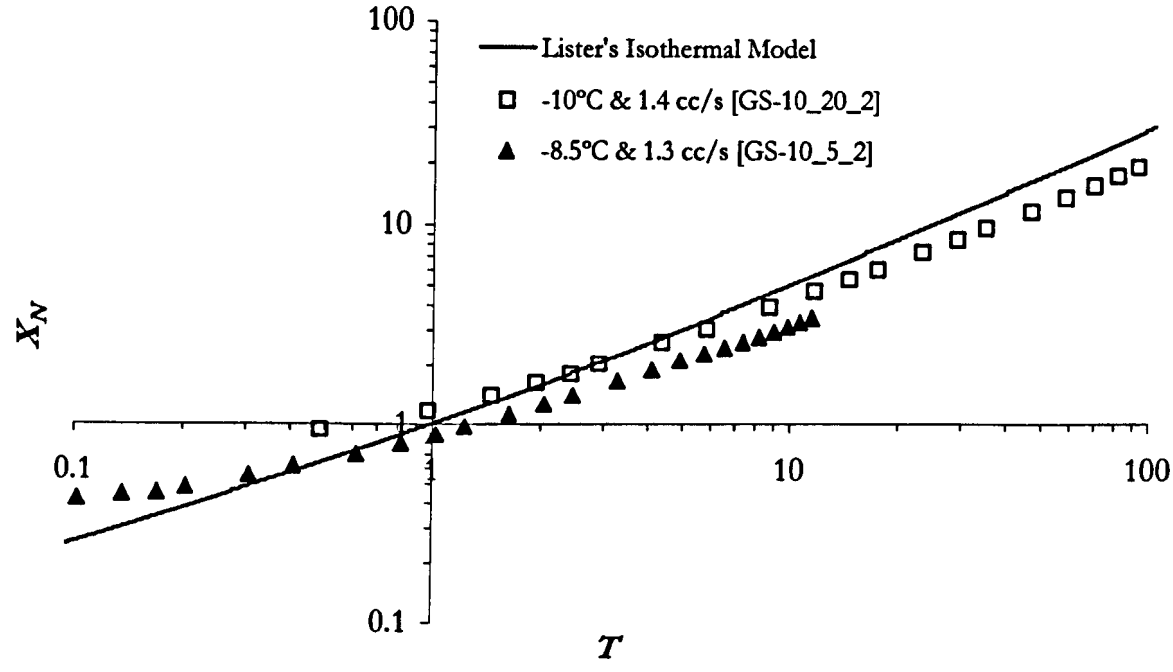

Figure 3.12 Plot of the maximum dimensionless downslope extents of two flows (X_N) with dimensionless time (T), extruded into the same set temperature (-10°C) at similar flow rates, but onto different slopes. Experimental parameters: **GS-10_20_2**—T_a –10°C, T_c 18.5°C, slope angle 20°, Q 1.4 x10^{-6} m^3 s^{-1}, X^* 3.4, T^* 10.3, η_c 75.3 Pa s, η_a ~46,000 Pa s; **GS-10_5_2**—T_a –8.5°C, T_c 20°C, slope angle 5°, Q 1.3 x10^{-6} m^3 s^{-1}, X^* 12.8, T^* 146.3, η_c 59 Pa s, η_a ~29,000 Pa s.

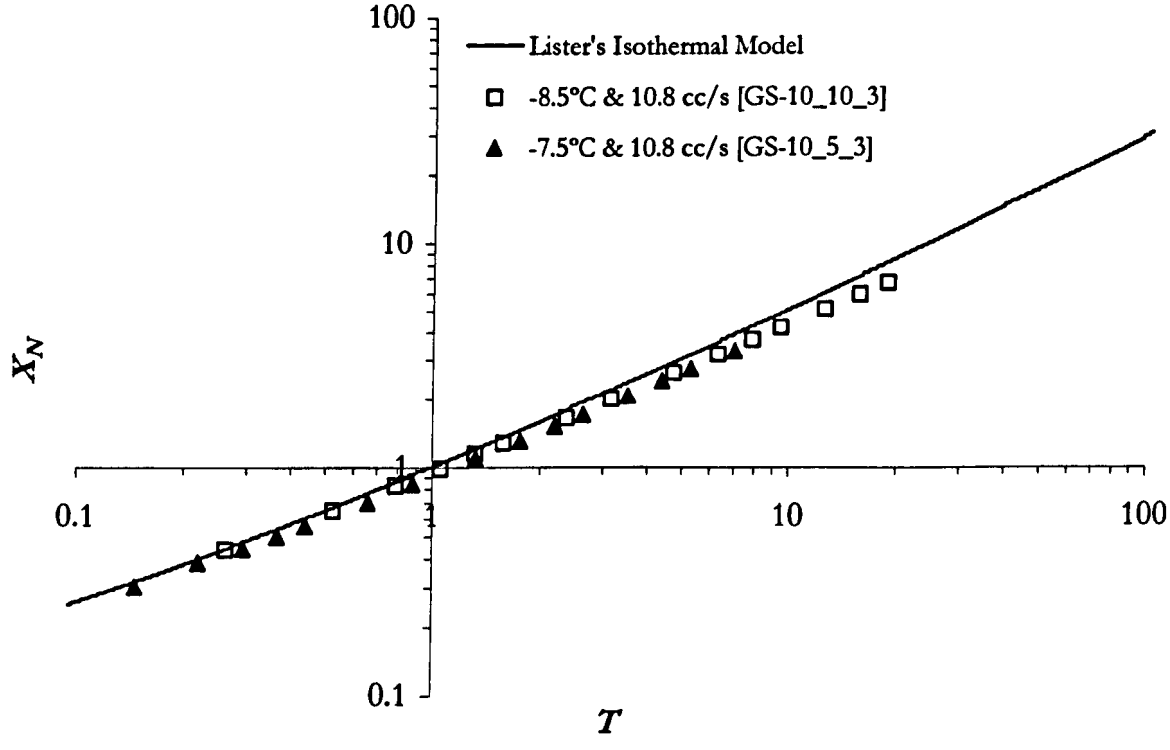

Figure 3.13 Plot of the maximum dimensionless downslope extents of two flows (X_N) with dimensionless time (T), extruded into the same set temperature (-10°) at similar flow rates, but onto different slopes. Experimental parameters: **GS-10_10_3**—T_a –8.5°C, T_c 21°C, slope angle 10°, Q 10.8 x10^{-6} m^3 s^{-1}, X^* 10.5, T^* 18.9, η_c 50.5 Pa s, η_a ~ 29,000 Pa s; **GS-10_5_3**—T_a –7.5°C, T_c 22°C, slope angle 5°, Q 10.8 x10^{-6} m^3 s^{-1}, X^* 20.3, T^* 67.9, η_c 43.3 Pa s, η_a ~ 22,000 Pa s.

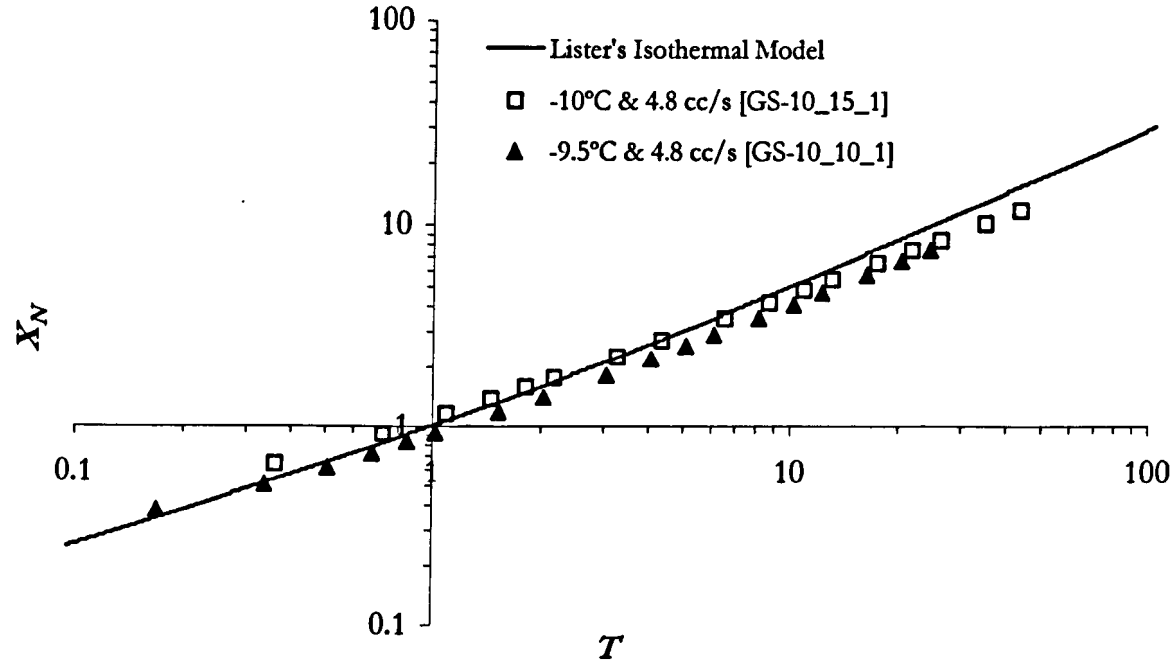

Figure 3.14 Plot of the maximum dimensionless downslope extents of two flows (X_N) with dimensionless time (T), extruded into the same set temperature (-10°) at similar flow rates, but onto different slopes. Experimental parameters: **GS-10_15_1**—T_a -10°C, T_c 18.5°C, slope angle 15°, Q 4.8 x10^{-6} m^3 s^{-1}, X^* 6.3, T^* 13.7, η_c 75.3 Pa s, η_a ~46,000 Pa s; **GS-10_10_1**—T_a -9.5°C, T_c 19°C, slope angle 10°, Q 4.8 x10^{-6} m^3 s^{-1}, X^* 9.3, T^* 29.4, η_c 69.4 Pa s, η_a ~39,500 Pa s.

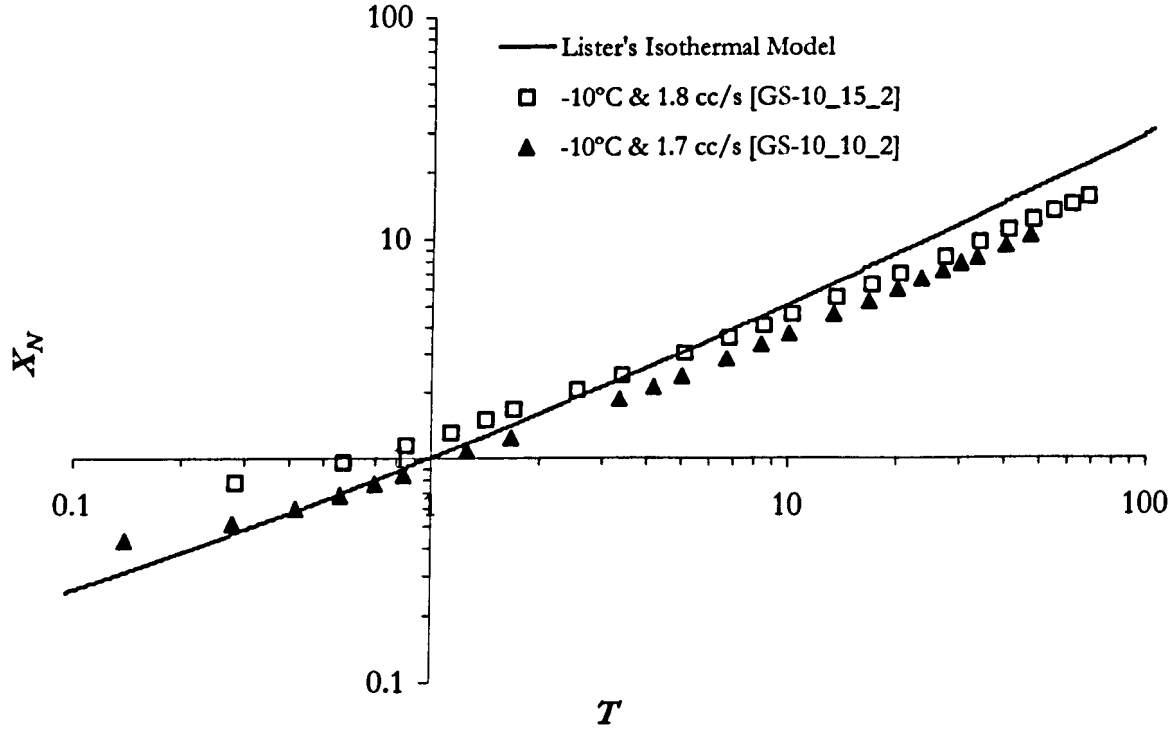

Figure 3.15 Plot of the maximum dimensionless downslope extents of two flows (X_N) with dimensionless time (T), extruded into the same set temperature (-10°) at similar flow rates, but onto different slopes. Experimental parameters: **GS-10_15_2**—T_a -10°C, T_c 18.5°C, slope angle 15°, Q 1.8 x10^{-6} m^3 s^{-1}, X^* 4.9, T^* 17.6, η_c 75.3 Pa s, η_a ~46,000 Pa s; **GS-10_10_2**—T_a -10°C, T_c 19.5°C, slope angle 10°, Q 1.7 x10^{-6} m^3 s^{-1}, X^* 7.0, T^* 35.8, η_c 64 Pa s, η_a ~46,000 Pa s.

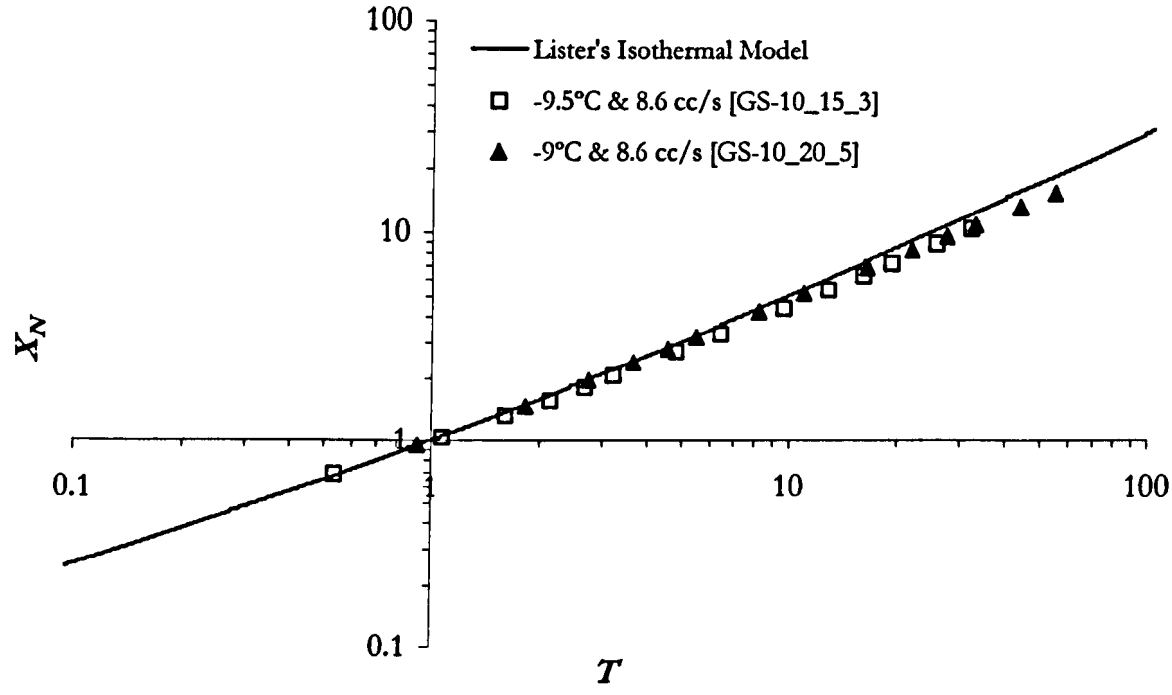

Figure 3.16 Plot of the maximum dimensionless downslope extents of two flows (X_N) with dimensionless time (T), extruded into the same set temperature (-10°) at similar flow rates, but onto different slopes. Experimental parameters: **GS-10_15_3**—T_a –9.5°C, T_c 20.5°C, slope angle 15°, Q 8.6 x10^{-6} m^3 s^{-1}, X^* 6.7, T^* 9.3, η_c 54.6 Pa s, η_a ~ 39,500 Pa s; **GS-10_20_5**—T_a –9°C, T_c 20°C, slope angle 20°, Q 8.6 x10^{-6} m^3 s^{-1}, X^* 5.1, T^* 5.5, η_c 59 Pa s, η_a ~ 34,000 Pa s.

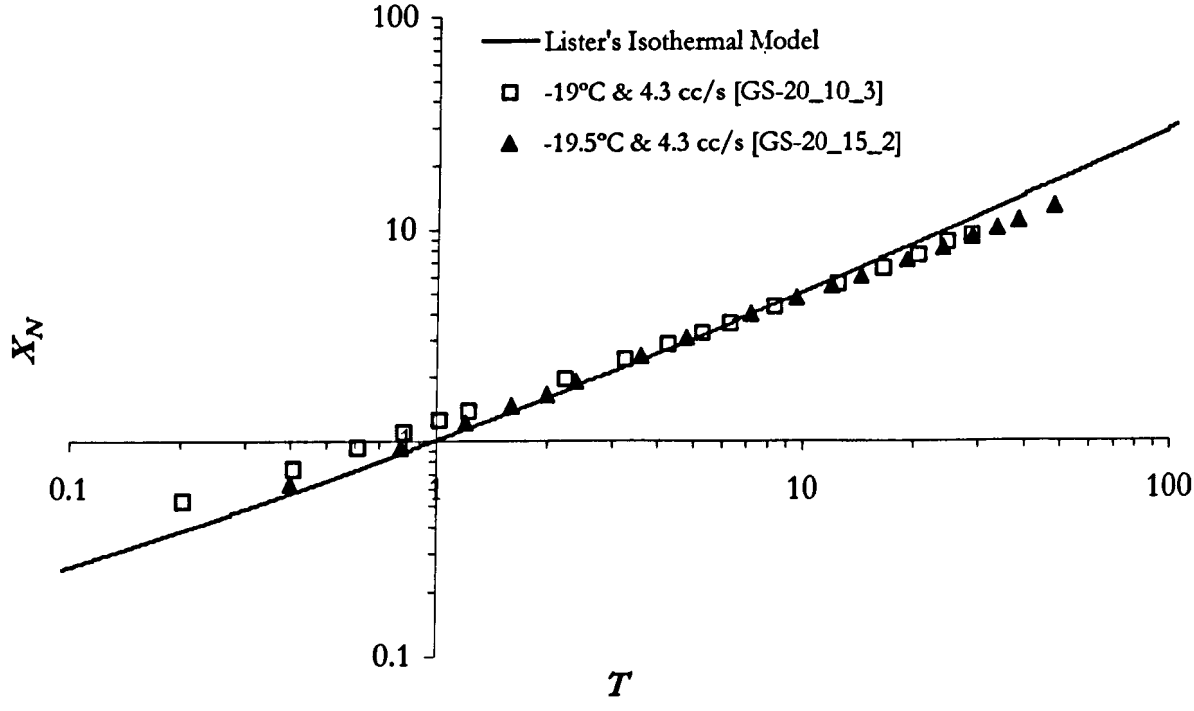

Figure 3.17 Plot of the maximum dimensionless downslope extents of two flows (X_N) with dimensionless time (T), extruded into the same set temperature (-20°) at similar flow rates, but onto different slopes. Experimental parameters: **GS-20_10_3**—T_a –19°C, T_c 20.75°C, slope angle 10°, Q 4.3 x10^{-6} m^3 s^{-1}, X^* 8.4, T^* 24.5, η_c 52.5 Pa s, η_a ~1.1 x10^6 Pa s; **GS-20_15_2**—T_a –19.5°C, T_c 19.5°C, slope angle 15°, Q 4.3 x10^{-6} m^3 s^{-1}, X^* 5.9, T^* 12.5, η_c 64 Pa s, η_a ~1.3 x10^6 Pa s.

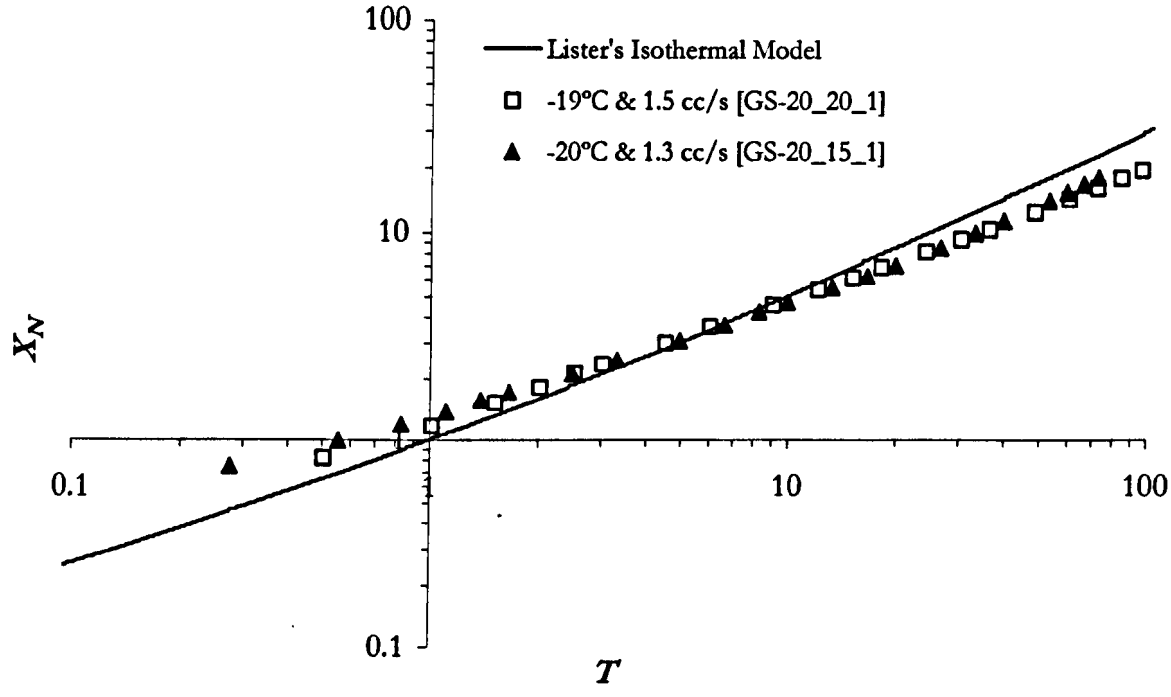

Figure 3.18 Plot of the maximum dimensionless downslope extents of two flows (X_N) with dimensionless time (T), extruded into the same set temperature (-20°) at similar flow rates, but onto different slopes. Experimental parameters: **GS-20_20_1**—T_a –19°C, T_c 18.75°C, slope angle 20°, Q 1.5 x10^{-6} m^3 s^{-1}, X^* 3.4, T^* 9.9, η_c 72.3 Pa s, η_a ~1.1 x10^6 Pa s; **GS-20_15_1**—T_a –20°C, T_c 20°C, slope angle 15°, Q 1.3 x10^{-6} m^3 s^{-1}, X^* 4.4, T^* 18.0, η_c 69.4 Pa s, η_a ~1.6 x10^6 Pa s.

propagation of X_N (T) in GS-10_5_2 is seriously retarded compared to GS-10_20_2 (**Figure 3.12**). This difference is exacerbated by the fact that the low-slope flow was actually extruded into a marginally cooler environment to its counterpart.

Generally speaking, the importance of slope on divergences from the model can be seen to decrease with increasing angles of inclination and higher flow rates. At extreme values of Q (~11 $cm^3\ s^{-1}$), little if any variation between experiments and the model can be witnessed in **Figure 3.13**. A closer correlation can be seen between the flows and the model in **Figure 3.14** (Q ~5 $cm^3\ s^{-1}$), than those in **Figure 3.15** (Q ~2 $cm^3\ s^{-1}$), which depart more from the predicted case. Highly inclined flows show little variance when slope angle is changed. There is no discernible difference between the experiments GS-10_15_3 and GS-10_20_5 in **Figure 3.16**, where Q is also high (~8.6 $cm^3\ s^{-1}$), and the flows only appear to diverge from the model as a direct function of cooling. Though the divergence in dX_N/dT in the model is most apparent at lower ambient temperatures (**Figure 3.17**), differences between runs are negligible. Even at low extrusion rates (~1.5 $cm^3\ s^{-1}$), the inclinations of experiments GS-20_20_1 and GS-20_15_1 are sufficiently high that no discernible difference is witnessed in a 5° change in slope (**Figure 3.18**).

3.5.1.2 Development of cross-slope extent with time

A preliminary analysis of the expansion of y_M (t) follows the criteria and methods established above. Plots of y_M (t) accompany those of x_N (t) collected in **Appendix A**. An example of the effects of cooling is displayed in **Figure 3.3b**. It is apparent that the cooled experiments flow across slope more slowly than predicted in Lister's solutions (eqs. 3.11 & 3.14), with the rate of advance, dy_M/dt, less than the isothermal case. Further, we now present the results in non-dimensional form, normalising y_M and t with the scales Y^* and T^*. Again, it should be reiterated that the scale Y^* has no direct bearing on the dynamics of the cooled flows, but serves to contrast experimental values with Lister's theory.

Plots of Y_M vs. T are displayed in **Figures 3.19a** to **3.22b**, sorted by ambient temperature and slope. As per related in 3.5.1.1, all cooled experiments systematically spread more slowly than the numerical model for an equivalent isothermal flow, with lower values of Y_M at all ranges of T, relative to the model. Furthermore, the gradients dY_M/dT typically fan away from the model, likewise possessing a more shallow habit. Recognition of differences in magnitude of Y_M (T) is complicated by the fact that even isothermal flows underestimate the numerical and similarity solution predictions for expansion (see section 3.4 and Lister, 1992).

Nevertheless, the data groupings frequently display a clear spread in values of Y_M (T) and trends of dY_M/dT, with a systematic decrease in the relative magnitude of Y_M and rate of increase of Y_M with T, inversely proportional to the flow rate. Such features are clearly displayed in **Figures 3.19a**,

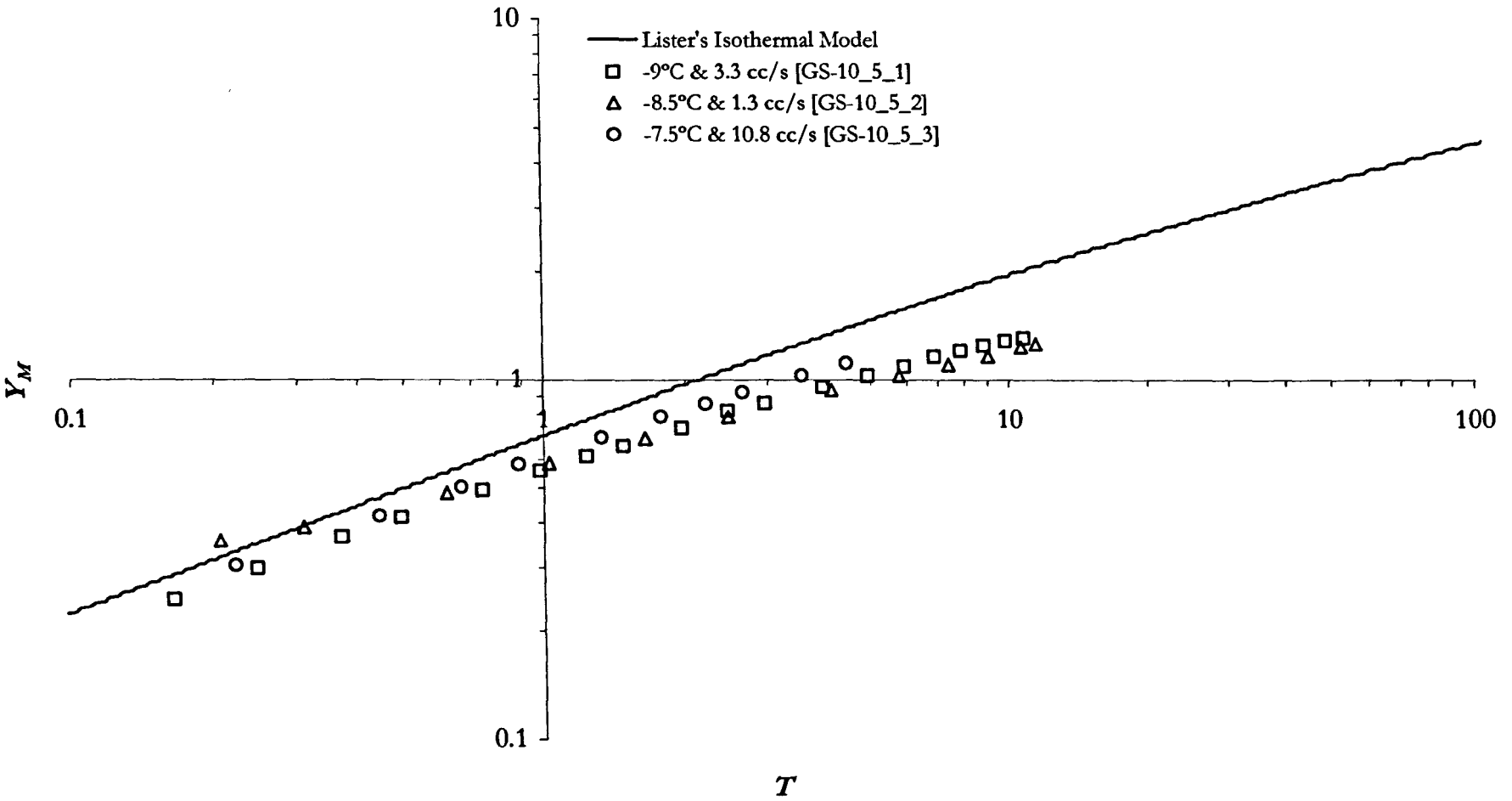

Figure 3.19a Plot of the maximum dimensionless cross-slope extent of a flow (Y_M) versus dimensionless time (T). Recorded experimental values of y_m for a given t are normalised by the scales Y^* and T^*, respectively. The cold room was set to –10°C and the tank slope to 5°. Experimental parameters: **GS-10_5_1**—T_a –9°C, T_e 19.5°C, Q 3.3 x10^{-6} m^3 s^{-1}, Y^* 16.7, T^* 122.3, η_e 64 Pa s, η_a ~34,000 Pa s; **GS-10_5_2**—T_a –8.5°C, T_e 20°C, Q 1.3 x10^{-6} m^3 s^{-1}, Y^* 12.8, T^* 146.3, η_e 59 Pa s, η_a ~29,000 Pa s; **GS-10_5_3**—T_a –7.5°C, T_e 22°C, Q 10.8 x10^{-6} m^3 s^{-1}, Y^* 20.3, T^* 67.9, η_e 43.3 Pa s, η_a ~ 22,000 Pa s.

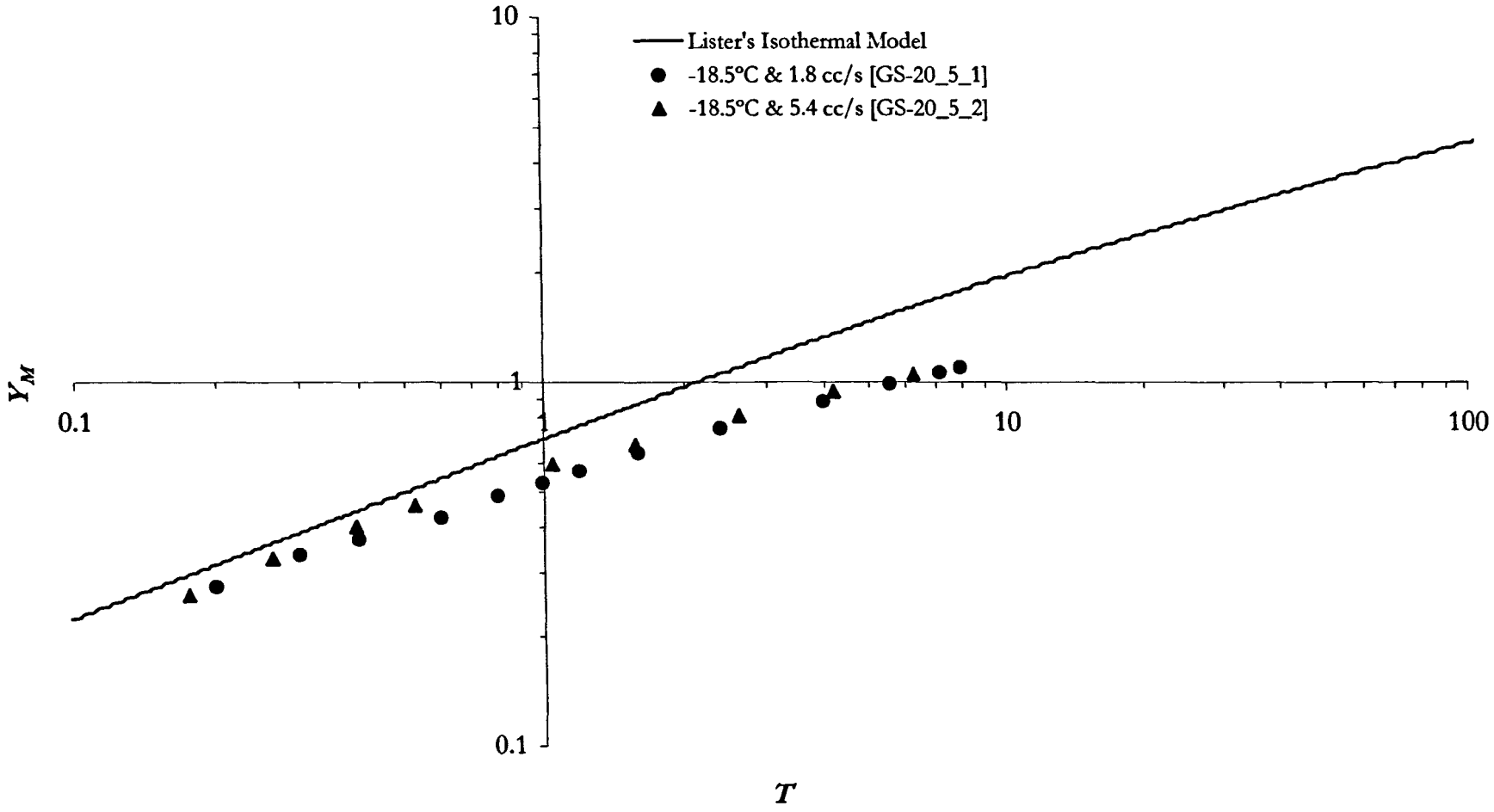

Figure 3.19b Plot of the maximum dimensionless cross-slope extent of a flow (Y_M) versus dimensionless time (T). The cold room was set to –20°C and the tank slope to 5°. Experimental parameters: **GS-20_5_1**—T_a –18.5°C, T_c 19°C, Q 1.8 x10^{-6} m^3 s^{-1}, Y* 14.6, T* 151.5, η_c 69.4 Pa s, η_a ~8.9 x10^5 Pa s; **GS-20_5_2**—T_a –18.5°C, T_c 19°C, Q 5.5 x10^{-6} m^3 s^{-1}, Y* 19.2, T* 115.1, η_c 69.4 Pa s, η_a ~8.9 x10^5 Pa s.

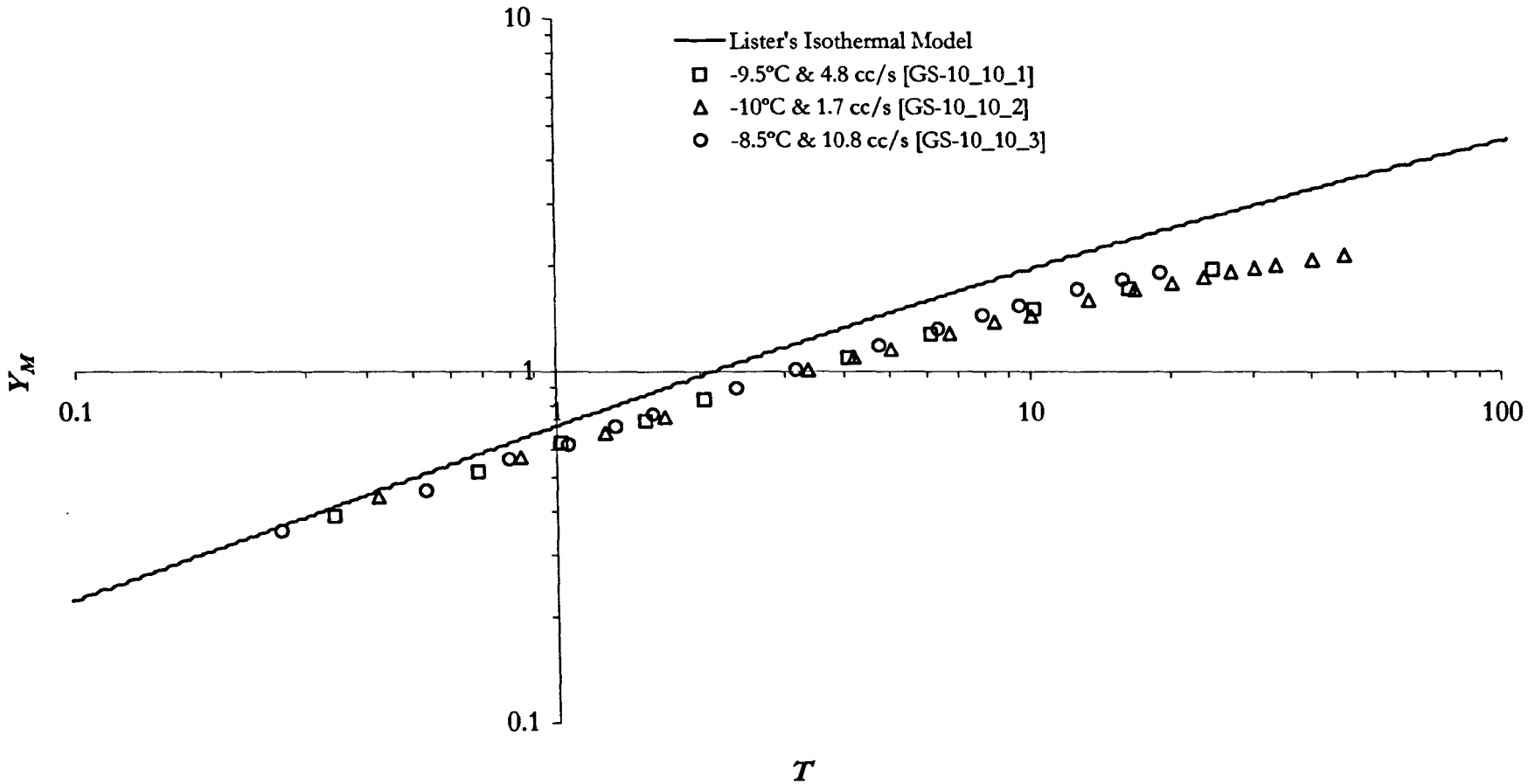

Figure 3.20a Plot of the maximum dimensionless cross-slope extent of a flow (Y_M) versus dimensionless time (T). The cold room was set to –10°C and the tank slope to 10°. Experimental parameters: **GS-10_10_1**—T_a –9.5°C, T_e 19°C, Q 4.8 x10^{-6} m^3 s^{-1}, Y^* 9.3, T^* 29.4, η_e 69.4 Pa s, η_a ~39,500 Pa s; **GS-10_10_2**—T_a –10°C, T_e 19.5°C, Q 1.7 x10^{-6} m^3 s^{-1}, Y^* 7.0, T^* 35.8, η_e 64 Pa s, η_a ~46,000 Pa s; **GS-10_10_3**—T_a –8.5°C, T_e 21°C, Q 10.8 x10^{-6} m^3 s^{-1}, Y^* 10.5, T^* 18.9, η_e 50.5 Pa s, η_a ~ 29,000 Pa s.

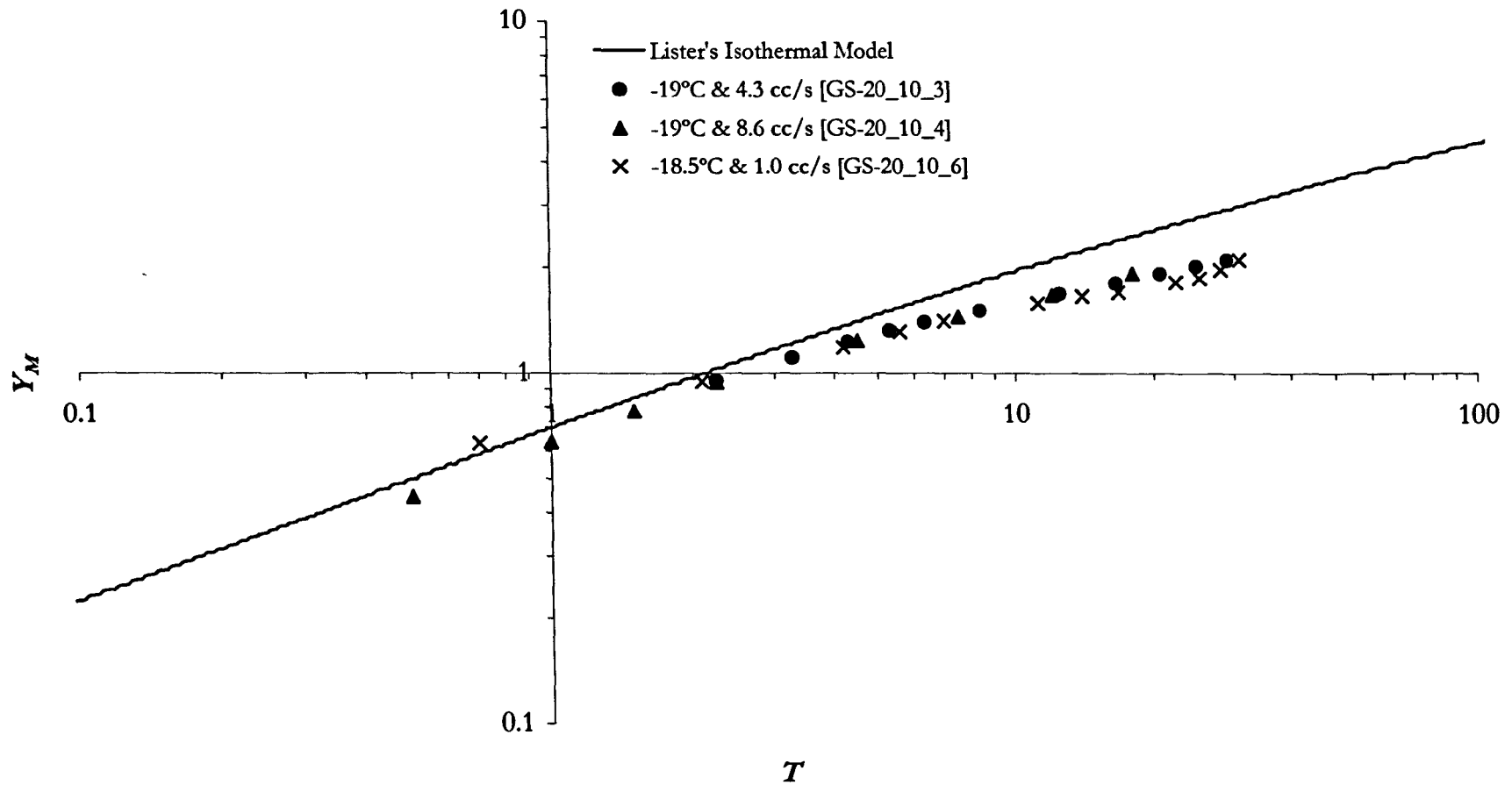

Figure 3.20b Plot of the maximum dimensionless cross-slope extent of a flow (Y_M) versus dimensionless time (T). The cold room was set to –20°C and the tank slope to 10°. Experimental parameters: **GS-20_10_3**—T_a –19°C, T_e 20.75°C, Q 4.3 x10^{-6} m^3 s^{-1}, Y^* 8.4, T^* 24.5, η_e 52.5 Pa s, η_a ~1.1 x10^6 Pa s; **GS-20_10_4**—T_a –19°C, T_e 21°C, Q 8.6 x10^{-6} m^3 s^{-1}, Y^* 9.9, T^* 20.0, η_e 50.5 Pa s, η_a ~1.1 x10^6 Pa s; **GS-20_10_6**—T_a –18.5°C, T_e 19°C, Q 1.0 x10^{-6} m^3 s^{-1}, Y^* 6.3, T^* 43.0, η_e 69.4 Pa s, η_a ~8.9 x10^5 Pa s.

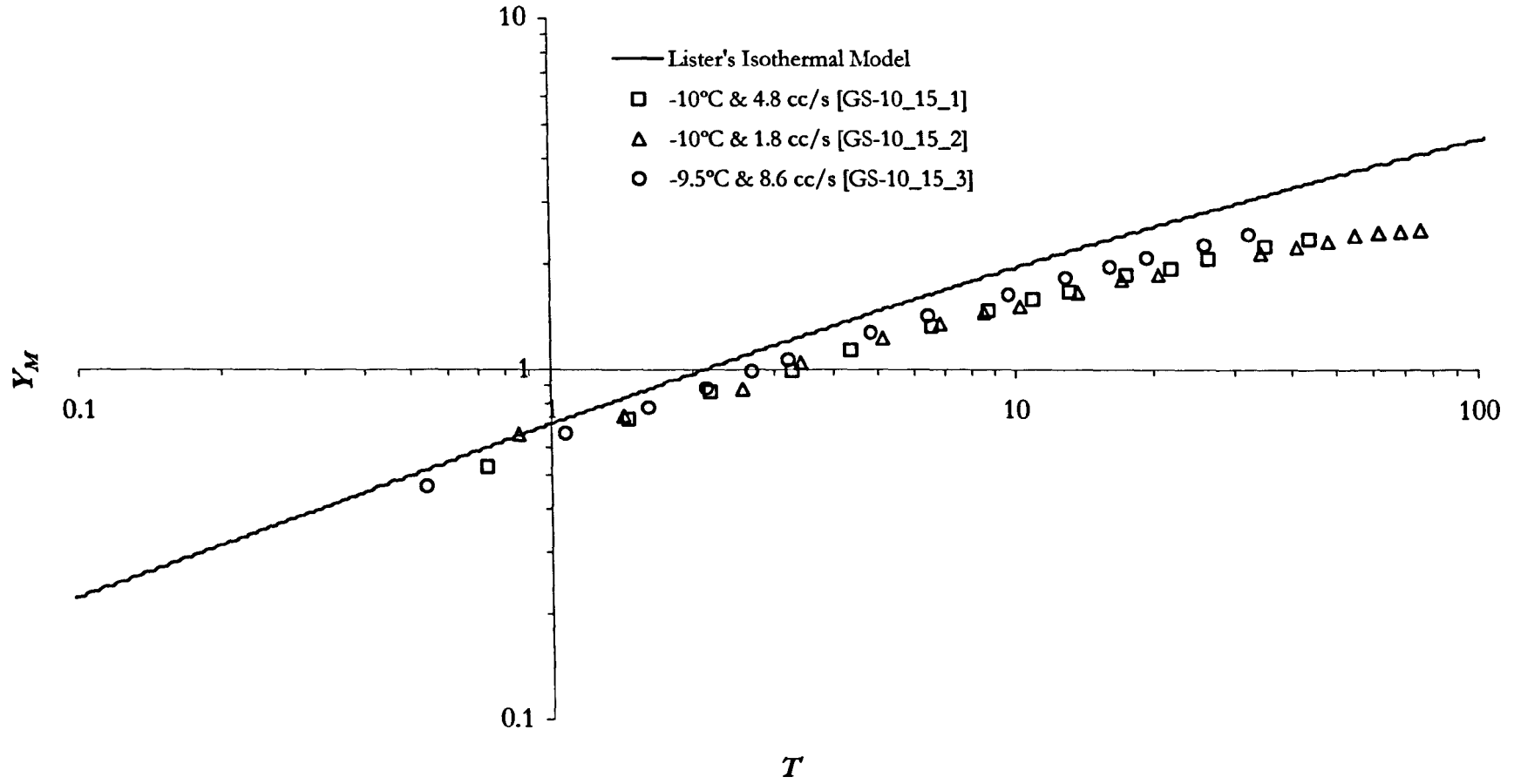

Figure 3.21a Plot of the maximum dimensionless cross-slope extent of a flow (Y_M) versus dimensionless time (T). The cold room was set to –10°C and the tank slope to 15°. Experimental parameters: **GS-10_15_1**—T_a –10°C, T_e 18.5°C, Q 4.8 x10^{-6} m^3 s^{-1}, Y^* 6.3, T^* 13.7, η_e 75.3 Pa s, η_a ~46,000 Pa s; **GS-10_15_2**—T_a –10°C, T_e 18.5°C, Q 1.8 x10^{-6} m^3 s^{-1}, Y^* 4.9, T^* 17.6, η_e 75.3 Pa s, η_a ~46,000 Pa s; **GS-10_15_3**—T_a –9.5°C, T_e 20.5°C, Q 8.6 x10^{-6} m^3 s^{-1}, Y^* 6.7, T^* 9.3, η_e 54.6 Pa s, η_a ~ 39,500 Pa s.

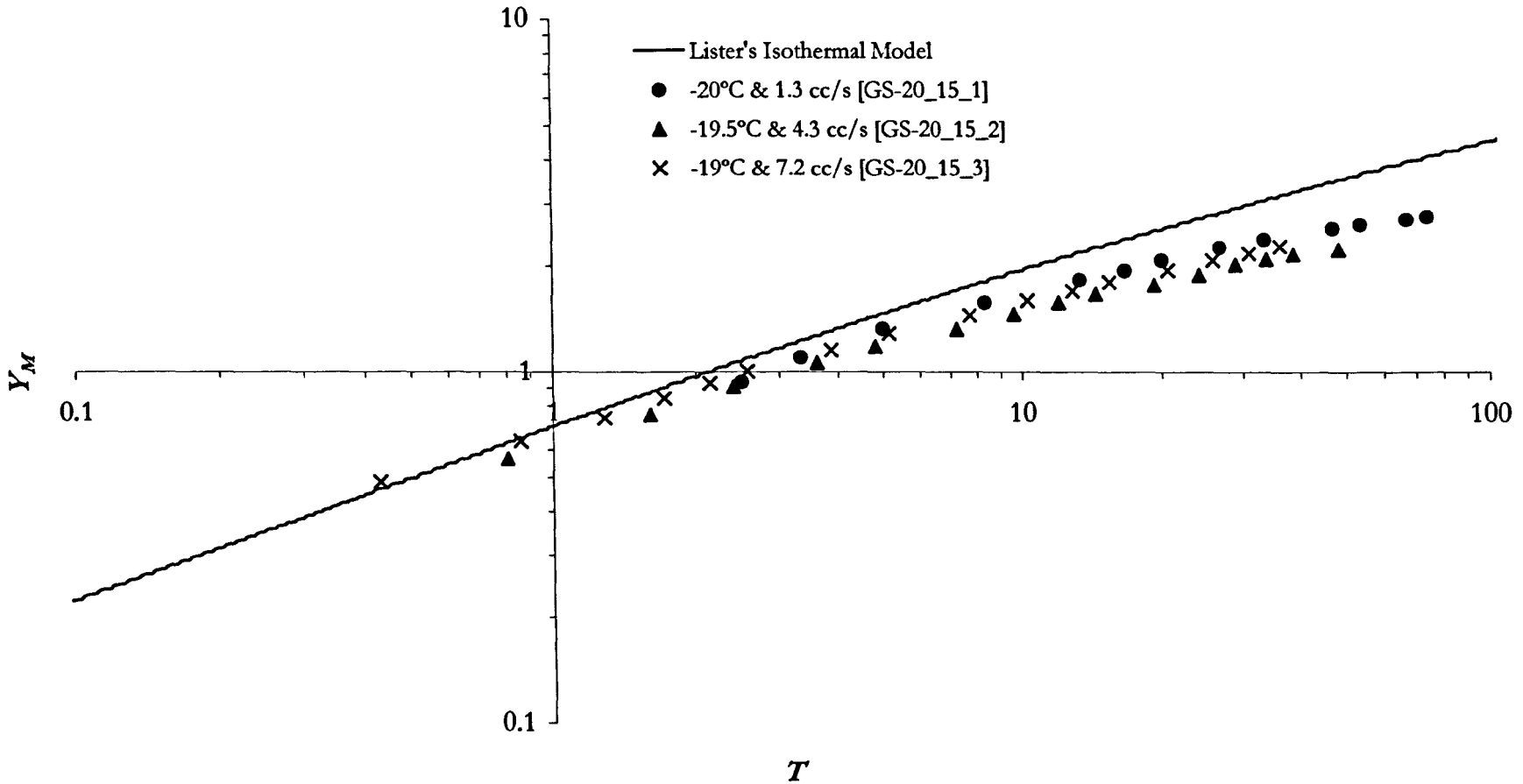

Figure 3.21b Plot of the maximum dimensionless cross-slope extent of a flow (Y_M) versus dimensionless time (T). The cold room was set to –20°C and the tank slope to 15°. Experimental parameters: **GS-20_15_1**—T_a –20°C, T_e 20°C, Q 1.3 x10^{-6} m^3 s^{-1}, Y^* 4.4, T^* 18.0, η_e 69.4 Pa s, η_a ~1.6 x10^6 Pa s; **GS-20_15_2**—T_a –19.5°C, T_e 19.5°C, Q 4.3 x10^{-6} m^3 s^{-1}, Y^* 5.9, T^* 12.5, η_e 64 Pa s, η_a ~1.3 x10^6 Pa s; **GS-20_15_3**—T_a –19°C, T_e 20°C, Q 7.2 x10^{-6} m^3 s^{-1}, Y^* 6.8, T^* 11.7, η_e 69.4 Pa s, η_a ~1.1 x10^6 Pa s.

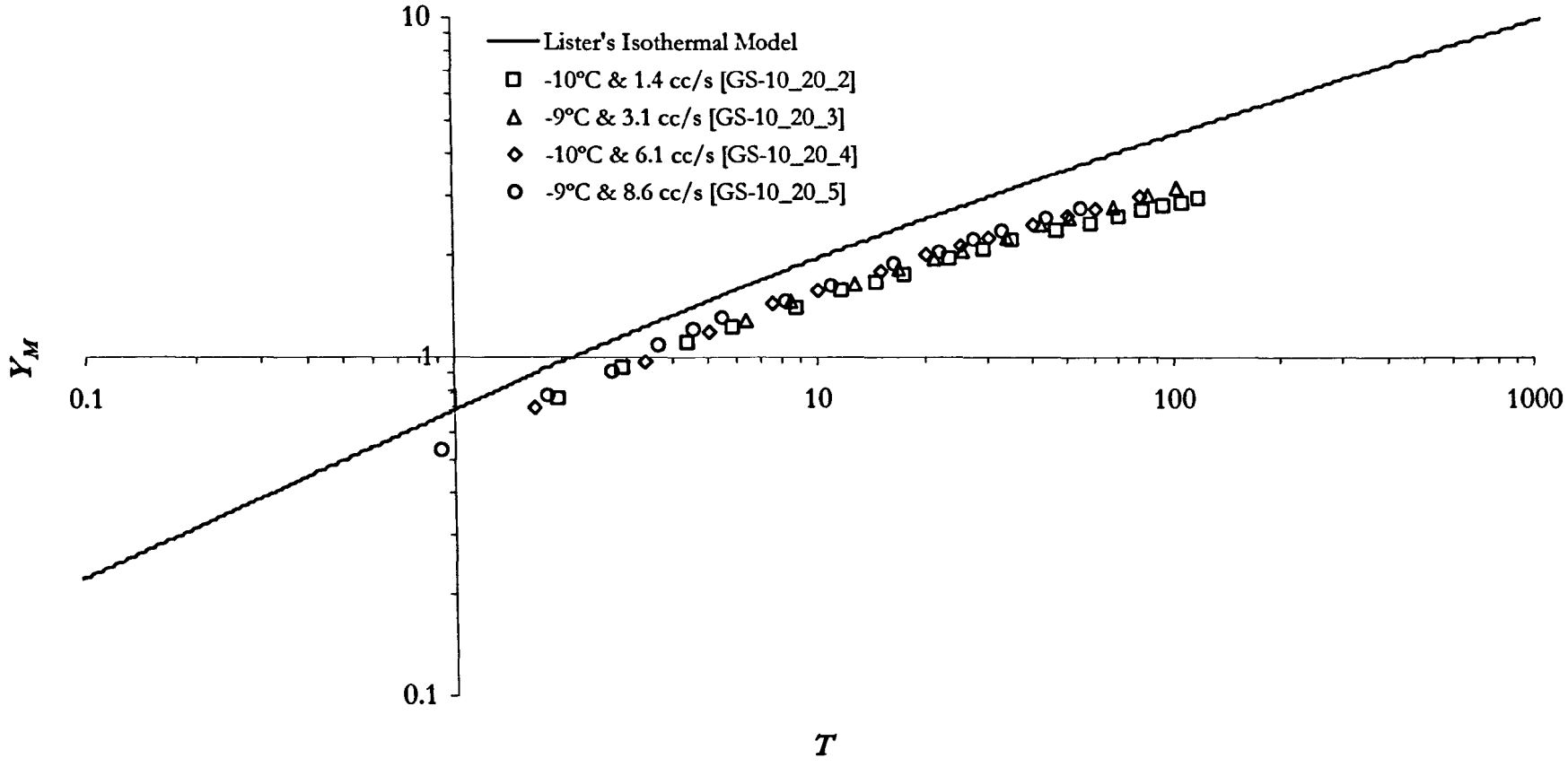

Figure 3.22a Plot of the maximum dimensionless cross-slope extent of a flow (Y_M) versus dimensionless time (T). The cold room was set to –10°C and the tank slope to 20°. Experimental parameters: **GS-10_20_2**—T_a –10°C, T_e 18.5°C, Q 1.4 x10^{-6} m^3 s^{-1}, Y^* 3.4, T^* 10.3, η_e 75.3 Pa s, η_a ~46,000 Pa s; **GS-10_20_3**—T_a –9°C, T_e 20°C, Q 3.1 x10^{-6} m^3 s^{-1}, Y^* 3.9, T^* 7.1, η_e 59 Pa s, η_a ~34,000 Pa s; **GS-10_20_4**—T_a –10°C, T_e 20°C, Q 6.1 x10^{-6} m^3 s^{-1}, Y^* 4.6, T^* 5.9, η_e 59 Pa s, η_a ~ 46,000 Pa s; **GS-10_20_5**—T_a –9°C, T_e 20°C, Q 8.6 x10^{-6} m^3 s^{-1}, Y^* 5.1, T^* 5.5, η_e 59 Pa s, η_a ~ 34,000 Pa s.

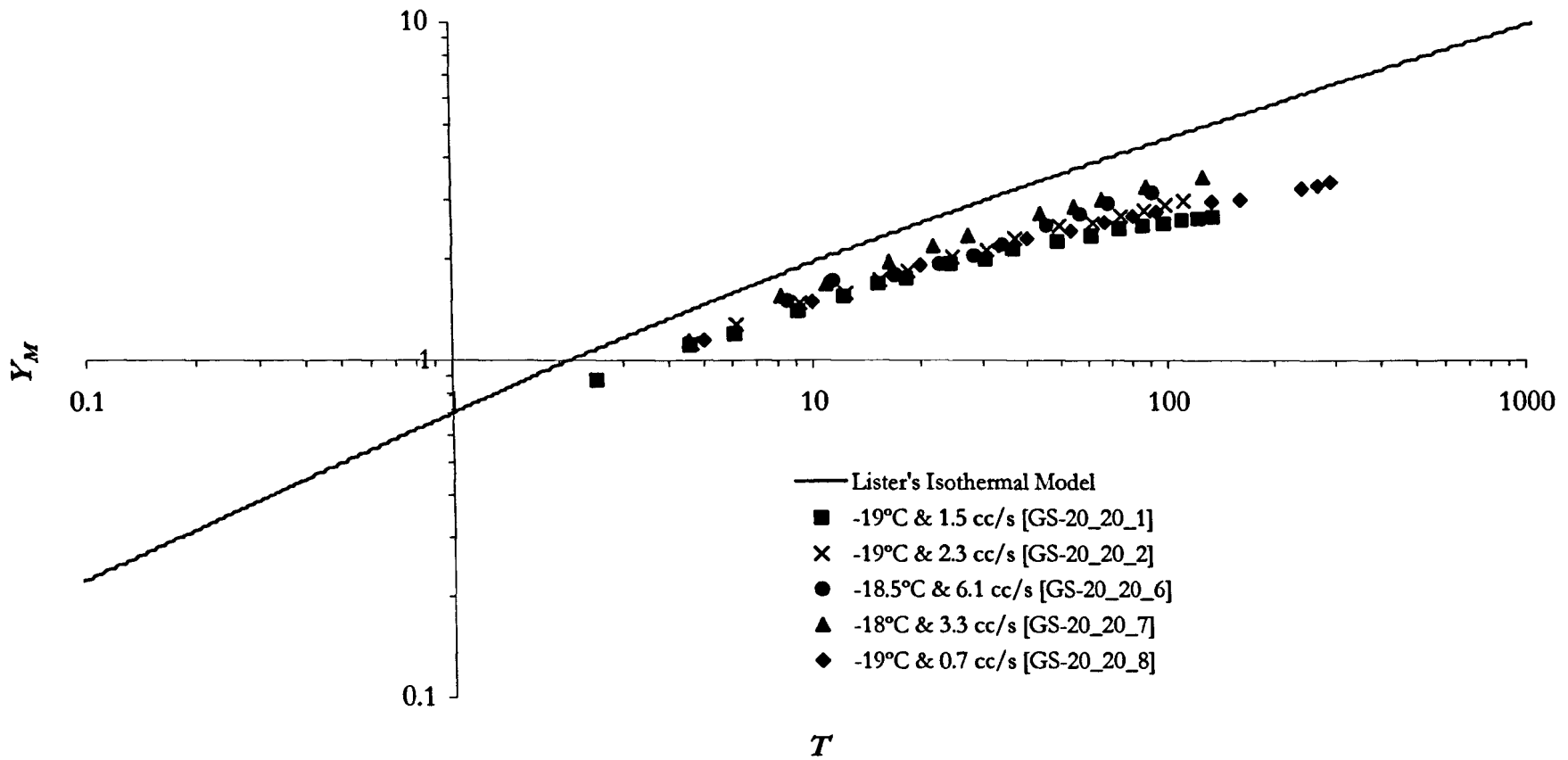

Figure 3.22b Plot of the maximum dimensionless cross-slope extent of a flow (Y_M) versus dimensionless time (T). The cold room was set to –20°C and the tank slope to 20°. Experimental parameters: **GS-20_20_1**—T_a –19°C, T_e 18.75°C, Q 1.5 x10^{-6} m^3 s^{-1}, Y^* 3.4, T^* 9.9, η_e 72.3 Pa s, η_a ~1.1 x10^6 Pa s; **GS-20_20_2**—T_a –19°C, T_e 18°C, Q 2.3 x10^{-6} m^3 s^{-1}, Y^* 3.9, T^* 9.7, η_e 81.7 Pa s, η_a ~1.1 x10^6 Pa s; **GS-20_20_6**—T_a –18.5°C, T_e 21°C, Q 6.1 x10^{-6} m^3 s^{-1}, Y^* 4.5, T^* 5.3, η_e 50.5 Pa s, η_a ~8.9 x10^5 Pa s; **GS-20_20_7**—T_a –18°C, T_e 22°C, Q 3.3 x10^{-6} m^3 s^{-1}, Y^* 3.7, T^* 5.5, η_e 43.3 Pa s, η_a ~7.3 x10^5 Pa s; **GS-20_20_8**—T_a –19°C, T_e 21°C, Q 0.7 x10^{-6} m^3 s^{-1}, Y^* 2.6, T^* 9.0, η_e 50.5 Pa s, η_a ~1.1 x10^6 Pa s.

3.20a, 3.20b, 3.21a and **3.22a**. Extruded at similar temperatures, the flows of series GS-10_5 (**Figure 3.19a**) display greater magnitudes of Y_M at given values of T than the model, and the gradients dY_M/dT decrease relative to the theoretical predictions with decreasing flow rate. Similar trends are displayed in series GS-10_10, but as explained above, a slight but systematic decrease in ambient temperature across the series complicates the issue. Though other series mimic these trends with a good degree of accuracy, the trend is harder to discern in series GS-20_5 (**Figure 3.19b**) and GS-20_10 (**Figure 3.20b**), and absent in series GS-20_15 and GS-20_20.

Experiments where ambient temperature and slope are held constant and flow rate is varied are displayed in **Figure 3.21b**. The retarding effect on lateral spreading is clearly observed with the departure from the isothermal case becoming more prominent with time. There are, however, no systematic differences for the three flow rates. The increasing effect of cooling is also observed in the decrease of the gradient (dY_M/dT) with time.

The effects of varying temperature on cross-slope development, at similar flow rate and slope, are displayed in **Figures 3.23** to **3.25**. Comparisons of GS-10_20_2 and GS-20_20_1 show that the flow extruded into a cooler ambient environment is clearly retarded, in both magnitude of Y_M (T) and the development of dY_M/dT, with respect to the less-cooled comparison and the numerical model (**Figure 3.22**). This retardation is most pronounced at low flow rates (GS-10_20_2 and GS-20_20_1 were extruded at 1.4 and 1.5 $cm^3\ s^{-1}$, respectively). As flow rate increases, to c. 3 (**Figure 3.24**) and 6 $cm^3\ s^{-1}$ (**Figure 3.25**), the differences in the cross-slope development disappear. Although **Figure 3.24** does indicate that the cooler flow is less retarded than its warmer counterpart, it was extruded at a slightly higher flow rate, and there is evidence of it possessing a shallower gradient at extreme values of T.

Likewise, the effects of slope on the development of Y_M can be analysed at common values of Q and tank inclination. **Figure 3.26** displays the varied expansion of experimental flows GS-10_20_3 and GS-10_5_1. At near identical flow rates and ambient temperatures, the flow extruded onto the gentler slope is more retarded in magnitude and rate of cross-slope expansion, relative to the model. This trend is repeated (for example: experiments GS-10_15_2 and GS-10_10_2 in **Figure 3.27**), and exacerbated at lower flow rates, but any changes in cross-slope expansion relative to the angle of slope are less systematic than those described for downslope expansion in Section 3.5.1.1. Occasionally, experiments extruded onto steeper inclines display greater absolute retardation relative to the model, as in GS-10_20_5 vis-à-vis GS-10_15_3, but they nevertheless possess gradients of dY/dT that diverge less from the model than in counterparts extruded onto gentler slopes.

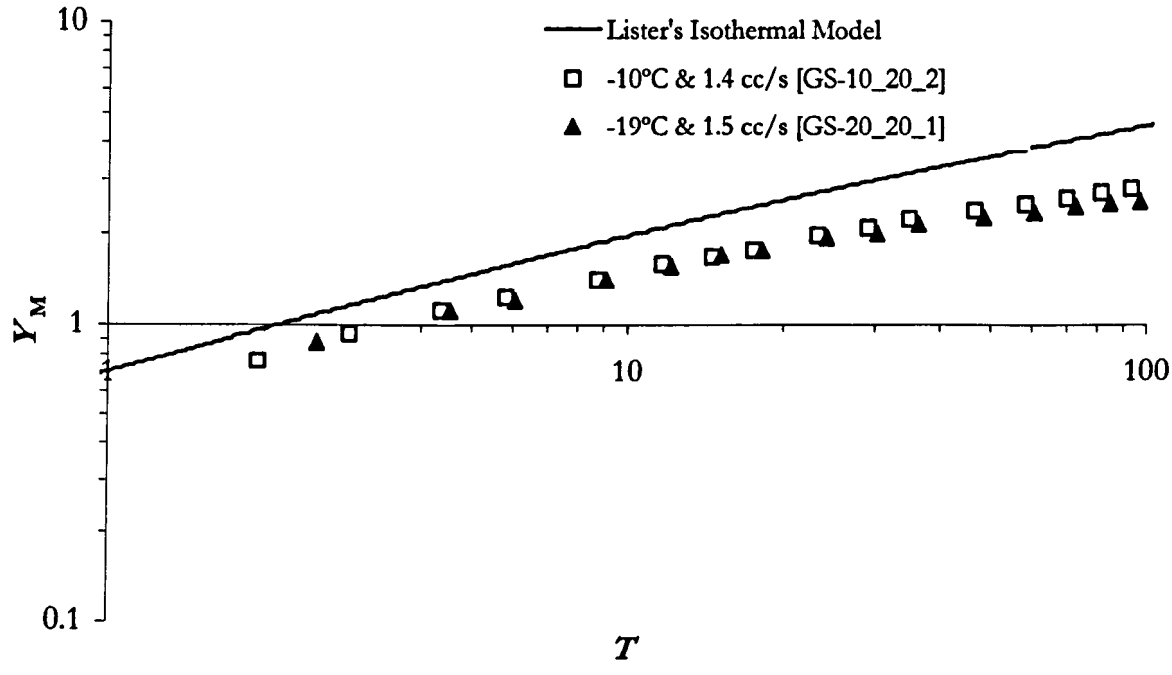

Figure 3.23 Plot of the maximum dimensionless cross-slope extents (Y_M) of two variably cooled flows with dimensionless time (T), extruded onto the same slope (20°) at similar flow rates. Recorded experimental values of y_M for a given t are normalised by the scales Y^* and T^*, respectively. Experimental parameters: **GS-10_20_2**—T_a –10°C, T_c 18.5°C, Q 1.4 x10^{-6} m^3 s^{-1}, Y^* 3.4, T^* 10.3, η_c 75.3 Pa s, η_a ~46,000 Pa s; **GS-20_20_1**—T_a –19°C, T_c 18.75°C, Q 1.5 x10^{-6} m^3 s^{-1}, Y^* 3.4, T^* 9.9, η_c 72.3 Pa s, η_a ~1.1 x10^6 Pa s.

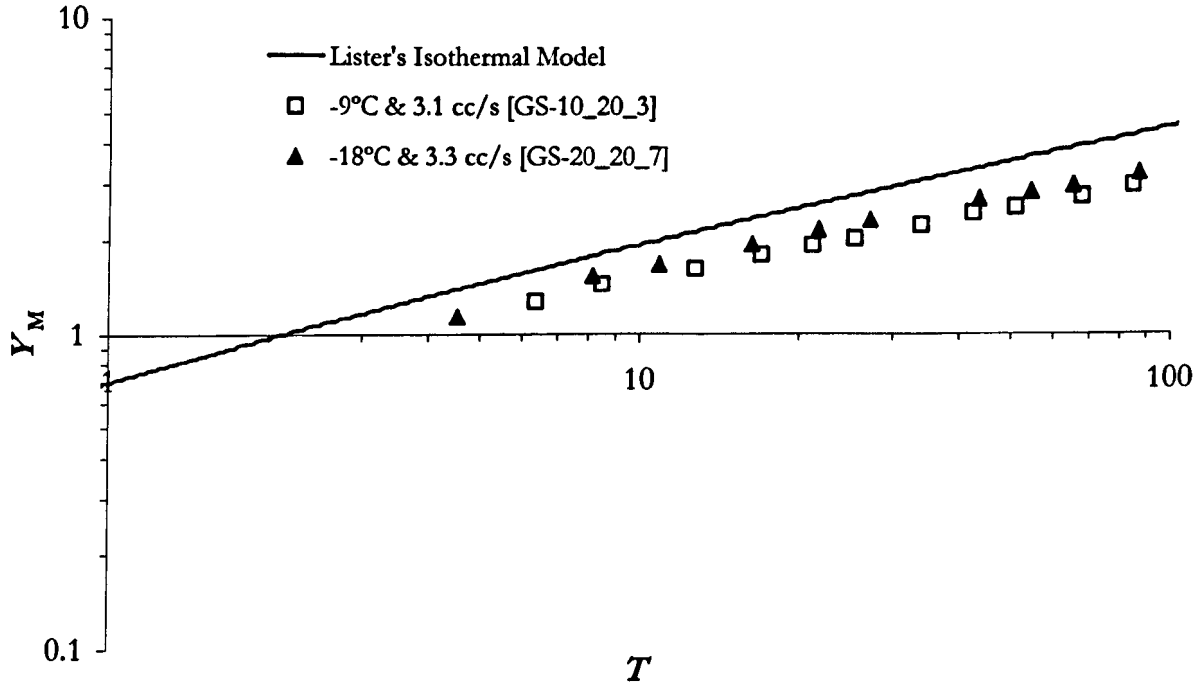

Figure 3.24 Plot of the maximum dimensionless cross-slope extents (Y_M) of two variably cooled flows with dimensionless time (T), extruded onto the same slope (20°) at similar flow rates. Experimental parameters: **GS-10_20_3**—T_a –9°C, T_c 20°C, Q 3.1 x10^{-6} m^3 s^{-1}, Y^* 3.9, T^* 7.1, η_c 59 Pa s, η_a ~34,000 Pa s; **GS-20_20_7**—T_a –18°C, T_c 22°C, Q 3.3 x10^{-6} m^3 s^{-1}, Y^* 3.7, T^* 5.5, η_c 43.3 Pa s, η_a ~7.3 x10^5 Pa s.

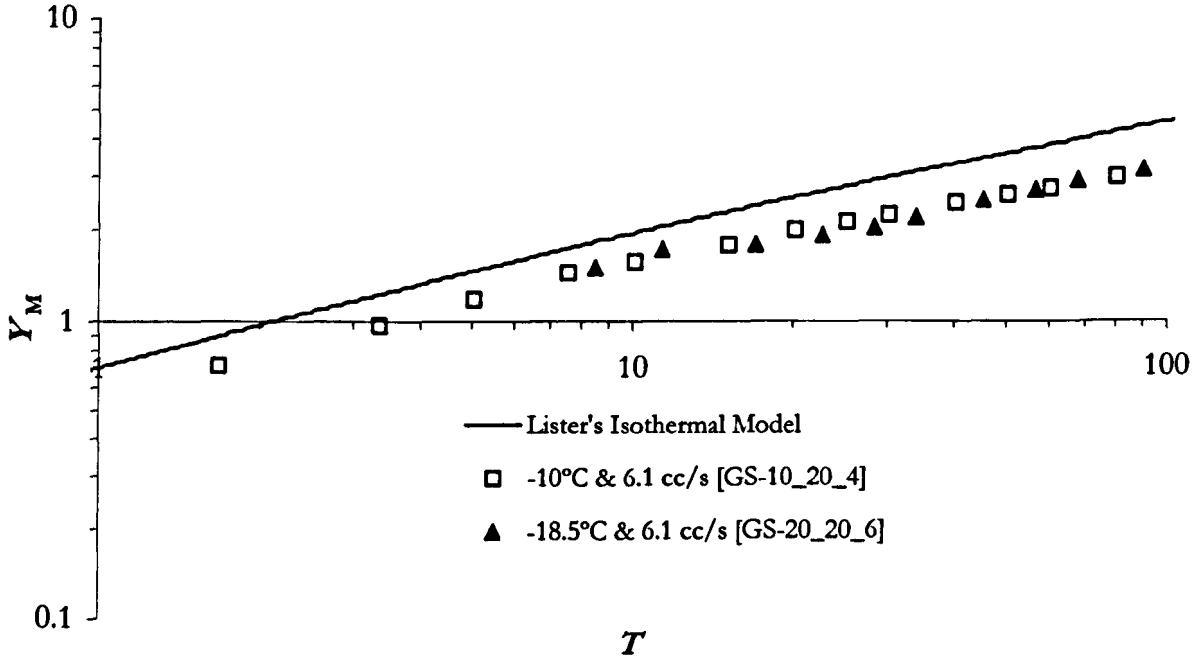

Figure 3.25 Plot of the maximum dimensionless cross-slope extents (Y_M) of two variably cooled flows with dimensionless time (T), extruded onto the same slope (20°) at similar flow rates. Experimental parameters: **GS-10_20_4**—T_a –10°C, T_e 20°C, Q 6.1 x10^{-6} m^3 s^{-1}, Y^* 4.6, T^* 5.9, η_e 59 Pa s, η_a ~ 46,000 Pa s; **GS-20_20_6**—T_a –18.5°C, T_e 21°C, Q 6.1 x10^{-6} m^3 s^{-1}, Y^* 4.5, T^* 5.3, η_e 50.5 Pa s, η_a ~8.9 x10^5 Pa s.

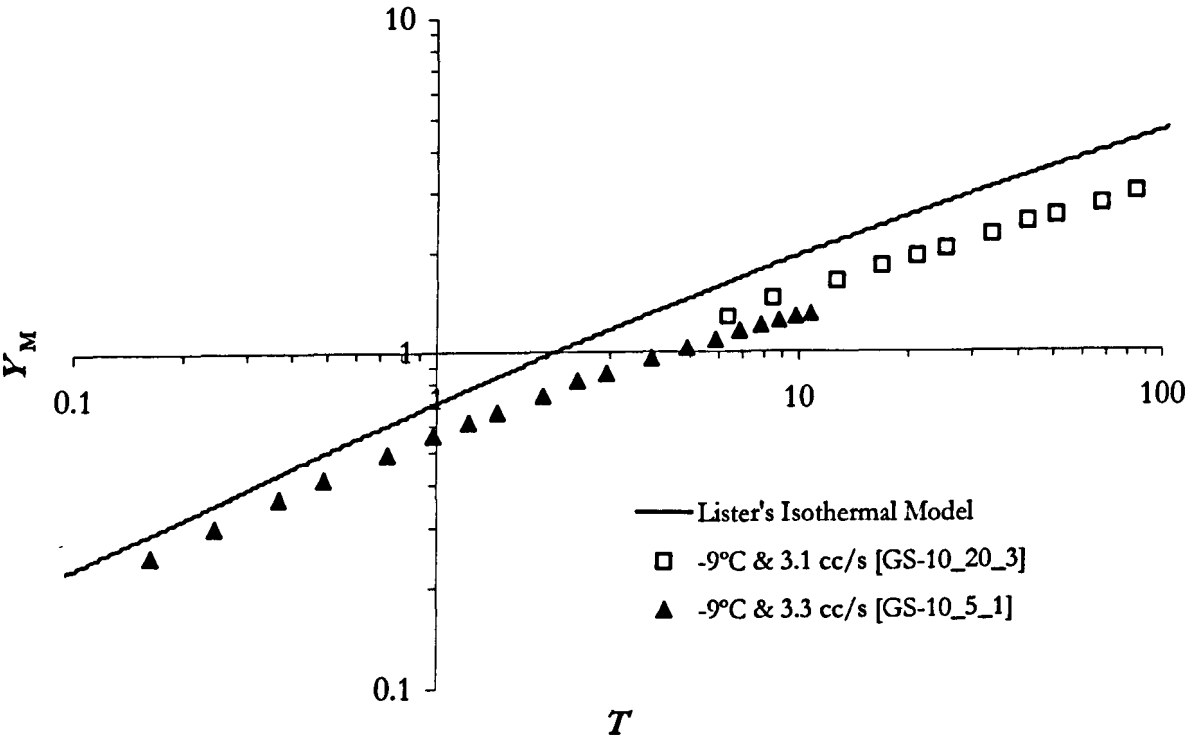

Figure 3.26 Plot of the maximum dimensionless cross-slope extents (Y_M) of two similarly cooled flows with dimensionless time (T), extruded at similar flow rates onto different slopes. Experimental parameters: **GS-10_20_3**—T_a –9°C, T_e 20°C, slope angle 20°, Q 3.1 x10^{-6} m^3 s^{-1}, Y^* 3.9, T^* 7.1, η_e 59 Pa s, η_a ~34,000 Pa s; **GS-10_5_1**—T_a –9°C, T_e 19.5°C, slope angle 5°, Q 3.3 x10^{-6} m^3 s^{-1}, Y^* 16.7, T^* 122.3, η_e 64 Pa s, η_a ~34,000 Pa s.

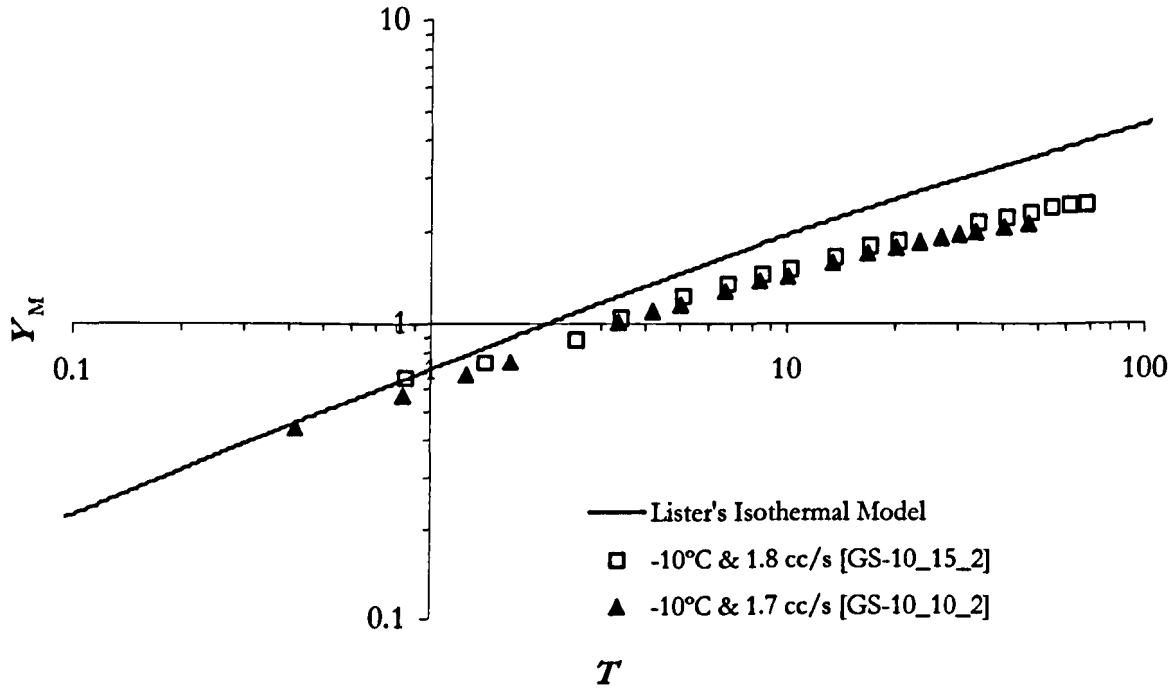

Figure 3.27 Plot of the maximum dimensionless cross-slope extents (Y_M) of two similarly cooled flows with dimensionless time (T), extruded at similar flow rates onto different slopes. Experimental parameters: **GS-10_15_2**—T_a –10°C, T_e 18.5°C, slope angle 15°, Q 1.8 x10^{-6} m^3 s^{-1}, Y^* 4.9, T^* 17.6, η_e 75.3 Pa s, η_a ~46,000 Pa s; **GS-10_10_2**—T_a –10°C, T_e 19.5°C, slope angle 10°, Q 1.7 x10^{-6} m^3 s^{-1}, Y^* 7.0, T^* 35.8, η_e 64 Pa s, η_a ~46,000 Pa s.

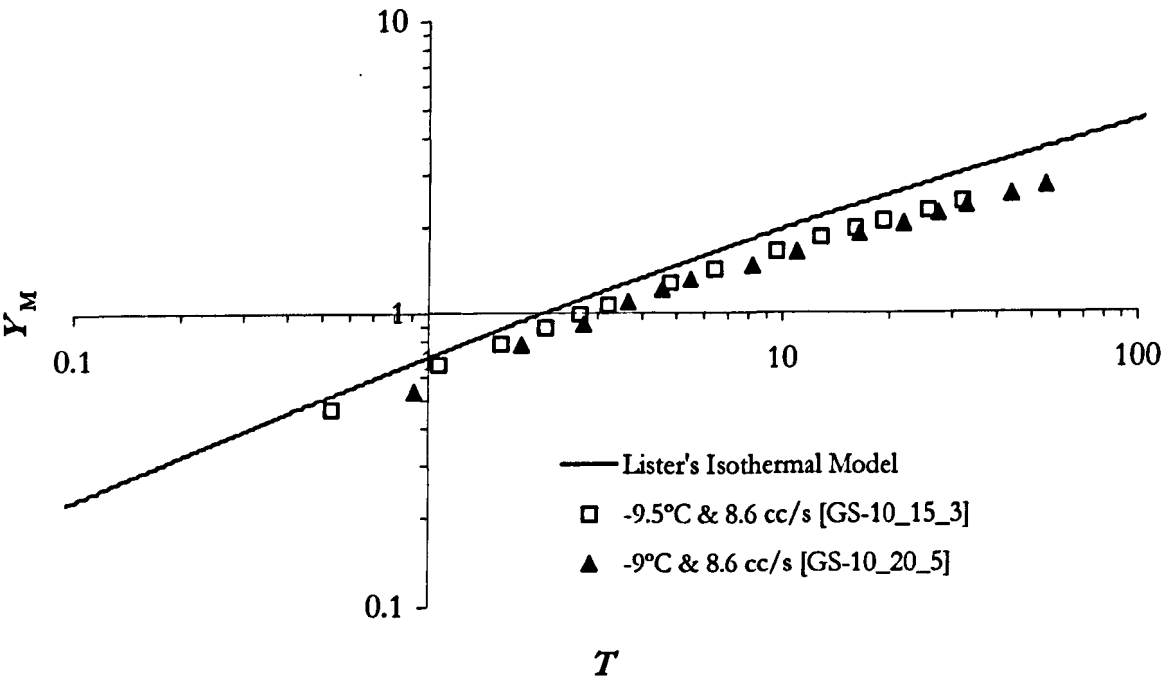

Figure 3.28 Plot of the maximum dimensionless cross-slope extents (Y_M) of two similarly cooled flows with dimensionless time (T), extruded at similar flow rates onto different slopes. Experimental parameters: **GS-10_15_3**—T_a –9.5°C, T_e 20.5°C, slope angle 15°, Q 8.6 x10^{-6} m^3 s^{-1}, Y^* 6.7, T^* 9.3, η_e 54.6 Pa s, η_a ~39,500 Pa s; **GS-10_20_5**—T_a –9°C, T_e 20°C, slope angle 20°, Q 8.6 x10^{-6} m^3 s^{-1}, Y^* 5.1, T^* 5.5, η_e 59 Pa s, η_a ~34,000 Pa s.

3.5.1.3 Development of aspect ratio with time

Sections 3.5.1.1 and 3.5.1.2 illuminate clear, and mostly systematic, variances from Lister's model. Cooling has a clear influence on flow expansion, with the effects of cooling (i.e. divergence from the model) exacerbated at different values of the parameters Q and tank incline. The question of whether down- or cross-slope expansion is retarded preferentially, given the interaction of thermal and dynamic processes, can be explored with reference to the development of flow aspect ratio with time.

Aspect ratio, defined as the ratio of downslope to cross-slope extent (i.e. x_N/y_M or here, non-dimensionally, X_N/Y_M) is plotted against dimensionless time (T). Experiments are grouped by slope, as series GS-10_5 & GS-20_5 (**Figure 3.29**), GS-10_10 & GS-20_10 (**Figure 3.30**), GS-10_15 & GS-20_15 (**Figure 3.31**) and GS-10_20 & GS-20_20 (**Figure 3.32**).

At first glance, all series of experiments appear to follow the trend remarkably accurately, indicating that the cooling regime does not adversely affect the expansion in a given dimension preferentially. Naturally, the absolute downshift in values of Y_M characteristic of all the experiments means that X_N/Y_M will typically be greater than predicted by the model, but nevertheless possess trends in $d(X_N/Y_M)/dT$ that follow the theory closely.

Close analysis of **Figure 3.29** indicates that at higher values of T, O (5-10), some flows might display a *slight* rise in $d(X_N/Y_M)/dT$ relative to the model. This is subjective and within the realm of experimental variability; the data preclude irrefutable conclusions as to a clear departure from the model. However, in **Figure 3.30** this trend is clearly evidenced at large T, O (10+), for the most slowly extruded flow, GS-20_10_6 (1 $cm^3\ s^{-1}$), which clearly possess higher aspect ratios and $d(X_N/Y_M)/dT$ than predicted by Lister's model; GS-10_10_2 (1.7 $cm^3\ s^{-1}$) shows a moderate, though less extreme trend over its lifetime. The final three data points of GS-20_10_6 in **Figures 3.5b** and **3.20b** deviate radically from the model (and their previous trend)—a function of a rapid increase in flow rate engendered by the sudden entrainment of air in the system, as the syrup reservoir was emptied below the level of the pressure vessel feed tube (see **Figure 2.2**)—and can be ignored; yet the trends and favourable development of X_N are clear. A lesser increase in $d(X_N/Y_M)/dT$ relative to the model is evidenced by GS-10_10_1, which is in turn more preferentially extended downslope than the less rapidly effused GS-10_10_3.

Figure 3.31 displays more complex relationship between X_N/Y_M and T. After an initial phase wherein $d(X_N/Y_M)/dT$ is typically slightly lower than predicted, the experimental flows mimic the numerical predictions. Then, at large T the most slowly extruded flows move into a regime of preferential extension downslope. This is most prevalent for the highly cooled GS-20_15 series,

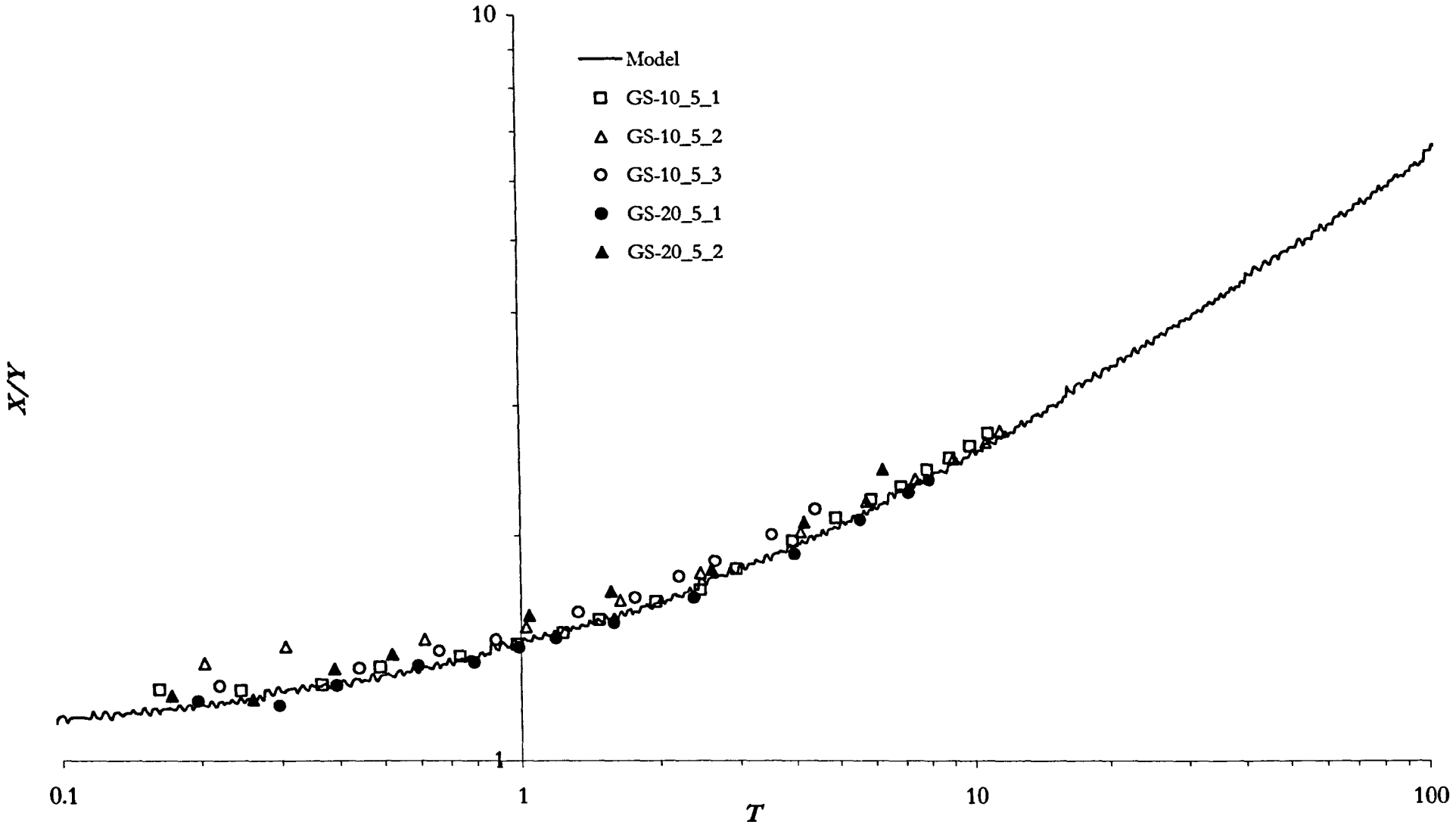

Figure 3.29 Plot of the aspect ratios of flows (X/Y) versus dimensionless time (T). Experimental parameters are as described in **Figures 3.3** and **3.18.**

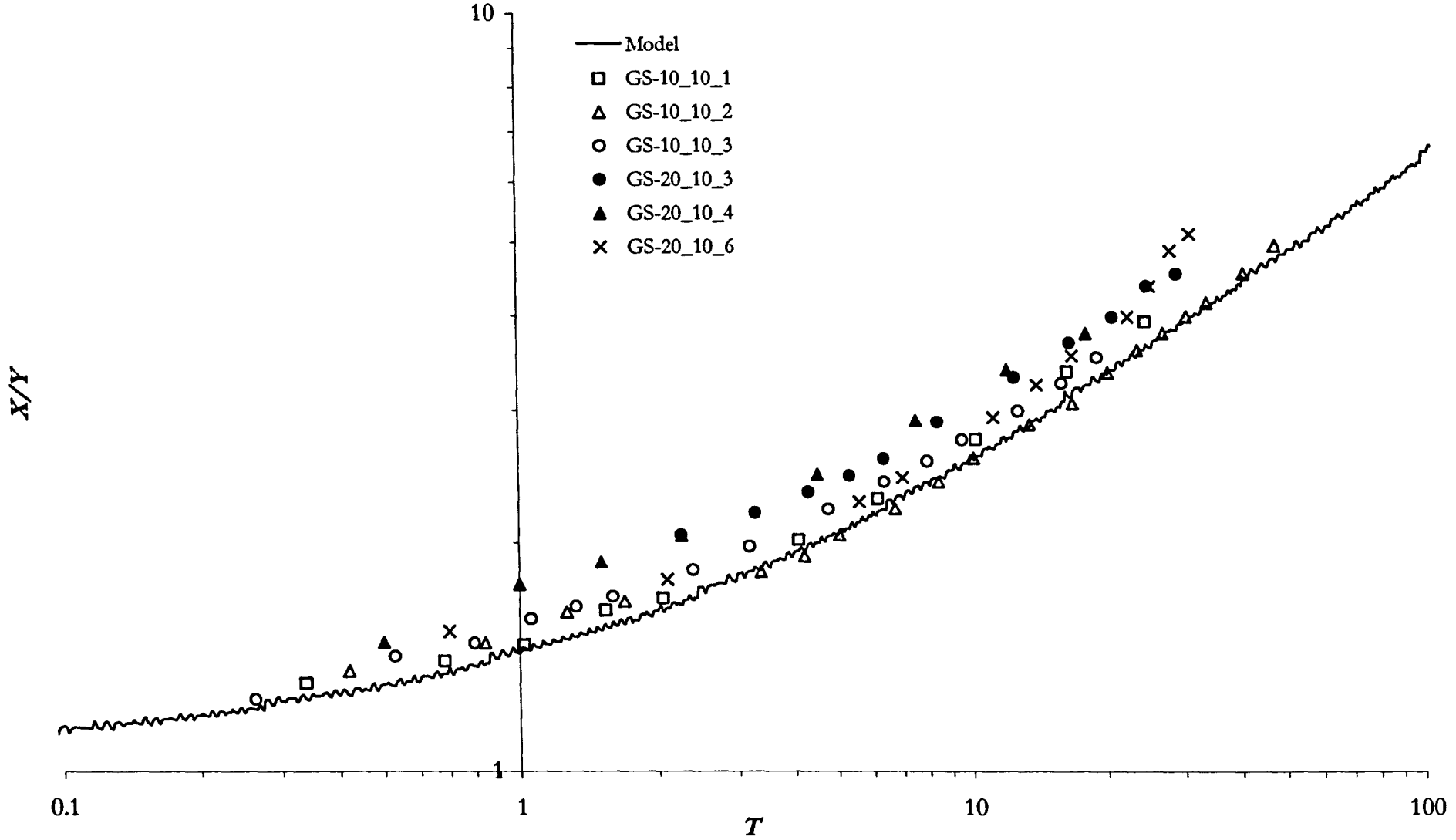

Figure 3.30 Plot of the aspect ratios of flows (X/Y) versus dimensionless time (T). Experimental parameters are as described in **Figures 3.4** and **3.19.**

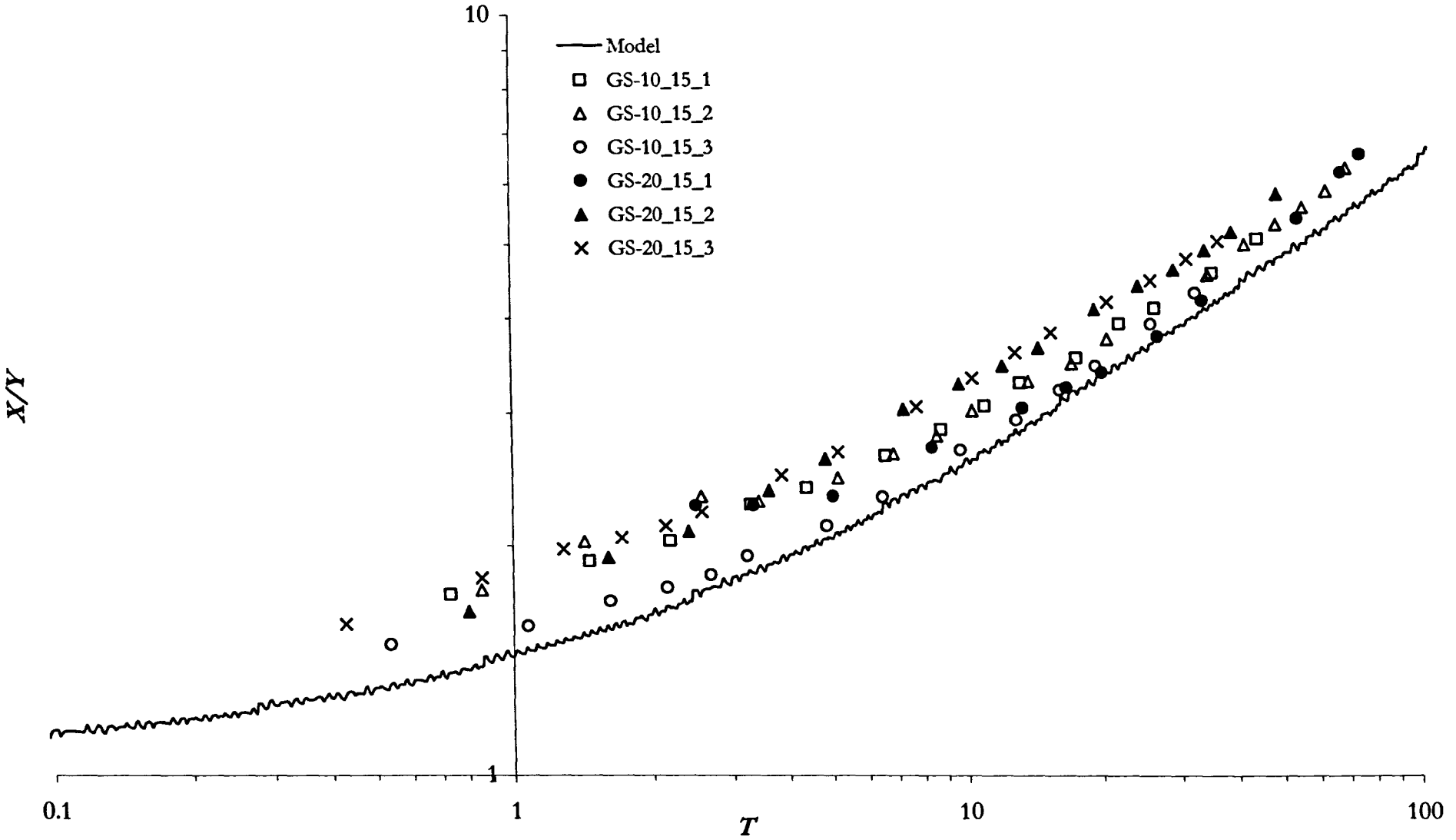

Figure 3.31 Plot of the aspect ratios of flows (X/Y) versus dimensionless time (T). Experimental parameters are as described in **Figures 3.5** and **3.20.**

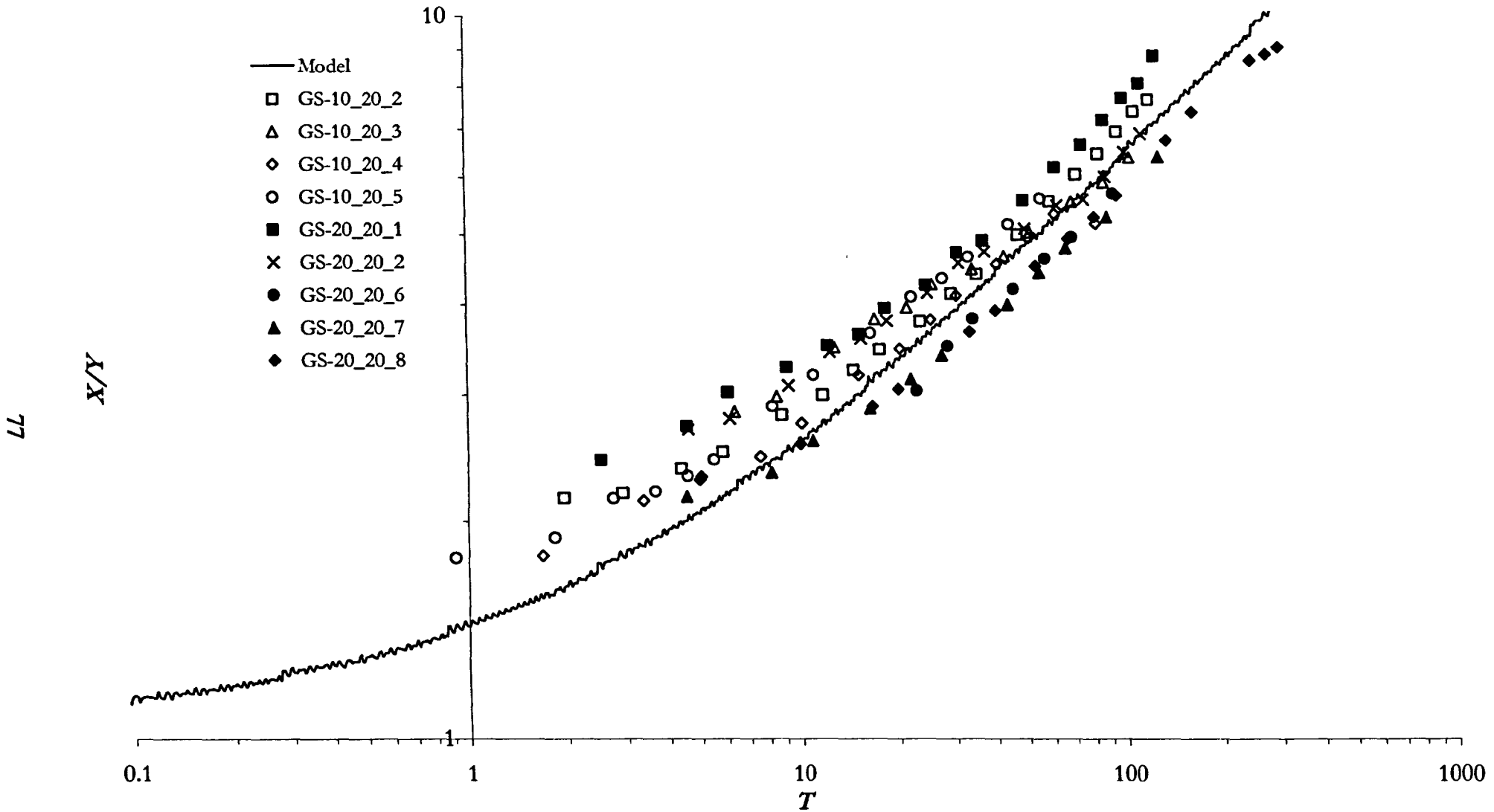

Figure 3.32 Plot of the aspect ratios of flows (X/Y) versus dimensionless time (T). Experimental parameters are as described in **Figures 3.6** and **3.21**.

with GS-20_15_1 entering this regime at $T \sim O$ (30). A similar, if less distinct change is evidenced in GS-10_15_2, yet on the whole any trend is harder to distinguish at higher slopes.

The final series, GS-10_20 and GS-20_20, are displayed in **Figure 3.32**. Again, the data describe trends of $d(X_N/Y_M)/dT$ less than predicted at low values of T, accommodating to the model at $T \sim O$ (10). Of series GS-10_20 only the most slowly effused, GS-10_20_2, displays a *slight* increase in $d(X_N/Y_M)/dT$ at extreme values of T, $\sim O$ (100). Series GS-20_20 describes a similar pattern: at long times, most flows mirror the theory, with only *slight* increases in $d(X_N/Y_M)/dT$ in GS-20_20_1 and GS-20_20_2 at $T \sim O$ (100). Again, these elements are weakly—if at all—defined, and must be considered with reference to natural experimental error and variability.

3.5.1.4 Development of height with time

Descriptions of flow kinematics have so far considered only the down- and cross-slope extents, and analyses of the aspect ratios (and preferential developments in one dimension) are themselves hampered by a lack of consideration of the third spatial dimension. Lister's model does not allow for readily accessible comparison with heights with the experimental data, in the manner undertaken in preceding sections for x_N and y_M.

Plots of centreline height (h) with respect to downslope position (x) for different time-steps are arranged according to ambient temperature and slope angle, and displayed in **Figures 3.33** to **3.39**. Error bars indicate the ± 1 mm degree of inaccuracy present in the vertical measurements (said inaccuracy in horizontal position being too small to indicate). At early stages in their evolution, all experiments develop the smooth centreline profiles described by Lister (1992) and Smith (1973) for isothermal flows, marked by a constant decrease in h with x as one proceeds away from the source.

A pronounced bulge is present in the source region, as a function of the entry conditions of the flow into the tank; this bulge is mimicked in the experimentally similar extrusions of Stasiuk et al. (1993). The height of this bulge above the source is usually stable throughout the life of a given experiment and, generally speaking, is proportional to the flow rate, Q. This is amply displayed in series GS-10_15 (**Figure 3.37**) and GS-10_20 (**Figure 3.39**)

As the flows expand downslope, however, *all* develop into a habit that is quite different to that predicted by Lister (1992) and Smith (1973), or witnessed in isothermal experiments. This development follows a two or three-stage process, beginning with an apparent bulking up of the cooler flow front. This distorts the centreline height profile, and results in one that instead describes a more gentle, if not horizontal, plateau from the source bulge to the flow front. Though isothermal flows will at some point develop this as a matter of course—they are after all thin flows

with extreme x/h ratios—this early development is compounded by a continuing inflation of the flow front, and a 'bulking up' of the flow to heights in excess of those predicted by Lister (1992).

Cooled flows develop one or two rises in addition to the source bulge, thus defining a profile that possesses inflection points beyond the one displayed in isothermal theory or practice. Typically the first one develops as a region of the 'plateau' immediately behind the flow front, or in-between such and the centre, bulks up in response to downslope retardation. Such features are clearly shown in all experimental profiles, and can frequently reach altitudes beyond those of the source bulge, exacerbating the difference from the isothermal case.

Beyond this development, flows may continue to inflate as a function of downslope stiffening, retaining the bimodal height distribution, or 'back-up', as the warmer material behind the downslope bulge preferentially accommodates the increases in height required by down- and cross-slope expansion relative to the model. It is not uncommon for flows that form a thick plateau in such a manner to subsequently develop one or two further topographic highs, close to the flow front or centre.

Experiments cooled to –20°C display thicker profiles than similarly parameterised flows cooled to –10°C, and while more rapidly extruded flows possess higher and more prominent source bulges, experiments extruded at the lowest flow rates typically achieve the highest absolute height profiles within an experimental series. At the lowest flow rates the source bulge is often nearly obscured, as the flow rises in absolute height to form the frontal and central plateau and/or bulge, lacking a prominent trough in between.

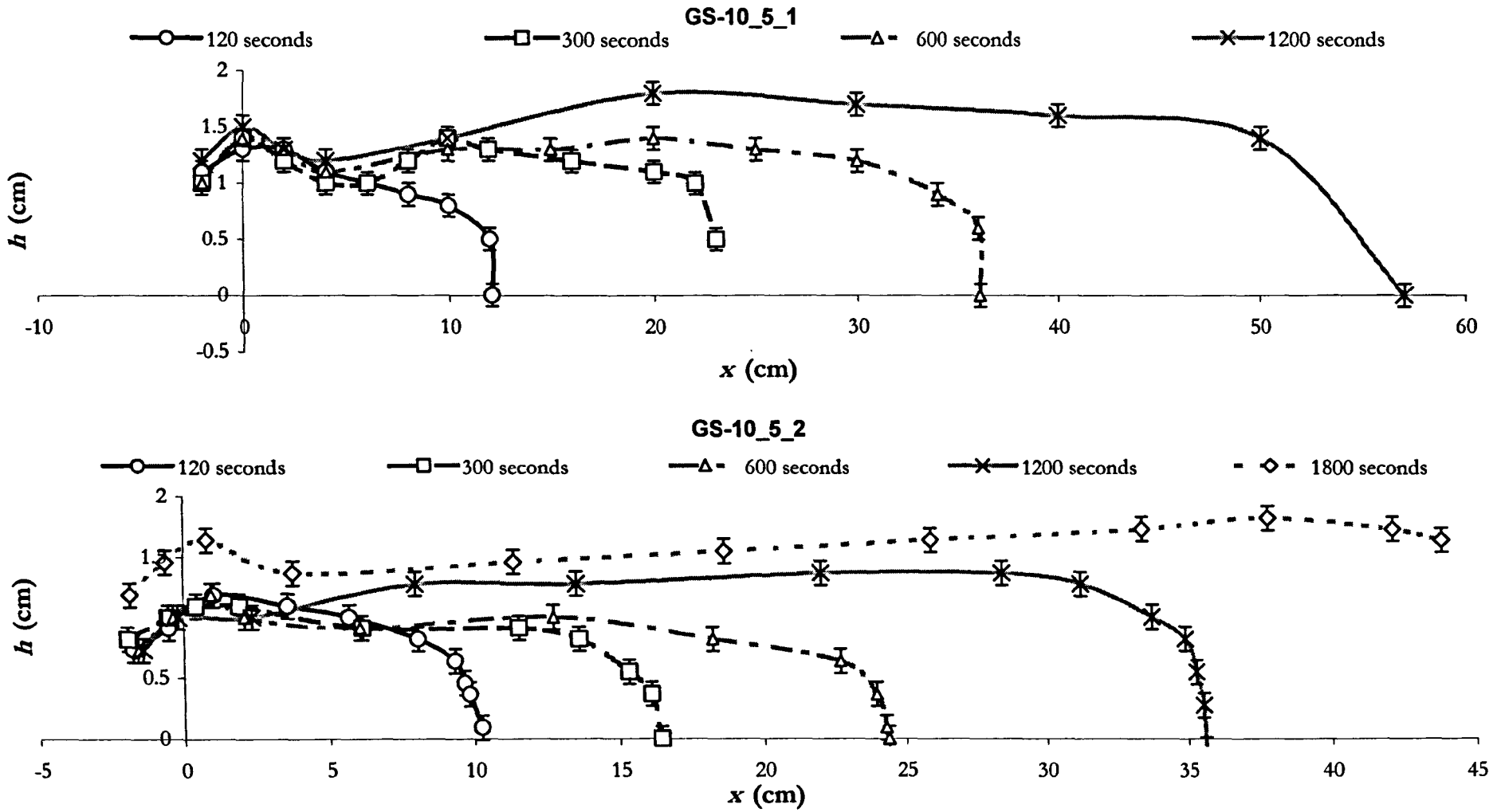

Figure 3.33 Profiles of the height (h) along downslope coordinates (x), taken at different times (t). Experimental parameters: **GS-10_5_1**—T_a –9°C, T_e 19.5°C, slope angle 5°, Q 3.3 x10^{-6} m^3 s^{-1}, η_e 64 Pa s, η_a ~34,000 Pa s; **GS-10_5_2**—T_a –8.5°C, T_e 20°C, slope angle 5°, Q 1.3 x10^{-6} m^3 s^{-1}, η_e 59 Pa s, η_a ~29,000 Pa s.

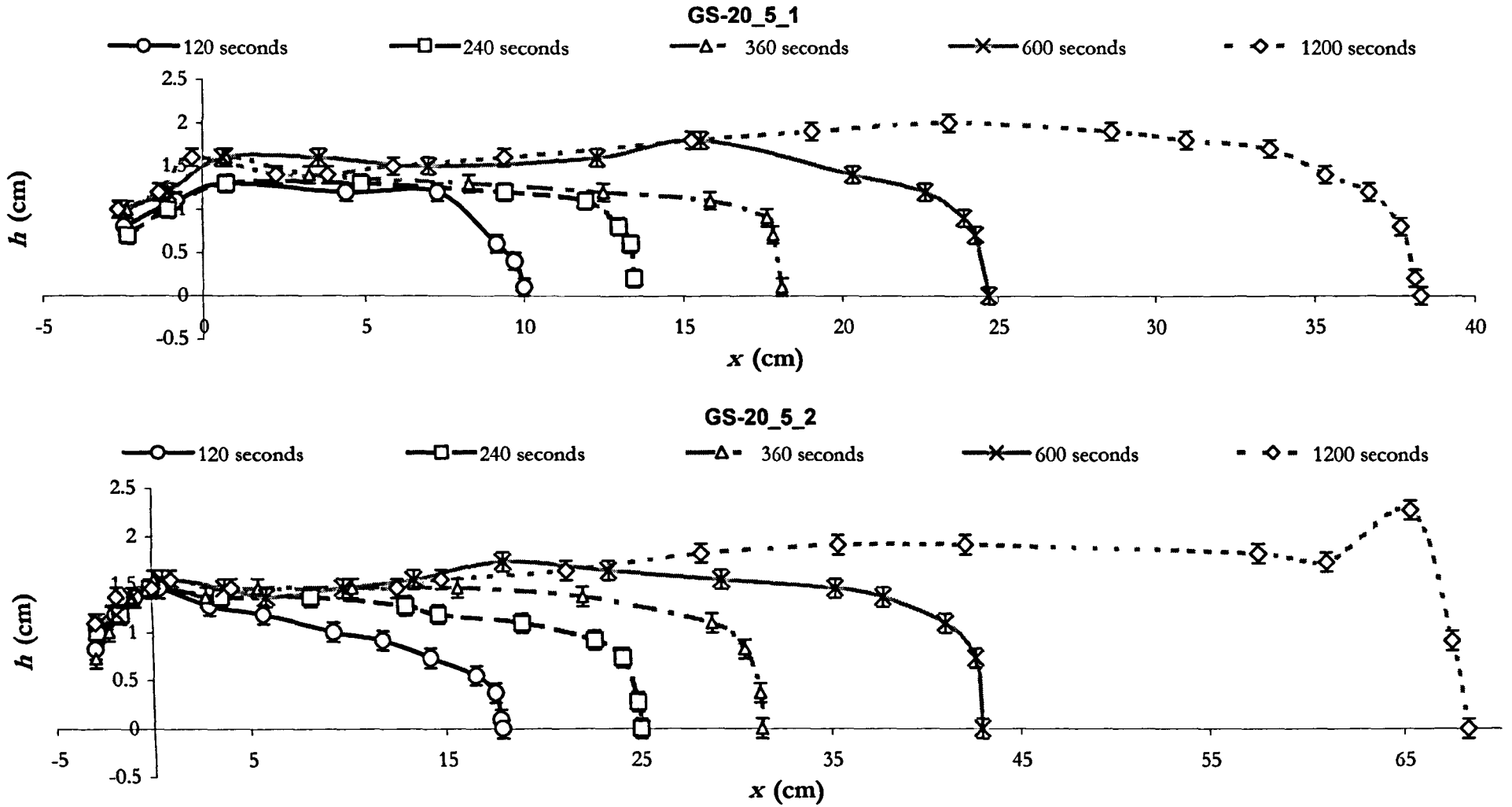

Figure 3.34 Profiles of the height (h) along downslope coordinates (x), taken at different times (t). Experimental parameters: **GS-20_5_1**—T_a –18.5°C, T_c 19°C, slope angle 5°, Q 1.8 x10^{-6} m^3 s^{-1}, η_c 69.4 Pa s, η_a ~8.9 x10^5 Pa s; **GS-20_5_2**—T_a –18.5°C, T_c 19°C, slope angle 5°, Q 5.5 x10^{-6} m^3 s^{-1}, η_c 69.4 Pa s, η_a ~8.9 x10^5 Pa s.

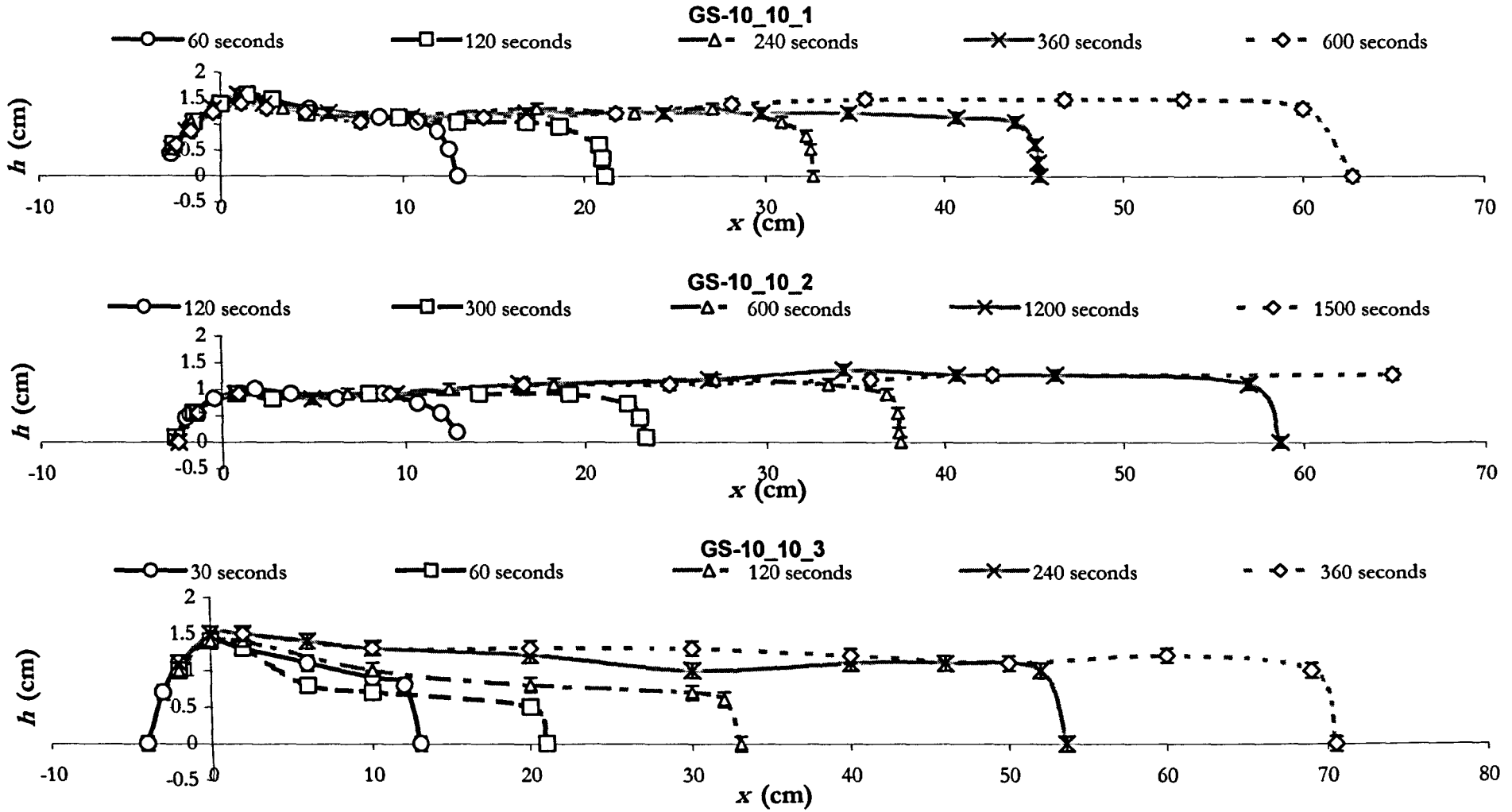

Figure 3.35 Profiles of the height (h) along downslope coordinates (x), taken at different times (t). Experimental parameters: **GS-10_10_1**—T_a –9.5°C, T_c 19°C, slope angle 10°, Q 4.8 x10^{-6} m^3 s^{-1}, η_c 69.4 Pa s, η_a ~39,500 Pa s; **GS-10_10_2**—T_a –10°C, T_c 19.5°C, slope angle 10°, Q 1.7 x10^{-6} m^3 s^{-1}, η_c 64 Pa s, η_a ~46,000 Pa s; **GS-10_10_3**—T_a –8.5°C, T_c 21°C, slope angle 10°, Q 10.8 x10^{-6} m^3 s^{-1}, η_c 50.5 Pa s, η_a ~ 29,000 Pa s.

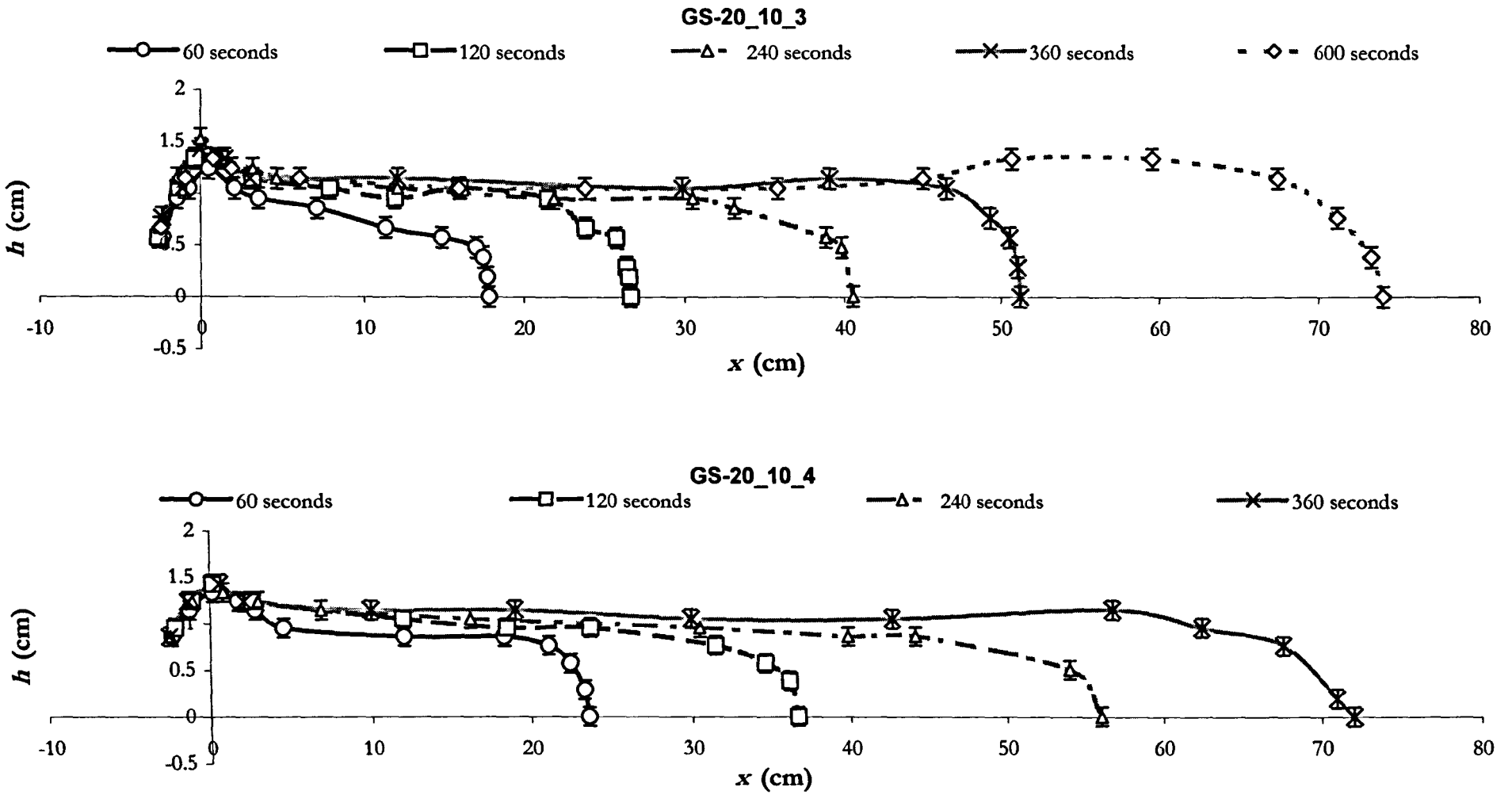

Figure 3.36 Profiles of the height (h) along downslope coordinates (x), taken at different times (t). Experimental parameters: **GS-20_10_3**—T_a –19°C, T_e 20.75°C, slope angle 10°, Q 4.3 x10^{-6} m^3 s^{-1}, η_e 52.5 Pa s, η_a ~1.1 x10^6 Pa s; **GS-20_10_4**—T_a –19°C, T_e 21°C, slope angle 10°, Q 8.6 x10^{-6} m^3 s^{-1}, η_e 50.5 Pa s, η_a ~1.1 x10^6 Pa s.

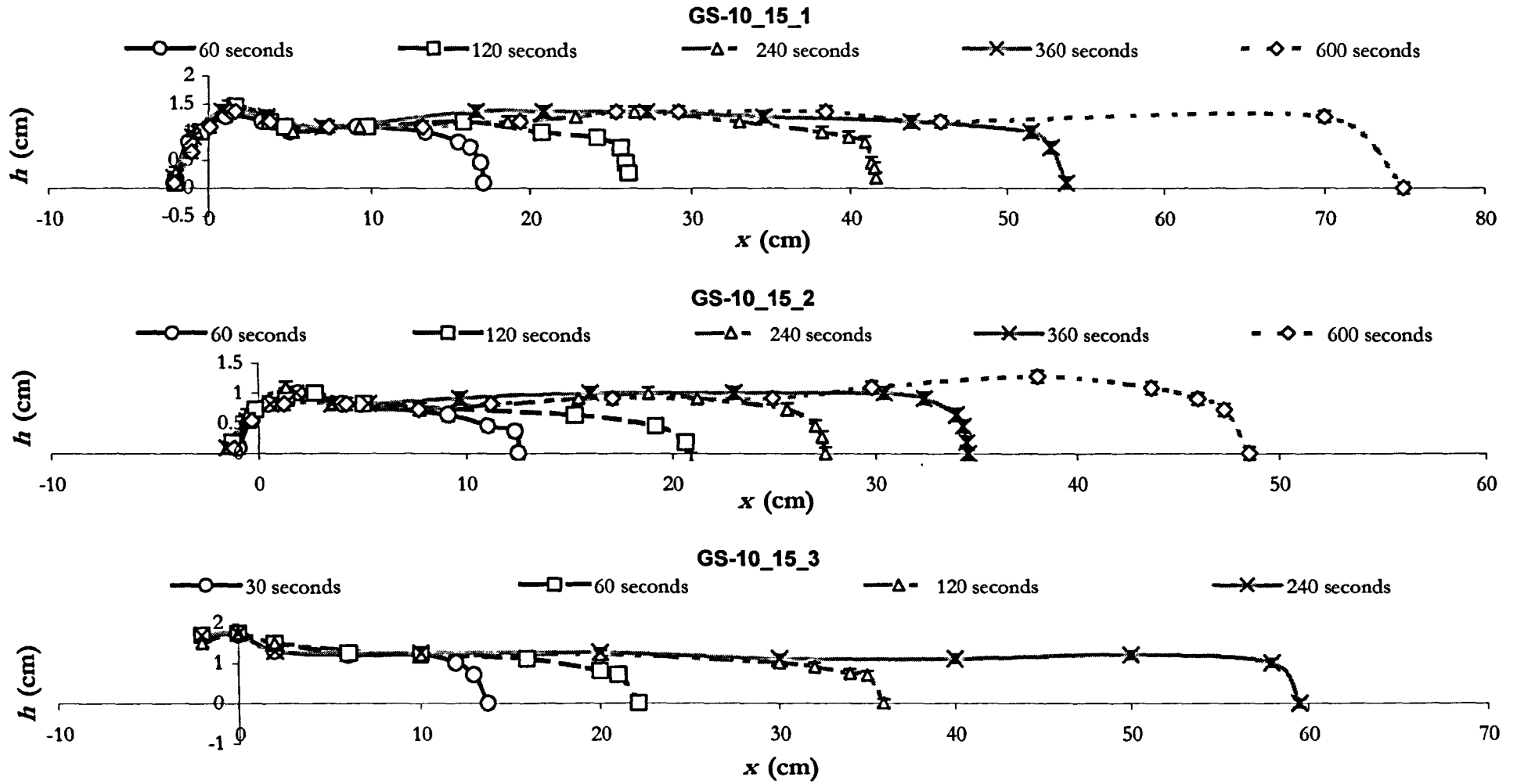

Figure 3.37 Profiles of the height (h) along downslope coordinates (x), taken at different times (t). Experimental parameters: **GS-10_15_1**—T_a –10°C, T_e 18.5°C, slope angle 15°, Q 4.8 x10^{-6} m^3 s^{-1}, η_e 75.3 Pa s, η_a ~46,000 Pa s; **GS-10_15_2**—T_a –10°C, T_e 18.5°C, slope angle 15°, Q 1.8 x10^{-6} m^3 s^{-1}, η_e 75.3 Pa s, η_a ~46,000 Pa s; **GS-10_15_3**—T_a –9.5°C, T_e 20.5°C, slope angle 15°, Q 8.6 x10^{-6} m^3 s^{-1}, η_e 54.6 Pa s, η_a ~ 39,500 Pa s.

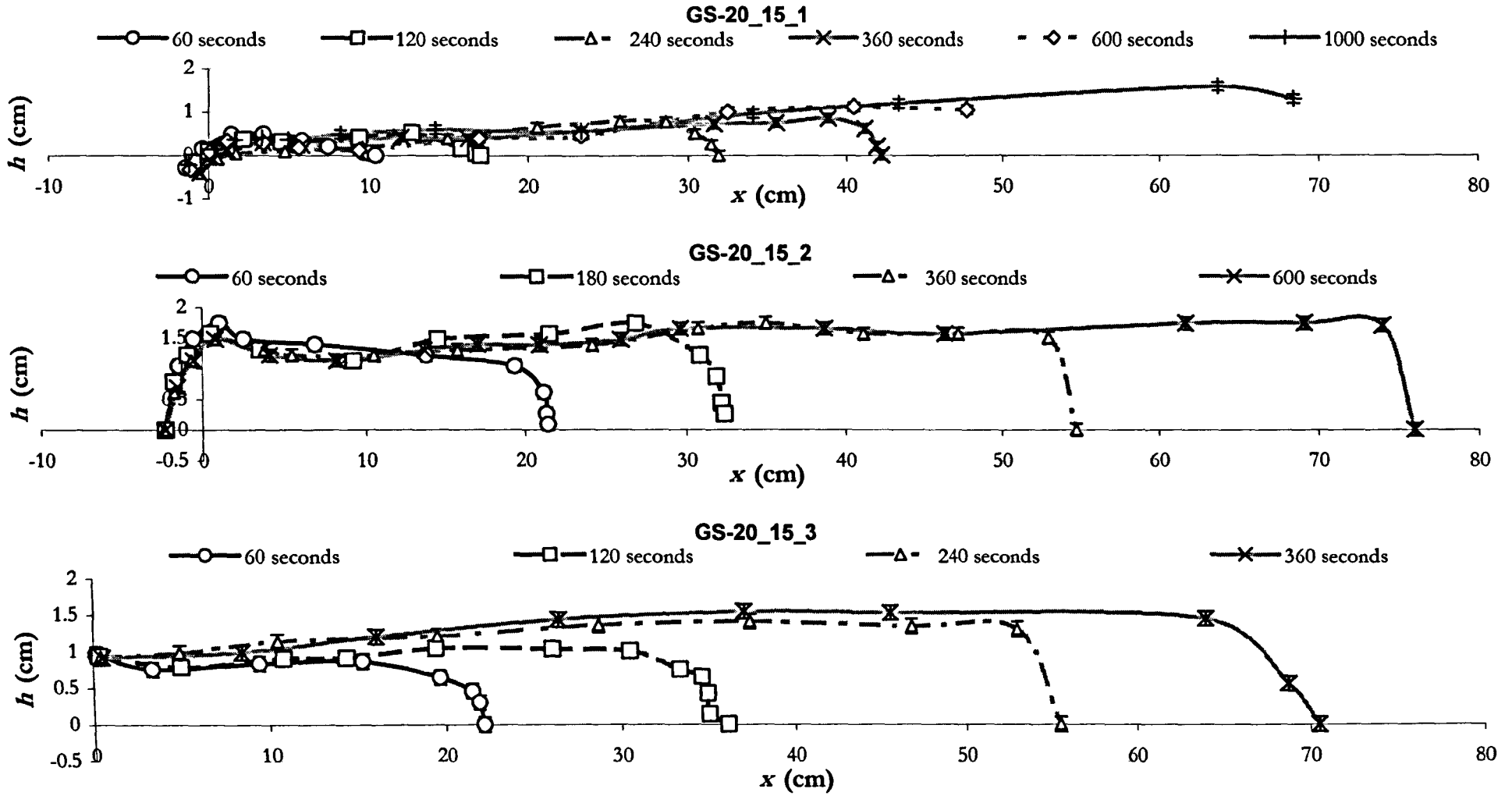

Figure 3.38 Profiles of the height (h) along downslope coordinates (x), taken at different times (t). Experimental parameters: **GS-20_15_1**—T_a –20°C, T_c 20°C, slope angle 15°, Q 1.3 x10^{-6} m^3 s^{-1}, η_c 69.4 Pa s, η_a ~1.6 x10^6 Pa s; **GS-20_15_2**—T_a –19.5°C, T_c 19.5°C, slope angle 15°, Q 4.3 x10^{-6} m^3 s^{-1}, η_c 64 Pa s, η_a ~1.3 x10^6 Pa s; **GS-20_15_3**—T_a –19°C, T_c 20°C, slope angle 15°, Q 7.2 x10^{-6} m^3 s^{-1}, η_c 69.4 Pa s, η_a ~1.1 x10^6 Pa s.

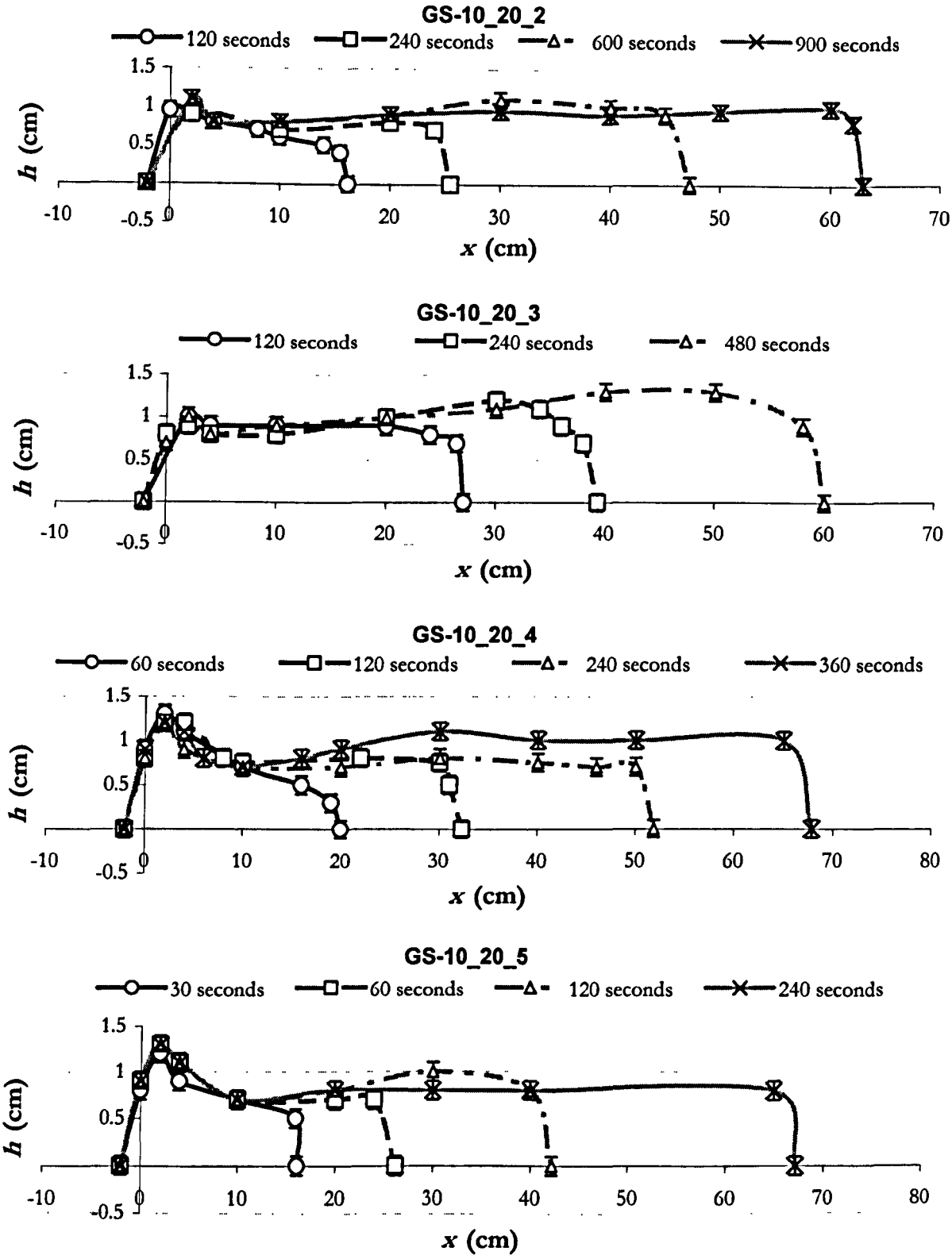

Figure 3.39 Profiles of the height (h) along downslope coordinates (x), taken at different times (t). Experimental parameters: **GS-10_20_2**—T_a –10°C, T_c 18.5°C, slope angle 20°, Q 1.4 x10^{-6} m^3 s^{-1}, η_c 75.3 Pa s, η_a ~46,000 Pa s; **GS-10_20_3**—T_a –9°C, T_c 20°C, slope angle 20°, Q 3.1 x10^{-6} m^3 s^{-1}, η_c 59 Pa s, η_a ~34,000 Pa s; **GS-10_20_4**—T_a –10°C, T_c 20°C, slope angle 20°, Q 6.1 x10^{-6} m^3 s^{-1}, η_c 59 Pa s, η_a ~ 46,000 Pa s; **GS-10_20_5**—T_a –9°C, T_c 20°C, slope angle 20°, Q 8.6 x10^{-6} m^3 s^{-1}, η_c 59 Pa s, η_a ~ 34,000 Pa s.

3.5.2 Morphological observations

Beyond the formation of rivulets in some extremely parameterised experiments, the analogue extrusions of Lister (1992) were marked by their homogenous character and smooth bounding surfaces. The uncooled experiments pictured in **Plate 3.1** wholly mimic this isothermal paradigm. Yet as cooling takes effect, the flows rapidly depart from these simple forms, and three main morphological features become readily evident: the formation of a thin, folded, highly viscous skin, which could buckle and tear; a clear near source flow channelisation delineated by areas of clear hot syrup and the cooled skin (as described above); and a significant flow boundary perturbation.

3.5.2.1 Fold and skin formation

In each cooled experiment, a noticeable change in the surface appearance and morphology of substantial areas of the flow was made manifest quite early on in the extrusion. Whereas isothermal (and hence isoviscous) syrup extruded at room temperature into a similarly heated environment forms constructs that are smooth, transparent and to all effects homogenous throughout their eruption history, cooled flows very rapidly develop a marked variation in surface appearance.

Areas of the flow develop what appears to be a highly translucent (and ultimately near opaque) skin; typically, this change began of the order of 100 s into the experiment. The skin develops first towards the flanks and rear of the experiment; proceeds to grow in two arms towards the front and centre of the flow; and ultimately develops to cover all but a central channel (see 3.5.2.2; **Plate 3.6**).

Closer inspection shows that this skin is not a cooled solid crust per se, of radically different rheological properties, but rather a thin surface layer of deformed syrup, formed by the tens to hundreds of small mm- and sub mm-scale folds (**Plates 3.2** to **3.5**). It is these folds that coalesce to form a visibly distinct surface layer, and the interplay of light with their morphology that gives the effect of translucency (**Plates 3.3** and **3.4**).

Direct observation shows this crust to behave in a ductile manner at low strain rates, indistinctly different from 'warm' syrup. This is no better highlighted than by the fact that in half the flows a second, subsequent generation of 'folding' occurs (highlighted in **Plate 3.2**). These second-generation compression features are typically of very low amplitude, and possess a wavelength of the order of 1-10 cm. The relief of these folds is so low that they are undetectable in the videos taken of the height profiles of the experiments, and are instead (literally) illuminated by the interaction of the Cold Room lights on the perturbed syrup surface.

Table 3.2 displays a number of data taken from the experiments, correlating the number of folds observed with the time of the measurement, the spatial range of the compressive features and the

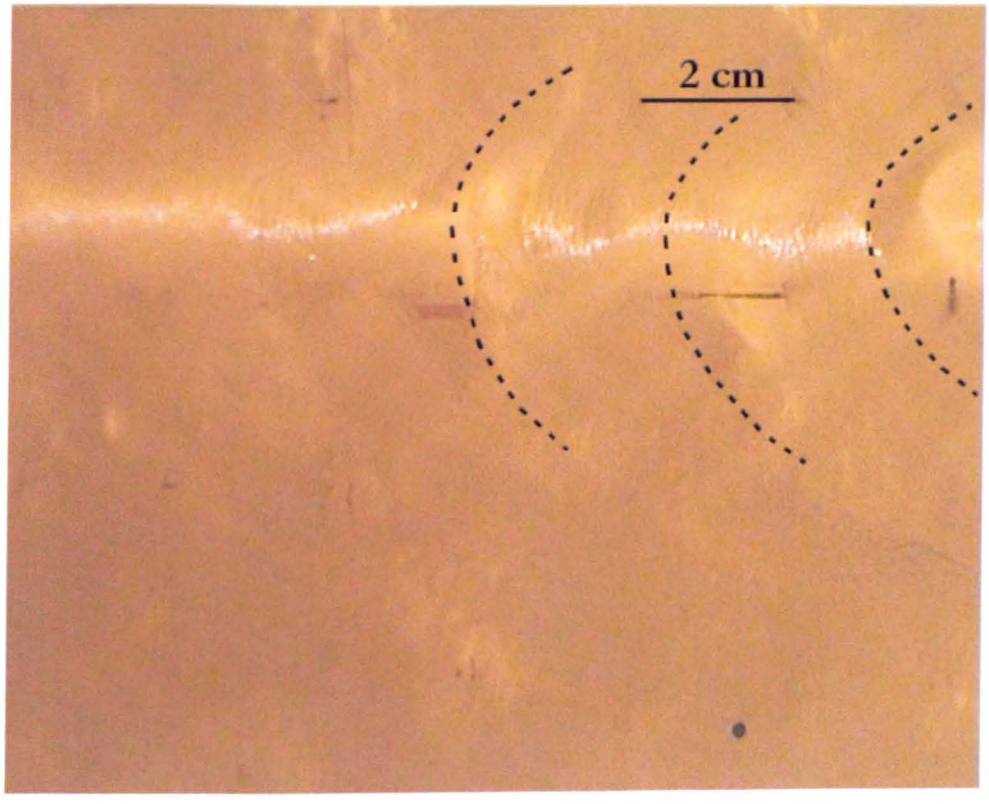

Plate 3.2 Second-generation 'large wavelength' folds, distinguished by perturbations in the reflection of light and marked for clarity. Flow is **GS-20_20_8**—T_a –19°C, T_e 21°C, slope angle 20°, Q 0.7 x10^{-6} m^3 s^{-1}, η_e 50.5 Pa s, η_a ~1.1 x10^6 Pa s.

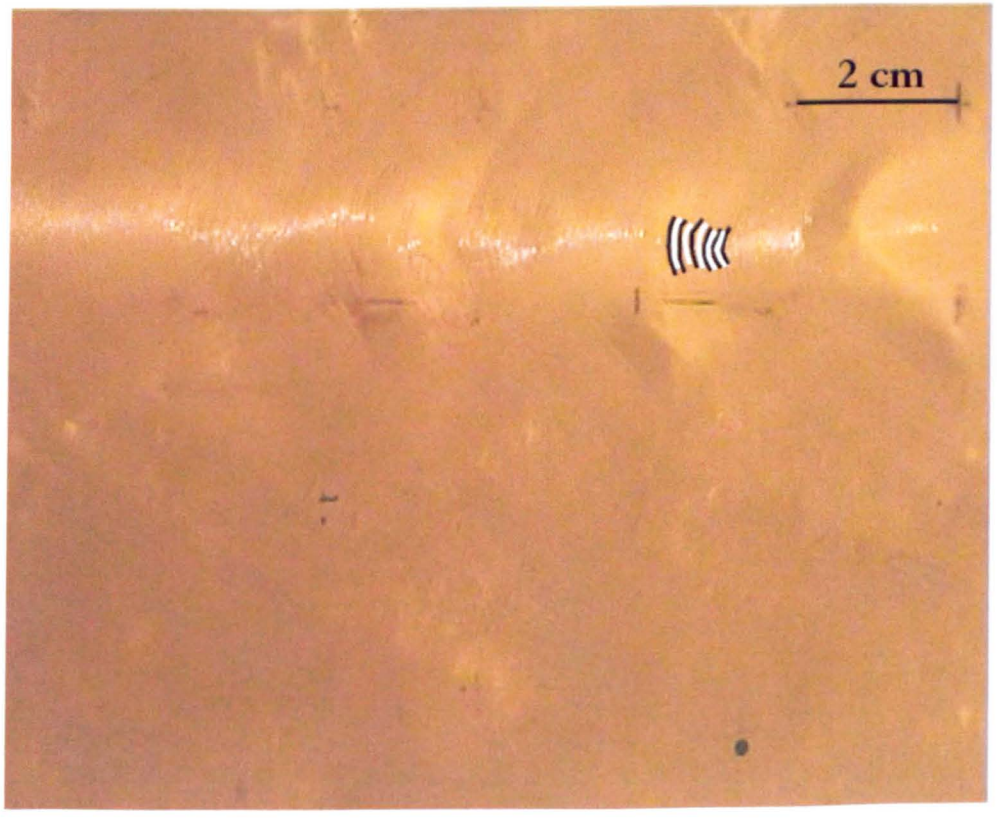

Plate 3.3 First-generation 'small wavelength' folds, with crests highlighted by the light; a series of folds are marked for clarity. Flow is **GS-20_20_8**.

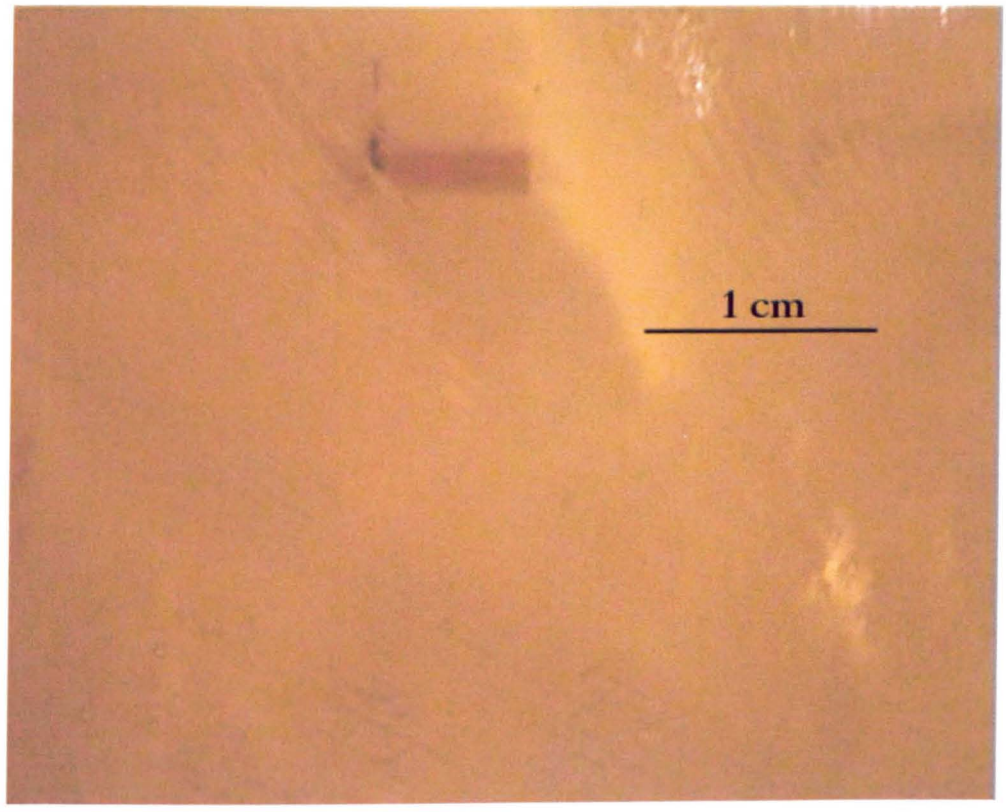

Plate 3.4 Close-up view of first generation, small wavelength folds, also clearly displaying areas of negligible skin formation. Flow is **GS-20_20_8**.

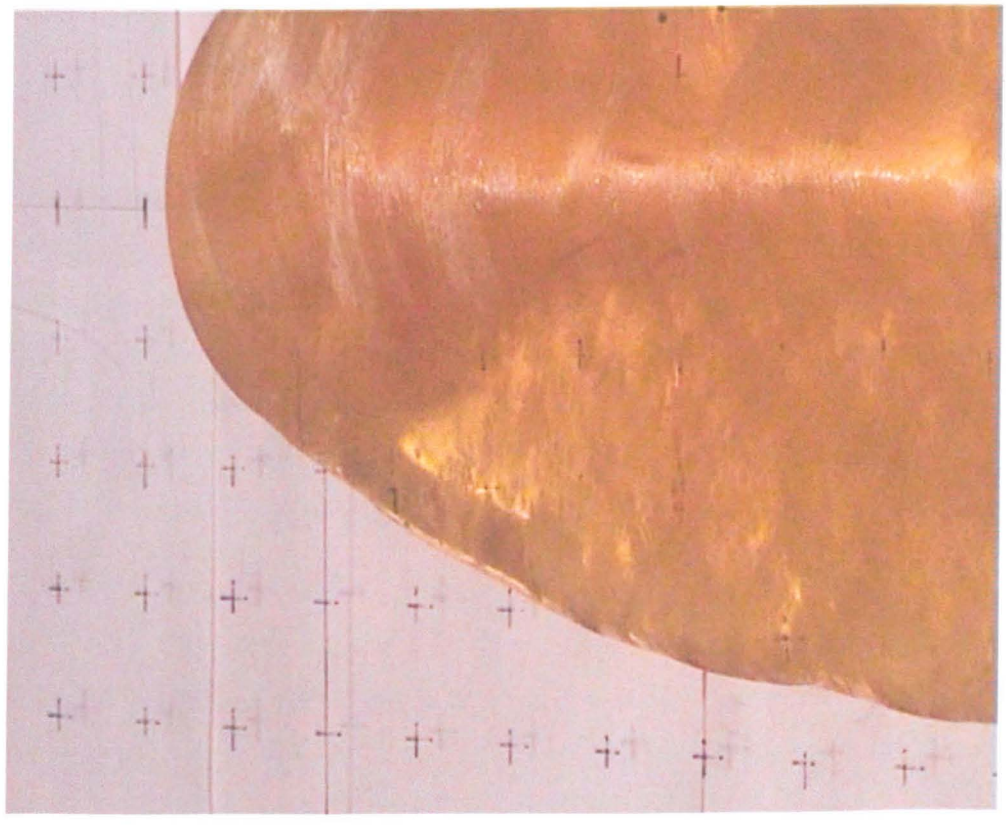

Plate 3.5 Flow front of **GS-20_20_8**, displaying two generations of compression. Contrast the strong, pervasive skin formation at the flow toe with the mottled patchy skin adjacent, between the central region and the flanks.

Table 3.2 Large wavelength (second generation) fold data taken from a variety of experiments.

Experiment	Time of reading (s)	Folded Range	Number of Folds	Average Fold Wavelength (cm)
GS-10_5_1	-	-	0	-
GS-10_5_2	1685	-	1	2.6
GS-10_5_3	-	-	0	-
GS-10_10_1	-	-	0	-
GS-10_10_2	1445	37 cm to 66.3 cm	5	5.9
	1680	40 cm to 74 cm	7	4.9
GS-10_10_3	-	-	0	-
GS-10_15_1	-	-	0	-
GS-10_15_2	1185	36.4 cm to 75 cm	7	5.5
GS-10_15_3	-	-	0	-
GS-10_20_2	880	41.9 cm to 58.4 cm	4	4.1
	1020	38 cm to 65.7 cm	6	4.6
	1185	40 cm to 73.8 cm	9	3.8
GS-10_20_4	-	-	0	-
GS-10_20_5	-	-	0	-
GS-20_10_3	555	40 cm to 56.7 cm	3	5.6
	645	39 cm to 72 cm	5	6.6
	670	-		9
GS-20_10_4	-	-	0	-
GS-20_10_6	1220	25.8 cm to 55 cm	6	4.9
GS-20_20_2	415	18.2 cm to 35.8 cm	5	3.5
	615	20.5 cm to 46.7 cm	9	2.9
	915	26.8 cm to 60 cm	11	3.0
	1315	25 cm to 80 cm	16	3.4
	1315	24.3 cm to 39 cm	5	2.9
GS-20_20_7	685	36.2 cm to 75 cm	9	4.3
	745	63.5 cm to 80 cm	8	2.1

average fold wavelengths thus defined. Correlation with **Table 3.1** will show that the flows that developed clear, second-generation compression features are those with lowest flow rates. Although at a glance counter-intuitive—as one might expect a heavy source flux vis-à-vis a cooled viscous flow front to be a crucial factor in favouring compression—this is simply a factor of the efficacy of experimental observation. Experiment lifetimes were limited by the length of the tank available. Slowly effused flows were therefore more able to proceed to a 'thermally evolved' state in the experimental space and timeframe than their more rapidly extruded counterparts.

Second-generation folds form in the central portions of the flow downslope, and possess a distinctly parabolic plan. Their formation is not uniquely compressive, however. At high strain rates, the microscopically folded, cooled skin does not readily accommodate to the warm mobile syrup underneath, and tears. Clearly the compound surface possesses some tensile strength, and these tears occur along the central channel's lateral boundary (see section 3.5.2.2).

A careful study of experimental video shows that tears forming at an angle of ~ 45° to the channel boundary (closing downslope; one such tear can be seen on the lower flank of **Plate 3.7d**, ~ 14 cm

from the source) can grow or heal, depending on the localised dynamics. Tears that grow define an arm of cooled, rippled skin that, on account of its obvious thermal, mechanical and viscous maturity, acts as a nucleus for further small-scale fold generation. As these areas of rippled surface pass downflow, they further interact with any compressive stress regime—itself a function of natural height gradient, frontal cooling and the curious height profiles described in section 3.5.1.4—to form secondary features.

The second-generation folds are therefore more complex compressive products than those of a simple, homogenous viscous surface layer that is buckled by a simple stress regime. Instead, areas of cooled skin torn away on the strained channel margins are ultimately recompressed downflow, ultimately forming a more simple folded skin layer towards the toe (**Plate 3.5**). In areas of localised skin formation that have a history of tearing and shear but are *not* especially recompressed, the surface can develop a mottled appearance. This is aptly displayed in **Plate 3.5**: as compression focused along the downslope axis of expansion, there is an area directly to the left of the toe and downflow channel that is expanding slowly enough to possess a close accumulation of skin-covered areas, yet freely enough to prevent coalescence and recompression of same.

An analysis of the potential mechanics behind these features is discussed in Chapter 6.

3.5.2.2 Flow channelisation

The most striking morphological feature observed was the clear channelisation that developed in the majority of the 25 cooled experimental runs, over a wide range of parameters. Even those flows which did not develop channel structures (those of highest flow rates and lowest slopes) developed what will be seen as the precursory stages to channel growth, and one might fairly envisage that they would develop channels in due course.

The channels were delineated by the sharp contrasts between areas of near opaque cooled, rippled 'skin' (described in section 3.5.2.1, above) and transparent hot, undeformed syrup. Whilst syrup naturally possesses a colour somewhat like deep amber, the skin is far lighter in hue, a mix between a light amber and straw yellow. Previous experiments with cooled syrup (Stasiuk et al. 1993) did not report the presence of such a skin, even though ambient temperatures in their experiments would have produced similar rates of cooling to those witnessed here. The axisymmetric flows of Stasiuk et al. (1993), however, lack the more extreme velocities and senses of shear that flows on an inclined plane exhibit.

The growth of this rippled skin follows a well-described, systematic pattern, forming a series of sequential morphological flowtypes that remain constant for all experiments. This development from visibly homogenous transparent syrup to a well-developed channel structure is described in

Plate 3.6. The six images follow the experiment GS-10_10_2 through its evolution over more than twenty minutes.

The flow begins as a simple, near-isothermal extrusion, still influenced by the early-time model of Lister (1992; and thus Huppert 1982; **Plate 3.6a**). After six minutes' extrusion, areas of cooled rippled skin, no more than a cm or so wide, begin to form on the rearward flanks and margins (**Plate 3.6b**). By eight minutes' evolution, these have grown to some five or six cm width, bracketing a clearly defined, 9 cm wide central channel (**Plate 3.6c**). The channel is not perfectly centred, but it generally uniform.

After ten and a half minutes of expansion, the rippled margins are forming arms that are curving round to join in the centre (**Plate 3.6d**), and by sixteen minutes this process is well and truly complete, with skin covering all the flow but a central, stable channel and a small lip at the flow toe (**Plate 3.6e**). The 'long-time' flowtype is ultimately defined by a clear central channel, followed by a skin-covered channel region that develops second-generation compression features, with both central areas flanked by slower moving portions covered with well-developed skin that is occasionally torn and remobilised (**Plate 3.6f**).

This sequence is shown in simplified form in **Figure 3.40** and **Plate 3.7**. For all fully developed experimental channels there was usually a notable (though not large) decrease in channel width with distance from the source. This decrease was approximately linear, but such a decrease did not continue *ad infinitum*. The channel reached some extinction point, at which the area of hot fluid syrup ended, and there was an abrupt change to an area of cooled rippled skin, as displayed in **Figure 3.40**, and **Plates 3.6d, 3.6f** and **3.7d**.

Beyond local, marginal changes in the channel-skin interface caused by tearing and recoalescence, and a slight variability in the position of channel extinction point down slope (by no more than a couple of centimetres), by the time the flow reached the stage depicted in **Figure 3.40d** (and **Plate 3.7d**) the near source channel structures were extremely stable. For all experiments, average channel widths at this stage were seen to vary linearly with extrusion rate for a given ambient temperature, and over a range of slope angles. Measurements of channel width are plotted against source flow flux measurements in **Figures 3.41** and **3.42**. The basic linear relationship between channel width and flow rate is clearly evidenced. Furthermore, subsequent investigations into the dynamics of these channels, in Chapter 6, will show that the intercept of these graphs is an inverse function of the tan of the slope angle.

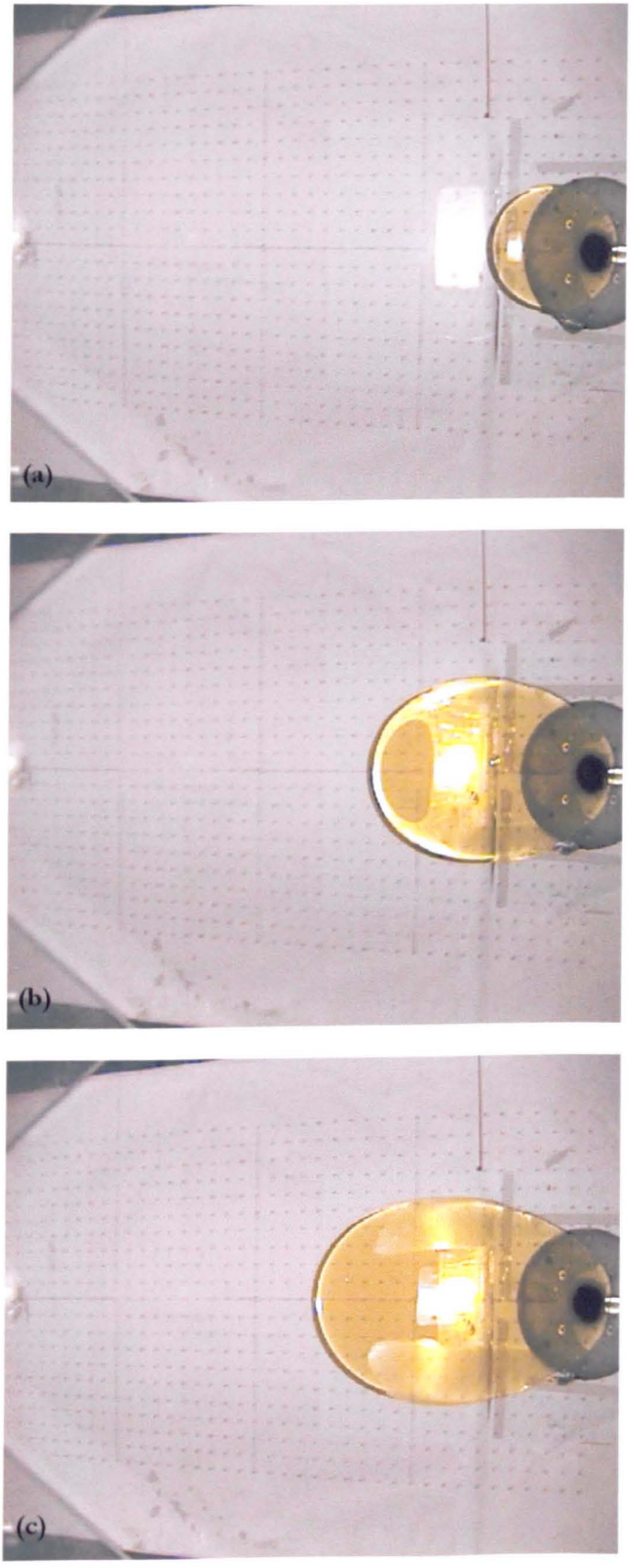

Plate 3.6a-c Progression of an experimental flow from a homogenous, warm extrusion to a cooled, morphologically heterogeneous flow form. Experiment is **GS-10_10_2**—T_a –10°C, T_e 19.5°C, slope angle 10°, Q 1.7 x10^{-6} m^3 s^{-1}, η_e 64 Pa s, η_a ~46,000 Pa s; (a) ~ 110 s, (b) ~ 360 s, (c) ~ 490 s.

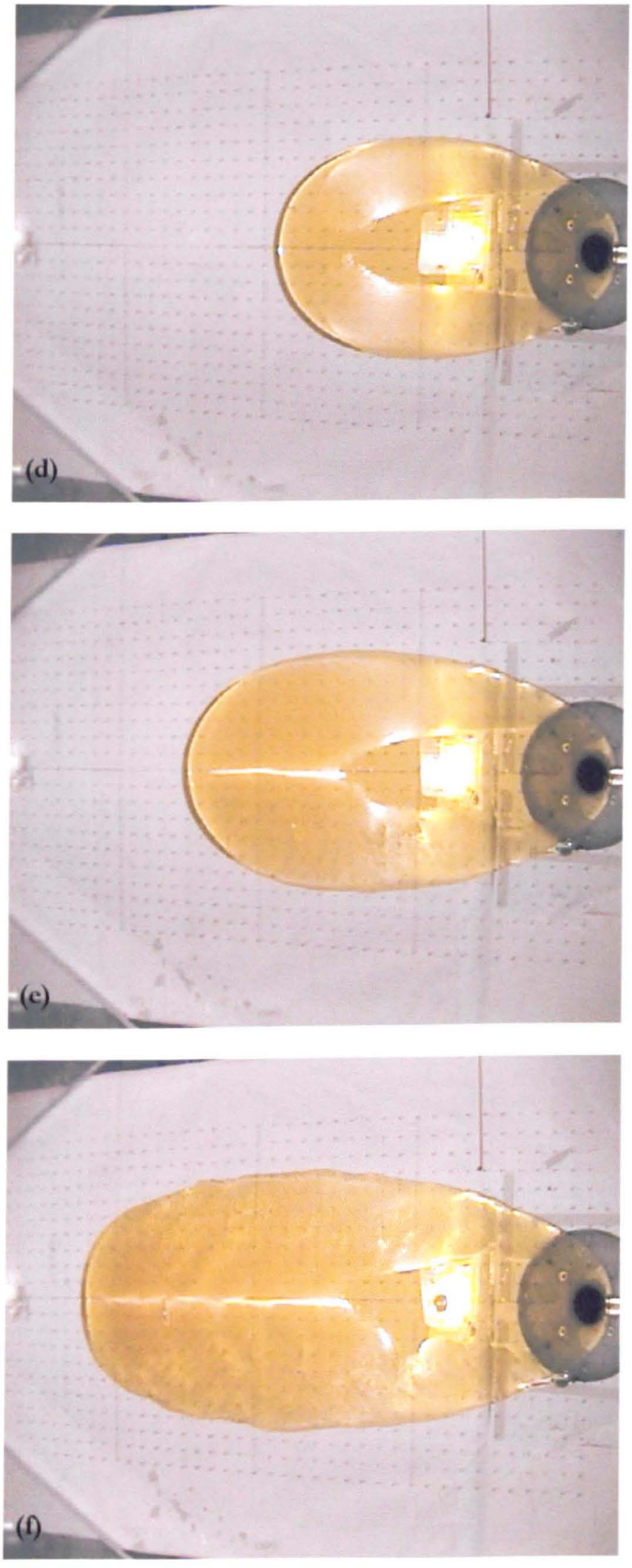

Plate 3.6d-f Progression of an experimental flow from a homogenous, warm extrusion to a cooled, morphologically heterogeneous flow form. Experiment is **GS-10_10_2**—T_a –10°C, T_e 19.5°C, slope angle 10°, Q 1.7 x10^{-6} m^3 s^{-1}, η_e 64 Pa s, η_a ~46,000 Pa s; (d) ~ 635 s, (e) ~ 950 s, (f) ~ 1420 s.

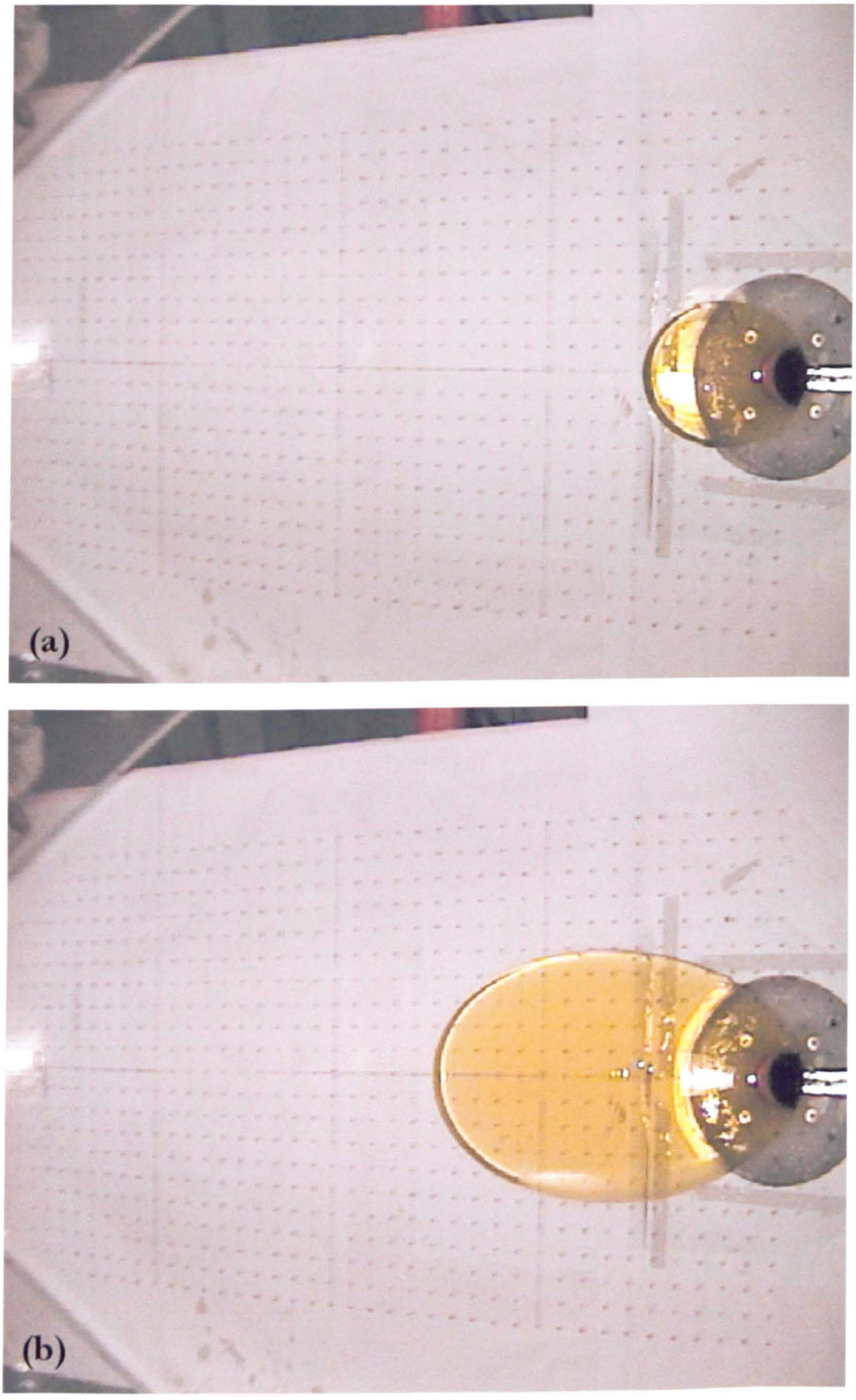

Plate 3.7a-b Experimental examples of the sequential stages depicted in Figure 3.40. Flow is **GS-20_15_3**—T_a –19°C, T_e 20°C, slope angle 15°, Q 7.2 x10^{-6} m^3 s^{-1}, X^* 6.8, T^* 11.7, η_e 69.4 Pa s, η_a ~1.1 x10^6 Pa s; (a) ~ 20 s, (b) ~ 90 s.

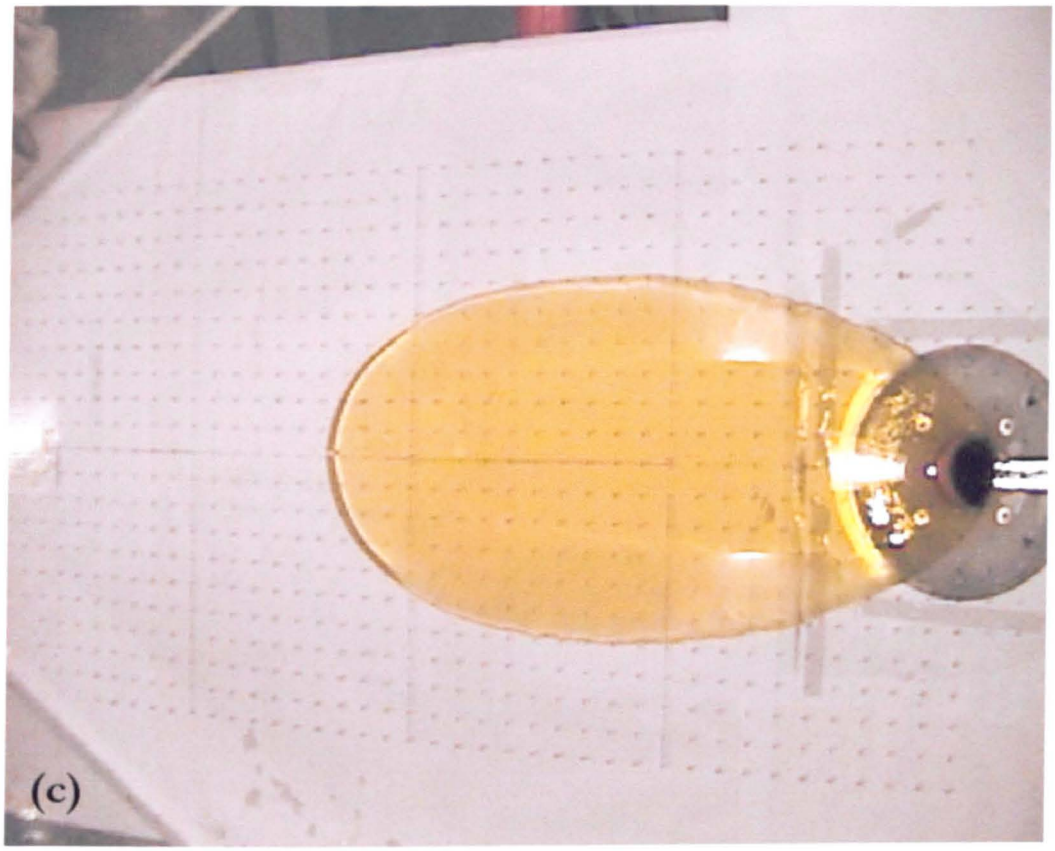

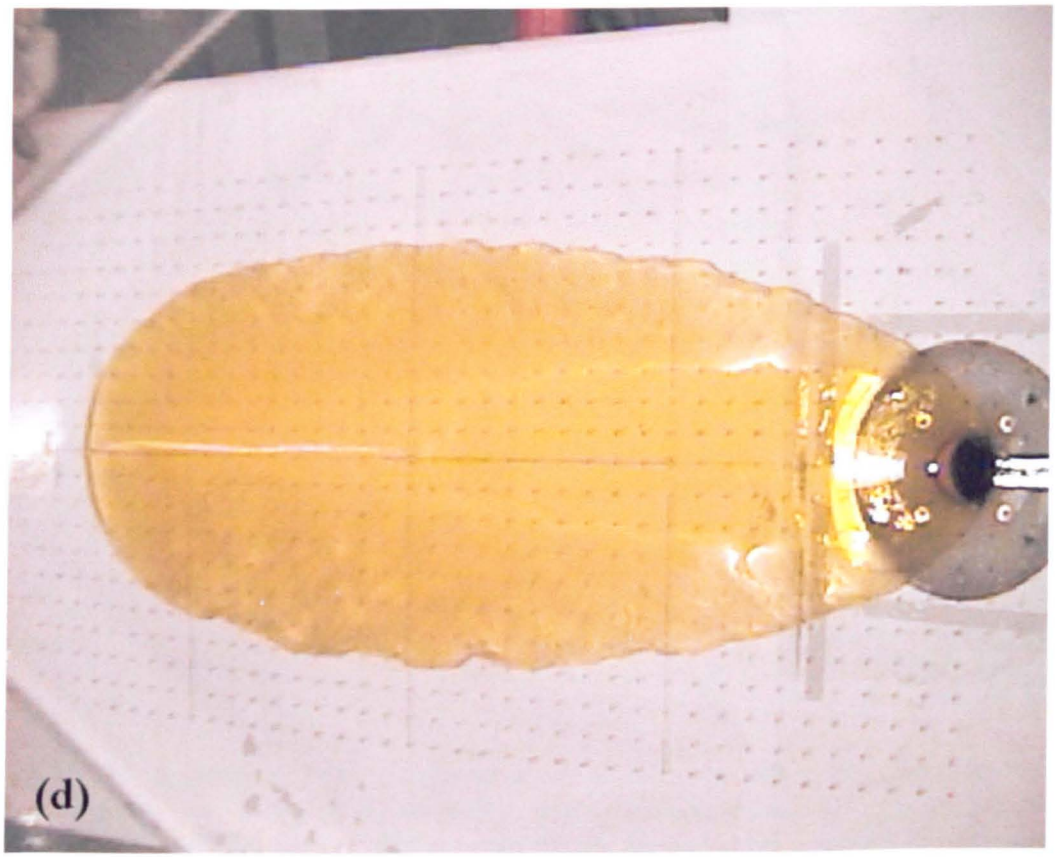

Plate 3.7c-d Experimental examples of the sequential stages depicted in Figure 3.40. Flow is **GS-20_15_3**—T_a –19°C, T_e 20°C, slope angle 15°, Q 7.2 x10^{-6} m^3 s^{-1}, X^* 6.8, T^* 11.7, η_e 69.4 Pa s, η_a ~1.1 x10^6 Pa s; (c) ~ 185 s, (d) ~ 365 s.

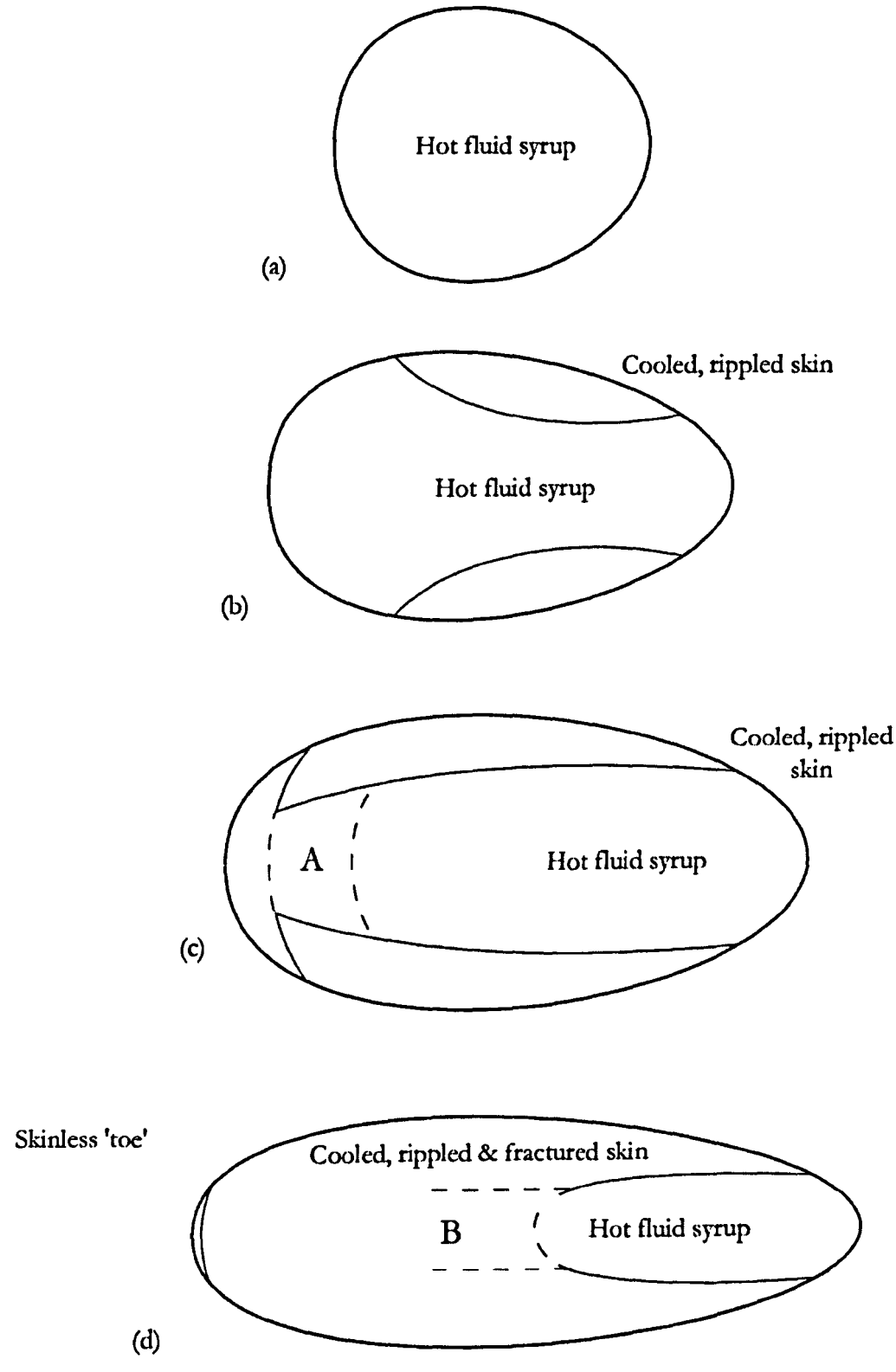

Figure 3.40 The sequence of channel formation and stabilisation commonly displayed in cooled experimental flows (not to scale): (a) no visible skin formation; (b) cooled rippled surface layer noticeable on flanks; (c) the arms of skin-covered surface formed in (b) converge to form a rippled region, A; (d) a fully developed flow with channel system. Although regions A and B are skin-covered, they are dynamically linked to the hot fluid channel, displaying considerable shear along the boundaries with the cooled flanks [the solid lines flanking A in (c) and the dashed lines in (d)]. Flow-plans are not to scale, and extrusions do not decrease in y_M as the experiment proceeds.

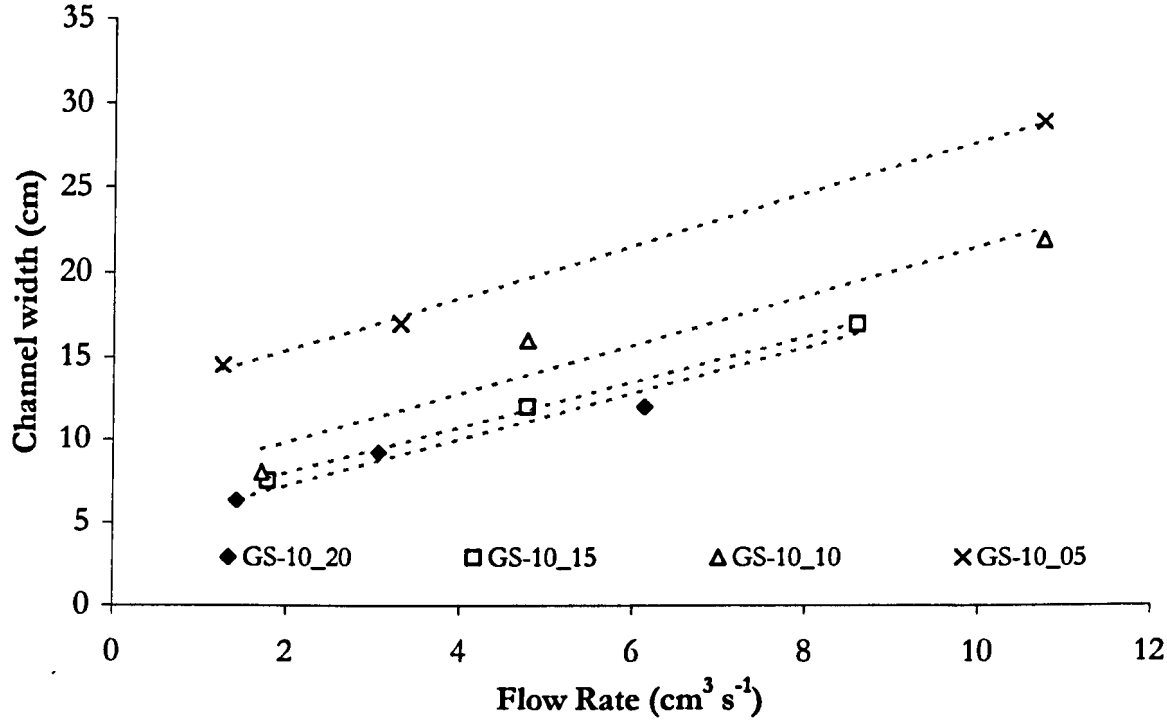

Figure 3.41 Plot of measured average channel widths versus recorded flow flux, for flows extruded into an ambient temperature of –10°C. Linear regression lines have been fitted to the data, to illustrate a general trend; regression fits in terms of channel width (w) and flow rate (Q) are as follows: GS-10_20 $w = 1.4Q + 4.3$ ($R^2 = 0.975$); GS-10_15 $w = 1.4Q + 5.1$ ($R^2 = 0.998$); GS-10_10 $w = 1.5Q + 6.8$ ($R^2 = 0.931$); GS-10_5 $w = 1.6Q + 12.2$ ($R^2 = 0.998$).

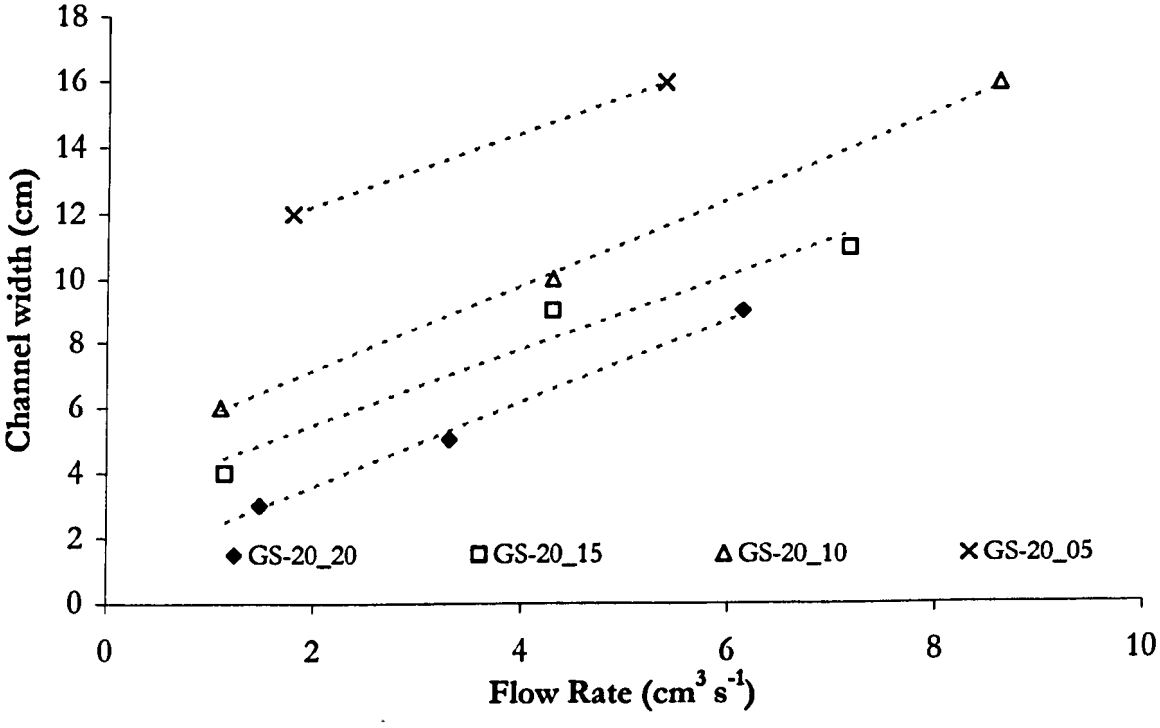

Figure 3.42 Plot of measured average channel widths versus recorded flow flux, for flows extruded into an ambient temperature of –20°C. Linear regression lines have been fitted to the data, to illustrate a general trend; regression fits in terms of channel width (w) and flow rate (Q) are as follows: GS-20_20 $w = 1.3Q + 1.0$ ($R^2 = 0.997$); GS-20_15 $w = 1.2Q + 3.1$ ($R^2 = 0.955$); GS-20_10 $w = 1.3Q + 4.4$ ($R^2 = 0.999$); GS-20_5 $w = 1.1Q + 10.0$ ($R^2 = 1$).

While the channel structure is clear and well-defined, it is not especially pervasive. Golden syrup's low thermal diffusivity (described in Chapter 2) precludes a rapid propagation of a thermal boundary layer through the depth of the flow, though its highly temperature-dependent viscosity does allow for considerable mechanical changes in the boundary layer to develop.

That the subsurface fluid is considerably warmer and more mobile than the cooled flow top is aptly shown in the processes of skin disruption. The viscous rippled skin possesses a very small tensile strength that is readily overcome by the levels of shear present between the warm central channel and cooled, near stagnant flow margins. This process is seemingly caused by an interaction of two factors: (a) a steep velocity gradient across the clear channel and adjacent skin-covered surface interface, wherein hot elements of syrup shear and draw out the cooler material on passing; and (b) the presence of warmer, more mobile syrup beneath the cooled surface, which provides a similar level of drag underneath the surface.

Though the former is the most apparent, it is no doubt aided by the process of underskin drag at the channel interface, and the appearance of tears in skin-covered areas beyond the channel is not at all uncommon. Further analyses of channel velocity and structure are considered in Chapter 6.

3.5.2.3 Flow boundary perturbation

As the analogue flows develop, the flow margins diverge from the smooth profiles predicted by numerical models (e.g. Smith 1972, Lister 1992) and seen in isothermal experiments, and instead gravitate toward the corrugated appearance seen in **Plates 3.8** and **3.9**, and shown schematically in **Figure 3.43**.

Plates 3.8 and **3.9** display a clear series of sheared, bulbous lobes situated on the flanks. All cooled flows develop these features, given time. When first observed, it was thought that these might signify overflow features, analogous to the lobes seen on a great many lava flows. Cooling is accentuated at the flow margins, where velocities are reduced and hence the ratio of the loss of heat by diffusion to the replenishment of heat by advection is greater than it is in the flow centre. Hot, less viscous material from the flow centre would then overflow this cooled viscous region and form a new frontal lobe. In a material such as Golden Syrup this would not necessarily be readily apparent, as strong viscosity gradients can exist with negligible change in the syrup's visual properties.

However, a cursory look at **Figure 3.43** and **Plate 3.9** shows that such a hypothesis is incorrect. For these to be overflow features, one would expect the crease structures to lie at a 90° angle to that actually observed (i.e. on the bottom flank of the flow shown in Plate **3.9**, they would run from top right to bottom left, rather than top left to bottom right). Rather than central, hot portions of

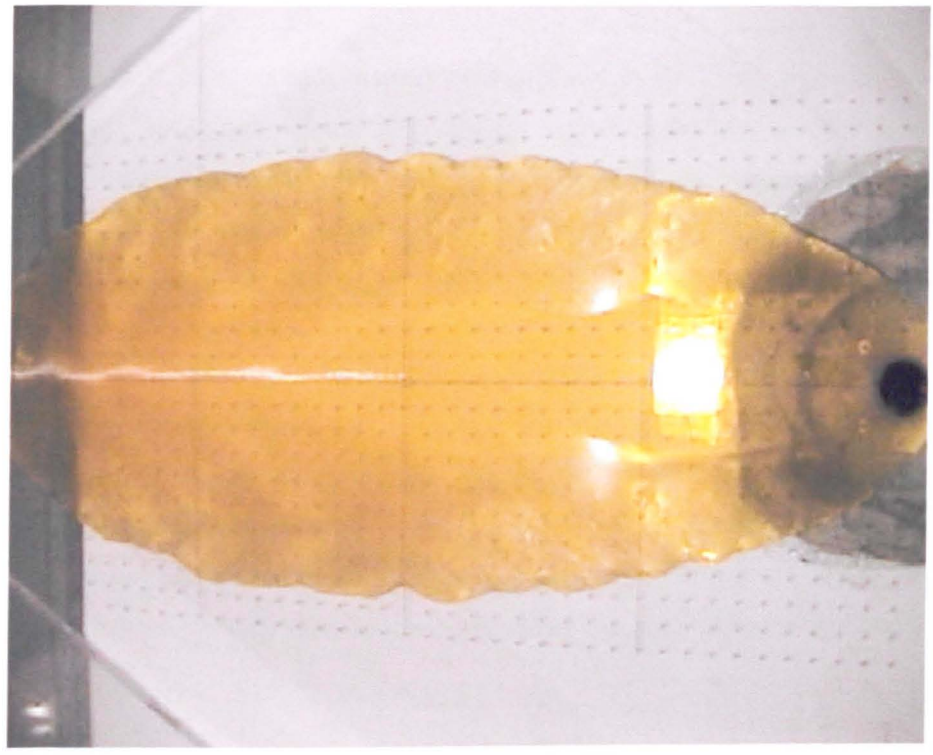

Plate 3.8 Experiment **GS-20_10_3**; still image captured after 625 seconds. Scale grid at 2 cm intervals. Note the variable lobe diameter and lobe placement asymmetry between the flanks. Parameters: T_a –19°C, T_e 20.75°C, slope angle 10°, Q 4.3 x10^{-6} m^3 s^{-1}, X^* 8.4, T^* 24.5, η_e 52.5 Pa s, η_a ~1.1 x10^6 Pa s.

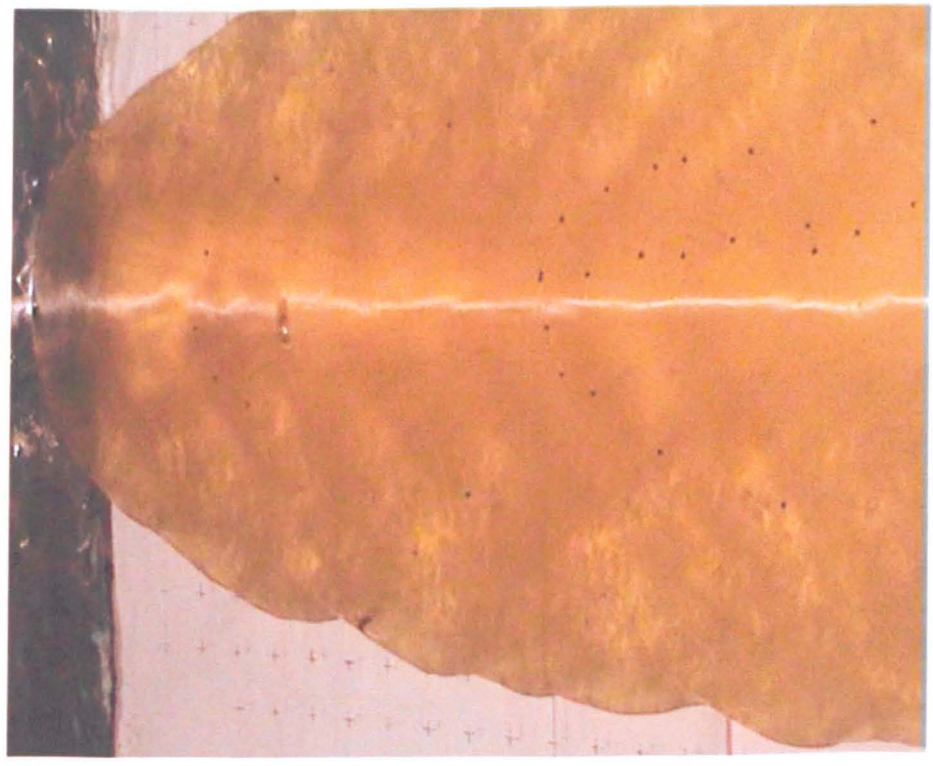

Plate 3.9 Experiment **GS-20_20_7**; still image captured after 750 seconds. Scale grid at 2 cm intervals. Note the crease structures on the lower flank, and their direction (bottom right to top left). The small particles were placed to measure flow velocities (see Chapter 5). Parameters: T_a – 18°C, T_e 22°C, slope angle 20°, Q 3.3 x10^{-6} m^3 s^{-1}, X^* 3.7, T^* 5.5, η_e 43.3 Pa s, η_a ~7.3 x10^5 Pa s;

the flow having overridden the cooled, viscous material at the frontal flanks, it is apparent that the rearward lobes or large perturbations instead overlap those to the front, at some point *after* the lobes' development. Close observation reveals that a point of stagnation is reached on the flanks of the flow, and any lateral movement at this point is temporarily halted. Given the incompressibility of the fluid, and the local lateral component of the flux then focus fluid into the surrounding areas, which perturbs the smooth flank profile and forms the shall amplitude lobes seen.

As Lister (1992) evidenced, accurately analysing the spatial and temporal characteristics of the origin of a small perturbation on the flow margins is difficult. The curved flow surface renders an accurate description of exactly when the perturbation started to grow difficult to obtain. The perturbations grow variably with time, depending on the local velocity profile. Perturbations relegated to the trailing margins of the flow cease to grow almost immediately, while those situated near more active flow margins continue to develop and overlap in the manner described.

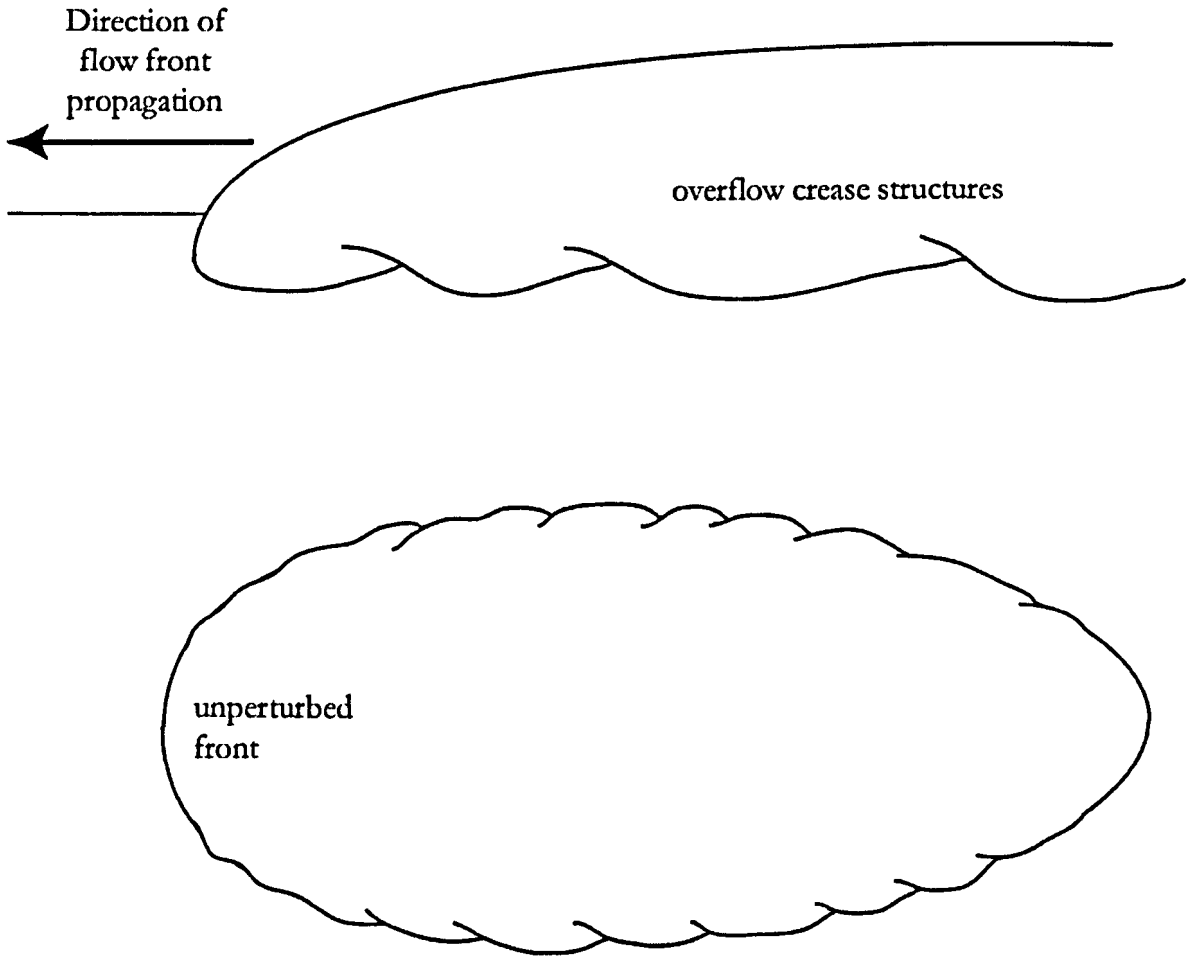

Figure 3.43 Schematic representation of the habit of the perturbed flow margins present in many cooled flows, and the resultant deformation of flow lobes caused by continued motion (not to scale).

3.6 Summary of experimental observations

In summation, it will be seen that the isothermal extrusions described in section 3.4 give good approximation with the similar extrusions of Lister (1992), but that the cooled experiments differ in clear and often systematic fashion from said extrusions and the isothermal theory of Lister (1992). Such deviations from the isoviscous case embrace both kinematic and morphological changes, which are described in section 3.5 of this chapter. Generally, at any given time (t), the values of the variables downslope extent (x_M) and maximum cross-slope extent (y_M) in cooled flows, and their rates of increase with time, are diminished with respect to the values predicted by Lister's (1992) numerical solution of (eq. 3.11) and the long-time similarity solution (eq. 3.15), for similar flow parameters. Such deviations from the model often appear to display a systematic character, though such phenomena are frequently subtle, and any attempt to resolve trends in the data must contemplate the presence of small changes in parameters between experiments and any other experimental inaccuracies.

Attempts to model these apparently systematic deviations from the model are analysed in Chapter 5, but it can be suggested that the *relative cooling* of a flow is itself dependent upon the other experimental parameters: flow rate (Q) and slope incline (θ). Otherwise-similarly parameterised flows display increased retardation (with respect to the model) in normalised x_M and y_M at lower values of Q or θ, with the influence of changes in the latter diminishing at higher values of θ. The relative rate of increase of normalised x_M and y_M, or changes in the aspect ratio with time, is hard to discern; but there is some evidence for preferential retardation of y_M with respect to x_M, and an increase in aspect ratio, at long times.

In addition to providing rather different kinematics to the isothermal and isoviscous flows of Lister (1992), the cooled extrusions display a suite of novel morphologies in their flow-forms; these features are hitherto unencountered – and unpredicted – in experimental viscous flows, yet highly pertinent in form and origin to real lavas. Firstly the development of the height profiles of the extrusions showed a marked deviation from the solutions predicted by Smith (1973) and Lister (1992) for an isoviscous fluid. Flows typically developed multi-modal height distributions, with both a source bulge and a raised, downstream flow plateau behind a viscous flow-front toe. Secondly, three further categories of phenomena have been classified in the extrusions: the development of a cooled, folded skin, showing two stages of fold generation; centrally sited channels of warm, undeformed and relatively uncooled syrup, whose widths are observed to be a clear function of experimental flow-rate and slope at a given ambient temperature; and perturbations and over-folds at the flow margins. These phenomena are further investigated in a quantitative manner in Chapter 5.

Chapter 4: Field investigation of the morphologies and structures of the 1999 lava flows, Mount Cameroon

4.1 Introduction

Mount Cameroon (**Fig. 4.1, Plate 4.1**) constitutes one of the most active of Africa's volcanoes, experiencing no fewer than seven eruptions over the period 1909-2000. With the exception of the summit eruption of 1954 (which produced only explosive activity), all events have produced a variety of volcanic phenomena, including a suite of extensive basanite lava flows and associated mild explosive activity along flank fissures. The 1922, 1999 and 2000 eruptions were characterised by activity at two vent sites: one near the summit (generating explosive and effusive phenomena) and one of lower altitude on the volcano's flank (producing mostly lava, and only weakly explosive).

The lava flows provide an ideal source of study for the volcanologist concerned with mafic flow processes, and a refreshing corollary to the extant literature, which is dominated by investigations of flows on Hawaii and Etna. Flow products of the earlier eruptions of the 20th century have been colonised by vegetation to various degrees, inhibiting detailed field investigation, and alternative methods have been undertaken to investigate broadly emplacement processes and conditions (see Appendix B). Conversely, the flows generated by the 1999 and 2000 eruptions are fresh, offering 100% exposure, and eruption processes (beyond relict fumarolic activity) have ceased, rendering the lavas fully open to field analysis.

Of the two eruption events, this study chooses to focus solely on the 1999 lavas. These flows originated from two non-contiguous sites on the south eastern flank of Mount Cameroon, and at Bakingili very nearly reach the sea (**Fig. 4.2**), offering greater accessibility than the 2000 flows which are close to the summit. The considerable length (~10 km) of the 1999 lower vent flow suggests an environment that will develop a greater range of flow morphologies, and yield greater information on the interaction of flow processes and the commensurate formation of appropriate lava structures. In addition, the duration of the 1999 episode exceeded that of the 2000 episode by a few days, and produced an order of magnitude more lava (Suh et al. 2003).

Although the eruption has been documented previously, such studies have focused on seismologic effects (Suh et al. 2001) or general eruptive behaviour and petrology (Suh et al. 2003). No study has described in detail the physical aspects of the 1999 lava flows, nor attempted to relate morphological features and flow structure to emplacement history and process. This chapter shall proceed to set out the range of flow-types, morphologies and structures observed on Mount Cameroon's 1999 flows, and qualitatively assess their development. Further quantitative analyses

are documented in Chapter 5, assessing similarities between natural flow products and the experimental flows discussed earlier in this thesis.

4.2 An overview of the 1999 eruption of Mount Cameroon

4.2.1 Geological setting

Mount Cameroon (**Fig. 4.2**) is a large stratovolcano, situated at 4.20°N, 9.17°E in South West Cameroon. At 4,095 m high it is the second highest mountain in Africa. A recent estimate by Suh et al. (2003) placed the structure's volume at 1,200 km^3. The volcano displays an elliptical planform, with its basal dimensions stretching 50 km in a NE-SW direction, as opposed to 35 km NW-SE, with the structure becoming more markedly elliptical at higher altitudes (Gèze 1953).

The volcanic edifice is covered with a variety of historical lava and fall-out tephra deposits. Basanite and hawaiite lavas dominate the stratigraphy, representing a near continuous period of eruptive activity (Suh et al. 2003). Whilst Fitton et al. (1983) estimate a start date of activity of 10 Ma before present, Marzoli et al. (2000) place most eruptive activity in the last 3 Ma. Such dates may be over-estimates of the volcano's age; volumetric considerations point to the production of approximately 10^8 m^3 of lava over the past century, whilst a substantially smaller figure of $4x10^7$ m^3 per century would be required to build the edifice in a period of 3 Ma. In the absence of a good suite of reliable age determinations, therefore, the age of the volcano remains uncertain.

Though weak Strombolian activity is occasionally observed, the eruption of less violently effused lavas form the dominant phenomenon. Over one hundred subsidiary cinder cones form along the Mount Cameroon's flanks and summit, focused along the same NE-SW trend discussed earlier (Suh et al. 2003). This trend itself derives from the volcano's position on the Cameroon Line, a 1,600 km long linear volcanic zone that stretches from maritime Pagalu in the southwest to Biu in northeastern Nigeria.

The Cameroon Line is described in greater detail by Fitton (1987), and is divided into two provinces: oceanic (characterised by the production of dominantly basaltic lava, with minor volumes of nephelinite, phonolite and trachyte; Fitton and Hughes 1977, Halliday et al. 1988) and continental (marked by a wider suite of rocks of varying characteristics and age, including felsic and basaltic lavas, and more silicic and alkaline plugs; Nono et al. 1994, Marzoli et al. 2000, Ngounouno et al. 2000). Mount Cameroon's satellite volcano, Etinde, is located at the boundary between provinces, and Mount Cameroon is the sole remaining active centre of the continental arm.

The volcanic products are deposited on a schistose and gneissose basement of Precambrian age (Toteu 1990, Toteu et al. 1994), and intrusive syenites and granites younger than 70 Ma (Suh et al. 2003). The Central African and Foumban Shear Zones transect the basement; the former area has been of considerable import to magma transport in the Cameroon Line, with ascent in the NE section of the continental province focused along a complementary suture zone (Poudjom Djomani et al. 1997).

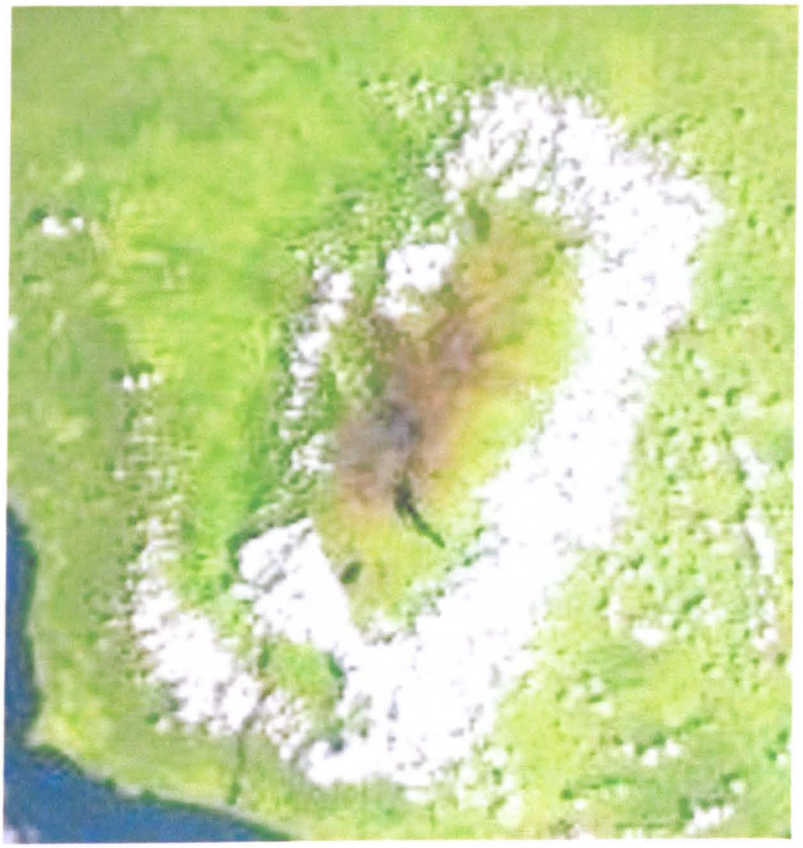

Figure 4.1 A satellite image of Mount Cameroon, taken on the 10th December 2000 (north is towards the top of the image, which depicts a region a 100 km wide). The 1999 site 2 flow can be seen in the southern portion of the image, partially obscured, by cloud, trending SSW and reaching the coast near Bakingili.

Plate 4.1 Photograph of Mount Cameroon, taken from Buea, looking west.

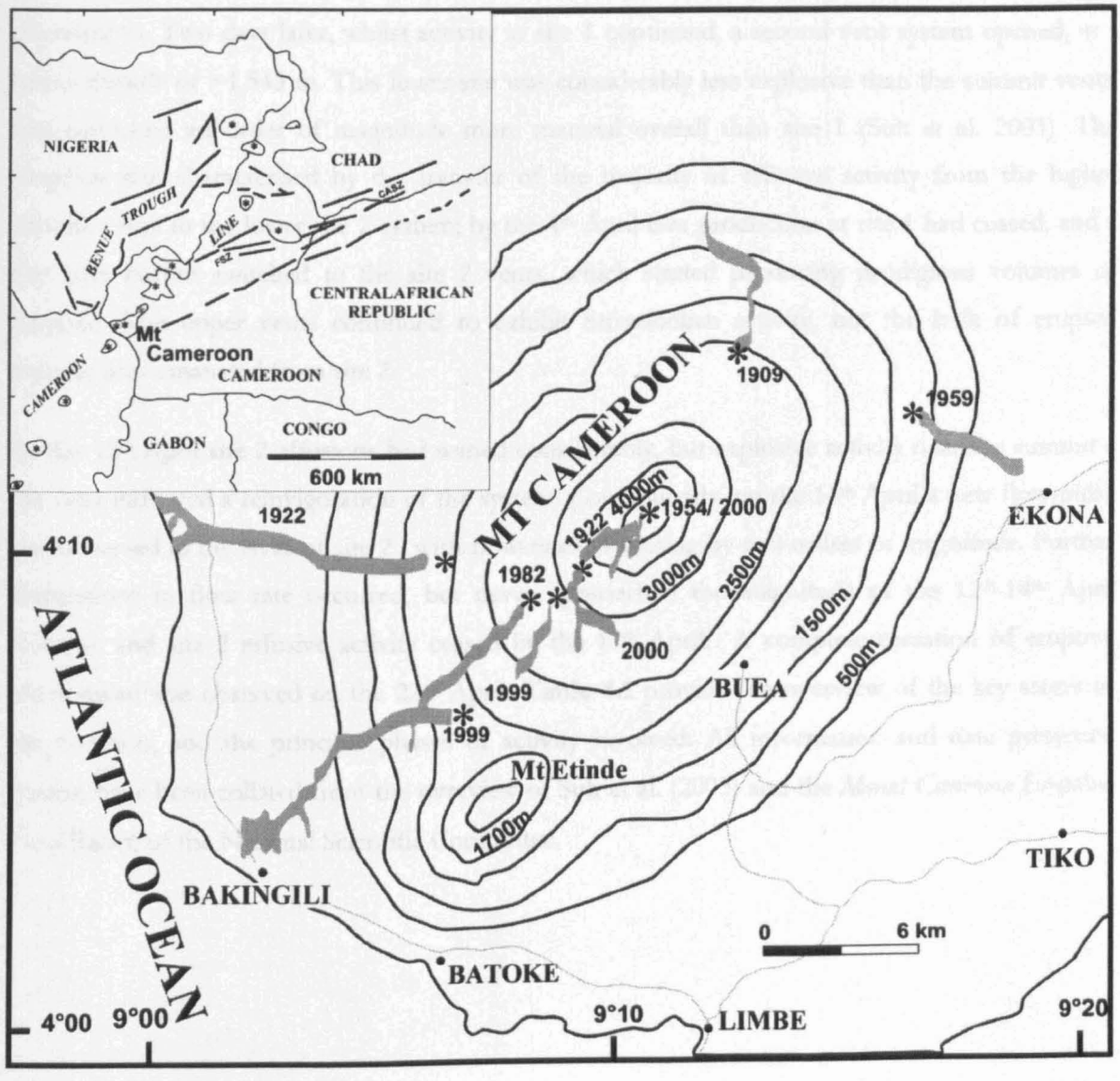

Figure 4.2 Contour map of Mount Cameroon displaying the 20th Century lava flows, with and insert depicting its position on the Cameroon Line (from Suh et al. 2003).

4.2.2 Eruption chronology

Following precursory earthquake swarms on 26th and 27th March 1999, the 1999 eruption occurred over the period 28th March to 22nd April 1999, inclusive (Suh et al. 2003). During this time lava erupted from two non-contiguous vent systems, at different altitudes. The first vent system, named site 1, opened at ~2,807 m on the 28th March, and produced a mix of explosive and effusive phenomena. Two days later, whilst activity at site 1 continued, a second vent system opened, at a lower altitude of ~1,545 m. This lower site was considerably less explosive than the summit vents, and produced an order of magnitude more material overall than site 1 (Suh et al. 2003). The eruption was characterised by the transfer of the majority of effusive activity from the higher altitude vents to the lower site 2 system; by the 4th April lava production at site 1 had ceased, and a day later output switched to the site 2 vents, which started producing prodigious volumes of basanite. The upper vents continued to exhibit Strombolian activity, but the bulk of erupted volume now emanated from site 2.

By the 12th April site 2 effusions had waned considerably, but explosive activity near the summit a day later indicated a reinvigoration of the system. Consequently, on the 14th April a new flow-pulse was observed in the lavas of site 2 , with flow-rates increasing by two orders of magnitude. Further fluctuations in flow rate occurred, but never approached the magnitude of the 12th-14th April changes, and site 2 effusive activity ceased by the 17th April. A complete cessation of eruptive phenomena was observed on the 22nd April. **Table 4.1** provides an overview of the key stages in the eruption, and the principal phases of activity involved. All information and data presented therein have been collated from the overview of Suh et al. (2003) and the *Mount Cameroon Eruption: Final Report*, of the National Scientific Committee.

Date	Site 1	Site 2
28th March	Eruption begins; following an explosion, there is aa effusion at a vent ~2,650 m asl.	
30th March		New vents open on the SE flank, at ~1,500 m asl, accompanied by an initial explosion and subsequent fire fountaining.
3rd April	12 vents can be observed, lying along a SW-NE oriented fissure ~1.5 km long. The vents opened from SW to NE (Suh et al. 2001). Phenomena ranged from post-eruptive steam emission (SW), through to explosive Strombolian activity (NE); latter continues through to 13th April. The total volume of the cones is ~4.8×10^6 m^3, equivalent to 2.4×10^6 m^3 of solid material.	
4th April	Aa lava flow fronts (erupted 28th March) stagnate 3 km from the vents, and effusive activity ceases. An estimated 2.7×10^6 m^3 of lava was produced.	
5th April	*Continuing Strombolian activity*	20 vents are observed, sited along a ~1500 m long, SW-NE fissure; they discharge large volumes of lava, which flows towards the coast. As the eruption progresses, areas between vents collapse, forming fissures.
10th April		Front of main lava flow field erupted recorded was 10 km from vents, and ~400 m wide and ~10 m thick. An estimated 4×10^7 m^3 of lava erupted so far.
12th April		Flow rates vary according to topography and local flow morphology, but by the 12th April the rate of advance of the flow front had slowed considerably (to 10 m day^{-1}).
13th April	Only 4 vents remain active. Nested cone formed at NE end of fissure, which experiences explosions approximately every hour and subsequent fire fountaining. Explosive activity ceases and is followed by strong degassing and prevalent 'rumbling', continuing to 22nd April.	
14th April		Following site 1 explosive activity on 13th April, the rate of flow front advance increases, by over two orders of magnitude (to 350 m day^{-1}).
15th April		Fresh lava still erupting from vents, but downstream lava flow front is temporarily stagnant.
16th April		Flow resumes; a lobe 100 m wide and 12 m thick overflows the Limbe-Idenau highway, stopping 20 m from the sea & 12 km from the site 2 vents.
17th April		Lava production ceases. An estimated 6×10^7 m^3 of lava has been produced from Site 2.
22nd April	Eruptive phenomena at Site 1 cease.	

Table 4.1 Mount Cameroon eruption timeline, 1999 phase: dates and data are taken from Suh et al. 2003. Volumetric totals are taken from Suh et al. (2003), and are estimated values, often derived from distal morphologies and processes, or isolated data. No detailed observations were recorded in the 'blank' days.

4.2.3 Lava properties

The following analyses of lava petrochemistry are provided as an overview of an aspect that lies beyond the scope of our field investigations, yet is important in relation particularly to the physical properties of the erupting magma. We draw on the petrographic overview of Suh et al. (2003). Although a variety of lava products were produced by the 1999 flows, general petrographic traits are shared by most massive lava samples, irrespective of source and proximity.

Typical bulk rock compositions for 1999 lavas are displayed in **Table 4.2.** The lavas are silica poor (44-47% SiO_2) basanites with occasional, rare hawaiites (specifically sample BA20; see below). The compositional variations amongst samples are slight with most showing similar major and trace element composition. One sample documented in Suh et al. (2003) has a slightly more differentiated composition, with lower Ni (40 ppm) and higher Zr (432 ppm) than the majority of samples (Ni ~70 ppm, Zr ~360 ppm). No systematic differences in bulk rock composition are observed between samples from site 1 and 2.

Hand specimens of massive lava collected from a variety of locations reveal a well-developed porphyritic texture, with olivine, clinopyroxene and plagioclase phenocrysts set in a fine-grained, often partly glassy groundmass. Heterogeneity is common, with areas enriched in certain phases relative to others. Relative abundances of these phases as reported by Suh et al. (2003) are displayed **Table 4.3**; samples as collected in the field in this study corroborate these values.

Olivine forms typically sub- to euhedral crystals (0.3-15 mm), with a dominant mode of 2-3 mm. Following microprobe analyses, Suh et al. (2003) have interpreted the larger (1 cm+) crystals as

Table 4.2 Chemical compositions of the Mt. Cameroon 1999 lava (from Suh et al. 2003)

	13 (proximal site 1)	BA20 (proximal site 2)	BA1 (distal site 2)
SiO_2	45.79	46.94	46.07
Al_2O_3	15.4	15.39	15.34
Fe_2O_3	12.12	11.51	12.23
MgO	6.41	6.11	6.5
CaO	10.37	10.52	10.63
Na_2O	4.17	3.75	3.92
K_2O	1.61	1.54	1.57
TiO_2	3.11	3.17	3.12
MnO	0.2	0.18	0.2
P_2O_5	0.7	0.69	0.69
LOI	-0.08	-0.07	-0.37
Total	99.8	99.73	99.9

Major element data collected from XRF analyses of whole-rock composition. Analyses are taken to show typical values for both vents. Subtle variations (outside of analytical error) exist, particularly with reference to trace element propensities, and are detailed in Suh et al. (op. cit.). Sample 13 originates from a site 1 vent, sample BA20 is from a lava flow ~400 m S of the site 2 vents and BA1 is from the distal Bakingili flow front.

Table 4.3 Modal mineralogy of the 1999 Mt. Cameroon lavas (selected from Suh et al. 2003)

	BA4 (proximal site 1)	BA20 (proximal site 2)	BA1 (distal site 2)
Phenocrysts/microphenocrysts	*18*	*15*	*20*
Olivine	6	6	8
Clinopyroxene	8	6	7
Plagioclase	2	2	4
Titanomagnite	2	<1	1
Groundmass	*82*	*85*	*80*
Microlites	84	76	70
Glass	16	24	30
Vesicles	-	-	-

Data derived from optical point counting of samples BA4 (3,000 points), BA20 (2,000 points) and BA1 (2,500 points), and checked under a scanning electron microscope. Provenance is as described in Table 4.2, with the exception of sample BA4, which is from a site 1 lava flow.

xenocrysts, wherein forsteritic cores (Fo83-85) are overgrown by more fayalitic rims (Fo77-82). The contacts, though varying in habit, are sharp, and several examples of such overgrown xenocrysts can be readily made out in hand specimen. The majority of smaller, more predominant olivines are unzoned phenocrysts and possess compositions in the Fo77-85 range (Suh et al. 2003). Sub-mm olivines occasionally appear as distinct chadacrysts or aggregates, enclosed by larger clinopyroxene oikocrysts, to form a locally poikilitic texture (see below).

Clinopyroxene is typically as abundant as olivine in the phenocrystal assemblage (**Table 4.3**), forming sub- to euhedral prismatic crystals, with clear octagonal (or cleavage formed hexagonal) geometries, and typical dimensions of 0.3-1 mm. As mentioned above, larger clinopyroxenes often enclose olivine crystals; closer analyses of the nature of some these grains show that olivine forms along dominant, cleavage-guided fractures. Suh et al.'s (2003) analyses give a clinopyroxene composition that varies between $Wo_{47}En_{41}Fs_{12}$ to $Wo_{51}En_{34}Fs_{15}$, with phenocrysts displaying normal chemical zoning, with a decrease in Mg from core to rim.

Plagioclase occurs as a subsidiary member of the phenocrystal assemblage, typically only 2% of the rock, and in some samples wholly absent in dimensions >0.3mm. Late, degassed viscous site 1 lavas displayed unoriented 1-2 mm laths, and smaller microphenocrysts of plagioclase amongst the mafic groundmass, yet these were still a minor mode relative to the olivine and clinopyroxene. In contrast a Hawaiite bomb (SEG4) displayed abundant sub-mm plagioclase phenocrysts and microphenocrysts, with larger olivines and clinopyroxenes virtually absent. Suh et al. (2003) describe basanite plagioclase compositions of An_{49-67}, with >1 mm zoned phenocrysts displaying

homogenous calcic cores (An_{82-84}) and sodic rims (An_{51-59}). Hawaiite plagioclase is more uniformly sodic: An_{49-54}. Apart from rare titanomagnetite phenocrysts, the remainder of the rock consists of a dominantly crystalline groundmass, composed of microlites of olivine, clinopyroxene, plagioclase and titanomagnetite. Subsidiary glass is typically trachytic in composition (Suh et al. 2003).

Vesicle distribution and microscale morphology are discussed later (see 4.3.1). Simple analyses show that blocks of massive, avesicular lava (taken from distal site 2 flows) have a mean density of 2592 kgm^{-3}. An estimate of the temperature of the lava at varying times in its emplacement can be derived using the olivine geothermometer of Roedder (1974). Firstly, taking the modal volume data of Suh et al. (2003), and typical mineral densities, we calculated the mean abundances of the phenocrysts and groundmass phases of the 1999 lava suite, in wt%. These average values are approximately olivine 8%, clinopyroxene 5%, plagioclase 3% and magnetite 1%, with the groundmass making up 83% of the rock mass. We derived average bulk rock compositions from the same data sets and normalise to 100%. Mass balance calculations give a residual melt on eruption of hawaiite composition. The results are displayed in **Table 4.4**.

With reference to the data of Thompson (1974), Suh et al. (2003) state that the equilibrium compositions of phenocrysts suggest a crystallisation depth of ~40 km. At this depth, for a lava of bulk composition defined in **Table 4.4**, in equilibrium with the forsteritic (Fo_{83}) cores of olivine phenocrysts, the olivine geothermometer infers a temperature of 1166°C (± 30°C). All values are calculated using the ratio of MgO in the olivine and liquid phases, as the oxidation state of iron is not known, and formula in Roedder (1974). In contrast, a residual hawaiite melt, in equilibrium with more fayalitic microlites and phenocryst rims (Fo_{69}), gives an eruption temperature of 1042°C (± 30°C). We note that this temperature estimate is consistent with measured temperatures of hawaiite lavas on Etna of 1070-1090°C (Pinkerton and Sparks 1976). In comparison, Suh et al.

Table 4.4 Averaged bulk rock and phenocryst compositions (adapted from Suh et al. 2003)

	Bulk Lava	Olivine	Clino-pyroxene	Plagioclase	Magnetite	Residual Melt
SiO_2	46.5	38.9	47.0	53.9	-	47.5
TiO_2	3.2	-	2.9	0.2	22.6	3.4
Al_2O_3	15.7	-	6.5	28.6	-	17.5
FeO	10.9	21.2	7.1	0.8	71.9	9.8
MgO	6.4	39.6	12.8	-	5.5	3.2
CaO	10.6	0.3	23.1	11.5	-	10.9
Na_2O	4.2	-	0.5	4.5	-	4.8
K_2O	1.7	-	-	0.4	-	2.0
MnO	0.2	-	0.1	-	-	0.2
P_2O_5	0.6	-	-	-	-	0.7

Residual melt compositions calculated through a mass balance method, with reference to averaged bulk rock and phenocryst compositions and modal propensities of phenocryst phases (in wt%) stated above.

(2003) measured field temperatures of 950-975°C 40 cm into the stagnated site 1 flow fronts (4th April) and 1000°C at the site 2 lava fronts ~10 km from the fissure (10th April). These latter direct measurements provide lower bounds on the lava temperature.

With these temperatures and compositions, one can estimate lava viscosity. Using the empirical method of Shaw (1972), an aphyric magma at depth, with a bulk composition as described in **Table 4.4** gives a Shaw viscosity of 15 to 28 Pa s (at 1196 and 1136°C respectively, accounting for the uncertainty in the olivine geothermometer). Viscosity figures have been rounded to the second significant figure. In comparison, a residual melt of hawaiite composition erupted at between 1012 and 1072°C yields a Shaw viscosity of between 145 and 320 Pa s. One can modify the Shaw viscosity by use of the Einstein-Roscoe relation

$$\eta = \eta_0 (1 - 1.67\phi)^{-2.5}$$

where η is the suspension viscosity, η_0 the viscosity of the melt phase (i.e. the Shaw viscosity), ϕ the volumetric crystal fraction of the lava and the integer 1.67 is a constant derived from particle geometry (e.g. Marsh 1981, Pinkerton and Stevenson 1992). Using this equation, a lava composed of 17% phenocrysts and 83% residual hawaiite has an estimated viscosity of between 710 to 320 Pa s for the temperature range 1012 to 1072°C.

As the lava thermally and chemically matures, it develops into a bimodal suspension of phenocrysts and microlites in an evolved melt. Residual glasses in lava samples have trachytic composition (Suh et al. 2003). Taking a typical composition of the groundmass glass from Suh et al. (op. cit.; SiO_2 62.62%, TiO_2 1.435, Al_2O_3 22.45%, FeO 4.28%, MnO 0.04%, MgO 0.79%, CaO 0.53%, K_2O 2.11%, Na_2O 3.65%), and assuming this phase represents the late stage melt, one derives a Shaw viscosity for this residual melt of between 3.2×10^6 and 10^6 Pa s for the temperature range 950 to 1000°C. These estimates are very much a lower bound on the viscosity in the flow front region, because the phenocrysts and microlites will result in much higher viscosities.

The Einstein-Roscoe relationship was originally parameterised to calculate the viscosity of relatively dilute suspensions, in the above case with $\leq$ 60% by volume of particles, and is based on the experimental analysis of the behaviour of wholly Newtonian suspensions of uniform spheres in a Newtonian fluid. Its validity as a model is therefore dubious with regard to the analysis of distal flows, where crystal proportions become high, with extreme values of ϕ (> 75% crystalline). Such a crystalline mush will instead behave in a strongly non-Newtonian manner, with elements of dilatancy or shear-thinning, time dependent visco-elastic effects, and apparent yield strengths, as witnessed for basaltic lavas in the field (this issue is referenced further in Chapter 1; see, for

example, Robson 1967, Shaw et al. 1968, Shaw 1969, Hulme 1974, Pinkerton and Sparks 1978, Chester et al. 1985, Pinkerton and Stevenson 1992, Dragoni and Tallarico 1994, Lejeune and Richet 1995, Pinkerton and Norton 1995). Nevertheless, for reference, the equation produces viscosities of the order 10^{11} for trachytic melts with 59% crystallinity. This result can be compared to estimates of apparent viscosity of the flow fronts of the lava in the order of 10^{8} Pa s from application of the Jeffreys equation to data on frontal speeds, thicknesses and slopes. These latter estimates are described in more detail in Chapter 5.

Plate 4.2 Hand specimen of a typical olivine-clinopyroxene-phyric basanite.

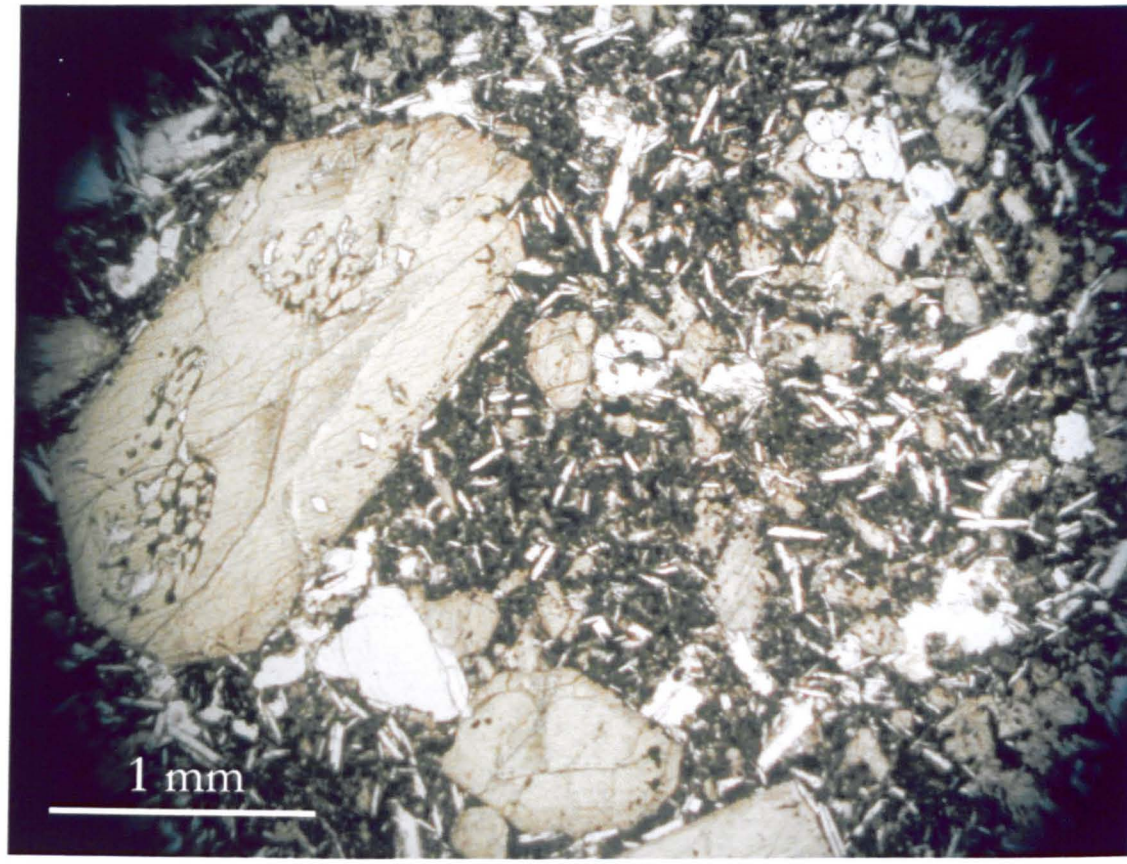

Plate 4.3 Thin-section of a typical olivine-clinopyroxene-phyric basanite in plane-polarised light.

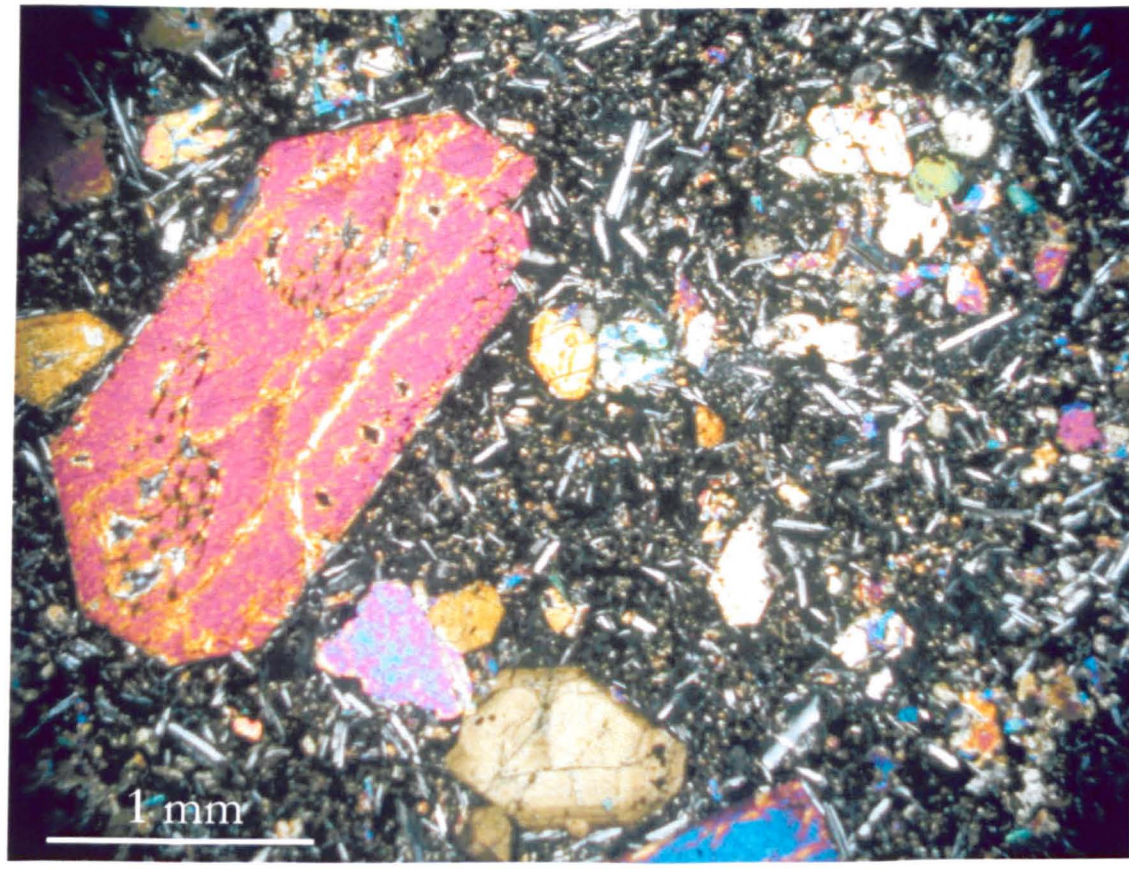

Plate 4.4 Thin-section of a typical olivine-clinopyroxene-phyric basanite in cross-polarised light.

4.2.4 General effusive behaviour

Volumetric flow rate and total volume erupted

A lack of accurate pre-eruption topographical maps and aerial, syn-eruption field data preclude a detailed analysis of the volcano's volume and rate of discharge. Further, in-depth mapping and aerial and photographic analysis will hopefully expand on the broad values presented below.

The spatter and cinder cones formed at site 1 are typically of the order of ~50-100 m high, with a basal diameter of ~150-200 m; the total volume of the dozen cones was therefore estimated at ~4.8×10^6 m^3 (Suh et al. 2003), though this neglects the component provided by wind-blown scoria and ash deposited beyond the cinder cones, and will therefore be a low estimate. Assuming 60% porosity, this translates into 2.4×10^6 m^3 of solid lava. Suh et al. (2003) also estimated gross volume estimates for the site 1 lava flows, from their general habit and dimension. From their stated typical dimensions (3 km in long, 30-120 m wide and with flow fronts 15 m high) they quote a volumetric figure of ~2.7×10^6 m^3 – i.e. an approximate median value of 60 m is used for common flow width. Variability in flow dimensions could place potential errors of a factor of 2 to 3 around this estimate.

As the eruption began at 8pm local time, on the 28th March, and effusive activity ceased by the morning of the 4th April, the lavas were erupted over a period of 6 to 6.5 days. This gives an average lava effusion rate of 5.2 to 4.8 $m^3 s^{-1}$ (Suh et al. 2003). As the total erupted volume in the same period was 5.1×10^6 m^3, this infers an overall, early site 1 eruption rate of 9.1 to 9.8 $m^3 s^{-1}$.

The site 2 flows were greater in extent and volume. On the 10th April, the main site 2 lava stream possessed a flow front that was ~10 km from the source and of dimensions ~400 m wide by ~10 m thick; from these figures Suh et al. (2003) derive a 10th April lava volume total of ~4×10^7 m^3. If one assumes this lava had been developing since the start of site 2 activity (30th March), this gives an approximate lava discharge rate of ~40 $m^3 s^{-1}$. Locally flow rates varied, but for the entire eruption Suh et al. (2003) suggest a conservative volume estimate of ~6×10^7 m^3, indicating an average effusion rate of 40 $m^3 s^{-1}$ for the duration of the eruption from site 2; although such a rate would indicate little apparent waning in averaged flux between the mean value up to the 10th April and the same figure up to the 17th April. At first the lack of difference is curious, as Suh et al. (2003) define abundant volume-limited field structures, and we shall return to reconsider these figures later.

Lava advance

The site 1 lava flows were limited in their extent, with the longest having ceased motion ~3 km from the vents. Their early relative inaccessibility and short period of eruption (~six and a half days) resulted in a cessation in flow before accurate velocities and time-series developments could

be recorded. One is therefore left to investigate lava structures and morphologies in an attempt to discern dynamical processes (see Chapter 5).

In contrast, the advance and kinematics of the main site 2 flow were better recorded. Over a dozen velocity measurements were recorded over the period 5th to 15th April. Some of these data are summarised on **Figure 4.3**, a map of the distal extent of the site 2 flow front, near Bakingili. Whilst occasional data also appear in Suh et al. (2003), the following figures are field measurements, kindly supplied by Dr. Emmanuel Suh of the University of Buea (pers. comm.).

A little after the start of the eruption, well-formed, proximal channels focused lava flux downstream, with high levels of heat advection. One such channel section ~100 m from the vents gave a central channel velocity of ~5 m s^{-1} on 5th April. Subsequent measurements record velocities for the main site 2 flow as it reached Dr. Tatani's farm near Bakingili on the coast. Here the flow developed into three distinct lobes, as illustrated on **Figure 4.3**.

On the 8th April, the eastern lobe of the main flow, which had reached the edge of the forest by the coastal plantations, encroached on the farm at a speed for the flow front of $2x10^{-3}$ m s^{-1}. Distal changes in rheology and morphology had displayed a notable effect on the rate lava advance, with observed lava velocities differing by three orders of magnitude from proximal, channel fed flow readings. Local changes in flow pattern could radically alter recorded values; at a shallowing break in slope ~7 km from the vents a 9th April measurement recorded channel flow speeds of ~2.1 m s^{-1}.

By the 10th April, the flow had encroached onto Dr. Tatani's plantation; speeds of frontal advance for the western and central lobes were recorded as being $1.3x10^{-3}$ and $2x10^{-3}$ m s^{-1}, respectively. From the 10th April to the morning of the 11th a lobe of the front ~150-200 m wide and ~30 m thick advanced 30 m in a 12 hour period, giving an average flow front velocity of $6.9x10^{-4}$ m s^{-1}. Flow advance diminished noticeably between the 11th and 12th of April, with the front travelling a mere 10 m; though occasional areas of quicker development were observed as a function of topography and lava inhomegeneity: an estimate of $1.4x10^{-3}$ m s^{-1} was recorded on the 12th, for example.

Following an explosive episode at site 1 on the 13th April, the velocities of the main flow from site 2 increased: by the evening of the 14th April, the flow front had advanced 350 m in 24 hours, indicating an average velocity of ~$4.1x10^{-3}$ m s^{-1} over the period. Subsequent to this 'surge', the main flow front remained stationary, although a reading of $2.8x10^{-3}$ m s^{-1} was recorded for the subsidiary western lobe. Despite temporary frontal stagnation, lava continued to be effused in the proximal region. On the 15th April, a measurement in the proximal channel (~30 m from the vent) recorded

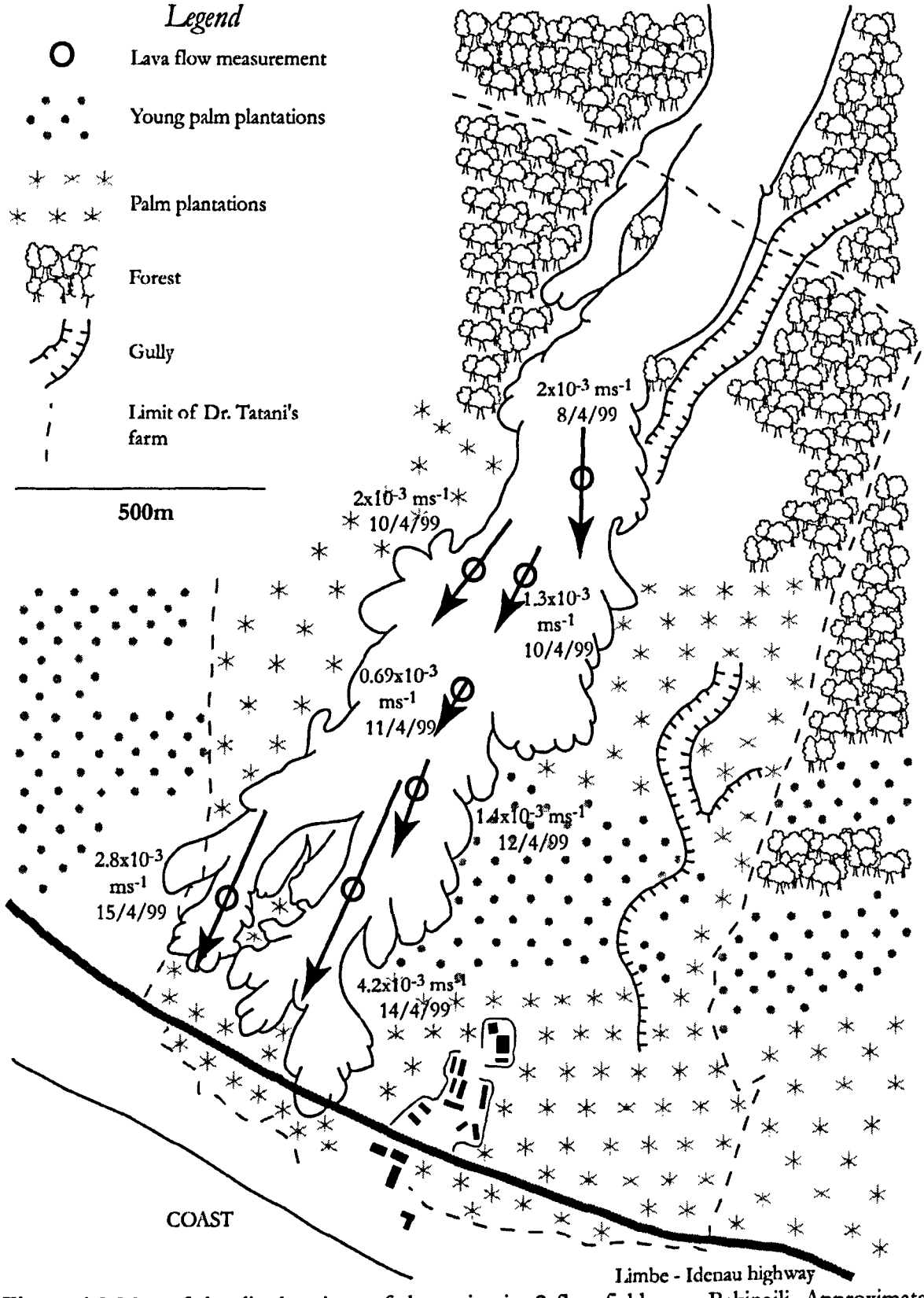

Figure 4.3 Map of the distal regions of the main site 2 flow-field, near Bakingili. Approximate velocity vectors are plotted with arrow length indicating the magnitude of the flow-speed. North is to the top of the figure.

a velocity of ~2 m s^{-1}. Clearly flux had waned overall over the period 5th to 15th April, and this simple interpretation suggested by the data agrees well with the volume-limited lava morphologies described by Suh et al. (2003) and discussed herein later.

On the 16th April, part of the main flow front remobilised, as a lobe ~100 m wide and ~12 m thick remobilised and advanced across the main Limbe-Idenau highway, stopping ~200 m from the shore. Effusive activity from the site 2 vents ceased on the 17th April. By this time the main flow had travelled approximately 12 km down-slope from the site 2 vents, through rainforest, scrub and plantation.

4.3 Lava flow morphology, field textures and structures

4.3.1 General features

The 1999 flows display a wide variety of morphologies, practically covering many commonly observed basaltic lava features. Field structures vary strongly according to proximity to vent, underlying topography and local flow evolution. Even the most simple of near-vent or bocca channel sections tend to display two types of lava and three types of levees, and distal flow portions commonly comprise of an anastamosing, compound geomorphology (e.g. **Fig. 4.3**). Such a plethora of flow features offers a challenge to the field volcanologist, but is also an important tool. Distinct features form as a function of often well-described flow processes, and a careful appreciation of the geometry and relative timing of various flow structures allows us to garner a dynamic overview of the flows' evolution, and general volcanic behaviour.

The flows are effused onto a variable landscape, of varying relief and vegetation. Proximal site 1 flows were extruded from vents onto gently sloping (~12°) montane savannah, occasionally blanketed by recent ash or older flows; the burying of existing flows was common, but older topographic features did not affect proximal flow evolution to any noticeable degree. The site 2 flows erupted at a lower altitude, closer to the upper limit of montane rainforest, and are more heavily guided by topography, forming several valley-fill sections closer to the vents. They also cross the extensive 1982 lava flow (**Fig. 4.2**).

Detailed cross-sectional profiles were taken of nearly 20 lava sections, along with several channel profiles across minor lava units. This project was a collaborative effort, involving the surveys of Gerald Ernst, Steve Njome, Emmanuel Suh, Steve Sparks, Stewart Stansfield and the University of Buea. These sections were completed through field surveys, using tape, compass and abney level. Where possible the contact with the underlying pre-eruption topography was partially quantified using marginal levee-topography contact geometry, and then further qualified as a function of general channel depth. Unfortunately, the lack of an accurate DEM or maps of pre-eruption relief often make the choice poorly constrained.

Four large sections were taken of the distal flow front of the main site 2 flow near Bakingili (**Sections I** to **IV**); eight surveyed a long proximal-distal flow that emanated from site 1 (**Sections V** to **XII**); two were gathered from a late-effused viscous flow near the site 1 vent (**Sections XIII** and **XIV**); and four were profiled from another proximal site 1 flow (**Sections XV** to **XVIII**). All sections are enclosed as separate sheets at the rear of the thesis, for the reader's convenience. Smaller profiles are used as data or figures throughout the text.

4.3.1.1 Large-scale morphologies—levees and channels

With one exception, all the lava cross-sections reveal a single consistent feature: the flows comprise a single (or multiple) channel(s), bounded by a well-defined and easily discerned set of levees. The dimensions and geometry of the channels and their levees vary widely according to the local character of the lava, the local flow regime and topography. The structure and formation of channels and levees shall be described in more detail later (see 4.3.2 and 4.3.3); an overview of the general considerations shall suffice here.

Channel width varies greatly; proximal pahoehoe channels emerging from boccas (1 m in diameter; **Plate 4.5**) are as much as two orders of magnitude smaller in width than distal blocky-aa channels (some over a 100 m in diameter; **Plate 4.6**). Marginal levees similarly range in character, but a common factor emerges: successive sets of levees are frequently encountered as one passes from a flow's margin to its centre and the extant end-of-eruption channel surface. These stranded levee sequences (**Plate 4.7**) are interpreted to represent an overall decrease in local flow flux with time.

These sequences can be discussed with reference to **Sections XII** and **XVII**, the easternmost flow-unit of **Section IV** or the interior flow-units of **Sections I, II** and **III**. Of the *extant* levee structures, the outermost, flow-unit bordering levees form first, as the active flow region of the flow narrows and thickens, building the marginal levee constructs. The highest point of this outer levee marks the high-stand line of the flow that formed the most extensive lava lobe or channel. As this channel drains, the lava leaves this initial outer levee stranded. The further, interior levees can be formed through a variety of processes (see 4.3.2). Typically they represent subsequent flow pulses, or further inflation in the channel through rheological stiffening down-slope exerting a local backpressure, which leads to further thickening. The draining of this channel would expose another set of younger levees, and so the process can continue.

The processes forming such levee sequences result from an interplay of flow conditions and parameters, including the source flux and its fluctuation, the rheological stiffening at the downstream flow-front, local outbreak-focused drainage, and heterogeneous channel flow regimes. Not all internal levees are depressed relative to the stand of the outer levees, as observed by Naranjo et al. (1992) for the Lonquimay lava of Chile. While **Section XII** and the eastern levee sequences of the next-to-easternmost units of **Section I** and **III** show such a sequence clearly, with a cumulative draining of the flow channel throughout the flows' evolution, the western levees of the western flow-unit of **Section I** show an increase in levee high-stand level across the channel, as do the levees of the eastern unit of **Section III**. It is common for younger, interior levees to rise

Plate 4.5 Proximal pahoehoe channel emerging from a near-source bocca, by the Site 2 vents.

Plate 4.6 Distal blocky aa flow channel, near Bakingili. The central channel depicted is approximately 100 m wide.

Plate 4.7 Sequence of stranded levees. The photograph is taken from the top of an outer, bounding levee, looking up flow. Professor Steve Sparks is kindly standing on an interior levee, bounding the main flow channel to the left.

above their flow bounding neighbours, with the actual height depending on the amount of inflation in the narrowed channel, and modified local flux per unit length.

In the distal profiles of **Sections I** to **IV**, it is rare to be able to trace interior levees contiguously from one profile to another; only the outermost, eastern levee of the main eastern flow-units of **Sections III** and **IV** can be traced with any certainty. Changes in underlying topography and the compound structure of the flow-field in this distal region, with multiple axes of flow focus across the field, lead to longitudinally fluctuating flow dynamics.

The only profile to lack clear levees, **Section V**, lies 3 m back from the flow front, and corresponds with the zone of dispersed flow/flow toe as described by Lipman and Banks (1987), in a situation where one would not expect a well-developed channel and levee morphology to have developed so early. This situation shares commonality with the eastern most lobe of **Section II**; a small side-flow which has broken out from the main channel, but ceased motion before it could proceed further and thence develop a channel zone.

Whilst topography naturally affects the flow's direction, habit and local morphology, the influence varies from acute to minimal in the flow profiles. Flows on steeper slopes preserve clear channel structures and single, as opposed to compound or multi-channel, flow units. As slope decreases, lava can pond and spread laterally, as a function of a decrease in flow front speed or an increase in lateral velocity components related to thickening. Ponding therefore typically occurs at breaks in slope, in wells and rifts in the topography, or irrespective of topography, behind a stagnant flow front. Typically, the flows were approximately freestanding or focused along shallow river valleys, and were not channelled down existing ravines in the terrain in an extreme manner, with the predominant exception of the near bocca site 2 channels.

4.3.1.2 Medium-scale morphologies—observed types of lava

The surface characteristics of the lava varied according to the *thermal maturity* of the flow surface itself (Naranjo et al. 1992). This concept relates to the length of time that a region of the lava surface has been cooled, and its level of crustal development and deformation, before it comes to rest. When erupted from a vent or bocca, cooling rapidly changes the surface regions of the lava from an incandescent fluid with increasing levels of plasticity to a cooled, brittle solid. If the flow ceases motion before the surface becomes sufficiently cooled to deform by semi-ductile or brittle mechanisms then smooth pahoehoe surfaces develop. With further cooling and crustal thickening deformation can no longer be accommodated in a ductile manner, and consequently plates and surfaces of lava tear or fracture, disaggregating first into slabs and rafts, then into clinker, and ultimately into blocks.

The proximal site 1 and site 2 pahoehoe flows occur locally near the vents and are examples of thermally immature lavas. Having cooled little, they deform in a ductile fashion, readily forming ropes and folds on an otherwise relatively smooth surface (e.g. Fink and Fletcher 1978, Fink 1980). The degree to which this surface can be retained, and preserved further down flow, depends on the characteristics of the channel and the general flow parameters. In a clear, unobstructed channel, or better yet a lava tube, low viscosity pahoehoe can flow considerable distances from the vent or bocca before cooling takes a more noticeable effect.

With cooling, lavas will develop an increasing level of plasticity, as crystallinity increases and crystal-fluid and crystal-crystal interactions become more frequent (see Chapter 1). As this process continues, there is a gradual transition from ductile to brittle behaviour. It is during this transitional process that aa lava surfaces form. Chilled elements are twisted by the channel torque (Moore 1987, Kilburn 1990, Rowland and Walker 1990) to coagulate into 'pasty clots', which combined with lava elements torn from the pahoehoe crust deform to produce small, highly recognisable clinkers (Jaggar 1930, Peterson and Tilling 1980, Kilburn 1989)

In laminar flow the central regions of the channel move faster than the flow margins where shear is highest. Thus lava surfaces in the centre have experienced less cooling than lava surfaces at the channel margins and have experienced less shearing. As a consequence the flow centre can remain as pahoehoe whereas the cooler and more sheared margins develop an aa clinker texture.

As lava evolves further, and develops a cooler, thicker crust, the tensile and shear stresses that build in a flow are accommodated by brittle failure. As the lava becomes more thermally mature the depth of solid-ductile transition increases, the most thermally mature lavas are produced, with surfaces analogous to the blocky flows of Macdonald (1953). Although blocky flows are commonly associated with the more viscous lavas of andesite and rhyolite flows (Macdonald 1953), primarily as a function of their slower emplacement times (and hence opportunity to thermally mature), they are also witnessed at long-lived basaltic flows (e.g. Booth and Self 1973). The upper surface of the flow deforms more as a granular flow, with blocks milling, fracturing and rearranging to accommodate channel movement.

The distal Bakingili flow fronts are composed of blocky aa, and facies transitional between clinker and block lava. Elements of rooted clinker are rare, occurring only as squeeze-ups, and most clinker is an abraded component of the rubbly veneer. The progress from clinker to blocky aa is both gradual and gradational, with many thermally mature aa lavas possessing a mixture of semi-ductilely sheared and brittley fractured material. With distance from the vent maximum and average clast size increases, from aa cauliflowers of the order of 1-10 cm to blocks 1 m in diameter, and the propensity of blocky aa relative to clinker aa increases.

4.3.1.3 Small-scale morphologies—textural characteristics of pahoehoe, aa and blocky lavas

Pahoehoe

Pahoehoe forms only a small fraction of the effusive products of the 1999 flows. Surface samples from the site 1 upper vents (Cone IV outflows, UTM 32 515227E 0459007N, 2690 m asl) consist of glassy, vesicular pahoehoe, with finely drawn-out, bladed surface texture (Kilburn 1990). Blades are highly deformed, typically 2-4 mm in relief and contiguous for 1-2 cm, and commonly carry mm and sub-mm-sized parasitic stubbly spines and knobs (**Plate 4.8**). A sample taken from overflow drapes at the same locality shows a deformed, finely filamented and platy surface, with filaments of mm-relief changing direction over lengths of ~3 cm. The drape is highly vesicular (>60%).

Site 2 pahoehoe (collected from near to the uppermost spattercone of the lower vents; UTM 32 510390E 0456404N, 1540 m asl) displays similar surface texture features. Flakes of surface lava collected from later, slowly effused, ropy channels (Dr. Emannuel Suh, pers. comm.) display a fairly glassy surface texture intermediate between coarsely filamented and bladed pahoehoe (Kilburn 1990). Less vesicular samples possess a glassy sheen, with a highly deformed surface texture. Blades, and fine and coarse filaments <1 mm to 4 mm in width, have folded and coagulated into 'fine ropes' (up to 2 cm across) and irregular protrusions, with a parasitic stubbly texture.

Samples from the interior of pahoehoe lava display lower levels of vesicularities (5%), with vesicles flattened and slightly elongated in the direction of flow. The lava is typically phyric, with subhedral 0.5-10 mm crystals of olivine and clinopyroxene (avg. 2-3 mm) and plagioclase (avg. 0.8 mm) existing in a mixed glassy-microcrystalline groundmass. The surface texture is finely to coarsely filamented (0.5-2.5 mm) and occasionally bladed.

Clinker aa

Thermally immature aa displays the classically irregular clinker appearance that "defies verbal description" (Macdonald 1953). Samples are analogous to the cauliflower aa of Kilburn (1990): lava forms an irregular surface habit reminiscent of a "field of maltreated cauliflowers", with aa forming small, irregular protrusions of order 1 to 10 cm in size, with similar inter-cauliflower distances, and a typical relief of 5 to 20 cm. Cauliflowers are typically homogenous, or split and branched into uneven 'florets' (micro-cauliflowers) of cm dimensions. The surfaces of cauliflowers and florets are composed of mm-sized spines that display a bladed ('stiletto') or stubby habit similar to those described by Kilburn (1990) for Etna.

A sample of clinker from a small (90 cm thick on a 15° slope) aa flow front (site 1, UTM 32 514924E 0458351N, 2513 m asl) displays stubby and occasional stiletto spines on 2.5-3 cm florets

(**Plate 4.9**). A similar sample from a flow further downslope (UTM 32 514487E 0457186N, 2242 m asl) contains only stubby spines, formed on a partially micro-cauliflowered surface, with florets ~1-1.5 cm in diameter. These cauliflowers may be contiguous with massive, underlying lava, or have broken off to supply a loose, clinkery carapace. The massive interior lava of clinker aa is typically poorly vesicular with only fine, angular vesicles. Phenocrysts of olivine and clinopyroxene (with occasionally visible subophitic textures), with subsidiary, sub to mm-sized, unoriented plagioclase laths, lie within a dominantly crystalline groundmass.

Blocky aa

Thermally mature blocky aa is typically composed of a variety of clasts: abraded clinker, fractured angular blocks of massive lava and fragments of welded breccia. The propensity of breccia and massive lava increases with distance from the vents. The clinker conforms to the description above, but is more heavily worked: few large cauliflowers retain their characteristic morphology, having fractured into small, sub-equant blocks.

Blocks of massive lava, inferred to have originated from flow material brecciated beneath the clinker or rubbly top, or blocky material that has been further reworked, are similar to the sub-clinker lavas described previously. They are typically olivine-clinopyroxene-phyric lavas with low vesicularity. Vesicles are commonly subangular and plastically deformed, but show no preferred orientation. **Plate 4.10** shows a typical fragment of thermally mature massive, blocky aa

The welded rubble facies varies heavily in consistency, crystallinity and degree of welding. A sample taken from a site 2 flow (UTM 32 510295E 0456305N, 1512 m asl) exhibits a crumbly, stubby texture (**Plate 4.11**). The rock varies between clast and matrix supported, and clasts may be angular, or stubby and rounded. Occasionally, large 0.5-0.8 mm sized crystals of clinopyroxene provide clasts in their own right. The matrix consists of fine to medium sand grade volcanic breccia, and many clasts appear to be reworked granules of earlier breccias. This welded breccia frequently grades into areas of massive (commonly vesicular) lava, typically olivine-clinopyroxene-phyric basanites analogous to those described above.

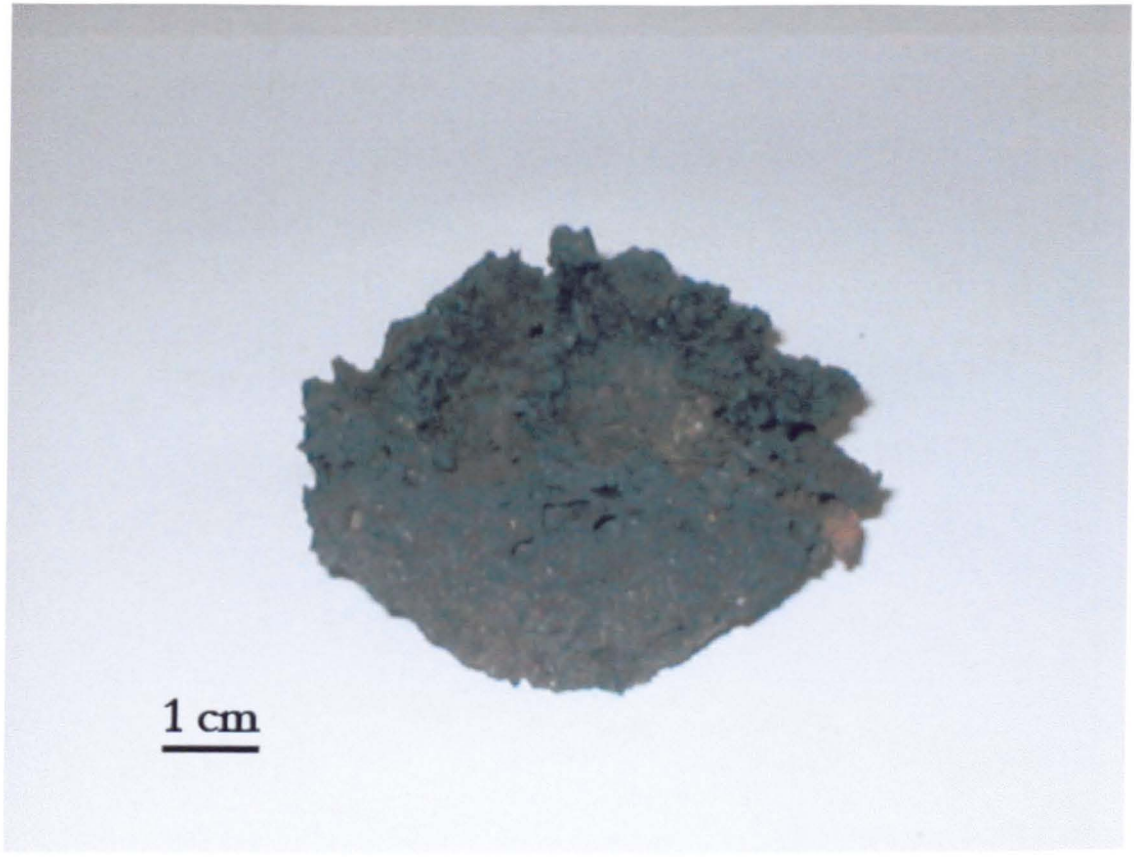

Plate 4.8 Typical hand specimen of thermally immature vesicular Cameroonian pahoehoe.

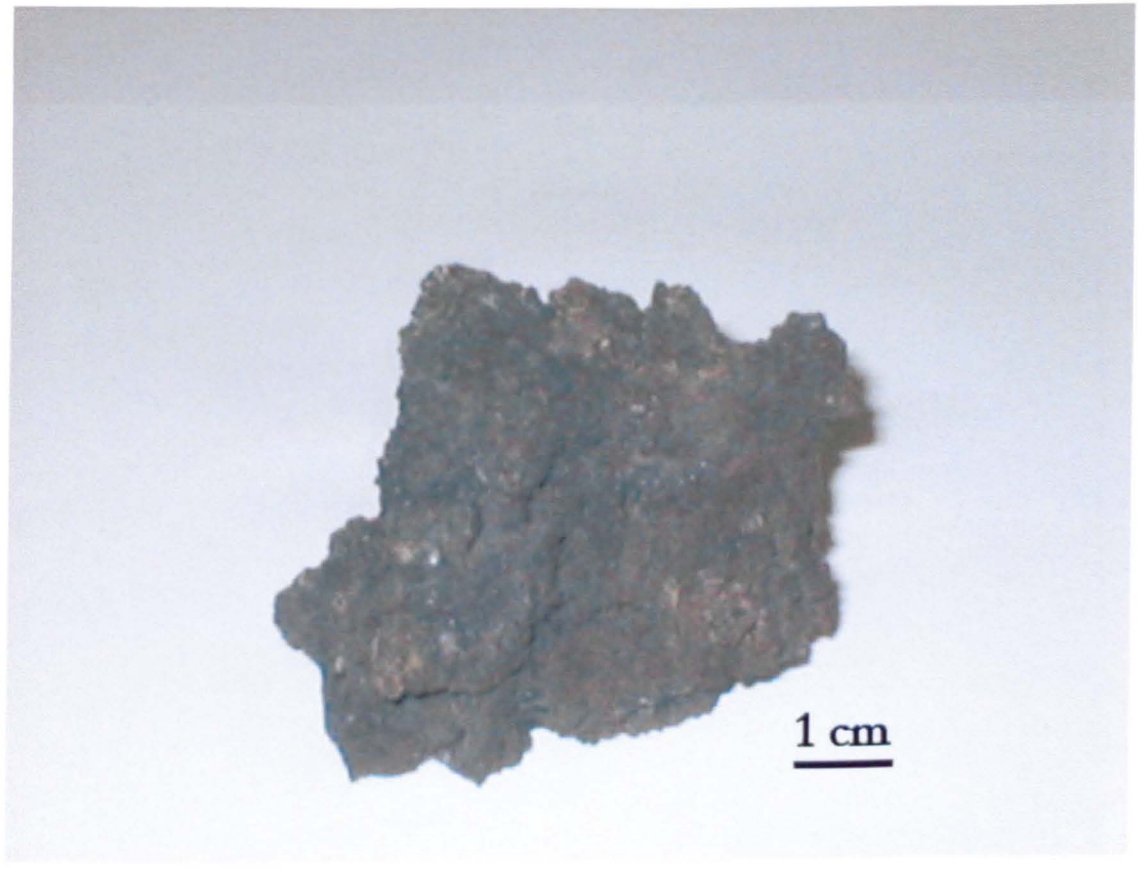

Plate 4.9 Hand specimen of relatively thermally immature aa clinker, displaying micro-cauliflowering.

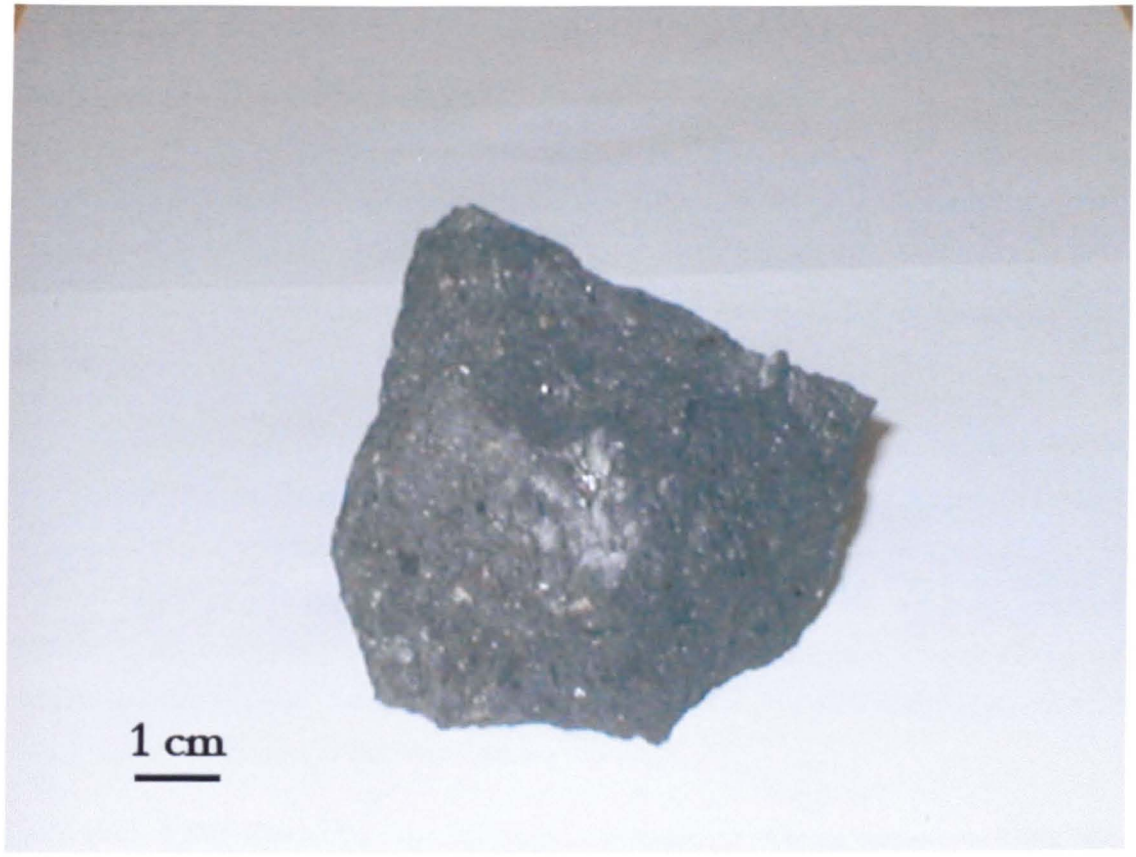

Plate 4.10 Sample hand specimen of thermally mature, massive blocky aa.

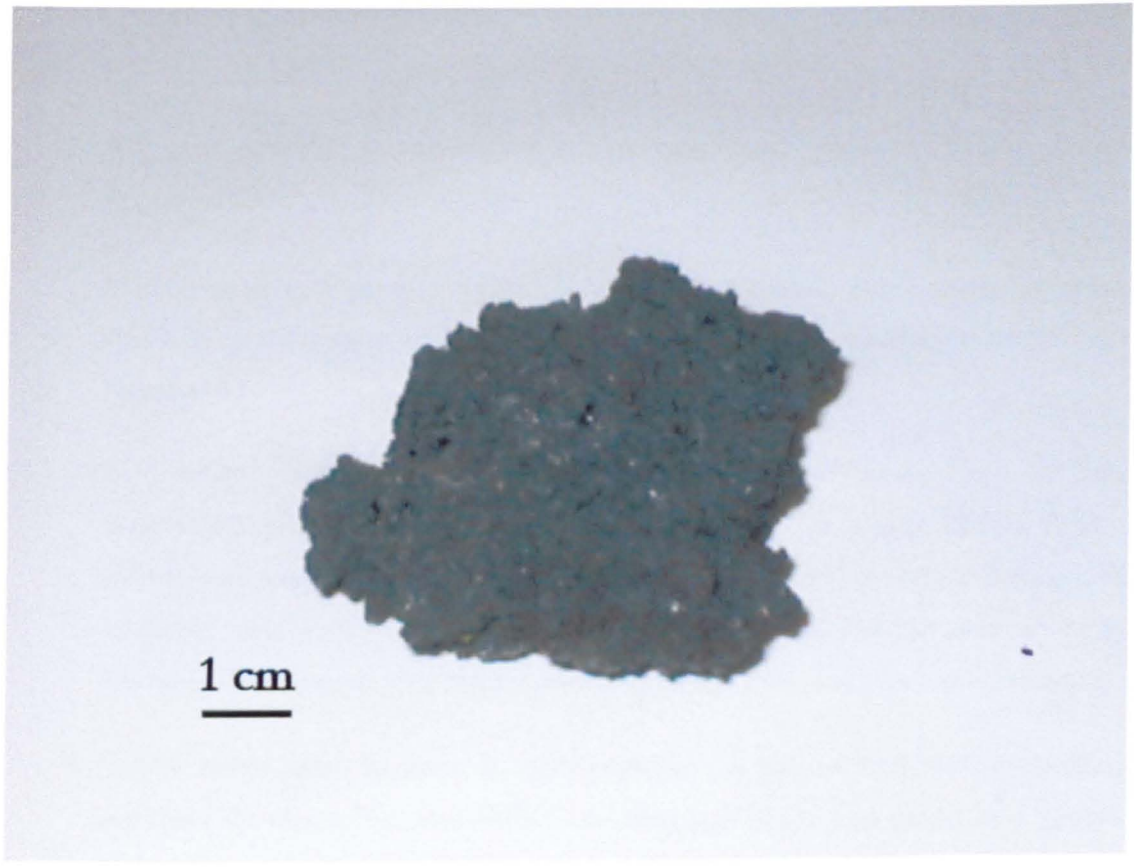

Plate 4.11 Hand specimen of welded fine-grained rubble and breccia.

4.3.2 Levee structure & texture

Lava levees are a common lava construct in Mount Cameroon lavas, whose structure and habit are directly related to the dynamical processes a flow has experienced in its emplacement history. Extant levee structures are therefore a key tool in the analysis of historical flows, where syn-eruptional data are limited, or wholly absent. The flows of Mount Cameroon possess numerous examples, and partial draining of some channels allows observation and analysis of their internal structure.

These levees can be either 'exterior', that is bounding a discrete flow unit, or 'interior', where they lie within the flow profile itself, as a secondary construct. Varying factors influence the degree and nature of levee formation; external and internal structures may be formed by similar, or wholly different, processes. The parameters that influence levee development are numerous: lava rheology; channel surface morphology; physical channel structure, orientation and curvature; local gradient and changes in such; local emplacement history, dynamics and flow rate; character and structure of channel and flow adjacent to the levee forming region etc.

Sparks et al. (1976) defined four specific types of levees from their experiences on Etna, garnered from lavas that are partially analogous to the flows seen on Mt. Cameroon; Etna lavas are hawaiites and not very different in composition to Cameroon basanites. To reiterate briefly, the distinctions they choose are:

Initial levees – formed by nascent, still incandescent, 'fluid' flows, as a function of the lava's yield strength.

Accretionary levees – typically formed by proximal pahoehoe flows, where marginal, still ductile clinker is sheared and welded into a solid levee margin, building up as more material is accreted.

Rubble levees – commonly found in fully developed aa flows, where the more thermally mature lava produces a heavily fractured and clinkery or blocky surface habit. This unwelded material avalanches and resettles as the flow moves, typically following a Mohr-Coulomb failure criterion and coming to rest at angle of between 30° and 35°. In reality, this rubble is frequently a superficial feature that hides more complex levee structures.

Overflow levees – whilst Sparks et al. rarely observed this type on Etna, they form when lava overflows the channel or levee sides (increasing their height and width), as a function of increasing magma discharge and lava backing up from the cooled front.

As Sparks et al. (1976) state, it is rare to find levees that perfectly match these descriptions; most levees are hybrids of two or more of the above archetypes, reflecting a more complex interplay of dynamical processes. Other workers, in adapting the system of Sparks et al, have created further distinctions, like the 'deformation' and 'accreted levees' of Lipman and Banks (1987) and the 'walled levees' of Naranjo et al (1992).

All four archetypes of levee are present, to varying degrees and combinations, in the 1999 flows of Mt. Cameroon. Using as a basis the categories of Sparks et al., we shall now describe their propensity, situation and morphology.

4.3.2.1 Observed levee structures

Initial levees

Initial levees are rarely preserved. They were observed to form on Mount Etna (Pinkerton and Sparks 1977), but were almost always destroyed by later levee forming processes. Naranjo et al (1992) describe well-preserved levees composed of massive lava at Lonquimay Volcano, Chile, but such are formed by andesite lava. The greater rate of shear and high flow velocities of the Cameroon basalts compared to the low effusion rate Etna lavas studied by Pinkerton and Sparks (1976) leads to a different dynamic regime. Initial, incandescent viscoplastic levees on Mt. Cameroon soon develop a solid character on further cooling, and fracture. Furthermore, the welding of marginal clinkers or actions of localised flow surges can overprint them with an 'accretionary' or 'overflow' character.

Rarely, the emptying of both proximal and distal channels reveals massive lava on the inside walls of levees, underlying areas of welded breccia, clinker or overflow drapes. Such material is frequently striated, and hence not contemporaneous with the last surge of channel flow. This may likely represent the parcel of lava Lipman and Banks (1987) describe as 'sluggish flow... developed... through degassing, drag, and cooling', which then develops a 'solidified crust, beneath which a plastic core remains' (see for example figures 57.9C & 57.9D, Lipman and Banks 1987). In character if not always in age, such plastic aa bulwarks represent the clearest observable analogue to an initial levee the 1999 flows possess.

Accretionary levees

In contrast to initial levees, accretionary levees are commonly preserved in their entirety, but preferentially are preserved only in the proximal flow regions of site 2. The 'accretionary process' does indeed play a part in the formation of certain types of rubble levee, but this shall be considered later.

Plate 4.12 displays a classic accretionary levee, bordering a narrow lava channel with a pahoehoe and clinker margins. It was extruded from a small bocca near the uppermost of the 1999 site 2 spatter cones (~1545 m asl). The channel is 1.9 m wide at the base, and 1.5 m wide at the levee tops. Such flows are typical of the small ephemeral vent flows of Etna, and have been well documented (see, for example, Polacci and Papale 1997). The levee walls are composed of welded clinkers, and a distinctive feature of many accretionary levees is their common possession of outwardly sloping inner walls. **Plate 4.13** clearly illustrates this geometry, wherein the interior levee walls slope steeply outwards at an angle of 70°; the outer walls slope outwards at and angle of ~40-50°.

A closer analysis of **Plate 4.12**, however, shows a more complex picture. Whilst the upper portions of the levee are clearly welded clinker, there is also evidence of more solid lava lying below the accretionary structures, and pahoehoe overflows (see below) draping them above. Polacci and Papale (1997) describe long undulations (with axial trace parallel to flow direction) in the near-bocca flows of Etna, wherein the marginal clinker overlies solid lava ridges. In such a system, the latter ridge providing the levee of the flow, the levees have a strong to dominant 'initial' component. This simply serves to highlight the rarity of finding simple end member levee archetypes, where a single levee is unmodified by other flow processes. The levee in **Plate 4.13** could be better described as a composite of initial, accretionary and overflow stages of levee construction (see below).

Rubble levees

Rubble levees provide the most common levee archetype of the 1999 flows, and in the distal regions they are the near exclusive levee construct. Of the approximate 82 levee structures contained within cross-sectional lava profiles, 80 are classed as rubble levees (including the subclass, 'accreted levees' – see below), and they are found in all but the most proximal regions of sites 1 and 2; only **Section XVIII** lacks rubble levees. This study gave an opportunity to examine rubble levees in more detail than previous work. Sparks et al. (1976) placed emphasis on the role of loose talus on the outer side of such levees both as a major feature and in restraining the spreading of the lava. Here we show that rubble levees are internally quite complex and that the talus is not such an important feature. Rather such levees are found to be predominantly composed of massive lava and welded breccia with high viscosity and strength.

Rubble levees are composed of highly brecciated clinker, blocks and rubble, of varying sizes, which can be loose, packed or commonly welded. Typically the levee will display two distinct parts: a more gently resting outer slope and a steeper inner wall. These sectors and their characteristic facies are shown in **Figure 4.4**. The lower outer slopes of exterior (i.e. flow bounding) levees are

Plate 4.12 Accretionary levees developed in a small, proximal bocca-fed lava channel, near the Site 2 vents. The central pahoehoe channel is flanked by clinker. The levees also display evidence of overflow activity, indicating a more complex, compound structure.

Plate 4.13 Another view of the channel described in Plate 4.12, clearly displaying the steep and outwards sloping walls. The top of the channel by the hammer is 1.5 m wide, the base 1.9 m wide.

composed of loose, unconsolidated talus (**Plates 4.14 & 4.15**). The size of the material varies from sub mm-sized coarse sand, through granules and small blocks, to larger blocks and m-sized boulders. Clasts are typically subangular to rounded, and the whole deposit is moderately to poorly sorted. Generally speaking, there is a gradation in particle size as one travels down the outer levee, with a slight decrease in mean grain size overall. This talus apron usually accounts for between 60 and 90% of the outer slopes' length, and lies at the angle of rest of the material. This angle varies according to the sorting and rounding of the clasts: the sections display a range of recorded values between 21° and 42°, with the vast majority of readings lying in the 27° to 34° range.

The upper portion of the outer slope is composed of welded clinkery rubble and breccia (**Plate 4.16**). This material is dominantly the same facies as is seen on the inner wall: it may be solid, fractured or wholly disaggregated into large blocks. Where solid it typically stands out above the lower talus apron at slopes of 45° to 60°, well above the angle of rest. This 'outer top' welded rubble facies may account for between 10 and 40% of the outer slopes' length; a mix of 66% talus and 33% welded breccia is most typical. The welded breccia is frequently overlain at the top by poorly sorted, unconsolidated angular blocks of rubble and massive lava (**Plate 4.17**). Such material is typically coarser and more angular than the outer levee talus, and greater than 10 cm in diameter.

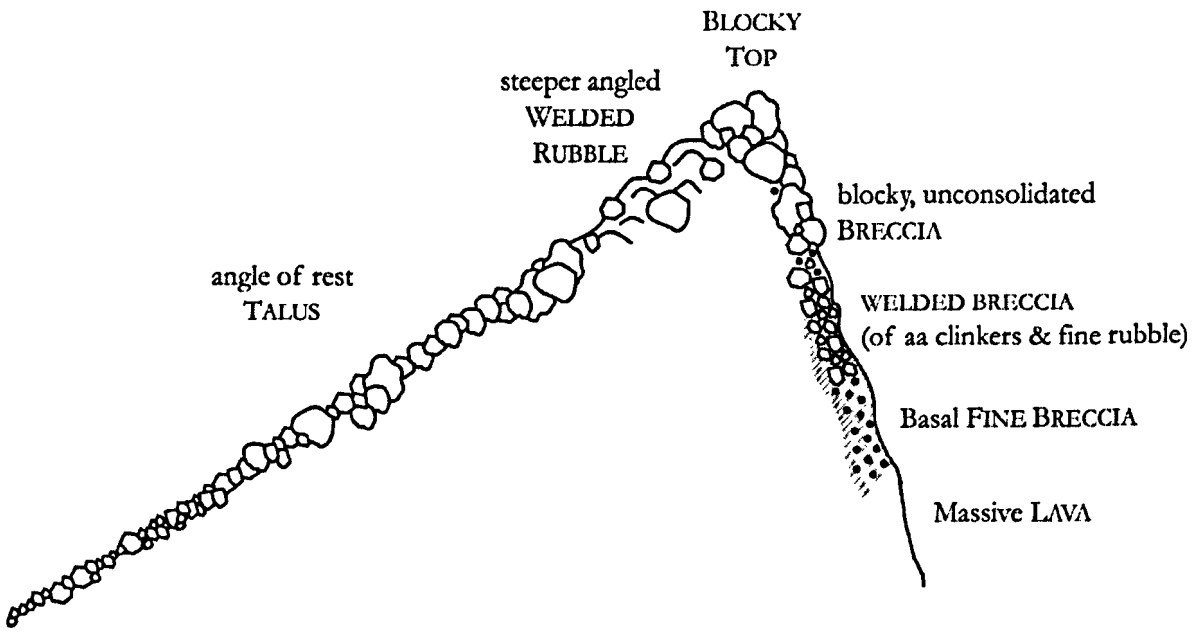

Figure 4.4 Typical rubble levee geometry and structure. The grey lines symbolise welding, or (if hashed) partial welding on the inner wall. The outer slope dips at the angle of rest (~30°) whilst the inner wall is considerably steeper (~70°). The section as shown represents an archetypal levee; many extant examples do not possess all the facies depicted.

Plate 4.14 Outer surface of a rubble levee, displaying the typically loose, angle-of-rest talus. The Site 1 cone from whence this flow originated may be seen in the background. Dr. Gerald Ernst kindly provides a Belgian scale.

Plate 4.15 Outer rubble levee 'wall', again showing unconsolidated talus. The level of sorting in marginal talus slopes can vary considerably. Areas of more consolidated, welded rubble are apparent in the upper third of the structure.

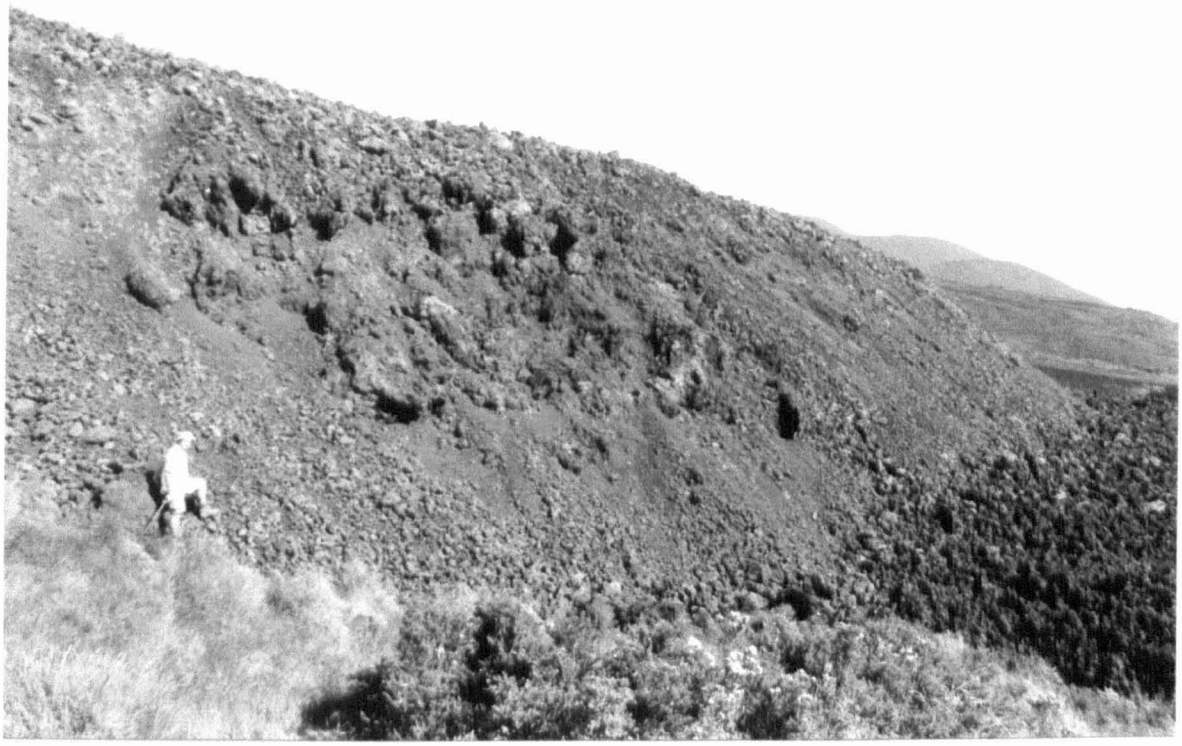

Plate 4.16 View of 1999 lava flow from the Site 1 vents, overriding an earlier flow unit, looking downstream (south). The upper half of the bounding rubble levee's outer slope displays areas of welded breccia, thrusting out of the surrounding talus at a steeper angle.

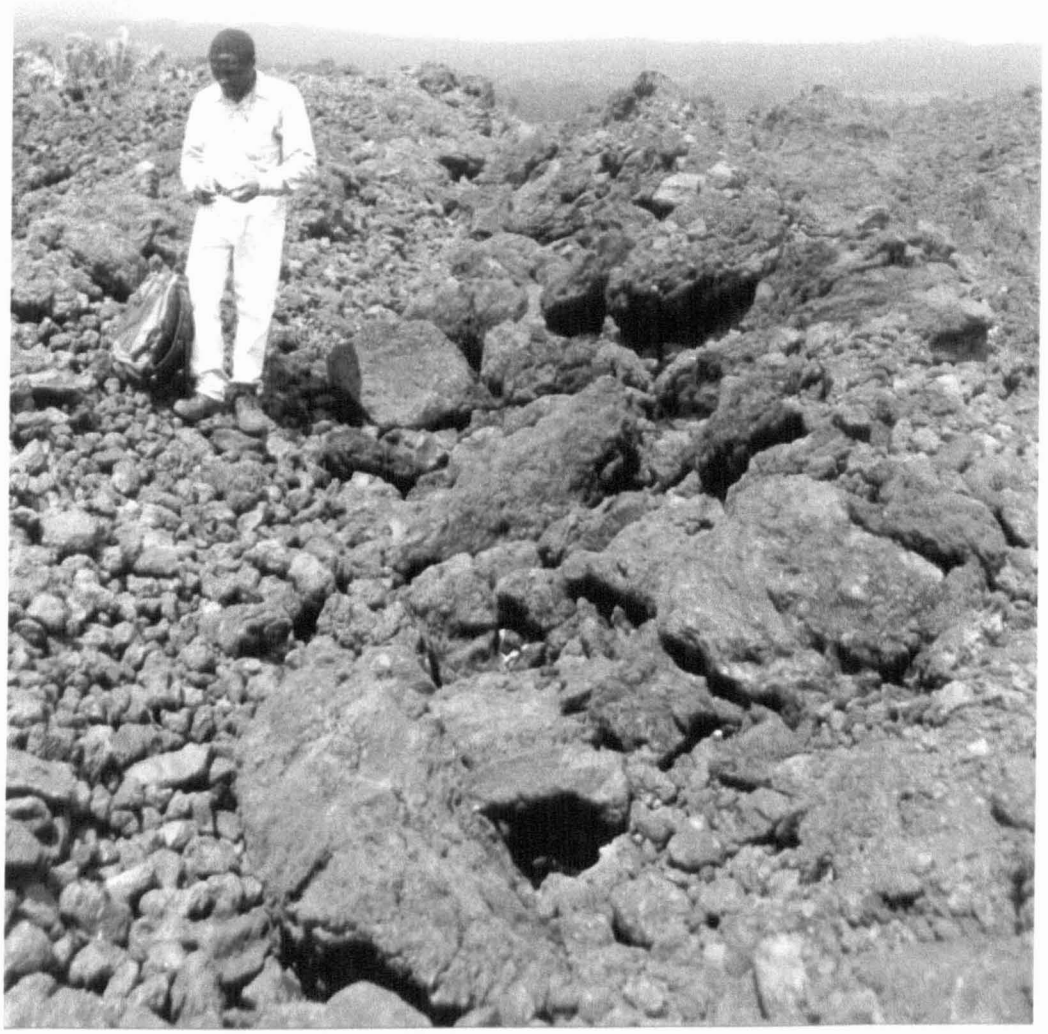

Plate 4.17 A typical rubble levee top facies, with a poorly sorted, unconsolidated collection of angular and semi-rounded blocks of welded rubble and avesicular block aa. Dr. Emmanuel Suh is actually standing in a small gully between two levees, the outer bounding levee being on the left of the picture. Photograph taken at the distal Bakingi flow fronts of the Site 2 flows, looking upslope (NNE).

The inner levee walls dip much more steeply, sloping inwards at angles of 45° to 85°. The facies of the inner levee vary considerably, as a function of the history of the local flow regime and its affect on levee development. What follows is a description of *all* the typical facies that appear in the Cameroon sections, as they would appear in an archetypal rubble levee profile. Inner walls revealed by channel drainage rarely display all these facies, or exhibit variations on the general theme.

Below the blocky top described above, one commonly sees a small (sub-m) section of blocky, unconsolidated breccia, fining downwards. This is in effect a continuation of the blocky top. In some levee walls, this material grades rapidly into a poorly sorted, matrix-supported breccia, with partial, incipient welding (**Plate 4.18**). These facies bear some similarity to the basal breccia of Naranjo et al. (1992) but display a far greater variety of clast size and heterogeneity. The level of welding varies greatly, with some blocks and rubble held in place by little more than a semi-consolidated sandy matrix.

The upper breccia facies is typically underlain by a strong, massive deposit of incipiently welded clinkery breccia. This provides the dominant facies of the inner wall, and provides its typically steep inner slope (**Plate 4.19**). This material is also similar in appearance to the upper welded rubble facies of the levee outer wall. The contact between the more massive welded breccia and the overlying breccia is usually sharp; any gradation between the two layers is focused in a band no greater than 15 cm in depth. The welded breccia facies comprises clasts of clinker and pre-mobilised rubble, of sub-angular to sub-rounded habit, and heterogeneous grain size (typically 1 to 10 cm). The facies commonly shows 'standlines', which are interpreted as various levels of interaction between the flow in the channel and the levee walls during channel fall, typically appearing ~10 cm apart (**Plate 4.19**).

This clast-dominated facies can fine downwards into a matrix-dominated basal breccia. The gradation appears gradual, and at times this basal breccia is less welded than the overlying clinkery deposit (**Plate 4.18**). On many inner walls, the welded breccia does not display any change from clast to matrix dominance with depth, appearing as a heterogeneous texture throughout the facies that is intermediate between a matrix and clast-dominated consistency (**Plate 4.20**). The level of welding and nature of clast size appears to heavily influence the steepness of the inner wall strongly. Incipiently welded clinkers can retain steeper angles of slope than fine, matrix-dominated rubble.

Rarely, solid lava is found beneath the base of the welded breccia, and forms the basal facies of the inner wall. Although inner levees are typically steeper than the outer slopes, the drop in channel depth can lead to structures that are initially unstable, local fracturing and in some examples avalanching, leading to the formation of talus or an apron of blocky rubble along the inner wall-channel boundary (**Plate 4.21**). Levees of outlying lobes are typically similar to the blocky flow

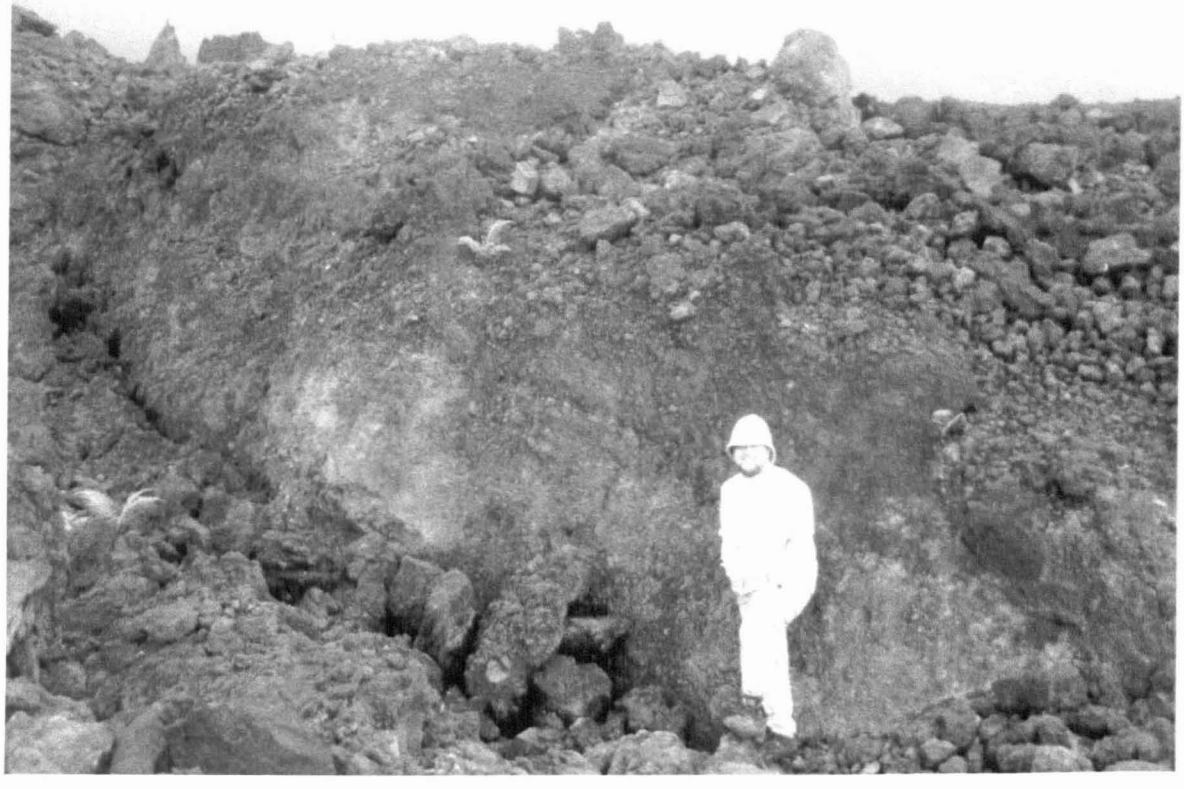

Plate 4.18 Inner rubble levee wall from the distal Bakingili flows. The wall is composed of a fine, poorly sorted breccia, partially welded. Towards the levee top the breccia coarsens into a more clast-dominated facies, and thence to a loose rubble and blocky top, as described in **Figure 4.4**. Intrepid explorer for scale.

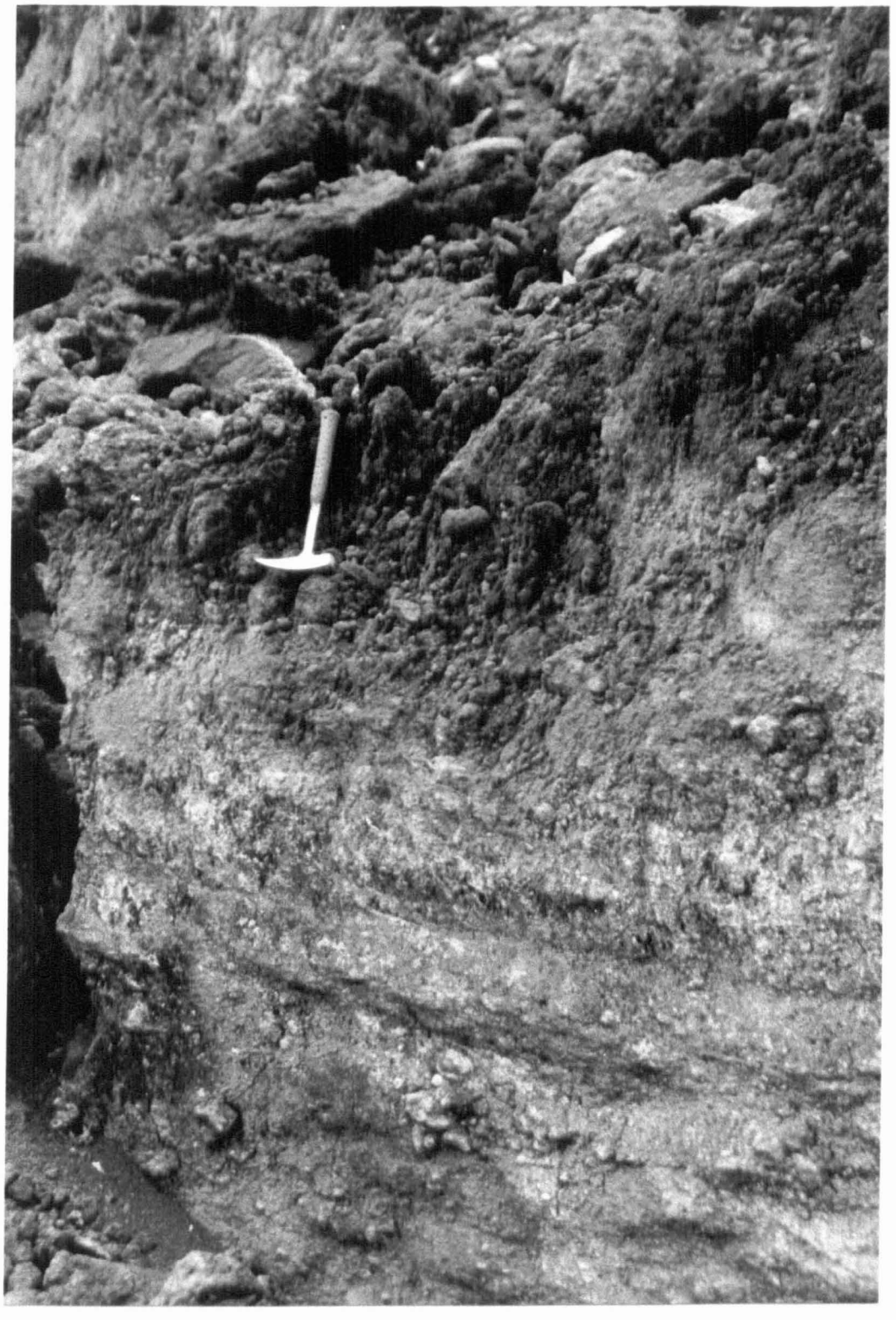

Plate 4.19 Steep inner wall of a rubble levee at the distal Bakingili flow fronts. The material here consists of a fine, matrix-supported welded breccia at the base, which grades upwards into a deposit of incipiently welded aa clinker and rubble. The clinkery breccia displays several 'standlines', typically 10 cm apart, interpreted as levee-channel interactions in response to changing flow level. The welded clinker grades into a less consolidated breccia richer in fines, and ultimately into a clast-rich rubbly top.

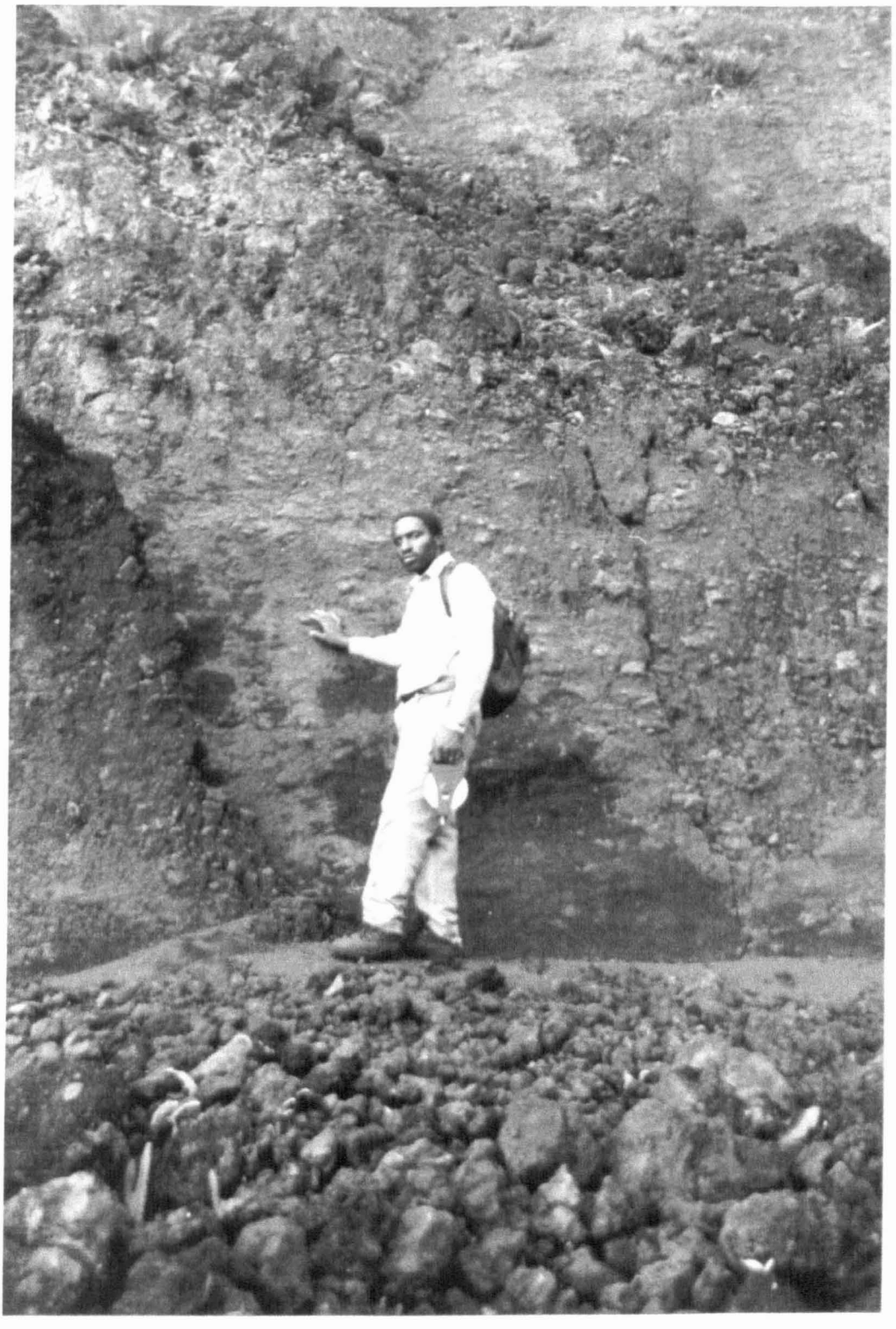

Plate 4.20 Dr. Emmanuel Suh stands by another interior rubble levee wall at the Bakingili flows. The welded breccia here possesses a heterogeneous texture, with an overall consistency intermediate to clast and matrix-dominated breccias.

fronts of aa flows; outer and inner levee surfaces (which are rarely revealed) depict poorly sorted, blocky talus. Such levees are immature, with far less reworking on the outer surfaces.

Interior rubble levees (**Plate 4.22**) typically mimic the habit of exterior levees, with an inner wall of welded breccia, blocky top, and outer slope of talus. The latter lacks the development or fining of the strongly developed and more extensive exterior levee outer slopes, and is typically little more than a continuation of the blocky top. If sets of interior levees are particularly close, the processes of new *active* levees (Guest et al. 1987) can impinge upon the morphology of older *static* levees, with lava reworking and talus avalanching burying bordering welded rubble facies with block and talus. Through such processes many rubble levees may appear simply as blocky ridges aligned parallel to the flow margins; in such cases it is impossible to discern if they formed through the typical process of channel inflation and subsequent fall, or through a wholly different mechanic, as *accreted levees.*

Our observations suggest that the loose talus component of rubble levees is less significant than originally envisaged by Sparks et al. (1976). The levees are predominantly composed of partly to densely welded breccia and clinker, and some contain a massive core. The resemblance to facies found at flow fronts suggests that rubble levees are formed by flow front material being pushed aside and then modified by channel flow. This concept is developed in more detail below.

Accreted levees

Accreted levees, as described by Lipman and Banks (1987), differ in mode of formation from the rubble levees, but exist as physically similar structures: shallow blocky ridges marked by sub-angular to angular coarse blocks, no more than a couple of metres high. They are often difficult to distinguish from the blocky tops of rubble levees buried by the activity of neighbouring levees (**Plate 4.23**).

Overflow levees

Overflow levees are observed in near-vent or bocca flows by the proximal site 1 or 2 regions. They are defined by thin pahoehoe overflows that cover existing initial, accretionary and overflow levees. In a vesicular pahoehoe flow that breaks out from the third of the site 1 cones (see **Section XVIII**), pahoehoe wells out of the channel, forming thin overflow drapes 15-30 cm thick on existing pahoehoe accretionary levees (**Plate 4.24**). Thinner drapes occur on steeper slopes, with measurements of 15 cm made for overflows on up to 50° slopes.

Plate 4.25 shows the behaviour of an overflow levee covering an accretionary levee discussed previously (see **Plate 4.13**). The strictly localised nature of the overflow and its ropey appearance are readily apparent in this site 2 proximal bocca outflow; drapes only travel approximately 2.3 m down existing levee slopes, and are typically 8 cm (on 45° slopes) to 18 cm thick (on 30-40° slopes).

Plate 4.21 This inner wall from a rubble levee near Bakingili displays steep portions of welded breccia., interspersed with avalanched, rubble rich in fines. The loose material is derived from areas of the level that were built from poorly consolidated, matrix-rich breccia The contrast in angles of repose post-avalanche is clear.

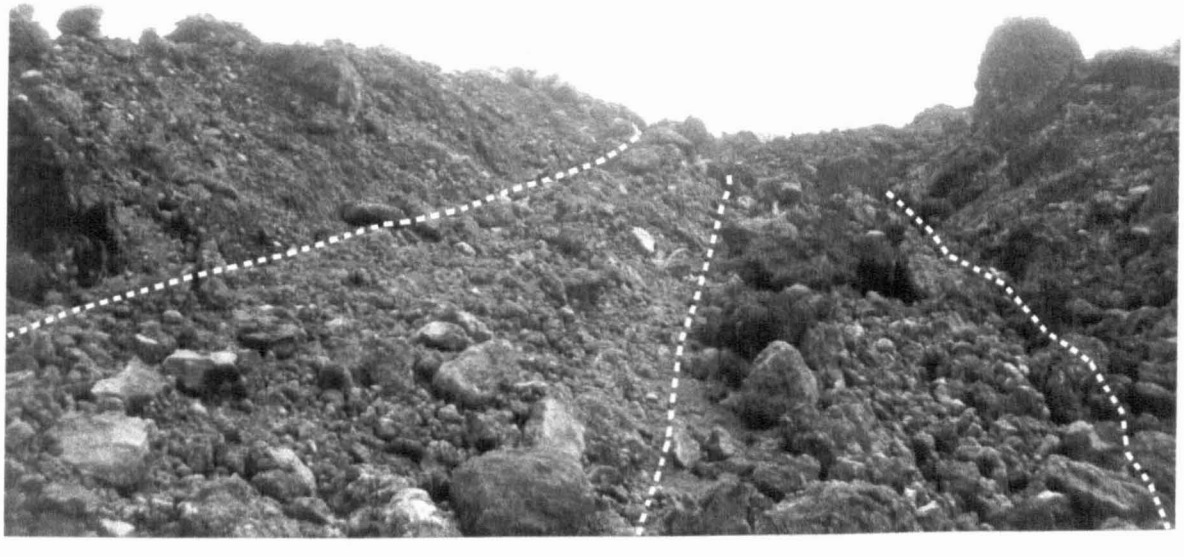

Plate 4.22 A series of three internal levees in the distal Bakingili blocky aa flows, looking downstream. The lava channel is the rise marked in the extreme right of the photograph.

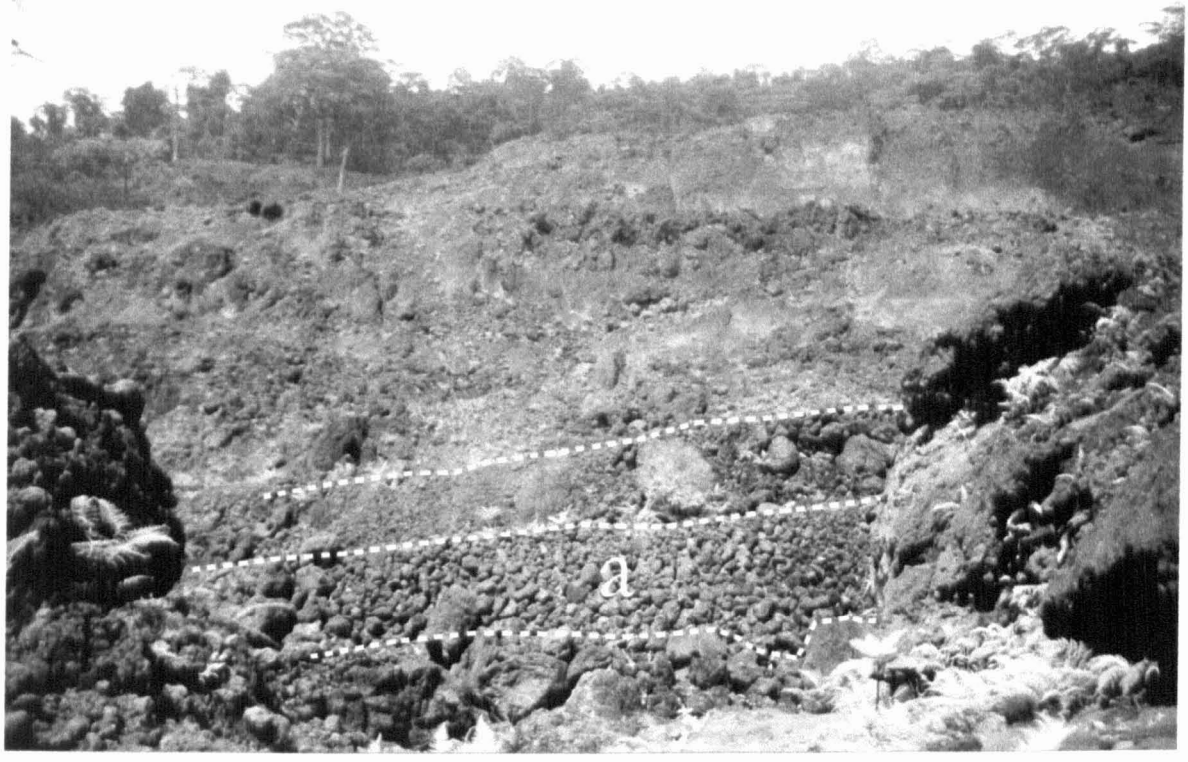

Plate 4.23 Photograph looking across a channel section of a blocky aa flow near Bakingili, standing on one bounding levee and facing the inner wall of the bounding levee opposite. The blocky region marked 'a' is a well-defined internal levee, quite possibly of accreted origin.

Plate 4.24 Outer wall of a levee of a small Site 1 vesicular pahoehoe flow that broke out from a vent cone, clearly displaying overflow drapes 15 to 30 cm thick.

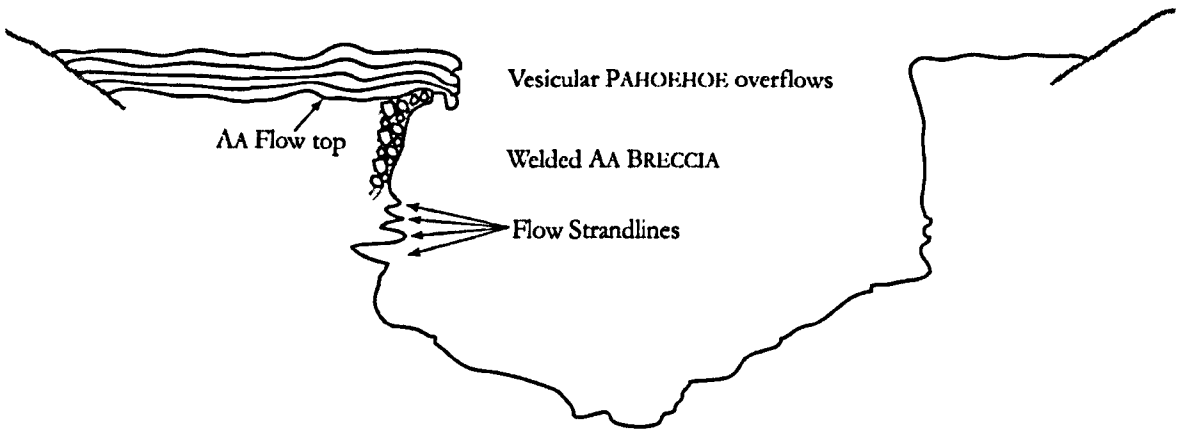

Figure 4.5 Proximal site 2 flow channel, focused down an existing valley (UTM 32 510177E 0456208N, 1484 m asl) – one of the two main feeders of the distal Bakingili flow front. In this example the central depth of the channel is 6 m.

A similar overflow levee on the opposite side of the channel is displayed in **Plate 4.26**. Further examples of overflow levees are found in a deep, valley-filling channel section downstream of the previous example (**Plate 4.27, Fig. 4.5**). Here four distinct pahoehoe drapes form a composite overflow levee ~0.7 m thick, overlying existing aa channel fill. The individual drapes were each ~10-25 cm thick.

4.3.2.2. Interpretation of levee structures: modes of formation

Initial levees

Irrespective of their post-eruption propensity, initial levees form a protostructure that can be masked or altered by subsequent levee building processes. Hence a brief discussion of the factors controlling initial levee formation shall be presented, as a basis for further discussion. Whilst elements have been presented previously, concepts like viscous levees (discussed in Chapter 3) are new to the literature.

Basaltic lava is commonly erupted as an incandescent fluid. Its exact rheology will depend on its chemistry, crystallinity and temperature (see Chapter 1), but hot basalt can be simply described as a simple viscous, or viscoplastic fluid, with a small yield strength (for clarity we shall henceforth ignore potential, 2nd order effects like visco-elasticity, shear dilatancy, or the presence of a gaseous phase). As basalt flows cool rapidly via conduction to a radiating, convecting free surface, two rheological changes occur:

(i) an increase in the lava viscosity, as a function of increasing crystallinity and melt polymerisation (e.g. Shaw et al. 1968, Shaw 1969, Marsh 1981)

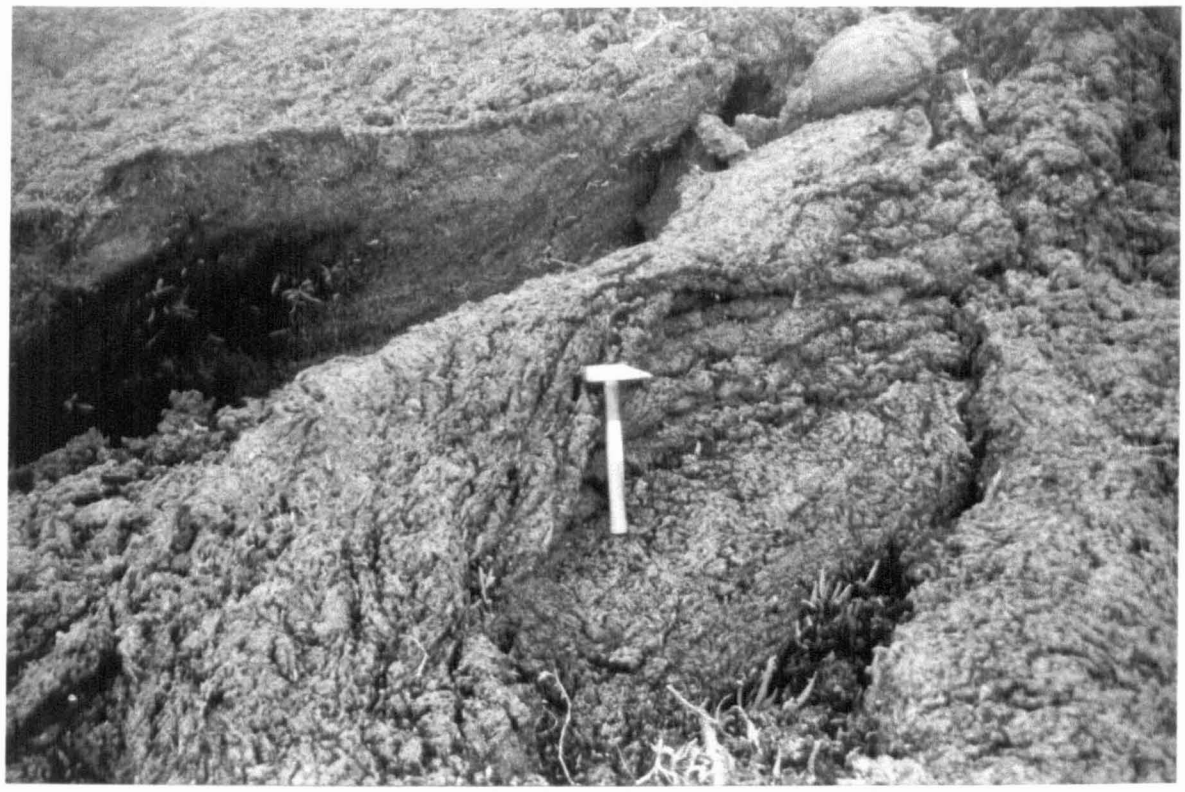

Plate 4.25 Ropy pahoehoe overflow on a proximal Site 2 flow (as also depicted in **Plates 4.12** and **4.13**). Drape thickness are on the order of ~10 to 20 cm thick, and are thicker on shallow slopes.

Plate 4.26 Pahoehoe overflow levee, on the opposite side of the channel to **Plate 4.25**. The overflows are localised, with drapes typically in the order of a few metres in width.

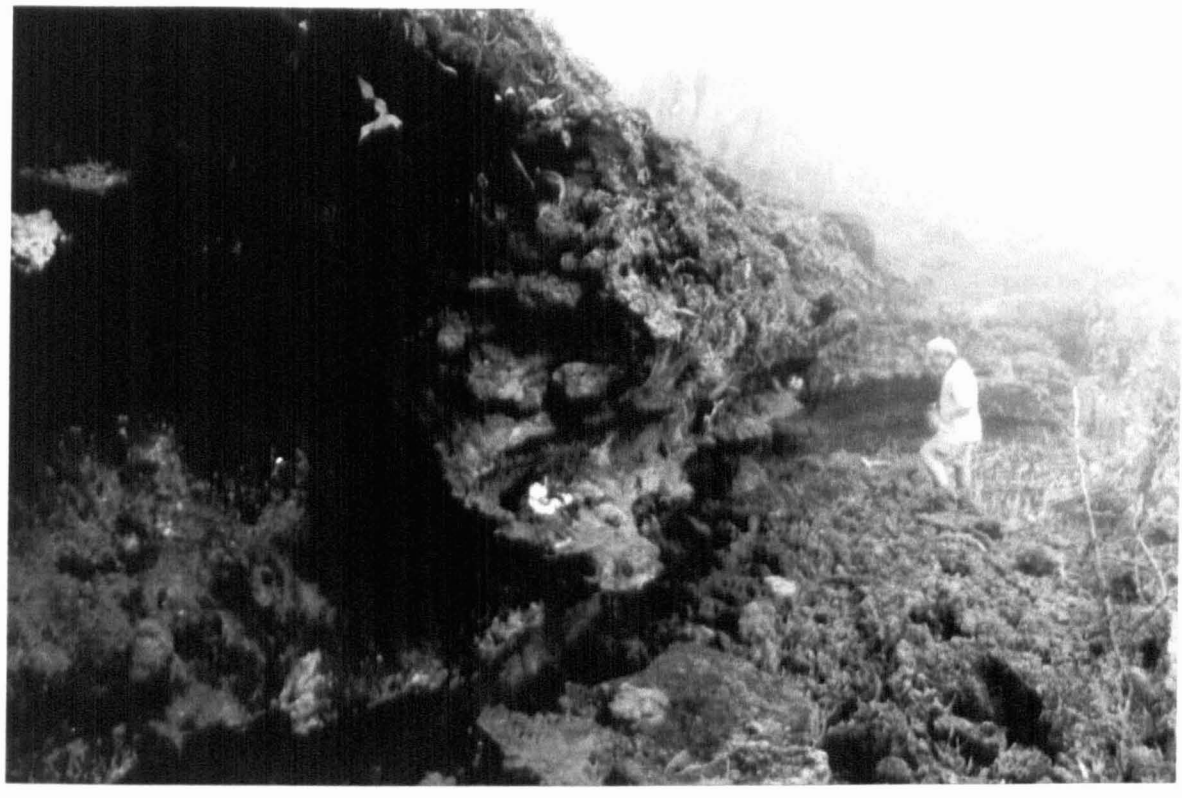

Plate 4.27 Internal wall of a Site 2, valley-filling lava flow, downstream of the channel described in **Plates 4.25 and 4.26**. Four pahoehoe drapes overlie aa channel fill; also described in **Figure 4.5**.

Plate 4.28 Photograph looking upstream at a proximal Site 2 pahoehoe channel with clinker margins, bounded in the near-source region by accretionary and overflow levees. Same channel as displayed in **Plates 4.12, 4.13, 4.25, 4.26, 4.29** and **4.30**.

(ii) an increase in the lava yield strength, as a function of increasing crystallinity, wherein crystal-crystal interactions provide a non-Newtonian plasticity (e.g. Shaw et al 1968, Murase and McBirney 1973, Pinkerton and Sparks 1978)

It is the latter to which Hulme (1974) attributes the initial formation of a bimodal levee-channel structure. Hulme argued that as flows were extruded, they would possess a lateral velocity, as a function of the height. As this lateral component *diminishes*, a state of static equilibrium will be reached, where the lateral basal shear stress near the boundary is equal to the yield value of the Bingham lava, and sideways movement ceases. Though cooling can indeed increase the magnitude of the yield stress of the lava, Hulme assumed a constant value related to partial cooling of the lava. Hulme's predictions found some valediction when applied to simple proximal flows in the field, though more complex lava geometries on variable topographies cause considerable errors and problems in analysis (Sparks et al 1976).

Though Hulme investigated the effects of yield strength on levee formation, none have considered the influence of a strongly temperature-dependent viscosity. Yet experimental evidence (see Chapter 3) has shown that structures like lava levees can form in cooled, temperature-dependent viscous flows on a slope, irrespective of a change in surface plasticity or the imposition of yield strength.

A simple indicator of the relative effectiveness of cooling in such cases is the Peclet Number (*Pe*), a dimensionless parameter that describes the ratio of the heat lost by diffusion to that which is replenished by advection. In our system this equates to the ratio of (i) heat lost by a parcel of lava through conduction to a cooled surface, to (ii) heat replenished by the advection of hot lava from the source.

$$Pe = \frac{Uh}{\kappa}$$

where U is the flow velocity or a velocity scale, h is the flow height and κ the thermal diffusivity. As κ is approximately a constant, the relative effects of cooling will be greatest when the term Uh is smallest i.e. when the flow velocity is low, and the flow depth is shallow. Both criteria are satisfied in the marginal regions of the flow, and consequently the Peclet number there is smallest.

For a given lateral cross-section, the marginal regions will be more affected by loss of heat than the fast, fluid interior, where the quantity is more rapidly replenished by advection. As lavas possess a strongly temperature dependent viscosity, this preferential cooling will develop a heterogeneous viscosity distribution across the flow cross-section, with more viscous margins flanking a relatively inviscid channel. This development generates a feedback loop, which further develops the situation. As the lava's viscosity increases, there is a commensurate reduction in U (relative to which the increase in h that may arise from marginal bulking can be considered a minor effect), which again decreases Pe. A decrease in Pe again increases the effects of cooling relative to the channel, and a strongly bimodal viscous structure develops.

Most importantly, the above processes interact with and exacerbate the rheological changes caused by an unbounded lava flow's motion. Cooler, viscous material at the flow front is pushed aside by warmer, fluid lava advected from the source. The cooled material forms nascent levees; as these are already considerably stiffer than freshly erupted lava, their relative cooling is accentuated further. By mechanical manipulation of the cooled flow front and accentuated cooling of the flow flanks, a two-phase flow is rapidly developed. The resulting marginal 'levee' is neither statically stable nor distinct in composition from the material it borders, but provides a considerable dynamic barrier nonetheless. Such highly viscous constructs will form in lava flows, irrespective of their plasticity, and contribute to the initial levee construction phase.

Accretionary levees

Following the development of initial levees (viscous or visco-plastic) the focus of flow down a channel produces high rates of shear at the levee-channel interface. The newly erupted lava is sheared too quickly to form fluid pahoehoe, and instead accommodates deformation in a plastic manner, forming small, irregular clinkers (Peterson and Tilling 1980). With the generally parabolic profile of the flow kinematics, modified by an added lateral component supplied by a typically convex upwards surface, hot and plastic marginal clinkers are accreted together along the initial levee margins, further developing the levee structure.

Sparks et al (1976) reason that accretionary levees form through a 'steady, slow rise of lava level'; such an increase may arise from an increase in the effusion rate, or from the cooling of more distal regions, especially the flow front. The latter causes a change in the rheology, and fluid lava bulks up behind this more viscous frontal toe and its margins, thence increasing flow depth all the way back to the bocca. As discussed, the slower moving channel margins will display the effects of cooling preferentially to the more mobile interior. The two factors promoting accretion are both greatest at the upper portions of the channel sides: shear, aiding the smearing and consolidation of clinkers, and cooling, which promote the solidification and stabilisation of the levee. Successive rises in flow

level, to accommodate the narrowing of the flow channel or as a function of global flow effects, will therefore accrete material from an increasingly smaller channel, and build outwardly sloping inner walls - unless a flow surge or blockage downstream causes a more rapid rise, in which case overflows will likely occur.

There is often considerable interplay between *initial*, *accretionary* and *overflow* levee building processes, as discussed previously. Yet irrespective of this complexity, the relative timing and influence of these stages can be rendered discrete. In **Plate 4.12** Pahoehoe overflows overlie much of the welded clinker, indicating a later, possibly surge-fed genesis. Likewise, areas of welded material overlie more massive lava, and one would therefore expect the accretionary constructs to post-date, or be contemporaneous with, the initial levee-forming lava.

Rubble levees

The methods for the creation and growth of initial and accretionary levees centre on the consolidation and deformation of incandescent, ductile lava, yet lava surfaces rarely retain these characteristics for long. As the lava thermally matures, it becomes increasingly susceptible to brittle deformation. Shear along the levee margin and flow front, accompanied by pressure from the weight of the channel itself, brecciates the cooled levee, channel top and frontal material. The onset of brittle deformation initiates a two-stage process of rubble levee building.

The flow fronts of thermally mature lavas will develop a distinct spatial gradation, from the loose or heavily fractured blocky aa carapace to a hot, thermally immature fluid interior (e.g. Sparks et al. 1976, Lockwood and Lipman 1980, Lipman and Banks 1987; **Fig. 4.6**). The core of the flow will display a Newtonian or weakly visco-plastic (Robson 1967, Walker 1967, Hulme 1974) rheology, and will grade into a cooler, highly viscous (and probably plastic) margin, where lava still deforms in a fluid manner. Beyond this cooled fluid boundary layer, the lava will be significantly cooled, to suffer plastic tearing due to shear and brittle failure. In between the fluid and solid strata it is common to find areas of welded clinker or autobreccia, incipiently forged by contact with the relatively hotter material adjacent. Thus a strong rheological zoning will develop in the front region as depicted in **Figure 4.6.**

Stage I rubble levees begin to form in response to the backpressure created by the rheologically stiffened flow front. As the front advances, the rheological and texturally zoned material is pushed aside by the caterpillar motion of the cooled surface, aided by the mobile fluid interior (Peterson and Tilling 1980; **Fig. 4.6**), in a manner similar to that described for the formation of initial levees. This new flow front soon cools and brecciates, and is itself marginalized by more thermally immature material or, more commonly, the thermally developed flow surface, building marginal rubble levees which display a gradation from external rubble, through welded clasts into a sluggish

visco-plastic interior. These structures are modified by the subsequent passage of warmer channellised lava, forming Stage II of the process. Additional material is provided by the transport of blocky material from the channel to the levee margins, and occasional 'blocky overflows' (similar to fluid overflow levees, only using clastic material). For the inner walls of the rubble levees, marginal shear and lateral channel pressure will mill initially fractured material so that it degrades in size, and sorts through to the basal regions of the shear zone, forming an incipiently welded fine basal breccia. As rheological changes downflow cause a backpressure to build up, resulting in flow thickening, and local narrowing of the channel as a function of cooling similarly occurs, the flow channel will inflate, and flow level will rise.

The upper surface will accommodate this movement by blocky avalanching, further developing and thickening the angle of rest talus that develops on the levee's outer slopes. Along the inner margin, the rise in level effectively raises the level of the hot, interior portion of the flow. This serves to further weld the initial rubble and breccia that accumulated, giving the levee stability, and also welding newer, warmer clinker to the wall, in a manner similar to that displayed in an accretionary levee. When the lava reaches its maximum height, upwards building of the lava ceases. The material deposited at the top represents the youngest material accrued to the levee, consisting of cool, thermally mature blocky lava, deposited from the channel. It is loose, having been deposited in a relatively cooled environment, and as it has not been milled for long, consists of course clasts and blocks. A subsequent decrease in lava level will strand this material here, leaving the classic rubble levee profile.

Accreted levees

Accreted levees form when existing channel structures, such as elements of pressure ridges or shear lenses, are marginalized and accreted to existing levee walls, merging with said same, or forming smaller internal levees. A further discussion of these phenomena is featured in 4.3.3.3.

Overflow levees

Overflow levees are generally formed following a flow surge, or a gradual backing up of the lava level as a function of downslope cooling (Sparks et al. 1976). They are most commonly evidenced in the proximal, near vent or near bocca region, where fluid, thermally immature lava is better suited to accommodate rapidly to the change in conditions and produce the cohesive overflow drapes evidenced. Both pahoehoe drapes and aa overflows are relatively common, occasionally in the same flow - with pahoehoe most likely signifying a vent induced surge of hotter less thermally mature lava, and aa depicting a backpressure derived raise in marginal clinker. Overflow levees also occur in distal blocky flows, though the products of an overflow of blocky lava would be near indistinguishable to those resulting from avalanching attending the natural growth of rubble levees.

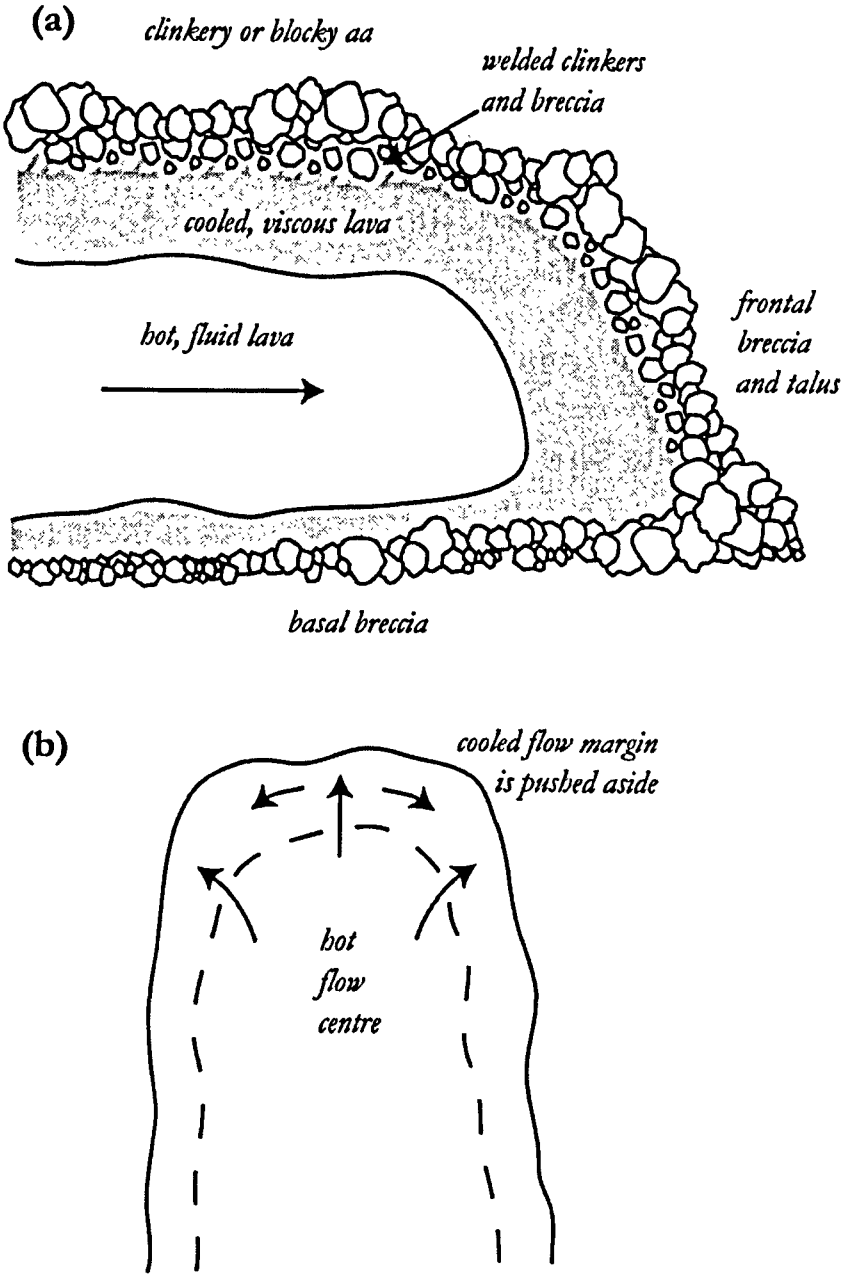

Figure 4.6 Structural and thermal zonation in block aa flows. Cooling causes initially Newtonian or weakly pseudoplastic material to stiffen, become increasingly non-Newtonian and ultimately cease behaving as a fluid pass into a regime of solid mechanics and brittle failure. As cooling is focused along the flow margins, and flow-top material is deposited at the flow toe by a caterpillar-like motion, frontal regions produce a flow profile similar to (a). While the core can deform in a ductile manner, the marginal carapace consists of torn clinkers and fractured blocks and rubble. The advance of the flow produces continual milling and further fracture; the high basal rates of shear and 'conveyer-belt' style of advance of the flow front produce a similar layer of autobrecciated material on the flow base. As the flow toe advances (b), the surface clinker or blocky aa pushes aside the sluggish, partially brecciated margins, whose structure forms the proto-rubble levees that are further developed by adjacent channel motion.

4.3.3 Lava channels

Strongly developed levee-bounded channel systems are the dominant morphology of the 1999 Mount Cameroon lava flows. As the character of levees varies according to proximity to the bocca or vent, the geometry and morphology of channels likewise displays a strong variance between proximal and distal channel facies. The differences are a function of an array of factors: slope and topography, cooling and channel building history, local and global lava flux, local lava rheology and shear rate, and downslope changes in lava viscosity and channel structure.

Irrespective of position, sequential and complex levees have shown that, with the exception of distal lobes and occasional breakouts, most channels have experienced repeated episodes of filling, inflation and draining. Stranded and exposed levees depict the general history of channel formation; the extant channel fill preserves the most recent (and perhaps dominant) mode of activity, exhibited before effusive activity ceased.

4.3.3.1 General channel morphology

Pahoehoe channels

Proximal pahoehoe channels occur by the site 1 and site 2 vents, and related boccas. They are typically more prevalent in the site 2 region, with the higher altitude lavas rapidly developing a more thermally mature character. Bounded by initial, accretionary or overflow levees, pahoehoe channels are typically narrow (<2 m wide at site 2, ~6 m wide at site 1), and relatively thin: the pahoehoe channel in **Section XVIII** is defined by flow drapes that were only 15-30 cm thick. The accretionary levees of **Plate 4.13** and **Figure 4.3** describe a channel that at its bocca was a mere 75 cm deep, thickening only to 1 m deep a few yards downstream.

These ephemeral proximal channels customarily display a zoned structure. No extant channels display a surface composed entirely of pahoehoe; rather, the channel surface consists of a central region of ropy or slabby pahoehoe, bordered by heavily sheared aa clinker margins (**Plates 4.28 & 4.29**). The central, ropy pahoehoe is typically no wider than 50 cm in a channel ~2 m wide. To either side there is an abrupt transition from pahoehoe into variably disaggregated clinker. There is no visible narrowing of the pahoehoe region as one progresses 10 to 15 m from the bocca (**Plate 4.29**), but a notable change in texture. The superproximal ropy pahoehoe facies (**Plate 4.12**) grades into slabby, fractured pahoehoe downstream (**Plate 4.30**), displaying an increased propensity for plastic as opposed to viscous deformation, as the cooled surface layer stiffens and thickens, becoming more thermally mature.

The transition from pahoehoe to aa is perhaps the most debated topic in the study of 'long lava flows'. A brief introduction to the arguments put forth can be found in Chapter 1. It shall suffice

Plate 4.29 Another view of the channel section described in **Plate 4.28**, looking upstream. The central region of pahoehoe is no wider than 50 cm at its greatest extent, and grades from a ropy facies into slabby, fractured pahoehoe downstream. The change to disaggregated aa clinker at the pahoehoe margins is abrupt.

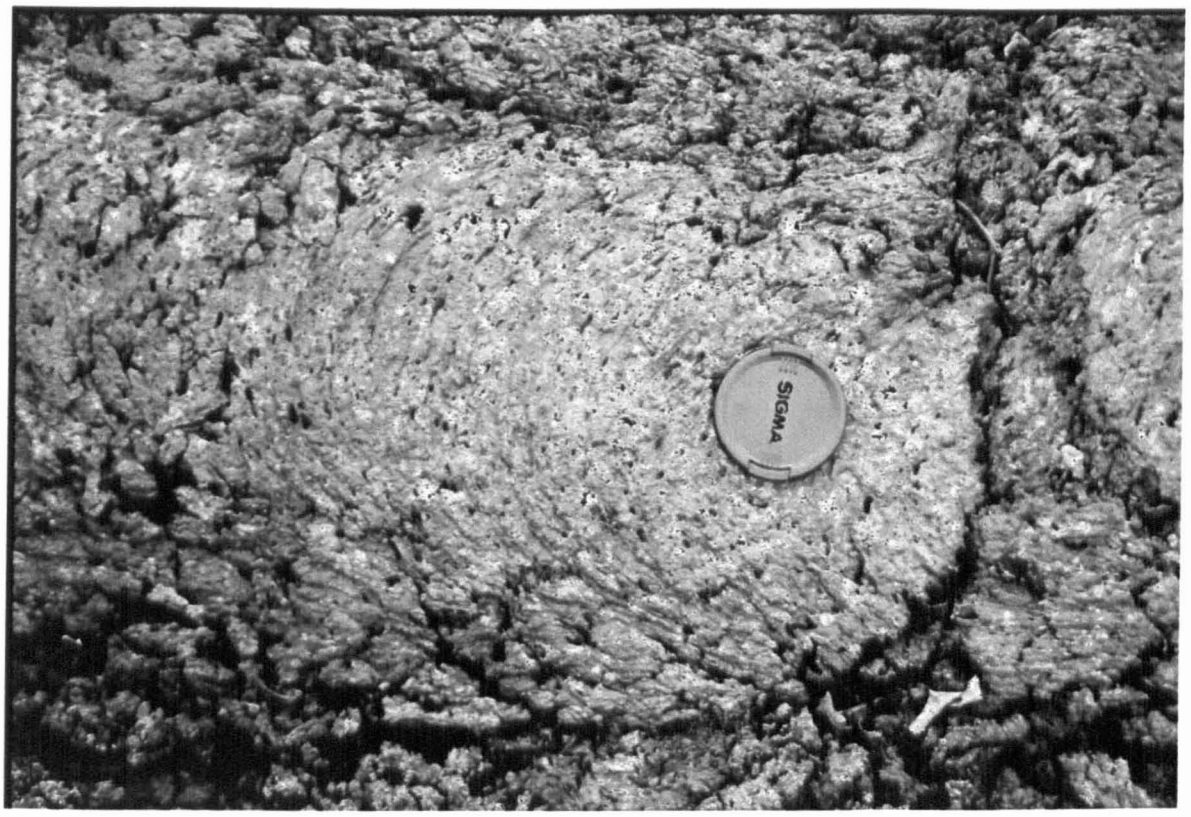

Plate 4.30 Section of slabby, fractured pahoehoe, downstream of the ropy pahoehoe facies depicted in **Plate 4.12**.

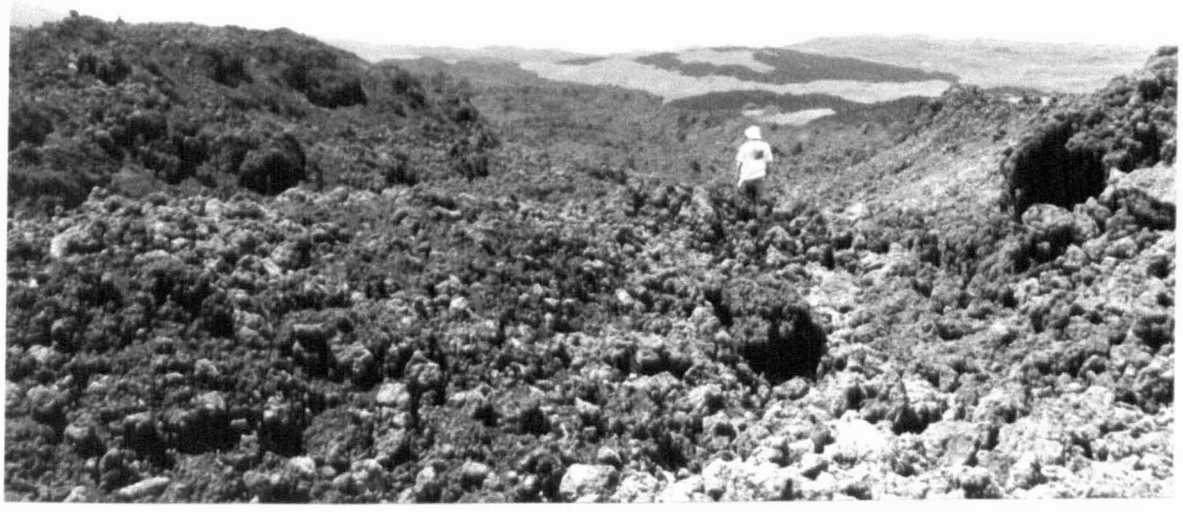

Plate 4.31 Aa channel, from a Site 1 flow. Channel widths are typically an order of magnitude greater than in pahoehoe flows. The channel surface is composed of highly irregularly formed, variably spinose, jagged and scoriaceous clinkers of aa, of the order 1 to 50 cm in diameter.

here to state that two factors are necessary to promote aa formation: (i) a significantly crystalline groundmass to provide a yield strength, and (ii) a high enough rate of shear to deform this plastic material (Cashman et al. 1999).

The relative propensities of both these factors are increased towards the channel margins: the rate of shear naturally increases as one moves away from the centreline of the flow channel, whilst the Pe number decreases along the same axis, promoting the effects of cooling relative to the channel centre. The pahoehoe surfaces preserved are typically late-stage, slow effusion rate effusion products. **Figure 4.5** and **Plate 4.27** describe a channel that was formed initially by aa clinker, and was only later reused by less viscous, slowly effused fluid pahoehoe.

The formation of this fractured slabby pahoehoe (also called slabby aa; Macdonald 1953, Peterson and Tilling 1980, Lipman and Banks 1987) marks the process of a lava channel through an intermediary transitional regime and into full aa development. The distance and time taken to develop full aa texture will depend on the factors described above: should the lava possess a crystalline enough groundmass to deform plastically, an increase in shear in the flow channel, perhaps arising from an increase in underlying slope, flow depth or a flow surge, will exacerbate aa formation.

Aa channels

Aa channels display a morphology analogous to the descriptions of scoriaceous and classic clinkery aa (e.g. Macdonald 1953, Lipman and Banks 1987; or 'cauliflower aa' Kilburn 1989). The channel surface comprises a highly irregular form, of variably spinose, jagged, scoriaceous and/or roughly angular lava (**Plate 4.31**). The clasts can be wholly loose and disaggregated, welded or massive and deeply rooted in the flow's interior (Jaggar 1930). Typically, clinkers are a couple of centimetres to half a metre in dimension, and overlie a more massive lava interior (as seen by Macdonald 1945). Aa channels are typically accompanied by accretionary or rubble levees, formed by welded or mechanically brecciated and reworked clinker.

These channels are wider than pahoehoe channels, forming flows 20+ m wide, and feature a more dispersed patterns of flow emplacement. Whereas pahoehoe is usually focused down a single, clearly defined channel, distal aa channels commonly possess a fairly hummocky appearance, indicating a slightly more heterogeneous mode of emplacement, possibly encapsulating the shear lenses described by Lipman and Banks (1987).

Blocky aa channels

In terms of megascale channel morphology, there is little to differentiate developed aa flow channels from the thermally mature blocky aa flows of more distal regions. These latter flows are

Plate 4.32 View of a large blocky lava channel bordered by rubble levees, at the Bakingili lava fronts, looking upstream (NNE). The channels in this region are typically 10 to 100 m wide, forming a broad flow field half a kilometre across.

Plate 4.33 Small upwelling of thermally immature clinker among distal blocky flows near Bakingili. This feature, running parallel to the flow direction, is depicted in detail in **Plates 4.39** to **4.41**.

Plate 4.34 Upthrown slabs or spinacles of welded rubble in the central region of a blocky channel, of the distal Site 2 flows by Bakingili. These examples reach a height of 4 m.

Plate 4.35 Further examples of rafts of welded flow breccia, thrust out of blocky channels near Bakingili.

especially well developed in the Bakingili flow front, with a series of interdigitating flow lobes describing a flow field ~500 m wide at its greatest lateral extent. The blocky aa flows described in **Sections I-IV** display channel morphologies broadly similar to those of clinkery aa, with dispersed flow features in broad channels bordered by rubble levees (**Plate 4.32**).

In contrast to the aa flows, the surface is near uniformly unconsolidated, consisting of angular to rounded blocks of massive lava and welded breccia (0.1-2 m), with rarer rounded balls and patches, breakouts and upwellings of clinker (**Plate 4.33**; see 4.3.3.4). Occasional spinacles and rafts of welded breccia up to 4 m high thrust out of the surface rubble (**Plates 4.34 & 4.35**). Consolidated, massive lava is rarely seen, in that it is usually covered by a dense carpet of rubble.

The transition from clinkery aa channel surfaces to blocky aa is gradual, and in even the most distal of the 1999 flows not wholly or uniformly developed. Clinker surfaces form as hot visco-plastic lava wells up between fractures or existing aa cauliflowers, or forms from consolidating clots in more incandescent fluid flows, and is then milled and brecciated (e.g. Macdonald 1953, Peterson and Tilling 1980, Lipman and Banks 1987, Kilburn 1989). As aa surfaces develop and thermally mature, the fluid underlying them cools to the extent that it becomes a brittle solid; deformation subsequently brings heavy fracturing of the cooled surface region, and the formation of blocks.

4.3.3.2 Levee-channel interface geometry in blocky aa flows

During the field investigations that produced **Sections I** to **XVIII**, we noted that aa channels could be readily categorised according to their morphology. From these field observations we describe six broad geometries, related to the nature the levee-channel intersection:

(i) is the channel 'continual' with the levee top, or 'offset', meeting the inner levee wall some distance beneath the top?

(ii) is the channel shape convex upwards, concave downwards or flat?

Combining elements of (i) and (ii) produces six distinct geometries, each of which is observed at least once in the 1999 flow sections. These simple descriptions do not always perfectly classify the morphologies of aa channels; there are occasions where channel shape changes away from the margin, and more detailed descriptions are required. Yet this terminology creates a simple, qualitative handle that can be applied to the field study of aa channels and, as will be seen, predicts the later emplacement patterns of lava channels to a fair degree of accuracy. While stranded levee sequences can illuminate the overall history of a flow-unit's evolution, these levee-channel interface geometries can reveal specific information on the most recent channel flow processes.

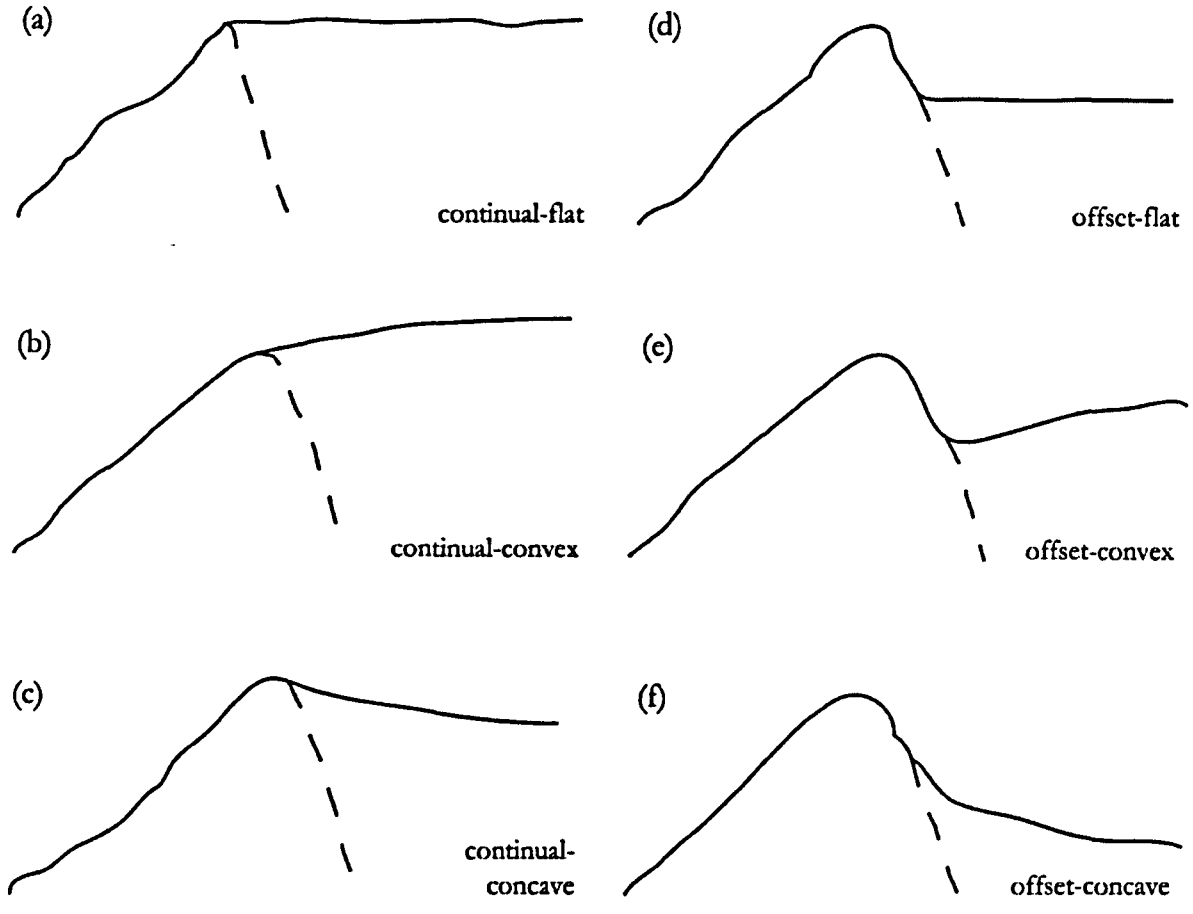

Figure 4.7 Levee-channel interface geometries. Broadly speaking, these six archetypes indicate relative modes of channel evolution on flow stagnation. *Continual* interfaces (a, b, c) indicate a channel that was in relative mechanic equilibrium with its bounding levees, and in the case of (a) and (b) a locally 'cooling-limited' (Kilburn et al. 1995) development. *Offset* interfaces (d, e, f) suggest a significant period of draining following the last episode of levee building, and generally a 'volume-limited' mode of emplacement. *Convex* geometries (b, e) arise from the bulking up of the central, more fluid region of the flow as a function of a surge or cooling-induced backpressure from the sluggish flow front. *Concave* geometries (c, f) result from a gradual draining of the channel, more clearly evidenced in the hotter, fluid channel centre than the stiffer, more viscous channel margin. *Flat* geometries (a, d) naturally accompany initial levee building, and are on the whole less indicative of distinctive flow processes.

Continual geometries

Continual geometries form when the channel margin is level with its bounding levee. The levee can usually be considered *active* (see 4.3.2; Guest et al. 1987) at the time that the flow stagnates: the motion of channel fill adjacent to the levee top is probably sufficient to cause lateral avalanching and brecciation of the levee material. Continual interfaces therefore infer a channel whose most recent phase of development was contemporaneous with the activity of its bounding levees. It is possible that the reinflation of a flow channel could cause an existing, drained profile to readjust exactly to the level of its last bounding levees, but there is no recorded evidence of such events in the 1999 flows, and this seems unlikely to be a general explanation.

Lipman and Banks (1987) recognised both convex upward and flat geometries in aa sections on Hawaii; the former in slower flows, the latter in rapidly advancing flows. These are valuable field observations, but do bear further discussion, and we suggest that the prevalence of convex vs. flat profiles is not defined only by velocity, but is a function of the interplay between lava influx and backpressures supplied through channel constriction and rheological stiffening.

We theorise that a ***continual-flat*** geometry infers a period of steady flow prior to the flow's stagnation, contemporaneous with the reworking and activity of the levees. The flow channel has seen a recent episode of inflation and building in the construction of the levees, but displays no strong draining or inflation structures; however a slight period of deflation may have occurred, if the channel originally possessed a broadly convex profile.

A ***continual-convex*** interface may arise when a continual-flat channel experiences a surge or backpressure that raises its central channel height; the channel bounding levees typically remain active. With an increase in channel transport efficiency and drainage, continual interfaces may develop ***continual-concave*** geometries. These suggest a period of well-drained flow near the time of stagnation, with a decreased activity near the bounding levees, which experience less pressure and shear from the channel.

Offset geometries

Offset interfaces form when a channel has drained, exposing its bounding levees' inner walls. The channel surface is therefore younger than the levee; in the absence of significant contact with the channel boundary the levee can probably be classed as *inactive* (Guest et al. 1987). Offset geometries infer that the channel has experienced a recent decrease in flow rate, and are usually indicators of the flows being of the volume-limited category (Kilburn et al. 1995). This decrease would have been accommodated well before the time of flow cessation; a channel readjusting to a decrease in flux at the time of its parent unit's stagnation might instead describe a *continual-concave* geometry.

An *offset-flat* geometry infers a relatively free moving channel in equilibrium with its surroundings, and with a constant flux close to the time of stagnation; in distal blocky aa facies it would be rare to find instantaneous channel fall or rise.

An *offset-convex* interface forms in reply to a deepening of the flow, as a function of a flow surge or a cooling induced backpressure. If this inflation is followed by a subsequent draining event, one will see the formation of a new set of interior levees.

Finally, an *offset-concave* geometry indicates a period of draining near contemporaneous to the flow's stagnation, though following previous significant draining episodes. It could indicate a drainage event distinct from previous level changes, or simply be the expression of a longer, continuous draining trend (i.e. a further developed *continual-concave* interface).

The preferential cooling of the margins of flow channels, and commensurate rheological stiffening, results in channel margins that accommodate more slowly to changes in pressure. This provides a sense of timing that can be applied to infer recent flow history. A *continual-concave* geometry might form when a channel gradually drains, with the sluggish margins reacting slowly to the situation compared to the more fluid channel core. An offset interface instead suggests that drainage occurred rapidly and in a relatively newly formed hot channel. Convex geometries typically occur when the local increase in flow height is accommodated in the less viscous, more readily deformable centre, as opposed to the stiff margins, and the greater centreline velocities exacerbate surge and backpressure effects.

4.3.3.3 Implications for the distal Bakingili flows of Mount Cameroon

We now present a discussion of how these interface geometries are distributed amongst the distal, Bakingili flows from site 2 (**Sections I** to **IV**), and the implications they infer. These flow units display volume-limited, offset levee-channel interfaces. The easternmost channel of **Section IV** displays a sequence of stranded levees, bracketing an *offset-flat* channel whose surface lies ~7 m beneath the last high-stand line, and 18 m beneath that indicated by the tops of exterior levees. Against these features the westernmost *continual-convex* channel of the same section seems incongruous; while its eastern neighbour is highly drained, this unit was active and full at the time of stagnation.

Section IV was recorded a few metres north of where the main flow wraps around a small island of vegetation. The western *continual-convex* channel could have formed to accommodate the backpressure provided by the inward curve of the flow. Lava supply to this bulked up channel may have deteriorated as it was preferentially supplied to the free draining channel to the east, leaving the sluggish westernmost channel to cool into its present habit.

The next profile down-flow, **Section III**, displays a largely dichotomous nature. The two central channels can be traced to the flow systems of **Section IV**. The eastern channel of the central pair displays *offset-flat* to *offset-convex* geometries within a sequence of stranded levees, and several pressure ridges. This suggests a period of volume-limited flow and general draining to the flow-front, followed by a late period of backpressure-induced compression that develops from frontal cooling and a nearby break-in-slope, and affects the channel dregs. The western channel of the central pair displays a general drop in levee level and a slight convexity to the channel

The easternmost, *continual-convex* lobe of **Section III** represents a breakout that has stagnated through cooling and stiffening rather than a draining of lava. The westernmost channel represents a similar archetype, though one that is far better developed and indicative of the formation processes. The Bakingili plan map shows this to be an offshoot channel that developed just north of **Section IV** (and was not profiled there) and flowed alongside the main flow for ~400 m. The depth of this channel is considerable (~22 m at the western margin), and it is probable that this unit was highly cooling-limited. A cessation of flux to this smaller, sluggish channel would occur as lava was preferentially directed to the easily drained main flow, producing the *continual-flat* geometry.

Section II is more than half a kilometre down-flow of **Section III**. Earlier flow units formed as the lava splayed out past the break in slope, and possess continual interfaces with relatively flat flow habits. These flows represent early toes and dispersed-flow lobes of the developing distal flow and hence display contemporaneous levee-channel activity. In contrast, the westernmost channel is huge (~185 m between exterior levees), and displays prominent volume-limited morphologies. Yet whilst the western channel margin possesses a *continual-concave* interface, the eastern portion of the westernmost channel displays an *offset-convex* geometry. This apparent paradox can be resolved through reference to the heterogeneous and dispersed flow patterns of distal blocky aa channels.

In the westernmost channel of **Section II**, it appears that the main episode of channel drainage occurred at the same time, producing the stranded exterior levees. As the channel responded to the rheological stiffening of the front, it will have experienced a period of inflation (perhaps exacerbated by the explosion of the 13th April, and subsequent surge) and the building of new levees. Natural drainage reveals these levees, but a concentration of more fluid material towards the flow-field centre led to an offset response in the eastern portion, compared to a more sluggish, continual-concave type accommodation along the western margin. The convexity of the eastern channel region would naturally result from this fluid area preferentially accommodating flow-front induced backpressures.

The most distal profile, **Section I**, shows six thermally mature channels with a variety of geometries. Lobes and channels interdigitate. As the flow expanded little past this section (<100 to

~400m), prominent volume-limited morphologies and offset geometries are limited. The westernmost channel displays a slight *offset-convex* interface near to the flow front, indicating a relaxation as lava influx ceased, and the channel consequently responded. This draining would supply the little forward movement the channel further experienced; relative inconsistencies in the direction of lava movement, or a slight influx of lava following the post-explosion surge or upflow reorganization, could have accounted for the localised convexity.

Elsewhere channels display variable profiles, with slight to absent amounts of offset, and gently convex through concave profiles that are masked by the noise of the blocky nature of the lava. Early offshoot lobes show *continual-convex* geometries typical of their *cooling-limited* emplacement. Although *younger in formation* than their adjacent channels, they are distinctly *older in the cessation of their activity*. This factor must be acknowledged when dating flow lobes. Activity in a given channel's levee may bury another flow unit, superficially indicating a younger age; yet this just points to a more recent period of levee activity. The adjoining flow could have been emplaced at later date than the burying flow, yet experienced an earlier cessation in levee activity.

4.3.3.4 Pressure-formed features and structures

Lava flows develop compressive stresses during emplacement. A freestanding, isothermal flow on a slope experiences length-shortening phenomena naturally, as a function of smaller speeds at the front than in the flow behind (as discussed in Chapter 3; see also Lister 1992). In a homogenous isoviscous fluid, stresses are accommodated through simple viscous diffusion, and no visible structures emerge. In lava flows, these compressive stresses are exacerbated by the process of cooling. Older, distal parcels of lava are considerably more viscous and plastic than freshly erupted hot magma from vents. This frontal rheological stiffening and subsequent slowing supplies a backpressure that adds to the stress field. Similarly, as lavas are erupted onto complex topographies, breaks in slope and ponding can also result in a sudden decrease in the forward speed, and a compressive regime.

In a cooled lava flow, one rapidly develops a distinct rheological boundary layer, which can possess a strongly enhanced viscosity, a plasticity or a wholly solid character. The bimodal rheology of the flow forces a different response to the compressive stresses than a homogenous fluid might otherwise experience. Structures as distinct in magnitude as cm-sized ropes and m-sized blocky ridges actually form from very similar stress regimes, with dimensional variance a function of differing rheologies. This section presents an overview of the compressive structures formed in the Mount Cameroon lavas. Whilst habit, dimension and frequency are discussed, an in depth analysis of the dynamics suggested is presented in Chapter 5.

Pahoehoe ropes

Ropy pahoehoe is best exhibited in the ephemeral bocca flow extruded near the site 2 vents (pictured previously in **Plates 4.12, 4.13, 4.25** and **4.26**). **Plate 4.12** displays a parcel of pahoehoe ropes that curve convexly in the flow direction. 20 well-formed and easily distinguished ropes are present in a 2 m section, implying a mean wavelength of 10 cm. The ropes typically display amplitudes of 5 cm on average (to a maximum of 10 cm). A few metres down the channel, and over a small break in slope, the ropy texture disappears, as ropes coalesce and weld.

Pahoehoe ropes are the most proximal compressive features seen on the 1999 lavas. As early pahoehoe generates a cooled surface skin, compressive stresses are accommodated ductilely in the formation of shallow amplitude, small wavelength folds. The mechanism for the deformation of this thin viscous boundary layer has been suggested by Fink and Fletcher (1978), with further elaborations on the geological applications of the theory presented by Fink (1980) and Gregg et al. (1998). It shall suffice here to say that the compressive stress encourages the growth of perturbations in the flow surface and buckles the viscous skin. An analysis of fold-forming dynamics is discussed in Chapter 5.

Pressure ridges

Pressure ridges are exposed as rubbly linear hummocks, contiguous over distances ranging from a few to several tens of metres, displaying an orientation which varies from parallel to perpendicular to the flow direction. They are commonly observed following a break in slope. A change in the angle of slope underlying a site 1 (Cone III) flow, from 17° to 6°, produced three strong, transverse pressure ridges (**Plate 4.36**). The ridges possess amplitudes of 0.6, 1.3 and 1.5 m, and an average wavelength of 8.2 m. The arms of the ridges slope at a relatively gentle angle of ~24°. A similar set of structures can be found in a more distal site 1 lava field, possessing several flow units. The approach to the locality is shown in **Plate 4.37**, and transverse, curved ridges are clearly evident in two of the flows, beyond an evident break in slope. A profile across four of these ridges gave an average amplitude of 0.83m and a mean wavelength of 6.7 m.

Pressure ridges are also observed in the distal site 2 flow front near Bakingili. The eastern channel of the central flow pair (see also 4.3.3.2 for a description) of **Section III** displays primitive blocky surfaced pressure ridges 5 to 7 m in wavelength, commonly baulked up against adjacent channels' levees, parallel to the flow direction. These are typical of pressure ridges marginalizing and forming accreted levees (**Fig. 4.8**; 4.3.2.4; Lipman and Banks 1987). The main channel of **Section II** also contains pressure ridge structures, picked out on **Plate 4.38**. These structures possess 10-12 m wavelengths; considerably greater than those of **Section III**.

Plate 4.36 Pressure ridges in a Site 1 transitional blocky-aa channel. The terrain makes them hard to define, but George is leaning against one, and the approximate positions of three ridge crests have been highlighted. These ridges are part of a series of break-in-slope derived pressure features displayed in **Plate 4.37**. The average structure wavelength was 8.2 m. Photograph looks upstream.

Plate 4.37 A series of Site 1 lava channels form clear compression features (highlighted by the distribution of shadows) following a break in slope, from 17° to 6°. Photograph looks downstream.

Plate 4.38 Pressure ridges formed in the distal Site 2 blocky lavas. Again, the ridges are far easier to distinguish in the field. Dr. Emmanuel Suh stands before the crest one ridge, and other ridge crests have been marked. Typical wavelengths in this locality were 10 to 12 m.

Plate 4.39 Ridge-like squeeze-up of clinkery aa emplaced between two adjacent lobes of blocky lava, in the Site 2 distal flow region, near Bakingili. Irregular, spinose clinker overlies a massive avesicular interior.

As ropy surface textures are produced in fluid pahoehoe undergoing compressive stresses, pressure ridges are the analogous product of more thermally mature lava surfaces. Blocky pressure ridges can form through the simple accommodation of the blocky veneer to local compressive or extensive mechanics, but many are produced by a more pervasive flow deformation. Compression is accommodated by brittle failure and slip, or visco-plastic buckling (or a combination of the two) in the sub-blocky, massive lava. Though thermally mature flows naturally buckle, break and shear as a function of flow development, a larger and more sudden imposition of a compressive stress typically results in pressure ridge development.

Breaks in slope are common examples of such situations. Beyond a break in slope, the forward momentum flux (heavily governed by the angle of the incline a lava is flowing on; see Chapter 3, and also e.g. Fink and Fletcher 1978, Lister 1992) is diminished, resulting in a strong compressive regime after the break. Furthermore, this can lead to a backpressure that affects lava prior to the break, and induces pressure ridge formation there: **Section III** depicts a dynamic regime before a break in slope, with considerable compression, while **Section II** profiles a splayed out flow-field in considerable advance of the break, where compression is supplied through flow-front stiffening and stagnation. One may also expect the **Section II** lavas to be more thermally mature, resulting in a thicker, stronger rheological boundary layer, which promotes an increase in fold wavelength (Fink and Fletcher 1978).

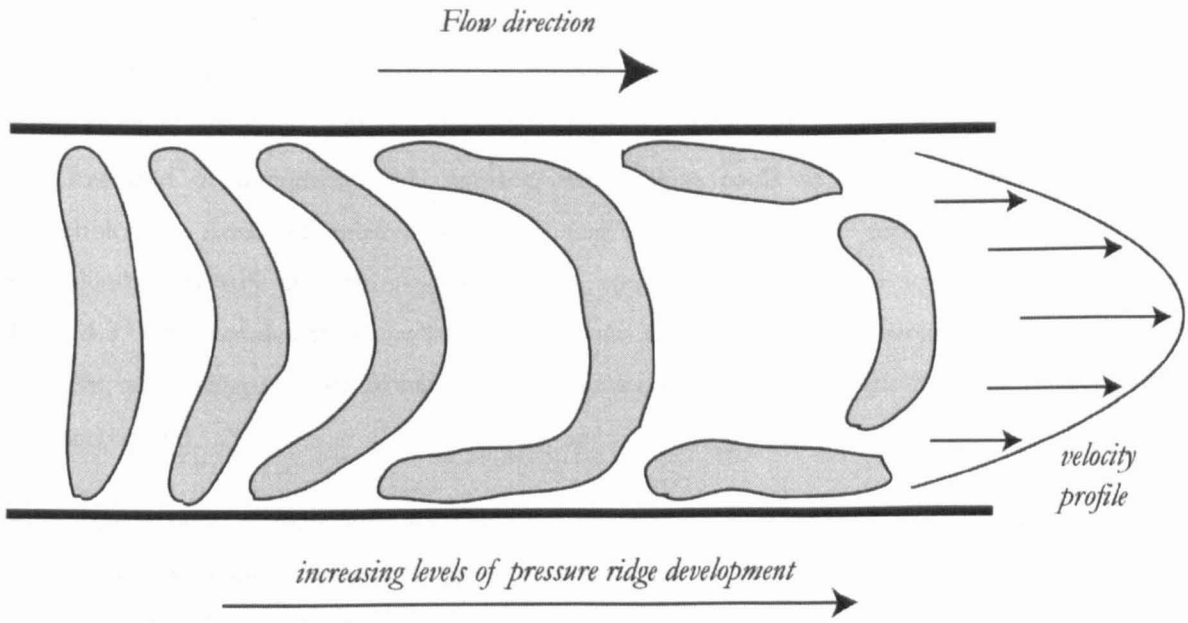

Figure 4.8 The time-staged evolution of pressure ridges (positive relief marked grey) in a levee-bordered channel. Ultimately, the extreme marginal rate of shear causes lateral portions to detach, and bulk against the channel margin as accreted levees (Lipman and Banks 1987). A simple Newtonian velocity profile is indicated for illumination, although central areas will perhaps experience visco-plastic 'plug'-flow.

'Squeeze-ups'

Squeeze-up features, consisting of more thermally immature lava pushed through the solid/blocky flow carapace, are commonly observed in the 1999 lava flows, particularly in the blocky aa flows near Bakingili. In **Section I**, a prominent ridge-like lobe of clinker aa ~5 m wide squeezes out between two adjacent lobes of blocky aa (**Plate 4.39**). The ridge's structure is further displayed in **Plate 4.40**. Spinose, vesicular clinker aa overlies a core of solid avesicular lava. The massive lava displays well-developed lineations: near horizontal striations in the direction of flow, and sub-vertical, shallow tensile fractures a few cm-deep. Eruptional visual evidence states that the blocky aa lobes were emplaced first, and the clinker squeezed out of the gap between them as the flow advanced (Dr. Emmanuel Suh, pers. comm.).

Squeeze-ups of thermally immature aa are also observed adjacent to the westernmost channel of **Section IV**. The vesicular spinose clinker forms a 3 m wide ridge of olivine-clinopyroxene-phyric aa distinct from blocky facies of the channel and welded rubble of the levee top. Similar features are found in-between channels and levees in **Sections II** and **III**. One such formation in **Section II** appears to spread beyond the channel margin, burying the blocky channel facies with thermally immature clinker (**Plate 4.41**). Pinnacles (or 'spinacles') and rafts of welded clinker and flow breccia are also thrust above the blocky carapace of distal flows, commonly in the centre of convex channels (see 4.3.3.1, **Figs. 4.34** and **4.35**).

Pressure ridges form as the lava surface accommodates to compressive stresses in the flow; the habit of the pahoehoe or aa surface may change, and perhaps break or fracture, but the surface facies remains consistent. Squeeze-ups occur when the stress regime forces hotter material through the fractured or unconsolidated carapace, which then cools to form less thermally mature morphologies. Areas of relative weakness (e.g. highly brecciated surfaces), or experiencing considerable pressure are natural sites for such structures to form. The squeeze-up displayed in **Plate 4.39** was extruded from the well between two lava lobe toes. Such an area is higher than the adjacent, more sluggish lobe fronts, and experiences a greater hydrostatic pressure from the lava damned behind.

Along the channel margins, high rates of shear produce a brecciated flow surface with mobile lava underneath. Although we have inferred that marginal regions experience exacerbated cooling relative to the higher velocity centre, the crust is rapidly disaggregated, distinct from the poorly sheared, plug-like centre. Lava in these marginal regions lava is more freely able to squeeze through the carapace in response to surges or compression, particularly if shear-derived, viscous heating keeps the lava mobile at depth.

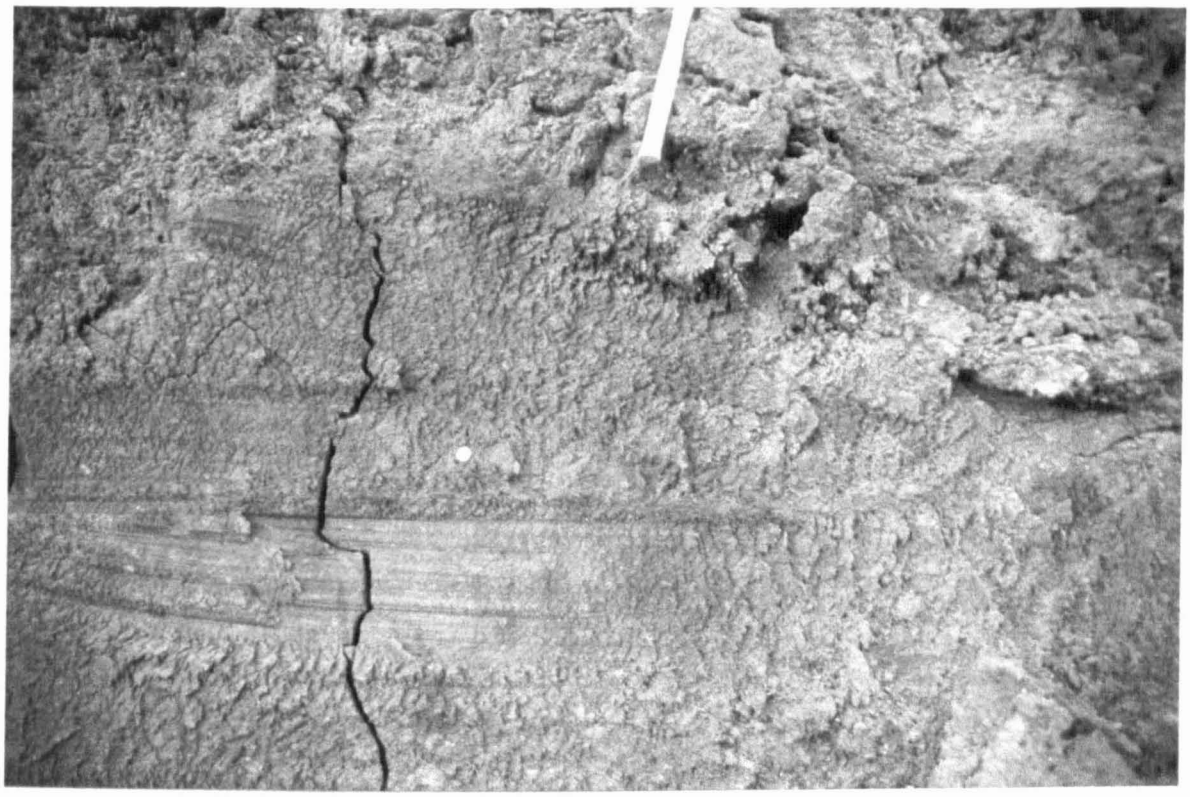

Plate 4.40 Closer view of a thermally immature clinker-topped aa 'squeeze-up' ridge, also displayed in **Plate 4.39**. Massive, poorly vesiculated lava forms the main body of this feature and displays two well-developed lineations: fine near-horizontal striations parallel to the flow direction; and shallow, sub-vertical fractures typically a few cm deep.

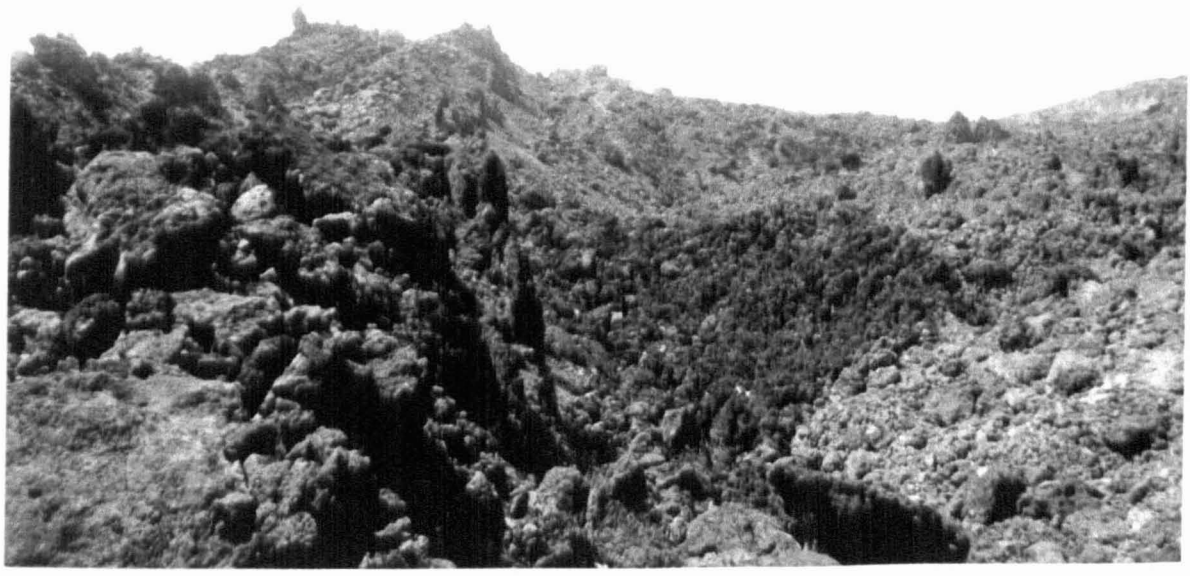

Plate 4.41 Near Bakingili a small region of clinker (marked by the dark material in the centre-right of the photograph) spreads out from the channel and partially buries the local blocky facies.

Pinnacles, spinacles or rafts are inferred to form from two processes. The welded rubble facies is analogous to the lower facies of inner levee walls, and many rafts appear to have originated as fragments of levee that have broken away as a function of post-drainage instability or channel pressure. Some bear similarity to the 'lava boats' described by Lipman and Banks (1987).

Some rafts and pinnacles appear more rooted in the underlying lava, though the rubbly surface precludes exact qualification of their depth and contiguity. Such welded clinker forms may instead arise from the fracture, buckling and up-thrust of the solid or semi-solid material that underlies the blocky veneer. These forms are distinct from the tumuli and 'lava rises' described by Walker (1991), but are inferred to form in not too dissimilar circumstances. Their prominence in the centres of convex channels, which have experienced local inflation and backpressure, indicates a mode of formation involving inflated crust rising and buckling as a function of compression, followed by rotation of the rafts or pinnacles to new geometries.

4.3.4 Flow fronts

Lava flow fronts are dominantly composed of thermally mature clinker or blocky aa. While pahoehoe toes and the generation of toothpaste lava are evidenced in the super-proximal site 2 regions, most flows effuse far and long enough to generate aa morphologies at the flow front. These flow-front facies are near indistinguishable from the outerslope rubble levee facies discussed earlier (**Plate 4.42**; 4.2.3.3). More thermally immature aa flows possess fronts of poorly sorted (5-100 cm), occasionally welded clinker, with occasional large cauliflowers (Kilburn 1989) and finer abraded and brecciated clasts (**Plate 4.43**). These less developed aa flows are often shallow, with heights of ~1.7 m.

More thermally mature aa flows have develop an increasingly blocky nature. Breakaway lobes from one of the main site 1 (Cone III) aa flows form short lava flows that possess typical flow-front textures. Two flows possessed rubbly fronts of intermediate height. One flow toe consists of aa clinker and welded breccia, sloping at 33° on a 8° slope, with an overall height of ~3.2 m (**Plate 4.44**). The other toe features a far greater amount of welded breccia, which raises the angle of rest to 39° (on a 12° slope) and supports a flow height of ~4 m.

The most distal blocky aa flows develop highly irregular, poorly sorted blocky fronts, like those at Bakingili (**Plate 4.45**), with a significant level of fine sand and dust, resulting from continual aggradation. Large rafts and spines of welded breccia and massive lava are common, thrusting out of the rest talus and locally increasing the slope of the front, and supporting frontal heights of between 12 and 20m. Syn-eruption video evidence demonstrates that the Bakingili flow-front advanced through creeping flow and repeated avalanching.

Plate 4.42 A typical, relatively thermally mature blocky or transitional blocky-aa flow front, photographed on a Site 1 flow. The morphology of the lava toe is essentially indistinguishable to the outerslope rubble levee facies displayed in **Plates 4.14** and **4.15**.

Plate 4.43 Site 1 aa flow front, consisting of a poorly sorted, partially disaggregated mix of clinkers welded clinkers, large aa 'cauliflowers' (Kilburn 1990) and finer brecciated material. The height of this small, thermally immature flow front was 1.7 m.

Plate 4.44 Aa flow, more thermally mature than that displayed in **Plate 4.43**. This small breakout lobe from a blocky lava flow has developed a greater proportion of welded, rubbly material than superproximal aa. The height and angle of repose of the flow front was found to increase with the amount of welded rubble visible in the flow makeup.

Plate 4.45 Flow front of a thermally mature Bakingili blocky flow that had overridden the Limbe-Idenau highway, typically composed of large rafts of welded rubble and a highly abraded fine talus.

4.4 Summary of field investigations

In addition to providing an overview of the geological characteristics of the 1999 eruption of Mount Cameroon, and the overall development of lava emplacement phenomena, Chapter 4 has presented detailed field analyses of the basic lava flows produced by the volcanic activity. Lava flows generated by both site 1 and site 2 1999 activity were systematically mapped and profiled, producing the sections appended to this thesis. This research constitutes the first major appreciation of the character and dynamics of the 1999 lava flows, and analyses their genesis, development and habit in light of the large *corpus* of literature on basaltic flow phenomena. Such literature, largely formed from investigations of flows at Hawaii or Etna, is pertinent, for Mount Cameroon exhibits many broadly similar eruption characteristics. The mega-, macro- and micro-scale morphologies of the 1999 lava flows display the suite of basic flow-types. The concept of *thermal maturity*, especially developed by Naranjo et al. (1992) is used to great extent in categorising and understanding Mount Cameroon flow phenomena, from the proximal, thermally immature pahoehoe with early-stage levee formation, through the development of clinker aa, to the ultimate development of thermally mature, blocky products in the distal flow regions.

In addition to using the extant literature to inform analyses of Mount Cameroon, the 1999 flows offer many opportunities to further define flow phenomena, or offer examples distinct to basaltic flow 'archetypes' that allow the scientist to expand upon the literature with Cameroonian examples. This is particularly true in the case of ubiquitous features, such as levees and lava channels, which are commonly described yet relatively little understood. Abundant levees on Mount Cameroon allowed dedicated, qualitative analyses of levee formation for long lava flows—particularly in the case of distal, rubbly levees—to be formulated, producing analyses that expand upon the work of Sparks et al. (1976) and Naranjo et al. (1992) to better describe levee processes. Levees from the 1999 flows are categorised into five types: *initial*, *accretionary*, *rubble*, *accreted* and *overflow*.

Similarly, transects made of the 1999 Mount Cameroon flows show the benefits of careful field investigations of large-scale lava morphologies. These support a classification of levee-channel interface geometry, and provide suggestions as to local and global flow dynamics at the time of stagnation. *Concave* or *convex* channels can indicate local draining or retardation, while an *offset* or *continual* interface between channels and inner levee walls can illustrate such processes in the history of the flow. Both geometrical considerations can help define flows within the context of cooling- or volume-limited flow arguments, and are used in conjunction with recorded flow rates to better understand the interaction between effusion rate and flow development in the 1999 Mount Cameroon eruption.

Chapter 5: Analysis of field, historical and experimental data, and conclusions

5.1 Introduction

The previous three chapters have sought to investigate in greater detail the processes relevant to lava emplacement dynamics. Chapter 4 presents an historically-founded analysis of earlier periods of volcanic activity on Mount Cameroon, and on that level serves also as a stand alone chapter; but elements of its data provide scope for quantitative analysis. Chapters 3 and 4 describe the morphological development of experimental and real flows in great detail, and present thoughts on the physical processes that lead to certain modes and character of emplacement. Elements of the results are discussed in further detail here.

This final chapter provides an analysis of the emplacement data in light of new and previous models, develops new criteria on which such data can be investigated, compares and contrasts the development of real and experimental lava flows, and offers conclusions as to the relative merits of current hypotheses on lava emplacement, in light of the results of this thesis. This chapter focuses on three central elements to the emplacement of lava flows: the propagation of the leading flow front; the creation and development of compressive features within the flow; and the development of a channel bounded by levees, central to so many real lavas. Other experimental results shall be discussed with greater brevity.

5.2 Flow Propagation

Lava flows vary in dimension considerably, extending from over a few tens of metres to several hundred kilometres in length, and forming products that range of from simple single streams to compound flow fields of great expanse. The manner in which a lava flows will depend on its initial chemical and physical character; the mechanics and rate of effusion; its thermal and physical development and history, and the topographical character of the environment into which is emplaced. The propagation of the flow front is the most commonly measured attribute of a flow's dynamics. With reference to theoretical and empirical models flow front advancement might enable estimations of a lava's physical and chemical properties, and it dictates the threat of a flow to the human and natural environment. Both the experimental and Cameroonian flows develop as shallow, slope-borne extrusions, extruded onto moderately gentle inclines (in the areas studied of the order of 20°) with similar Reynolds numbers. The experimental flows have Newtonian rheology

Table 5.1 Typical flow parameters for syrup and lava flows

Parameter	Golden Syrup	Basalt	Rhyolite
Density ρ (kg m^{-3})	1438	2600	2600
Eruption viscosity η_e (Pa s)	60 (20°C)	10 to 10^2 (1100 to 1300 °C)	10^7 to 10^9 (700 to 900°C)
Viscosity at relevant temperature η_r (Pa s)	10^4 (-10°C) 10^6 (-20°C)	10^2 to 10^9	10^{11+}
Thermal diffusivity κ (m^2 s^{-1})	1.2×10^{-7}	0.8×10^{-6}	0.8×10^{-6}
Effusion rate (m^3 s^{-1})	1×10^{-6} to 1×10^{-5}	10-100	1-10
Typical flow velocity u (m s^{-1})	0.001	0.001 to 10	0.001to 1
Typical flow height h (m)	0.02	1 to 30	10 to 100
Typical flow length L (m)	1	10^3 to 10^4+	10^2 to 10^3
Reynolds number ($\rho uh/\eta$)	10^{-4} to 10^{-8}	10^3 to 10^{-8}	10^{-3} to 10^{-9+}
Peclet number (uh/κ)	10^2	10^4 to 10^8	10^5 to 10^8

and the natural flows, while very likely non-Newtonian, can be approximated in terms of an 'apparent' Newtonian viscosity in certain conditions. Both are thus affected by the thermal and physical changes initiated by cooling, developing strong viscosity gradients at their margins. The experimental syrup flows do not crystallise or vitrify, and therefore develop neither a non-Newtonian suspension rheology nor a solid crust. As syrup is a purely viscous fluid, it will (in the absence of surface tension effects) flow indefinitely. The increasing development of a thermal boundary layer may raise the viscosity values wherefore movement is very slow, but the flow will continue to creep. In contrast, real lava will develop a strength in its cooled margins, and will cease to flow when the body forces of a flow unit fail to overcome the retardational stresses provided by a plastic or solid boundary.

Viscosity is a key parameter within formulations of lava dynamics. It is simplest to compare the viscous effects with those of plasticity, and derive scaling arguments as to their relative importance in differing flow regimes, for varying parameters and at different stages in a flow's development (e.g. Blake 1990, Griffiths and Fink 1993). Such models give good first order appraisals of complex systems. However, simple plastic or viscous models differ from real systems in certain respects. In complex multiphase lava systems, with suspended crystals and bubbles, the rheology may be both non-linear and time-dependent. For example once body forces overcome the yield stress crystals

are deformed and have to accommodate to a new static or dynamical equilibrium by complex adjustments between the crystals and surrounding viscous melt.

For this reason the experiments of Chapter 3 seek to illuminate the influence of a temperature-dependent viscosity on lava dynamics, to provide a basic framework for more complex visco-plastic formulations. It was not the scope of this thesis to seek to provide a full numerical solution of a slope-borne flow with coupled dynamic and thermal evolution. Therefore analyses of the influence of temperature-dependent viscosity on the propagation of gravity currents must simplify the system in the interests of tractability. The most common manner in which this is achieved is through the introduction of a 'bulk viscosity'.

As a flow develops a heterogeneous thermal (and thus rheological) profile, one can simplify the issue by assuming the disparate elements conflate to produce one simple fluid. Such a fluid flows with a rheology that averages all physical components: a single parameter can thus describe the effects of cooling. The use of a bulk viscosity in such a manner should be made with due care. It is a gross simplification of a complex system, and allows only leading order formulations of the flow problem. With reference to equation 3.15a, one can see that the downslope extent of a flow at a given time is inversely proportional to the viscosity, as follows

$$x_N \sim \left(\frac{1}{\eta^3}\right)^{\frac{1}{9}} \tag{5.1}$$

wherein x_N is the downslope extent at a given time (t) and η is the fluid viscosity. If one assumes that deviations in the values of x_N (t), as compared to those predicted by the isothermal model of Lister (1992), are a function of a changing viscosity alone, one can cast (eq. 5.1) in two forms:

$$x_{N\,(experimental)} \sim \left(\frac{1}{\eta_B^3}\right)^{\frac{1}{9}} \quad \text{and} \quad x_{N\,(theory)} \sim \left(\frac{1}{\eta_e^3}\right)^{\frac{1}{9}} \tag{5.2a,b}$$

where η_e and η_B are the eruption viscosity of uncooled syrup and an apparent bulk viscosity, respectively. At any given value of t, the *apparent bulk viscosity* can be calculated with reference to how 'underdeveloped' the down slope extent is, i.e.

$$\eta_B \sim \eta_e \left(\frac{x_{N\,(theory)}}{x_{N\,(experimental)}}\right)^3 \tag{5.3}$$

Values of η_B have been calculated for all experimental flows during their evolution, and plotted in **Figures 5.1 to 5.6.** Apparent viscosities calculated in this manner will underestimate the *effective bulk viscosity* at any value of t, as the value of η_B takes into account an average bulk viscosity required to produce the flow's extent over t, and at early times the viscosity will have been much less, and therefore flow propagation proportionally greater. More temporally representative values for the bulk viscosity may be gained from use of the Jeffreys simplified equation for motion in a channel:

$$\eta_j = \frac{\rho g h^2 \sin\theta}{\alpha u} \tag{5.4}$$

where η_j is the effective Jeffreys bulk viscosity, ρ is the fluid density, g the acceleration due to gravity, h the fluid depth, θ the angle of the incline on which the fluid flows, u the fluid velocity and α a constant (3 for broad flows). If one considers two values of x_N at closely spaced values of t, an approximate flow front velocity $u(t)$ can be calculated over these time-steps, and used in (eq. 5.4) to discern η_j. Values of η_j are plotted alongside those of η_B in **Figures 5.1 to 5.6.** Most of the data are observed to approximate to a linear relationship with logarithmic axes, suggesting that they can be described by a power law relationship.

With cooling areas of a syrup flow's surface will cool to the ambient temperature; heat will be lost by convection from this thermal boundary, and lead to the development of a conductive thermal boundary layer in the surface region of the flow. One may expect the thickness of this boundary layer (δ) to develop ~ $(\kappa/t)^{0.5}$, where κ is the thermal diffusivity and t the time. Such a feature was used by Griffiths and Fink (1993) to suggest that the time-dependent growth of δ could be incorporated into dynamical models. By supposing that the thickness of a cooled viscous crust provided the dominant resisting force in a dynamic equilibrium, they derived a scale based on the use of a crust viscosity and thickness. Effectively, from a point source this results in a radial gravity fluid extruded at a constant flux expanding according to

$$\text{radius}(t) \sim \left(\sqrt{\kappa}\frac{\eta_s}{\eta_e}\right)^{-\frac{1}{7}} t^{\frac{1}{2}} \tag{5.5}$$

where η_s is the viscosity of a fluid cooled to the ambient temperature and η_e is the eruption viscosity (Balmforth et al. 2003). This relationship, wherein the flow still spreads according to the square root of time as in the isothermal case, is not reproduced in the flows of Stasiuk (1993)

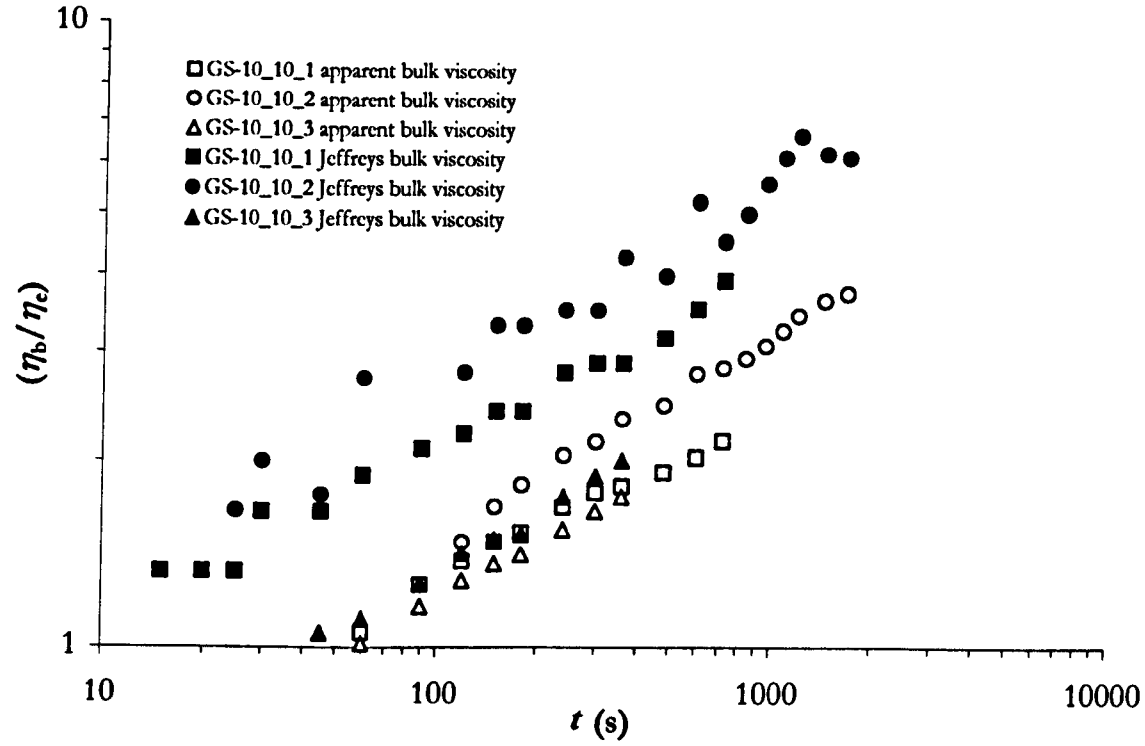

Figure 5.1 Variation of viscosity ratio with flow rate. The flows were extruded onto an incline of 10°, into an ambient temperature of ~-10°C. Flow rates were: GS-10_10_1—4.8 cm^3s^{-1}; GS-10_10_2—1.7 cm^3s^{-1}; GS-10_10_3—10.8 cm^3s^{-1}.

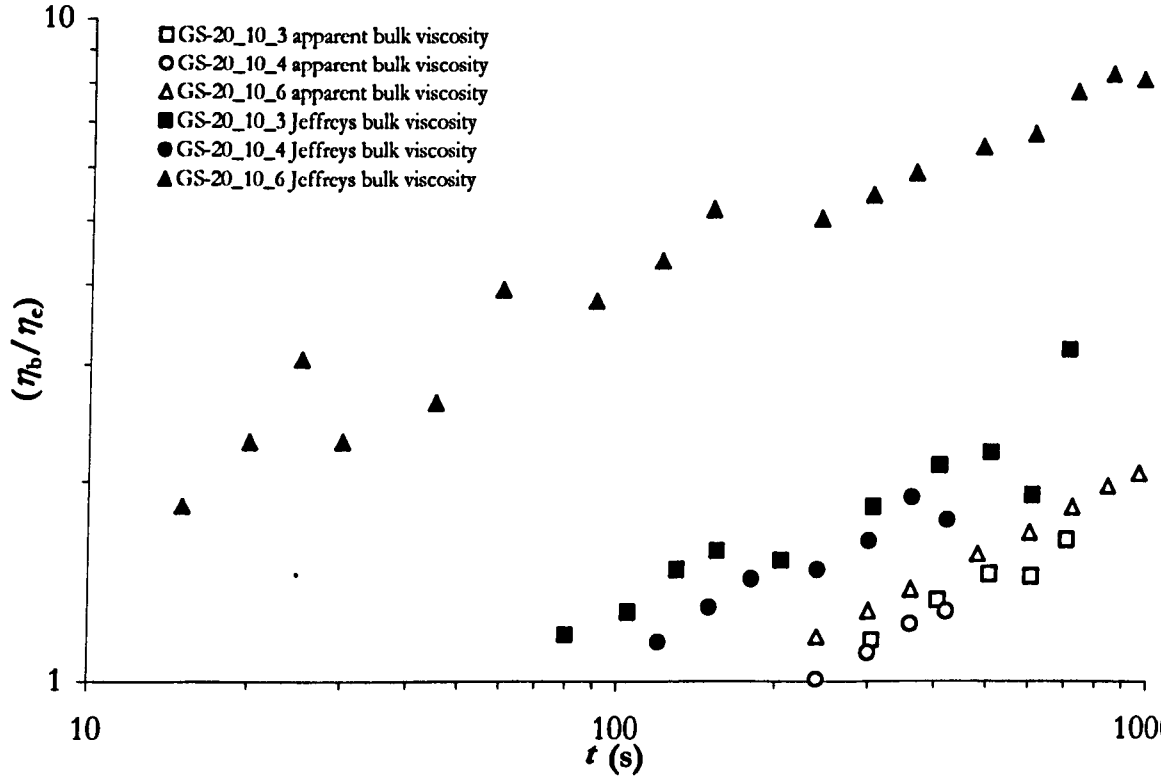

Figure 5.2 Variation of viscosity ratio with flow rate. The flows were extruded onto an incline of 10°, into an ambient temperature of ~-20°C. Flow rates were: GS-20_10_3—4.3 cm^3s^{-1}; GS-20_10_4—8.3 cm^3s^{-1}; GS-20_10_6—1.0 cm^3s^{-1}.

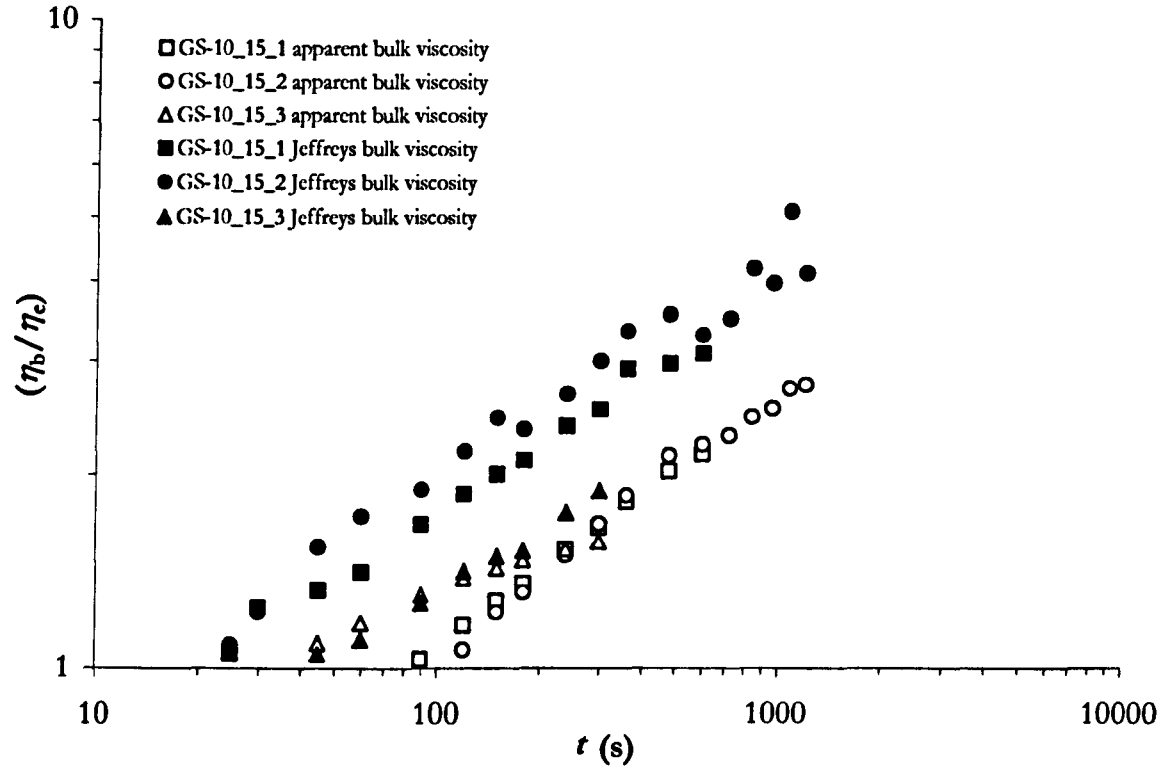

Figure 5.3 Variation of viscosity ratio with flow rate. The flows were extruded onto an incline of 15°, into an ambient temperature of ~-10°C. Flow rates were: GS-10_15_1—4.8 cm^3s^{-1}; GS-10_15_2—1.8 cm^3s^{-1}; GS-10_15_3—8.6 cm^3s^{-1}.

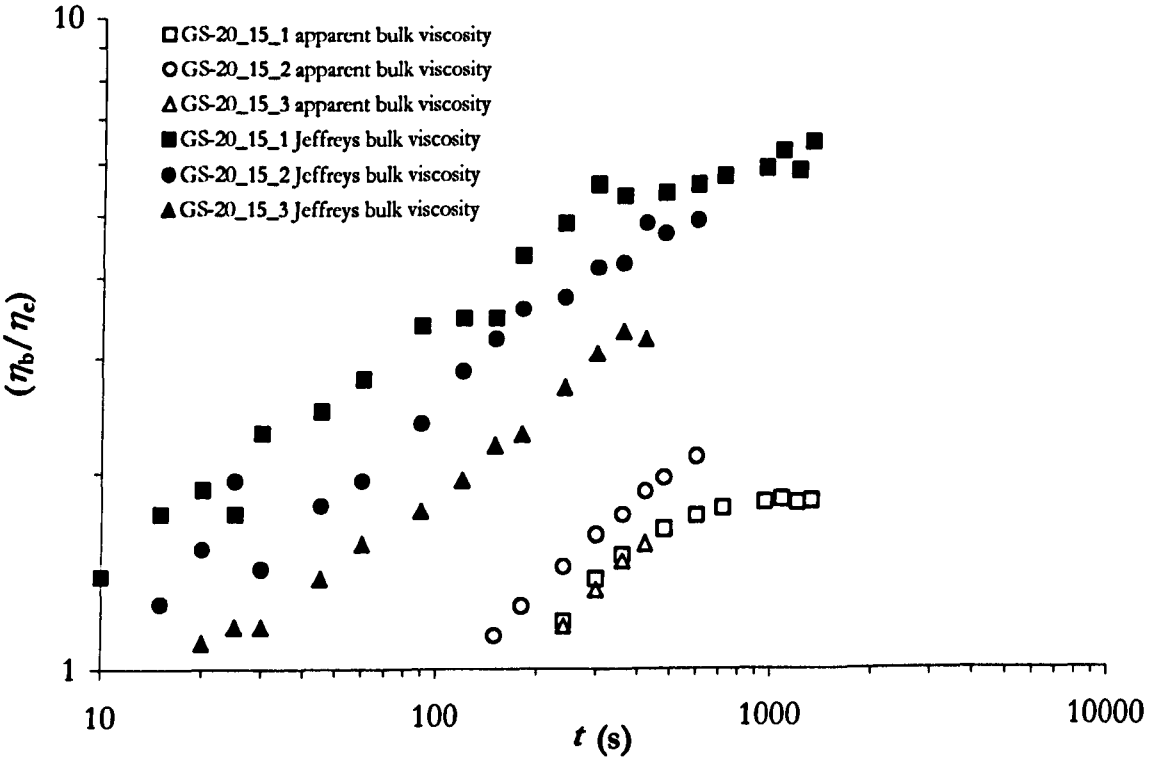

Figure 5.4 Variation of viscosity ratio with flow rate. The flows were extruded onto an incline of 15°, into an ambient temperature of ~-20°C. Flow rates were: GS-20_15_1—1.3 cm^3s^{-1}; GS-20_15_2—4.3 cm^3s^{-1}; GS-20_15_3—7.2 cm^3s^{-1}.

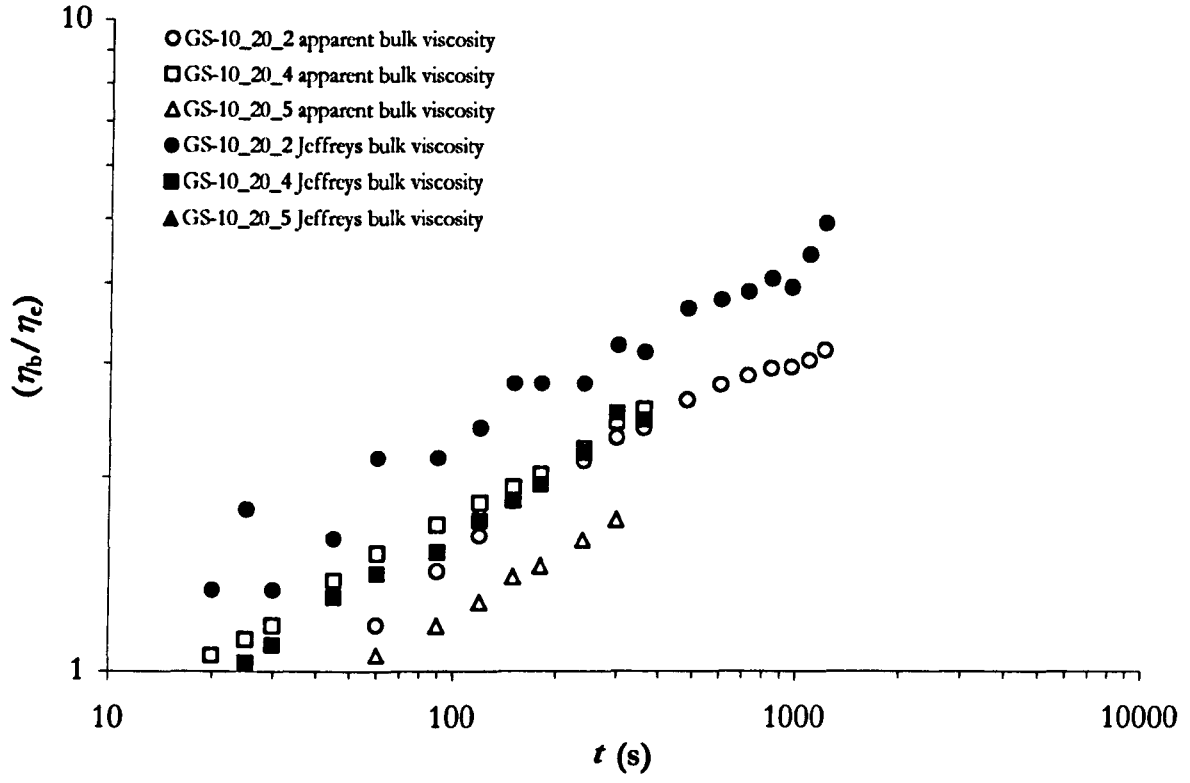

Figure 5.5 Variation of viscosity ratio with flow rate. The flows were extruded onto an incline of 20°, into an ambient temperature of ~-10°C. Flow rates were: GS-10_20_2—1.4 cm^3s^{-1}; GS-10_20_4—6.1 cm^3s^{-1}; GS-10_20_5—8.6 cm^3s^{-1}.

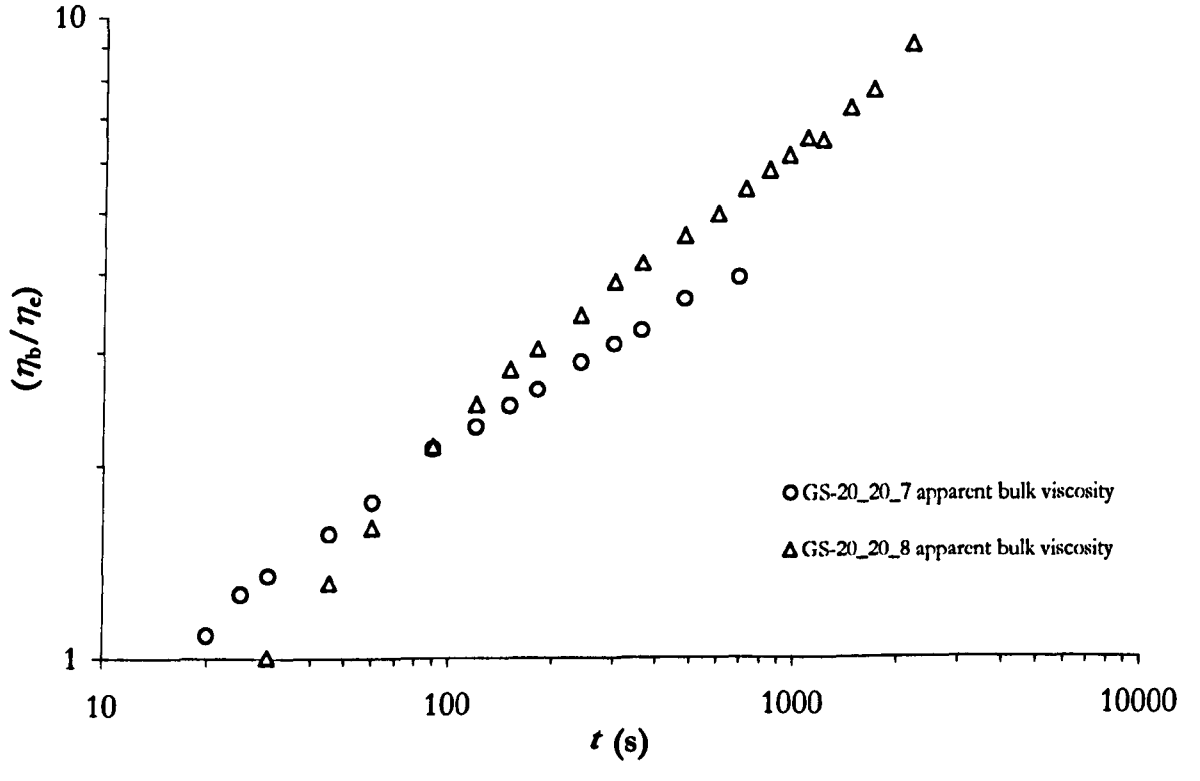

Figure 5.6 Variation of viscosity ratio with flow rate. The flows were extruded onto an incline of 20°, into an ambient temperature of ~-20°C. Flow rates were: GS-20_20_7—3.3 cm^3s^{-1}; GS-10_20_4—6.1 cm^3s^{-1}; GS-20_20_8—0.7 cm^3s^{-1}.

which spread at some exponent of time less than 0.5, and furthermore display evidence of a changing exponent of t as the flows evolve.

Stasiuk et al. (1993) and Lister and Kerr (1994) sought to model the cooled radial flows with a single bulk viscosity. This value was achieved with reference to the data, which were interpreted as showing that the area of a radial flow soon adapted to a linear growth later in their development. This seeming adherence to isothermal theory was used to demonstrate that the flows had developed a stable bulk viscosity. Yet close analysis of Stasiuk et al. (1993) shows that the progression of area with time adheres to a power law, not a linear, trend. The supposed trend is a function of the *relative* linearity of the data over a period investigated. This model is problematic, as Stasiuk et al. (1993) themselves acknowledge that the model does not account for the ultimate progression of the thermal layering as lavas cool, and does not reference early changes, when the viscous skin develops and strongly affects cooling. The bulk viscosity theory they adopt is therefore severely constrained by its applicability to the experimental analogue and subjective analysis of the data.

Another alternative is the formulation of Sakimoto and Zuber (1995), who in modelling cooling radial viscous flows suggested a time-dependent bulk viscosity of the form

$$\eta_b = \eta_e t^{\beta} \tag{5.6}$$

where η_b is the actual bulk viscosity, η_e is the initial eruption viscosity, t is time elapsed and β is a constant. An apparent value of β can therefore be found at any time through

$$\beta = \frac{\log \eta_b - \log \eta_e}{\log t} \tag{5.7}$$

though this considerably underestimates values of η_b and suggests changes of the form $\partial \eta_b / \partial t$ when locally η_b is stable with time. In our experiments, η_b can be approximated by the apparent bulk viscosity η_B, or the effective Jeffreys bulk viscosity η_j. β is considered a constant by Sakimoto and Zuber (1995), and encapsulates all the influences of cooling on the fluid. Therefore β must reference the magnitude of the change in viscosity of a fluid on cooling

$$R = \frac{\eta_s}{\eta_e} \tag{5.8}$$

and the manner in which the system allows the cooling to manifest itself, effectively a comparison between the rate at which heat is lost to the cooled surface by conduction, and the rate at which heat is locally replenished, as a function of advection from the source. This latter feature can be approximated as the Peclet number

$$Pe = \frac{ub}{\kappa} \tag{5.9}$$

wherein u is the flow velocity or a velocity scale, b is a flow height or scale and κ is the thermal diffusivity. Observed values of the parameters u and b are of course variables in the experimental system, and Peclet numbers may thus vary in time and space. For example, one may assign a bulk Peclet number, Pe_B, to describe the overall thermodynamics of a flow, or the concept can also be analysed locally within a given flow, to differentiate between variable magnitudes of cooling e.g. Pe_f (related to the sluggish velocity at the flow front), or Pe_c (for a more mobile, proximal channel region).

Analysis of **Figures 5.1** to **5.6** shows that bulk viscosity increases with time, as predicted by (eq. 5.6). Typically these increases are not large, and of the order 2 to 10 times the magnitude the original values; η_i is usually larger than η_B. The trends of the logarithms of viscosity ratio, when plotted against the logarithm of time of measurement, are for most experiments strikingly linear. Though there are some exceptions, the general stability of this linearity would suggest that during the experimental lifetimes observed, β is a constant, as is considered by Sakimoto and Zuber (1995). Curve-fits are not shown for clarity of presentation, but values of β are obtained from linear regression coefficients calculated for the trends of $\partial\eta_b/\partial t$, and displayed in **Table 5.2.**

Clearly the range of values of β varies according to the value of the ambient temperature, T_a, into which the flows are extruded, which in turn affects R, and ultimately *Pe*. Typically flows cooled at a T_a of –10°C display $\beta(\eta_B)$ of 0.19-0.47, while those extruded into a T_a of –20°C possess $\beta(\eta_B)$ of ~0.32-0.79. Fewer values of η_i were calculated on account of available height profiles, but typically for T_a of –10°C $\beta(\eta_i)$ of 0.25-0.35, while those effused at T_a of –20°C show $\beta(\eta_i)$ of ~0.31-0.43. Thus there is a clear tendency of β to increase with more pronounced cooling. At a specified T_a and angle of slope, some experimental series (i.e same T_a and slope) display tendency to a trend of increasing $\beta(\eta_B)$ with decreasing Q. Certainly the highest values of $\beta(\eta_B)$ are uniformly returned at the very lowest flow rates for each experimental series, with the sole exception of GS-20_10_6, which displays rather low values of β in comparison with other slowly effused flows at T_a ~-20°C.

Table 5.2 Values of β, gained from the coefficients of the regression fits of the data, plotted as the log of the viscosity ratio vs. the log of time. The three values obtained for GS-20_20_8 describe the tri-modal character of the data.

Experiment	η_B		η_j	
	β	R^2	β	R^2
GS-10_10_1 (4.8 $cm^3 s^{-1}$)	0.25	0.991	0.28	0.979
GS-10_10_2 (1.7 $cm^3 s^{-1}$)	0.32	0.994	0.31	0.962
GS-10_10_3 (10.8 $cm^3 s^{-1}$)	0.30	0.998	0.31	0.992
GS-10_15_1 (4.8 $cm^3 s^{-1}$)	0.40	0.999	0.35	0.989
GS-10_15_2 (1.8 $cm^3 s^{-1}$)	0.41	0.987	0.32	0.960
GS-10_15_3 (8.6 $cm^3 s^{-1}$)	0.19	0.981	0.25	0.997
GS-10_20_2 (1.4 $cm^3 s^{-1}$)	0.47	0.999	0.30	0.963
GS-10_20_4 (6.1 $cm^3 s^{-1}$)	0.30	0.997	0.33	0.990
GS-10_20_5 (8.6 $cm^3 s^{-1}$)	0.30	0.997	-	-
GS-20_10_3 (4.3 $cm^3 s^{-1}$)	0.50	0.988	0.36	0.938
GS-20_10_4 (8.6 $cm^3 s^{-1}$)	0.44	0.999	0.38	0.953
GS-20_10_6 (1.0 $cm^3 s^{-1}$)	0.41	0.999	0.31	0.956
GS-20_15_1 (1.4 $cm^3 s^{-1}$)	0.58	0.990	-	-
GS-20_15_2 (4.3 $cm^3 s^{-1}$)	0.46	0.995	0.43	0.981
GS-20_15_3 (7.2 $cm^3 s^{-1}$)	0.53	0.998	0.41	0.992
GS-20_20_1 (1.5 $cm^3 s^{-1}$)	0.46	0.989	-	-
GS-20_20_2 (2.3 $cm^3 s^{-1}$)	0.47	0.995	-	-
GS-20_20_7 (3.3 $cm^3 s^{-1}$)	0.32	0.997	-	-
GS-20_20_8 (0.7 $cm^3 s^{-1}$)	0.69, 0.42, 0.79	0.999,0.997,0.988	-	-

This overall trend is supported by the proposed dependence of β on R and Pe. In a simple system a change in global flow rate will serve to increase u and h at a given point in the flow, and thus increase Pe. Flows extruded at higher flow rates will experience less *relative cooling* than effusions of low Q, all other things being equal. Assuming that all flows adhere to the power-law dependence of viscosity on time, flows exhibiting greater relative cooling and lower Pe will develop higher viscosities more rapidly, and thus display higher values of β. Similarly, experiments that possess higher values of R will develop far more viscous margins than extrusions of lower R, which will raise the value of bulk viscosity, and its rate of increase, β.

Some experiments display slight variations around, or departures from this trend. **Table 5.2** lists three separate values of β (η_B) for the experiment GS-20_20_8. While the data in **Figure 5.6** describe a single linear trend to a moderate degree of accuracy, they are better modelled by three successive regression fits of excellent accuracy. These successive trends—with $\beta \sim 0.69$, 0.42 and 0.79—may be little more than variability in the experimental data (and it should be remembered

that the values in question are calculated from *apparent* bulk viscosities, η_B) but trends away from constant β with increasing time are intimated in a few flows.

GS-10_10_1&2 (**Figure 5.1**), GS-10_15_3 (**Figure 5.3**), GS-10_20_2 (**Figure 5.5**) and especially GS-20_15_1 (**Figure 5.4**) show such behaviour at stages in their evolution, as β is seen to decrease slightly with increasing time. Such departures are usually small, and variably take the form of a very shallow non-linear trend over the times measured, or an adaptation to a different linear trend of β with t. Even with these elements, the trend of $\partial R/\partial t$ is apparently linear at larger values of t. Such is again predicted with reference to the Peclet number.

A decrease in *Pe* (thus favouring cooling via diffusion) would suggest an increase in β. As cooling via the conduction of heat across a small thermal boundary layer is greatest at early times, one could expect that changes to *Pe* imposed as a function of cooling are proportionally larger at the early stages of a flow's evolution. Thus one might expect any variation in $\partial\beta/\partial t$ to be greatest as $t \rightarrow 0$. Naturally *Pe* will vary dependent upon the velocity used in its construction. A real or scaled velocity for the flow front, indicative of cooling in the distal portion of the flow, will decrease with respect to time, as a function of natural flow dynamics and frontal stiffening. A velocity calculated for the proximal warm channel will be approximately constant, as changes to centreline height and velocity are relatively small.

For the experimental flows a slight variation in β at earlier times might be natural, for several additional reasons. The source condition (x_N and y_M at t=0 are typically 2 cm) means that at early times the flow will have advanced further than the model predicts; in defining a floating η_B this extension manifests itself in a bulk viscosity that is *lower* than η_e. Also values of η_B are calculated with reference to the long-time similarity solution of Lister (1992). Prior to T^* and up to $10T^*$, the flows will be influenced by the early-time spreading regime, though an increase in effective viscosity will lower T^*; see Chapter 3 and Lister (1992). Again this will manifest itself in a change to any value of η_b.

Beyond these changes, however, the processes of cooling may themselves alter β. While we would expect the ratio of surface to interior viscosities to remain relatively constant, it will in reality take some amount of time for the surface to cool to T_a, and thus display η_s. As thermal diffusivity is taken as a constant, the remaining key parameter whose variability would alter β is *Pe*. Even if we assumed a bulk *Pe* for the flow, global changes in the flow velocity and height as a function of cooling would affect the ratio of advective to diffusive thermodynamics—in effect creating a feedback loop that leads to an increase in bulk viscosity, which further decreases *Pe*. Changes to *Pe*

may be incorporated into a simple equation for a time-dependent viscosity, as in (eq. 5.6), but the addition of such feedback loops and effective time-dependence in *Pe* itself may complicate the nature and behaviour of β.

Real lava flows observed in Cameroon differ from those observed in the laboratory in that they are affected by visco-plasticity and solidification, and are more pervasively channelised. Furthermore the Cameroonian lavas are not extruded onto a uniformly flat plane, and instead onto a varied topography. As discussed in Chapter 3, the 1999 lava streams are in many cases what Pinkerton and Wilson (1994) class as *captured flows*, flows that are "restricted by pre-existing topographic depressions for more than 25% of their length". Such depressions may vary from gentle valleys to steep ravines, but still serve to focus lava propagation along their course. In such a case one would expect their dynamics to differ considerably from those of an unimpeded flow on a sloping plane.

When the site 2 flow fronts reached Bakingili by the coast, the flow fronts dilated, forming a flow field that was less immediately affected by underlying topography. If we assume that the relief of the substrate had negligible effect on the flow dynamics, simple application of the Jeffreys equation can suggest the apparent viscosity of the flow front. For example, on the 11th April, a lobe ~150-200 m wide and 30 m thick advanced at an average rate of 6.9×10^{-4} ms^{-1} over a period of 12 hours. Using (eq. 5.4) and a value of α of three, appropriate for a broad flow front, provide an apparent Jeffreys viscosity of 7.7×10^{8} Pa s. Other velocity measurements are not so tied to lobe morphology, but in general, assumptions of flow thickness of 10 to 30 m suggest apparent viscosities of 10^{7} to 10^{8} Pa s, but time-series comparisons are impossible.

However, a comprehensive data set exists for the Lonquimay eruption of 1988-90 (Naranjo et al. 1992). Distance versus time data were used to derive local flow front velocities, and values of velocity, height and slope analysed within the Jeffreys channel equation to derive apparent viscosities for the lava. Naranjo et al. (1992) plotted velocity and viscosity as functions of distance, but did not consider viscosity as a function of time, or further analyse its dependence on *Pe*.

If one considers that the Lonquimay lava's viscosity follows time-dependence like (eq. 5.6), the value of β can be calculated at any time with reference to the apparent and eruption viscosities. **Figure 5.7** displays the development of log R with log *t*, showing excellent agreement with (eq. 5.6) and the experimental trends displayed earlier. The trend is linear, indicating a stable value of β. The linear regression fit indicates that $\beta \sim 1.38$. This indicates a considerably different trend and dynamics than active in the expansion of Golden Syrup. With $\beta < 1$, the importance of cooling is greatest at early times, and η_b asymptotes towards some value of η_s at long (or infinite) time-scales. When $\beta > 1$, as in the Lonquimay lava, apparent viscosity rapidly increases with time, perhaps more

as a function of plastic and non-Newtonian effects than simple viscous stiffening, and attains a maximum value and retardational effect rather more quickly. Similar trends in β are displayed for Puu Oo basalts (Fink and Zimbelman 1990).

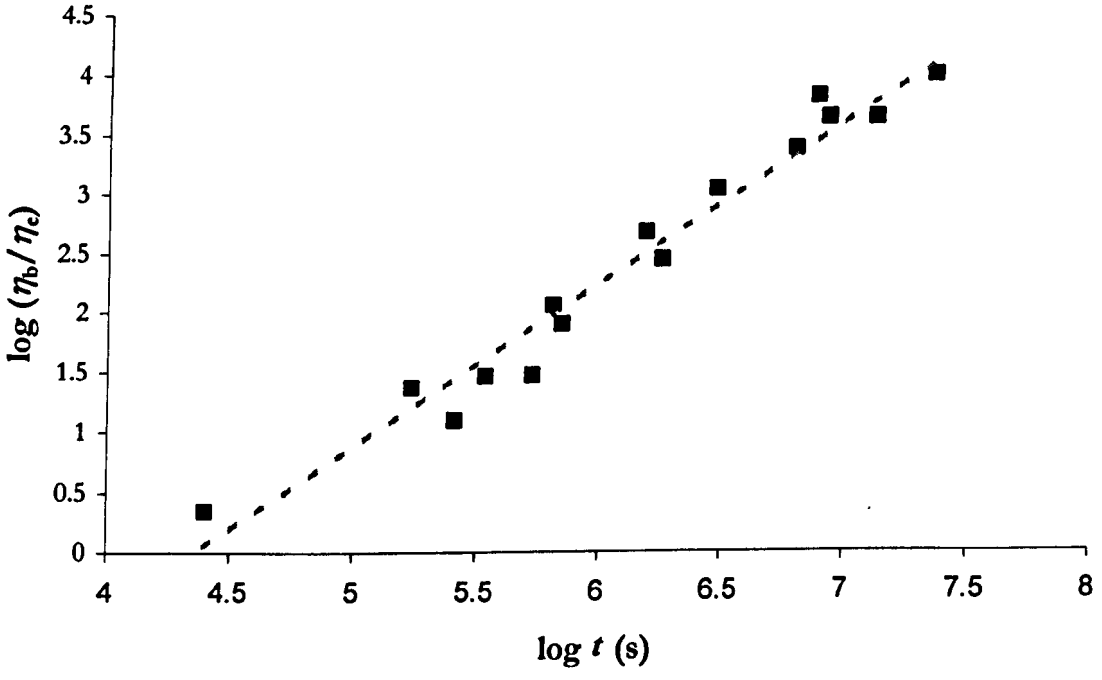

Figure 5.7 The variation of viscosity ratio with time for the 1988-1990 andesite lava of Lonquimay Volcano, Chile. Data are taken from Naranjo et al. (1992), and are fitted with a linear regression, wherein β is equal to 1.38 ($R^2 = 0.962$).

5.3 Fold Formation

Both the experimental and field flows investigated developed clear compression structures. As a viscous gravity current with a strong temperature-dependent viscosity, like syrup or lava, cools, it will develop an inhomogeneous thermal and rheological profile. The cooler elements provide a stiff mechanical layer that will deform in a manner distinct from the steady diffusion of a homogenous isoviscous fluid. The deformation and buckling of such layers in rocks has been widely studied (e.g. Biot 1960, Biot 1961, Ramberg 1961, Ramberg 1963, Donath and Parker 1964, Treagus 1973, Fletcher 1974, Castro and Cashman 1999), but direct analyses for lava flows have been few. Fink and Fletcher (1978) developed a model that applied elements of folding theory to lava flows, with specific reference to the development of ropey structures in pahoehoe. The analysis was extended to folding of rhyolite (Fink 1980), and most recently multiple generations of folds in flows of varying compositions (Gregg et al. 1998).

Analogue models of lava emplacement have developed folds during the extrusion of polyethylene glycol wax (Fink and Griffiths 1990, 1992; Griffiths and Fink 1992; Gregg and Fink 1995; Gregg et al. 1998). PEG possesses a weakly temperature-dependent viscosity over the range of extrusion temperatures ($\Delta\eta$ ~30 Pa s over 5°C) but a relatively rapid onset of solidification at which viscosity can increase and non-Newtonian effects and brittle regimes develop. Such experiments have provided excellent morphological comparisons with real lavas, developing a variety of structures. Fink, Fletcher and Gregg have related structural processes to the dimensionless parameter Ψ, a ratio of the time a solid crust takes to develop to a typical timescale for the advection of warm material from the source. The syrup flows described herein lack the onset of solidification and highly non-Newtonian or brittle deformation, but do possess a strongly temperature-dependent viscosity (($\Delta\eta$ ~10^6 Pa s over 40°C), which proves useful in the study of large viscosity contrasts in viscous flows.

Merle (1998) investigated the development of strain in lava flows through experimental analogue modelling. His isothermal material lacked any viscosity contrast but illuminated the manner in which folds could develop on the introduction of rheological heterogeneities with cooling. Merle (1998) concluded that the dominance of layer parallel shear and layer parallel extension would make folding unlikely in a fluid extruded onto a horizontal plane or constant incline. Folding may result from friction along the lateral margins which could interact with viscosity contrasts to initiate folding at an angle of 45° to the flow direction, the axes of which are then rotated by lateral shear so as to be parallel with the flow margins; if a channel is large and the effects of the margin are felt

across the flow and may produce parabolic fold profiles (Merle 1998; see also the experimental results of Fink and Griffiths 1992 and Gregg and Fink 1995).

Beyond lateral friction, compressive stress regimes may also arise from a deceleration of the flow front and change in local dynamics. A progressive decrease in flow front velocity may occur as (i) a function of the natural progression and divergence of an unbounded flow (even isoviscous radial and slope-borne flows emplaced at a constant flow rate experience shortening parallel to the direction of radial and downslope expansion; Huppert 1982, Lister 1992); (ii) from extended flow divergence beyond the above, as a function of a lava proceeding from a confined channel (e.g. Ramberg 1964, and Merle 1998) or splaying out beyond a break in slope; (iii) due to the influence of a change in angle of slope over which a lava flows itself, altering the local dynamics (Nye 1952, Fink and Fletcher 1978); (iv) and through a rheological stiffening of material downflow (e.g. Kilburn and Lopes 1991, Dragoni et al. 1992). The imposition of obstacles under a flow may also cause local changes in dynamics convivial to folding (see Merle 1998 for a brief overview).

The syrup experiments develop compressive regimes as a function of (i), down and cross-slope shortening, and (iv), rheological stiffening. Cameroonian lavas develop features that were congruent with all four factors, though the focus of the flow down channel largely limited (i). The interaction of compression with the effects of cooling creates a system in which a rheologically stiffer layer may deform into a sequence of parallel folds.

The folding model of Fink and Fletcher (1978)

Fink and Fletcher (1978) define a simplified mathematical system in which folds may be created, amplified and analysed. They considered an infinitely deep layer or half-space of a Newtonian viscous fluid, of viscosity $\eta=\eta_e$ (where η_e is the interior viscosity of the flow; here approximated as equalling the 'eruption' viscosity), overlain by a layer of cooled fluid H deep. The viscosity of this layer decreased with depth, from a bounding surface viscosity, η_s, to an interior layer viscosity η, which developed as $\eta_s e^{\gamma z}$, where z is the vertical co-ordinate and γ is an inverse length scale to be defined later. At the base of the layer, the interior viscosity must match that of the layer at depth H, and therefore $\eta_e=\eta_s e^{-\gamma H}$.

The model is considered applicable only in the first stages of fold generation, when the dominant wavelengths of folds are defined and the slope of the disturbances is infinitesimally small. In this analysis, initial small perturbations in the lava-air interface are selectively amplified as a function of a rate of shortening parallel to the flow surface, $\dot{\varepsilon}_{xx}$, and the wavelength that grows most rapidly defines a dominant fold wavelength in the flow. The growth in the amplitude of perturbations along the lava-air interface can be modelled as

$$\frac{dA}{dt} = (1+q)(-\dot{\varepsilon}_{xx}) \tag{5.10}$$

where A is the amplitude of the disturbance, t the time and q a 'mechanical amplification factor' that depends on the wavelength (L) and physical properties of the lava (Fink and Fletcher 1978, Fink 1980). The amplification factor is greatest at some intermediate dimensionless dominant wavelength $L_d\gamma$ and tends towards 0 at very long or short wavelengths (see Fink and Fletcher for a more detailed analysis of the derivation of q). When $q > 10$, mechanical amplification will dominate over passive kinematic amplification of disturbances, and a well-defined fold wavelength L_d will result, proportional to the thickness of the rheological boundary layer.

From Fink and Fletcher's (1978) analysis, therefore, it is seen that the development of the folding instability and regular wavelengths are a function of three elements: (i) the ratio of surface to interior viscosities; (ii) the thickness of the thermal and hence rheological boundary layer over which the contrast is evidenced; and (iii) the ratio of compressive to body stresses in the surface region of the flow.

The ratio of viscosities is defined by the parameter $R = \eta_s/\eta_e$, and folding is favoured if R is large. Given the viscosity relationships in the surface boundary layer assumed above, the thickness of this layer, H, can be calculated as

$$H = \frac{1}{\gamma}\ln R \tag{5.11}$$

The ratio of surface-parallel compressive stresses to body stresses resulting from the weight of the fluid is defined by the parameter S, which varies as

$$S = \frac{\rho g(1/\gamma)}{4\eta_s(-\dot{\varepsilon}_{xx})} \tag{5.12}$$

where ρ is the lava density, g the acceleration due to gravity, γ the inverse length scale and exponent of viscosity dependence in the boundary layer, η_s the surface viscosity and $\dot{\varepsilon}_{xx}$ a compressive strain rate. Folding is favoured for small values of S.

By comparing the relationships between $L_d\gamma$ and q as functions of R and S, Fink and Fletcher (1978) derive a series of criteria for the application of the model to real flows. A clear mechanical instability requires large values of q, and Fink and Fletcher (1978) suggest that the limiting case for application to real flows must be $q \geq 10$, when mechanical amplification dominates. Taking such a limit produces limiting bounds on the values of R, S and γ. When R is infinite, the criterion that $q \geq 10$ requires $S \leq 0.02$. Similarly, when S trends towards zero, R increases with q, and for $q \geq 10$, $R \geq 35$. With these criteria $L_d\gamma$ must ≥ 28 for mechanical folding to be defined (Fink 1980, Figure 5; note the increase on the value of ≥ 16, proposed by Fink and Fletcher 1978).

Folds in experimental extrusions of Golden Syrup

In the analogue flows of cooled syrup, two wavelengths are clearly defined. Following Gregg et al. (1998), we define the first generation of folds as L_1, and the second as L_2, and the ratio of the two, L_2/L_1, as Λ. While Fink and Fletcher (1978) consider the development of subsequent generations of folds, they do not expressly analyse their manifestation. Continued cooling and mechanical shortening as a result of folding will expand the depth of the rheological boundary layer. Compression will be accommodated by a thicker surface skin, and thus suggest a new, longer wavelength of deformation. Amplification of disturbances proceeds as defined, but the perturbations are not random, rather the form of the first fold generation (Gregg et al. 1998). Gregg et al. (1998) suggest that the geometry of a mechanically thickened layer does not necessarily abrogate the use of the folding theory for second-generation folds, and that the thickened layer leads to an increase in H and thus decrease a decrease in γ.

Observed first generation fold wavelengths in the syrup experiments are typically ~1 mm. Such folds take the form of a cooled rippled skin, whose formation is described in Chapter 3. One cannot be more exact as the magnitude of their wavelength was approximate with the resolution of the visual data recorded by the digital video cameras. A few experiments were recorded in a manner that saw a manually operated, local zooming in on flow features, though in general this practice was limited to reduce heating of the ambient environment. However, manual and occasional digital observations of these first generation folds confirm the length scale, and its *apparent* invariability with temperature, flow rate or slope. Any variations were beyond the accuracy of our measurements. As these ripples are quite tightly buckled, it will prove more accurate to suggest that the fold arc length is a better measure of the initial value of L_1 on fold generation than measured wavelengths at later times (e.g. Fletcher and Sherwin 1978, Fink and Fletcher 1978, Fink 1980). As sub-mm accurate measurements of fold arc length are not possible, we assume a simple enlarged value of L_1 of 2 mm.

With reference to the framework of Fink and Fletcher (1978), for $q \geq 10$, $L_1\gamma \geq 28$; i.e. with an observed L_1 of 0.002 m, $1/\gamma \leq 7 \times 10^{-5}$ m. We assume that by the onset of folding the surface has cooled to the ambient temperature T_a, forming a boundary layer that grades thermally to an interior of eruption T_e, resulting in an exponential viscosity as described above, $R \sim 420$ (T_a –8°C) to 27,000 (T_a -20°C). From (eq. 5.11), this would suggest that $H \leq 0.7$ mm (T_a –20°C) and $H \leq 0.4$ mm (T_a -8°C) at the onset of folding.

These estimates compare well with a simple estimate of the development of a conductive thermal boundary layer over time, with a thickness $\delta \sim (\kappa t)^{0.5}$, where κ is the thermal diffusivity (1.2×10^{-7} $m^2\ s^{-1}$ for Golden Syrup) and t the time. After 10 s of steady-state, one-dimensional conduction, $\delta \sim 1$ mm; after 100 s, $\delta \sim 3.5$ mm. First generation folds typically start to form over these timescales, whether they relate to the onset of folding at the flow margins, or the time taken to advect a parcel of fluid from the source to an area of fold formation downflow. If we consider that the boundary layer will propagate somewhat slower into the interior of a flow with time due to advection from the source, revised estimates of δ give good agreement with H. Values of L_1 are therefore commensurate with those predicted by the mechanics of Fink and Fletcher's (1978) model.

Analyses of S, the ratio of compressive to body stress, require an estimation of the syrup flows' strain rates. As the limiting value of $1/\gamma$ is 7×10^{-5} m, use of syrup densities and viscosities at T_a (see Chapter 2) means that for the criterion $S \leq 0.02$, the model requires strain rates $\dot{\varepsilon}_{xx} \geq \sim -8 \times 10^{-6}\ s^{-1}$ (T_a –20°C), or $\dot{\varepsilon}_{xx} \geq \sim -5 \times 10^{-4}\ s^{-1}$ (T_a –8°C), where negative rates of strain are compressive. Naturally these minute values are exceeded in experimental flows. Strain rates in the extrusions of syrup can be estimated in several ways.

First generation folds form in two regions: towards the flow flanks and rear, with axes trending at an angle of ~45° or greater to the downslope flow direction, and in the distal, skin-covered extension of the central flow channel, with clear parabolic axes (see section 3.5.2.1). It is simplest to analyse the latter, as these are better recorded with respect to values of L_1 and exist as the basis for the generation of L_2. An appropriate strain rate $\dot{\varepsilon}_{xx}$ for the development of fold axes perpendicular to the direction of downslope expansion is equal to the downstream velocity gradient, $\partial u_0/\partial x$, where u_0 is the centreline velocity and x the distance downflow from the source. One might consider the application of scales developed from Lister's (1992) isothermal theory, placing sluggish and time-dependent flow front expansion to the propagation of fluid elements advected from the hotter proximal regions. However a frontal roll-over criterion means that flow surface velocities at the flow front are somewhat greater than those of the bulk advance of the flow toe itself.

Analyses of the centreline velocities of experiments GS-20_10_6, GS-20_15_1 and GS-20_20_8 suggest that a simpler formulation is accurate to a first order and far more tractable (see section 5.4). Empirical arguments show that in the near source u_0 decreases linearly with x, and can be modelled to a simple order of accuracy by simple application of the Jeffreys channel equation. Slight non-linearities occur at higher values of x as cooling takes increased affect and the surface mechanically reacts to its increased viscosity. Velocities of the order of 1-5 mm s^{-1} supply centreline strain rates of the order of $-0.005s^{-1}$ to $-0.01s^{-1}$, clearly in excess of those required for $S \leq 0.02$.

Second generation folds display such shallow amplitudes that crest-to-crest measurements are accurate indicators of an initial L_2 wavelength. In contrast to L_1, L_2 is readily measured from the recorded flow profiles, and values for a range of flows collated in **Table 3.2** (see section 3.5.2.1). Care was taken to choose values of L_2 that were recorded as early in the flow's evolution as possible, to render the greatest applicability to model of Fink and Fletcher (1978) and eliminate the effects of the initial second generation folds squashing together near the flow front. Repeating the analysis performed for L_1, given the criterion $L_1\gamma \geq 28$ maximum values of $1/\gamma$ can be calculated, followed by the upper limit on H, and suggested lower limits for $\dot{\varepsilon}_{xx}$ dictated by S. The results for several flow data are collated in **Table 5.3**.

The wavelengths of second-generation folds, L_2, are an order of magnitude greater than L_1; for the data in **Table 5.3**, Λ = 17.5 - 29.5. Such values are greater than those witnessed by Gregg et al. (1998) in PEG flows ($\Lambda \sim 8$) or real lavas ($\Lambda \sim 4$ to 6 for basalts, $\Lambda \sim 2$ for rhyolites). Even the smallest values of L_2 measured in the distal toe of a syrup flow, produce $\Lambda \sim 10.5$. Values of Λ in lavas are suggested by Gregg et al. (1998) to be a function of the relative rates of crust growth through thermal cooling and mechanical shortening. In highly strained flows where crust growth through shortening is much greater than that provided by cooling, a small L_1 will generate at early times with an extremely thin skin; folds will further tighten and deform until the crust has thickened to an extent that compressive stresses must be accommodated in larger wavelength second-generation folds. In more gently strained lavas, the relative influence of cooling on crust development is far greater, and fewer folds with larger initial L_1 will form from a thicker carapace, before a still-thicker crust necessitates a new wavelength (Gregg et al. 1998).

Beyond a strongly-temperature dependent viscosity, the experimental syrup flows possess low thermal diffusivities and relatively high rates of strain, with many similarities to basalts. L_1 develops from a very thin skin, and is thus rather small. If the values of H for second-generation folds are taken as accurate, the boundary layer effectively covers the depth of the flow by the time second-generation folds form. As apparent and effective Jeffreys bulk viscosities are typically only an order of magnitude greater than the eruption viscosity (section 5.2), L_1 is of the order of 2 mm, and it

Table 5.3 Second generation (L_2) fold data, displaying the limiting values of ($1/\gamma$), H and $\dot{\varepsilon}_{xx'}$ suggested by application of the model of Fink and Fletcher (1978).

Experiment	L_d (cm)	$1/\gamma$ (cm)	R	H (cm)	$\dot{\varepsilon}_{xx'}$ (s^{-1})
GS-10_10_2	5.9	≤ 0.211	719	≤ 1.39	≥ 0.008
GS-10_15_2	5.5	≤ 0.196	611	≤ 1.26	≥ 0.008
GS-10_20_2	4.1	≤ 0.146	611	≤ 0.94	≥ 0.006
GS-20_10_3	5.6	≤ 0.200	20618	≤ 1.99	≥ 0.008
GS-20_10_6	4.9	≤ 0.175	12805	≤ 1.66	≥ 0.007
GS-20_20_2	3.5	≤ 0.125	13249	≤ 1.19	≥ 0.005
GS-20_20_7	4.3	≤ 0.154	16898	≤ 1.50	≥ 0.006

would take over 30 minutes of steady-state conduction to advance a thermal boundary layer that far, H must be taken as a figurative limit only.

With Golden Syrup, folds are not dampened or resisted by nascent plastic effects or even a veneer of glassy, brittle crust. Compression is accommodated entirely in the buckling of the viscous skin, and one might suggest that the large value of Λ is a function of the free and rapid development and amplification of folding instabilities in a thin skin at very early times, followed by a later episode that was linked to a mechanically thicker and stiffer skin. The rates of compressive strain parallel to downslope flow typically encountered in the experiments (-0.01 s^{-1}) are of the order of those considered necessary for mechanical amplifications of L_2 disturbances (Fink and Fletcher 1978; **Table 5.3**). The weak amplitudes of second generation folds suggest that, alongside the quantitative evidence, the dynamics of the syrup extrusions just touch on the folding regime predicted by Fink and Fletcher (1978).

Folds in the 1999 Mount Cameroon lava flows

The lava flows investigated on Mount Cameroon differed from the extrusions of syrup in that they are typically channelised, and noticeably developed compression structures as a function of toe stiffening in the distal channels, and changes in local dynamics initiated by a break in slope. Although ropes were witnessed in the proximal pahoehoe flows of the Site 1 and Site 2 vents, they are not considered here. Rather we document the large pressure ridges described in Chapter 4 that formed in aa, blocky and transitional blocky-aa channels. Only a single generation of pressure features of this type is observed.

The distal flow lobes at Bakingili react to a compressive stress regime that is not too dissimilar to that experienced in the experiments. Frontal stiffening and small levels of flow front dilation provide for backpressures that require a rheologically stiffer lava top to buckle and deform. Of

course blocky lavas are thermally mature; their very habit indicates a significant crossover into a regime of brittle deformation in the upper flow region. Below the fractured, brecciated top, cooling will have generated a stiff, mushy layer of relatively crystalline viscous basanite. Fink and Fletcher (1978) do not consider a visco-plastic rheology in their folding model but, because complex rheologies can often be approximated by the concept of a bulk viscosity, it is reasonable to assess the pressure structures via this approach, and compare the data with other predictions.

Accreted levees may develop as indicated by Lipman and Banks (1987), indicated in **Figure 4.8**, or perhaps as suggested by Merle (1998), with a more marginal genesis along the angle of shortening, caused by a wrenching motion against the channel margins. The ridges described on p. 203 possess a mean L_d of 6 m, suggesting $1/\gamma \leq 0.21$. As this is a measured wavelength rather than arc length, and the ridges have been compressed against the side of the channel, one would expect the actual value of L_d to be slightly larger. Estimating a viscosity contrast, R, of ~4 x 10^4 (see section 4.2.3), we gain a crust depth, H, of $\leq$ 2.26 m.

With regard to strain rates, if we use the marginal formation analogy of Merle (1998) rather than that of Lipman and Banks (1987), we might assume that measured values of L_d are similar to those witnessed in the field, as the ridge will have encountered less mechanical squeezing beyond the initial amplification of disturbances. We refer to Fink and Fletcher's (1978) formulation of the maximum strain encountered at the edge of a semicircular channel

$$\dot{\varepsilon}_{xx} = \left(-\frac{\rho g \phi}{2\eta_e} \right) a \tag{5.13}$$

where the parameters are as described before, with the exception of ϕ, the slope angle in radians, and a, the radius of the channel. **Section III** indicates a ~ 10 m (the channel is more rectangular than semi-circular, with a half-width, 15 m, greater than the suggested depth, 10 m; the latter value is used for reference) and the altimetric trend of Sections a slope of ~ 7°. With an interior viscosity of the order of 10^6 Pa s, this produces a strain rate of ~ -0.002 s^{-1}, though the surface value will be somewhat lower as a function of the increased stiffness. For comparison, for $S \leq 0.02$, $\dot{\varepsilon}_{xx} \geq \sim 2 \times 10^{-6}$.

For a second series of distal pressure ridges near Bakingili, on **Section II**, average wavelengths of ~ 11 m were recorded, suggesting $1/\gamma \leq 0.39$ and, with similar values of R as above, $H \leq 4.14$ m. Velocity profiles recorded for the development of the flow region were 2 x 10^{-3} m s^{-1}, while a day later speeds 225 m downflow had fallen to 0.69 x 10^{-3} m s^{-1}. Assuming linear surface strain parallel

to the flow direction, this translates to an $\dot{\varepsilon}_{xx}$ of ~ 6 x 10^{-6}. This barely satisfies the criterion that for $S \leq 0.02$, $\dot{\varepsilon}_{xx} \geq$ ~ 3 x 10^{-6}, but the strain rate estimated is undoubtedly a low estimate. The pressure ridges in this area may also have formed as the product of two different flow surges interacting in an exceptionally wide channel (see section 4.3.3.4).

Fold formation and breaks in slope

These latter ridges occurred a few hundred metres beyond a break in slope, which may have exerted an influence of their dynamical development. Following Fink and Fletcher (1978), we use a simple model to display the effects on a flow that experiences a change in underlying slope angle at some point in its development. For flow in a simple semi-circular channel, the local flux through the channel cross-section at any time can be modelled as

$$Q = \frac{2\pi\rho g \phi a^4}{3\eta_e} \tag{5.14}$$

where Q is the local flux and all other parameters are as previously defined. With a change in slope, the retention of a uniform local flow rate necessitates the increase of a with decreasing ϕ, with both varying with x as follows

$$\frac{1}{a}\frac{\mathrm{d}a}{\mathrm{d}x} = -\frac{1}{4\phi}\frac{\mathrm{d}\phi}{\mathrm{d}x} \tag{5.15}$$

The application of the above to the equations for straining flow at the centre of a semicircular channel produce a maximum rate of shortening along the centreline of

$$\dot{\varepsilon}_{xx} = \frac{\rho g a^2}{4\eta_e}\frac{\mathrm{d}\phi}{\mathrm{d}x} \tag{5.16}$$

Assuming plane strain of a surface experiencing stresses proportional to $-4\eta_s\dot{\varepsilon}_{xx}$, we can substitute the above into (eq. 5.12) to gain a modified S:

$$S = -\left[\frac{\eta_s}{\eta_e}\gamma a^2 \frac{\mathrm{d}\phi}{\mathrm{d}x}\right]^{-1} \tag{5.17}$$

In the lava flows that extruded from site 1 cones, two excellent examples of flows developing ridges beyond a break in slope were recorded, and described in section 4.3.3.4. In the first example, a change in slope of 17° to 6° produced folds with an average wavelength of 8.2 m. This would suggest limiting values of $1/\gamma \leq 0.29$ and $H \leq 3.1$ m. Using (eqs. 5.16 and 5.17) one arrives at suggested values of $\dot{\varepsilon}_{xx} \sim 0.006\ s^{-1}$ and $S \sim 9.5 \times 10^{-5}$, well within the limits prescribed by Fink and Fletcher for mechanical folding (1978). The second example displayed folds with a mean L_d of 6.7 m, sited beyond a break in slope of ~ 7°. With the model of Fink and Fletcher (1978) this wavelength suggests $1/\gamma \leq 0.24$ and $H \leq 2.5$ m. The flow parameters suggest $\dot{\varepsilon}_{xx} \sim 0.004\ s^{-1}$ and $S \sim 1.8 \times 10^{-4}$.

Further ridges were detailed on other investigations of the 1999 flows, and were kindly communicated to the author by Dr. Emmanuel Suh. A change in slope angle from ~24° to 6° occurred approximately 114 m behind a site 1 flow front, resulting two zones of folding. The first contained six pressure ridges occupying a zone some 46 m long before (i.e. upstream from) the break in slope. The wavelengths of folds witnessed generally decreased as the flow channel approached the slope, from 7.89 m through 7.10 m, 6.90 m and 6.10 m to 6.90 m. Beyond (i.e downstream from) the break in slope three folds were present, with a very tight wavelength of 2 m immediately after the change in angle, opening out to 8.90 m between the ridge following. Though the depth of the channel (estimated at 1.5 to 2 m) in which these ~1.6 m amplitude folds occur is somewhat smaller than the half-width (typically 3.25-4 m), use of the above theory suggests that if we approximate the break in slope as a change in angle of 18° over 60 m, with a mean L_d of 6.7 m, $\dot{\varepsilon}_{xx} \sim 5 \times 10^{-4}\ s^{-1}$ and $S \sim 1.3 \times 10^{-3}$.

5.4 Channel Development

Clear, well-defined channels containing hotter fluid than in sluggish, cooled margins are observed in both experimental extrusions of Golden Syrup and Cameroonian basanite lavas. Though there are distinct differences in the development of rheological changes in what is considered to be a purely viscous syrup, compared with a complex lava that might develop a range of visco-plastic, visco-elastic and brittle characters during deformation, the experimental results highlight that the issue of channel development cannot be regarded simply.

In any flow a noticeable channel is observed when there is a clear difference in flow behaviour and appearance between a more fluid centre and its adjacent margins. In lava flows, this development manifests itself as a function of changes to the flanks—i.e. a channel is formed as a function of alterations to the flow margins delineating a central region relatively unchanged from its initial condition. This central flow region then dynamically adapts to the new physical system. The overall process is the same in the development of channels in cooled syrup.

The potential differences lie in the manner in which the alterations to the flow flanks are manifested and develop. Following the work of Hulme (1974), concepts on levee, and thus channel, development have centred on the theory that initial levees form as a function of plasticity in the flow margins (e.g. Sparks et al. 1976). Once the local stresses exerted by the weight of the fluid fail to overcome a yield strength developed as a result of cooling, the lateral expansion of the flow halts. From the dimensions of a levee a yield value may be predicted, or vice-versa. Although the nature and application of Hulme's theory has been criticized by some, with particular reference to the artificially uncoupled levees and channels, and the resultant application of an essentially 2D model to a 3D problem (e.g. see Sakimoto and Gregg 2001), it remains the accepted theorem, with the merits of simplicity. In Chapters 3 and 4 we sought to suggest further criteria that add to and modify the levee building process, not least of all the influence of a temperature-dependent viscosity.

Channelisation in cooled viscous flows

Syrup cannot replicate the production of statically equilibrated plastic levees; the margins of syrup will never develop a strength and thus will continue to expand laterally across the slope. Yet syrup flows do clearly show the effects of a temperature-dependent viscosity in their expansion. Cross-slope height gradients in the near source regions of the experimental flows are significant, especially at early times. The fall in velocity as one travels towards the lateral margins causes a significant amount of compression. As the syrup cools, the thin surface layer can no longer accommodate this

rapid compression by viscous diffusion, and instead buckles, forming a series of small wavelength folds. This process is exacerbated by the fact that due to the low velocities at the flow margins, there is little local advection of heat, and less replenishment of any heat lost via thermal diffusion. Hence, relative to the hot, free flowing central region, the flow margin surfaces will cool considerably quicker. This will serve to enhance the local differences in surface velocity described above, as in effect a cooled margin further retards lateral surface flow, increasing the compressive effect.

As this viscous 'surface levee' builds up, expansion across-slope is limited, and the flux is concentrated in the downslope direction. By contrast, the compressive effect parallel to the downslope co-ordinate is much smaller than that in the cross slope direction, and the large flow velocities along the centreline of the flow allow significant advection of hot material downslope, minimising effective cooling. Overall this leads to small to negligible compressive effects in the proximal flow region and a highly thin to effectively absent surface thermal boundary layer. Given time, parcels of fluid advected down flow will cool, and the flow front may also retard as cooled viscous material is accumulated at the foremost regions, leading to downslope deformation and an increase in flow height. The central channels produced by the cooling of marginal areas were measured and detailed in Chapter 3. Average values of flow width are plotted against flow rate in **Figures 3.41** and **3.42.** The data can be described by good trends of the (not dimensionally accurate) form

$$w = kQ + c \tag{5.18}$$

where w is the average channel width (measured after it had fully developed and stabilised), Q the flow rate (measured at the source), and k and c are presented, at this stage, as numeric factors. The data show that for a given amount of cooling, w increased linearly with increasing Q for extrusions on a given slope. The numeric factor k is relatively constant, falling into the range 1.4-1.6 (for flows cooled to ~–10°C) or 1.1-1.3 (for flows cooled to ~–20°C). The slight variance in k between the flows extruded into ~–10°C and ~–20°C suggests that this factor is a function of temperature, and perhaps the viscosity ratio, R (see above). While especially close inspection shows that experimental series extruded at lower *actual* temperatures overall generate marginally lower values of k (c.f. GS-10_15 and GS-10_20 vs. GS-10_5) and the –10°C flows also display a slight increase in k with decreasing slope, there are relatively few data and the magnitude of the changes is not significant enough to assuredly indicate anything beyond experimental variability.

Among flows extruded into a given ambient temperature, the influence of slope can be clearly categorised. For a given value of Q, the channel width w varies according to $\cot\theta$, or the inverse

tangent of the angle of the slope. For the –10°C and –20°C data sets c therefore takes the form $c=\cot\theta + n$, where n is ~-1.88 (-10°C) and ~1.25 (-20°C), and suggestively a function of temperature/viscosity contrast. c effectively places a limiting value on w as one trends towards Q = 0. One may also have considered n to be a function of the source condition, though w is not explicitly limited to the diameter of the vent (4 cm), as is displayed in **Figure 3.42.**

The exact variation of k, c and n with eruption parameters (effectively Q, $\cot\theta$ and R) cannot be defined accurately with the current data. Two values of T_a (ambient temperature) were considered adequate to conduct a primary analysis of first order effects of cooling on the flow dynamics. The values of T_a were constrained by (i) the slight variability in ambient temperature recorded for a given set value of T_a, necessitating a wider range to provide a clearer contrast; (ii) the noted onset of non-Newtonian properties and visco-elasticity in syrup at lower temperatures (see Stasiuk 1993); and (iii) the under-performance of the cold room at temperatures ~0 to -5°C, when it displays greater variability in recorded temperatures.

While the isothermal examples provide a mark against which cooled experiments can be compared, the isothermal flows naturally develop no channel structures or folds, and channelisation data can only be considered with reference to two levels of cooling. Further data are required to study accurately the geometries of channel formation and generate empirical models, but early results suggest that the width of channels in cooled syrup flows varies as

$$w = f_1(\text{temperature; R})Q + f_2(\text{temperature; R?})\cot\theta \tag{5.19}$$

wherein the term fQ is probably more accurately a combination of viscosity ratio and Peclet Number (Pe). Again, it should be highlighted that this is an empirical formulation, and not dimensionally accurate. Physically, these formulations are consistent with an appreciation of the modes of formation of surface channel structures. Warm central channels are delineated through the gradual growth of a cooled, rippled skin. The skin will therefore form when surface elements of the syrup possesses the three properties necessary to allow fold generation: a high value of R (always present in syrup at –10°C and –20°C, even if the skin has not cooled completely to T_a); a thermal boundary layer thick enough to necessitate buckling on observable wavelengths; and a high enough rate of strain to allow deformation.

One can suggest that the most important control on skin formation is Pe. High values of flow velocity promote the advection of fresh, hot syrup from the source to a given flow region, and stymie the slow process of diffusion necessary to form a stiff rheological boundary layer. A simple appreciation of the dynamics of a slope-borne syrup flow validates the above criteria. Once the

flow develops into something similar to Lister's (1992) long-time solution, lateral movement is very much reduced compared to downslope expansion. Skin does not form in the source region, or in the central portion downflow where the flow is deepest and focused downslope; these areas possess the highest velocity components and *Pe*. Skin first forms in the rear and flank margins, where replenishment of heat from the source is negligible and flow advance slow.

With time a central flow plateau develops, spreading as a function of $\partial h/\partial x$ decreases, and flow elements are advected far enough from the source that they can cool and deform into a viscous skin. The point at which the central channel is extinguished marks the change from advection-dominated to diffusion-dominated thermodynamics. It will be recalled that a skinless toe typically formed at the very front of the flow. Although the flows develop a roll-over motion at the front that can eliminate this feature, the flow front retains large $\partial h/\partial x$, driving local flow motion and minimising the effects of compression compared to those felt on the plateau building behind the flow toe. Higher flow rates suggest increasing importance of advection of heat from the source, which would favour the generation of larger channels. Slight changes in the ambient temperature would exacerbate or denigrate the counter to source advection—cooling by thermal diffusion. Therefore while the few data cannot be taken to indicate a clear dependence of k on temperature, such is highly likely.

Motion in a channel

Full models of contemporaneous levee and channel development in cooling flows require solutions of an often-transient regime involving a coupling of complex thermal and physical processes and a moving contact line. No such models currently exist, and it is most common to decouple levee and channel formation in a manner similar to Hulme (1974). Levees are described as a function of their visco-plastic rheology and then assumed fixed. Though this is frequently true, it is far from uncommon for levees to continue to develop and deform in reaction to channel flow processes (see for example Guest et al. 1987 and Chapter 4). The elements of levee-channel interaction need to be better studied, and given the difficulties of numerical approaches, scaled, dimensionally consistent analogue models provide the most useful lead.

Nevertheless, in the absence of such models, the uncoupled levee-channel system remains useful, and often provides accurate correlations with real lava dynamics. Channel or infinite sheet flow models provide estimates of flow velocities, from which important flow parameters can be resolved. These models are now compared with experimental and field data. Particles were deposited on the centre of the flow surface in three experiments, GS-20_10_6, GS-20_15_1 and GS-20_20_7, and their positions recorded with time, and displayed in **Figures 5.8** to **5.10**. From

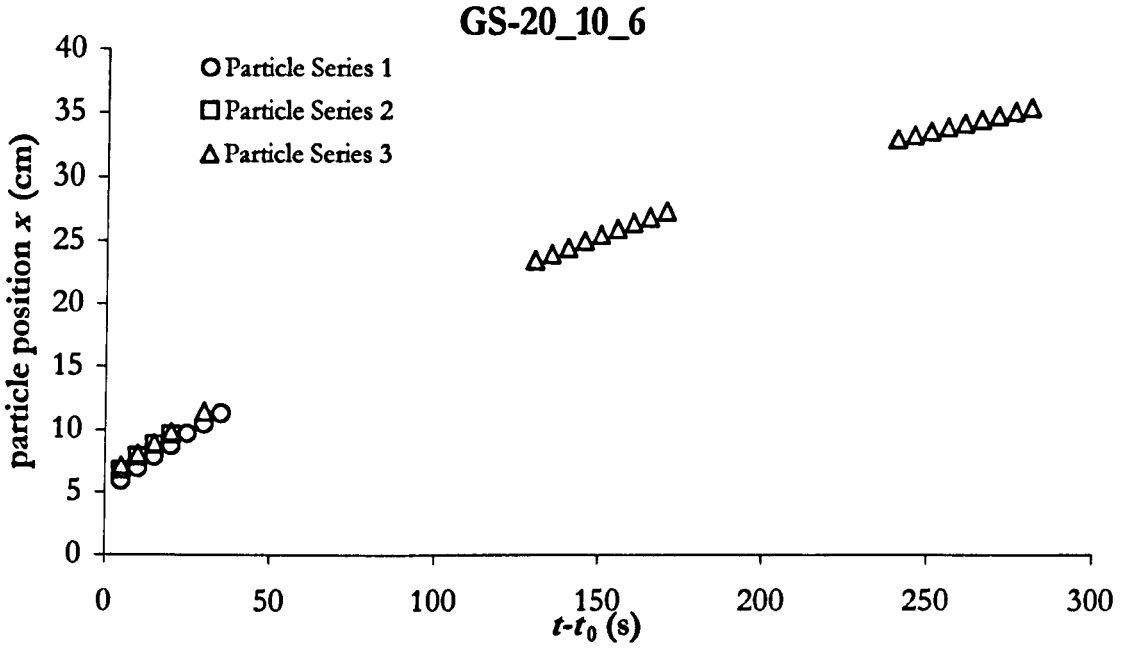

Figure 5.8 Distance travelled downslope (x) by a small mm-sized round particle, deposited on the centre-top of the flow, tracked as a function of the time expended since the deposition of the particle (t-t_0). For the three series, the values of t_0 at which the particle was deposited (in the overall duration of the experiment) were: Series 1 t_0 = 180 s; Series 2 t_0 = 360 s; Series 3 t_0 = 565 s.

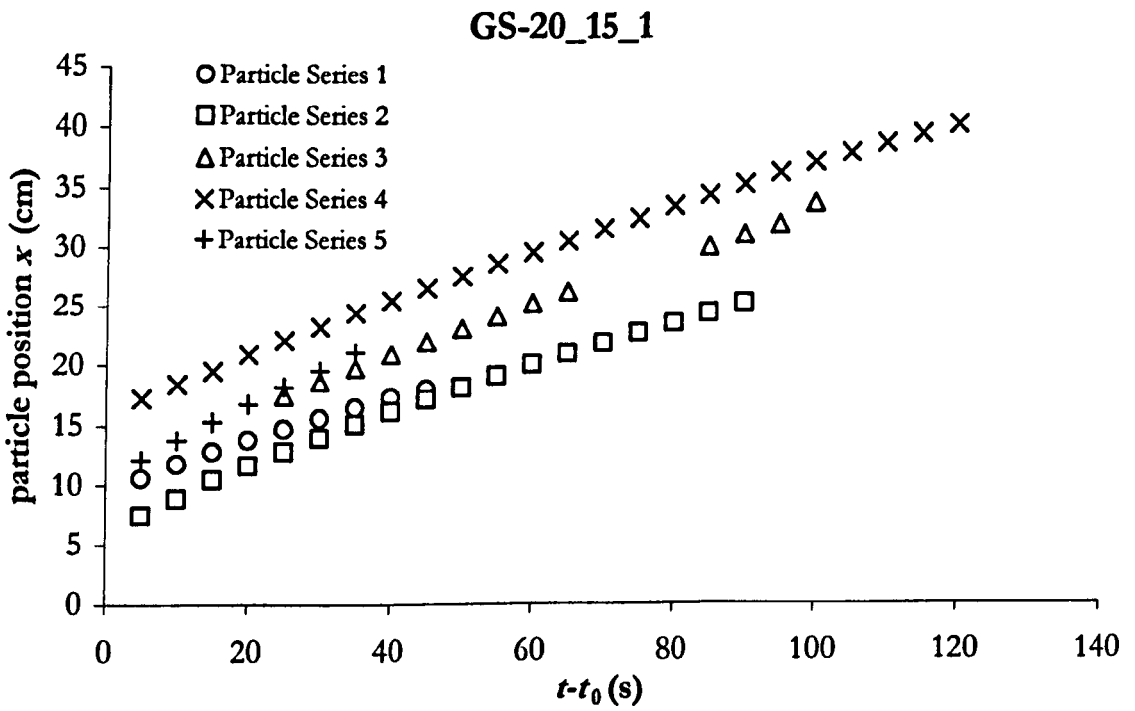

Figure 5.9 Distance travelled downslope (x) by a small mm-sized round particle, deposited on the centre-top of the flow, tracked as a function of the time expended since the deposition of the particle (t-t_0). For the five series, the values of t_0 at which the particle was deposited (in the overall duration of the experiment) were: Series 1 t_0 = 150 s; Series 2 t_0 = 410 s; Series 3 t_0 = 785 s; Series 4 t_0 = 895 s; Series 5 t_0 = 1080 s.

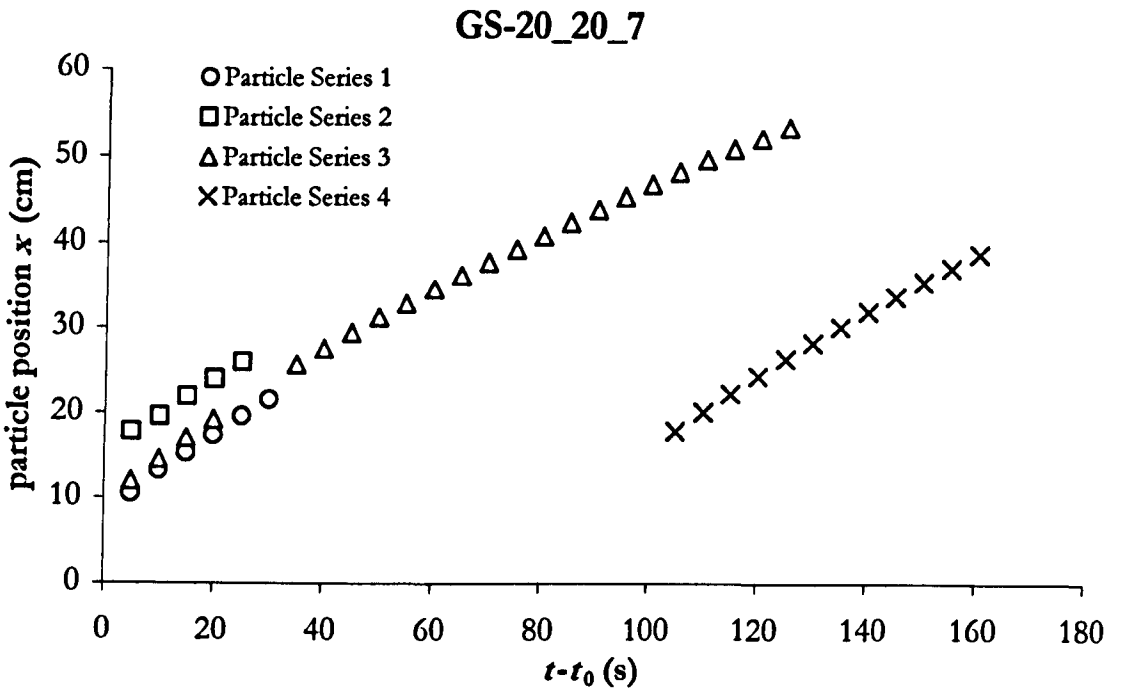

Figure 5.10 Distance travelled downslope (x) by a small mm-sized round particle, deposited on the centre-top of the flow, tracked as a function of the time expended since the deposition of the particle (t-t_0). For the four series, the values of t_0 at which the particle was deposited (in the overall duration of the experiment) were: Series 1 t_0 = 180 s; Series 2 t_0 = 255 s; Series 3 t_0 = 515 s; Series 4 t_0 = 610 s.

these distance–time series the variation of velocity with distance for measurements over a given time sequence was calculated, and the results are displayed in **Figures 5.11** to **5.13.**

As distance/time measurements for the progress of a given particle were recorded over small ranges of t, we can assume that the series of velocities calculated as it progressed downslope is appropriate for a single time-step. At any give time, centreline velocities are shown to be approximately inversely linear functions of downslope distance. While there is occasionally an apparent shallowing of $\partial u/\partial x$ within a given series, it is not well defined, though a gradual decrease in $\partial u/\partial x$ across all series and large ranges of x is more prominent (e.g. GS-20_10_6, **Fig. 5.11**). The velocities for GS-20_20_7 were recorded over a period of ~500 s, and show little variation between series (**Fig. 5.13**). In **Figure 5.12,** however, there is a clear trend towards increasing u at a given magnitude of x in GS-20_15_1, with increasing t (the series were recorded over ~1000 s).

Several theories exist for the development of velocity in a Newtonian flow, and we present and analyse the data with the two most commonly used and readily applicable. With the development of at least a surface channelisation, we use the model for Newtonian flow in a rectangular channel, presented by Tallarico and Dragoni (1999; an alternate approach is developed by Sakimoto and

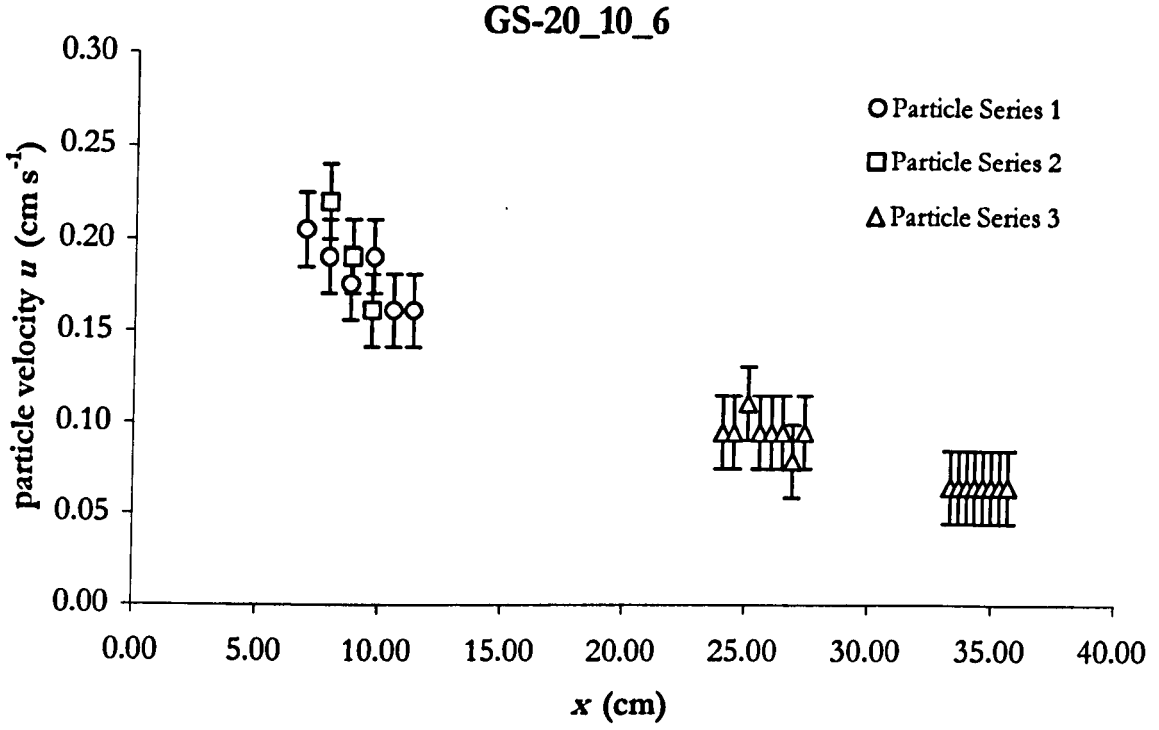

Figure 5.11 Variation of centreline flow velocities (u) with distance from the source (x), recorded for three particles over a range of times displayed in **Figure 5.8.** Flow rate was 1.0 $cm^3\ s^{-1}$.

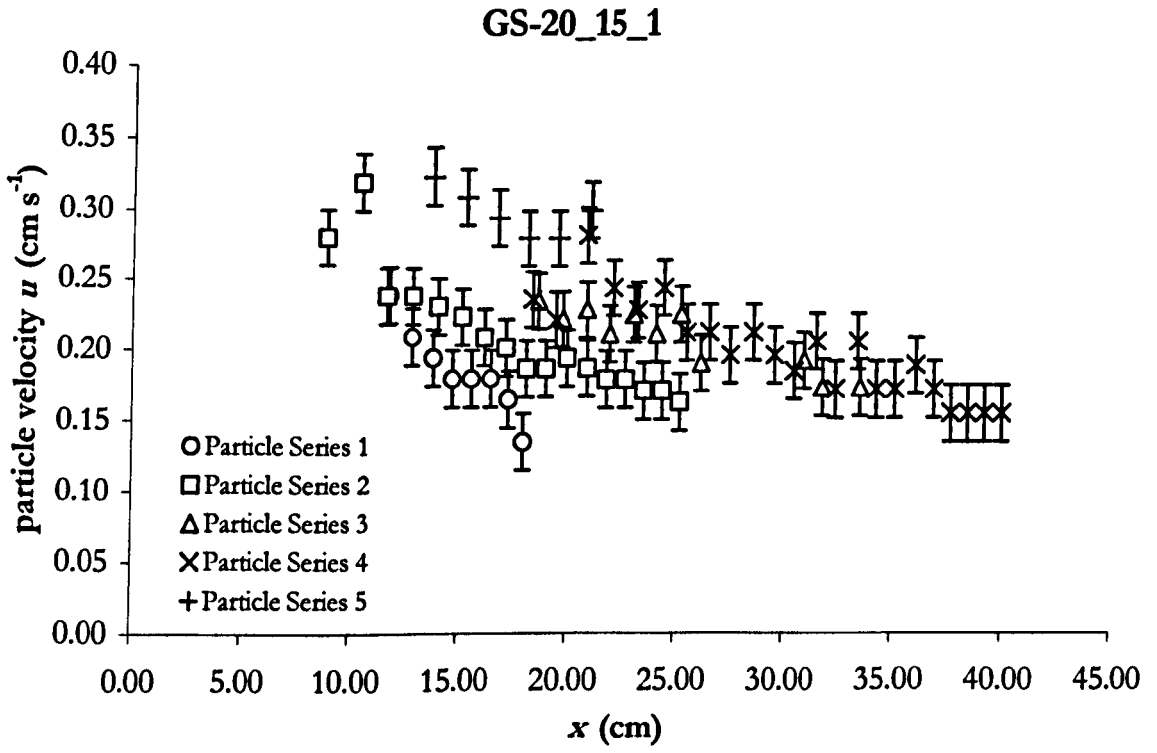

Figure 5.12 Variation of centreline flow velocities (u) with distance from the source (x), recorded for three particles over a range of times displayed in **Figure 5.9.** Flow rate was 1.3 $cm^3\ s^{-1}$.

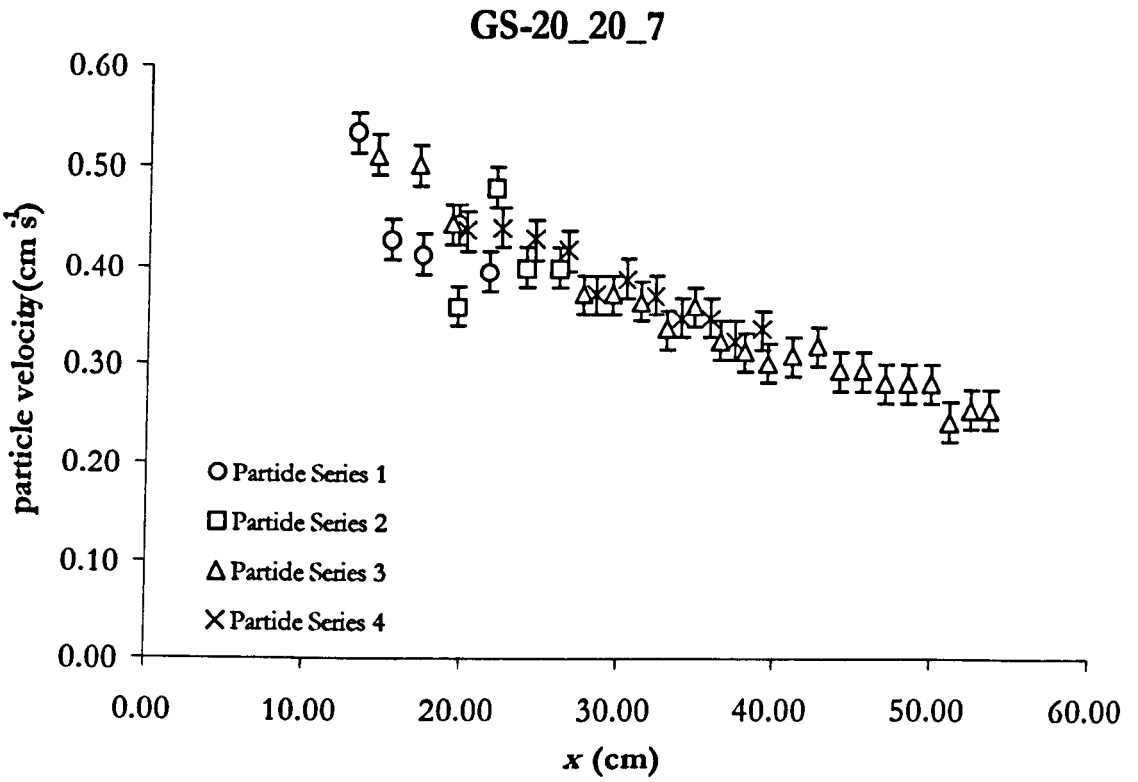

Figure 5.13 Variation of centreline flow velocities (u) with distance from the source (x), recorded for three particles over a range of times displayed in **Figure 5.10**. Flow rate was 3.3 $cm^3\ s^{-1}$.

Gregg 2001). A full development is presented in the above paper, but for ease of analysis we present the formulation for a typical centreline velocity. For flow in a rectangular conduit with a constant slope θ, height $2h$ and width a, with uniform density ρ, viscosity η and steady laminar flow, the centreline velocity u can be modelled as (Tallarico and Dragoni 1999)

$$u = \frac{\rho g \sin\theta}{2\eta} h^2 \left[1 - \frac{32}{\pi^3} \sum_{n=1,3,5}^{\infty} \frac{1}{n^3} (-1)^{(n-1)/2} \operatorname{sech} \frac{n\pi a}{4h} \right] \tag{5.20}$$

A simpler formulation, which might also be appropriate to the thin spreading slope-borne flows, is to assume that the fluid flows as if infinite in the y coordinate. While planform flows do display parabolic velocity gradients with y and $-y$, this model shall be used for comparison. Simply, this two dimensional model gives (e.g. Dragoni et al. 1995)

$$u_{2D} = \frac{\rho g \sin\theta}{2\eta} h^2 \tag{5.21}$$

It will be seen that the two models are proportional, and that the difference in centreline velocity predicted can be identified by the term in square brackets in (eq. 5.20).Centreline velocities from GS-20_15_1 are compared with model predictions in **Figures 5.14**. The velocities calculated using (eqs. 5.20 and 5.21) are applicable for a given flow or channel cross-section, and do not take into account dynamic processes and changes up and downflow. Each value is calculated according to values of a and b measured from flow profiles and **Figure 3.38** (corrected for an error that caused a dip in camera positioning).

In general, the models produce a useful order of magnitude correlation with the experimental data, given the accuracies of experimental measurement (to 1 mm when assessing x), with flow velocities typically accurate to within that limit. Model flow velocities depend on the square of height, which itself was measured to an accuracy of 1 mm (typically a 5 to 10% error). Fluctuations in the model velocities are a function of multimodal height distributions (as described in Chapter 3), and the manifestation of this inaccuracy. For clarity, errors in the centreline velocity model, intended as a guide, are not produced on this composite plot. Nevertheless, beyond experimental errors it is clear that the models predict an increase in velocity downflow, as a function of an increase in flow height.

However such models ignore the importance of downstream stiffening, and the influence this has on upstream dynamics. Surface temperature (and thus viscosity) was not measured as a function of x, but the pervasiveness of the warm channel suggests that advection was strong and cooling weak in the proximal channel; but rheological changes may be approximated by increasing viscosity with downslope distance. This would be a simple solution to dynamically complex effect, but would factor in the frictions involved to a first order analysis. Furthermore, though syrup does develop clear surfacial channel constructs, they are not pervasive, and a Newtonian rectangular channel or infinite sheet model does not account for a more complex velocity distribution.

The 1999 Cameroonian lavas are better suited for channel velocity analysis, displaying clear channel structures of dominantly rectangular habit. While more complex models for Bingham channel flow have recently been formulated (Tallarico and Dragoni 2000), we restrict analysis to a more immediately tractable Newtonian model. Channel widths of Cameroonian lavas are of the order 10-100 m, and 1-10 m deep. Tallarico and Dragoni (1999) show that for the comparison of viscosities derived from channel flow models, the simpler cylindrical model compares well with a rectangular model when a/b is between 1 and 1.13 (< 10% error); while the infinite sheet flow model offers less than 10% error compared to the rectangular model when $a/b > 3.9$.

The parameterisation of the Newtonian rectangular channel model means that if any four of channel width, depth, slope, centreline velocity or viscosity are known, the fifth parameter can be calculated. While a great many excellent channel sections were observed and measured in

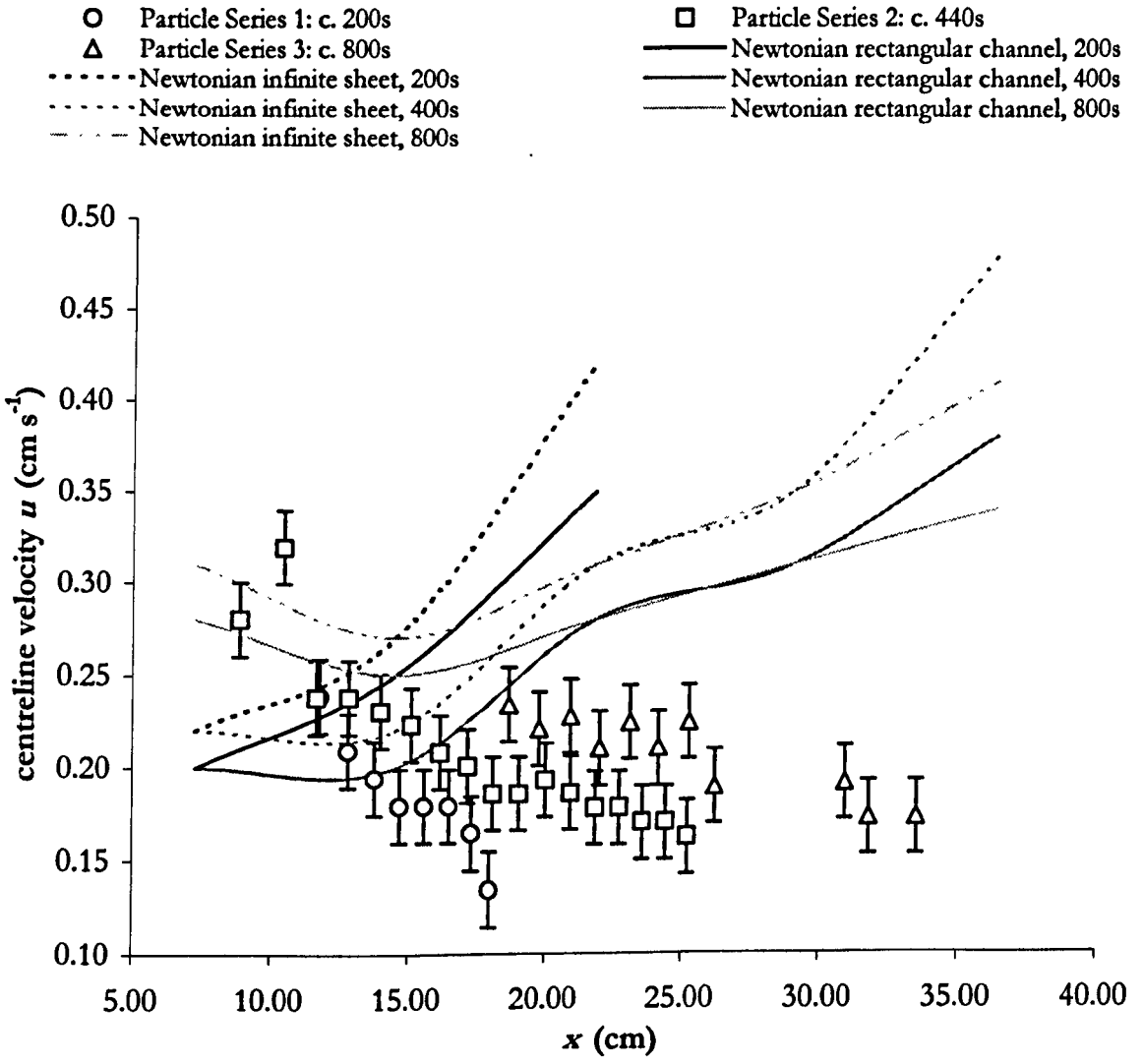

Figure 5.14 Comparisons between experimental tracer particle centreline velocities, and those predicted by a Newtonian infinite sheet flow model (Dragoni et al. 1995) and Newtonian rectangular channel flow model (Tallarico and Dragoi 1999).

Cameroon (see **Sections I** to **XIV**), the data provide only a and good estimates of h and θ. Only a few active velocity measurements were recorded, and allow the calculation of an apparent flow viscosity and flow rate. Otherwise assumptions of typical viscosities from lava temperatures may allow approximate estimates of likely flow rates or, more importantly, local flow rates.

Proximal to the site 2 vents, lava channels 3-6 m deep and 3-5 m wide typically recorded centreline channel velocities of 5 ms^{-1}. Assuming that the distance from the vent (c. 100 m) allows us to

approximate the thermally immature lavas as Newtonian, reference to such channels typically rectangular channel and subsequent use of (eq. 5.20) suggests lava viscosities of 1350 Pa s to 3910 Pa s (on a 15° slope), and 635 Pa s to 1845 Pa s (on a 7° slope). Such viscosities are typical for a highly thermally immature, proximal basanite. If we take such viscosities as typical for site 2 proximal channels, local mass and volume flow rates for other near-vent structures can be estimated. A local volumetric flow rate for a rectangular channel can be calculated as (Tallarico and Dragoni 1999)

$$Q = \frac{\rho g \sin\theta}{3\eta} a h^3 \left(1 - \frac{384}{\pi^5} \frac{h}{a} \sum_{n=1,3,5...}^{\infty} \frac{1}{n^5} \tanh \frac{n\pi a}{4h} \right) \tag{5.22}$$

where parameters and variables are as described before, and Q is a local volumetric flow rate.

Assuming that the height of a channel marks the high-stand mark of a lava flow and channel at its maximum flow rate, the small near-bocca channel depicted in **Plates 4.12, 4.13, 4.25** etc. would suggest flow rates of 0.33 to 0.1 $m^3 s^{-1}$. If one assumes, given its proximity to the source, that the above viscosity estimates are on the high side, the flow rate could rise to 1 to 2 $m^3 s^{-1}$. Downstream of this narrow channel lay a larger structure, described in **Plate 4.27.** With a depth of 6 m and sited on a 14° slope, this channel would suggest exceedingly high flow rates for the viscosities estimated above (200 to 10^3 $m^3 s^{-1}$!). Although this channel was one of the main feeders of the distal Bakingili flows, the rates for 'source' viscosities are absurdly excessive, and viscosities of the order of 10^5 Pa s produce volumetric flow estimates of ~8 $m^3 s^{-1}$.

A further channel near the site 2 vents, approximately 5.7 m wide and 1.4 m deep on a 14° slope, suggests $Q \sim 5.2$ $m^3 s^{-1}$ at higher viscosity estimates (3910 Pa s). Distal channels are more difficult to analyse in that considerable heights and low angles of slope, combined with the necessity of charting flow propagation, produced measurements of flow front kinematics, rather than channel velocity. Furthermore, the extreme thermal maturity of the Bakingili flow fronts would suggest that a simple isoviscous Newtonian model of channel dynamics for the distal channels is grossly over-simplistic.

5.5 Summation

In summation, experimental and field investigations have sought to shed greater light on elements of the processes of lava emplacement dynamics. Though the syrup flows are not wholly reconcilable with the more complex lavas of Mount Cameroon, they inform their analysis considerably. Processes that occur in lavas, previously considered a function of plastic mechanics alone, also develop in cooled viscous flows. While plasticity and brittle mechanics may still provide a dominant force in many examples of lava flow development, they need to be considered alongside the effects of a stiff viscous phase that can initiate or exacerbate folding and channelisation, and influence lava propagation overall.

The influence of cooling on extrusions of syrup has been described qualitatively, and expanded upon with reference to the concept of a Peclet number (Pe) and viscosity contrast between syrup at cooled and extrusion temperatures (R). While absolute cooling and rheological change as a function of the ambient temperature and R are important, the effects are exacerbated by a *relative cooling* of the flow as a function of the ratio of heat transport via advection to diffusion in a flow. The advection of hot syrup from the source is governed by the flow rate (Q) and the angle of slope (θ) onto which the syrup is extruded; increasing the value of either increases the level of advection and thus decreases the amount of relative cooling.

In the absence of a full dynamical model, coupling thermal and spatial evolution of a cooling viscous slope-borne flow, a simple analysis shows that syrup flows propagate downslope in a manner similar to isothermal extrusions, but with an apparent bulk viscosity that increases to some power of time. This exponent of time, β, is typically a constant, and itself varies with Pe and R. The delineation of trends based on gradients and variable power laws is problematic, and exact formulations of Pe and β are difficult to extract from the data. Nevertheless the general trends are clear. Though we lack the data to apply such models to Cameroonian flows, the Lonquimay lavas are well-modelled by a time-dependent bulk viscosity, following the trends noted by Fink and Zimbelman (1990).

Similar flow morphologies develop in experimental analogues and real lavas. The folding results obtained for the experiments suggest that the folding model of Fink and Fletcher (1978) accurately explains the distribution and size of the pressure ridge features developed in Cameroon, and the folds witnessed in the experimental extrusions of cooling Golden Syrup. Though the reasons for compression in both mediums (real and analogue) can vary, the apparent applicability of a viscous buckling model to complex rheological fluids such as lava does imply that the development of

strong viscosity gradients with cooling remain an active component in lava deformation, even in thermally mature lavas that have propagated some distance from their vents.

Levee structures in the 1999 Mount Cameroon lavas display characters indicative of a range of geneses. *Accretionary*, *rubble* and *overflow* levees require levels of solidification, plasticity, thermal interaction and variations in flow rate that are not present in syrup, or for that matter other analogues. However the proto-levees of lava flows, *initial levees*, form at early times from a largely simple viscoplastic fluid. In such a process, the results of cooled viscous flows are highly appropriate for cross-analysis. Although syrup does not possess a yield strength, the effects of cooling are exacerbated by the development of surface textures. Cooling in a temperature-dependent viscous system repeats many of the processes of marginal stiffening and stagnation that lead to levee formation.

Cooling of the surface skin provides a group of changes that will affect levee development, and the dynamic feedback loops caused by cooling serve to accentuate and perpetuate its effects at the flow flanks. Crystallisation and solidification are therefore favoured along a flow's margins. Levees form not only as a function of limited local movement being unable to supply stresses that overcome yield values, but also as a function of the channelisation of a flow through purely viscous processes. Such processes help create a system in which the effects of any plasticity are exacerbated. Therefore viscous effects must be considered alongside the development of 'plastic levees', and it is hoped that future models of more complex flow systems, incorporating visco-plastic rheologies and solidification, will better demonstrate the interplay between viscous and plastic effects in the generation of lava flow structures.

The concept of channel width as a function of *Pe* is effectively the same as Jon Fink and Ross Griffiths' Ψ (see, for example, Fink and Griffiths 1990, 1992, 1998; Griffiths and Fink 1993, 1997). Detailed models of coupled channel and levee development do not exist, other than by effect in isothermal Bingham flows (Balmforth et al. 2002), yet flow structures such as these can have as dominant an effect on flow dynamics as the rheology, flow rate or slope. Experimental examples will hopefully better inform modellers of the flow behaviour and regimes of lava analogues, and both test and encourage applications of greater complexity.

Rheological effects as a function of cooling are becoming increasingly better modelled. If a temperature-dependent viscosity has in the past been ignored for practical reasons, as a function of its relative importance vis-à-vis plasticity and solidification, it can now be rightly reinserted into analytical systems. This thesis hopes to display a temperature-dependent viscosity's effects in an ideal analogue, illustrates for modellers the processes and structures that accompany its extrusion in slope-borne flows, and highlights its applicability in the study of lava emplacement dynamics.

Appendix A: Experimental Results

The following appendix contains tables of raw data collated from the cooled experiments described in section 3.5, and plots of non-normalised dimensional and temporal variables on liner axes. The eruption parameters displayed in Table 3.1 are repeated here for ease of reference.

Name	Ambient Temp. (°C)	Eruption Temp. (°C)	Slope (°)	Erupt. Pressure (x 10^{-1} M Pa)	Flow Rate (x 10^{-6} m^3 s^{-1})	Viscosity (Pa s)	T^* (s)	X^* &Y^* (cm)
GS-ISO_20_1	22	22	20	0.6	1.9	43.3	6.3	3.2
GS-ISO_10_1	21	21	10	1	3.1	50.5	25.9	7.7
GS-ISO_10_3	23	23	10	0.6	1.9	37.3	23.2	6.3
GS-ISO_15_1	23.5	23.5	15	0.4	1.3	34.6	10.5	3.7
GS-ISO_15_2	23.8	23.8	15	0.8	3.1	33	8.3	4.6
GS-ISO_5_1	22	22	5	0.5	1.8	43.3	105.6	13.0
GS-20_10_3	-19	20.75	10	0.6	4.3	52.5	24.5	8.4
GS-20_10_4	-19	21	10	1	8.6	50.5	20.0	9.9
GS-20_10_6*	-18.5	19	10	0.4	1.0	69.4	43.0	6.3
GS-20_20_1	-19	18.75	20	0.4	1.5	72.3	9.9	3.4
GS-20_20_2	-19	18	20	0.6	2.3	81.7	9.7	3.9
GS-20_20_6	-18.5	21	20	1.1	6.1	50.5	5.3	4.5
GS-20_20_7	-18	22	20	0.8	3.3	43.3	5.5	3.7
GS-20_20_8	-19	21	20	0.3	0.7	50.5	9.0	2.6
GS-20_15_1*	-20	20	15	0.4	1.3	69.4	18.0	4.4
GS-20_15_2	-19.5	19.5	15	0.7	4.3	64	12.5	5.9
GS-20_15_3	-19	20	15	1.1	7.2	69.4	11.7	6.8
GS-20_5_1	-18.5	19	5	0.5	1.8	69.4	151.5	14.6
GS-20_5_2	-18.5	19	5	1	5.4	69.4	115.1	19.2
GS-10_5_1	-9	19.5	5	0.8	3.3	64	122.3	16.7
GS-10_5_2	-8.5	20	5	0.4	1.3	59	146.3	12.8
GS-10_5_3	-7.5	22	5	1.2	10.8	43.3	67.9	20.3
GS-10_15_1	-10	18.5	15	0.8	4.8	75.3	13.7	6.3
GS-10_15_2	-10	18.5	15	0.4	1.8	75.3	17.6	4.9
GS-10_15_3	-9.5	20.5	15	1.2	8.6	54.6	9.3	6.7
GS-10_10_1	-9.5	19	10	0.8	4.8	69.4	29.4	9.3
GS-10_10_2	-10	19.5	10	0.5	1.7	64	35.8	7.0
GS-10_10_3	-8.5	21	10	1.2	10.8	50.5	18.9	10.5
GS-10_20_2	-10	18.5	20	0.4	1.4	75.3	10.3	3.4
GS-10_20_3	-9	20	20	0.6	3.1	59	7.1	3.9
GS-10_20_4	-10	20	20	0.8	6.1	59	5.9	4.6
GS-10_20_5	-9	20	20	1.2	8.6	59	5.5	5.1

Table 3.1 Experimental runs and their parameters. The eruption temperature refers to the temperature of the syrup measured at the point of extrusion into the tank, while the eruption pressure is that placed upon the syrup in the pressure vessel. Flow rate is measured as stated in section 2.2, and viscosity is calculated from the eruption temperature, using the relationships described in section 2.1. T^*, X^* and Y^* are represented time and length scales, based on the work of Lister (1992), and explained in detail in section 3.3.

GS-ISO_5_1

t (s)	x_N (cm)	y_M (cm)	x_N *late-time model* (cm)	y_M *late-time model* (cm)
0	2.0		0.0	
5	2.8		1.0	
10	3.5		1.7	
15	3.9		2.4	
20	4.6		3.0	
25	5.3		3.6	
30	5.8		4.1	
45	7.0		5.6	
60	8.7		7.0	
90	11.0		9.6	
120	13.1		12.0	
150	15.0		14.3	
180	16.8		16.5	
240	20.3		20.6	
300	23.6		24.6	
360	27.0		28.3	
480	33.2		35.4	
600	39.0		42.1	
720	44.7		48.5	
900	52.8		57.7	
1080	60.3		66.5	

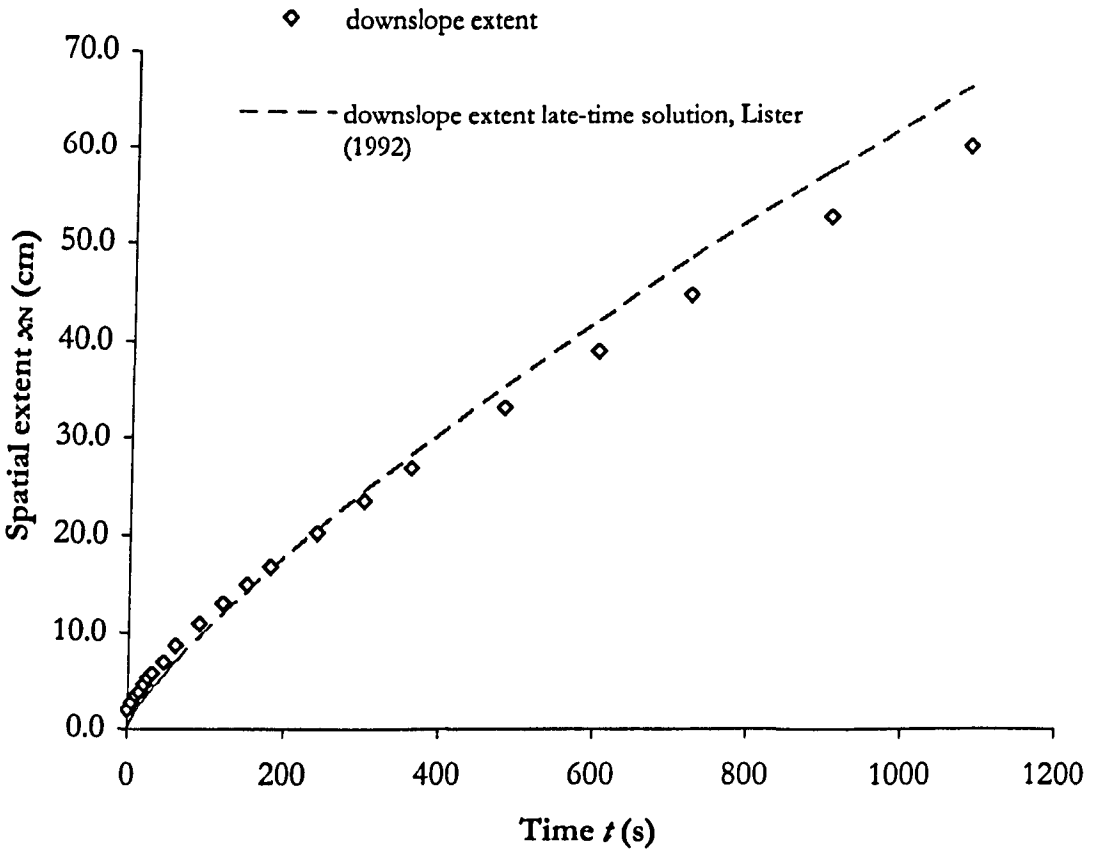

GS-ISO_10_1

t (s)	x_N (cm)	y_M (cm)	x_N *late-time model* (cm)	y_M *late-time model* (cm)
0	2.0		0.0	0.0
5	3.3		1.7	4.4
10	4.9		3.0	5.5
15	6.0	4.0	4.1	6.3
20	6.8		5.1	7.0
25	7.8		6.1	7.5
30	8.8		7.0	8.0
45	11.2		9.7	9.1
60	13.3	7.0	12.1	10.0
90	17.5		16.6	11.5
120	22.1	10.0	20.7	12.7
150	25.5		24.6	13.6
180	28.4	11.0	28.4	14.5
240	35.0		35.5	15.9
300	41.1	13.0	42.3	17.2
360	47.2		48.7	18.3
480	59.0		60.9	20.1
600	70.2	17.0	72.5	21.6

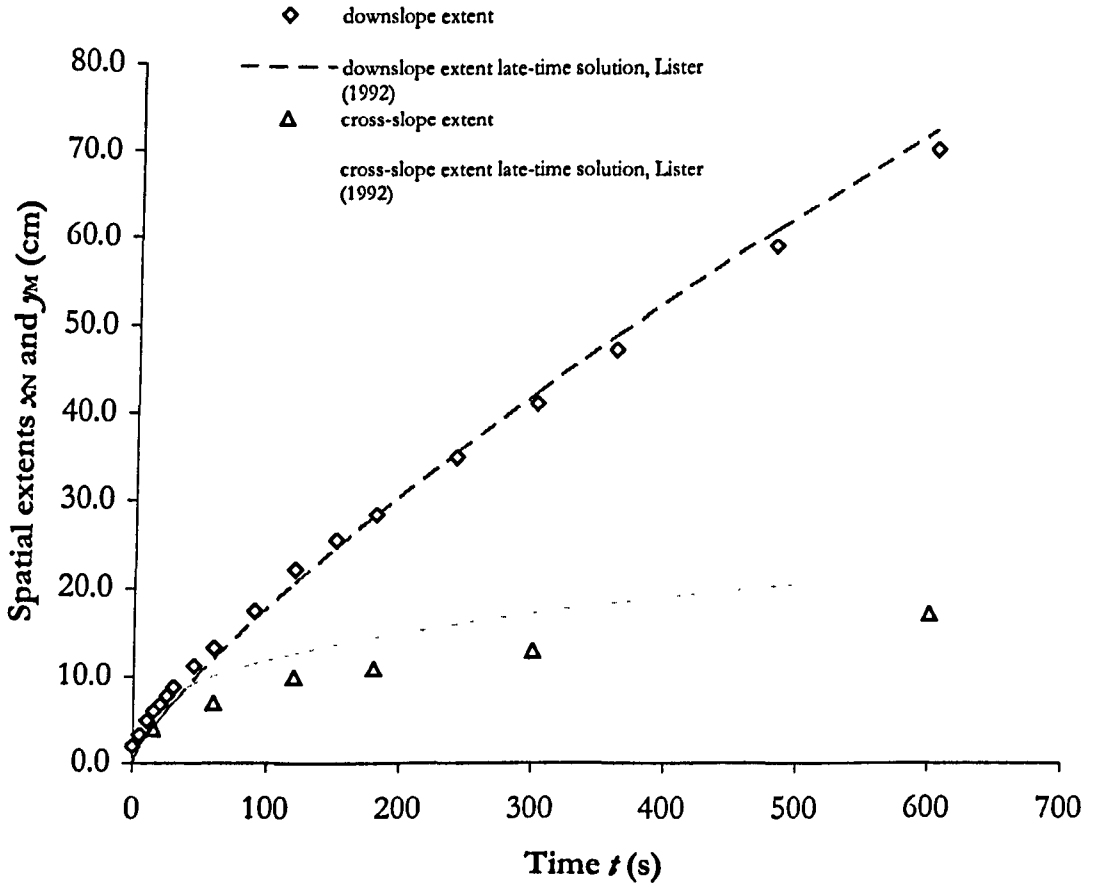

GS-ISO_15_1

t (s)	x_N (cm)	y_M (cm)	x_N *late-time model* (cm)	y_M *late-time model* (cm)
0	2.0		0.0	0.0
5	2.7		1.7	2.9
10	3.4		3.0	3.6
15	4.2		4.0	4.2
20	4.9		5.1	4.6
25	5.7		6.0	5.0
30	6.5	3.0	6.9	5.3
45	8.6		9.5	6.0
60	10.5	3.8	11.9	6.6
90	14.2		16.3	7.6
120	17.5	5.0	20.4	8.4
150	20.6		24.2	9.0
180	23.9	6.0	27.9	9.6
240	29.8		34.9	10.5
300	35.5	6.6	41.6	11.3
360	40.8		47.9	12.0
480	51.1		59.9	13.3
600	61.2		71.3	14.3
720	71.0		82.1	15.2

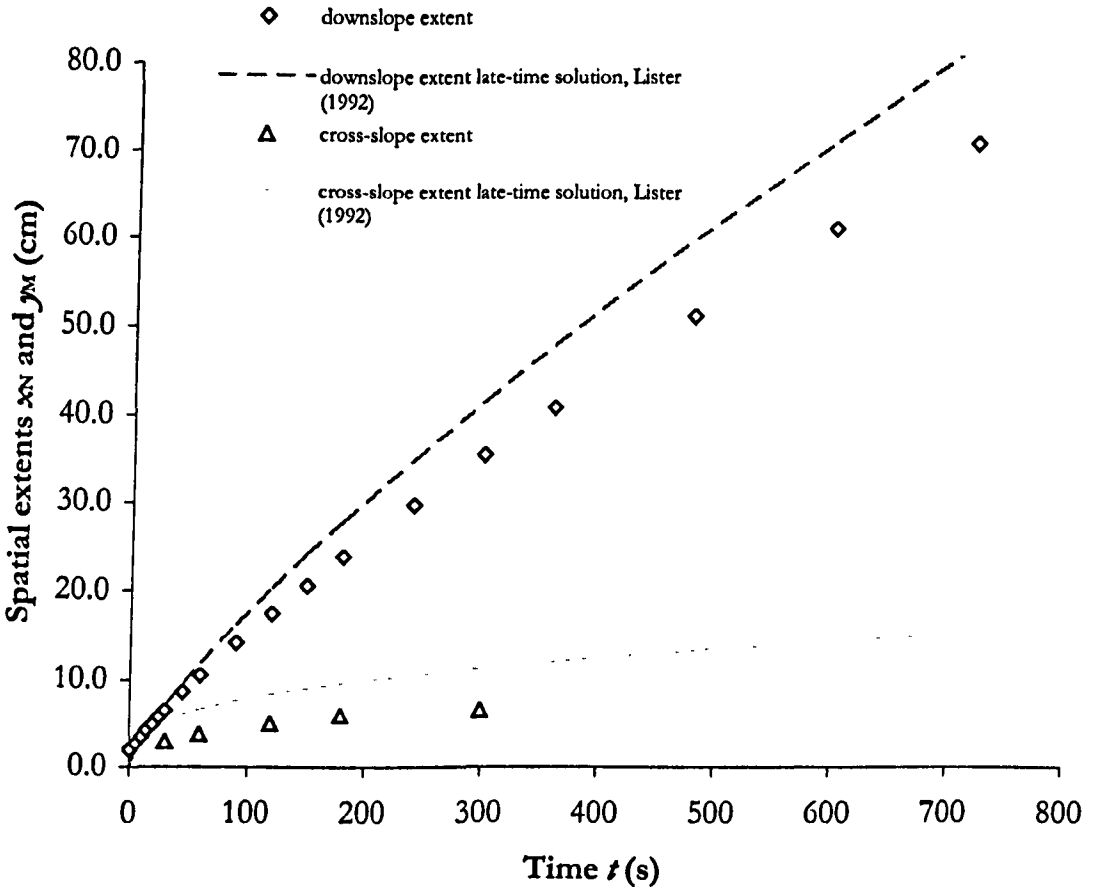

GS-ISO_15_2

t (s)	x_N (cm)	y_M (cm)	x_N *late-time model* (cm)	y_M *late-time model* (cm)
0	2.0		0.0	
5	4.2		2.5	
10	5.5		4.3	
15	7.3		5.9	
20	8.2		7.4	
25	9.5		8.8	
30	11.5		10.2	
45	15.9		14.0	
60	19.2		17.5	
90	25.8		23.9	
120	32.0		29.9	
150	37.5		35.6	
180	42.9		41.0	
240	52.9		51.3	
300	61.6		61.0	
360	69.2		70.3	

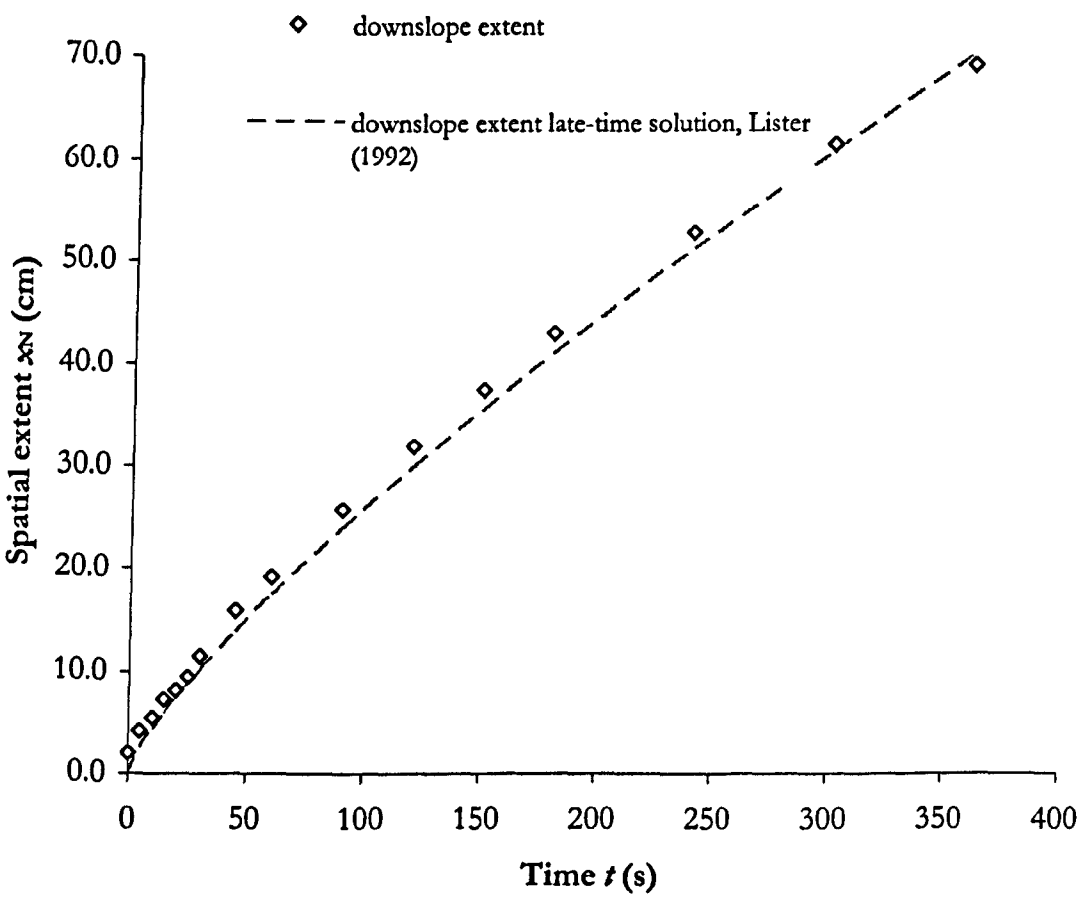

GS-ISO_20_1

t (s)	x_N (cm)	y_M (cm)	x_N *late-time model* (cm)	y_M *late-time model* (cm)
0	2.0		0.0	0.0
5	2.4		2.2	2.9
10	3.7		3.8	3.7
15	5.0		5.1	4.2
20	6.3		6.4	4.7
25	7.6		7.7	5.0
30	8.7		8.8	5.3
45	12.2		12.1	6.1
60	14.9	4.8	15.1	6.7
90	20.3		20.7	7.7
120	25.4	7.0	25.9	8.5
150	30.1		30.9	9.1
180	34.8	7.5	35.6	9.7
240	43.3		44.5	10.7
300	51.6	8.5	52.9	11.5
360	59.4		61.0	12.2
480	74.0		76.3	13.4

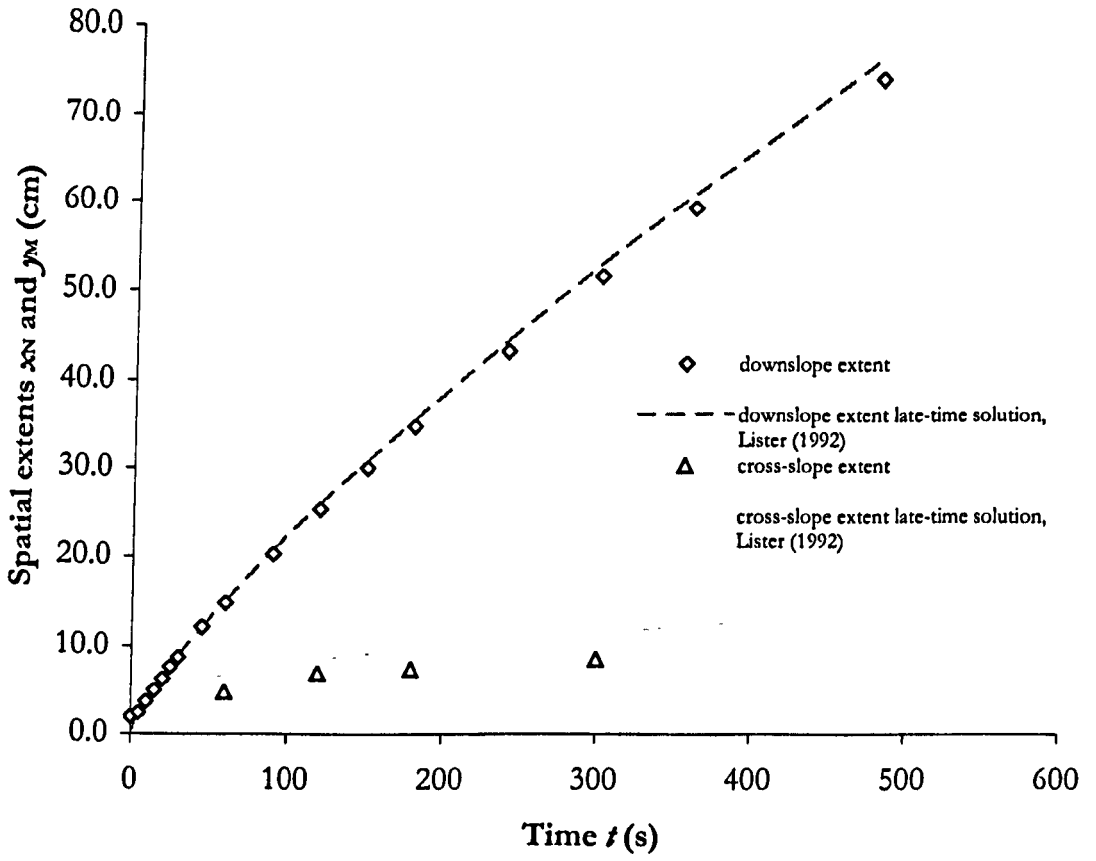

GS-10_5_1

t (s)	x_N (cm)	y_M (cm)	x_N *late-time model* (cm)	y_M *late-time model* (cm)
0	2		0.0	0.0
5	2.8		1.1	5.7
10	3.7	3.3	1.9	7.2
15	4.4		2.7	8.2
20	5.1	4.1	3.3	9.0
25	5.7		4.0	9.7
30	6.2	5	4.6	10.3
45	7.7	6.1	6.3	11.8
60	9.2	6.9	7.9	13.0
90	11.3	8.2	10.8	14.9
120	13.3	9.3	13.5	16.4
150	15.1	10.2	16.0	17.7
180	16.8	10.9	18.5	18.8
240	19.9	12.2	23.1	20.7
300	23	13.6	27.5	22.2
360	25.8	14.3	31.6	23.6
480	31.3	15.9	39.6	26.0
600	36.2	17.1	47.1	28.0
720	40.6	18.1	54.3	29.8
840	45	19.3	61.2	31.4
960	49.2	20	67.9	32.8
1080	52.8	20.7	74.4	34.1
1200	56.4	21.3	80.7	35.3
1320	59.8	21.7	86.9	36.5
1440	63.4		93.0	37.5
1560	66.8		99.0	38.5

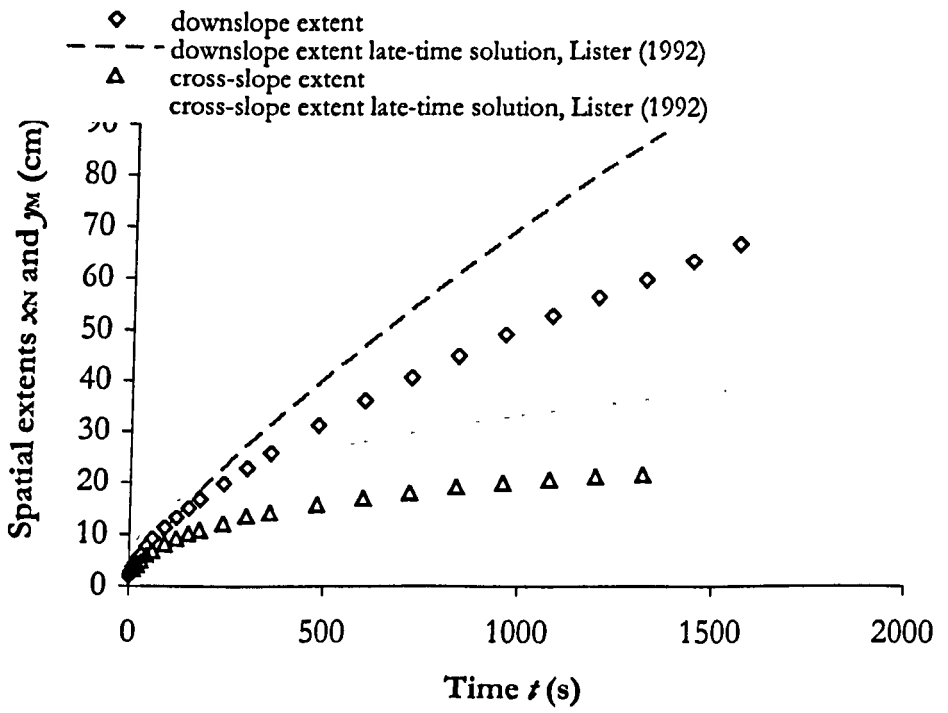

GS-10_5_2

t (s)	x_N (cm)	y_M (cm)	x_N *late-time model* (cm)	y_M *late-time model* (cm)
0	2		0.0	0.0
5	4.7	3.6	0.8	4.1
10	5		1.3	5.2
15	5.4		1.8	5.9
20	5.7		2.2	6.5
25	5.8		2.7	7.0
30	6.2	4.6	3.1	7.5
45	7.1	5	4.2	8.6
60	7.9		5.3	9.4
90	9	6.2	7.2	10.8
120	10.2		9.0	11.9
150	11.3	7.5	10.7	12.8
180	12.4		12.3	13.6
240	14.4	8.8	15.4	15.0
300	16.2		18.4	16.1
360	18	10.1	21.2	17.1
480	21.3		26.5	18.9
600	24.3	12	31.5	20.3
720	27.2		36.3	21.6
840	29.4	13.2	40.9	22.7
960	31.5		45.4	23.8
1080	33.7	14.1	49.7	24.7
1200	35.7		54.0	25.6
1320	37.9	14.9	58.1	26.4
1440	40.2		62.2	27.2
1560	42.3	15.8	66.2	27.9
1680	44.6	16.1	70.1	28.6

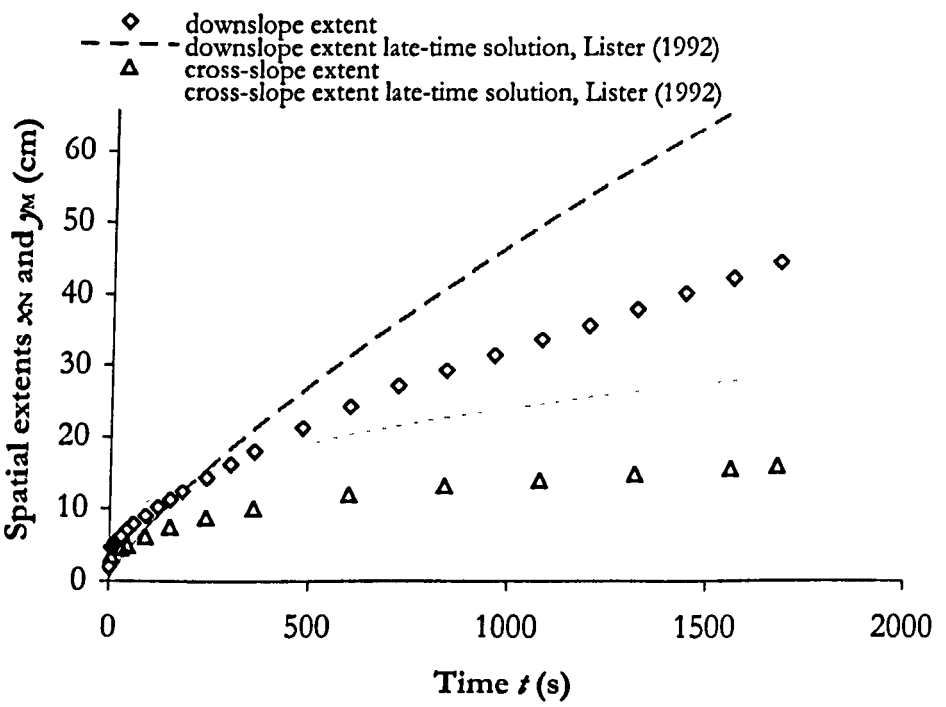

GS-10_5_3

t (s)	x_N (cm)	y_M (cm)	x_N *late-time model* (cm)	y_M *late-time model* (cm)
0	2		0.0	0.0
5	4.2	3.7	2.2	8.4
10	6.1		3.7	10.6
15	7.8	6.2	5.1	12.1
20	9		6.4	13.4
25	10.2		7.6	14.4
30	11.3	8.5	8.8	15.3
45	14.3	10.2	12.1	17.5
60	17.1	11.8	15.1	19.3
90	22.1	14	20.7	22.1
120	26.4	16	25.9	24.3
150	30.7	17.4	30.8	26.2
180	34.6	18.7	35.5	27.8
240	41.8	20.8	44.4	30.6
300	48.9	22.5	52.8	32.9
360	55.4		60.8	35.0
480	66.7		76.1	38.5

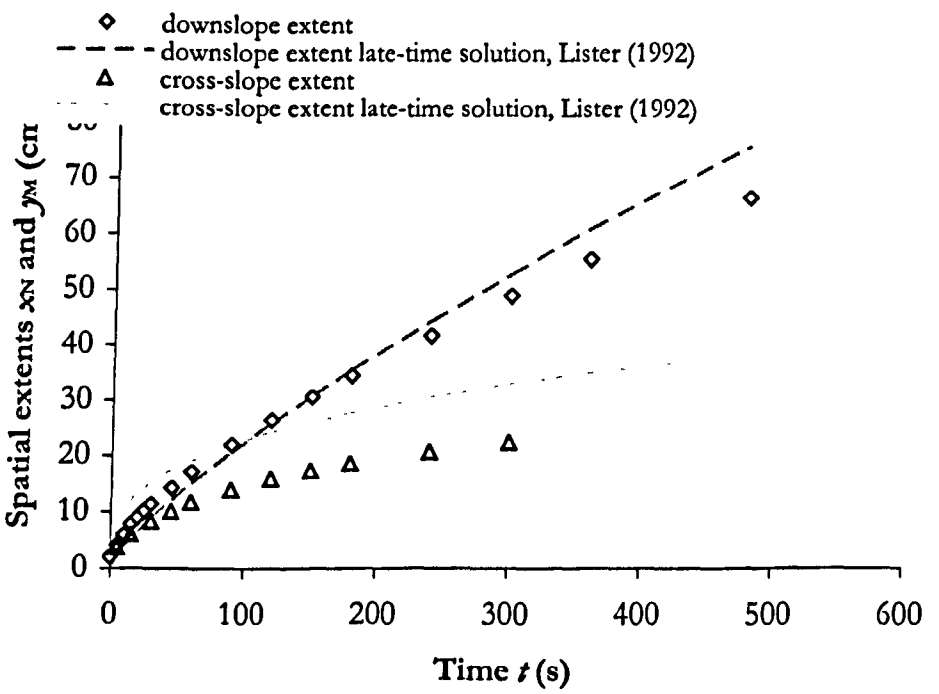

GS-10_10_1

t (s)	x_N (cm)	y_M (cm)	x_N *late-time model* (cm)	y_M *late-time model* (cm)
0	2		0.0	0.0
5	3.5		1.9	5.1
10	4.7	3.6	3.3	6.4
15	5.7		4.5	7.3
20	6.7	4.8	5.6	8.1
25	7.7		6.7	8.7
30	8.5	5.8	7.7	9.2
45	10.9	6.7	10.6	10.6
60	13	7.7	13.2	11.6
90	16.8		18.1	13.3
120	20.4	10.1	22.7	14.7
150	23.7		27.0	15.8
180	27	11.8	31.1	16.8
240	32.7		38.9	18.5
300	38.2	13.9	46.3	19.9
360	43.7		53.3	21.2
480	53.7	15.9	66.7	23.3
600	62.7		79.3	25.1
720	70.8	18	91.4	26.7

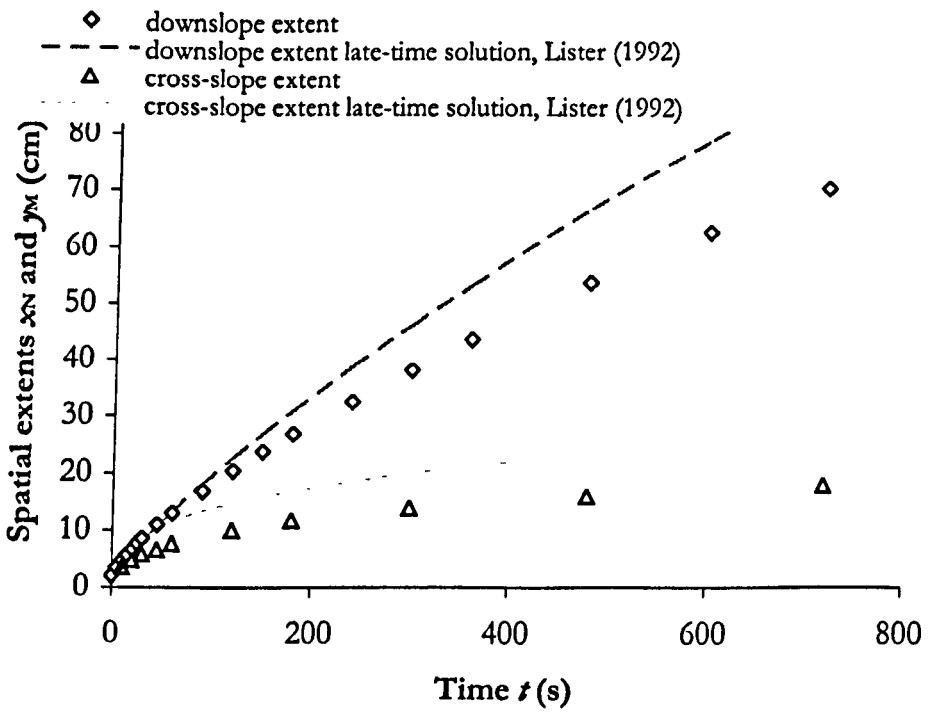

GS-10_10_2

t (s)	x_N (cm)	y_M (cm)	x_N *late-time model* (cm)	y_M *late-time model* (cm)
0	2		0.0	0.0
5	3		1.2	3.6
10	3.6		2.1	4.6
15	4.2	3.1	2.9	5.2
20	4.8		3.7	5.7
25	5.4		4.4	6.2
30	5.9	4	5.0	6.6
45	7.6	4.7	6.9	7.5
60	8.7	5.2	8.6	8.3
90			11.8	9.5
120	13	7.1	14.8	10.4
150	14.8	7.7	17.6	11.2
180	16.6	8.1	20.3	11.9
240	20	9	25.4	13.1
300	23.4	9.7	30.2	14.2
360	26.2	10.1	34.8	15.0
480	32.2	11.2	43.5	16.6
600	36.8	12	51.8	17.8
720	42.1	12.5	59.6	19.0
840	46.9	13	67.2	20.0
960	51.2	13.5	74.6	20.9
1080	55.1	13.8	81.7	21.7
1200	58.7	14.1	88.7	22.5
1440	66.4	14.6	102.2	23.9
1680	74.2	15	115.3	25.1

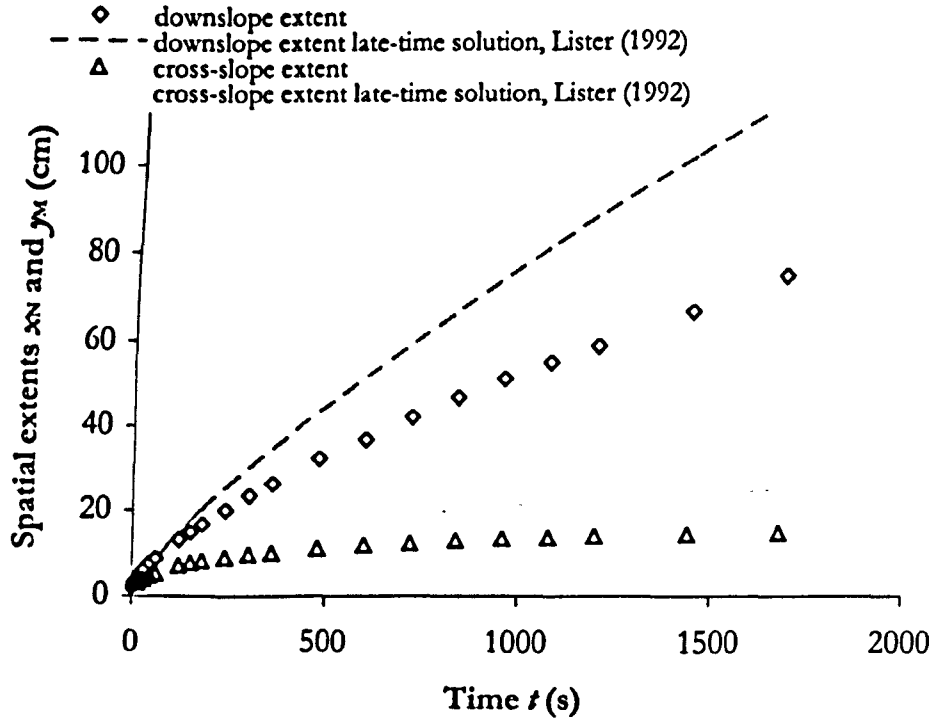

GS-10_10_3

t (s)	x_N (cm)	y_M (cm)	x_N *late-time model* (cm)	y_M *late-time model* (cm)
0	2		0.0	0.0
5	4.6	3.7	3.1	6.7
10	6.8	4.8	5.2	8.4
15	8.7	5.9	7.2	9.6
20	10.3	6.5	9.0	10.6
25	12	7.3	10.7	11.4
30	13.4	7.9	12.3	12.1
45	17.3	9.4	16.9	13.9
60	21	10.6	21.1	15.3
90	27.5	12.4	28.9	17.5
120	33.3	13.8	36.2	19.2
150	38.8	15.1	43.0	20.7
180	44.2	16.1	49.6	22.0
240	53.6	17.9	62.0	24.2
300	62.3	19.1	73.8	26.1
360	70.5	20	85.0	27.7
480			106.3	30.5

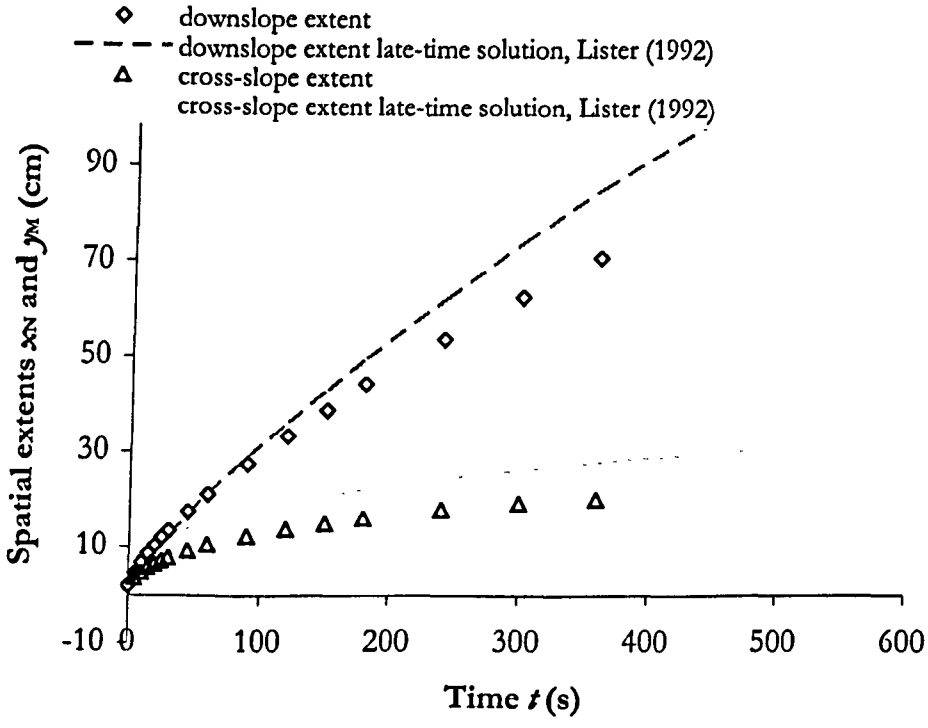

GS-10_15_1

t (s)	x_N (cm)	y_M (cm)	x_N *late-time model* (cm)	y_M *late-time model* (cm)
0	2		0.0	0.0
5	4		2.3	4.4
10	5.7	3.3	4.0	5.6
15	7.2		5.5	6.4
20	8.6	4.5	6.9	7.0
25	9.9		8.2	7.6
30	11	5.4	9.4	8.0
45	14.1	6.2	12.9	9.2
60	17	7.1	16.1	10.1
90	21.9	8.3	22.1	11.6
120	26.3	9.2	27.7	12.8
150	30.4	9.9	32.9	13.7
180	34.3	10.4	37.9	14.6
240	41.2	11.6	47.5	16.1
300	47.7	12.1	56.5	17.3
360	53.3	12.9	65.1	18.4
480	64.3	14	81.4	20.3
600	74.9	14.7	96.8	21.8

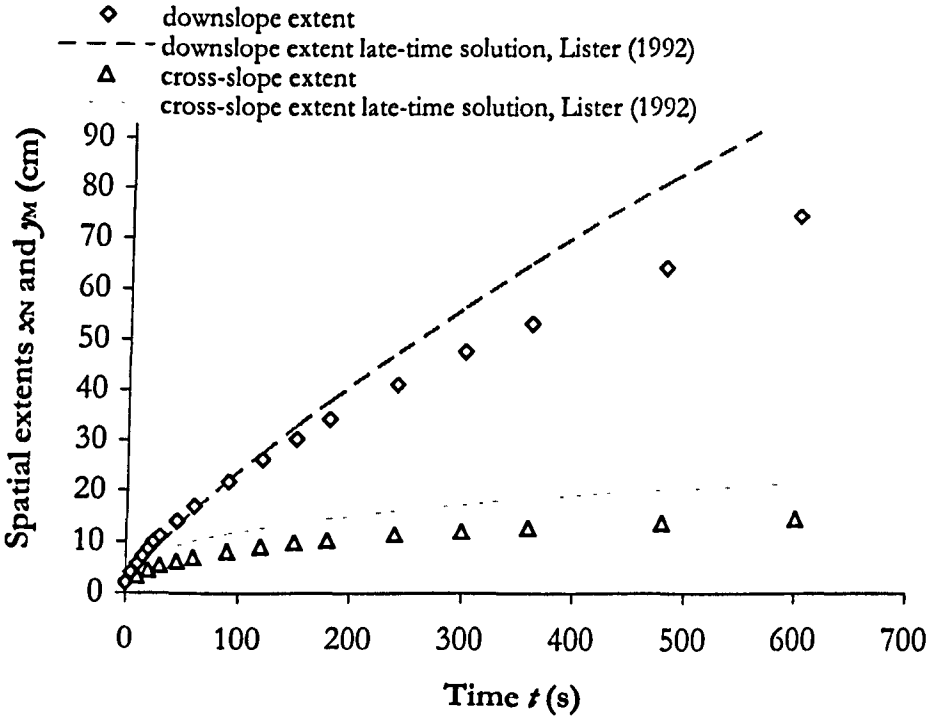

GS-10_15_2

t (s)	x_N (cm)	y_M (cm)	x_N *late-time model* (cm)	y_M *late-time model* (cm)
0	2		0.0	0.0
5	3.8		1.5	3.2
10	4.7		2.6	4.0
15	5.6	3.2	3.5	4.6
20	6.4		4.4	5.1
25	7.3	3.6	5.3	5.5
30	8.1		6.1	5.8
45	10	4.3	8.3	6.6
60	11.7	5.1	10.4	7.3
90	14.8	6	14.3	8.4
120	17.5	6.6	17.9	9.2
150	19.9	7.1	21.3	9.9
180	22.4	7.4	24.5	10.5
240	26.8	8.1	30.7	11.6
300	30.7	8.8	36.5	12.5
360	34.2	9.1	42.0	13.3
480	40.8	9.9	52.6	14.6
600	47.9	10.5	62.6	15.7
720	54.6	10.9	72.1	16.7
840	60.2	11.3	81.3	17.6
960	66.1	11.8	90.2	18.4
1080	70.7	12	98.8	19.1
1200	76.4	12.1	107.2	19.8
1320		12.2	115.5	20.5

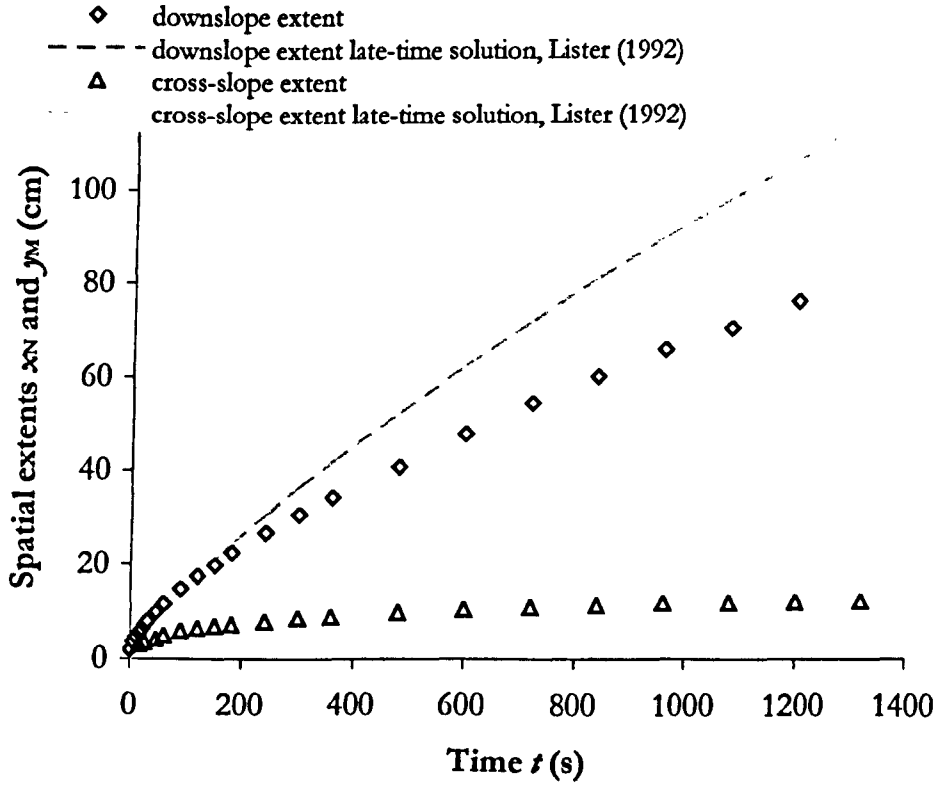

GS-10_15_3

t (s)	x_N (cm)	y_M (cm)	x_N *late-time model* (cm)	y_M *late-time model* (cm)
0	2		0.0	0.0
5	4.6	3.1	3.4	5.4
10	6.9	4.4	5.8	6.8
15	8.8	5.2	7.9	7.8
20	10.4	5.9	9.9	8.5
25	12.1	6.6	11.8	9.2
30	13.8	7.1	13.6	9.8
45	18.1	8.5	18.7	11.2
60	22.1	9.5	23.3	12.3
90	29.3	10.9	32.0	14.1
120	35.9	12.2	40.0	15.5
150	42.2	13.1	47.6	16.7
180	48.2	13.9	54.8	17.8
240	59.5	15.1	68.6	19.6
300	70.1	16.2	81.6	21.1

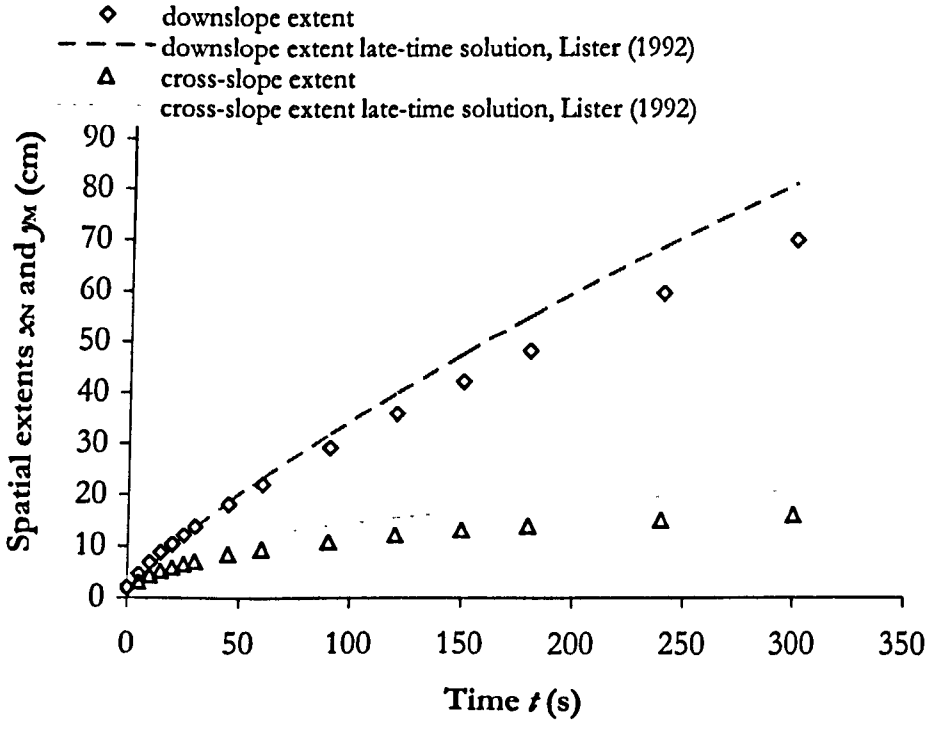

GS-10_20_2

t (s)	x_N (cm)	y_M (cm)	x_N *late-time model* (cm)	y_M *late-time model* (cm)
0	2		0.0	0.0
5	3.2		1.6	2.7
10	4		2.8	3.4
15	4.8		3.8	3.9
20	5.6	2.6	4.7	4.2
25	6.2		5.6	4.6
30	7	3.2	6.5	4.9
45	9	3.8	8.9	5.6
60	10.5	4.2	11.1	6.1
90	13.5	4.8	15.2	7.0
120	16.2	5.4	19.0	7.7
150	18.5	5.7	22.6	8.3
180	20.8	6	26.1	8.8
240	25.4	6.7	32.6	9.7
300	29.4	7.1	38.8	10.5
360	33.5	7.6	44.7	11.1
480	40.5	8.1	55.9	12.2
600	47.3	8.5	66.5	13.2
720	53.9	8.9	76.6	14.0
840	60.2	9.3	86.4	14.7
960	66.7	9.6	95.8	15.4
1080	72.5	9.8	105.0	16.0
1200	77.7	10.1	114.0	16.6

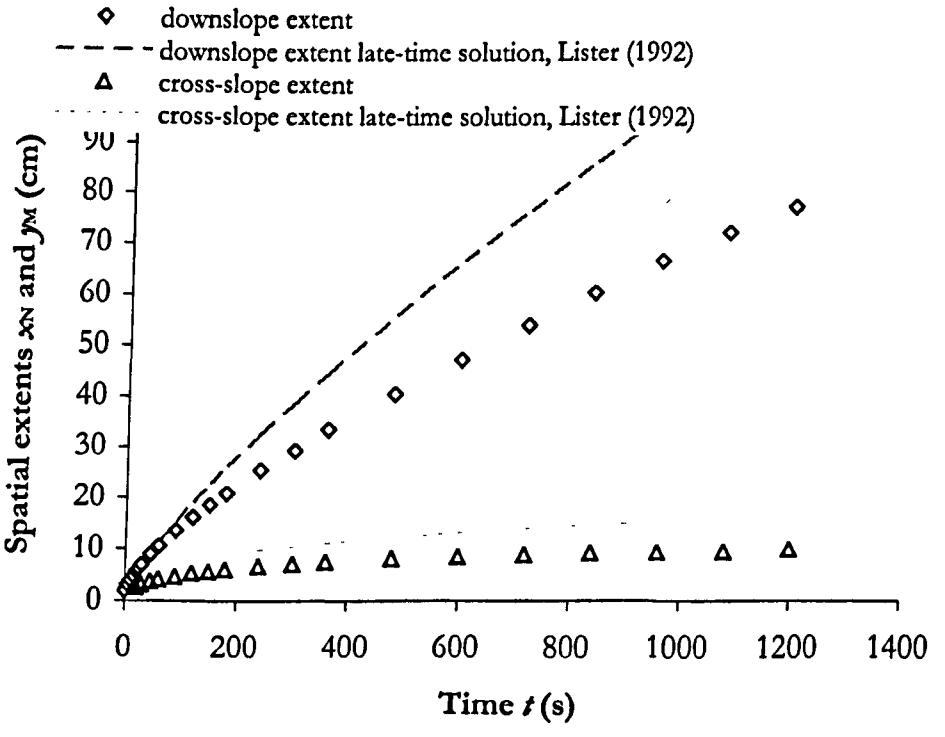

GS-10_20_3

t (s)	x_N (cm)	y_M (cm)	x_N *late-time model* (cm)	y_M *late-time model* (cm)
0	2		0.0	0.0
5	4.4		2.4	3.4
10	5.2		4.2	4.3
15	7.1		5.7	5.0
20	8.7		7.2	5.5
25	9.5		8.6	5.9
30	10.1		9.9	6.3
45	14.2	5	13.5	7.2
60	17	5.7	16.9	7.9
90	22.3	6.4	23.2	9.0
120	27.1	7.1	29.0	9.9
150	30.1	7.6	34.5	10.7
180	34.1	8	39.7	11.4
240	39.4	8.8	49.7	12.5
300	44.8	9.6	59.1	13.5
360	50.3	10	68.1	14.3
480	60	10.8	85.2	15.8
600	69.2	11.7	101.3	17.0
720	78.6	12.3	116.7	18.1
900			138.9	19.5

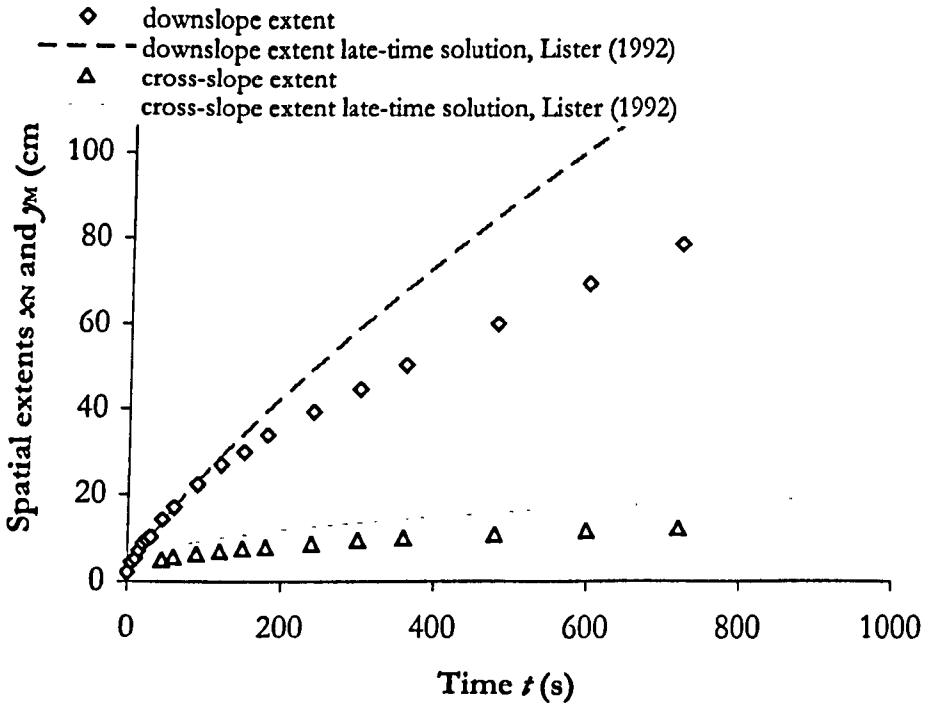

t (s)	x_N (cm)	y_M (cm)	x_N *late-time model* (cm)	y_M *late-time model* (cm)
0	2		0.0	0.0
5	4		3.3	4.3
10	5.9	3.3	5.7	5.5
15	8		7.8	6.3
20	9.6	4.5	9.8	6.9
25	11.2		11.6	7.4
30	12.7	5.5	13.4	7.9
45	16.5	6.7	18.4	9.0
60	20	7.3	23.0	9.9
90	26.5	8.3	31.5	11.4
120	32.3	9.3	39.4	12.5
150	37.7	9.9	46.9	13.5
180	42.8	10.4	54.0	14.3
240	51.9	11.4	67.6	15.8
300	59.8	12.1	80.4	17.0
360	67.9	12.7	92.6	18.1
480	71.5	13.8	115.9	19.9

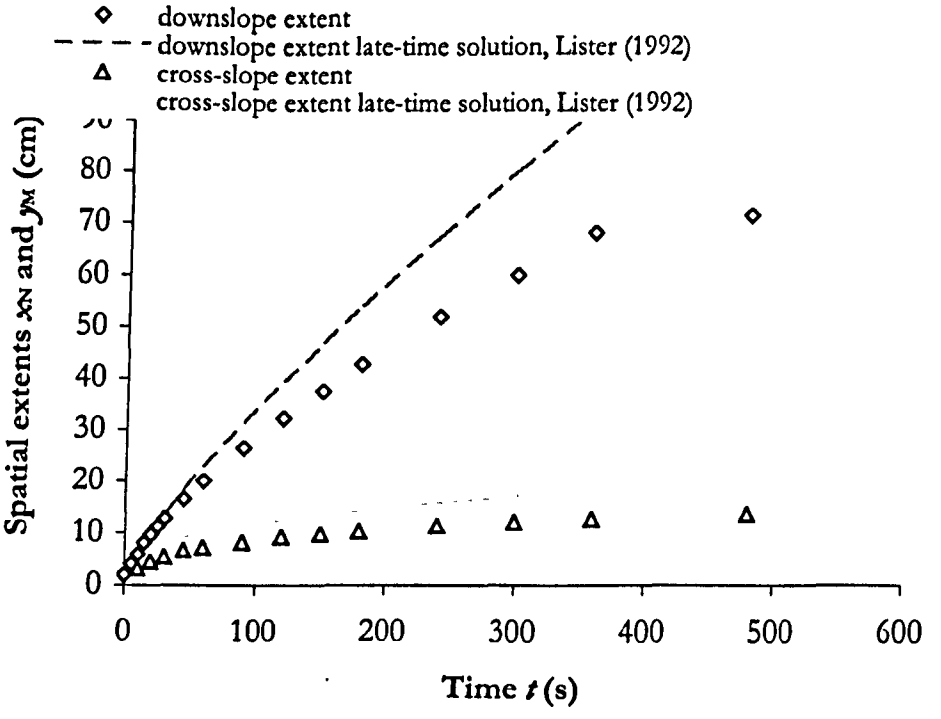

GS-10_20_5

t (s)	x_N (cm)	y_M (cm)	x_N *late-time model* (cm)	y_M *late-time model* (cm)
0	2		0.0	0.0
5	4.8	2.7	3.9	4.9
10	7.4	3.9	6.6	6.1
15	9.9	4.6	9.1	7.0
20	12.1	5.5	11.4	7.7
25	14.1	6.1	13.5	8.3
30	16.1	6.6	15.6	8.8
45	21.4	7.4	21.4	10.1
60	26.2	8.2	26.7	11.1
90	34.7	9.5	36.6	12.7
120	42.2	10.3	45.8	14.0
150	48.7	11.2	54.5	15.1
180	55.4	11.9	62.8	16.0
240	67.2	13	78.5	17.7
300	78	13.9	93.4	19.0
360			107.6	20.2
480			134.6	22.2

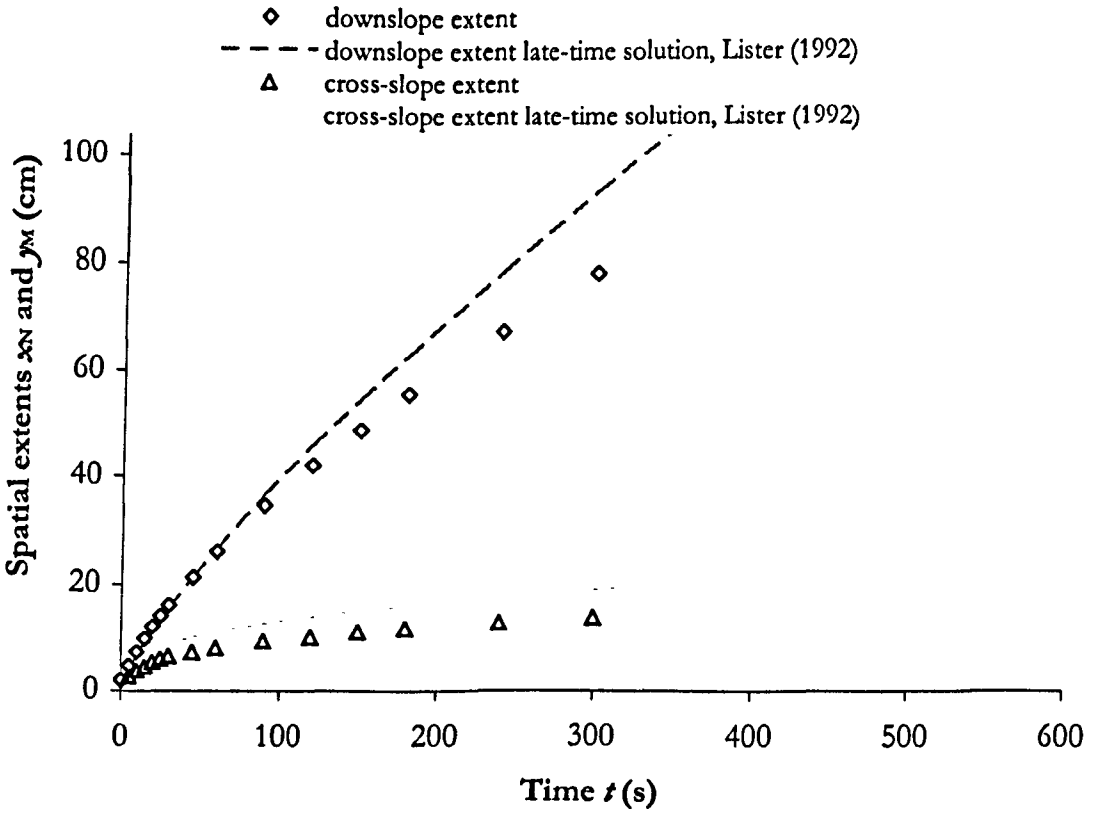

GS-20_5_1

t (s)	x_N (cm)	y_M (cm)	x_N *late-time model* (cm)	y_M *late-time model* (cm)
0	2		0.0	0.0
5	2.6		0.8	4.6
10	3.2		1.4	5.8
15	3.6	3.1	2.0	6.7
20	4		2.5	7.3
25	4.4		2.9	7.9
30	4.8	4	3.4	8.4
45	5.8	4.9	4.7	9.6
60	6.8	5.4	5.8	10.6
90	8.3	6.2	8.0	12.1
120	9.6	7.1	10.0	13.4
150	10.9	7.7	11.9	14.4
180	12.1	8.3	13.7	15.3
240	14.2	9.3	17.1	16.8
300	16.2		20.3	18.1
360	18	10.9	23.4	19.3
480	21.3		29.3	21.2
600	24.4	12.9	34.9	22.8
720	27.5		40.2	24.3
840	30.3	14.4	45.3	25.5
960	33		50.3	26.7
1080	35.5	15.5	55.1	27.8
1200	38.1	16	59.8	28.8

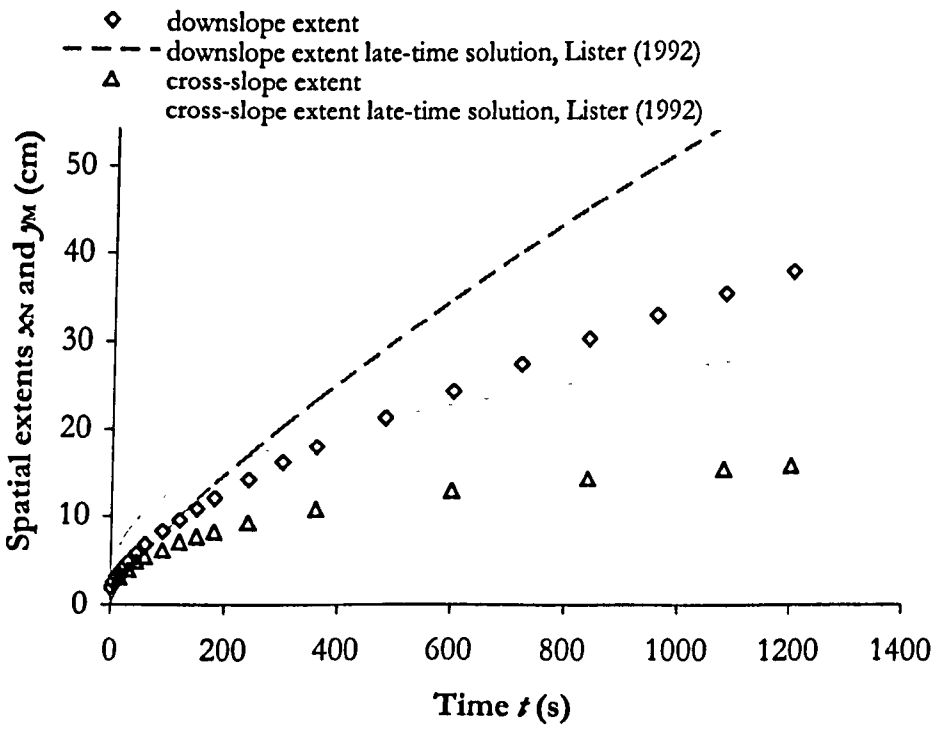

t (s)	x_N (cm)	y_M (cm)	x_N *late-time model* (cm)	y_M *late-time model* (cm)
0	2		0.0	0.0
5	2.9		1.4	6.7
10	4.1	3.5	2.4	8.4
15	5.2		3.2	9.6
20	6.1	5	4.0	10.6
25	6.9		4.8	11.4
30	7.6	6.3	5.5	12.1
45	10.2	7.7	7.6	13.9
60	12.2	8.8	9.5	15.3
90	15.5		13.0	17.5
120	17.8	11.4	16.3	19.3
150	20		19.3	20.8
180	21.7	12.9	22.3	22.1
240	24.9		27.9	24.3
300	27.9	15.5	33.2	26.2
360	31.2		38.2	27.8
480	37.8	18.1	47.8	30.6
600	43.9		56.9	33.0
720	49.7	20.2	65.5	35.0
840	54.9		73.9	36.9
960	60		82.0	38.5
1080	64.3		89.8	40.1
1200	68.3		97.5	41.5

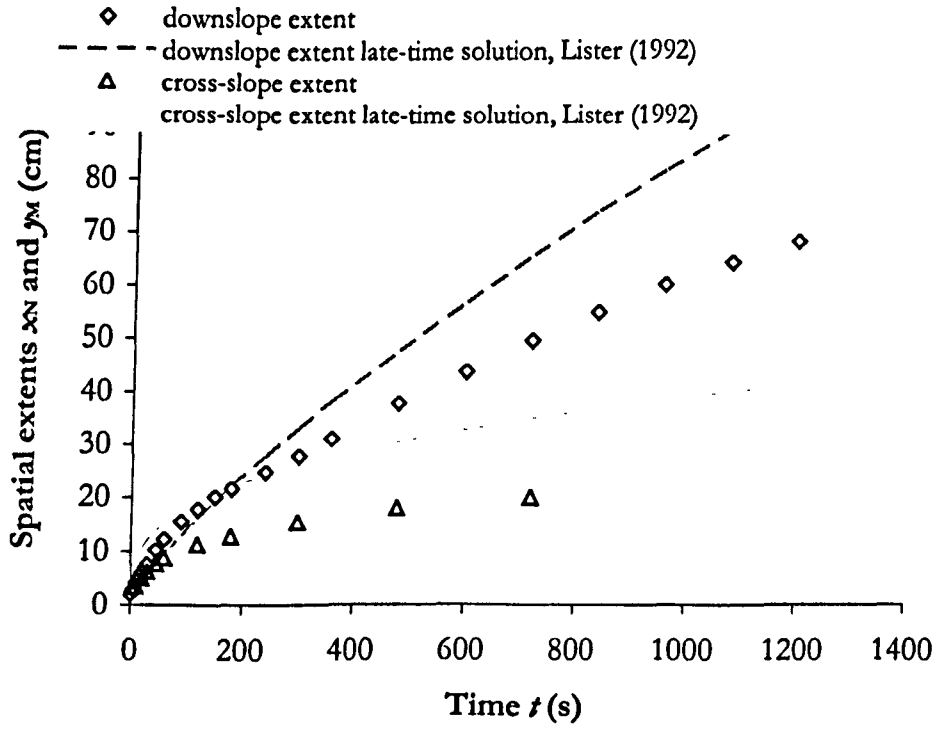

GS-20_10_3

t (s)	x_N (cm)	y_M (cm)	x_N *late-time model* (cm)	y_M *late-time model* (cm)
0	2		0.0	0.0
5	4.4		2.0	4.9
10	6.2		3.4	6.2
15	7.8		4.7	7.1
20	9.2		5.9	7.8
25	10.5		7.0	8.4
30	11.6		8.1	8.9
55	16.4	8	13.0	10.9
80	20.4	9.3	17.3	12.4
105	24.1	10.3	21.4	13.5
130	27.3	11.1	25.3	14.5
155	30.3	11.7	29.0	15.4
205	36.5	12.6	36.0	16.9
305	46.8	14.1	49.1	19.3
405	55.7	15.1	61.2	21.2
505	64.2	16.1	72.6	22.9
605	74.1	16.9	83.6	24.3
705	80	17.6	94.2	25.6

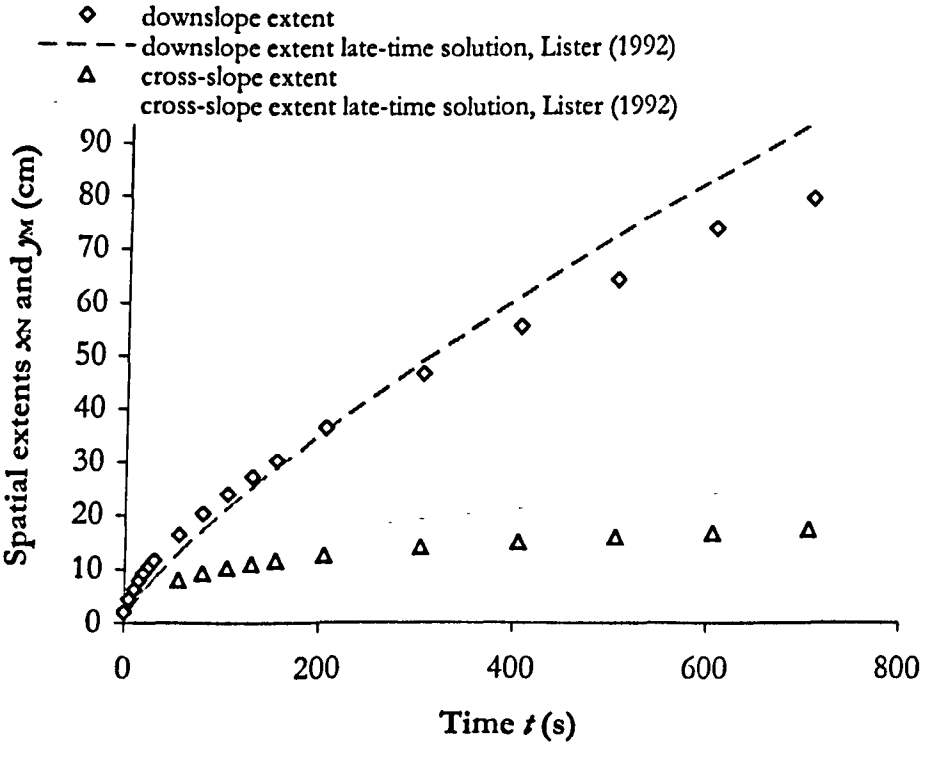

GS-20_10_4

t (s)	x_N (cm)	y_M (cm)	x_N *late-time model* (cm)	y_M *late-time model* (cm)
0	2		0.0	0.0
5	3.6		2.8	6.2
10	6.5	4.4	4.7	7.8
15	9		6.5	8.9
20	11.1	6.3	8.1	9.8
25	12.8		9.7	10.6
30	14.5	7.7	11.1	11.2
45	19	9.3	15.3	12.9
60	23.1		19.1	14.2
90	30.1	12.2	26.2	16.2
120	36.2		32.8	17.8
150	41.6	14.3	39.0	19.2
180	46.5		44.9	20.4
240	56	16.5	56.2	22.5
300	64.6		66.8	24.2
360	72	19	77.0	25.7
420	80		86.8	27.1
480		20.5	96.3	28.3

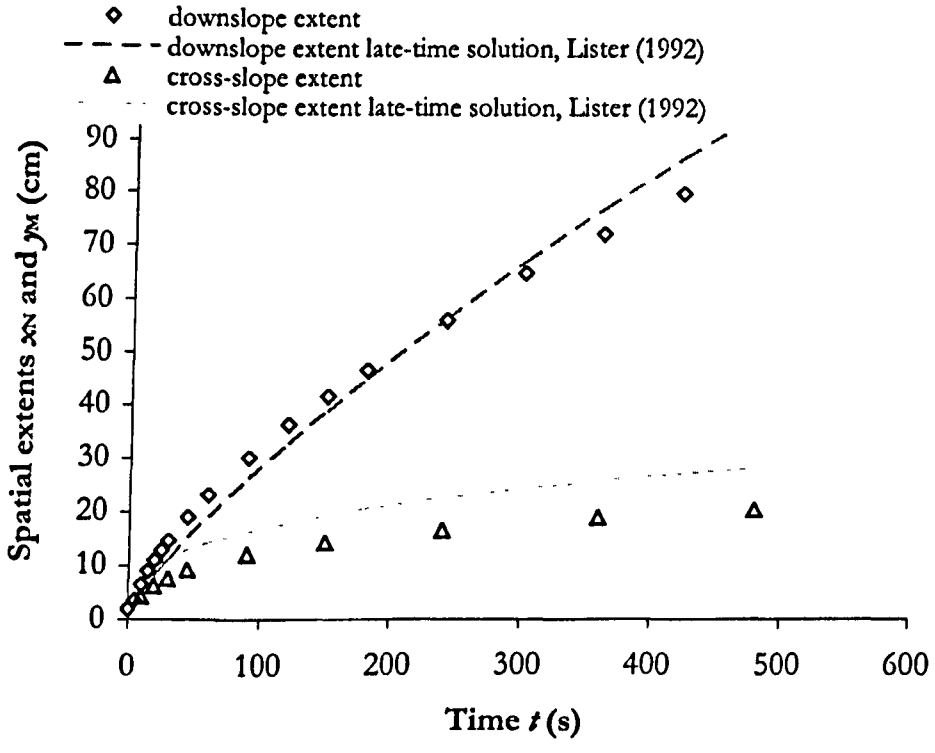

GS-20_10_6

t (s)	x_N (cm)	y_M (cm)	x_N *late-time model* (cm)	y_M *late-time model* (cm)
0			0.0	0.0
5	3.1		1.1	3.1
10	3.8		1.9	3.9
15	4.5		2.6	4.4
20	5.1		3.2	4.9
25	5.5		3.8	5.2
30	6.1	4	4.4	5.6
45	7.6		6.0	6.4
60	8.6		7.5	7.0
90	10.7	6	10.3	8.0
120	12.6		12.9	8.9
150	14.1		15.3	9.5
180		7.5	17.6	10.1
240	18.8	8.3	22.1	11.2
300	21.7	8.9	26.2	12.0
360	24.4		30.2	12.8
480	29.4	10	37.8	14.0
600	34.1	10.5	45.0	15.1
720	38.1	10.75	51.8	16.1
840	41.9		58.4	16.9
960	45.8	11.5	64.8	17.7
1080	51.6	11.8	71.0	18.4
1200	60.9	12.5	77.1	19.1
1320	68.2	13.3	83.0	19.7

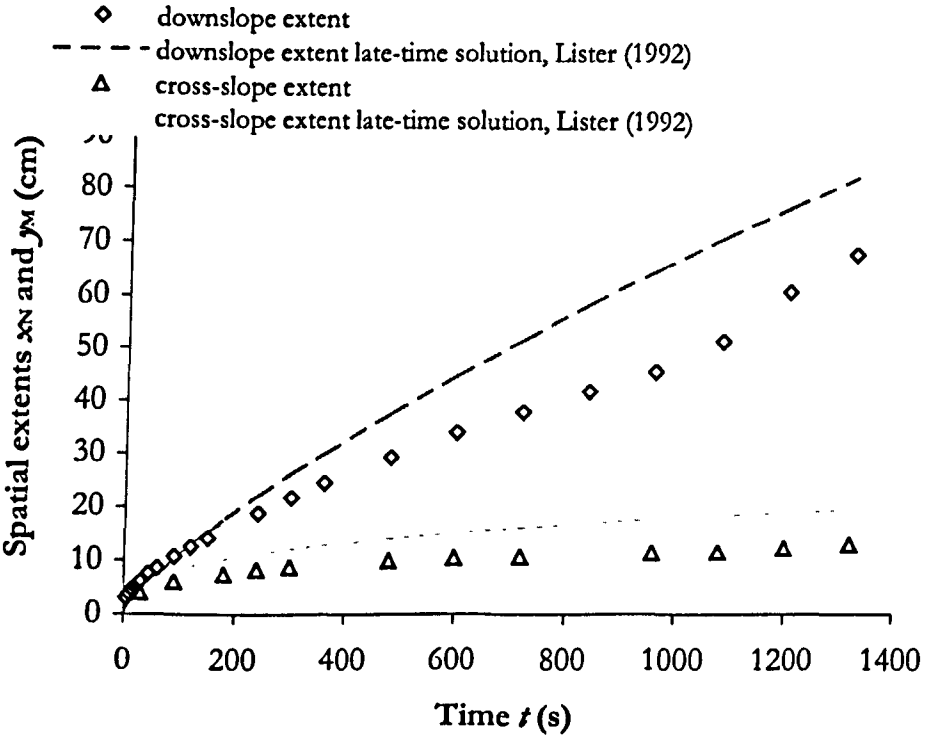

GS-20_15_1

t (s)	x_N (cm)	y_M (cm)	x_N *late-time model* (cm)	y_M *late-time model* (cm)
0	2.0		0.0	0.0
5	3.3		1.3	2.7
10	4.4		2.2	3.5
15	5.2		3.0	4.0
20	6.0		3.7	4.4
25	6.9		4.4	4.7
30	7.5		5.1	5.0
45	9.3	4.1	7.0	5.7
60	10.9	4.8	8.8	6.3
90	13.5	5.8	12.0	7.2
120	16.1		15.0	7.9
150	18.7	6.9	17.9	8.5
180	20.7		20.6	9.1
240	24.4	8	25.8	10.0
300	27.6	8.5	30.7	10.7
360	30.9	9.1	35.4	11.4
480	37.5	9.9	44.2	12.6
600	44.0	10.4	52.6	13.5
720	50.2		60.6	14.4
840		11.2	68.3	15.1
960	62.4	11.5	75.8	15.8
1080	68.1		83.1	16.5
1200	74.2	11.9	90.2	17.0
1320	79.8	12.1	97.1	17.6

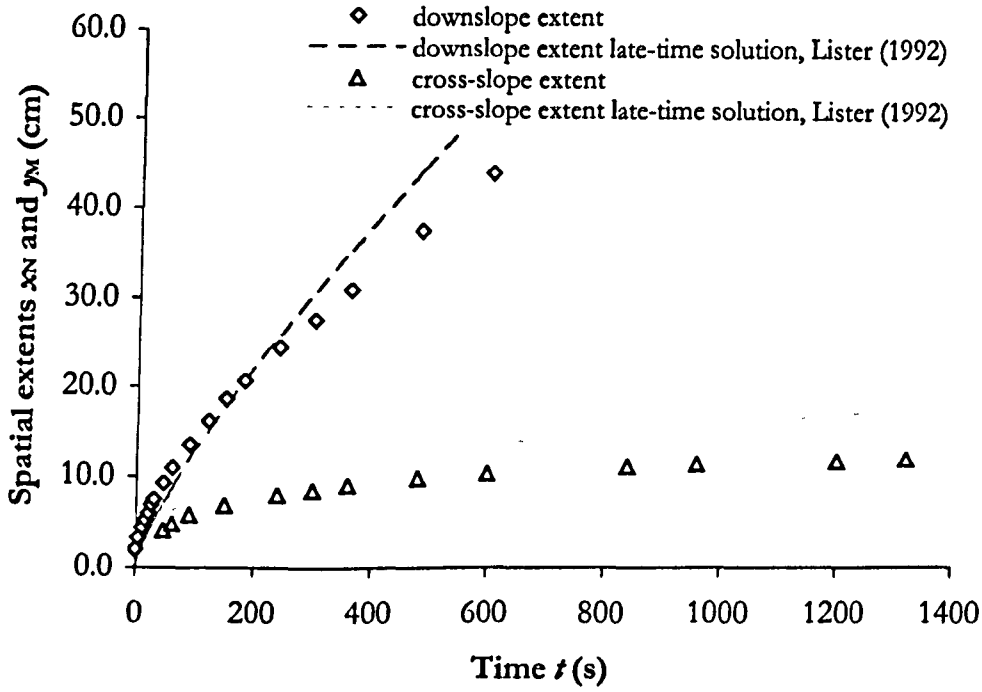

GS-20_15_2

t (s)	x_N (cm)	y_M (cm)	x_N *late-time model* (cm)	y_M *late-time model* (cm)
0	2		0.0	0.0
5	3.7		2.4	4.3
10	5.4	3.3	4.0	5.4
15	7.1		5.5	6.2
20	8.5	4.4	6.9	6.8
25	9.6		8.2	7.3
30	11.1	5.3	9.5	7.8
45	14.7	6.2	13.0	8.9
60	18	6.9	16.3	9.8
90	23.4	7.7	22.3	11.2
120	27.9	8.5	27.9	12.3
150	31.9	9.2	33.2	13.3
180	35.5	9.7	38.2	14.1
240	42.4	10.3	47.8	15.5
300	48.6	11	56.9	16.7
360	54.7	11.8	65.5	17.8
420	60	12.2	73.9	18.7
480	65.5	12.6	82.0	19.6
600	76	13	97.5	21.1

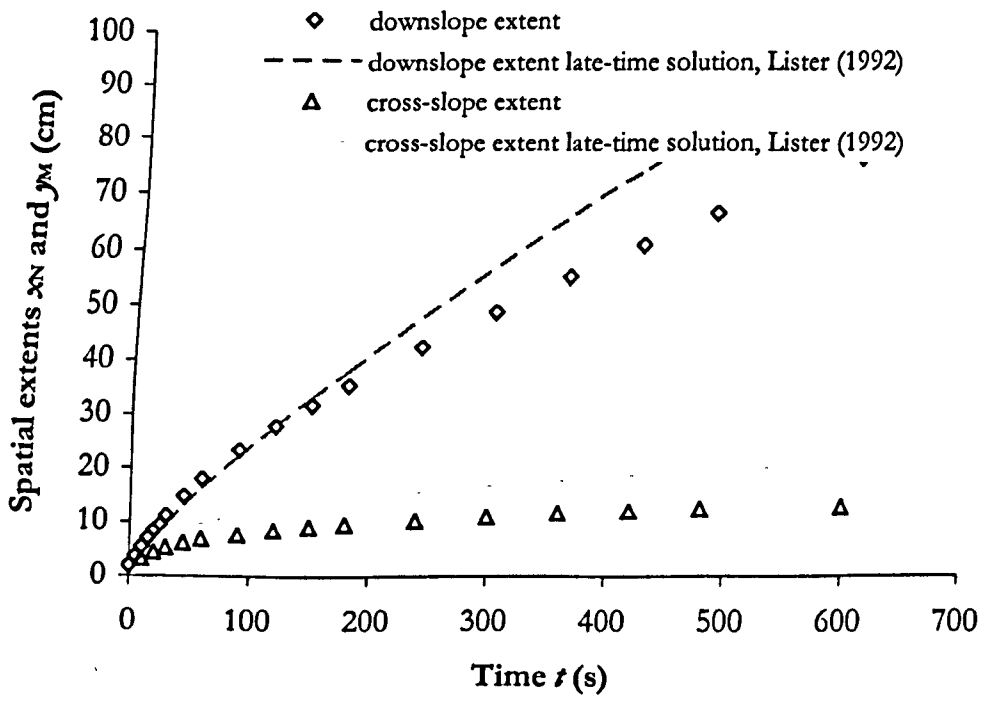

GS-20_15_3

t (s)	x_N (cm)	y_M (cm)	x_N *late-time model* (cm)	y_M *late-time model* (cm)
0	2		0.0	0.0
5	5.2	3.3	2.9	5.1
10	7.8	4.3	4.9	6.4
15	9.9	5	6.8	7.3
20	11.7	5.7	8.5	8.0
25	13.4	6.3	10.1	8.7
30	15.1	6.8	11.6	9.2
45	19.4	7.8	15.9	10.5
60	23.2	8.7	19.9	11.6
90	30	9.8	27.2	13.3
120	36.1	10.8	34.1	14.6
150	41.5	11.5	40.5	15.7
180	46.7	12.2	46.7	16.7
240	55.5	13.2	58.4	18.4
300	63.3	14.1	69.5	19.8
360	70.5	14.7	80.1	21.1
420	77.9	15.4	90.2	22.2

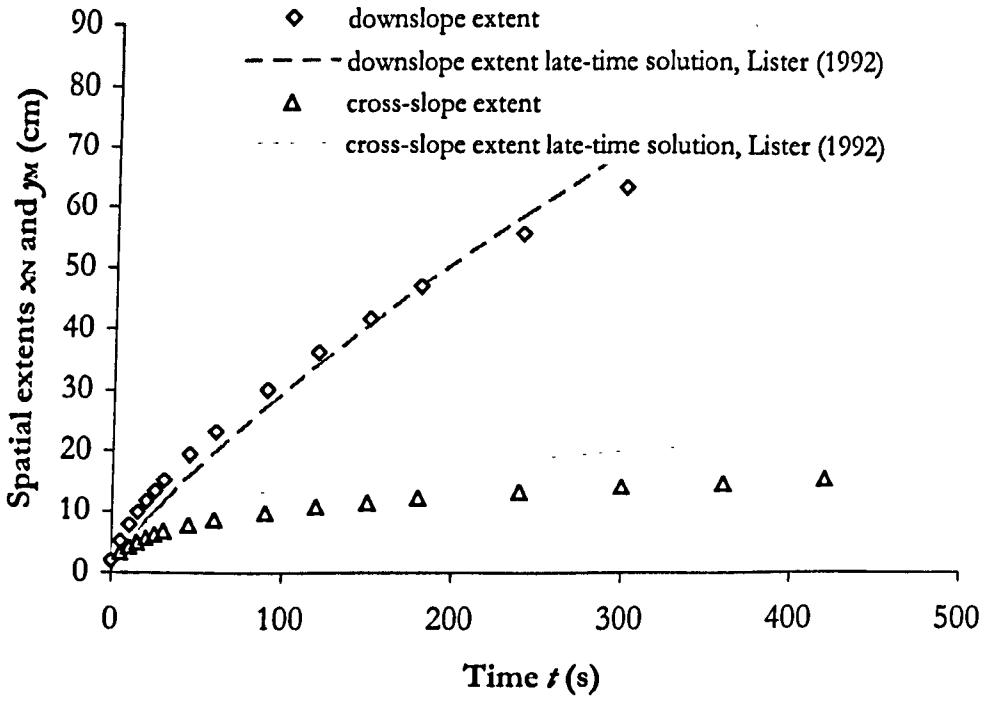

GS-20_20_1

t (s)	x_N (cm)	y_M (cm)	x_N *late-time model* (cm)	y_M *late-time model* (cm)
0	2		0.0	0.0
5	2.8		1.7	2.7
10	4		2.8	3.4
15	5.2		3.9	3.9
20	6.2		4.9	4.3
25	7.3	3	5.8	4.6
30	8.1		6.7	4.9
45	10.3	3.8	9.1	5.6
60	12.4	4.1	11.4	6.2
90	15.7	4.8	15.7	7.1
120	18.6	5.3	19.6	7.8
150	21.1	5.8	23.3	8.4
180	23.7	6	26.8	8.9
240	28.1	6.6	33.6	9.8
300	32.1	6.8	39.9	10.6
360	35.8	7.3	46.0	11.2
480	43	7.7	57.5	12.4
600	49.6	8	68.4	13.3
720	55.9	8.4	78.9	14.2
840	62	8.6	88.9	14.9
960	67.2	8.7	98.7	15.6
1080	72	8.9	108.1	16.2
1200	79.5	9	117.3	16.8
1320		9.1	126.4	17.3

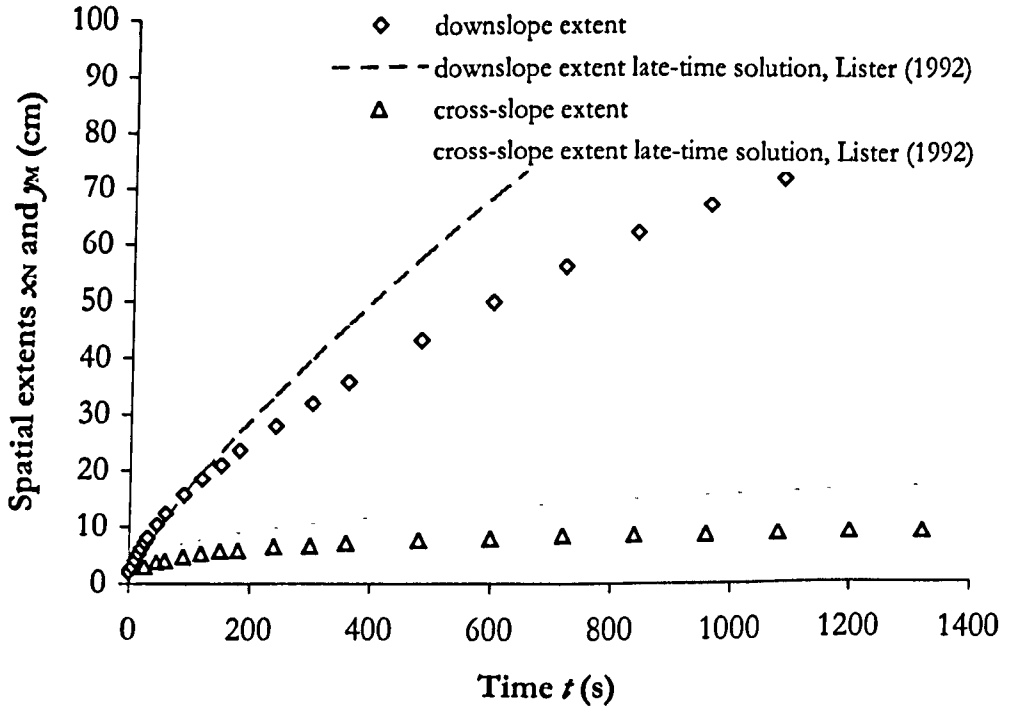

GS-20_20_2

t (s)	x_N (cm)	y_M (cm)	x_N *late-time model* (cm)	y_M *late-time model* (cm)
0	2		0.0	0.0
5	3.4		1.9	3.1
10	4.8		3.3	3.9
15	6		4.5	4.5
20	7.1		5.6	4.9
25	8.3		6.7	5.3
30	9.2		7.7	5.7
45	11.8	4.4	10.6	6.5
60	13.9	5	13.2	7.1
90	17.9	5.8	18.1	8.2
120	21.3	6.2	22.7	9.0
150	24.4	6.8	27.0	9.7
180	27.3	7.2	31.1	10.3
240	32.8	7.9	38.9	11.3
300	37.9	8.3	46.3	12.2
360	42.6	9	53.3	12.9
480	49.9	9.8	66.7	14.2
600	54.9	10	79.3	15.3
720	58.7	10.5	91.4	16.3
840	65.5	10.9	103.0	17.2
960	73.5	11.3	114.3	18.0
1080	80	11.6	125.3	18.7
1200			136.0	19.3

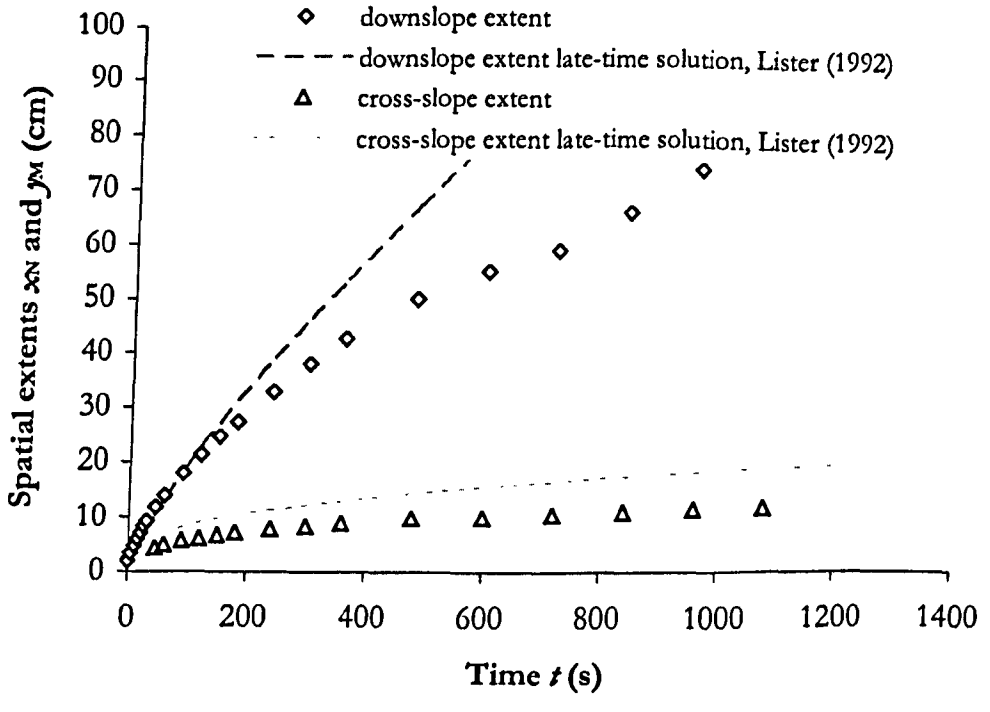

GS-20_20_6

t (s)	x_N (cm)	y_M (cm)	x_N *late-time model* (cm)	y_M *late-time model* (cm)
0	1.9	2	0.0	0.0
5	4.2		3.5	4.3
10	6.3		6.0	5.5
15			8.2	6.3
20			10.3	6.9
25			12.3	7.4
30			14.1	7.9
45		6.7	19.4	9.0
60		7.7	24.2	9.9
90		8	33.2	11.4
120	26.1	8.6	41.5	12.5
150	31.9	9.1	49.4	13.5
180	37.5	9.8	56.9	14.3
240	47.0	11.2	71.2	15.8
300	56.1	12.1	84.7	17.0
360	64.4	13	97.6	18.1
480	79.9	14	122.0	19.9

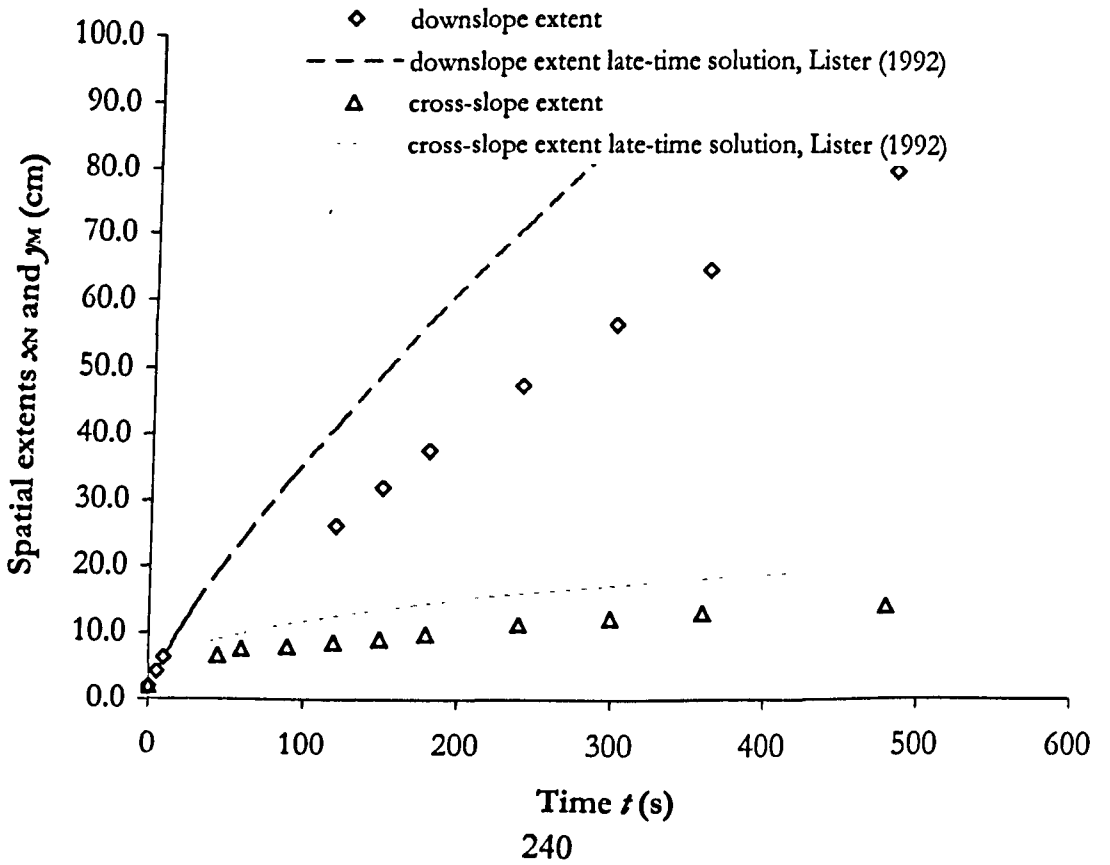

GS-20_20_7

t (s)	x_N (cm)	y_M (cm)	x_N *late-time model* (cm)	y_M *late-time model* (cm)
0	2.0		0.0	0.0
5	3.6		2.7	3.5
10	5.2		4.6	4.5
15	6.6		6.3	5.1
20	8.0		7.8	5.6
25	9.1	4.2	9.3	6.0
30	10.2		10.7	6.4
45	13.3	5.7	14.7	7.4
60	16.1	6.2	18.4	8.1
90	20.7	7.2	25.2	9.3
120	25.2	8	31.6	10.2
150	29.2	8.6	37.5	11.0
180	33.1		43.2	11.7
240	40.0	10	54.1	12.8
300	46.5	10.5	64.3	13.8
360	52.7	11	74.1	14.7
480	63.5	12	92.7	16.2
690	82.0	12.8	123.0	18.3

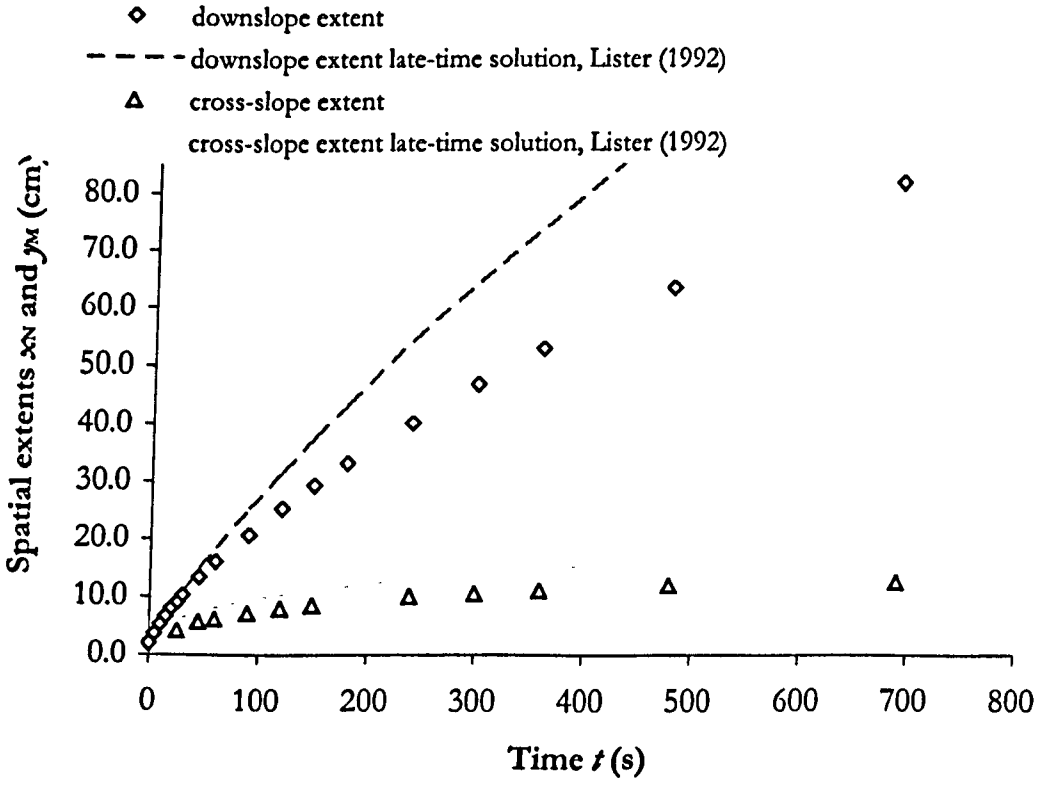

t (s)	x_N (cm)	y_M (cm)	x_N *late-time model* (cm)	y_M *late-time model* (cm)
0	2.0		0.0	0.0
5	2.6		1.0	2.1
10	3.3		1.6	2.7
15	3.9		2.2	3.1
20	4.5		2.8	3.4
25	5.0		3.3	3.7
30	5.5		3.8	3.9
45	6.9	3	5.3	4.4
60	8.0		6.6	4.9
90	10.0	3.9	9.0	5.6
120	11.9		11.3	6.2
150	13.6	4.7	13.4	6.6
180	15.3	5	15.4	7.0
240	18.3		19.3	7.8
300	20.9	5.7	23.0	8.4
360	23.6	6	26.5	8.9
480	28.5	6.3	33.1	9.8
600	33.1	6.7	39.4	10.5
720	37.0	7	45.4	11.2
840	40.8	7.2	51.2	11.8
960	44.5		56.8	12.3
1080	47.8		62.2	12.8
1200	52.0	7.7	67.6	13.3
1440	57.6	7.8	77.9	14.1
1680	63.6		87.8	14.8
1920			97.4	15.5
2160	73.2	8.4	106.7	16.1
2400	76.3	8.6	115.8	16.7
2610	79.9	8.8	123.6	17.2

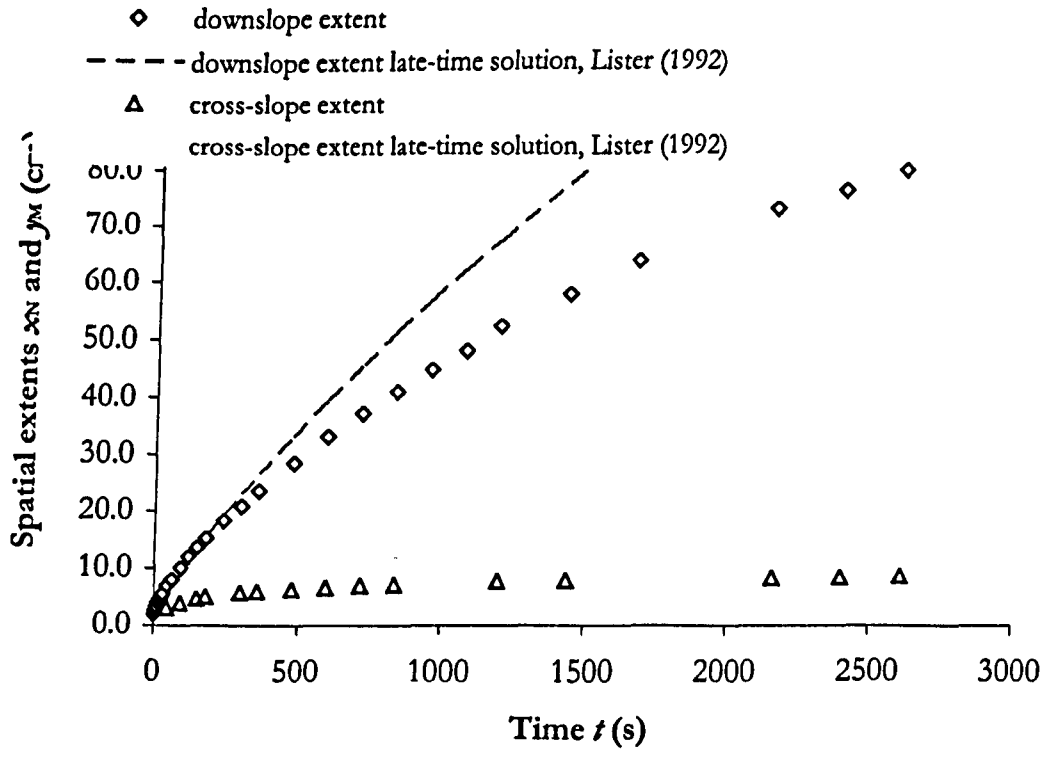

Τέτταρας δ' ἡμέρας φερόμενοι,
νυκτὸς τὴν γῆν ἀφεωρῶμεν φλογὸς μεστήν.

Ἐν μέσῳ δ' ἦν ἡλιβατόντι πῦρ τῶν ἄλλων μεῖζον
ἁπτόμενον, ὡς ἐδόκει, τῶν ἄστρων.

Τοῦτο δ' ἡμέρας ὄρος ἐφαίνετο μέγιστον
Θεῶν ὄχημα καλούμενον.

"After hastening-away for four days,
we saw the land ablaze by night.

In its midst a leaping flame towered above the others,
and appeared to reach the stars.

By day it was revealed to be a mountain of tremendous height,
which was named the Chariot of the Gods."

***The Periplus of Hanno*, 16.**

Appendix B: An historical analysis of the eruptive behaviour of Mount Cameroon in the early 20th Century

B.1 Introduction

Mount Cameroon has captured the imagination of generations, be they of the Bakweri of the mountain's slopes or travellers from across the world. For some it is the explorer Hanno's *Theôn ochèma*, the 'Chariot of the Gods', and source of the fires that were engraved in Punic in the Carthaginian temple of Baal Hammon.[1] Though one of the African continents most active volcanoes, experiencing no fewer than seven eruptions over the last century, Mount Cameroon has only recently been the subject of rigorous scientific study. The work of Godfrey Fitton, Emmanuel Suh and others, on the nature and dynamics of the Cameroon Line and the mountain of 'Fako' itself, provide the groundwork for an increasing geological interest in Mount Cameroon and its environs.[2]

Yet if, prior to 1982, the eruptions of Mount Cameroon receive little modern analysis, partially through the scientific paradigm of the times, previous eruptions of the mountain were not entirely unstudied. In the current climate of volcanological research, wherein the increasing efficacy of numerical methods, geochemical analysis and render tractable extremely complex geological problems, it is perhaps too easy to detract the work of amateur personnel with no geological knowledge, written several generations ago. Geology, not least volcanology, was founded as an observational science. Though coloured—in a manner oft amusing or perplexing to a contemporary audience—by the prejudices and limited objective knowledge of the period, as works of observation the records of military explorers, colonial administrators and plantation managers rival

[1] Mount Cameroon is associated by some authors with two particular passages in Hanno's *Periplus*; the passages in question are reprinted on the frontispiece to this appendix. The *Periplus was* a stylised travelogue of Hanno's supposed exploratory voyages along the coasts of Africa. The original is lost, but was translated into Greek; two surviving copies of this translation exist in the Codex Palatinus Graecus 398A and Vatopedinus 655. The Roman historian Pliny the Elder recorded that the Greek Polybius retraced Hanno's voyage, and wrote of such in his *Natural History*: *"a media eius parte imminens mari mons excelsus aeternis ardet ignibus, Theon Ochema dictus Graecis"* (VI.35.197—'a mountain of great height, close to the sea, perpetually burning with fire'). The arguments as to whether Mount Cameroon constitutes *Theôn ochèma* (or the emendation *Theôn oikèma*, 'throne of the gods', as the Bakweri *Monga-ma-Loba* translates as 'seat of the gods', comments on the efficacies of exact linguistic continuities over the past two millennia not withstanding) rage on, based on attempts of exact interpretations of Hanno's emended text and concepts of the capability of ancient mariners; one author's lava flow is another's bush fires. Two passionate proponents of the link connected to this narrative are Sir Richard F. Burton in his 'Account of the Ascent of the Cameroons Mountain, in Western Africa', *Proceedings of the Royal Geographical Society of London*, Vol. 6, No. 5 (1862), 238-248, p. 238; and J. de Hart and Capt. Mateer, 'Notes on the Exploration of Africa among the Ancients: With Special Reference to Hanno', *Journal of the Royal African Society*, Vol. 25, Iss. 99 (Apr. 1926), 264-277, pp. 271-273.

[2] See the introduction of Chapter 4 for an overview of the recent forays into the volcanology of Mount Cameroon, and p. 107 for a map of the disposition and general habit of 20th century lava flows.

the quality of field observations provided by modern field scientists. They provide a useful source of historical information for the geologist willing to engage even the most rudimentary historical analysis or programme of archival research.

This appendix seeks to illuminate in particular the early 20th Century eruptions of Mount Cameroon, and the volcanological phenomena that followed, prior to the more documented 1959 event. In investigating the 1909 eruptions, it draws on the official reports of the German colonial administration that was centred in Buea, and experienced the phenomena first hand, and the accounts of a radically different witness, a British explorer engaged in Pan-African exploits. For the 1922 events, the analysis turns to the accounts of the plantations managers, whose charges lay in the path of the encroaching lava fields. Indications of further activity are also studied with reference to the records of the colonial administration.

B.2 The eruption of 1909

By the spring of 1909, Cameroon (Ger. *Kamerun*) had been a German 'colony' for nigh on twenty-five years. In his famous *volte-face* of 1884, German Chancellor Prince Otto von Bismarck had cast aside his colonial antipathy and put in motion an aggressive imperial policy that would soon create an African empire five times the size of the Reich. Cameroon was the second pawn to fall to Germany in this *Kolonialtummel*, with the noted explorer Dr. Gustav Nachtigal running up the German flag on the 14th July, 1884.[3]

The *Shutzgebiete Kamerun* grew into a prominent piece in the German colonial jigsaw, exporting such plantation commodities as cocoa, bananas, palm oil and tobacco, and most importantly, natural rubber from the forests. Rubber was critical to the industrial powers of the world, and export tariffs on rubber provided the colony's major revenue. It was such that Cameroon was administered from Buea, near the heart of plantation country, and by 1912, the German governor oversaw a population of 2,600,000.[4]

Yet the German occupation of Buea and rise to hegemony on the slopes of Mount Cameroon had not come readily. Imperial designs on the slopes of Fako had first to negate the influence of Kuva Likenye and his Bakweri. The first expedition in 1891, led by *Hauptmann* Karl Freiherr von Gravenreuth and composed of a motley *askari* force, met with disaster at the Namonge ravine in Buea. Gravenreuth was killed and the local colonial effort left in tatters. By the time a more

[3] For an overview of Bismarck's colonial coup and British prevarication, see Thomas Pakenham, *The Scramble for Africa* (London 1992), p. 180 *ad passim*, and pp. 200-17.
[4] H. Rudin, *Germans in the Cameroons: a Case Study in Modern Imperialism* (New York 1968) contains the most useful overview of Imperial German policy.


Halbi.
B A R O M B I
Tolaum-Abrechnahöhe

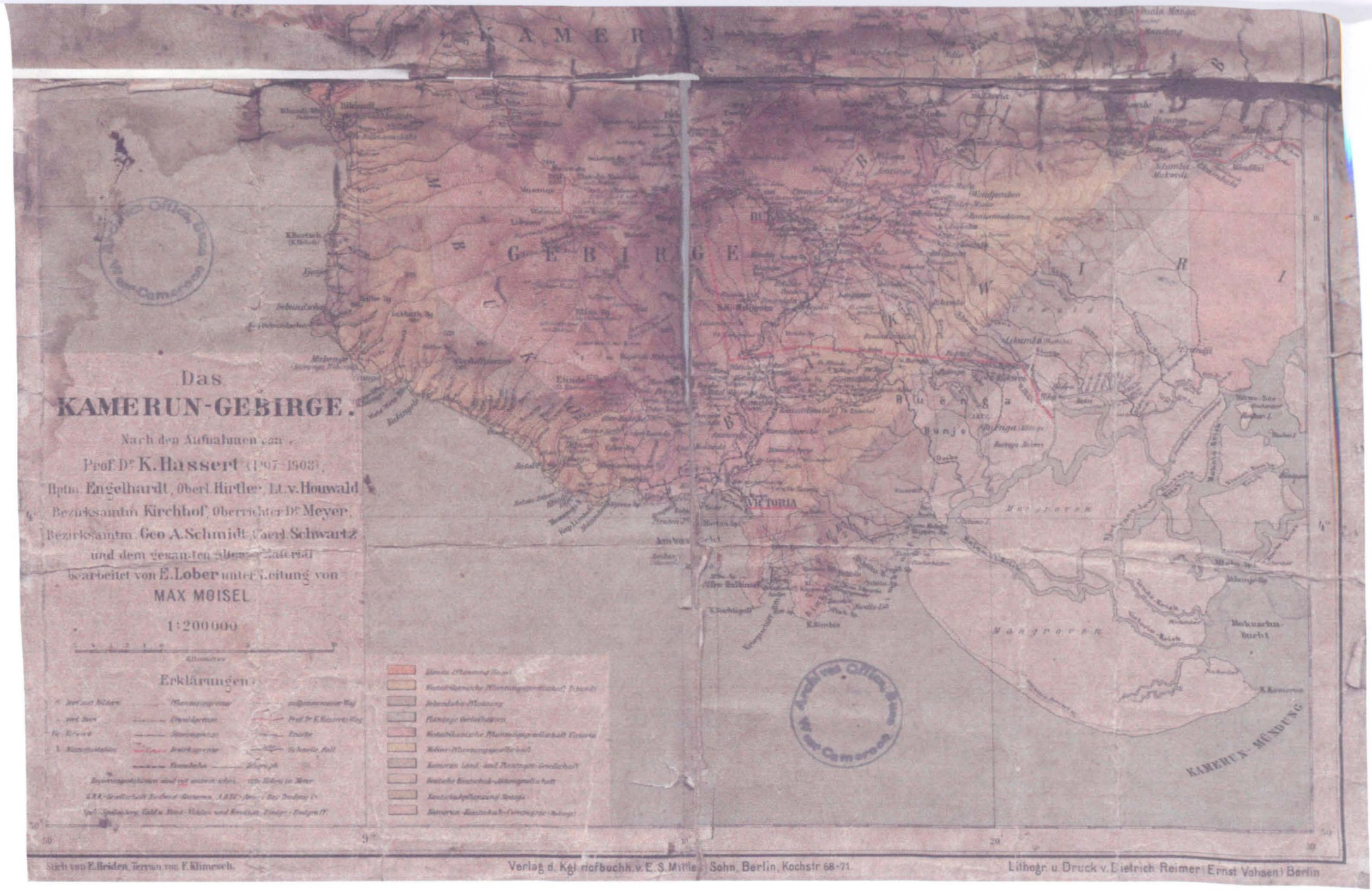

Figure B.1 Photographic reproduction of Professor Dr. Hassert's map of the Mount Cameroon region.

cohesive operation was launched in 1894, commanded by *Rittmeister* von Stetten, Gravenreuth's lieutenant at Namonge, Germany had learnt her lessons well. Stetten's better-organized Schutztruppen defeated Kuva's Bakweri and forced a harsh peace on the tribe. Buea became the capital of German Cameroon in 1902, and its importance placed a large number of concerned colonial administrators in close proximity to an often-truculent volcano.[5]

The eruptions of 1909, therefore, were the first to be recorded in any great detail, with data taken by a significant and concerned colonial administration, well ensconced in the locality. Prior to 1909, several eruptive episodes had been witnessed, or rumoured to have occurred in the 19th Century and before, as reported by a variety of ephemeral witnesses. In their *Volcanoes of the World*, Tom Simkin and Lee Siebert list nine recorded eruptions, of varying veracity, occurring in the years 450 BCE, 1650, 1807, 1838, 1852, 1865, 1866 and 1871.[6] Simkin and Siebert acquaint many of these dates to a significant margin of error. Such is due in the main to the work of Bernard Gèze, who in his 1943 volume *Géographie Physique et Géologie du Cameroun Occidental*, provides the most comprehensive appraisal of the merits of the eruption dates suggested by a variety of sources.[7]

The closest phase of activity to the 1909 eruption must lie in that intimated at by the Reverend T.J. Comber of the Baptist Missionary Society, at an evening meeting of the Royal Geographical Society, 10th February 1879. In answering a query of Sir Richard Burton on the question of recent activity, Comber stated that the local people spoke of an eruption *"having occurred some six or seven years [before his visit]"*.[8] The German administration that turned to analyse the aftermath of the 1909 eruption was less accurate—or more resolutely selective—in its appreciation of recent activity. Their report spoke of an eruption fifty years previous, which was accompanied by strong earthquakes that caused the inhabitants to evacuate the villages (a phenomenon not repeated in 1909). Centred on 'Robert Meyer Crater', some 8 km west of Ekona (see **Figure B.1**), the 'preceding eruption' also caused earthquakes that were felt in the southwest, by Mann's Spring. Beyond these few details, little was known of the previous event, yet by all belief it was somewhat stronger than that of 1909.[9]

---

[5] The best analysis of this situation is contained in Edwin Ardener, *Kingdom on Mount Cameroon: Studies in the History of the Cameroon Coast, 1500-1970* (Oxford 1996). Though some Bakweri approaches to the issue are rather emotive, a useful adjunct is provided in 'Kuv'a likenye and the Bakweri Armed Resistance to the Germans: 1891-4', *Fako International*, Vol. 2, No. 1 (January 1995).

[6] T. Simkin and L. Siebert, *Volcanoes of the World* (Tuscon AZ 1994).

[7] Bernard Gèze, *Géographie Physique et Géologie du Cameroun Occidentali*, Mémoire du Muséum National D'Histoire Naturelle, tome XVII (Paris 1943).

[8] The Reverend T.J Comber, 'Explorations Inland from Mount Cameroons, and Journey Through Congo to Makuta', *Proceedings of the Royal Geographical Society and Monthly Record of Geography*, Vol. 1, No. 4 (Apr. 1879), 225-240; p. 239.

[9] O. Mann, 'Aus dem Schutzgebiete Kamerun: Bericht, betreffend die Ergebnisse einer Unterschung des Vulkanausbruches im Kamerungebirge im April—May 1909', *Mitteilungen aus den Deutschen Schutzgebieten*, XXII.

The Germans had assumed the volcano dormant or extinct, until the observations of workers such as assessor Diehl (sulphur layers on the northern craters), *Oberrichter* Dr. Robert Meyer (CO_2 emissions from the crater that bears his name), and Professor Hassert and Thorbecke (who reached similar conclusions after observing the northeast of the mountain). Though the author of the report, Dr. Otto Mann, namesake of Gustav Mann, the companion of Richard Burton after whose water-fetching deeds Mann's Spring was gladly named, stated that there had been several earthquakes felt in Buea in the last decade, these movements were mostly weak, of short duration, and had been forgotten.[10]

The onset of strong earthquake activity on the evening of the 26th April 1909 came as something of a shock to the inhabitants of Buea, therefore, with the fear generated exacerbated by the knowledge of recent activity of a similar manner in Italy (*"...und besonders in Erinnerung an die jüngsten schweren Erdleben in Italien usw. alles mit Schrecken erfüllten"*). During the night of the 26th/27th and following day, earthquakes followed one another in sequence, after varyingly timed breaks. Between the onset of activity and 8pm on the evening of the 27th April, there were counted sixty earthquakes, of which 20 were considered 'strong'.[11]

Attempts to define the source and expression of the earthquakes were of limited effect. Mann himself felt that most shocks emanated from the north and the northwest, and that most earth movements were expressed in the vertical plane. The period of intense earthquake activity lasted until between 9.30 and 10 o'clock on the 28th April, when the last major earthquakes were felt. Following this time, the earthquakes that occurred were rapidly reduced in number and strength.[12] Herr Dr. Mann writes that these earthquakes were felt across the area of the mountain, in Mapanja and Victoria, and as far afield as Douala. With some colour, he stated that

> *"Die Wirkung der Stöße äußerte sich in Buea dadurch, daß bei stärkeren Stößen z. B. Wein aus der Gläsern herausgespritzt wurde, daß Lampen ins Shcwanken kamen und Porzellanfiguren umgeworfen wurden. Auch Bücher und Akten sollen aus den Regalen herausgefallen sein."*[13]

Not withstanding the slopping of wine from the glass or the unseemly violence caused to the German colonial establishment's porcelain, the earthquakes caused more lasting damage, in the form of fractures to local buildings. Dr. Otto Mann was not alone in observing these features and

---

Band. IV. (ed. Freiherr v. Danckelman), pp. 277-284. On the characteristics and timing of the previous eruption, see Mann, 277.

[10] *"Im letzten Jahrzehnt wurden im Buea zu wiederholten Malen Erderschütterungen gespürt. Meist sind dieseaber nur scwach und von recht kurzer Dauer gewese, so daß ihnen keine besondere Wichtigkeit beigelegt wurde und sie bald in Vergessenheit gerieten."* Mann, op. cit., p. 277.

[11] Ibid, 277-278.

[12] *"Die letzten stärkeren Stöße wurden an diesem Tage zwischen 9½ und 10 Uhr beobacht."* Ibid, 278. Mann fails to define whether this time in the morning or evening.

[13] Ibid, 278.

the severity of the earthquake swarms afflicting Buea and its environs. A fellow European witness to the phenomena was one Boyd Alexander.

Lieutenant Boyd Alexander was born in 1873, the eldest son of Colonel Boyd Francis Alexander. He held a Queen's commission in the Rifle Brigade, and participated in the relief of Kumassi in the Ashanti War of 1900. Yet his real fame and talents lay in the field of exploration. Between the years 1904 and 1907, he led the Alexander-Gosling expedition across Africa, from the Niger to the Nile. Alexander was the only European to survive the journey, Captain Gosling and his own brother Claud perishing on the route. It was in recognition of these exploits that he was awarded the Royal Geographical Society Founders Gold Medal in 1908. Boyd Alexander would not live long beyond the eruption, and was killed in Wadai on 2nd April the following year, aged 37.[14]

Boyd Alexander's account provides a useful corollary to the German report. His thoughts and manner are those of the quintessential English explorer, different in tone and focus to the German account. Alexander had arrived in Victoria on 27th March, accompanied by his faithful attendant José Lopes, a veritable Passepartout, employed on a further exploration of West Central Africa. He departed Buea to ascend the mountain on 29th March, and reached the peak some eight days later. Boyd recorded some apparent evidence of continuing activity on the peak, noting that *"the cinder [looked] as fresh as if it had been thrown up yesterday"*.[15]

He spent the next few weeks hunting and collecting specimens, until he was disturbed by the onset of earthquake activity on the 26th April. His thoughts bear a full transcription:

> *"[The night of April 26th] was very dark, and at eight o'clock, while I was sitting in my tent, I had a suspicion that the ground trembled; it was ever so little, but it made me call José, who at once confirmed my suspicion. Not two minutes had elapsed before a terrible trembling shook the mountain-side, and it seemed as if the whole earth would break in two. After this shocks came at intervals of five to six minutes, always preceded by terrific booms from the hill above our camp. Torrents of stones poured down the mountain not half a mile from our camp. Forest trees kept crashing down and snapping in two like matchsticks, and the cries of terrified monkeys fleeing before the torrent added, if that was possible, to the dreadful scene."*[16]

[14] A calendar of Boyd Alexander's relatively short life can be found in Sir Harry H. Johnston's obituary, *Geographical Journal*, Vol. 36, No. 1 (Jul. 1910), pp. 108-110. A fuller account of the man can be found in the familiar biography: J. Alexander, *Whom the Gods Love: Boyd Alexander's expedition from the Niger to the Nile, 1904-7, and his last journey, 1908-10* (London 1977).

[15] B. Alexander, 'Lieut. Boyd Alexander's Expedition in West Africa', *Geographical Journal*, Vol. 34, No. 1 (Jul. 1909), 51-55; p. 51.

[16] B. Alexander, op. cit., 52.

Beyond this, Alexander added that he manfully *"stuck it till three o'clock,"* but with shocks only increasing in intensity, he was forced to abandon camp and repair for Buea. An hour later his campsite had been covered by stones that had *"rained down from the mountain"*.[17]

The rockfalls Alexander described are mirrored in the report of Mann, the latter describing the initiation of landslides (*Erdrutsche*) above Buea, causing highly visible smoke and dustclouds (*Rauchwolken* and *Stuabwolken*). Rockslides were well evidenced on the steeper sides of valleys, sometimes forming slides 20 to 30 m wide, sometimes composed of only a few blocks of weathered lava. Mann contested that many of the rocks would have fallen anyway, and that the earthquakes only speeded up the process, yet noted a variety of other shock induced phenomena, including the collapse of lava caves and the propagation and generation of fractures.[18]

Alexander departed for Buea on the night of the 26th/27th, experiencing over one hundred shocks during the period. On arriving in Buea he found the town *"practically deserted"*, stating that *"all the white men [had] gone to Duala [sic]"*. It is not without some glee that Alexander stated that *"the natives...say that I have been the cause of this earthquake—that I went up to the top of the mountain, fired into the crater, and moved to wrath the devil that dwells therein."* Of further interest, Alexander also noted that the Bakweri of Buea placed the last 'outburst' of the mountain occurred *"about thirty-six years ago."* This would place it contemporaneous with that described by Comber.[19]

If Alexander's depiction is accurate, Mann's comment that on the evening of the 28th April, the citizens of Buea saw a 'fire-glow' (*Feuerschein*) over the northern flank of the volcano for the first time, might be ascribed to the indigenous population alone. Though a later British account does make reference to one German remaining in Buea during the crisis[20], Alexander's contestation that all the Germans had fled to Douala is in partial error, as Mann's first expedition to the Okoli site of the eruption occurred over the period 30th April to 2nd May, necessitating his presence in the immediate area of the mountain.[21]

The Germans conducted two initial expeditions to the source of the *Feuerschein*, the first as described above, the second over the dates 12th to 24th May. Alexander himself reconnoitred the

---

[17] Ibid, 52.
[18] Mann, 278.
[19] B. Alexander, 52.
[20] Cameroon Archives, Buea (hereafter cited as CAB), QK 1920/2, M.P. 367/1920 F. H. Ruxton, Resident, Cameroons Province, Buea, to Director, Geological Survey, 26th February 1922. Ruxton states: *"...members of the late administration deserted Buea, leaving only the Treasurer in charge, for which act he is said to have received the Iron Cross."* Yet on the same day, Ruxton writes *"every German fled from Buea."* As the Iron Cross was a military distinction, and before its reinstitution in 1914 last awarded in 1871, the story is clearly anglocentric apocrypha. CAB, QK 1920/2, Pt. 3, MSS M.P. 367/1920 Ruxton to Sir John Scott Keltie, Royal Geographical Society.
[21] Mann, 277.

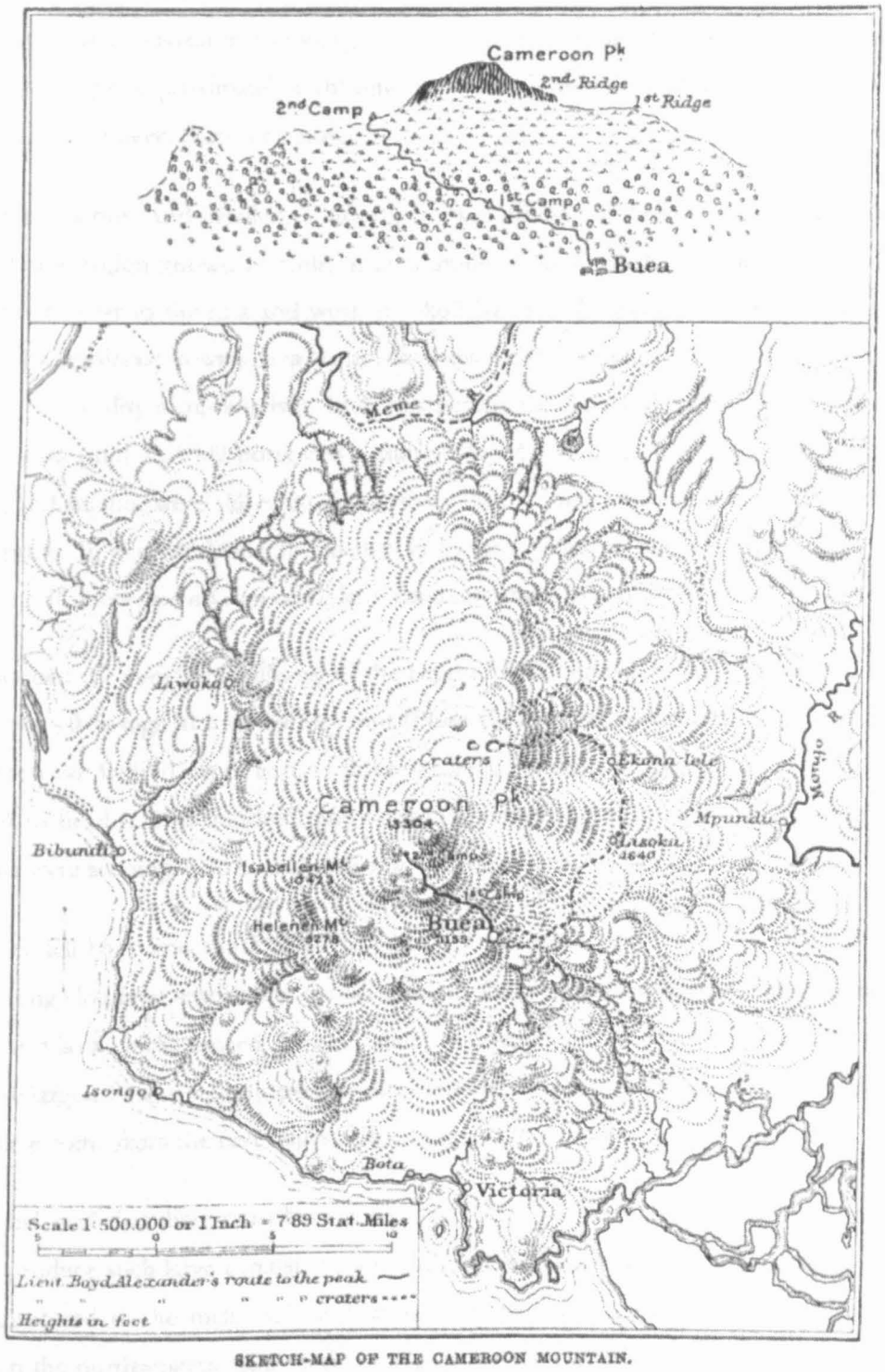

SKETCH-MAP OF THE CAMEROON MOUNTAIN.

Figure B.2 Boyd Alexander's peregrinations on Mount Cameroon, April-May 1909. This figure is reproduced from B. Alexander, 'Lieut. Boyd Alexander's Expedition in West Africa', *Geographical Journal*, Vol. 34, No. 1 (Jul. 1909), 51-55; p. 53.

site, and his route is displayed in **Figure B.2.** It is unknown as to when the Briton actually witnessed the Okoli craters, or when he departed for them; he arrived back in Buea on the 7th May, and suggests that he stayed in the village of Ekuria for two nights prior to reaching the craters. Given the journey is approximately eight miles as the crow flies, an observation between the 2nd and the 5th May is most likely (also see below).[22]

Mann's report is calm and detailed. *Vulkan Okoli* was placed on the northeastern flank of Fako, in an old volcanic region known as Kole, at an altitude of 2,400 m. A brief description of the Kole region revealed that to the east and west of Okoli lay two older craters, with the one to the east breached by a northeast flowing lava stream that was weathered and old. Further to the south there were more cones, displaying relatively little weathering; the Robert Meyer-Krater, site of the most recent eruption prior to 1909 possessed a funnel (*Schlot*) 100 m deep and 10 m wide at the open bore. CO_2 and sulphur were still emitted, but there were no more violent phenomena, linked to the Okoli eruption. In general, Mann found that in the area between Mann's Spring in the southeast and Okoli itself, there was no sign of violent, contemporaneous activity.[23]

Mann described the vent (*Krateröffnung*) of the largest Okoli cone as being 50 to 60 m in diameter, with the cone 70 m high at the highest point (**Plate B.1**). It was racketed by explosions inside the funnel (*Innern des Schlotes*) every two to three seconds, resulting in the violent ejection of spatter (*Lavafetzen*) to heights of a hundred, and its greatest extent, four to five-hundred metres. These phenomena were accompanied by a *donnerartiges Getöse*, or 'thunder-like din', and light quaking.[24]

Most spatter fell back into the *Schlund* or 'gullet' of the cone, or onto its rim, where they rolled down, forming clouds of smoke and contributing to the growth of the cone. Only a small amount of spatter and lava blocks ranged further, falling to become embedded in the soil and scorch the grass. These largest blocks typically possessed a diameter of 0.5 m or greater, and were presumed by Mann to have come from the first stages of the eruption.[25]

Dr. Mann believed that there must have been a significant amount of water vapour present in the magma to produce such large explosions, and the observed *Feuersäule* or fire-fountain is a function of water dissolved in the melt. Ash and lapilli were seen in only small amounts; ash rain was observed on the northwestern flank during the first few days of the eruption, but it was limited in extent and no samples were taken.[26]

---

[22] B. Alexander, 54.
[23] Mann, 280.
[24] Ibid, 280.
[25] Ibid, 280.
[26] Ibid, 280.

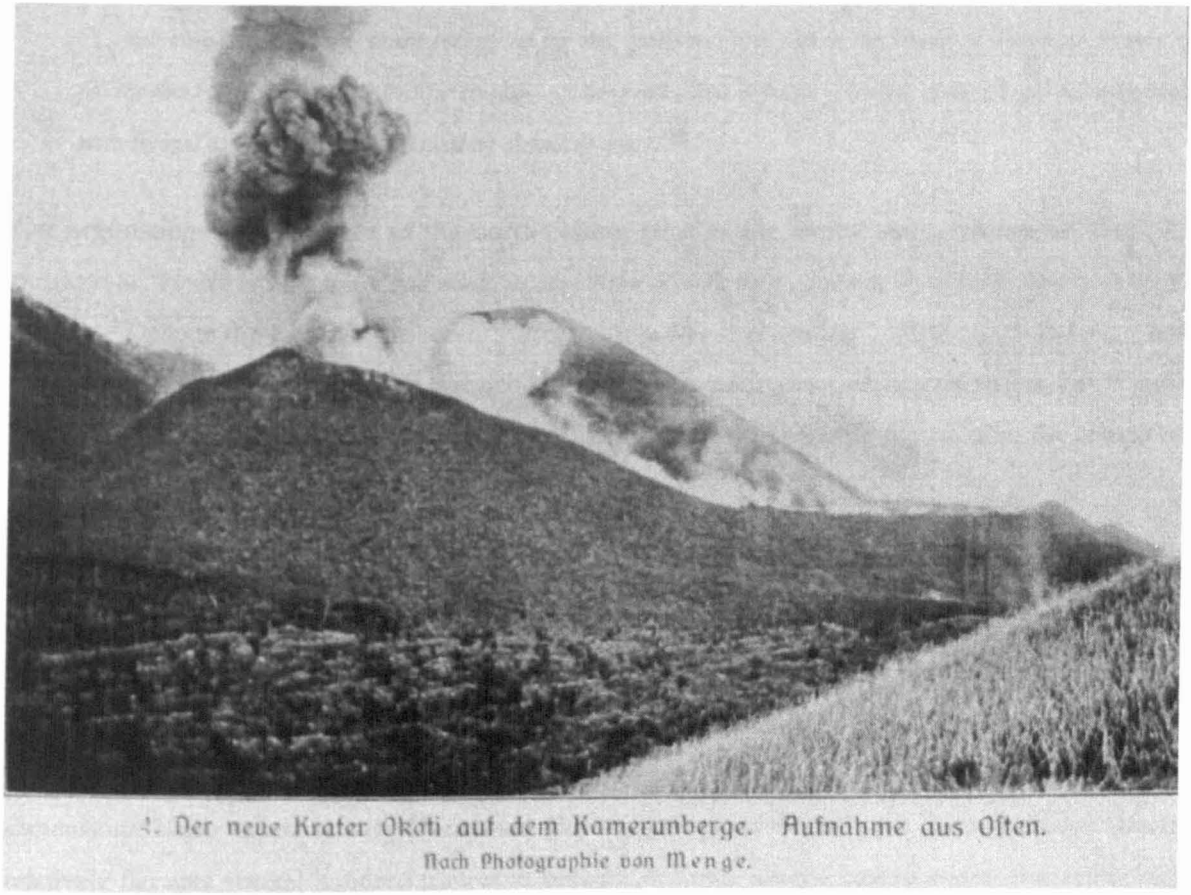

Plate B.1 View of the main Okoli 'crater', from the southeast. From *Das Deutsche Kolonialreich*, by Hans Meyer, 1909, Vol. I, p. 433.

Alexander's description of explosions at Okoli is short, but evocative, speaking of a *"wonderful sight… [that] almost baffles description."* In contrast to Mann, he defined two active craters, situated on the northeastern flank of the mountain, in a region *"studded with extinct craters"*. On managing to approach within two hundred yards of the larger of the two cones, Alexander wrote of its character:

> *"…the diameter of the top of which I should put at 60 yards. I got so close that ashes fell on my clothes, and several stones came perilously near me. The detonations were terrific, like the roar of many cannons; great volumes of smoke, blue and black as ink, towered into the sky, and were lit up by lurid flame; while enormous stones and fragments were hurled into the sky."*[27]

[27] B. Alexander, 54.

Of the small crater, Boyd Alexander noted that it was

> *"...not more than 30 yards to the east of the big one, [and] was only just in the process of formation. It was by far the most terrible, for there was no smoke—nothing but sheets of flame. Showers of stones, all red with heat, were thrown out rapidly, to be followed by appalling roars."*[28]

On negotiating a safe passage to the north-eastern edge of the largest cone, Alexander noted its outflow, a *"stream of lava which had made its way down a wide valley, running in a north-easterly by north direction."* Despite the fact that the recently effused lava was *"still smoking"*, Boyd seems to have been close enough to make the perhaps erroneously accurate measurement of lava thickness, of *"3 feet 4 inches"*. The flow itself was some 70 yards wide, and caused considerable destruction, the trunks of trees standing out like 'twisted iron'.[29]

Mann also described this flow, stating that a river of spatter lava—*"einen Strom von shlackiger, zerspratzter Lava"*—flowed out from a breach in the eastern side of the cone, heading northeast. The flow could be followed for approximately 4 km, until it passed into a forested gorge, which made further observation impossible. Mann rendered the flow 4 to 5 m in height, and at some points double that, and of highly variable width. At the cone breach it conformed to these limiting dimensions, being approximately 15 m wide. Beyond the source breach, the flow expanded over a relatively flat area several hundred metres in breadth, forming several anastamosing channels (*"sich teilend und Inseln umschließend, dann sich wieder vereinend"*). At the point of entry into the forested gorge, the flow was 30 m wide.[30]

Mann described the lava flow surface and sides as being covered in a *Schlackenkruste*, or scoriaceous cinder crust, which was partly disaggregated into a raw surface of individual blocks. The land forty to fifty metres either side of the flow was frequently scorched, with the grass completely burned away. Large blocks carried along on the top of the flow allowed Mann to estimate the (centreline) channel velocity, which he put at 4 to 5 m minute^{-1}. Further downstream, the Doctor noted that the flow was wrapped in a vapour cloud, and that small explosive events were seen within the regions of the flow itself.[31]

It is curious that Mann made no mention of the later, second cone, as witnessed by Boyd Alexander. While this is wholly congruent with an earlier visit than Alexander, on the 1st May when this cone might not have yet formed, his later expedition, from the 12th to 24th May, should have

---

[28] Ibid, 54.
[29] Ibid, 54.
[30] Data are as reported by Mann, 280-281.
[31] Ibid, 281. Mann's exact description of the lava surface runs *"Die Lava ist auf ihrer Oberfläche und an ihren Seitenwänden mit einer Schlackenkruste bedeckt, die sich teilweise in ein Haufwerk einzelner Blöcke aufgelöst hat."*

noted its presence. While Mann does not distinguish between observations made in each expedition, it is not beyond reason to equate the more wide-ranging, general analyses of the mountain were formed in the second longer expedition. Nevertheless, a return visit to Okoli is clearly implied (*"er warbei meinem ersten Besuche am 1. Mai bedeutend niedriger"*).[32]

Further observations are carried in an annex to Dr. Otto Mann's own paper, formed in the report of *Bezirkamtmann* ('district officer') Kirchhof, dated 23rd June 1909. Kirchhof's map is reproduced as **Figure B.3**. Approaching Okoli from the northwest, on the 15th June he found the foot of the Okoli *Krater* to lie at 2,390 m above sea level. Okoli was approximately three hours walk from the village of Mokona (990 m asl).[33]

Kirchhof described an Okoli region that was still active. Material ejected from the vent had created a mantle around it, forming a cone. On the western side, the cone was approximately 80 m high, while the eastern side rose only 60 m above the ground. Importantly, Kirchhof stated that the rim of the cone was intact, and not breached, with a diameter of approximately 50 m.[34] On the southern flank of the main cone's mantle, Kirchhof described a smaller, parasitic cone, positioned approximately a third of the way up the flank. Similar in form, Kirchhof suggested its activity would have been most vigorous after the observations of Herr Autenrieth (which are sadly lost to us). This smaller cone was nearly buried by the main cone, and no longer active.[35]

At the base of the active cone, on the northern flank, lay a lava field, consisting of several, separated glowing lava 'masses' or channels (*"werden glühende Massen ausgeshieden"*). One channel, approximately 10 to 20 m broad, could be followed for several hundred meters through the lava field.[36] The cone erupted continuously, and the mantle was still growing. The frequency of eruptions measured by Kirchhof was 8-10 min^{-1}, accompanied by strong rumbling. Occasionally the activity was less violently explosive, and discharged only ash, but mostly the one ejected molten scoria of considerable size. Scoriae as heavy as 10 kg were thrown 500 m into the air, and cinderblocks sized 1 m^3 or more were still found over 200 m from the vent. According to Kirchhof, scoriae were typically glowing, some white-hot, and exceedingly viscous when ejected from the crater whole.[37]

At night Kirchhof found the spectacle was particularly striking. He wrote that the lava 'appeared at the north side of cone from the base' (*"Die Lava tritt an der Nordseite des Kraters aus dem Boden"*), rather than cutting through the cone and forming a horseshoe shape, as most Cameroonian cones

[32] Ibid, 280.
[33] Ibid, 281-282.
[34] Ibid, 282.
[35] Ibid, 282.
[36] Ibid, 282.
[37] Ibid, 282.

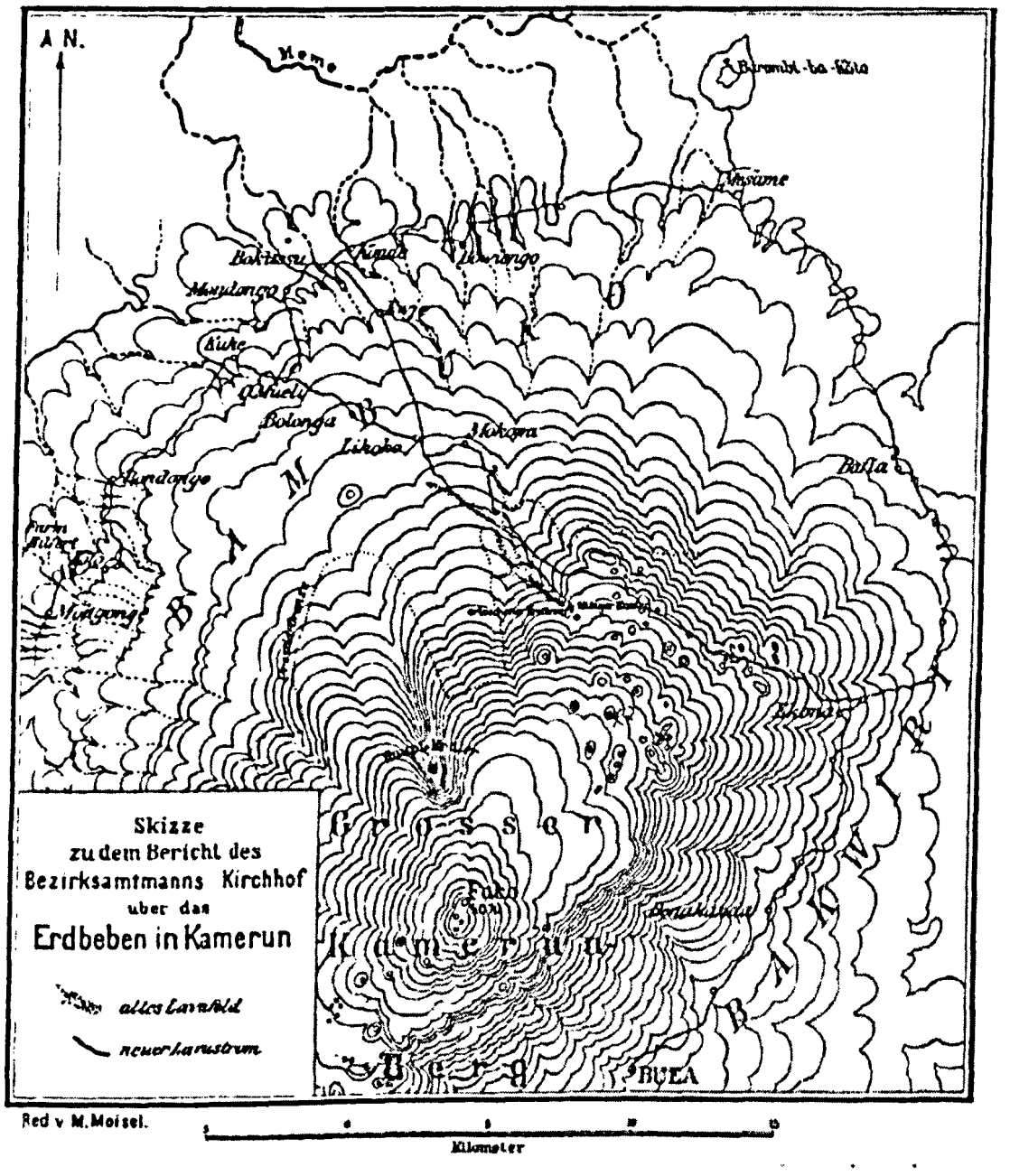

Figure B.3 Reproduction of Bezirksamtmann Kirchhof's sketch of the volcanism at Okoli, from his observations in June 1909. Reproduced from O. Mann, 'Aus dem Schutzgebiete Kamerun: Bericht, betreffend die Ergebnisse einer Unterschung des Vulkanausbruches im Kamerungebirge im April—May 1909', *Mitteilungen aus den Deutschen Schutzgebieten*, XXII. Band. IV. (ed. Freiherr v. Danckelman), 277-284, p. 283.

displayed. From this initial flow a lava field was formed, which is 800 to 1000 m wide and approximately 4000 m long. In the centre of this field there lay a glowing mobile channel approximately 20 m wide. The boundaries of the lava field were considerably bulked up, and in some places rose to 20 m in height.[38]

[38] Ibid, 282.

Beyond the lava field, Kirchhof saw three offshoots. The first consisted of a 100 m wide stream that flowed north. According to the *Bezirkamtmann*, the flow disappeared into the 'ground' as it reached the forest (*"verschwindet er im Boden"*), where it then travelled underground, only to reappear at the surface several hundred metres downslope (*"um einige hundert Meter abwärts wieder an die Erdoberfläche zu treten"*), wherefrom it could be followed for another kilometre, until the flow ended. Kirchhof noted that at the end the flow margins were still some 2 to 3 m high. While he stated that the jungle was completely flattened by the passage of the flow (*"Der Urwald ist durch den Strom völlig niedergelegt"*), with trees uprooted and burnt, he made a perplexing observation: that where the lava flowed underground, the Mokona-Ekona road passed over it (**Figure B.3**), and was fractured to display the black lava underneath![39]

Of the second flow, seemingly wider than 100 m, Kirchhof wrote that it progressed away from the lava field, towards the west and Likoko and Bolonga (**Figure B.3**). This flow *also* passed underground, under the rainforest, and halted after approximately 2000 m. It blocked the direct Ekona-Likoko path, and forced traffic to divert via Mokona. A third, smaller lava flow broke off from the field to the west (effectively upslope), but had ceased its motion rather quickly (**Figure B.3**).[40]

Kirchhof found the flow of the lava underground perplexing, and one would hazard that he's not alone. A relatively thin soil or dense rainforest and bush overlies a hard volcanic terrain; that a flow several kilometres from the source would possesses the thermal properties necessary to scour a tunnel under the forest is obviously discountable. That the viscous front of the flow was able to accommodate to and thus reactivate whatever lava tunnels might have existed in the area, without adapting to a more feasible passage elsewhere, is also highly improbable. Most probably, it would appear that Herr Kirchhof has made a rather elementary mistake in his field observations, if one that is rather understandable.

Countless historical lava flows form a base to the flanks of Mount Cameroon that deform the topography into a mass of shallow tongues, ridges and valleys. The local topographic interaction between a thin lava toe and pre-existing forested flow may have led Herr Kirchhof to assume that the flow had absconded underground. Dogged pursuit of the ridge may have led him to encounter a rather poorly vegetated area of lava downslope, which he assumed to be a continuation of the active lavas. In describing the lavas he stated that they had not completely cooled, and in many cases were still smoking; they were in the main black porous rock, and had an appearance like coal (*"Kohlenschlacken ähnlich"*). Yet these descriptions are not location specific, and elsewhere he

[39] Ibid, 282. Kirchhof writes: *"Die Übergangstelle hat zahlreiche bis zu 30 cm breite Risse, die im Innern die schwarze Lavamasse erkennen lassen."*
[40] Ibid, 282.

described the flows as being covered in a yellowish green layer, others with a white mass. While the latter is common in fumarolic areas of cooling flows, the former is typical of early moss-colonized, cooled flows in the damp forested environment; and is certainly discordant if linked to a flow that was emplaced a scant month previously.[41]

Beyond these problems, there now arises another, wholly justifiable situation of confusion. All three reporters neglect to state the exact date of their observations. We might pin Alexander's to the first week in May, but are unaware of whether Mann's are concordant with his first or second expeditions; and while Kirchhof places a date of 15th June on his altimetric measurement at Okoli, we cannot be sure if that is contemporaneous with his statements on eruption characteristics. It will therefore prove a little difficult to assess conflicting statements in light of natural vent evolution or observational (or recording) error.

Alexander neglects to inform us as to the length of the lava flow he observed, but clearly states that it flowed down a wide valley, in a 'north-easterly by north direction'. Though not so marked on his map, it appears that this flow might be indicated by the speckled trail that departs from the easternmost of the marked craters (whose distance between each other is too extreme to indicate that these are the two cones he speaks of in his narrative; rather the eastern crater indicated his 'larger' structure). Yet Alexander made no reference to any great violence in this stream, and simply stated that it was still smoking. Furthermore, one senses that the map's depiction of the speckled band neatly following the valley is the presumption of the journal's artist, based on the topographies of the maps he had to hand in London.

Mann, like, Alexander, stated that the flow ran in a north-eastern direction on leaving the Okoli cone, and was followable for four kilometres, until it reached a forested gorge. Reference to the distance from Okoli to the tree line depicted in **Figure B.3**, shows that this is dimensionally accurate. Furthermore, Mann's description of the lava expanding over a flat region several hundred metres in width is favoured by the shallower gradients to the northeast. However, Mann clearly stated that the only danger posed by the lava stream is to Likoko and its environs. While a flow to the northeast could pose a danger to Likoko if an offshoot was focused down the western side of the plateau, prior to reaching the tree line, this is highly lateral thinking. To this author at least, the way in which Mann simply phrases the Likoko sentence seems to bear reference to a flow heading *northwest.*

Bezirkamtmann Kirchhof perhaps indulged in certain errors in investigating the long-distance evolution of the flows, but his depictions of the lava field, vents and active channel region need not

[41] Ibid, 282-283. *"Manche Stellen sind mit einer gelbgrünen Schicht, manche Gesteinemit einer weissen Masse überzogen."*

be so tarred. He described a lava field similar to that of Mann, and if his stated directions of offshoots ('north' and 'west', though the latter is depicted as northwest on his sketch, reproduced in **Figure B.3**) are different than those of Mann, the sense—a possible threat to Likoko—is the same. Kirchhof also described two cones, one major with one parasitic to the south, an observation that is mirrored by Alexander (though his smaller cone is to the east) but not Mann. A charitable resolution of these historical accounts—one that allows for development of the vent region, that lava rarely follows an arrow straight course and the fact that the development of an anastamosing field hampers accurate directional measurements—might develop as follows:

An initial cinder cone developed in the region of Okoli no later than the 28th April, when there was clear fire-fountaining activity witnessed from Buea. This first cone may have been a wholly new creation, or developed within an existing edifice. A lava flow, possibly partly effused and partly spatter-fed, developed out of a breach in the northeastern wall of the cone, and for some time flowed in a northern or northeastern direction. As the eruption progressed, local changes in source character and flow rheology led to the flow forming a wide, anastamosing field on the gentler gradients that lay to the north of the cone. Elements of this field reached the tree line and were focused along conduits in topography. Further ejections of material from the vent built a mantle over the escaping lava, which may have subsequently been fed from within, or from accumulating spatter. As the lava accommodated to preferentially sited channels, subsidiary flows developed from and within this field, largely focused to the northwest, forming the threats to Likoko and Mokona described by Kirchhof.

The distance in time between the observations of Alexander (c. first week in May) and Kirchhof (c. second week in June), and the fact that Mann noted no second cone, allow for many theories in cone development. The similarity in 'large' cone diameter noted by all three observers need not preclude the idea that they are in fact different edifices, and that new cones developing above the vent progressively buried earlier centres of activity under their growing mantles. That said, it is perhaps more feasible to argue that the 'large' cone observed remained a constant feature of the Okoli eruption. Factoring in the rather unspecific statements of Alexander and Kirchhof as to the smaller cone's position (taken in arduous circumstances), and a slight development and building of the larger cone to the northeast, and it seems highly possible that the cones of Kirchhof are those of Alexander.

The eruption of 1909 thus occurred to the north, away from the administrative centres of Buea, and the plantations that crowded the littoral slopes of the mountain. Kirchhof noted that the activity in 1909 offered no danger to the plantations in the west. Such observations would not hold true during the next eruption, when the mountain chose a rather different focus for its effusions.

B.3 The eruptions of 1922

Subsequent to 1909, future observations of eruptions on Mount Cameroon would occur in a rather different political climate. With the onset of the Great War, the forces of the Entente colonial powers, France and Great Britain, rapidly assaulted German colonial possessions across the globe. *Deutsche Kamerun* possessed no Lettow-Vorbeck, and in 1916 the conquered territories of Cameroon were provisionally partitioned between the French and British occupiers. Following the restitution of civilian administration on 1st April 1916, the British controlled 'Cameroons Province' became one of the Southern Provinces of Nigeria. During the war the plantations that formed this administrative unit, originally controlled by such German interests as *Deutsche WestAfrikanische Handelgesellschaft* and the *WestAfrikanishe Plantagengesellschaft*, were organised into a 'Plantations Department', overseen by a supervisor of plantations. Following the war, and the mandate of the ex-German possessions to the British, these assets were vested in a Public Custodian for Enemy Property, in Lagos.[42]

It would therefore be a British administration that witnessed and recorded the 1922 eruption of Mount Cameroon. Since the activity at Okoli in 1909 (see section B.2) no major eruptive events had occurred, and any minor activity went unrecorded. The quiescence ended on the night of the 2nd-3rd February. A small party, led by Dr. T. Rice, C.M.G., Director of Medical Services, Nigeria, and Captain F. S. Mateer, F.R.G.S., occasioned to be up on Mount Cameroon as the first disturbances were felt. In a later report of events, Mateer wrote:

> *'On the night of February 2-3, Dr. Rice...and I slept on the first ridge in the open at a height of about 10,000 feet. About midnight I felt three distinct tremors. The temperature was about 40° Fahr. Later I was awakened by Dr. Rice, who drew my attention to a brilliant red sky over the top of the mountain. We had neither heard nor felt anything at that time. On the morning of the 3rd, at about 9 a.m. and at 12,000 feet... we felt a distinct shaking sufficient to make us sway. It appeared to be very close to the surface.'*[43]

Shortly following this disturbance, Mateer and Rice heard a noise

> *"...not unlike wind in the trees. The air was still at the time. I [Mateer] went ahead and towards the noise, passed over the second ridge in time to see a large spout of pink dust go up like a huge mushroom. As we*

[42] The most detailed overview of the situation and the British attempts at disposal of the German plantations is contained in Richard A. Goodridge's '"In the most effective manner"?: Britain and the disposal of the Cameroons plantations, 1914-1924', *International Journal of African Historical Studies*, Vol. 29, No. 2 (1996), 251-277.

[43] Mateer's report is reprinted in F. H. Ruxton, Capt. Mateer, G. Waldau, A. A. Reading and F. Evans, 'Volcanic Eruptions on the Cameroons Mountain', *Geographical Journal*, Vol. 60, No. 5 (1922), 135-141; p. 137. The Cameroon Archives in Buea hold only a single copied sheet of Mateer's report in CAB, QK 1920/2; the remainder is missing.

proceeded the noise increased. The dust cloud was not very large, and small stones were being thrown up incessantly.'[44]

Mateer noted that all the vegetation in a region running of three or four miles west of the eruption—mostly moss and lichen—was ablaze. The party failed to see the actual vents, as they were obscured by a ridge and time precluded a detour to the site, but did note that the noise and 'shower of stones' continued until approximately five o'clock in the evening, reaching their maximum intensity between 1 and 2 pm.[45] Mateer and Rice returned to Buea on the night of the 3rd, and found a town that had itself witnessed some of the eruptive phenomena. Captain F. H. Ruxton, Resident, Cameroons Province, stated that on the morning of the 3rd he had *"heard a curious rustling sound as of wind in the trees, and at night saw a glow in the sky at 7.30 p.m.'*[46]

Notice of these volcanic disturbances was not confined to Buea, or the southeast flank of the mountain. At Debundscha, lying on the coast, some fifteen miles southwest of the Mount Cameroon summit (**Figure B.4a**), plantation manager Mr. G. Waldau noted

'On February 3rd, in the morning we heard here in Debundscha a noise as from a tornado far away on the mountain, but it differed from a tornado in going on without interruption till 5 or 6 o'clock in the evening. Every now and then a sound reached us. Nothing was seen here. In Bibundi the noise was also heard... the next morning Mr. Reading said he could see smoke rising from west of the Peak, in 104° mag. (91° true).'[47]

Mr. A. A. Reading, the manager of the Bibundi Group of plantations, some thirteen miles west of the summit of the volcano (**Figure B.4a**), did not provide any written observations of this first phase of activity. However a panoramic sketch of his (**Plate B.2**), dated 23rd February and copied in Ruxton et al.'s *Geographical Journal* piece, features a note by the summit that states "Smoke observed here about 5/2/22", a day after Waldau placed Reading's comment.[48]

Following this initial activity, a period of relative quiet followed. Waldau recorded that plantation workers had heard noises emanating from the mountain at 5 pm on the 9th, of a lesser intensity than those heard previously. Waldau himself saw fire on the mountain at 10 pm that evening, which he placed at heading of 65° from magnetic North (or 53° true) from his position at Debundscha

[44] Ruxton et al., op. cit., p. 137.
[45] Ibid., p. 137.
[46] Ibid., p. 135. Ruxton's own report, attached as a covering sheet to the reports of Mateer, Waldau and Reading, and dispatched to Sir John Scott Keltie of the Royal Geographical Society, is preserved as a copy in CAB, QK 1920/2, M. P. No. 367/1920, attached to Memorandum No. 314/367/1920.
[47] Ruxton et al., op. cit., p. 138. An original copy of Waldau's report, identical apart from minor changes such as a retention of his thoughts on the link with sun spots, appears as CAB, QK 1920/2, M. P. No. D. 8/22 G. Waldau to Supervisor of Plantations, Bota, 16th February—attached to No. 155/12/22 of 18th February.
[48] CAB, QK 1920/2, No. 15/11/22 A. A. Reading to Supervisor of Plantations, Bota, 23rd February—attached to No. 175/12/22 of 24th February; Ruxton et al., op. cit., p. 136.

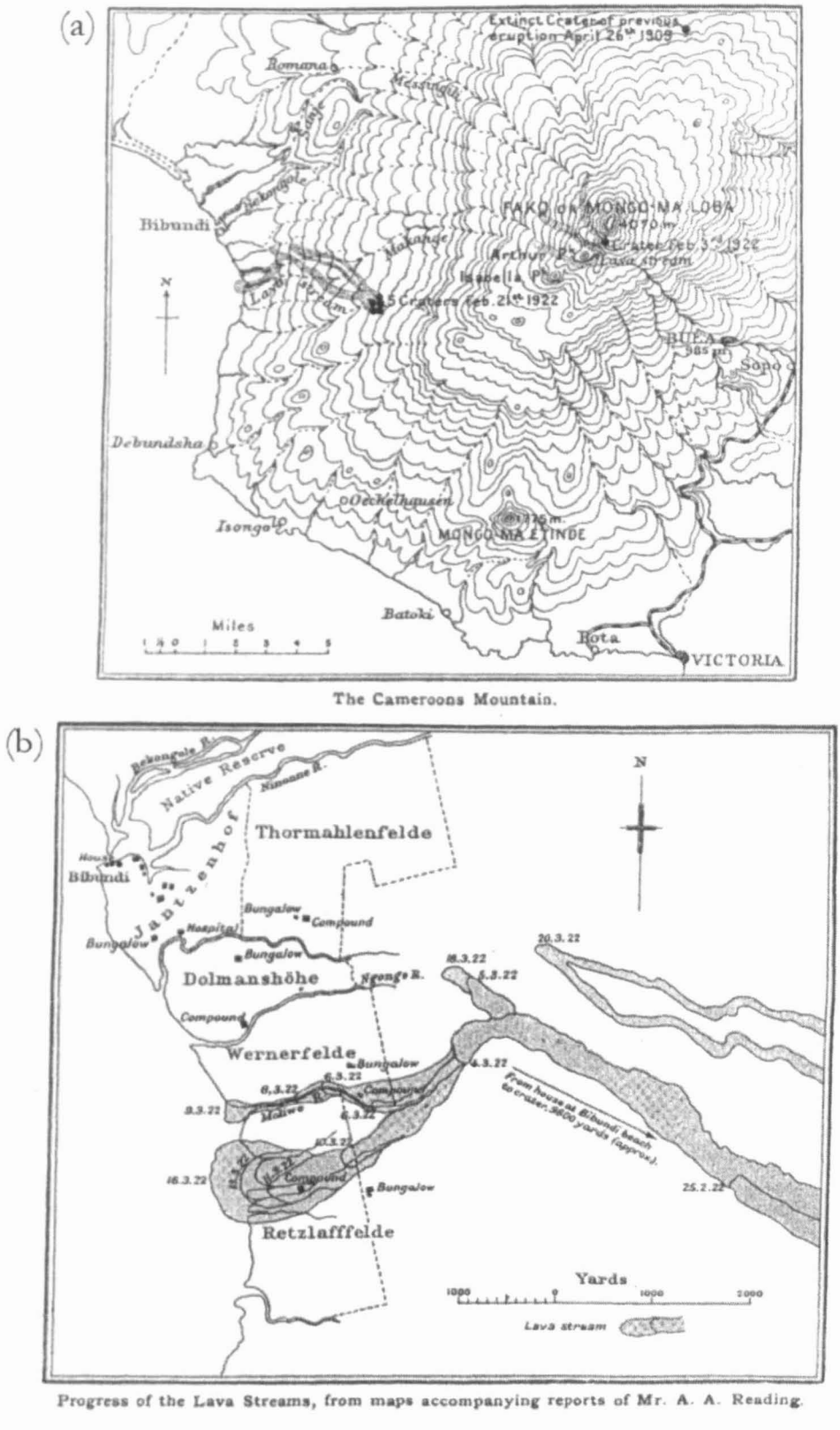

Figure B.4 Maps showing (a) the siting of the upper and lower vents, and (b) progression and development of the 1922 lava flows in the Bibundi region, up until the 20th March. Reproduced from F. H. Ruxton, Capt. Mateer, G. Waldau, A. A. Reading and F. Evans, 'Volcanic Eruptions on the Cameroons Mountain', *Geographical Journal*, Vol. 60, No. 5 (1922), 135-141; p. 139.

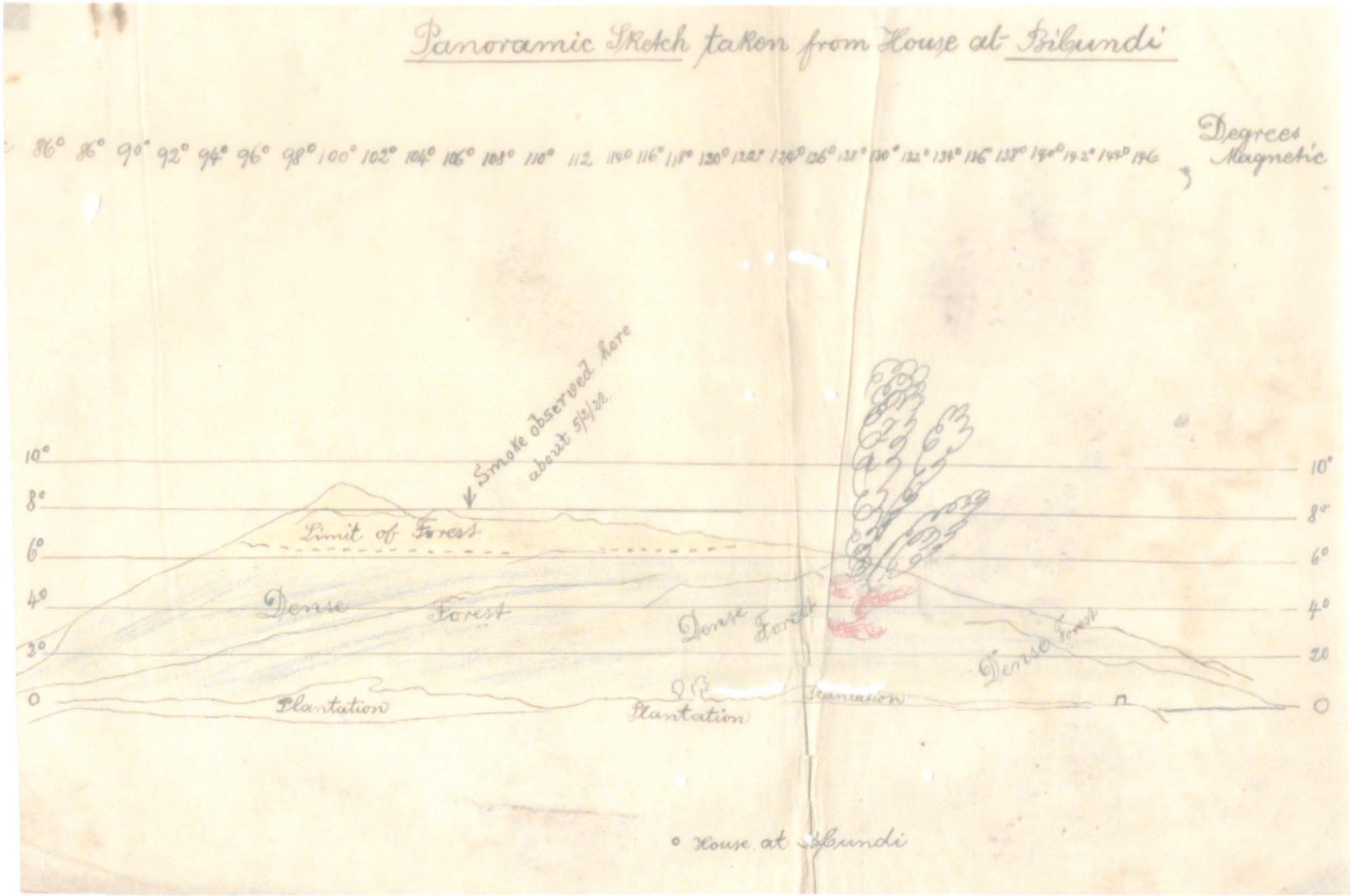

Plate B.2 Photographic reproduction of A. A. Reading's panoramic sketch of 23rd February. CAB, QK 1920/2, No. 15/11/22.

(**Figure B.4a**). The fire was *"constantly rising and falling, showing that the eruptions were coming in quick succession."*[49]

Though Waldau intimated of seismic and eruptive activity on the night of the 12th, all other contemporary sources made no mention of it. Fire was again seen on the mountain during the evening of the 14th, centred in the same area as witnessed five days before. Ruxton wrote that nothing further was observed in Buea until the 14th February, when a large tremor was felt at 1.20 am. Further 'slight shocks' were experienced until the 23rd February, but caused no damage. Writing on the 23rd, Reading records that in Bibundi they had experienced 'earthquake shocks' over the preceding ten or so days, with the frequency increasing towards the end of that period. An especially intense seismic event was experienced at 12.30 pm on the 18th, one of seven between 8 am and 2 pm.[50]

Mateer repaired again to the mountain on the morning of the 18th February. When he reached a hut at an altitude of about 10,000 feet, his party experienced a *"violent, rapid vibration lasting 10 seconds."* Mild tremors followed, interspersed with more violent events: at 7.08 pm there was a *"sharp shock, as though the hut had been hit"*; at 3.33 am the following day they experienced a seismic event that started violently, and then decreased in intensity, lasting for a period of 30 seconds. During the 19th Mateer visited the vents he had not been able to reach on his previous visit. He saw a new crater, from which two lava streams had emerged, "one dividing itself around Arthurberg, and the other bearing to the right" (**Figure B.4a**)[51]. Of the crater itself, Mateer noted

> *"The crater I estimated to be 150 feet by 80 feet, and rising to a height of 50 feet. A small column of smoke or steam was rising from the crater. The lava had set, but was too hot to examine very carefully... The ground in the vicinity was shaking almost incessantly."*[52]

On the 21st February, attentions were drawn to a new development. In the early morning of the 21st, Reading experienced two 'severe shocks' at Bibundi. At around 6.10 pm, he noted the appearance of a fire in the forest on the western side of the mountain, lower than the crater observed by Mateer. Although it at first appeared as a bush-fire might, it soon developed into a larger conflagration. Another fire was seen 4° to the left, as seen from Bibundi; both developed into highly violent phenomena, with *"spouts of flame... shooting high up into the sky, making it apparent that they were volcanic."* By 6.30 pm the two fires had conflagrated into one single 'blazing mass' out of which were cast 'five spouts of fire'. Lava could be observed flowing form the right (southern) edge of

[49] Ibid., p. 138; CAB, QK 1920/2 M. P. No. D. 8/22.
[50] Ruxton et al., pp. 135 & 138; CAB, OK 1920/2 Nos. M. P. D. 8/22, 15/11/22 & 367/1920.
[51] Mateer in Ruxton et al., op. cit., p. 137.
[52] Ibid., p. 137.

this system. Reading sketched this scene; his original representations are reprinted in Ruxton et al., but a copy made in Bota is reproduced in **Plate B.3.**[53]

The violent activity witnessed by Reading continued until approximately 9 pm that evening, when heavy palls of smoke in the region prevented further observation. This situation continued into the day of the 22nd February, when only the path of the lava flow descending the mountain could be seen. When a breeze cast aside the smoke near dusk that evening, however, Reading could see the entire mountainside, with visibility remaining good throughout the night. The system of explosive fires had altered, as Reading described

> *'Three spouts of flame only were now to be seen, but they were intensely brilliant, and the spectacle was quite as magnificent as before... The pyramid on the left, which had been formed by the burning masses thrown up, was a wonderful sight. The top and part of the way down the sides were an incandescent mass of white, which showed up in contrast to the red fountain of flame at its side. These spouts of fire were rushing out at a great velocity, and I estimate that at times they reached a height of 1000 feet from their base.'*[54]

A copy of Reading's sketch of these phenomena is displayed in **Plate B.4.** Through a simple system of bearings, Reading suggested that these lower vents existed at an altitude of 3000 to 3500 feet above sea level (c. 900 to 1050 m). Using these data, Reading constructed a sketch-map of the Mount Cameroon area, displaying the approximate positioning of the lower vents. A copy of Reading's map is reproduced in **Plate B.5,** to accompany the panoramic sketch in **Plate B.2.** Later the measured inclination of 8° from his position indicated a more rigorous measurement of 4150 feet above sea level (c. 1250 m) for the altitude of the vents, and by measuring the lag time of the noise of explosions at the source (27 seconds), Reading calculated that the craters lay some 9900 yards distant (c. 9050 m), on a magnetic bearing of 128°. He managed to approach within two miles of the lava flow, and witnessed firsthand the fires its passage caused amongst the adjacent vegetation. For the moment, the lava was still propagating through dense forest, and closer observation would prove difficult.[55]

Between the 23rd February (the date of Reading's report) and the 9th March, no primary sources survive to detail events. The map reproduced in **Figure B.4b** clearly demarcates the advance of lava towards Bibundi plantations over the period 25th February to 6th March (and beyond), but no specific records exist in the Cameroon Archives; only a later report of the Plantations Department stated that the lava flows entered the Bibundi Estate on 3rd March. Any diagrams made by Reading were not copied, or have since disappeared, though a later report contained three sketches of the

[53] Ibid., pp. 138 & 140; CAB, QK 1920/2, No. 15/11/22, 23rd February.
[54] Ibid., p. 140; CAB, QK 1920/2, No. 15/11/22, 23rd February.
[55] Ibid., p. 140; CAB, QK 1920/2, No. 15/11/22, 23rd February; CAB, QK 1920/2, No. 15/11/22 contd Re Seismic Disturbances, Reading to Sup. of Plantations, Bota, 22nd March.

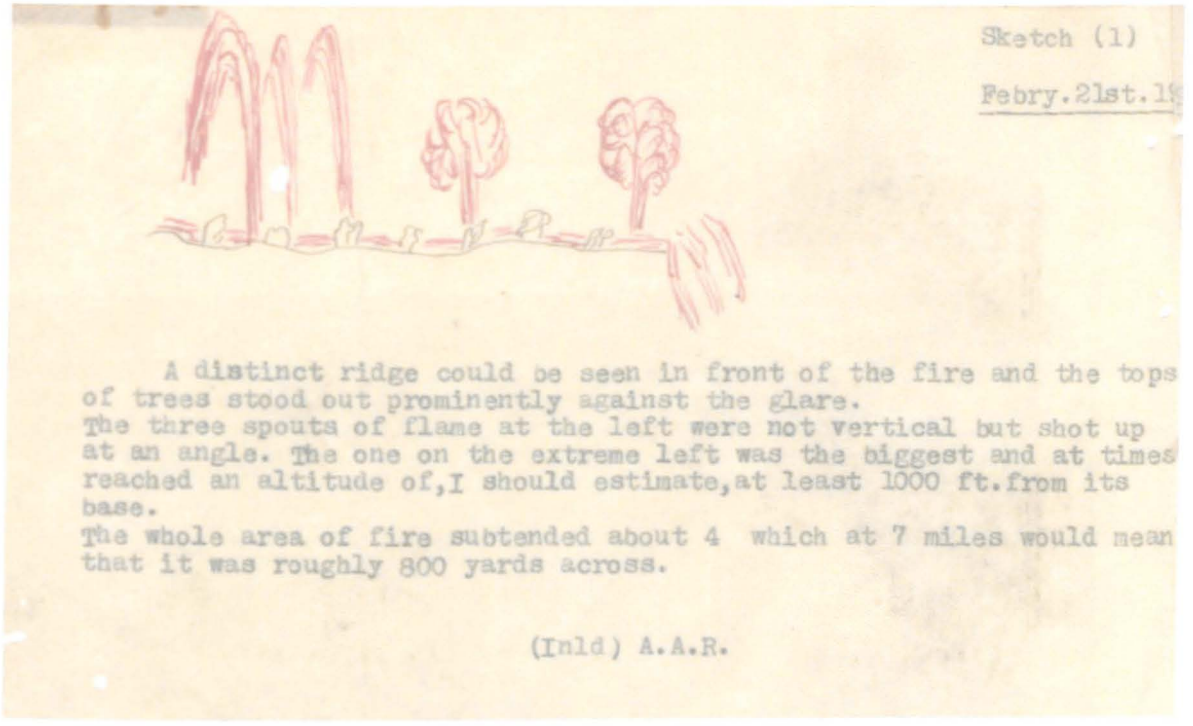

Plate B.3 Photographic reproduction of a Plantations Department *copy of* A. A. Reading's sketch of the vents on 21st February 1922. Reading's original caption is retained. CAB, QK 1920/2, No. 15/11/22.

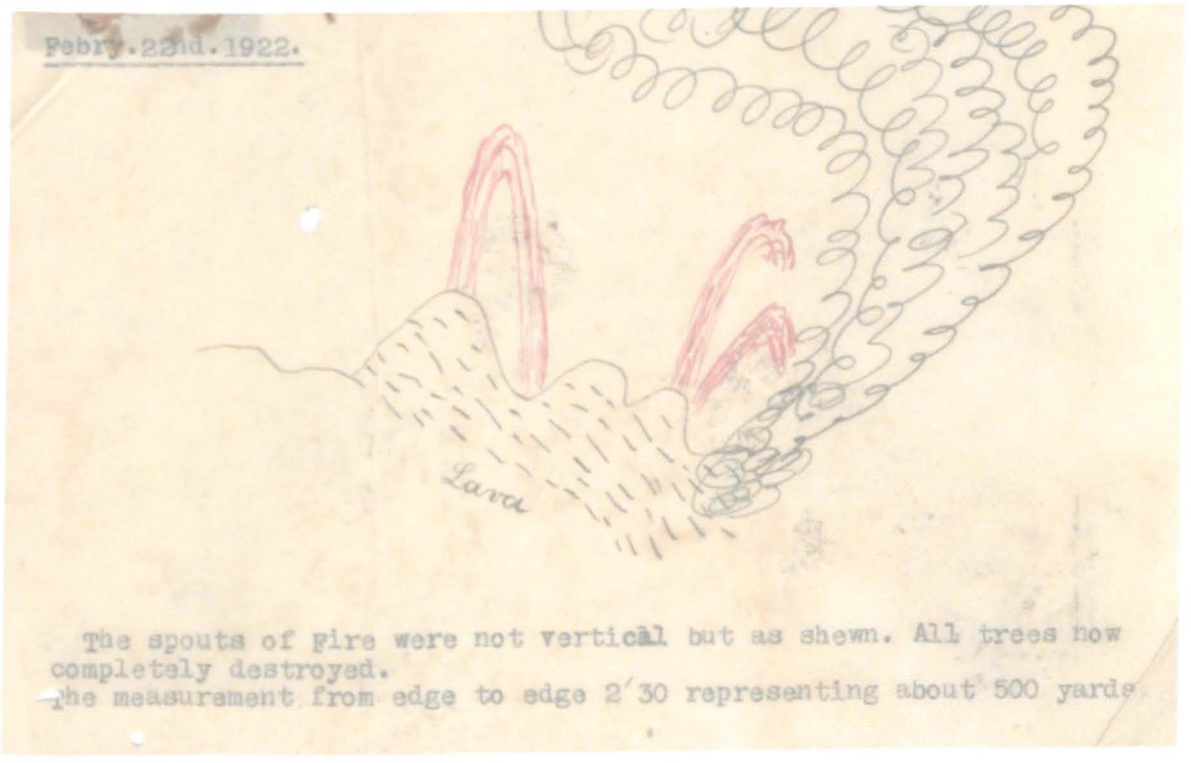

Plate B.4 Photographic reproduction of a Plantations Department copy of A. A. Reading's sketch of the vents on 22nd February 1922. Reading's original caption is retained. CAB, QK 1920/2, No. 15/11/22.

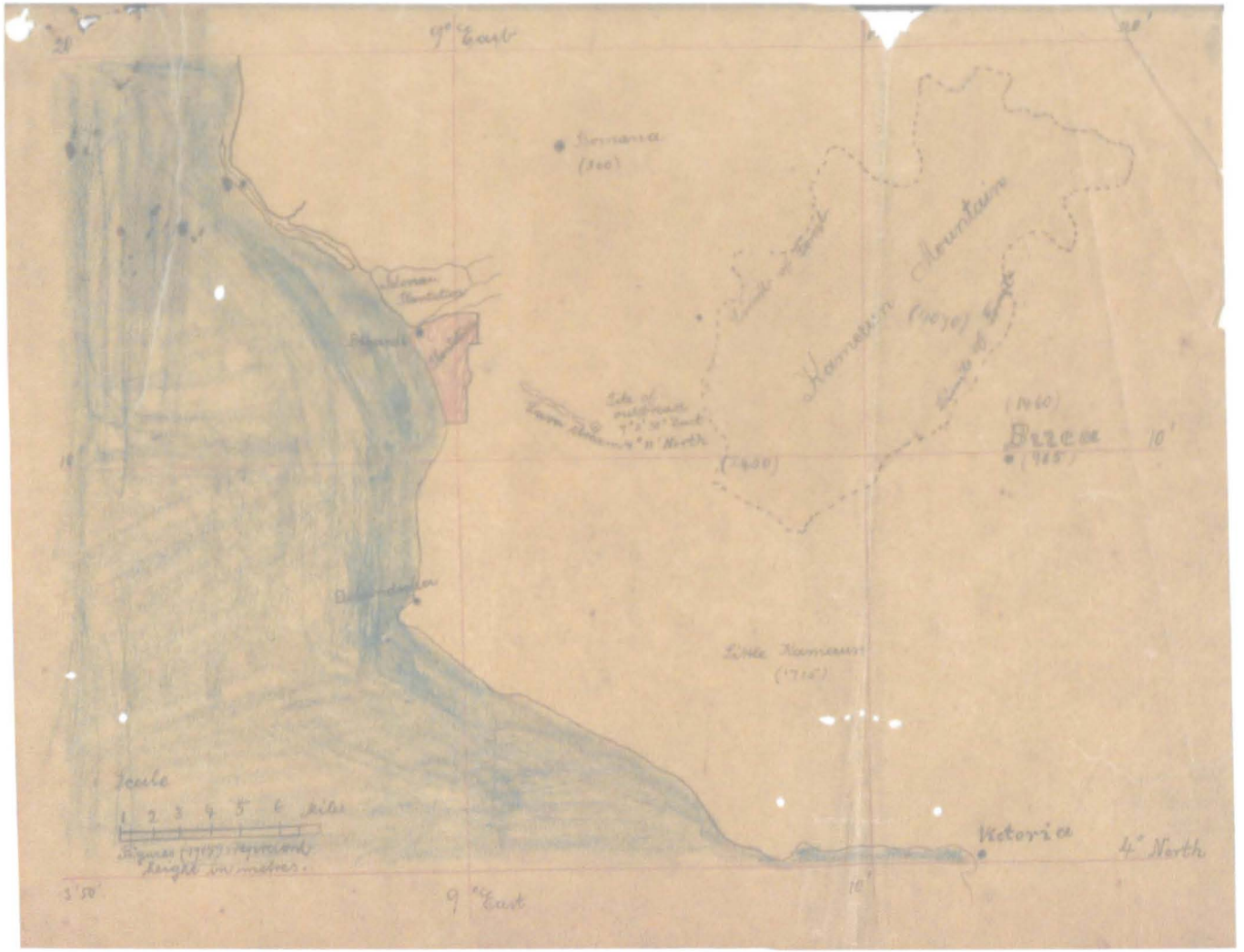

Plate B.5 Photographic reproduction of A. A. Reading's sketch map of the 23rd February 1922, displaying the position of the flank vents. CAB, QK 1920/2, No. 15/11/22.

vent region made in this period, which are reproduced as **Plates B.6, B.7** and **B.8.** That the evolution of the lavas towards, and into, the Bibundi plantations occurred and was greeted with alarm is clear from a memorandum dispatched to Reading from Bota, advising him to remove and safeguard furniture and stores, and send daily reports as to the advance of the lava and the plots it affected.[56]

The propagation of the lava streams had pre-empted this communiqué somewhat. The same day the above memorandum was dispatched, Reading wrote

> *"...the lava has now run completely through the plantation between Wernerfelde and Retzlafffelde farms, destroying the Government Road and telephone lines. This completely cuts us off from Victoria and I should be much obliged if you would let us have a Surfboat with crew of, say, four men so that we can establish communications on the Debundscha side. The lava stream runs right out into the sea, 200 to 300 yards and is extending all the time."*[57]

The advance Reading indicated is displayed in **Figure B.4b,** clearly following the line of the Moliwe River. In two notes written on the 9th and 10th, Reading emphasised position

> *"I am afraid that we are now cut off for good, as I have heard that the Bridge is down & the lava running into the area. This messenger is however going to get back somehow [...] doubt I can ferry him across if the lava really is right down to the sea."*[58]

And the day following

> *"I have just heard from Mr. Waldau who got a letter trough to me by canoe. As you will see from my letter addressed to Supervisor of Plantations I have asked for a Surf Boat. I really must have one... because it is essential that we should have some means of escape if any thing serious happened."*[59]

In response to the Acting Supervisor of Plantations' communiqué of 9th March, Reading appraised the administration in Bota of the situation at the time of writing (13th March)

> *"I understand that the [newer stream of] lava is now in the sea at Plot 2 of Retzlafffelde* (**Plate B.9**)*...The [older] lava stream between Wernerfelde and Retzlafffelde appears to have stopped but the [newer] one through the middle of Retzlafffelde is still going strongly...it has completely wiped out the native compound* (**Figure B.4b**) *& from the lie of the land I fear that many other plots in that farm will be destroyed. The Bungalow is*

[56] CAB, QK 1920/2, No. 198/12/22 Acting Supervisor of Plantations to Reading, 9th March 1922. On the date of entry, see CAB, QK 1920/2, No. 234/12/22, 21st March.
[57] CAB, QK 1920/2,No. 1[x]/11/1922 Reading to Act. Sup. of Plant., 9th March.
[58] CAB, QK 1920/2 Handwritten note from Reading to [illegible], 9th March.
[59] CAB, QK 1920/2 Handwritten note from Reading to [illegible], 10th March.

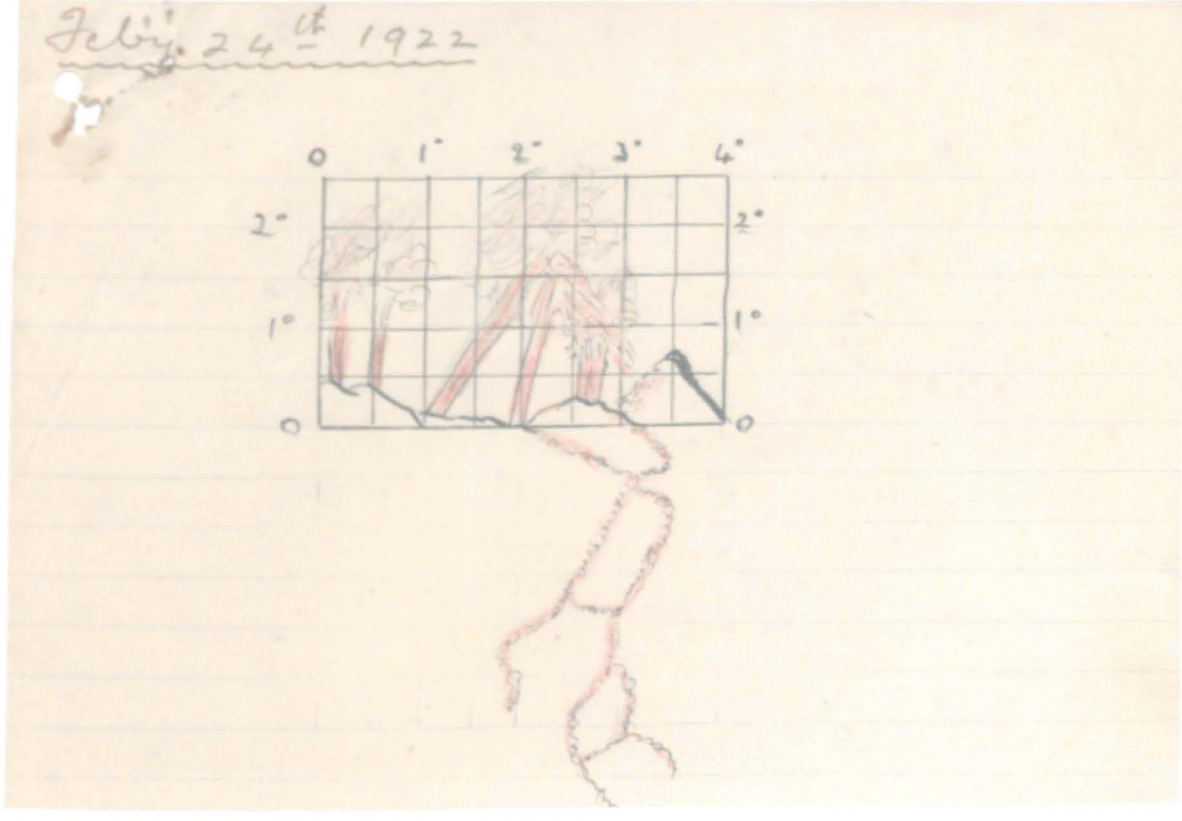

Plate B.6 Photographic reproduction of A. A. Reading's sketch of the vents, 24th February 1922. Reading's caption reads: *Visibility very good at night. The five spouts of fire distinctly seen. The wind was blowing from the right and the fire and pyramid on that side were brilliant, the streams of lava also were very bright. At 9900 yards a degree equals about 170 yards, so that the area shewn above is a matter of 680 yards across. The fire shot up to 1½ degrees or more at times, which would mean a height of between 700 and 800 feet.* CAB, QK 1920/2, No. 15/11/1922, Re Seismic Disturbances, 22nd March 1922.

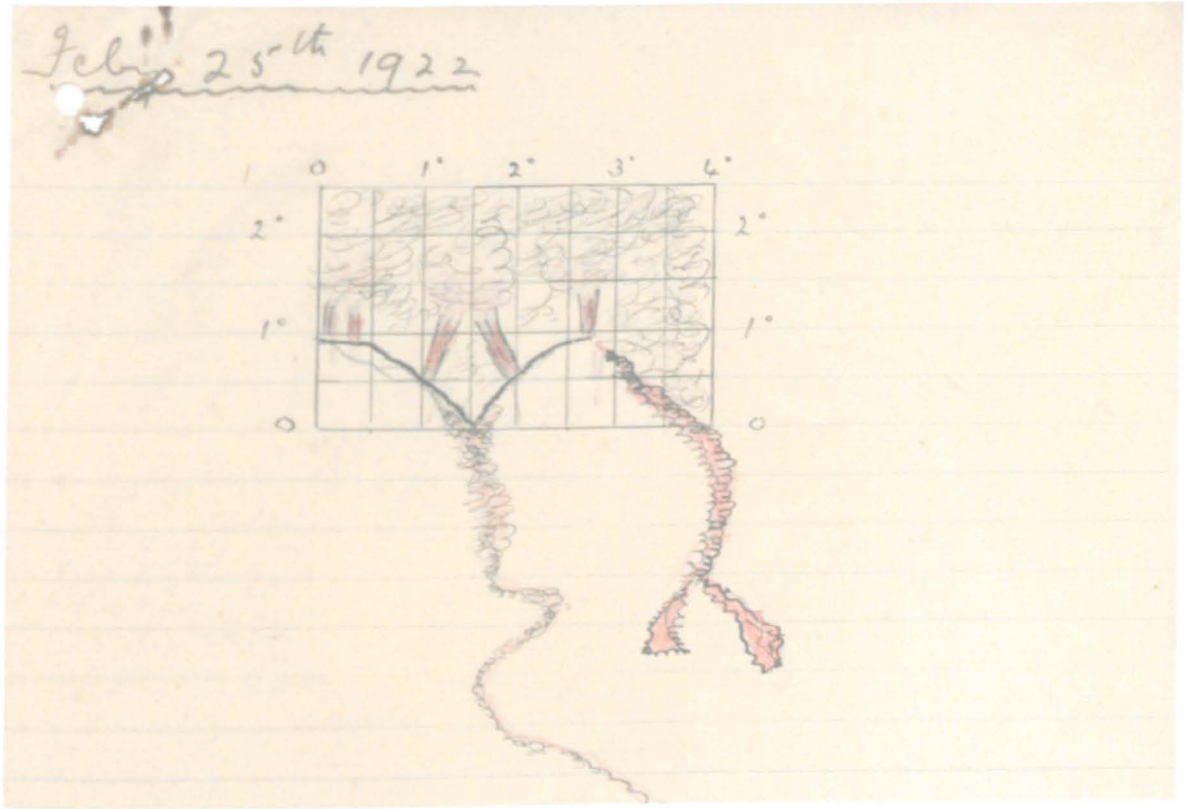

Plate B.7 Photographic reproduction of A. A. Reading's sketch of the vents, 25th February 1922. Reading's caption reads: *Visibility never really good and impossible to see details of craters. Lava stream on the right very bright and strong but does not seem to have come much further down the mountain the last couple of days, but it is spreading out more on both sides.* CAB, QK 1920/2, No. 15/11/1922, Re Seismic Disturbances, 22nd March 1922.

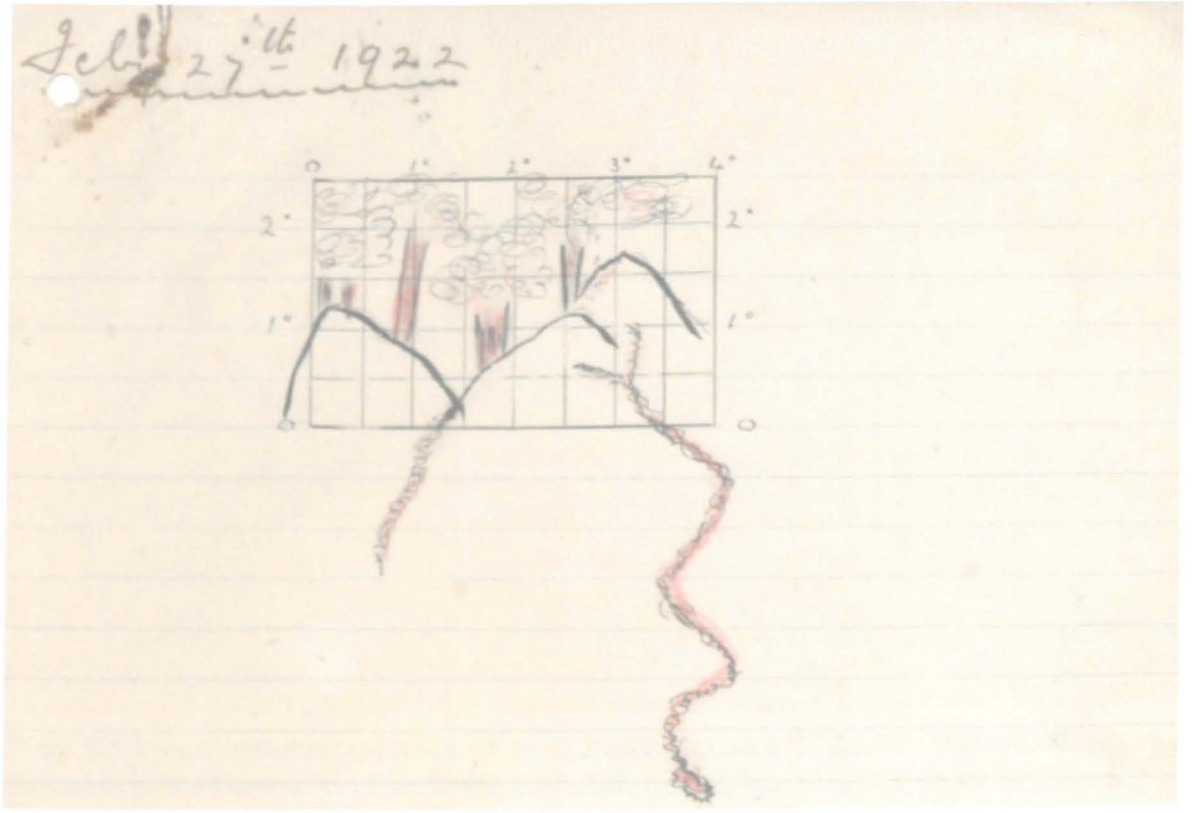

Plate B.8 Photographic reproduction of A. A. Reading's sketch of the vents, 27th February 1922. Reading's caption reads: *Visibility good at night, the huge mounds thrown up very distinctly seen, the general appearance is now very different to what it was on the 24th, the last time a good view was obtained. The five craters were all distinctly seen, though the two on the left were never so clear as the others, apparently they are situated rather behind the others. Lava stream very bright and burning fiercely at the end.* CAB, QK 1920/2, No. 15/11/1922, Re Seismic Disturbances, 22nd March 1922.

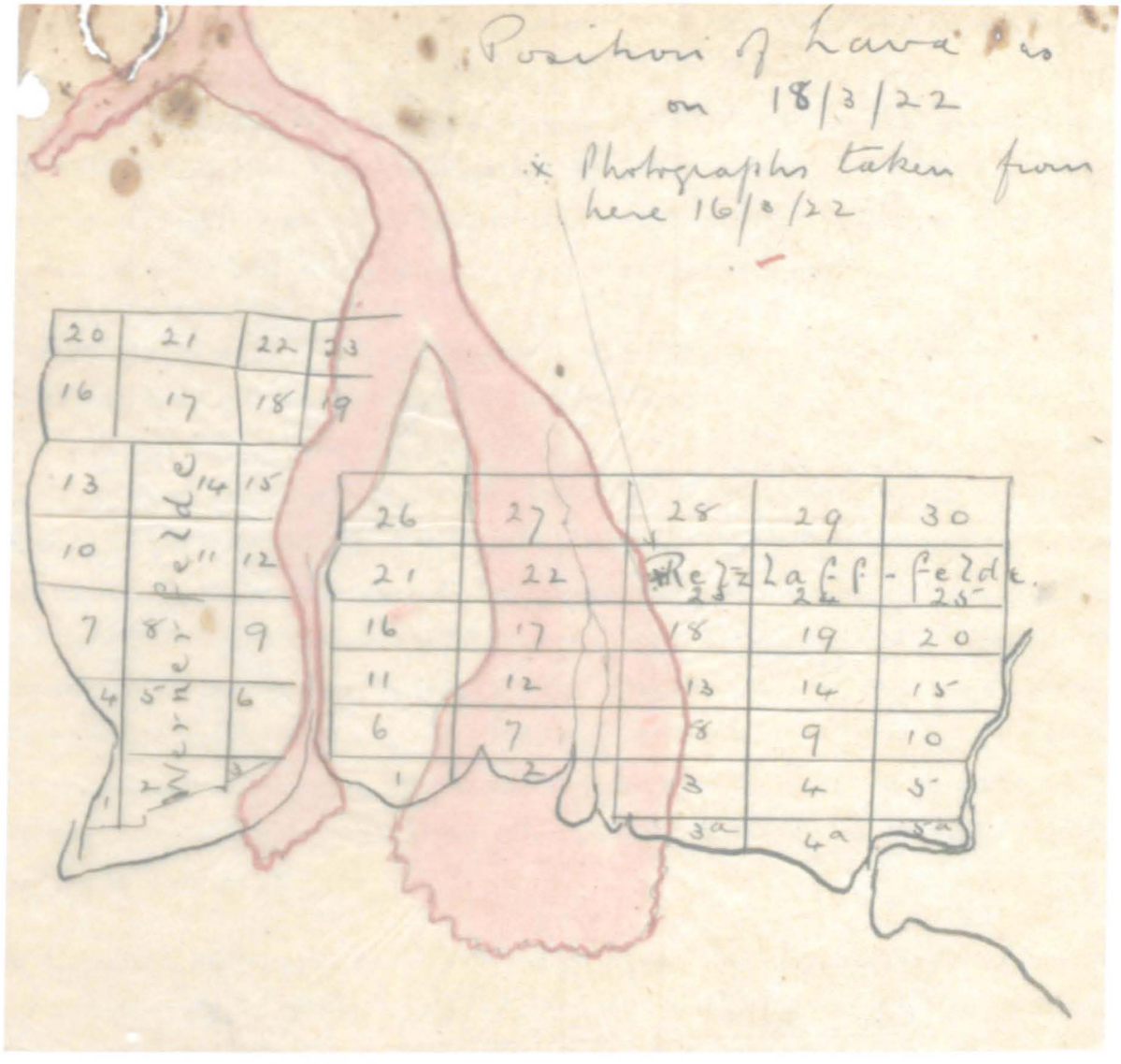

Plate B.9 Photographic reproduction of A. A. Reading's sketch of the 18th March 1922, showing the extent of the Bibundi lava flow fronts. CAB, QK 1920/2, No. 19/11/22 contd 18th March.

> *on a high hill & will I think escape destruction. The native compound on Wernerfelde also you will see has been overwhelmed, but there again I hope the Bungalow will escape as it stands high.'*[60]

The damage caused to the southernmost plantation farms, Retzlafffelde and Wernerfelde (**Figure B.4b**) was not the only danger Reading saw to his charge.

> *"It is that small stream of lava East of Dollmanshöhe that I fear, it ran down as shown on the map* (**Figure B.4b**) *a week ago but since then has made no apparent movement* [i.e. the 5.3.22 standline]. *Should that develop with a stream like the one through Retzlafffelde the whole Estate will be wiped out. The volcano is just as active as ever makes more noise now than at first, it is one continual roar day and night.'*[61]

[60] CAB, QK 1920/2 No. 19/11/1922 Reading to Supervisor of Plantations, Bota, 13th March.
[61] Ibid.

Reading diligently continued to make further observations of the development of the lava streams. A day after his report of the 13th, he noted that the general lava position at Bibundi was unchanged, except on Retzlafffelde, where the lava had 'extended considerably'. The flow field had expanded to the north, entering Plots 11, 6 and 1 (**Plate B.9**), and was "burning fiercely and from the sea huge columns of steam are going up." As had happened frequently in the past few days, the roughness of the surf prevented Reading from taking his canoe to sea to observe further.[62]

Smoother waters on the 15th allowed Reading to navigate around the front of the flow. The lava entered the water in the middle of Plot 1 and extended south to the middle of Plot 3a (**Plate B.9**). The water even three hundred yards from the lava *"was so hot, at times you could not even bear your hand in it,"* and Reading was able to approach no closer. The following day he examined the southern flank of the lava in Retzlafffelde, and reported that the flow extended about 700 yards into the sea. On the 18th, Reading produced a sketch of the coverage of the plantation thus far, reproduced here as **Plate B.9**, and noted that there was *"slight movement yesterday in Plots 23 and 19 of Wernerfelde* [i.e. an expansion of the flow upstream; **Plate B.9** and **Fig. B.4b**] *which are now both almost completely covered."* Poor visibility over the past few days had hampered observations of the craters, and the noise of the eruption had reduced somewhat, but seismic events were still felt on the night of the 17th. Reading also noted that the smaller stream of lava east of Dollmanshöhe had made slight progress (see **Figure B.4b**, '18.3.22').[63]

A. A. Reading's following update, dated 22nd March, reported little change in the development of the Wernefelde and Retzlafffelde streams, other than the observation on the 20th of two break-out lobes from the north flank of the latter, extending into Plot 26 (these are not depicted, but their locality can be appreciated in **Plate B.9**). A new development was marked in his observation: "a new lava stream appears to be developing in the left [sic] which looks as if it would enter Thormahlenfelde if it continues" (**Figure B.4b**). On the 20th this flow glowed brightly at night, but *"its progress [seemed] slow."*[64]

In a separate report of the same date, Reading added a little more character to the phenomena. The craters appeared to be *"just as active as ever, some days the noise [was] quite loud, just like a blast furnace, other days there [were] series of explosions which sound[ed] just like a big gun firing."* Some days they received showers of ash that fell like rain, falling so heavily that the ash broke the leaves of the palm trees. The lava itself, when it reached open ground, progressed like

[62] Ibid.
[63] Ibid.
[64] CAB, QK 1920/2, No. 19/11/22 contd Reading to Act. Sup. of Plantations, Bota, 22nd March.

> *"...a wall of red hot rock 30 or 40 feet high which keeps falling away as it advances, but when it came down the deep ravine between Wernerfelde and Retzlafffelde it flowed like a red hot river moving at the rate of about 2 feet a minute. I threw a big stone on it to see if it would make a splash, but although it was moving and looked liquid, the stone bound off it just as if it were solid rock."*[65]

The manager at Bibundi calculated that some 162 acres of his farms had been destroyed by lava (32 acres in Wernerfelde and 130 acres in Retzlafffelde). This is a somewhat smaller estimate than that passed in a report written on the 21st March, wherein the Plantations Department in Bota estimated that approximately 350 acres had been affected.[66] Reading's final report on the progress of the lava in the Bibundi plantation, was written on the 29th March, and was accompanied by a sketch of the extent of the lava on the 28th, reproduced in **Plate B.10**. Over the 23rd to 25th March, he noted little change, but suggested that a lava *"breakthrough on the left* [i.e. the north of the flow field] *[seemed] likely."*

By daybreak on the 26th, however, this breakthrough was made manifest, with lava advancing into Plot 21 of Wernerfelde (**Plate B.10**). Reading noted

> *"The suspected breakthrough had evidently taken place though luckily not as much to the left as anticipated. I immediately... started to save the Railway Line. I then went up to inspect the lava and found that it had already entered Plots 20 & 21 and was advancing rapidly."*[67]

The following day Reading recorded that lava had *"advanced considerably during the night, but was apparently slowing up."* Telephone connection with Bota had been re-established, as the lava in Retzlafffelde had cooled enough to allow a cable to be lain over it. By the morning of the 28th, the new lava stream spreading into Wernerfelde had advanced slightly, but then experienced a rapid surge in its movement in the afternoon, passing under and destroying the bridges linking Dollmanshöhe and Wernerfelde. Following this extension the lava field ceased, and on the 29th Reading recorded that the lava was "apparently stationary".[68]

On the 29th March, Reading reported that in addition to the damage to 162 acres of the farms of Wernerfelde and Retzlafffelde caused by the older lava streams, a further 100 acres had been

---

[65] CAB, QK 1920/2, No. 15/11/1922 contd, Re Seismic Disturbances, Reading to Sup. of Plantations, Bota, 22nd March.

[66] Reading's estimates are contained in CAB, QK 1920/20, No. 19/11/22 contd (22nd March) and No. 15/11/1922 contd (22nd March). The Plantation Department's initial estimations are in CAB, QK 1920/20, No. 234/12/22 Act. Sup. of Plantations to the Hon. the Secretary, Southern Provinces, Lagos, 21st March. In a further note, the Plantations Department clarify their original estimate, stating that it *"took into consideration the plots in the vicinity of the lava stream which are likely to be effected thereby."* CAB, QK 1920/2, No. 246/12/22 Act. Sup. of Plantations to the Hon. the Secretary, Southern Provinces, Lagos, 25th March.

[67] CAB, QK 1920/2, No. 19/11/22 contd Reading to Sup. of Plantations, Bota, 29th March.

[68] Ibid.

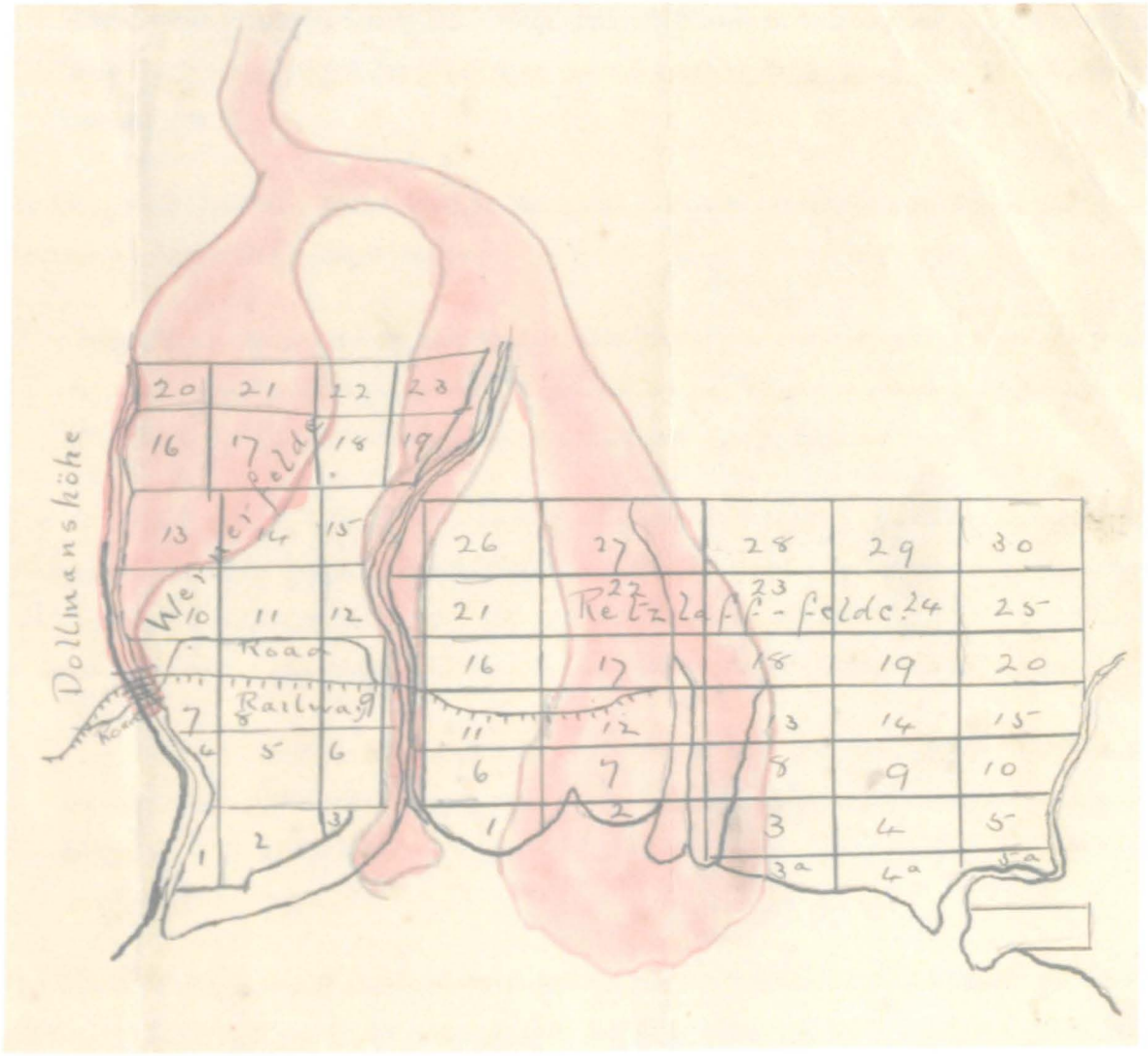

Plate B.10 Photographic reproduction of A. A. Reading's sketch of the 28th March 1922, showing the extent of the Bibundi lava flow fronts. CAB, QK 1920/2, No. 19/11/22 contd 29th March.

affected by the newer branch of flow. It had appeared that no further damage would be caused to the Bibundi plantations. In a memorandum of the 12th April, Reading stated that since his last report (29th March), he had nothing new to report. The vents remained as active as they had before, but no new lava had reached plantation.[69]

Things changed for the worse two months later, when on the 17th June flow activity at Bibundi recommenced. In a detailed report of the new activity, the Acting Supervisor of Plantations, Mr. Cameron, recorded

> *"On 17th June the Manager of Bibundi informed me by telephone that lava streams had commenced in flow again [and] also that heavy damage was being done by floods. On the 18th I went to Bibundi and going... to*

[69] Ibid.; CAB, QK 1920/2, No. 19/11/22 contd Reading to Sup. of. Plantations, Bota, 12th April.

> *Dollmanshöhe I found the roadway of the bridge entirely swept away by floods... I went up the river and in about a mile reached the first flow of lava which had been advancing the day before, but had cooled and was stationary."*[70]

As he crossed over into Wernerfelde to the south, Cameron's progress was shortly halted by advancing lava, forming a stream that was

> *"molten but its advance which was more "creeping" than "flowing" was over a very wide area and on a gentle slope, and it seemed probable that eventually it would cool and turn the main lava stream down the old course of the Njonge [Ngonge] river and extend into the sea which part of the flow was then doing."*[71]

The lava itself was not directly the greatest of Cameron's worries. Flooding damage was considerable; over fifty inches of rain had fallen in the first two and a half weeks of June and the blocking of old watercourses by the lavas had exacerbated the drainage problem.[72] On the 20th June a manuscript note from the manager of Bibundi, highlighted a more rapid trend of lava advance:

> *'Lava takes a turn to the left* [north; the breakout occurs near the 'Bungalow', **Figure B.4b**] *down the main road at Dollmanshöhe, this morning... Very fine sight... streamed down in such streams quite quickly that it got into the river in the afternoon. So I am afraid the main buildings will shortly suffer badly from flooding."*[73]

The following day a similar note recorded that the lava had advanced rapidly along the river splitting the Jantzenhof and Dollmanshöhe farms, and had reached the hospital (**Figure B.4b**). He was confident that once the river channel had filled with lava, the stream would be diverted to the north, towards the Bibundi house.[74]

On the 25th June, Cameron returned to Bibundi, accompanied by Mr. Waldau, who was still resident at Debundscha. Cameron reported that at Dollmanshöhe the whole of the farm to the east of the railroad (see **Plate B.10**; the railroad or 'iron road' runs approximately north-south through the Bibundi plantations) was covered by lava, and that *"molten lava was flowing down the banks of the ravine... The river* [the watercourse north of the Ngonge on **Figure B.4b**] *bed was full of detached flows of lava fed from the Dollmanshöhe plateau where it had been massing during the past week."* Tracing the length of the deposits, from the bungalow in Thormahlenfelde downflow, he found lava flowing

---

[70] CAB, QK 1920/2, 'Recommencement of Lava Flows on Bibundi Estate', Cameron, undated. However the report, asked for in a letter (CAB, QK 1920/2, B.421/1922, 7th July 1922), was dispatched to a variety of correspondents in mid-July, as recorded in CAB, QK 1920/2, No. 764/12/22, 13th to 16th July.
[71] Ibid.
[72] Ibid.
[73] CAB, QK 1920/2, unnumbered MSS McCallum (?) to Cameron, 20th June 1922.
[74] CAB, QK 1920/2, unnumbered MSS McCallum (?) to Cameron, 21st June.

'everywhere'; by 11 pm that evening the lava had crossed the north-south railroad in Dollmanshöhe, and was following the road that splayed from the rail and was bound for Bibundi.[75]

In a telegram dated 27th June, Cameron advised the Public Custodian of Enemy Property in Lagos of the then current status of the eruption. The greater part of Dollmanshöhe had been destroyed, and lava was beginning to flow rapidly into Jantzenhof as of the 26th, but in general he did not *"anticipate very rapid advance of lava as [the] slope is now gentle and [the] flow is wide."* McCallum's letters to Cameron over the 2nd and 3rd July compounded this general picture. Flooding was severe, and the lava was advancing slowly, if *'filling up everywhere."*[76]

On the 11th July, Cameron revisited Bibundi. Again he traced the lavas from the Hospital to near the Thormahlenfelde bungalow (**Figure B.4b**); though the lava had advanced considerably since his last visit, Cameron recorded that their activity was "gradually dying out." The effusion of lavas from the lower vents seemed as strong as ever, however, and further flow activity was expected to recommence at a later date. In assessing the damage to the Bibundi Estate, Cameron noted that, in addition to the damage already caused to Retzlafffelde and Wernerfelde, Thormahlenfelde had received lava and flood damage in the four plots closest to the southern river boundary. Jantzenhof had likewise been affected along the river course, with elements of four plots affected by the lava, and the hospital pulled down. Flooding spread north and west, causing damage to buildings and three feet of standing water.[77]

Dollmanshöhe had been near destroyed, with lava covering the eastern portions of the farm and floodwaters inundating the lower littoral regions. The flows that had followed the courses of the Moliwe and Ngonge rivers (**Figure B.4b**) had been focused onto the coast, and actually joined, serving to wall off the remaining portions of Wernerfelde in a manner that promoted considerable flooding.[78] On the 14th Cameron, as Acting Supervisor of Plantations, telegrammed the absent Supervisor, F. Evans, and reported that though the eruption was still active, lava advance had ceased for the present, with lava simply accumulating at the position of the hospital (**Figure B.4b**). A day later, McCallum in Bibundi sent a memorandum to Cameron, stating that the lava streams were quiet, but that for the previous three nights a bright new flow of lava had been seen coming down the side of the mountain, much closer in direction to Bibundi and the Ninonne river than the previous streams had been. Finally, on the 18th July 1922, McCallum wrote to Cameron in Bota,

[75] CAB, QK 1920/2, 'Recommencement of Lava Flows on Bibundi Estate', Cameron, undated.
[76] CAB, QK 1920/2, telegram from Plantations Department, Cameroons, to Public Custodian, Lagos, 27th June; CAB, QK 1920/2, letters from McCallum to Cameron, 2nd & 3rd July.
[77] Ibid.
[78] Ibid.

stating that while one could still see the glowing streams descending the mountainside, there had been no lava front advance at Bibundi.[79]

B.4 The activity post-1922 and movements toward the current situation

Following the cessation of flow activity at Bibundi, the most observed and potentially destructive elements of the 1922 eruption had ended. The sheer spatial and temporal extents of the eruption had fully awakened the new administration to the capabilities of the volcano, and the malign effects on the local ecosystem, and the human environment. The flows of the lower 1922 vents extended for twice the length of those from Okoli, and demonstrated that the volcano could develop outpourings of lava from the centre, or the north and west flanks. Concerns that the period of eruptive activity may not have ended following the cession of lava flow on the mountainside were raised during the 3rd-17th November 1922, when a series of seismic events were experienced in Victoria. H. S. Meilandt, the Executive Engineer of the Cameroons Division, Public Works Department (P. W. D.), noted

> *"...during the last 14 days there have been a great many underground rumblings and small shocks running through Victoria from South to North. In one day I have counted 8 to 19 separate reports lastings [sic] from 3 to 16 seconds. The average daily number is 9 to 10. We have also had 3 to 4 bad shocks daily for the last 7 days these shocks are increasing in violence. Last night at 9.pm. we experienced the worst shock we have had – my candlesticks and pictures were knocked over and I fully expected the house to fall."*[80]

Over the next two weeks these reports were passed onto the highest organs of the government in Lagos, but no further note of earthquake activity in the Cameroons in 1922 followed that of Meilandt's original memorandum.[81] Though there is apparent evidence of minor activity in 1924, with the Resident in Buea noting the appearance of fresh white ash near the summit crater and fumarolic activity around the craters and fissures in a memorandum to the Director of the Geological Survey in Jos, no further reports followed.[82] Seismic outbursts would mark the trend of Mount Cameroon and its environs' activity during the following volcanic events. On the 11th December 1946, the Provincial Engineer of the P. W. D. communicated in a telegram to his

---

[79] CAB, QK1920/2, 741/12/22, Telegram confirmation of 9th June Cameron to F. Evans, Esq., West Indian Club, 14th July; CAB, QK 1920/2, note from McCallum to Cameron (marked R829/30), 15th July; CAB, QK 1920/2, McCallum to Cameron, 18th July.

[80] CAB, QK 1954/1, No. 1172/92/22 Meilandt to Director of Public Works, P. W. D, 17th November 1922.

[81] The report was reached the Chief Secretary to the Government, Lagos, from the Secretary, Southern Provinces, on 2nd December. CAB, QK 1954/1, No. 8536/67/22 Director, P. W. D to Secretary, Southern Provinces, 20th November; CAB, QK 1954/1, B.1837/1922 Secretary, Southern Provinces to the Hon. the Chief Sec. to the Govt., 2nd December.

[82] Quoted in E. N. Gamnje, *The Cameroon Mountain, Its Eruptions and the Recent Tremors*, Report of the Ministry of Mines and Power, Department of Mines and Geology, 1975, p. 5.

administrators that *"A severe earth quake shock tenth December has caused damage several buildings Victoria. Am examining extent of damage and will report fully earliest x Works informed.'*[83]

In a subsequent telegram, the Provincial Engineer stated that the *"only buildings affected seriously [were houses] of Executive and Diworks. Minor damage only to remainder."* From this information further details were sought. The Resident, Cameroons Province, believed that initial reports overstated the intensity of the tremors:

> *"The earthquakes do not seem to have been so severe as the first report stated. In fact I only heard of it by accident as I was away at the time it took place. I understand there are cracks in the houses of DO Victoria and PE, but otherwise no damage. From previous papers in this file it seems sensible that it may be followed by an eruption on the mountain.'*[84]

A full report on the shocks, dated 7th January 1947 recounted the events. A. Leeming, the Senior District Officer, Victoria, stated:

> *"...an earth tremor occurred at Victoria and in the surrounding countryside at 3.47 a.m. on the morning of the 10th of December, 1946. The shock was felt at Buea at approximately the same time, but not damage to building has been reported. At Kumba ad Tiko the shock was even less pronounced. At Douala the shock was also felt, but no damage was sustained... The lighthouse staffs at Debundscha and Nachtigal report that they did not feel the shock. No personal injuries were suffered anywhere.'*[85]

It was considered that the shock consisted of *"one heavy tremor, followed after less than a second by four or five smaller tremors."* One witness stated that the earthquake was preceded by a "sound like heavy thunder", another by a sound *"that was exactly like a V.2 rocket exploding a hundred yards away (with the echo thundering up the mountainside)"*, followed immediately by the shocks. The Provincial Engineer stated that the shocks were felt in Victoria at approximately 3.50 am, and that the vibrations lasted for six seconds. Damage to the buildings (of which only European dwellings are apparently considered) was mainly limited to pre-1914 constructed residences, usually made of concrete walls and floors, with galvanised steel roofs. The concrete cracked in several dimensions, leaving hairline fissures and cracks up to an inch in width.[86]

---

[83] CAB, QK 1954/1, Copied from pp. 59 & 60 of P.W.D's file 557. (marked '6'), 1517 Diworks, Victoria to Adworks, Enugu, 11th December.
[84] CAB, QK 1954/1, Copied from pp. 59 & 60 of P.W.D's file 557. (marked '6'), 1562 Diworks, Victoria to Adworks, Enugu, 19th December; CAB, QK 1954/1, telegram 21346 (marked 3) Secretary, Enugu, to Resident, Buea 23rd December 1946; CAB, QK 1954/1, appended MSS, Resident, Cameroons to SEP, 7th January 1947.
[85] CAB, QK 1954/1, No.V.1396/5 (marked 6) Leeming to Resident, Cameroons Province, 7th January 1947.
[86] Ibid.

Further earthquakes and volcanic activity occurred in 1954, in a sequence of events that were best detailed by Dr. A. M. J. de Swardt, the Principal Geologist, Enugu. Additional primary data and information are collected in this thesis, to provide an adjunct to de Swardt, and overview the basic events of the activity of 1954. A telegram from the Resident in Buea, to the Civil Secretary in Enugu, dated 29th June 1954, stated:

> *"Two minor earth tremors in Buea during last two weeks. This morning and last evening puffs smoke rising from the top of Cameroons Mountain. No damage has occurred or is expected to do so. Local population undisturbed."*[87]

In a subsequent telegram of the 3rd July, the Resident communicated

> *"Earth tremors lasting from two to five seconds each felt in Buea and Victoria on four occasions at irregular intervals during past three weeks. Eruption first observed on evening of 27th June consisting of two enormous columns [of] black smoke estimated at between two and three thousand feet high situated westwards and behind shoulder of mountain."*

Following the initial eruption the smoke columns were *"noticeably whiter in colour and [a] reddish glow at the base of [the columns] was occasionally visible."* Activity continued and was observed for short periods every day, until 30th June, when a mist descended; no further tremors were experienced. Once visibility was restored on the 3rd July, no columns of smoke were observed, but a report from 10 miles south of Buea stated that three "huge puffs of smoke" had been observed on the 2nd, during a clear period of approximately two minutes; no mention of eruptive activity had yet been reported from other places of observation.[88]

Better visibility on the 5th July allowed better observations from Buea. Black columns of smoke appeared at "frequent continuous intervals", and it was thought that the 'reddish glow' previously observed may have resulted from the effect of the sunset and sunrise. No sign of any lava flow was witnessed (and this statement was repeated for emphasis). Such observations were confirmed by an aeroplane overflight, on which the pilot reported that he saw "columns of smoke coming from [the] crater at the summit and burning cinders appeared to be thrown up to [a] height of about one [hundred and] fifty metres."[89] A. M. J. de Swardt had ascended the mountain on 9th July, accompanied by Mr. K. J. O'Shaughnessy, Principal Surveyor, Buea. Their return to Buea on the 13th caused the Resident to report briefly on their findings:

---

[87] CAB, QK 1954/1, Telegram 4060 (marked 10A) Resident to Civsec Enugu, 29th June 1954.
[88] CAB, QK 1954/1, Telegram 4060 (marked 10B and B/14) Resident to Civsec Enugu, 3rd July 1954.
[89] CAB, QK 1954/1, Telegram 4060/14 (marked 11A) Resident to Civsec Enugu, 6th July; CAB, QK 1954/1, Telegram B.1 (marked 12) Resident to Civsec Enugu, 11th July.

"They report that there is only one repeat one active vent which is throwing out ash and solid large blocks up to size of ten feet diameter covering area with half mile radius. Smoke rising in puffs up to two thousand feet... there have been no repeat no lava flow... Geologist further reports that unless radical change occurs there is no imminent danger. Activity probably decreasing."[90]

For the sake of this narrative, it will prove useful to insert a description of de Swardt's field study, as presented to *The Easter Outlook and Cameroons Star*, and printed on the 22nd July:

"...the eruption is not on a large scale and is taking place on the opposite side of the mountain from Buea... At the time of the visits there was only one active vent emitting puffs of dark smoke at intervals of about half a minute. The eruption may have two feeding channels as pillars of smoke were often seen to rise almost simultaneously at opposite ends of the vent. The smoke from the volcano rises to a height of up to 2,000 ft. and even when there is a strong wind it ascends vertically for several hundred feet before being dissipated. The vent is situated on the north-west rim of the old extinct crater near the summit and about 500 to 600 yds. west-north-west of the peak."[91]

On the 1954 crater, de Swardt continues

"A few hundred yards away, in a valley, there is a low crater composed of rock fragments and ash, apparently associated with the present eruption, but which practically ceased activity. On the slope between the two vents there is a scar which looks fresh and is still smoking in places. This scar is almost certainly the result of the earth movements which caused the earth tremors in Buea and the surrounding country before the start of the eruption.

"About half the puffs are silent and composed only of smoke with a little ash. The others are accompanied by loud explosions and, apart from dense smoke, fragments of rock, up to 10 ft. across are thrown to a height of from 100 to nearly 1,000 ft. At the time of the examination these fell up to half a mile from the vent, but during the earlier stages of the eruption they travelled over a mile. This may suggest a decrease in activity, but it is also likely that the initial explosions, which opened up the vent, were more violent than those accompanying the present discharges which can escape along an established channel.

"The rock fragments travel through the air with a loud hissing noise and form deep holes where they hit the ground, and smoke for several minutes afterwards. Near the vent the hill-sides have been extensively scarred by falling debris. Most of the fragments are composed of vesicular lava. At night they look red-hot on leaving the vent and fade gradually as they approached the surface. The effect is that of a gigantic fireworks display. A little

[90] CAB, QK 1954/1, Telegram 460 (Marked 14B) Resident to Civsec Enugu, 14th July.
[91] *The Eastern Outlook and Cameroons Star*, 22nd July 1954, pp. 1 & 5.

ash is also emitted by the volcano, but it forms only a thin veneer over the surface within a mile of the eruption."[92]

Further developments in activity were observed at 10 am on the 17th July and 8 am 21st July, when a *"heavy rumble resembling [a] thunderclap or detonation was heard"*. Although unaccompanied by tremors, the phenomena were accompanied by large volumes of smoke covering a greater than normal area. A further explosion was heard on the 25th July, but observations conducted in the limited periods of visibility allowed the Resident to suggest that the activity at the summit was actually decreasing.[93] The authorities acted very much in an effort to quell earlier, sensationalist accounts of the eruption, in an effort to prevent undue panic and concern. De Swardt's article in The Eastern Outlook and Cameroons Star was very much an element of the strategy of *"preventing the eruption of a "molehill made" mountain."* Activity waned and on the 6th September 1954, the Resident in Buea was able to pass on the report of a geologist that had just returned from an inspection of the mountain, namely that *"...all activity practically ceased and no repeat no likelihood of any further disturbance."*[94]

In more recent times, eruptions have been better documented outside of archival sources; neither the eruption of 1959, earthquakes of 1967, 1973 and 1975, nor the eruption of 1982 are not discussed here. Data pertaining to the details of such volcanic events are within the reach of the volcanologist, and in the published record. It is hoped that the historically based investigation of this appendix has placed at the reach of geologists studying Mount Cameroon a variety of data that were hitherto confined to the Cameroon Archives in Buea. Such sources build on the scientific record, and offer corollaries to the somewhat poorly recorded events of previous eruptions, or offer comparison and analysis of diverse sources with occasionally conflicting accounts. This appendix has thus sought to bring a more illuminated description of the events of 1909, 1922, 1946 and 1954 to the volcanologist interested in the still little studied eruptive phenomena of Mount Cameroon.[95]

---

[92] Ibid.

[93] CAB, QK 1954/1, Telegram 4060 (Marked 15) Resident to Civsec Enugu, 21st July; a further note on the 21st July stated that "there was a large explosion from inside the mountain yesterday morning about 8 o'clock. The mountain was only visible for a short time at 08.15 a.m. but during that time two large puffs of smoke were seen." CAB, QK 1954/1, Note on sheet marked 15, dated 22nd July; CAB, QK 1954/1, Telegram 4060 (Marked 15; below above) Resident to Civsec Enugu, 27th July.

[94] CAB, QK 1954/1, Telegram 4060 (in reply to No. 50366/73 of 30th August) Resident to Civsec Enugu, 6th September.

[95] For example, the 1959 eruption is documented in: E. W. Ardener and D. W. Macrow, 'Cameroon Mountain', *Nigeria*, No. 62 (1959), 230-245 and J. H. Jennings, 'The eruption of Mt. Cameroon, February-March 1959', *Geography*, No. 44 (1959), 207-208.On the tremors felt in the 1960s and 1970s, brief notes are contained in Gamnje, op. cit., p. 7. On the 1982 eruption, the most accessible source is J. G. Fitton, C. R. J. Kilburn, M. F. Thirlwall and D. J. Hughes, '1982 Eruption of Mont Cameroon, West Africa', *Nature*, Vol. 306, 24th November 1983, 327-332.

References

Archive sources, manuscript and printed

Cameroon Archives, Buea

QK 1920/2

[The third part of QK 1920/2 was formally Plantations File 12/22. Although the 12/22 was reclassified, individual documents have not, and retain their original notation.]

QK 1954/1

West Cameroon Press Releases (Southern Cameroons Series), January-June 1959. West Cameroons Archives.

Journal articles and books

ALEXANDER, B. 1909 Lieut. Boyd Alexander's Expedition in West Africa. *Geographical Journal* **34** (1; Jul. 1909), 51-55.

ALEXANDER, J. 1977 *Whom the Gods Love: Boyd Alexander's expedition from the Niger to the Nile, 1904-7, and his last journey, 1908-10.* London.

ANON. 1995 Kuv'a likenye and the Bakweri Armed Resistance to the Germans: 1891-4. In *Fako International* **2** (1, January).

ARDENER, E. 1996 *Kingdom on Mount Cameroon: Studies in the History of the Cameroon Coast, 1500-1970.* Oxford.

BALMFORTH, N. J., BURBIDGE, A. S., CRASTER, R. V., SALZIG, J. & SHEN, A. 1999 Viscoplastic models of isothermal lava domes. *J. Fluid Mech.* **403**, 37-65.

BALMFORTH, N. J. & CRASTER, R. V. 2000 Dynamics of cooling domes of viscoplastic fluid. *J. Fluid Mech.* **422**, 225-248.

BALMFORTH, N. J., CRASTER, R. V. & SASSI, R. 2002 Shallow viscoplastic flow on an inclined plane. *J. Fluid Mech.* **470**, 1-29.

BALMFORTH, N. J., CRASTER, R. V. & SASSI, R. 2003 Dynamics of cooling viscoplastic domes II. *J. Fluid Mech.* (in press).

BARNES, H. A. 1999 The Yield Stress - a review or "παυτα ρει" - everything flows? *J. Non-Newtonian Fluid Mech.* **81**, 133-178.

BATCHELOR, G. K. 1967 *An Introduction to Fluid Dynamics.* Cambridge University Press.

BERCOVICI, D. 1994 A theoretical model of cooling viscous gravity currents with temperature-dependent viscosity. *Geophys. Res. Lett.* **21**, 1177-1180.

BERCOVICI, D. & LIN, J. 1996 A gravity current model of cooling mantle plume heads with temperature-dependent buoyancy and viscosity. *J. Geophys. Res.* **101**, 3291-3309.

BIOT, M. A. 1960 Instability of a continuously homogenous half space under initial stress. *J. Franklin Inst.* **270**, 190-201.

BIOT, M. A. 1961 Theory of folding of stratified visco-elastic media and its implications in tectonics and orogenesis. *Bull. Geol. Soc. Am.* **72**, 1595-1620.

BLAKE, S. 1990 Viscoplastic models of lava domes. In *Lava flows and domes: emplacement mechanisms and hazard implications* (ed. J.H. Fink), pp. 88-128. IAVCEI Proc. In Volcanology, vol. 2, Springer-Verlag, Berlin.

BOOTH, B. & SELF, S. 1973 Rheological features of the 1971 Mount Etna lavas. *Philos. Trans. R. Soc. London A* **274**, 99-106.

BRUNO, B. C., BALOGA, S. M. & TAYLOR, G.J. 1996 Modelling gravity-driven flows on an inclined plane. *J. Geophys. Res.* **101**, 11565-11577.

BURTON, R. F. 1862 Account of the Ascent of the Cameroons Mountain, in Western Africa. *Proc. R. Geog. Soc. London* **6** (5; 1861-1862), 238-248.

CASHMAN, K. V., THORNBER, C. R. & KAUAHIKAUA, J. P. 1999 Cooling and crystallization of lava in open channels, and the transition of Pahoehoe Lava to `A`a. *Bull. Volc.* **61**, 306-323.

CASTRO, J. & CASHMAN, K. V. 1999 Constraints on rheology of obsidian lavas based on mesoscopic folds. *J. Struct. Geol.* **21**, 807-819.

CHESTER, D. K., DUNCAN, A. M., GUEST, J. E. & KILBURN, C. R. J. 1985 *Mount Etna: the anatomy of a volcano.* Stanford University Press.

COMBER, REV. T.J. 1879 Explorations Inland from Mount Cameroons, and Journey Through Congo to Makuta. *Proceedings of the Royal Geographical Society and Monthly Record of Geography* **1** (4; Apr. 1879), 225-240.

CRISP, J. & BALOGA, S. 1990 A model for lava flows with two thermal components. *J. Geophys. Res.* **95**, 1255-1270.

CRISP, J. & BALOGA, S. 1994 Influence of crystallisation and entrainment of cooler material on the emplacement of basaltic `a`a lava flows. *J. Geophys. Res.* **99**, 11819-11832.

DANCE, M., HANCOCK, P., SPARKS, R. S. J. & WALLMAN, A. 2001 Fracture and surface crust development in a Holocene lava flow on the island of Tenerife, Canaries. *J. Struc. Geol.* **23**, 165-182.

DAVAILLE, A. & JAUPART, C. 1993 Trannsient high Rayleigh number thermal convection with large viscosity variations. *J. Fluid Mech.* **253**, 141-166.

DIDDEN, N. & MAXWORTHY, T. 1982 The viscous spreading of plane and axisymmetric gravity currents. *J. Fluid Mech.* **121**, 27-42.

DONATH, F. A. & PARKER, R. B. 1964 Folds and folding. *Geol. Soc. Am. Bull.* **75**, 45-62.

DRAGONI, M. 1989 A dynamical model of lava flows cooling by radiation. *Bull. Volc.* **51**, 88-95.

DRAGONI, M., PONDRELLI, S. & TALLARICO, A. 1992 Longitudinal deformation of a lava flow: the influence of Bingham rheology. *J. Volcanol. Geotherm. Res.* **52**, 247-254.

DRAGONI, M. & TALLARICO, A. 1994 The effect of crystallisation on the rheology and dynamics of lava flows. *J. Volcanol. Geotherm. Res.* **59**, 241-252.

FINK, J. H. 1980 Surface folding and viscosity of rhyolite flows. *Geology* **8**, 250-254.

FINK, J. H. & FLETCHER, R. C. 1978 Ropy pahoehoe: surface folding of a viscous fluid. *J. Volcanol. Geotherm. Res.* **4**, 151-170.

FINK, J. H. & GRIFFITHS, R. W. 1990 Radial spreading of viscous-gravity currents with solidifying crust. *J. Fluid Mech.* **221**, 485-510.

FINK, J. H. & GRIFFITHS, R. W. 1992 A laboratory analog study of the morphology of lava flows extruded from point and line sources. *J. Volcanol. Geotherm. Res.* **54**, 19-32.

FINK, J. H. & GRIFFITHS, R. W. 1998 Morphology, eruption rates and rheology of lava domes: insights from laboratory models. *J. Geophys. Res.* **103**, 527-546.

FINK, J. H. & ZIMBELMAN, J. 1990 Longitudinal variations in rheological properties of lavas: Puu Oo basalt flows, Kilauea volcano. In *Lava flows and domes: emplacement mechanisms and hazard implications* (ed. J.H. Fink), pp. 157-173. IAVCEI Proc. In Volcanology, vol. 2, Springer-Verlag, Berlin.

FITTON, J. G. 1987 The Cameroon Line, West Africa: a comparison between oceanic and continental alkaline volcanism. In *Alkaline igneous rocks* (eds. J. G. Fitton, B. G. J. Upton), pp. 273-291. Geol. Soc. Lond. Spec. Pub. **30**, London.

FITTON, J. G. & HUGHES, D. J. 1977 Petrochemistry of volcanic rocks of the Island of Principe, Gulf of Guinea. *Contrib. Mineral. Petrol.* **64**, 257-272.

FITTON, J. G., KILBURN, C. R. J., THIRLWALL, M. F. & HUGHES, D. J. 1983 1982 Eruption of Mount Cameroon, West Africa. *Nature* **306**, 5941, 327-332.

FLETCHER, R. C. 1974 Wavelength selection in folding of a single layer with power-law rheology. *Am. J. Sci.* **274**, 1029-1043.

FLETCHER, R. C. & SHERWIN, J. 1978 Wavelength selection in single layer folding. *Am. J. Sci.* **278**, 1085-1098.

GAMNJE, E. N. 1975 *The Cameroon Mountain, Its Eruptions And The Recent Tremors.* United Republic of Cameroon Ministry of Mines and Power, Dept. of Mines and Geology Report.

GÈZE, B. 1943 *Géographie Physique et Géologie du Cameroun Occidentali.* Mémoire du Muséum National D'Histoire Naturelle, **XVII**, Paris.

GÈZE, B. 1953 Les Volcans du Cameroon occidental. *Bull. Volcanol.* **13**, 63-92.

GOODRIDGE, R. A. 1996 "In the most effective manner"?: Britain and the disposal of the Cameroons plantations, 1914-1924. *International Journal of African Historical Studies* **29** (2), 251-277.

GREGG, T. K. P. & FINK, J. H. 1995 Quantification of submarine lava-flow morphology through analogue experiments. *Geology* **23**, 73-76.

GREGG, T. K. P., FINK, J. H. AND GRIFFITHS, R. W. 1998 Formation of multiple fold generations on lava flow surfaces: Influence of strain rate, cooling rate and lava composition. *J. Volcanol. Geotherm. Res.* **80**, 281-292.

GREGG, T. K. P. & FINK, J. H. 2000 A laboratory investigation into the effects of slope on lava flow morphology. *J. Volcanol. Geotherm.* **96**, 145-159.

GRIFFITHS, R. W. 2000 The Dynamics of Lava Flows. *Annu. Rev. Fluid Mech.* **32**, 477-518.

GRIFFITHS, R. W. & FINK, J. H. 1992 Solidification and morphology of submarine lavas: a dependence on extrusion rate. *J. Geophys. Res.* **97**, 19729-19737.

GRIFFITHS, R. W. & FINK, J. H. 1993 Effects of surface cooling on the spreading of lava flows and domes. *J. Fluid Mech.* **252**, 667-702.

GRIFFITHS, R. W. & FINK, J. H. 1997 Solidifying Bingham extrusions: a model for the growth of silicic lava domes. *J. Fluid Mech.* **347**, 13-36.

GUEST, J. E., KILBURN, C. R. J., PINKERTON, H. & DUNCAN, A. M. 1987 The evolution of lava flow-fields: observations of the 1981 and 1993 eruptions of Mount Etna, Sicily. *Bull. Volc.* **49**, 527-540.

HALLIDAY, A. N., DICKIN, A. P., FALLICK, A. E., FITTON, J. G. 1988 Mantle dynamics: a Nd, Sr, Pb and O isotopic study of the Cameroon Line Volcanic Chain. *J. Petrol.* **29**, 181-211.

HALLWORTH, M. A., HUPPERT, H. E. & SPARKS, R. S. J. 1987 A laboratory simulation of basaltic lava flows. *Mod. Geol.* **11**, 93-107.

HAMMER, J. E., MANGA, M. & CASHMAN, K. V. 1998 Non-equilibrium and unsteady fluid degassing during slow decompression. *Geophys. Res. Lett.* **25**, 4565-4568.

HARRIS, J. L. & ROWLAND, S. K. 2001 FLOWGO: a kinematic thermo-rheological model for lava flowing in a channel. *Bull. Volc.* **63**, 20-44.

DE HART, J. & MATEER, CAPTAIN 1926 Notes on the Exploration of Africa among the Ancients: With Special Reference to Hanno. *J. R. Afr. Soc.* **25** (99), 264-277.

HOOVER, S. R., CASHMAN, K. V. & MANGA, M. 2001 The yield strength of subliquidus basalts. Experimental Results. *J. Volcanol. Geotherm. Res.* **107**, 1-18.

HULME, G. 1974 The interpretation of lava flow morphology. *Geophys. J. R. Astr. Soc.* **39**, 361-383.

HUPPERT, H. E. 1982 The propagation of two-dimensional and axisymmetric viscous gravity currents over a rigid horizontal surface. *J. Fluid Mech.* **121**, 43-58.

HUPPERT, H. E. 1986 The intrusion of fluid mechanics into geology. *J. Fluid Mech.* **173**, 557-594.

HUPPERT, H. E., SHEPHERD, J. B., SIGURDSSON, H. & SPARKS, R. S. J. 1982 On lava dome growth, with application to the 1979 lava extrusion of the Soufrière of St. Vincent. *J. Volcanol. Geotherm. Res.* **14**, 199-222.

HUPPERT, H. E. & SPARKS, R. S. J. 1985 Komatiites I: Eruption and flow. *J. Petr.* **26**, 694-725.

IVERSON, R. M. 1990 Lava domes modelled as brittle shells that enclose pressurised magma, with application to Mount St. Helens. In *Lava flows and domes: emplacement mechanisms and hazard implications* (ed. J.H. Fink), pp. 47-69. IAVCEI Proc. In Volcanology, vol. 2, Springer-Verlag, Berlin.

JAGGAR, T. A. 1930 Distinction between pahoehoe and aa or block lava. *Volcano Lett.* **281**, 1-4.

JAUPART, C. 1991 Effects of compressibility on the flow of lava. *Bull. Volc.* **54**, 1-9.

JOHNSTON, H. H. 1910 Obituary: Lieut. Boyd Alexander. *Geographical Journal* **36** (1; Jul. 1910), 108-110.

KERR, R. C. & LISTER, J. R. 1991 The effects of shape on crystal settling and on the rheology of magmas. *J. Geol.* **99**, 457-467.

KILBURN, C. R. J. 1990 Surfaces of lava flow-fields on Mount Etna, Sicily: Morphology, rheology, crystallization and scaling phenomena. In *Lava flows and domes: emplacement mechanisms and hazard implications* (ed. J.H. Fink), pp. 129-156. IAVCEI Proc. In Volcanology, vol. 2, Springer-Verlag, Berlin.

KILBURN, C. R. J. & LOPES, R. M. 1991 General patterns of flow field growth: Aa and blocky lavas. *J. Geophys. Res.* **97**, 19739-19748.

KILBURN, C. R. J., PINKERTON, H. & WILSON, L. 1995 Forecasting the behaviour of lava flows. In *Monitoring active volcanoes: strategies, procedures and techniques* (eds. B. Mcguire, C. R. J. Kilburn, J. Murray), pp. 346-368. University College London Press, London.

KING, J. R., RILEY, D. S. & SANSOM, A. 2000 Gravity currents with temperature-dependent viscosity. *Comp. Assisted Mech. Eng. Sci.* **7**, 251-277.

LEJEUNE, A-M. & RICHET, P. 1995 Rheology of crystal-bearing silicate melts: an experimental study at high viscosities. *J. Geophys. Res.* **100**, 4215-4229.

LEJEUNE, A-M., WOODS, A. W., SPARKS, R. S. J., HILL, B. E.& CONNOR, C. B. In press. The decompression of volatile-poor basaltic magma from a dike into a horizontal subsurface tunnel. *Bull. Volc.*

LLEWELLIN, E. W. 2002 *The rheology of bubble-bearing magmas: theory and experiments.* PhD Thesis. University of Bristol.

LLEWELLIN, E. W., MADER, H. M. & WILSON, S. D. R. 2002 The rheology of a bubbly liquid. *Proc. R. Soc.* A **458**, 987-1016.

LINNEMAN, S. R. & BORGIA, A. 1993 Morphology and dynamics of emplacement of block lava flows at Arenal Volcano, Costa Rica. In *Monitoring lava flows* (eds. C. R. J. Kilburn, G. Luongo), pp. 25-72. University College London Press, London.

LIPMAN, P. W. & BANKS, N. G. 1987 Aa flow dynamics, Mauna Loa 1984. *US Geol. Surv. Prof. Pap.* **1350**, 1527-1567.

LISTER, J. R. 1992 Viscous flows down an inclined plane from point and line sources. *J. Fluid Mech.* **242**, 631-653.

LISTER, J. R. & KERR, R. C. 1993. Influence of cooling on lava-flow dynamics: comment. *Geology* **22**, 93-94.

LOCKWOOD, J. P. & LIPMAN, P. W. 1980 Recovery of datable charcoal beneath young lavas: lessons from Hawaii. *Bull. Volc.* **43**, 609-615.

MACDONALD, G. A. 1945 Structure of aa lava flows. *Geol. Soc. Am. Bull.* **56**, 1179-1180.

MACDONALD, G. A. 1953 Pahoehoe, aa and block lava. *Am. J. Sci.* **251**, 169-191.

MANGA, M. & STONE, H. A. 1994 Interactions between bubbles in magmas and lavas: effects of bubble deformation. *J. Volcanol. Geotherm. Res.* **63**, 267-279.

MANGA, M. & STONE, H. A. 1995 Collective hydrodynamics of deformable drops and bubbles in dilute suspensions at low Reynolds numbers. *J. Fluid Mech.* **300**, 231-263.

MANGAN, M. T., HELIKER, C. C., MATTOX, T. N., KAUAHIKAUA, J. P. & HELZ, R. T. 1995 Episode 49 of the Pu'u 'O'o Kupaianaha eruption of Kilauea Volcano: breakdown of steady-state eruptive era. *Bull. Volc.* **57**, 127-135.

MANN, O. 1909. Aus dem Schutzgebiete Kamerun: Bericht, betreffend die Ergebnisse einer Unterschung des Vulkanausbruches im Kamerungebirge im April—May 1909. In *Mitteilungen aus den Deutschen Schutzgebieten*, XXII. Band. IV. (ed. Freiherr v. Danckelman), pp. 277-284.

MARSH, B. D. 1981 On the crystallinity, probability of occurrence, and rheology of lava and magma. *Contrib. Mineral. Petrol.* **78**, 85-98.

MARZOLI, A., PICCIRILLO, E. M., RENNE, P. R., BELLIENI, G., IACUMIN, M., NYOBE, J. B. & TONGWA, A. T. 2000 The Cameroon line revisited: petrogenesis of continental basaltic magmas from lithospheric and asthenospheric mantle sources. *J. Petrol.* **41**, 87-109.

MCBIRNEY, A. R. AND MURASE, T. 1984 Rheological properties of magmas. *Annu. Rev. Earth Sci.* **12**, 337-357.

MERLE, O. 1998 Internal strain within lava flows from analogue modelling. *J. Volcanol. Geotherm. Res.* **81**, 189-206.

MEYER, H. 1909 *Das Deutsche Kolonialreich.* Leipzig.

MOORE, H. J. 1987 Preliminary estimates of the rheological properties of 1984 Mauna Loa lava. *US Geol. Surv. Prof. Pap.* **1350**, 1569-1588.

MURASE, T. & MCBIRNEY, A. 1973 Properties of some common igneous rocks and their melts at high temperatures. *Geol. Soc. Am. Bull.* **84**, 3563-3592.

NARANJO, J. A., SPARKS, R. S. J., STASIUK, M. V., MORENO, H. & ABLAY, G. J. 1992 Morphological, structural and textural variations in the 1988-1990 andesite lava of Lonquimay Volcano, Chile (38° S). *Geol. Mag.* **129**, 657-678.

NERI, A. 1998 A local heat transfer analysis of lava cooling in the atmosphere: application to thermal diffusion-dominated lava flows. *J. Volcanol. Geotherm. Res.* **81**, 215-243.

NGOUNOUNU, I., DERUELLE, B. & DEMAIFFE, D. 2000 Petrology of bimodal Cenozoic volcanism of the Kapiski plateau (northernmost Cameroon, Central Africa). *J. Volcanol. Geotherm. Res.* **102**, 21-44.

NONO, A., DERUELLE, B., DEMAIFFE, D. & KAMBOU, R. 1994 Tchabal Nganha volcano in Adamawa (Cameroon): petrology of a continental alkaline lava series. *J. Volcanol. Geotherm. Res.* **60**, 147-178.

NYE, J. P. 1952 The mechanics of glacier flow. *J. Glaciol.* **2**, 82-93.

OSMOND, D. I. & GRIFFITHS, R. W. 1998 Silicic lava domes on slopes. In *Proc. 13th Australasian Fluid Mech. Conf.* (ed. M. C. Thomson, K. Hourigan), pp. 827-830. Monash University, Melbourne.

OSMOND, D. I. & GRIFFITHS, R. W. 2001 The static shape of yield-strength fluids slowly emplaced on slopes. *J. Geophys. Res.* **106**, 16241-16250.

PAKENHAM, T. 1992 *The Scramble for Africa.* London.

PETERSON, D. W. & TILLING, R. I. 1980 Transition of basaltic lava from pahoehoe to aa, Kilauea Volcano, Hawaii: field observations and key factors. *J. Volcanol. Geotherm. Res.* **7**, 271-293.

PINKERTON, H. AND NORTON, G. 1995 Rheological properties of basaltic lavas at sub-liquidus temperatures: laboratory and field measurements on lavas from Mount Etna. *J. Volcanol. Geotherm. Res.* **68**, 307-323.

PINKERTON, H. & SPARKS, R. S. J. 1976 The 1975 sub-terminal lavas, Mount Etna: a case history of the formation of a compound lava field. *J. Volcanol. Geotherm. Res.* **1**, 167-182.

PINKERTON, H. & SPARKS, R. S. J. 1978 Field measurements of the rheology of flowing lava. *Nature* **276**, 383-385.

PINKERTON, H. & STEVENSON, R. J. 1992 Methods of determining the rheological properties of magmas at sub-liquidus temperatures. *J. Volcanol. Geotherm. Res.* **53**, 47-66.

POLACCI, M. & PAPALE, P. 1997 The evolution of lava flows from ephemeral vents at Mount Etna: insights from vesicle distribution and morphological studies. *J. Volcanol. Geotherm. Res.* **76**, 1-17.

POUDJOM DJOMANI, Y. H., NNANGE, J. M., DIAMENT, M., EBINGER, C. J. & FAIRHEAD, J. D. 1997 Effective elastic thickness and crustal thickness variations in west-central Africa inferred from gravity data. *J. Geophys. Res.* **100**, 22047-22070.

RAMBERG, H. 1961 Contact strain and folding instability of a multilayered body under compression. *Geol. Rundsch.* **51**, 405-439.

RAMBERG, H. 1963 Evolution of drag folds. *Geol. Mag.* **100**, 97-106.

RAMBERG, H. 1964 Note on model studies of folding of moraines in Piedmont glaciers. *J. Glaciol.* **5**, 207-218.

ROBSON, G. R. 1967 Thicknesses of Etnean lavas. *Nature* **216**, 251-252.

ROEDDER, E. 1974 Activity of iron and olivine solubility in basaltic liquids. *E. P. S. L.* **23**, 397-410.

ROSCOE, R. 1952 The viscosity of suspensions of rigid spheres. *Br. J. Appl. Phys.* **3**, 267-269.

ROSCOE, R. 1953 Suspensions. In *Flow Properties of Disperse Systems* (eds. J. J. Hermans), pp. 1-38. North Holland, New York.

ROWLAND, S. K. & WALKER, G. P. L. *1990* Pahoehoe and aa in Hawaii: volumetric flow rate controls the lava structure. *Bull. Volc.* **52**, 631-641.

RUDIN, H. 1968 *Germans in the Cameroons: a Case Study in Modern Imperialism.* New York.

RUXTON, F. H., MATEER, CAPT., WALDAU, G., READING, A. A. AND EVANS, F. 1922 Volcanic Eruptions on the Cameroons Mountain. *Geographical Journal* **60** (5), 135-141.

SAKIMOTO, S. E. H. & ZUBER, M. T. 1995 The spreading of variable viscosity axisymmetric radial gravity currents: applications to the emplacement of Venusian 'pancake' domes. *J. Fluid Mech.* **301**, 65-77.

SAKIMOTO, S. E. H. & DEANE, A. E. 1997 Eruption constraints for channelized lava flows: A general Bingham channel flow solution from CFD simulations. *Eos Trans. AGU* **78** (17), Spring Meet. Suppl. S332.

SAKIMOTO, S. E. H. & GREGG, T. K. P. 2001 Channeled flow: Analytic solutions, laboratory experiments, and applications to lava flows. *J. Geophys. Res.* **106**, 8629-8644.

SANSOM, A. 2000 *Gravity currents with a temperature dependent viscosity.* PhD Thesis. University of Nottingham.

SHAW, H. R. 1969 Rheology of basalt in the melting range. *J. Petrol.* **10**, 510-535.

SHAW, H. R. 1972 Viscosities of magmatic silicate liquids: An empirical model of prediction. *Am. J. Sci.* **272**, 438-475.

SHAW, H. R., WRIGHT, T. L., PECK, D. L. & OKAMURA, R. 1969 The viscosity of basaltic magma: an analysis of field measurements in Makaopuhi lava lake, Hawaii. *Am. J. Sci.* **266**, 255-264.

SIMKIN, T. & SIEBERT, L. 1994 *Volcanoes of the World.* Tuscon, AZ.

SMITH, P. 1973 A similarity solution for slow viscous flow down an inclined plane. *J. Fluid Mech.* **58**, 275-288.

SMITH, J. V. 1997 Shear thickening dilatancy in crystal-rich flows. *J. Volcanol. Geotherm. Res.* **79**, 1-8.

SPARKS, R. S. J., PINKERTON, H. & HULME, G. 1976 Classification and formation lava levées on Mount Etna, Sicily. *Geology* **4**, 269-271.

SPARKS, R. S. J. & PINKERTON, H. 1978 Effect of degassing on rheology of basaltic lava. *Nature* **276**, 385-386.

SPARKS, R. S. J., MURPHY, M. D., LEJEUNE, A-M., WATTS, R. B., BARCLAY, J. & YOUNG, S. R. 2000 Control on the emplacement of the andesite lava dome of the Soufriere Hills Volcano, Montserrat by degassing-induced crystallization. *Terra Nova* **12**, 14-20.

STASIUK, M. V. 1993 *Investigations of the dynamics of lava eruptions.* PhD Thesis. University of Bristol.

STASIUK, M. V., JAUPART, C. & SPARKS, R. S. J. 1993 Influence of cooling on lava-flow dynamics. *Geology* **21**, 335-338.

SUH, C. E., AYONGHE, S. N. & NJUMBE, E. S. 2001 Neotectonic earth movements related to the 1999 eruption of Cameroon Mountain, West Africa. *Episodes* **24**, 9-13.

SUH, C. E., SPARKS, R. S. J., FITTON, J. G., AYONGHE, S. N., ANNEN, C., NANA, R. & LUCKMAN, A. 2003 The 1999 and 2000 eruptions of Mount Cameroon: eruption behaviour and petrohemistry of lava. *Bull. Volc.* **65**, 267-281.

TALLARICO, A. & DRAGONI, M. 1999 Viscous Newtonian laminar flow in a rectangular channel: application to Etna lava flows. *Bull. Volc.* **61**, 40-47.

TALLARICO, A. & DRAGONI, M. 2000 A three-dimensional Bingham model for channeled lava flows. *J. Geophys. Res.* **105**, 25,969-25,980.

THOMPSON, R. N. 1974 Some high-pressure pyroxenes. *Mineral Mag.* **39**, 768-787.

TOTEU, S. F. 1990 Geochemical characterisation of the main petrographical and structural units of northern Cameroon: implications for Pan-African evolution. *J. Afr. Earth Sci.* **10**, 615-624.

TOTEU, S. F., VAN SCHMUS, W. R., PENAYE, J. & NYOBE, J. B. 1994 U-Pb and Sm-Nd evidence for Eburnian and Pan-African high grade metamorphism in cratonic rocks of southern Cameroon. *Precambrian Res.* **67**, 321-347.

TREAGUS, S. H. 1973 Buckling instability of a viscous single layer system oblique to the principal compression. *Tectonophysics* **19**, 271-289.

WALKER, G. P. L. 1967 Thickness and viscosity of Etnean lavas. *Nature* **213**, 484-485.

WEBB, S. L. & DINGWELL, D. B. 1990 Non-Newtonian rheology of igneous melts at high stresses and strain rates: experimental results for rhyolite, andesite, basalt, and nephelinite. *J. Geophys. Res.* **95**, 15,695-15,701.

WHITE, D. B. 1988 The planforms and onset of thermal convection with a temperature-dependent viscosity. *J. Fluid Mech.* **191**, 247-286.

WHITE, F. M. 1991 *Viscous Fluid Flow*. McGraw-Hill, New York.

WHITEHEAD, J. A. & HELFRICH, K. R. 1991 Instability of a Flow with Temperature-Dependent Viscosity: A Model of Magma Dynamics. *J. Geophys. Res.* **96**, 4145-4155.

Site 1 Flow Sections

Section 99XII [15/11/02]

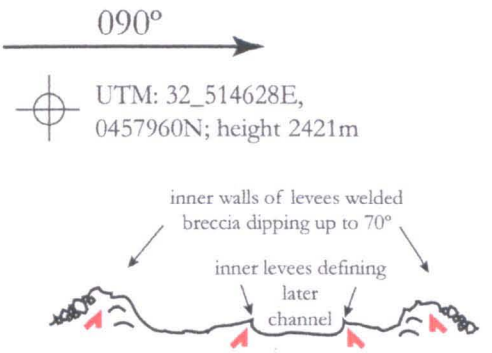

thermally immature aa clinker, with well-formed levees, pahoehoe slabs and welded breccia clasts

Section 99XI [15/11/02]

SCALE: 1cm=5m

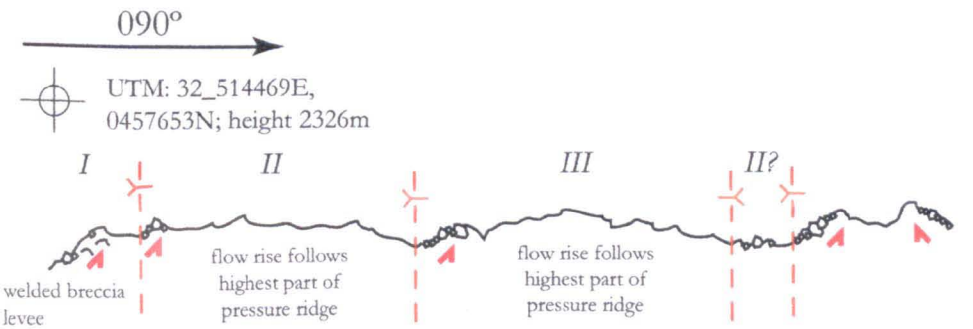

Section 99X [15/11/02]

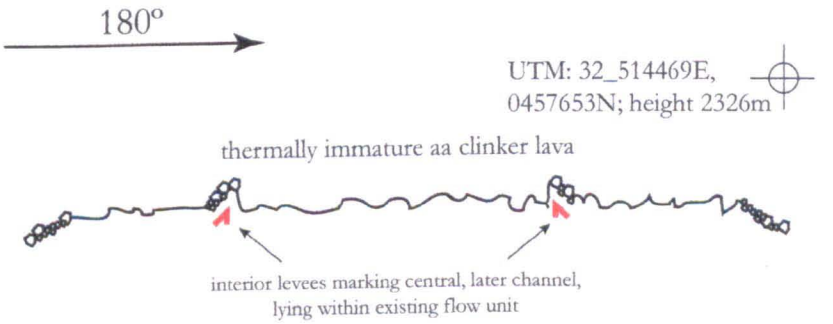

Site 1 Flow Sections (continued)

Section 99IX [Emmanuel Suh & Steve Njome]

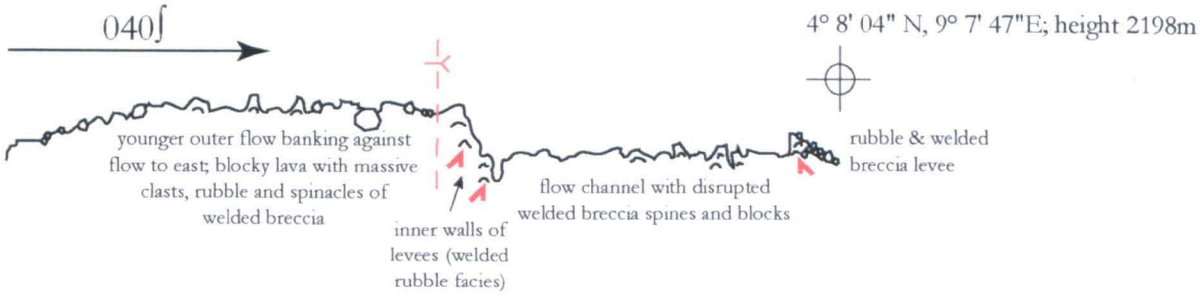

Section 99VIII [E.S. & S.N.]

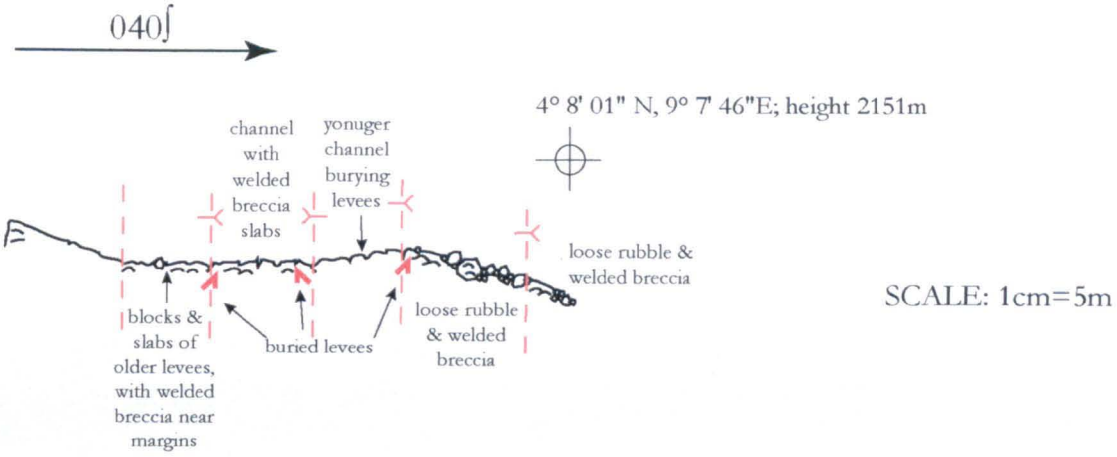

SCALE: 1cm=5m

Section 99VII [E.S. & S.N.]

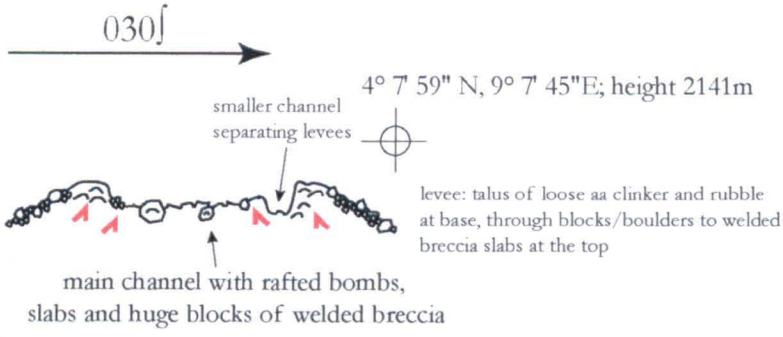

Section 99VI [E.S. & S.N.]

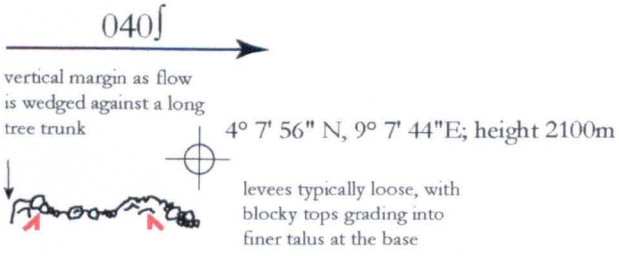

main flow channel consists of marginal loose blocks and rubble, with welded breccia clasts towards the centre

Section 99V [E.S. & S.N.]

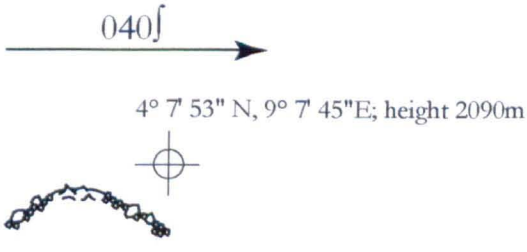

no distinct levees; lava is dominantly blocky and rubbly aa

CONE III FLOWS

SCALE: 1cm=5m

Section 99XVIII [14/11/02]

090°

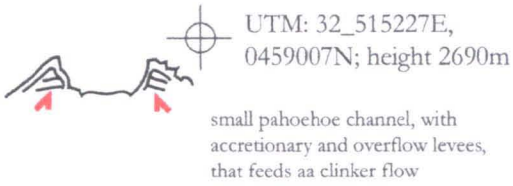

Section 99XVII [14/11/02]

145°

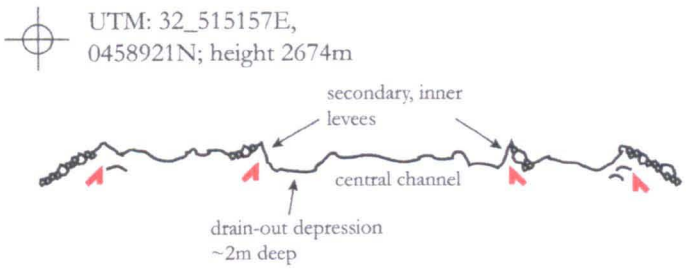

Section 99XVI [14/11/02]

100°

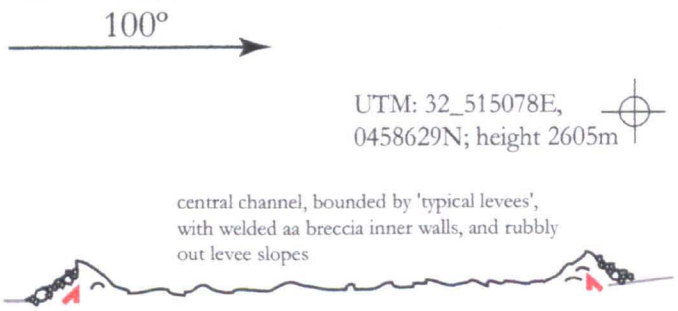

Section 99XV [15/11/02]

090°

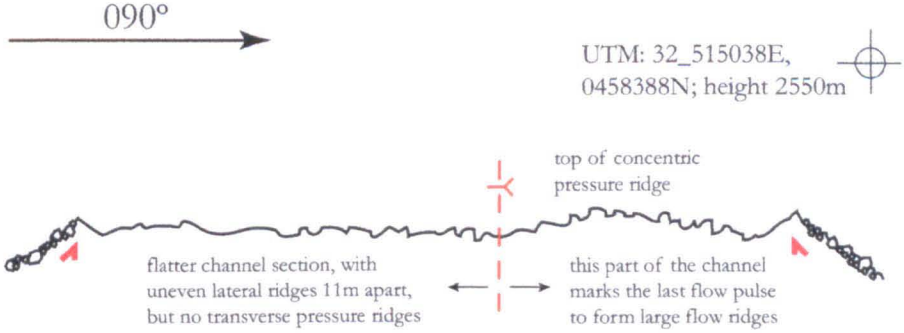

CONE V FLOWS

Section 99XIV [15/11/02]

SCALE: 1cm=5m

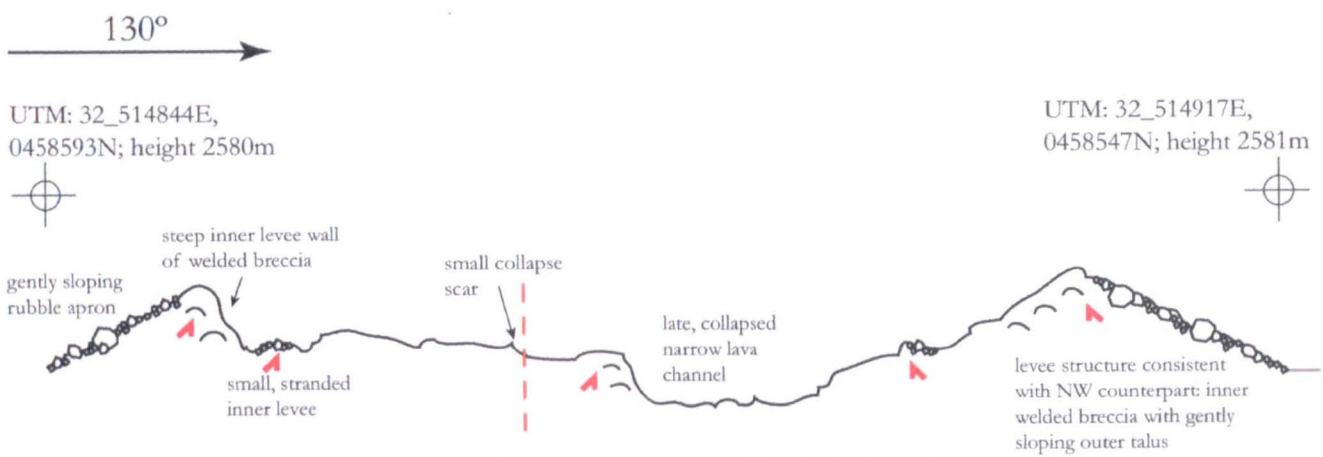

viscous, degassed, late-stage transitional blocky-aa lava

Section 99XIII [15/11/02]

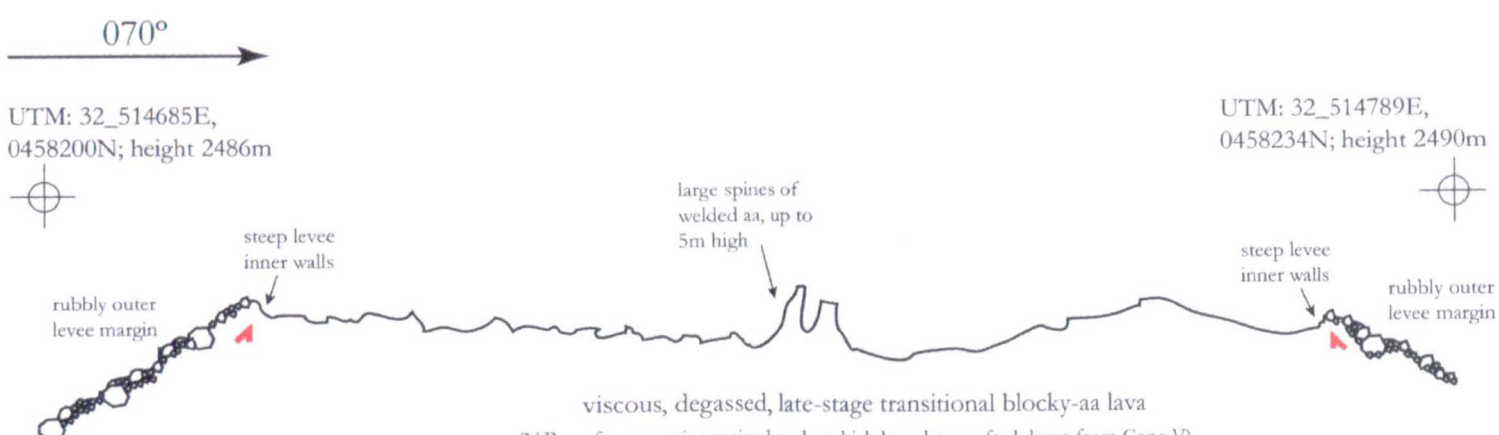

viscous, degassed, late-stage transitional blocky-aa lava

(N.B. surface contains mainy bombs which have been rafted down from Cone V)

Site 2 Flow Sections: Bakingili flow-front

10m

Legend

- Blocky lava surface
- Welded breccia
- Clinkery lava surface
- Talus
- Levee (inner wall / outer wall)
- Lateral position of GPS measurement on section
- Lava flow unit boundary; direction of younging if observed

Section 99IV [24/11/02]

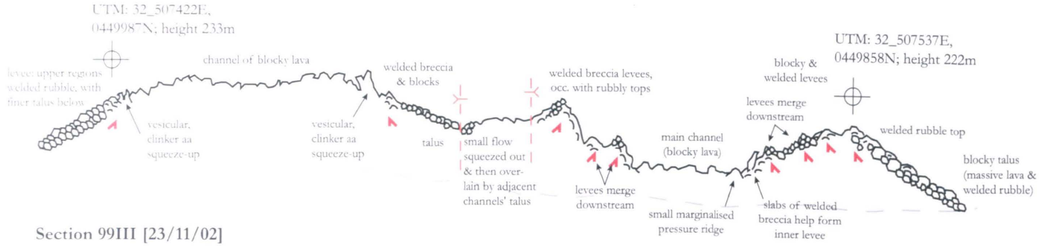

Section 99III [23/11/02]

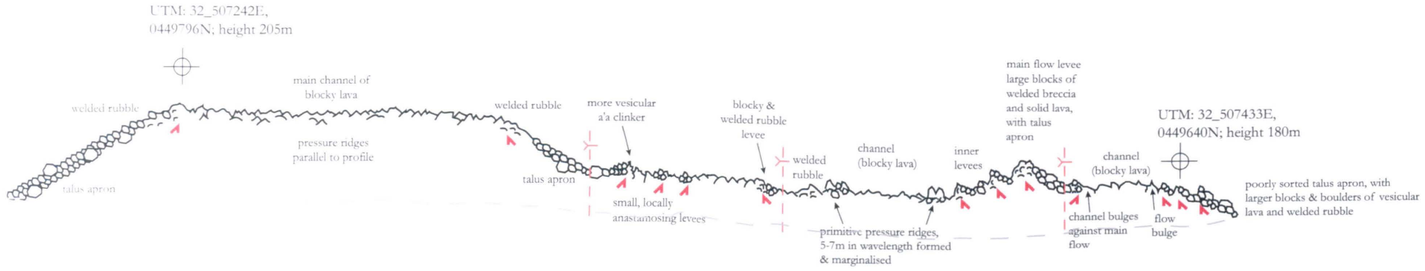

Section 99II [26/11/02]

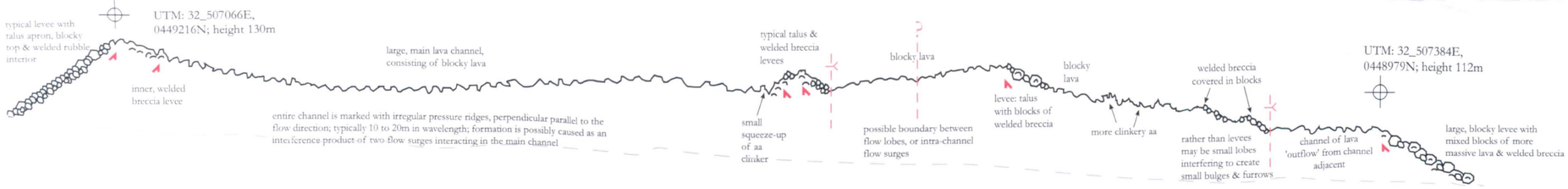

Section 99I [7&8/11/02]